SCHOLARLY PUBLICATIONS

A CURRENT AWARENESS BULLETIN
OF RESEARCH OUTPUT

@DTU

(26th Edition)

FEBRUARY 2015

BY: CENTRAL LIBRARY

DELHI TECHNOLOGICAL UNIVERSITY
(FORMERLY *DELHI COLLEGE OF ENGINEERING)*
GOVT. OF N.C.T. OF DELHI
SHAHBAD DAULATPUR, MAIN BAWANA ROAD
DELHI 110042

PREFACE

This is the **Twenty sixth** Issue of Current Awareness Bulletin started by Delhi Technological University, Central Library. The aim of the bulletin is to compile, preserve and disseminate information published by the faculty, students and alumni for mutual benefits. The bulletin also aims to propagate the intellectual contribution of Delhi Technological University (DTU) as a whole to the academia.

The bulletin contains information resources available in the internet in the form of articles, reports, presentations published in international journals, websites, etc. by the faculty and students of DTU. The publications of faculty and student which are not covered in this bulletin may be because of the reason that the full text either was not accessible or could not be searched by the search engine used by the library for this purpose.

The learned faculty and students are requested to provide their uncovered publications to the library either through email or in CD, etc to make the bulletin more comprehensive.

This issue contains the information published during **February 2015**. The arrangement of the contents is alphabetical. The full text of the article which is either subscribed by the university or available in the web is provided in this bulletin.

Central Library

CONTENTS

1. A Comparative Study of Biodiesel Production of Waste Cooking Oil Through Mechanical Stirring and Ultrasound Cavitations, ***3. AMIT PAL***, Mechanical Engineering, DTU

2. A New Metric for Predicting Software Change using Gene Expression Programming, ***3. Ruchika Malhotra*** and ***3. Megha Khanna***, Software Engineering, DTU

3. A New Time-Domain Solution to Transmission Through a Multilayer Low-Loss Dielectric Wall Structure for UWB Signals, Bajrang Bansal and Sanjay Soni, ECE, DTU

4. Case Study of the Nisarguna Based Biogas Plant Installed at Delhi Technological University, ***3.Mohit Gupta, 3.Aadish Jain*** and ***3.P.K Jain***, Mechanical Engineering, DTU

5. International conference on Science, Technology and Management (AN ANALYSIS OF REACTION TO GREEN PRODUCT INITIATIVES), (page 16 onwards) ***6. Gaurav Dawar*** and ***3. Dr. Seema Singh***, Department of Humanities, DTU

6. Consolidation of clayey gouge amid permeating rock masses, ***3. Ashutosh Trivedi***, Tanmay Banik, Tanay Sukumar, ***3. Naresh Kumar***, Akshay Jain, Amit Kumar, Civil Engineering, DTU

7. Crystal structure and mechanical properties of spark plasma sintered Cu2Se: An efficient photovoltaic and thermoelectric material, Kriti Tyagi, Bhasker Gahtori, ***Sivaiah Bathula, M. Jayasimhadri***, Sakshi Sharma, Niraj Kumar Singh, D. Haranath, A. K. Srivastava, Ajay Dhara, Applied Physics, DTU

8. Design and control of LCL filter interfaced grid connected solar photovoltaic (SPV) system using power balance theory, Ravi Nath Tripathi, ***3. Alka Singh***, Tsuyoshi Hanamoto, Electrical Engineering Department, DTU

9. Effect of Nickel–Cobaltite Nanoparticles on Production and Thermostability of Cellulases from Newly Isolated Thermotolerant Aspergillus fumigatus NS (Class:

Eurotiomycetes), ***3. Neha Srivastava***, Biotechnology, DTU & Rekha Rawat & Reetika Sharma & Harinder Singh Oberoi & Manish Srivastava & ***3. Jay Singh***, Applied Chemistry, DTU

10. Electrochemical-aided abrasive flow machining (ECA2FM) process: a hybrid machining process, B. S. Brar & ***3. R. S. Walia***, DTU & V. P. Singh

11. Enhanced thermoelectric performance of spark plasma sintered copper deficient nanostructured copper selenide, Kriti Tyagi, Bhasker Gahtori, ***3. Sivaiah Bathula, 3. M. Jayasimhadri***, Niraj Kumar Singh, Sakshi Sharma, D. Haranath, A.K. Srivastava, Ajay Dhar, Applied Physics, DTU

12. Enhancing Performance of Uricase Using Multiwalled Carbon Nanotube Doped Polyaniline, Kavita Arora & Meenakshi Choudhary and ***3. Bansi D. Malhotra***, Department of Biotechnology, DTU

13. Exergy analysis of a syngas fuelled cogeneration cycle for combined production of power and refrigeration, Mohd Parvez and ***3. Abdul Khaliq***, Mechanical Engineering, DTU

14. Experimental Analysis of SPF Based Secure Web Application, Nitish Pathak, ***7.1 Dr. Girish Sharma*** and Dr. B. M. Singh, Computer Technology and Application (2003), DTU

15. Giant enhancement in thermoelectric performance of copper selenide by incorporation of different nanoscale dimensional defect features, Bhasker Gahtori, ***3. Sivaiah Bathula***, Kriti Tyagi, ***3. M. Jayasimhadri***, A.K. Srivastava, Sukhvir Singh, R. C. Budhani, Ajay Dhar, Applied Physics, DTU

16. Graphene Oxide-Based Biosensor for Food Toxin Detection, Saurabh Srivastava & Md Azahar Ali & Sima Umrao and Upendra Kumar Parashar & Anchal Srivastava & Gajjala Sumana &, ***3. B. D. Malhotra*** & Shyam Sudhir Pandey & Shuji Hayase, Biotechnology, DTU

17. Hardware Design of Dynamic Time Warping Algorithm based on FPGA in Verilog, ***3. Kriti Suneja*** and ***3. Dr. Malti Bansal***, ECE, DTU

18. INVESTIGATION ON PROCESS PARAMETER OPTIMIZATION FOR SURFACE ROUGHNESS AND MICRO HARDNESS OF COLD SPRAYED COATINGS, Tarun Goyala, ***3. R.S. Walia***, T.S. Sidhu, DTU

19. MACRO ECONOMIC DETERMINANTS OF FOREIGN DIRECT INVESTMENT IN BRIC NATIONS ***6. Ms. Priya Gupta***; ***3. Dr. Archana Singh,*** Delhi School of Management, DTU

20. Magnetorheological Smart Automotive Engine Mount, ***3. Chiranjit Sarkar***, Harish Hirani and Abhijit Sasane, Mechanical Engineering, DTU

21. Methods for Improving Thermodynamic Performance of Vapour Compression Refrigeration Systems Using R134a Ecofriendly Refrigerant in Primary Circuit and Three Nano Particles Mixed with R718 used in Secondary Evaporator Circuit for Reducing Global Warming and Ozone Depletion, ***3. R. S. Mishra***, Mechanical Engineering, DTU

22. mit-o-matic: a comprehensive computational pipeline for clinical evaluation of mitochondrial variations from next-generation sequencing datasets, Shamsudheen Karuthedath Vellarikkal, Heena Dhiman, Kandarp Joshi, ***3. Yasha Hasija***, Sridhar Sivasubbu and Vinod Scaria, Biotechnology, DTU

23. Nanomaterial-Based Biosensors for Food Toxin Detection, ***3. Bansi D. Malhotra*** & Saurabh Srivastava and Md. Azahar Ali & Chandan Singh, Biotechnology, DTU

24. Neural Network Based Black Box Testing, ***3. Harsh Bhasin***, Computer Science, DTU and Esha Khanna

25. Non-Additive Entropy Measure and Record Values, Vikas Kumar, and ***3. H. C. Taneja,*** Applied Mathematics, DTU

26. Performance characteristics of a single cylinder diesel engine fuelled with1-octanol diesel blends, ***3. Rashi Koul,*** Mechanical Engineering, DTU

27. Piezoelectric and pyroelectric properties of zirconium substituted barium titanate ferroelectric ceramics, ***3. P A Jha*** and ***3. A K Jha***, Applied Physics, DTU

28. Prediction & Assessment of Change Prone Classes Using Statistical & Machine Learning Techniques, ***3. Ruchika Malhotra*** and Ravi Jangra, Software Engineering, DTU

29. Selecting competitive supply chain using fuzzy AHP and extent analysis, ***3. Rajesh Kumar Singh*** & Milind Kumar Sharma, Mechanical and Production Engineering, DTU

30. Synthesis and Characterization of Nano-Copper-Powder Based Magnetorheological Fluids for Brake, ***3. Chiranjit Sarkar***, Harish Hirani, Mechanical Engineering, DTU

31. Theoretical modeling of temperature dependent catalyst-assisted growth of conical carbon nanotube tip by plasma enhanced chemical vapor deposition process, Aarti Tewari and Suresh C. Sharma, Applied Physics, DTU

32. Transient Thermo Elastic Analysis of Disk Brake, ***3. Chiranjit Sarkar*** and Harish Hirani, Mechanical Engineering, DTU

1. Vice Chancellor	***1.1. Ex Vice Chancellor***
2. Pro Vice Chancellor	***2.1. Ex Pro Vice Chancellor***
3. Faculty	***3.1. Ex Faculty***
4. Teaching-cum-Research Fellow	
5. Alumni	
6. Research Scholar	***6.1. Ex Research Scholar***
7. PG Scholar	***7.1. Ex PG Scholar***
8. Undergraduate Student	***8.1. Ex Undergraduate Student***

BRCORP
TECHNOLOGY | INNOVATION | INDUSTRY

International Journal of
Applied Sciences, Engineering and Technology
Vol. 03, No. 01, Jan-Dec 2014

A Comparative Study of Biodiesel Production of Waste Cooking Oil Through Mechanical Stirring and Ultrasound Cavitations

AMIT PAL
Department of Mechanical Engineering, Delhi Technological University, New Delhi, India
Email: amitpal@dce.ac.in

Abstract: This paper presents the comparative details of biodiesel production process using low frequency ultrasonic cavitation (28-33 kHz) and conventional mechanical stirrer method. In this work Waste Cooking Oil (WCO) is used as a biodiesel feedstock. The experiments have been performed for molar ratio (alcohol/oil) 6:1 and 4.5:1, with three different catalyst percentages (0.5%, 0.75% and 1%) of Potassium Hydroxide. The important chemical and physical properties of WCO biodiesel were determined and compared with diesel. It is observed that the density and viscosity values of the biodiesels produced are within the permissible limits but still higher than petroleum diesel. It can be concluded from present study that the Biodiesel production through ultrasound energy is much better than mechanical stirrer process.

Keywords: *Biodiesel, Ultrasonic Cavitation, Waste Cooking Oil, Molar Ratio, Mechanical Stirrer*

1. Introduction:

Majority of the world's energy needs are supplied through petrochemical sources, coal and natural gas, with the exception of hydroelectricity and nuclear energy, all these sources are finite and will be consumed shortly [1]. Economic growth always comes with commensurate increase in the transportation requirement. Diesel fuel plays an important role in the industrial economy of developing countries and commonly used in transportation system, industrial and agricultural goods, etc. India's demand for diesel fuel is six times higher than gasoline [2]. Petroleum fuels are currently the main global source of CO_2 emissions and their combustion is creating stronger threat to clean environment. The recent interest in alternative sources for petroleum-based fuels is an outcome of these.

The requirements of any viable alternative fuel are that it should be easily available in huge quantity, environment friendly and techno-economically competitive. Bio-diesel is an alternative to petroleum-based fuels derived from vegetable oils or animal fats [3]. It is named biodiesel because it is derived from biological products and it may substitute the petro diesel in performance. Vegetable oils are extracted from different kind of plants and the glycerides present in the oils can be separated and used as by-product [4]. Bio-diesel production is a very advanced and technological area for researchers due to its environmental advantages the increase in the price of petroleum fuels [5]. The most common way of producing bio-diesel is the transesterification of vegetable oils and animal fats. Vegetable oils have good heating power and provide exhaust gas with almost no sulphur and aromatic polycyclic compounds. It possesses high biodegradability and lubricating property which makes it even better fuel. As vegetable oils are produced from plants, they are completely recyclable as it produces carbon dioxide (CO_2), which is consumed by the plants in photosynthesis [6].

Vegetable oils can be directly used as fuel for diesel engines, but their viscosities are much higher (10 to 20 times) than usual diesel fuel and require modifications of the engines [7]. The injection and atomization characteristics of the vegetable oils are significantly different than those of petroleum-derived diesel fuels, mainly due to their high viscosities [8]. Many of the vegetable oils are edible in nature; therefore their continuous use may cause shortage for food supply and prove far expensive to be used as fuel at present. So far a very few of non-edible vegetable oils have been tried on diesel engine leaving a lot of scope in this area. Different countries are looking for different types of vegetable oils as substitutes for diesel fuels that further depending upon the climate and soil conditions. [9].

India is a developing country and its energy demand is increasing day by day. Vegetable oils are good alternative source in Indian context because India is agriculture based country. Vegetable oil consists edible and non-edible oil, edible oil demand being higher than its domestic production, there is no possibility of diverting these oils for production of bio-diesel. Non-edible oil plants can be planted on under-stocked forest lands, farmer's field boundaries to provide protective hedge, fallow lands, public lands along railway tracks, highways, canals and community and government land in villages. Therefore biodiesel production through non-edible oil is major concerned field for India. The by-products of Bio-diesel from non edible oil are oil cake and glycerol which have good commercial value.

2. Biodiesel production history:

Basic reaction carried out in the biodiesel production is transesterification. In this reaction different catalysts can be used to enhance the transesterification reaction which is namely alkali catalyst, acid catalyst and lipase catalyst [10]. Different technique has been developed for biodiesel production like mechanical stirring, hydrodynamic cavitation, ultrasonic

IJASET 030102 Copyright © 2014 BASHA RESEARCH CENTRE. All rights reserved.

cavitation [11] and supercritical methanol [12]. Ji et al. [11] prepared biodiesel through Power Ultrasonic (PU) (19.7 kHz), Hydrodynamic Cavitation (HC) and Mechanical Stirring (MS). The yield of PU and HC are found to be almost similar and are better than MS. Power ultrasonic gave the shortest reaction time and the highest yield. It is found that the PU and HC processes require approximately a half of the energy that was consumed by the MS method. Stavarache et al. [6], studied low frequency ultrasound (40 kHz) with the aim of gaining more knowledge on intimate reaction mechanism with the KOH (potassium hydroxides). It was concluded by Stavarache et al. [13] that using ultrasounds the reaction time is much shorter (10–40min) than for mechanical stirring and the quantity of required catalyst is 2 or 3 times lower.

Gogate et al. [14] performed the similar experiment on hydrodynamic cavitation, ultrasonic cavitation and mechanical stirring technique for biodiesel production under optimum operating conditions. Production of fatty acid ethyl ester (FAEE) from oleic acid with short-chain alcohols (ethanol, propanol, and butanol) under ultrasonic irradiation was investigated by Hanh et al. [15] and it was concluded that Ultrasonic irradiation condition is efficient, time saving and economically functional for esterification of free fatty acid with short-chain alcohols to produce biodiesel fuel. The esterification of fatty acid with ethanol under ultrasonic irradiation provides a possibility for producing cheap alternative fuels, which could reduce air pollution and protect the environment.

In the open literature, experimental studies on application of ultrasound cavitation for biodiesel production of non-edible oils are not available. Therefore, the objectives of present experimental study are to explore the possibility of production of biodiesel from non-edible oils using ultrasound cavitation in comparison to mechanical stirring method.

3. Materials:

Waste Cooking Oil has been used for biodiesel production. The waste cooking oil (WCO a mixture of different kind of used frying oils) was obtained from Paris Hilton, the five star hotels in Delhi and commercially available diesel oil was purchased from the nearby Indian Oil Corporation Limited petrol pump in Delhi.

4. Experimental work:

4.1 Test rig for ultrasonic cavitation technique:

The transesterification reactions were carried out in the horn type ultrasonic reactor (Figure 1). In horn type reactor the horn is attached with the transducer which produces ultrasonic irradiation in the mixture. Ultrasonic processor frequency is ranging from 25 kHz to 30 kHz. There is an integrated arrangement for supporting the beaker (100 ml) so that the transducer horn may be submerged at the separating boundary of two immiscible liquids. The horn of the transducer was submerged approximately half the level of the mixture of methanol and fatty acid oil. The reaction started when a mixture consisting of desired amount of KOH was dissolved in methanol liquor and then poured into the reactor.

The reaction is carried out by ultrasonic irradiation from the acoustic rod horn incorporated with the transducer. Cavities are created by the irradiation of power ultrasonic with sufficient energy in immiscible liquid (oil and alcohol are not miscible with each other) as a result micro fine bubbles are formed and these bubbles are collapsing at various place of the reactor and disturb the phase boundary between two immiscible liquid which resulted in emulsification of the mixture.

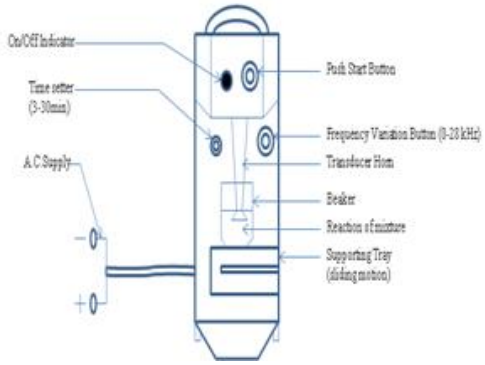

Figure 1: Schematic diagram of ultrasonic horn type reactor

4.2 Fuel properties:

Properties of the WCO biodiesel produced in comparison to diesel are shown in Table 1. Density for the WCO biodiesel is slightly higher than diesel. Kinematic viscosity of WCO biodiesel is also higher than diesel kinematic viscosity. Flash point of WCO biodiesel is much higher than the diesel. Water content (0.005 w/w %) is much lower in case of diesel oil. Sulphur content in biodiesel is negligible than diesel.

Table 1: *Comparison of the property of biodiesel and diesel as per BIS: 2796*

Property	**WCO**	**Unit**	**Limit**	**Diesel**
Appearance	clear	----	----	clear
Color	Yellow	----	----	----
Density at 15 ^{0}C	886	kg/m^3	860-900	840
Kinematic viscosity at 40 ^{0}C	4.3 x 10^{-6}	m^2/sec	3.5-5 x 10^{-6}	4.86 x 10^{-6}
Flash point	>110	^{0}C	< 100	51
Sulphur contents	>0.012	w/w %	Max 0.05	0.35-0.55
Water content	>0.04	w/w %	0.02 - 0.05	0.005

4.3 Preparation of biodiesel blends:
Biodiesel blends of WCO biodiesel with diesel oil has been prepared for engine performance testing. From the literature it is evident that dilution or blending of non edible oil with other fuels like alcohol or diesel fuel would bring the viscosity close to a specified range. Therefore WCO biodiesel blends with diesel in varying proportion is used to reduce its viscosity. Engine experiments are performed with different blends of biodiesel (pure diesel, B-10, B-20, and B-30).

4.4 Experimental setup for performance testing:
The setup consists of four cylinder, four stroke, Tata Indica diesel engine connected to eddy current type dynamometer for loading. It is attached with necessary instruments for combustion pressure and crank-angle measurements. The signals are interfaced to computer through engine indicator for p-θ diagrams. The set up has stand-alone panel box consisting of air box, fuel tank, manometer, fuel measuring unit and transmitters for air and fuel flow measurements. The setup enables study of engine performance for various engine parameters. The main aim of this experiment is to investigate the suitability and effect on performance of blending of biodiesel (produced through power ultrasound) in comparison to the petroleum diesel fuel.

4.5 Experimental data of biodiesel production:
WCO (50g) is taken in a 100 ml beaker and filtered it to remove impurities and heated up to 110 ^{0}C in order to remove water content of oil to avoid soap formation. This oil is allowed to cool up to 50 ^{0}C temperature. Methyl alcohol (CH_3OH) with a molar ratio of (1:4.5 & 1:6) and Catalyst KOH is taken as (0.5%, 0.75% and 1%) by weight of oil. Then mixer of methyl alcohol and KOH stirred until KOH dissolve in methyl alcohol. This mixture is mixed with vegetable oil. The mixture of oil, methanol and catalyst come in contact with ultrasonic processor transducer which works at the ultrasonic frequency of 28.5 kHz. During the reaction the temperature of mixture is kept between, 50 to 65^{0}C.

When reaction is completed the beaker is kept for the gravity separation. Fatty acid has higher specific weight therefore it will settle at the bottom. Separation of methyl ester and glycerol will take 1 to 1 ½ hour duration. After complete separation bio-diesel (methyl easter) is visible in the upper layer and the lower layer as glycerol. Bio-diesel is separated from beaker for purification process. To remove the catalyst, water at around 60 ^{0}C is mixed with the methyl ester and left for settling down. Water due to its higher specific gravity is separated and collected at bottom. Excess methanol present in biodiesel has been removed by distillation process. The experiments are performed with alcohol to oil molar ratio as 6:1 and 4.5:1(alcohol/Oil). The amount of oil, alcohol and catalyst taken is given in Table 2.

Table 2: Oil, alcohol and catalyst during the experimentation

Molar ratio	non-edible oil (gm)	methanol (gm)	Catalyst gm(KOH)		
			0.5 %	0.75 %	1.0 %
6:1	50	11	0.25	0.375	0.5
4.5:1	50	8.28	0.25	0.375	0.5

Time and yield produced for the different vegetable oils:
Experiments have been performed to prepare biodiesel from WCO by ultrasonic cavitation method and conventional magnetic stirring method. Main aim of this experiment is to obtain the optimum reaction time, catalyst percentage and molar ratio (alcohol/oil) for biodiesel production with maximum yield in comparison to the conventional method. If biodiesel produced on industrial scale, large amount of catalyst will be discharged in river or land causing harm to environment.

Our emphasis in the present study is to reduce the use of catalyst (KOH) and alcohol because catalyst (KOH) is pollutant for the water and land. Experimental data are collected by performing ultrasonic cavitation on the sample which is a mixture of WCO, methanol (CH_3OH) and catalyst (KOH). For every sample reaction time (20-50 minute) biodiesel production yield of methyl ester is obtained.

Experimental Data for Mechanical Stirring Method:
For comparison purpose experiment has also been performed with conventional magnetic stirrer. For every sample reaction time (30-60 minute) biodiesel production yield of methyl ester is obtained. Here minimum time 30 minute is used as in 20 minute no appreciable conversion is obtained.

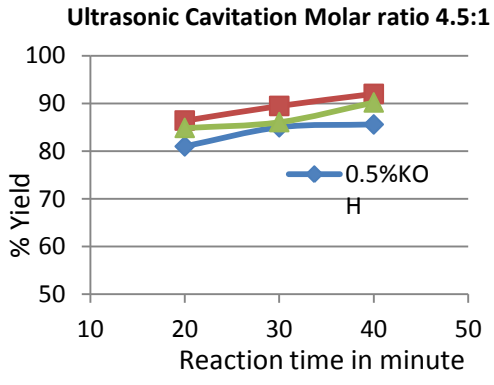

Figure 2(a): Comparison of yield for WCO biodiesel at molar ratio 6:1

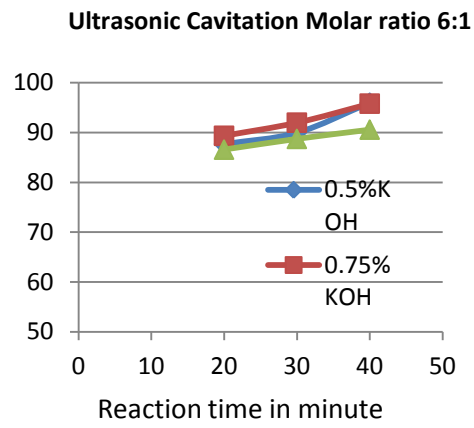

Figure 2(b): Comparison of time for WCO biodiesel at molar ratio 6: 1

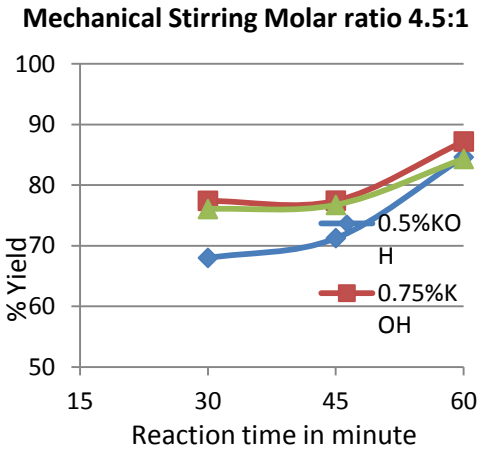

Figure 3(a): Comparison of yield for WCO biodiesel and molar ratio 4.5:1

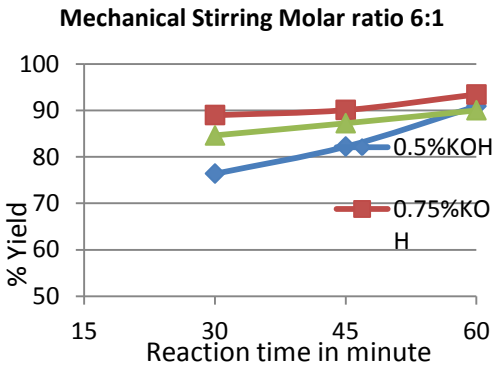

Figure 3(b): Comparison of time for WCO biodiesel and molar ratio 4.5:1

6. Discussion on experimental results:

With the help of experimental data obtained, graphs have been plotted to compare the power ultrasound and mechanical stirring methods applied for the WCO. Comparison of these two techniques for molar ratio 4.5:1 and 6:1 is carried out. It can be seen that using ultrasonic method reaction time is almost half compare to conventional method which is beneficial for industrial applications.

Slightly better production Yield is obtained for ultrasonic method for all catalyst (%) but time is much lower in case of ultrasonic cavitation method. For molar ratio 4.5:1 (alcohol to oil) Yield in case of ultrasonic method is higher for 0.5% and 0.75% catalyst of oil and it is lower for 1% compared to conventional method. Reaction time show similar pattern as above.

7. Conclusions:

Ultrasonic cavitation method is energy efficient, environmental friendly and industrially viable alternative for the biodiesel production. Following conclusions have been made from the experiments:

1. The reaction time required for Waste Cooking oil methyl ester formation is much shorter for ultrasonic cavitation method compare to conventional magnetic stirring method.
2. Relatively better yield has been obtained by ultrasonic cavitation technique compare to convention method of biodiesel production.
3. WCO biodiesel conversion is one of the best ways to safely dispose the WCO and it may prove to be a potential alternative to diesel.

References:

[1] A Srivastava, R Prasad, Triglycerides based diesel fuels. Renew Sustain Energy Rev 2000; 4: 111–33.

[2] D Hebbal, K. Vijaya kumar Reddy, K. Rajagopal, Performance characteristics of a diesel engine with deccan hemp oil. Fuel 2006; 85: 2187–2194.

[3] YD Wang, T Al-Shemmeri, P Eames, J McMullan, N Hewitt, Y Huang, An experimental investigation of the performance and gaseous exhaust emissions of a diesel engine using blends of a vegetable oil. Appl Thermal Eng 2006; 26: 1684–91.

[4] SL Dmytryshyn, AK Dalai, ST Chaudhari, HK Mishra, MJ Reaney, Synthesis and characterization of vegetable oil derived esters: evaluation for their diesel additive properties. Bioresour Technol 2004; 92: 55–64.

[5] JM Marchetti, VU Miguel, AF Errazu, Possible methods for biodiesel production. Renew Sustain Energy Rev 2005; 11: 1300–11.

[6] Carmen Stavarache, M Vinatoru, R Nishimura, Y Maeda, Fatty acids methyl esters from vegetable oil by means of ultrasonic energy. Ultrasonic Sonochemistry 2005; 12: 367–372.

[7] S Kerschbaum, G Rinke, Measurement of the temperature dependent viscosity of biodiesel fuels. Fuel 2004; 83: 287–91.

[8] KB Cigizoglu, T Ozaktas, F Karaosmanoglu, Used sunflower oil as an alternative fuel for diesel engines. Energy Sour 1997; 19: 559–66.

[9] A Murugesan, C Umarani, T R Chinnusamy, M Krishnan, R Subramanian, N Neduzchezhain, Production and analysis of bio-diesel from non-edible oils—A review Renewable and Sustainable Energy Reviews 2008; 825-834.

[10] V Miguel, G Trubiano, G Perez, DO Borio, AF Errazu, Kinetic analysis of enzymatic esterification of fatty acids and ethanol. Stud Surf Sci Catal 2001; 133: 619–24.

[11] Ji Jianbing, Wang Jianli, Li Yongchao, Yu Yunliang, Xu Zhichao, Preparation of biodiesel with the help of ultrasonic and hydrodynamic cavitation. Ultrasonics 2006; 44: 411–414

[12] A Demirbas, Biodiesel from vegetable oils via transesterification in supercritical methanol. *Energy Conv Mgmt* 2002; 43: 2349–56.

[13] Carmen Stavarache, M Vinatoru, R Nishimura, Y Maeda, Aspects of ultrasonically assisted transesterification of various Vegetable oils with methanol. Ultrasonics Sonochemistry 2007; 14: 413-417.

[14] Parag Gogate and Pandit Aniruddha, A review and assessment of hydrodynamic cavitation as a technology for the future. Ultrasonics Sonochemistry 2005; 12: 21–27.

[15] Hoang Duc Hanh, Nguyen The Dong, Kenji Okitsu, Rokuro Nishimura, Yasuaki Maeda. Biodiesel production by esterification of oleic acid with short-chain alcohols under ultrasonic irradiation condition. Renewable Energy 2009; 34: 780–783.

A New Metric for Predicting Software Change using Gene Expression Programming

Ruchika Malhotra
Department of Software Engineering
Delhi Technological University
Shahbad Daulatpur, Main Bawana Road,
Delhi- 110042, India
+919910290445
ruchikamalhotra2004@yahoo.com

Megha Khanna[*+]
[*]Acharya Narendra Dev College
University of Delhi
[+]Delhi Technological University
Delhi, India
+919911156446
meghakhanna86@gmail.com

ABSTRACT
Software metrics help in determining the quality of a software product. They can be used for continuous inspection of a software to assist software developers in improving its quality. We can also use metrics to develop quality models which predict important quality attributes like change proneness. Determination of change prone classes in an Object-Oriented software will help software developers to focus their time and resources on the weak portions of the software. In this paper, we validate the Chidamber and Kemerer metric suite for building an efficient software quality model which predict change prone classes with the help of Gene Expression Programming. The model is developed using an open source software. We further propose a new metric which can be used for identifying change prone classes in the early phases of software development life cycle. The proposed metric is validated on another open source software and the results show that it can be effectively used by the software industry to classify change prone classes. Identification of change prone classes may help in efficient refactoring and rigorous testing of these classes in the forthcoming releases of the software product.

Categories and Subject Descriptors
D.2 [**Software Engineering**]: D.2.8 Metrics, D.4.8 Performance

General Terms
Measurement, Performance, Reliability, Verification.

Keywords
Change Proneness, Empirical Validation, Gene Expression Programming, Object-Oriented Metrics, Software Quality.

1. INTRODUCTION
According to Tom DeMarco, "You can't control what you can't measure" [6]. Thus, the measurement of various Object-Oriented (OO) characteristics of a software, like coupling, cohesion, reusability or size is crucial to continuously assess and control a software product effectively. A number of OO metrics have been proposed in the literature [5, 11] which help the software practitioners in managing and improving the software process to yield good quality software products. These metrics can also be used for developing quality models which predict various software quality attributes like fault proneness and maintainability [1, 3, 14, 23-25]. One of an important software quality attribute is change proneness i.e. the probability of a class of a software to change in the forthcoming release of the software i.e. after it goes into operation [16]. Identifying change prone (CP) classes in a software is essential because of the following reasons: a) to manage and allocate adequate resources like cost, effort and time to these CP classes b) to take preventive design measures in the early phases of software development life cycle for such classes to prevent introduction of defects and c) to perform rigorous verification activities like reviews, inspections and walkthroughs in CP classes to detect changes in the initial phases of software development [12, 16]. These practices assure development of a low cost, good quality and maintainable product.

In order to develop quality models for predicting change proneness, certain researchers have applied traditional statistical techniques [15, 30], while few others have evaluated the use of the commonly used machine learning techniques like Bagging, Random Forests etc. [16]. However, there has been no study till date which examines the applicability of Gene Expression Programming (GEP) to the problem of classification of CP classes. GEP is an evolutionary algorithm which has various applications like real parameter optimization [28], dynamic multi-objective optimization [27] and protein structure prediction [17] amongst many others. Singh et al. [24], demonstrated efficient use of the GEP algorithm for software defect prediction. According to Sherrod, experiments have already proved that the GEP algorithm is up to 60,000 times faster than traditional genetic algorithms [21]. GEP is advantageous because the chromosomes of the GEP algorithm are simple and easy to interpret with various operations. The GEP chromosomes formulate precise expression trees even after undergoing operations like selection and reproduction with modification [9]. Thus, the motivation of this study was to investigate the usefulness of the GEP algorithm for the prediction of CP classes.

In order to determine the effectiveness of the GEP algorithm, this study validates the metric suite proposed by Chidamber and Kemerer (CK) [5], a widely used OO metric suite to build a software quality model which determines the CP classes using the GEP algorithm. The model was developed on Simutrans, an open source software data set developed using the C++ language. Based on the results, we propose a new metric which can be used by researchers and practitioners to identify CP classes. This metric

Permission to make digital or hard copies of all or part of this work for personal or classroom use is granted without fee provided that copies are not made or distributed for profit or commercial advantage and that copies bear this notice and the full citation on the first page. Copyrights for components of this work owned by others than ACM must be honored. Abstracting with credit is permitted. To copy otherwise, or republish, to post on servers or to redistribute to lists, requires prior specific permission and/or a fee. Request permissions from Permissions@acm.org.

WETSoM'14, June 3, 2014, Hyderabad, India
Copyright 2014 ACM 978-1-4503-2854-8/14/06...$15.00
http://dx.doi.org/10.1145/2593868.2593870

was validated on another open source data set (Glest) and yielded good results.

Hence, the primary contributions of this paper are a) validation of the CK metric suite using the GEP algorithm to ascertain CP classes b) development of a new metric for classifying CP classes c) validation of the proposed metric to assess its effectiveness.

The paper is organized as follows. Section 2 gives us a brief description of background literature while Section 3 gives an overview of the GEP algorithm, its basic process and operators. Section 4 states the dependent and independent variables of our study and the data collection procedure while Section 5 states the results of the GEP model. Section 6 introduces a new metric called Change Index while Section 7 states the conclusions of the study.

2. BACKGROUND LITERATURE

Researchers in the past have validated a number of metrics which predict various quality attributes in a software. Certain researchers have proposed new metrics which are indicators of specific quality attributes like fault proneness. Moser et al. [18] analyzed a number of change metrics like number of revisions, number of refactorings, number of bugfixes, code churn etc. for predicting defects in a software. Krishnan et al. [13] extended this work to a certain extent by analyzing the same change metrics for identification of defect prone classes in the Eclipse product line. Nagappan et al. [19] conducted an empirical study to observe the applicability of software dependencies and churn metrics for detecting post-release failures. Singh et al. [24] proposed a new metric named Fault Factor to classify defect prone classes in the earlier stages of software development life cycle. However, these studies were specific to the prediction of defect prone classes.

Badri et al. [2] proposed a new metric called quality indicator, which captures certain aspects of testability and maintainability in an OO software. The metric was based on control call graphs and captures the information provided by a large number of OO metrics. Zhang et al. [29] presented a change metric suite which can be further classified into added change metrics, deleted change metrics and modifying change metrics to assess and measure the impact of changes during the evolution of AspectJ software. Elish et al. [7] derived and empirically evaluated a set of evolution based metrics for predicting CP classes in an OO system. These metrics included birth of a class, total amount of changes to a class, first time changes introduced to a class, frequency of change of a class etc. They found that these metrics along with the CK metric suite are efficient change predictors. However, evolution based metrics [7] and change metric suite [29] can only be derived in the later phases of software development life cycle. Thus, there is a need for a metric which can assess the occurrence of change in a class in the early phases of a software's life cycle. The metric proposed in this study takes into account only the CK metrics and thus can be evaluated in the initial phases of a software product to determine CP classes. Such a metric is important for effective quality control during the lifecycle of a product and develop quality benchmarks to assess the capability of current processes used in the software industry.

3. GENE EXPRESSION PROGRAMMING

According to Candida Ferreira, the GEP algorithm is similar to Genetic Algorithms (GA) in terms of finding an efficient solution in a vast search space of candidate solutions [9]. Both the algorithms constantly improve their solutions with the help of various operators like mutation, selection, recombination etc. However, there is a dissimilarity in the representation of the candidate solutions for both the algorithms, while both the GA as well as the GEP algorithm use chromosomes whose length is fixed throughout, in the GEP algorithm the chromosomes are later represented as optimal expression trees [9]. Ferreira adapted this system in order to incorporate a diverse range of mutation, cross-breeding, transposition and recombination operators whose application does not inhibit efficient translation of the chromosome into an accurate expression tree. Thus, the advantage of the GEP algorithm is two-fold, a) at the initial stage chromosomes are simple, linear and small objects which are easily handled while performing various transitions and operations b) performing any operation on the chromosome would lead to an accurate and precise expression tree [9]. These specific traits make the GEP algorithm highly adaptable, efficient and fast.

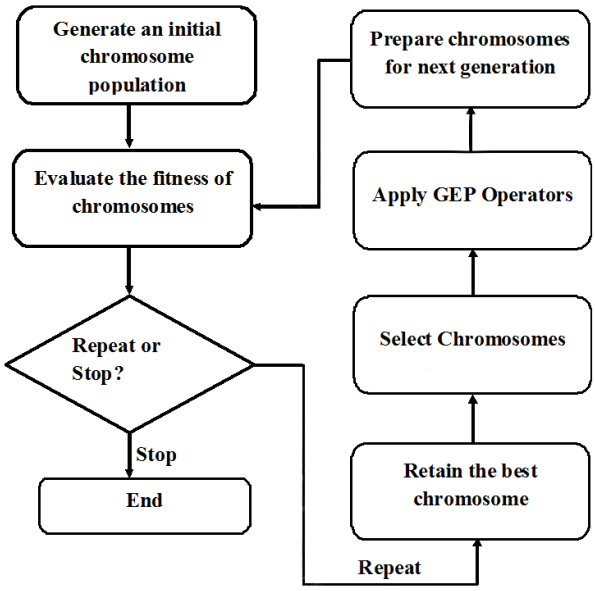

Figure 1. Flowchart of the GEP Algorithm

3.1 The GEP Algorithm

The basic flowchart of the GEP algorithm is given in Figure 1. The algorithm starts with an arbitrary generation of the chromosomes. The chromosomes should be represented in such a way so that they model the data efficiently. Each chromosome of the population is evaluated by ascertaining its fitness function. The best candidates are selected according to their fitness by performing the roulette wheel selection. After selecting the good chromosomes, we perform reproduction by applying the GEP operators (Section 3.3) to produce new candidates with better traits. Thereafter, we prepare the chromosomes for the next generation and repeat the steps until a fixed number of iterations or until we get the best solution from the population.

3.2 Genes and Chromosomes

A gene in the GEP algorithm consists of two parts, head and tail. While a tail can only have constants and variables, the head also includes functions in addition to constants and variables. Figure 2(a) demonstrates a GEP gene for the expression ((m + n) / (o +

r)). The gene expression tree can be encoded in Karva language by listing the nodes from the highest level to the lowest level and from left to right [9]. The gene in Figure 2(a) can be encoded as "/+*mnor", where "/+*" is the head part and "mnor" is the tail part. This encoding mechanism was devised by Ferreria for efficient application of a number of mutation and cross-breeding techniques which assure a valid syntactical expression tree [9].

A GEP chromosome is composed of one or more genes of equal length. A linking function is used to combine genes if required. Figure 2(b) shows a chromosome of two genes (Gene 1: "/mn" Gene 2: "*or") combined by the linking function "+".

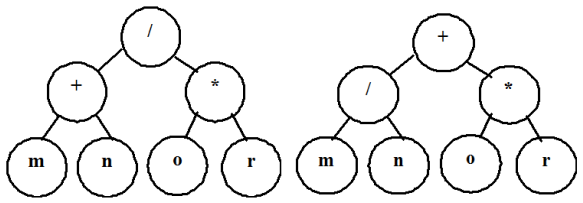

(a) (b)

Figure 2. a) Gene b) Chromosome

In order to train a GEP model, we first start with an initial population of chromosomes and progressively model the chromosomes which represent the data well. We then try to simplify the linking functions [24].

3.3 The GEP Operators

In order to traverse the solution space and constantly improve the solution candidates, the GEP algorithm uses the following operators:

3.3.1 Replication

While performing replication, the chromosomes are simply duplicated for the next generation. No change is made to the parent chromosome while replicating.

3.3.2 Mutation

Mutation can be performed at any part of the chromosome but care should be taken to maintain the structural organization. In order to maintain the structural composition, the terminals of the tail section can only be replaced by other terminals, while in the head section of the chromosome, any symbol can be changed into either a function or a terminal.

3.3.3 Transposition

Transposition corresponds to reordering of certain symbols within a gene. There are three different types of elements which can be transposed a) small fragments of a function or terminal which rearrange themselves at the head of the genes (IS transposition) b) small fragments of a function that rearrange at the root of the gene (Root transposition (RIS)) c) complete gene rearranging itself at the beginning of the chromosome (Gene Transposition).

3.3.4 Recombination

Recombination involves random selection of two chromosomes to perform crossover and exchange some portions to generate two new child chromosomes. Recombination could be a) One-point: Two chromosomes choose a random point for exchange b) Two point: Two chromosomes perform recombination at two separate randomly chosen points c) Gene Recombination: The complete gene is exchanged while performing the crossover.

4. RESEARCH BACKGROUND

This section explains the dependent and the independent variables of the study and also describes the data source and the data collection method.

4.1 Dependent and Independent Variables

The dependent variable of this study is change proneness. A class is said to be CP if there is a likelihood of change in a class in terms of the Source Lines of Code (SLOC) added, deleted or modified after the software has been released and goes into operation [16]. Previous studies [15-16, 30] have established the existence of a relationship between OO metrics and change proneness. This study validates the metric suite proposed by CK (independent variables) in order to predict change proneness of a class using the GEP algorithm. The details about the various metrics of the CK metric suite (Coupling Between Objects (CBO), Weighted Methods of a Class (WMC), Number of Children (NOC), Depth of Inheritance Tree (DIT), Response for a Class (RFC) and Lack of Cohesion amongst Methods (LCOM)) can be obtained from [5]. We also included SLOC, which is a count of lines containing the source code including the inactive regions. It is a metric which measures the length of the code but excludes comments. These metrics were computed with the help of Understand for C++ (http://www.scitools.com/) software.

4.2 Data Collection

In order to perform empirical validation, we collected data from an open source software data set named Simutrans, a transport simulation game developed in C++ language. It is a highly customizable network game with intelligent routing of the vehicles. We also validated the proposed metric on another open source software data set named Glest, which is a 3D strategy game developed in C++ language. Apart from being a game, Glest is also an engine to make other strategy games which are based on XML with the help of tools. The source code of the software data sets was available at http://sourceforge.net/ [10, 22]. The change was analyzed by examining two different versions of each of the software data set and computing the SLOC added, deleted or modified in the classes which were common to both the versions of the software. The details of the two versions (Ver.) of the software data sets namely release date and size (in SLOC) is given in Table 1.

Table 1. Data Set Details

Name	Ver.	Release Date	Size	DP	CC
Simutrans	111-3	17-06-2012	99,331	510	45%
	112-3	28-08-2013	1,17,568		
Glest	1.0.10	20-01-2005	13,764	108	66%
	3.2.2	03-04-2009	17,453		

We also compute the CK metrics for all the classes of the 111-3 version of the Simutrans data set and 1.0.10 version of the Glest data set with the help of Understand for C++ software. All abstract classes were discarded. The change statistics and the OO metrics for all the common classes were combined to form data points. Table 1 also shows the number of Data points (DP) and the percentage of Changed Classes (CC). According to Table 1, only 510 classes were found common in both the versions of the

Simutrans data set, out of which 231 classes (45%) were found to be changed. Similarly, only 108 classes were common to both the versions of the Glest data set. Out of 108 common classes, 71 classes (66%) were found to be changed. We define a new variable named ALTER which was set as "yes" for all the changed (Simutrans: 231, Glest: 71) classes and "no" for all the other common classes in both the data sets. A similar procedure was followed by Malhotra et al. [16].

5. ANALYSIS AND RESULTS

This section describes the analysis and results of the study. It states the descriptive statistics of the data sets used and also presents the results of the quality model developed using the GEP algorithm.

Table 2. Descriptive Statistics of Simutrans Data Set

Metric	Min.	Mean	SD	Max.	Med.
CBO	0	10.16	11.31	100	6
RFC	1	10.20	15.44	202	6
SLOC	5	154.19	344.86	4,897	59
NOC	0	0.95	5.48	82	0
LCOM	0	43.92	36.14	100	52.5
WMC	1	36.90	31.48	202	32
DIT	0	1.13	0.85	4	1

Table 3. Descriptive Statistics of Glest Data Set

Metric	Min.	Mean	SD	Max.	Med.
CBO	0	6	7.97	45	3
RFC	2	11.97	14.4	92	14
SLOC	10	110.34	223.41	1,972	48.5
NOC	0	0.11	0.54	4	0
LCOM	0	53.44	30.29	95	62
WMC	2	17.29	14.81	92	7
DIT	0	0.74	0.97	3	0

5.1 Descriptive Statistics

This section states the descriptive statistics of the Simutrans and the Glest open source data sets. Table 2 and 3 presents the Minimum (Min.), Mean (Mean), Standard Deviation (SD), Maximum (Max.), and Median (Med.) for all the CK metrics.

We make the following observations from Table 2 and 3.

(i) The size of the classes in the Simutrans data set ranges from 5 to 4,897 SLOC while the size of the classes in the Glest data set ranges from 10 to 1,972 SLOC.

(ii) The Simutrans as well as the Glest data sets have low mean values for the NOC metric (Simutrans: 0.95, Glest: 0.11) and for the DIT metric is (Simutrans: 1.13, Glest: 0.74) which signifies low use of inheritance in both the software data sets. Certain studies show similar results [3-4, 16].

(iii) The LCOM measure has high values (up to 95) in both the Simutrans as well as the Glest data sets.

5.2 Model Generation and Validation

In order to train and validate the software quality models which predict change proneness, we performed ten-fold cross validation [26] by randomly dividing the data into ten partitions. The GEP model trains itself on 9 partitions of the data set and validates the result on the 10^{th} partition. This procedure is again repeated with 9 different partitions of the data set and validated on the remaining 10^{th} partition. Such iterations are performed ten times.

The performance evaluation of the predicted models is assessed with the help of commonly known performance evaluators which are described as follows.

- *Specificity and Sensitivity:* Sensitivity (Sens.) is defined as the ratio of correctly predicted CP classes to the actual number of CP classes [16]. Specificity (Spec.) is defined as the ratio of correctly predicted not change prone (NCP) classes to the actual number of not CP classes [16].
- *Accuracy and Precision:* Accuracy (Acc.) is the percentage of number of classes which were correctly predicted to be CP or NCP [20, 23]. Precision (Prec.) is the ratio of correctly predicted CP classes to the total number of CP classes [20].
- *f -measure:* f-measure (f) is computed as the harmonic mean of precision and sensitivity [20].
- *Receiver Operating Characteristic (ROC) Analysis:* An ROC curve is plotted between sensitivity and 1-specificity values. While sensitivity values are represented on the y-axis, 1-specificity values are depicted on the x-axis [8, 16]. The model's effectiveness is measured by calculating the Area Under the ROC Curve (AUC).

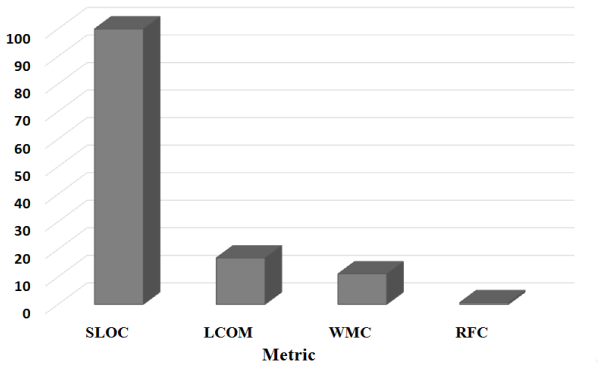

Figure 2. Variable Importance on the Simutrans Data Set

5.3 Variable Importance

We compute the importance of independent variables across each validation fold. The geometric mean of the variable importance is calculated, depicting the mean of cross validation importance for a particular variable across each fold. This method minimizes the importance of those variables which may be unimportant across any fold. After analyzing the variable importance across each cross validation fold using the GEP algorithm, the SLOC metric, the LCOM metric, the WMC metric and the RFC metric were computed as important variables while predicting change on the Simutrans project. Figure 2 shows their relative importance. According to Figure 2, the SLOC metric was highly important

with an importance percentage of 100%. The LCOM metric, the WMC metric and the RFC metric were also computed as important variables with an importance percentage of 16.86%, 11.07% and 0.63% respectively.

Table 4. Parameter Settings for GEP Algorithm

Population Size	50
Gene Per Chromosome	4
Gene Head Length	8
Simplification Generations	500
Linking Function	Addition
Fitness Function	Number of correct hits with penalty
Maximum Generations	2000
Stop if fitness reaches	1.00
Mutation Rate	0.044
Transposition Rates (IS, RIS, Gene)	0.1 each
Recombination Rate (One-point, Two-point)	0.3 each
Gene Recombination Rate	0.1

5.4 GEP Results

In this section, we present the results of the model predicted on the Simutrans data set using the GEP algorithm. As stated in Section 5.3, only 4 metrics out of 7 were used for developing the model. We also state the univariate results of each individual metric (Table 5) in order to determine the effectiveness of the GEP model. The parameter settings used while developing the model are specified in Table 4.

Table 5. Ten-fold Cross Validation Results

	Acc.	Sens.	Spec.	Prec.	f	AUC
CBO	70.00	58.87	79.21	70.10	64.00	0.691
RFC	66.08	51.95	77.78	65.93	58.11	0.650
SLOC	70.59	62.34	77.42	69.57	65.75	0.700
NOC	56.67	11.69	93.91	61.36	19.64	0.531
LCOM	54.51	49.78	58.42	49.78	49.78	0.541
WMC	65.29	46.75	80.65	66.67	54.96	0.632
DIT	57.45	32.03	78.49	55.22	40.55	0.545
Model	72.94	72.73	73.12	69.14	70.89	0.732

The fitness function for the GEP model is such that it counts the percentage of correct predictions (both CP as well as NCP). Moreover, it penalizes incorrect predictions of the target variable. The fitness function is actually the Accuracy measure (Section 5.2).

The model for predicting CP classes was generated with 510 data points of the Simutrans data set. Table 5 shows the ten-fold cross validation results after applying the GEP model using a combination of important metrics (Section 5.3) and the univariate results of each individual metric using ten-fold cross validation. The model developed using the GEP algorithm gave an AUC measure 0.732 and an accuracy measure of 72.94%. The specificity, sensitivity, precision value and f-measure of the GEP model was calculated as 73.12%, 72.73%, 69.14% and 70.89% respectively. Table 5 shows that the results of the predicted GEP model were clearly better than the univariate results of individual metrics.

6. CHANGE INDEX METRIC

This section describes a new metric, called the Change Index which can be used for ascertaining the CP nature of a class. We further validate the proposed metric on an open source data set.

6.1 Definition of Proposed Metric

Based on the results of the Simutrans data set using the GEP algorithm we propose a Change Index metric which can be used for ascertaining classes which would change in the forthcoming version of the software. The metric definition is as follows:

Metric Name: Change Index (CI)

Metric Definition: For a given class C_j, the CP for the given class can be computed by the following equation:

$$CI = ((((0.24 * RFC) + (2 * SLOC)) - WMC) - 59.62) - LCOM$$

Where RFC = Response for a class, SLOC = Source Lines of Code, WMC = Weighted Methods of a Class and LCOM = Lack of Cohesion amongst methods.

A class C_j is designated the CP status according to the following function:

$$ALTER\ (Cj) = \begin{cases} Yes, & if\ CI > 0 \\ No, & if\ CI \leq 0 \end{cases}$$

The function defines the ALTER variable (Section 4.2). A class is CP if the value of CI metric for the particular class is greater than zero otherwise it is NCP.

6.2 Validation of Proposed Metric

In order to validate the proposed CI metric, we used Glest, another open source data set and ascertained the CI metric value for all its 108 common classes. The results of the validation are shown in Table 6. The metric gave 72.22% accurate results with a specificity and sensitivity of 94.60% and 60.56% respectively. The precision value was computed as 95.55% and the f-measure as 74.59%. The AUC measure for the validation of the CI metric on the Glest data set was 0.776. Thus, the CI metric gave efficient validation results on the Glest data set.

Table 6. Validation Results for CI metric on Glest Data Set

	Acc.	Sens.	Spec.	Prec.	f	AUC
CI	72.22	60.56	94.60	95.55	74.59	0.776

6.3 Application of the CI Metric

The CI metric can be used by the software practitioners to identify classes which are CP in the early phases of software development life cycle. The primary sources of change in a software is defects and evolving requirements [16]. Thus, CP classes represent weak areas of a software and proper management of such classes is important. Determination of CP classes, helps in planning efficient resource allocation as more resources should be allocated to such classes. CP classes should be meticulously tested and rigorous verification activities like reviews and audits should be performed on such classes so that minimum changes occur in these classes. These steps lead to a good quality software.

All those classes where the CI metric value is greater than zero are considered as CP and the classes having negative CI metric value are considered as NCP. Developers should ensure that proper design measures are followed while coding such classes so that they can be efficiently refactored in the forthcoming releases of the software.

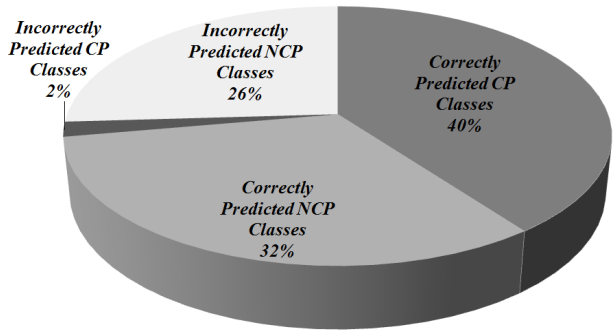

Figure 3. Validation Statistics of the proposed metric

Figure 3 shows the validation results of the CI metric. After analyzing the validation results, we found that 40% of the classes were correctly predicted as CP while only 2% of the classes were incorrectly designated CP status. Moreover, as shown in Figure 3, 32% of the classes were correctly predicted as NCP and only 26% of CP classes were not given proper status and adequate resources. Thus, the CI metric can be effectively used by the software practitioners for outlining resource usage and performing quality checks in the early phases of software development life cycle.

The CI metric can be used both during the maintenance and the testing phases to distribute limited resources effectively. This metric would also help in evaluating the efficiency of the present practices and processes of the software industry. The metric can be used as a quality benchmark to achieve good quality software. However, in order to provide universal results more studies should be conducted which ascertain the applicability of the proposed CI metric.

7. CONCLUSIONS AND FUTURE DIRECTIONS

The main focus of the study was to evaluate the effectiveness of the GEP algorithm for predicting CP classes. For this purpose, we validated the CK metric suite on an open source software named Simutrans. Based on the results produced by the application of the GEP algorithm, we propose a software quality metric named Change Index (CI). This metric can be used by researchers and practitioners for identifying CP classes in a software. The metric was validated on another open source data set named Glest. The conclusions of the paper are summarized below.

1) The metrics SLOC, LCOM, WMC and RFC were given importance while predicting change proneness of the Simutrans data set. The result indicates that change in a class of a software is dependent on the values of these metrics. Thus, these metrics should be monitored during the software development lifecycle for predicting the occurrence of CP classes.

2) The results indicate that the GEP algorithm can be efficiently used for developing models which predict software change. The model predicted using the GEP algorithm gave an accuracy of 72.94%, a sensitivity of 72.73%, a specificity of 73.12%, a precision value of 69.14% and an f-measure of 70.89%. The AUC measure for the model was computed as 0.732. (These results were better than univariate results of individual metrics).

3) A metric called Change Index (CI) was proposed which can be used by software practitioners to identify CP classes. The validation results of the metric (AUC: 0.776, Accuracy: 72.22%, Specificity: 94.60%, Sensitivity: 60.56%, Precision: 95.55% and f-measure: 74.59%) show that it can be used effectively for predicting classes which would undergo change in a software data set. An important application of the CI metric is to form quality standards which detect CP classes in the early phases of software life cycle and use this information for efficient quality control and resource allocation.

Our future work may involve repeated studies on different data sets to generalize our results. We also plan to replicate our study by using other unexplored machine learning techniques like genetic algorithms and evolutionary programming for predicting software change.

8. REFERENCES

[1] Aggarwal, K.K., Singh, Y., Kaur, A. and Malhotra, R. 2009. Empirical analysis for investigating the effect of object-oriented metrics on fault proneness: a replicated study. *Softw. Process*. 14, 1 (January 2009), 39-62.

[2] Badri, M., Badri, L. and Toure, F. 2009. Empirical analysis of object-oriented design metrics: Towards a new metric using control flow paths and probabilities. *Journal of Object Technology*. 8, 6 (September 2009), 123-142.

[3] Briand, L., Wust, J. and Lounis, H. 2001. Replicated case studies for investigating quality factors in object oriented designs. *Empir. Softw. Eng.* 6, 1 (March 2001), 11-58.

[4] CartWright, M. and Shepperd, M. 2000. An empirical investigation of an object-oriented software system, *IEEE Trans. Softw. Eng.* 26, 8 (August 2000), 786-796.

[5] Chidamber, S.R. and Kemerer, C.F. 1994. A metrics suite for object oriented design, *IEEE Trans. Softw. Eng.* 20, 6 (June 1994), 476-493.

[6] DeMarco, T. 1982. *Controlling Software Projects, Management Measurement & Estimation*, Prentice Hall, Upper Saddle River, NJ, USA.

[7] Elish, M.O. and Al-Khiaty, M. A.R. 2013. A suite of metrics for quantifying historical changes to predict future change-prone classes in object-oriented software, J. Softw.: Evol. and Proc. 25, 5 (May 2013), 407-437.

[8] Fawcett, T. 2006. An introduction to ROC Analysis. *Pattern Recogn. Lett.* 27, 8, (June 2006), 861-874.

[9] Ferreira, C. 2001. Gene expression programming: A new adaptive algorithm for solving problems, *Complex Systems*, 13, 2, 87-129.

[10] Glest Source Code: http://sourceforge.net/projects/glest/files/glest%20source/

[11] Henderson-sellers, B., 1996. *Object-oriented metrics: Measures of Complexity*. Prentice Hall, New Jersey.

[12] Koru, A.G. and Liu, H. 2007. Identifying and characterizing change-prone classes in two large-scale open-source products. *J. Syst. Softw.* 80, 1 (January 2007), 63-73.

[13] Krishnan, S., Starsburg, C., Lutz, R.R. and Popstojanova, K.G. 2011. Are Change Metrics Good Predictors for an Evolving Software Product Line?. *In Proceedings of the 7th International Conference on Predictive Models in Software Engineering*, (Banff, Canada, September 20-21, 2011). PROMISE'11. ACM, New York, USA, 7:1 – 7:10.

[14] Li., W. and Henry, S. 1993. Object oriented metrics that predict maintainability, *J. Syst. Softw.* 23, 2 (November 1993), 111-122.

[15] Lu, H., Zhou, Y., Xu, B., Leung, H. and Chen, L. 2012. The ability of object-oriented metrics to predict change-proneness: a meta-analysis. *Empiri. Softw. Eng.* 17, 3 (June 2012), 200-242.

[16] Malhotra, R. and Khanna, M. 2013. Investigation of relationship between object-oriented metrics and change proneness. *Int. J. Mach. Learn. & Cyber.* 4, 4 (August 2013), 273-286.

[17] Moreira, B.C., Fitzjohn, P.W., Offman, M., Smith, G.R. and Bates, P.A. 2003. Novel use of a genetic algorithm for protein structure prediction: searching template and sequence alignment space. *Proteins: Structure, Function, and Genetics*. 53, 6 (April 2003), 424-429.

[18] Moser, R., Pedrycz, W. and Succi, G. 2008. A comparative analysis of the efficiency of change metrics and static code attributes for defect prediction, *In 30th International conference on Software Engineering*, (Leipzig, May 12-18, 2008). ICSE'08. ACM, New York, NY, 181-190.

[19] Nagappan, N. and Ball, T. 2007. Using software dependencies and churn metrics to predict field failures: An empirical case study. In *Proceedings of 1st International Syposium on Empirical Software Engineering and Measurement*, (Madrid, September 20-21, 2007). ESEM'07. IEEE Computer Society, Washington DC, USA, 364-373.

[20] Peters, F., Menzies, T. and Andrian, M. 2013. Better cross company defect prediction. In Proceedings of the 10th Working Conference on Mining Software Repositories, (San Francisco, CA, May 18-19, 2013). MSR'13. IEEE Press, Piscataway, NJ, USA, 409-418.

[21] Sherrod, P. 2003. DTreg Predicting Modeling Software. http://www.dtreg.com/gep.htm.

[22] Simutrans Source Code: http://sourceforge.net/projects/simutrans/files/simutrans/

[23] Singh, Y., Kaur, A. and Malhotra, R., 2009. Empirical Validation of Object-Oriented Metrics for Predicting Fault Proneness Models. *Software Qual. J.* 18, 1 (March 2010), 3-35.

[24] Singh, Y., Kaur, A. and Malhotra, R. 2009. Prediction of software quality model using gene expression programming. In *Proceedings of 10th International Conference on Product Focus Software Process Improvement*, (Oulu, Finland, June 15-17, 2009). PROFES'09. 32, 43-58.

[25] Singh, Y., Kaur, A. and Malhotra, R. 2009. Software fault proneness prediction using support vector machines. In proceedings of the World Congress on engineering, (London, U.K., July 1-3, 2009). WCE'09. 1, ACM, New York, NY, 1-6.

[26] Stone, M., 1974. Cross-validatory choice and assessment of statistical predictions. *J. Royal Society Series B*. 36, 2 (December 1973), 111-114.

[27] Wang, W., Du, Y., Li, Q. and Fang, Z. 2011. Chaotic GEP algorithm for dynamic multi-objective optimization. In *Proceedings of 7th International conference on Natural Computation*, (Shanghai, July 26-28, 2011). ICNC'11. 2, IEEE Computer Society, Washington DC, USA, 1067-1071.

[28] Xu, K., Tang, C., Tang, R., Liu, Y., Zuo, J. and Zhu, J. 2008. Application of Gene Expression Programming to Real Parameter optimization. In *Proceedings of 4th International conference on Natural computation,* (Jinan, October 18-23, 2008). ICNC'08. 6, IEEE Computer Society, Washington DC, USA, 273-277.

[29] Zhang, S., Shen, H., and Zhao, J. 2008. *Metrics for Measuring Change Impacts in AspectJ Software Maintenance and Reuse*. Technical Report. Center for Software Engineering, SJTU.

[30] Zhou, Y., Leung, H. and Xu, B. 2009. Examining the potentially confounding effect of class size on the associations between object-oriented metrics and change proneness. *IEEE Trans. Softw. Eng.* 35, 5 (September 2009), 607-623.

APPENDIX

The appendix lists down some of the commonly used acronyms in the study.

A.1: Commonly used Acronyms

GEP	Gene Expression Programming
CP	Change Prone
NCP	Not Change Prone
OO	Object-Oriented
CK	Chidamber and Kemerer
GA	Genetic Algorithm
DP	Data Points
CC	Percentage of Changed Classes
CI	Change Index
CBO	Coupling Between Objects
RFC	Response for a Class
SLOC	Source Lines of Code
NOC	Number of Children
LCOM	Lack Of Cohesion amongst Methods
WMC	Weighted Methods of a Class
DIT	Depth of Inheritance Tree
ROC	Relative Operating Characteristic
AUC	Area Under the ROC Curve

Wireless Pers Commun (2014) 79:581–598
DOI 10.1007/s11277-014-1874-0

A New Time-Domain Solution to Transmission Through a Multilayer Low-Loss Dielectric Wall Structure for UWB Signals

Bajrang Bansal · Sanjay Soni

Published online: 27 June 2014
© Springer Science+Business Media New York 2014

Abstract In this work the time-domain solution for transmission through a multilayer wall structure has been presented. A time-domain transmission coefficient formulation for transmission through an interface between two low-loss dielectric mediums with different electrical properties is derived. Both hard and soft polarizations are considered. A novel ray tracing algorithm for multilayer wall structure has been presented with accuracy of ray-traced path as close as order of 10^{-5}. Further, in depth formulation for actual refracted angles for different layers of the wall has been presented and exact frequency-domain formulation for transmitted field at the receiver has been obtained. The exact formulation has been simplified under the condition of low loss assumption and this simplified formulation has been converted to time-domain formulation using inverse Laplace transform. The proposed time-domain solution has been validated with the inverse fast Fourier transform of the corresponding exact frequency-domain solution. Further the computational efficiency of both the methods has been compared.

Keywords Ultra wideband · Propagation model · Transmission · Frequency-domain · Time-domain

1 Introduction

Ultra wideband (UWB) technology has been the area of considerable attention of the research community in recent years due to its unique capabilities like high-speed connectivity, high-data rate, low equipment cost and low system complexity [1]. UWB communication systems employ the transmission and reception of very short duration pulses, usually a fraction of 1 ns [2–5], which cover extremely large bandwidth in the frequency-domain (FD). The possibility of very short duration pulses makes UWB signals resilient to multipath phenomena. The large

B. Bansal · S. Soni (✉)
Department of Electronics and Communication Engineering, Delhi Technological University, Delhi 110042, India
e-mail: sanjoo.ksoni@gmail.com

bandwidth of UWB signals offer salient features [2–6] like high data rates, accurate position location and ranging. Due to their low power density, they are perceived as noise by other communication systems that help in reducing the effect of interference.

The UWB signals, because of their huge bandwidth, get distorted at receiver as the channel response is frequency selective by nature which changes with frequency. The signal distortion brings challenges in channel modeling and receiver design in UWB system [7]. Considering the huge bandwidth of UWB signals, it is more efficient to study UWB propagation directly in time-domain (TD) where all the frequencies are treated simultaneously [5,8]. Also it is more efficient to work directly in the TD than applying the numerical inverse fast Fourier transform on each frequency separately as the latter would be very time consuming for the large bandwidth of UWB signals [9]. In TD, the path impulse response is calculated in simple closed form for each possible propagation path and then convolved with the transmitted signal to obtain the received field [5].

An overview on UWB propagation channels, their theory, measurement and modeling of UWB channels is presented in Molisch [7]. The main physical mechanisms considered in radio propagation are reflections, diffraction and transmission through the obstacles [5,10]. The TD reflection coefficient for a finitely conducting half space was presented in Barnes and Tesche [11]. For diffraction phenomena, uniform theory of diffraction (UTD) [12] is the most popular theory. The TD–UTD theory was first given by Veruttipong [13], and its applications to various scenarios involving single, double and multiple diffractions were discussed in [14–19]. The major drawbacks of TD-UTD theory were mathematical complexity and large computational time because of incorporation of higher-order diffraction coefficients. A new TD-UTD-PO approach was proposed in [9,20–22] to calculate the received field after multiple diffractions with much less computation time than the TD–UTD approach.

In urban microcellular scenario and indoor scenario especially in non-line of sight (NLOS) communication in deep shadow regions, where the reflected and diffracted field components are weak, transmitted field component proves to be very significant [10,23,24]. So it becomes important to analyze the effect of transmitted field through a wall for UWB communication in microcellular and indoor scenario.

The TD solutions for transmission of UWB signals through a dielectric slab were presented in [25,26]. Here multiple reflections inside the slabs were ignored due to their weak contribution. Another TD solution for transmission through a dielectric slab, considering a limited number of internal reflections, was presented in Qiu [27]. The measurements depicting the characterization of different materials within UWB range along with the discussion about dispersion suffered by UWB signals due to penetration through the walls were presented in Muqaibel et al. [28,29]. Another work in Yun [30] presented UWB pulse reflections and transmissions through complex wall structures, found in indoor propagation environments, through numerical FDTD simulations. A simplified TD model for transmission of UWB signals through a dielectric slab was presented in Yang et al. [31,32]. The TD solutions for the reflection and transmission through a dielectric slab incorporating the multiple internal reflections, was presented in Karousos et al. [33]. In Tewari and Soni [34], a TD transmission coefficient for transmission through an interface involving free space and dielectric material has been studied and structures like single wedge and single building scenarios have been analyzed. A FD model was developed in Yahalom et al. [35] for transmission through multiple layers in the 3–10 GHz band. Though a TD model for UWB signals transmitting through a dielectric slab with interface having free space and dielectric medium exists in literature [25,26,31,32], but the TD solution for received field calculation after penetration through multilayer wall structure having multiple layers with different dielectric materials has not yet been studied.

In this work, we propose an approximate TD solution for the field transmitted through a multilayer wall structure under the condition of low-loss assumption, in a microcellular propagation environment, for UWB signals. The proposed TD solution is based on the established FD transmission model of [24,36,37], upon which suitable approximations are applied to obtain a simpler, accurate and more computationally efficient TD solution. First a novel ray-tracing algorithm for a multilayer wall structure has been presented with accuracy of ray traced path as close as the order of 10^{-5}. The Generalized analytical TD transmission and reflection coefficients, for transmission through an interface between two low-loss dielectric mediums, considering oblique incidence, are derived for both soft and hard polarizations for UWB signals. Further, true refracted angles across each interface of the multilayer wall are derived. Through these TD formulations and actual refracted angles, the expression of the transmitted field through the multilayer wall is obtained. Here we have ignored the effect of weak multiple internally reflected signals following the condition in [24,26,31,32]. As mentioned in Muqaibel et al. [28], if the pulse duration is shorter than twice the travel time through the thickness of the slab, then, multiple reflections from the slab interior can be ignored. Also, given in Jing and Nai-tong [38], multiple internally reflected signals are not significant if the thickness of the obstacle is large compared to the wavelength of the incident signal and both the conditions are satisfied by the propagation profiles considered in this work. The TD results of the proposed work are validated against the inverse fast Fourier transform (IFFT) [39,40] of the corresponding exact FD solution results. At last, the computational efficiency of two approaches is compared to emphasize the significance of the proposed TD solutions.

The paper is organized as follows. In Sect. 2, the mathematical background on the inverse technique is presented. In Sect. 3, the propagation environment is presented. Section 4 presents the ray-tracing algorithm for transmission through the multilayer wall structure and discusses the TD transmission and reflection coefficients. This also discusses the in-depth analysis of true refracted angles when the signal propagates from one medium to another medium along with the TD formulation for the computation of the transmitted field component, for the multilayer wall profile. In Sect. 5, the aforementioned numerical TD results are calculated and validated against the numerical IFFT of the corresponding exact FD results and finally Sect. 6 concludes the paper.

2 Inverse Technique

The inverse continuous time Fourier transform (ICTFT) integral can be applied to find out the TD solution while knowing the FD solution [5], i.e.

$$f(t) = \frac{1}{2\pi} \int_{-\infty}^{\infty} F(\omega) \exp(j\omega t) d\omega = \int_{-\infty}^{\infty} F(f) \exp(j2\pi f t) df \tag{1}$$

where $f(t)$ is the TD solution of the corresponding FD representation $F(\omega)$ and ω is the angular frequency. In many cases it may not be possible to evaluate this integral for the whole interval and so maximum angular frequency may be introduced which should be greater than the maximum angular frequency of the transmitted signal to satisfy the Nyquist sampling rate in order to eliminate the effects of aliasing.

The ICTFT integral given in Eq. (1) can be approximated by discrete inverse fast Fourier transform (IFFT) [39] and the relationship between two is expressed below for a band limited FD function:

$$f(t) = \int_{-\infty}^{+\infty} F(f)\exp(j2\pi ft)\,df \simeq \Delta f \sum_{\substack{n=-\infty \\ \Delta f\to 0}}^{+\infty} F(n\Delta f)\exp(j2n\pi\Delta ft)$$

$$\simeq \frac{1}{N\Delta t}\sum_{\substack{n=0 \\ \Delta f\to 0}}^{N-1} F(n\Delta f)\exp(j2n\pi\Delta ft) \tag{2}$$

where Δf is the frequency step, Δt is the time step as per the Nyquist sampling criteria and N refers to the total number of frequency samples in IFFT-FD solution. The FD transmitted field has to be calculated up to a frequency, which follows the Nyquist sampling rate in order to eliminate the effects of aliasing. Secondly the frequency step size Δf has to be sufficiently small such that IFFT of FD result accurately approximates ICTFT Integral [39].

3 Propagation Environment

The propagation environment is shown in Fig. 1, where a single multilayer wall with layers of different dielectric materials is considered. As shown in Fig. 1, the parameters r_1, r_2, r_3, r_4, r_5 are the distances traversed by the transmitted field through the wall from the transmitter (Tx) up to the receiver (Rx). Angles $\theta_1, \theta_3, \theta_5, \theta_7$ are the incidence angles, and $\theta_2, \theta_4, \theta_6, \theta_8$ are the angles of refraction at points 'I', 'J', 'K' and 'L' respectively. The parameters h_t and h_r are the heights of the transmitter and the receiver and h_w is the height of the wall. Tx is at a distance d_1 from the wall and Rx is at a distance d_5 from the wall. Wall is assumed to be of three layers, each with different dielectric properties and width d_2, d_3 and d_4, respectively.

4 Proposed Transmission Model

4.1 The FD Model

The general expression for the received field after transmission through the wall for any polarization is given by [24,36,37]

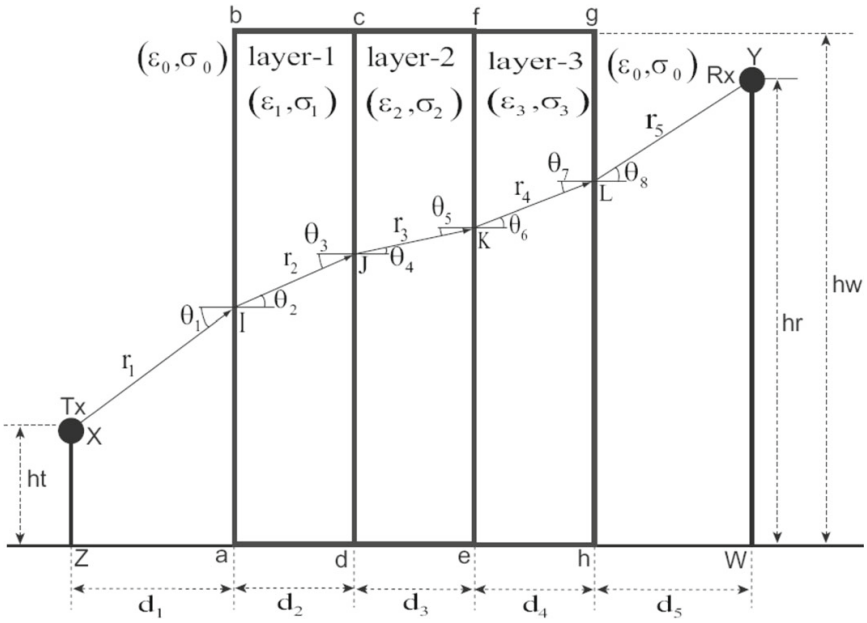

Fig. 1 Three-layer wall structure

$$E_{RX}(\omega) = \left(\frac{E_i}{r_{total}}\right) T_{total,s,h}(\omega) L_{total,s,h}(\omega) \tag{3}$$

where E_i is the relative amplitude of the spherical source in Fig. 1 [22, Eq. 2], r_{total} represents the total distance traversed by the transmitted field from Tx to Rx, $T_{total,s,h}(\omega)$ represents the total FD transmission coefficient, which is equal to the product of all the FD transmission coefficients occurring along a given transmission path between Tx and Rx in a given scenario and the 's' and 'h' subscripts refer to the soft and hard polarizations respectively. Here $L_{total,s,h}(\omega)$ [31,32] represents the total propagation path-loss suffered by the transmitted field during propagation between Tx to Rx. The total path-loss term of (3) includes all the losses during transmission between Tx and Rx, including the free-space propagation loss and the losses that depend on the internal architecture of the considered wall.

In general, the transmission coefficients for hard and soft polarizations are given as [24,37]

$$T_h(\omega) = 1 + R_h(\omega) = \frac{2\eta_2 \cos\theta_i}{\eta_2 \cos\theta_i + \eta_1 \cos\theta_t} \tag{4}$$

$$T_s(\omega) = \left(\frac{\cos\theta_i}{\cos\theta_t}\right)\{1 + R_s(\omega)\} = \frac{2\eta_2 \cos\theta_i}{\eta_2 \cos\theta_t + \eta_1 \cos\theta_i} \tag{5}$$

where θ_i is the angle of incidence, θ_t is the refracted angle, both considered with respect to the normal to the surface of incidence, $R_h(\omega)$ and $R_s(\omega)$ are the Fresnel reflection coefficients for hard and soft polarizations respectively. The parameters $\eta_1 = \sqrt{\mu_1/\tilde{\varepsilon}_1}$ and $\eta_2 = \sqrt{\mu_2/\tilde{\varepsilon}_2}$ are the characteristic impedances of first and second medium respectively, where μ and $\tilde{\varepsilon} = \varepsilon + (\sigma/j\omega)$ are the permeability and complex permittivity of the medium. Further $\mu = \mu_0\mu_r$ with μ_0 as the free space permeability and μ_r as the relative permeability of the medium. The real part of the complex dielectric permittivity is $\varepsilon = \varepsilon_o\varepsilon_r$ with ε_0 and ε_r as the free space permittivity and the relative dielectric permittivity of the medium respectively. The parameter σ is the conductivity of the medium.

The general expression for propagation constant is given by $\gamma(\omega) = \alpha(\omega) + j\beta(\omega)$, where α is the attenuation constant and β is the phase-shift constant for the given medium. In a general case, when mediums 1 and 2 are lossy materials (nonzero conductivity which implies $\alpha(\omega) \neq 0$), the refracted angle $\theta_t(\omega)$ is a complex frequency dependent number and the true real refraction angle $\psi_t(\omega)$ can be calculated with the help of Snell's law of refraction [37,41]. From [37, Section 5.4.2] and Fig. 2, the transmitted field in medium 2 is given as

$$E_2^t = E_2 \exp(-\gamma_2(\omega)(y \sin\theta_2(\omega) + x \cos\theta_2(\omega))) \tag{6}$$

For lossy medium, Snell's law of refraction across the interface in Fig. 2 can be written as [37]

$$\gamma_1(\omega) \sin\theta_1 = \gamma_2(\omega) \sin\{\theta_2(\omega)\} \tag{7}$$

For the geometry of Fig. 2,

$$\sin\theta_2(\omega) = \frac{\gamma_1(\omega)}{\gamma_2(\omega)} \sin\theta_1 = \frac{\alpha_1(\omega) + j\beta_1(\omega)}{\alpha_2(\omega) + j\beta_2(\omega)} \sin\theta_1 \tag{8}$$

and

$$\begin{aligned}\cos\{\theta_2(\omega)\} &= \sqrt{1 - \sin^2\{\theta_2(\omega)\}} = \sqrt{1 - \sin^2\theta_1[\gamma_1(\omega)/\gamma_2(\omega)]} \\ &= s(\omega)\exp[j\zeta(\omega)] = s(\omega)[\cos\zeta(\omega) + j\sin\zeta(\omega)]\end{aligned} \tag{9}$$

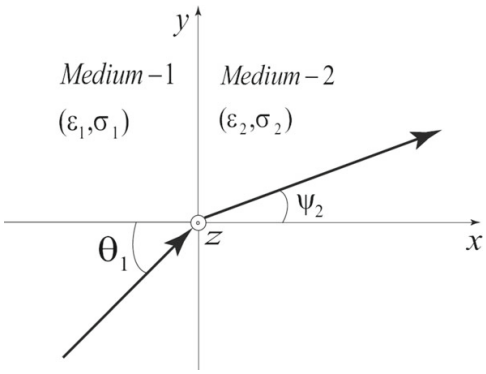

Fig. 2 Ray propagation in different lossy dielectric medium

Using (8) and (9), (6) can be written as

$$E_2^t = E_2 \exp\Bigg[-(\alpha_2(\omega)+\beta_2(\omega))\Bigg(y\frac{\alpha_1(\omega)+\beta_1(\omega)}{\alpha_2(\omega)+\beta_2(\omega)}\sin\theta_1 + xs(\omega)\left[\cos\zeta(\omega)+j\sin\zeta(\omega)\right]\Bigg)\Bigg] \tag{10}$$

This reduces to

$$E_2^t = E_2 \exp\begin{bmatrix} -y\alpha_1(\omega)\sin\theta_1 - xs(\omega)(\alpha_2(\omega)\cos\zeta(\omega) - \beta_2(\omega)\sin\zeta(\omega)) \\ -j\,(y\beta_1(\omega)\sin\theta_1 + xs(\omega)(\alpha_2(\omega)\sin\zeta(\omega) + \beta_2(\omega)\cos\zeta(\omega))) \end{bmatrix} \tag{11}$$

Finally (11) can be written as

$$E_2^t = E_2\exp(-\alpha_{e2}(\omega))\exp[-j\,(yt(\omega)+xq(\omega))] = E_2\exp(-\alpha_{e2}(\omega))\exp(-j\beta_{e2}(\omega)) \tag{12}$$

Thus the true refracted angle [37] is given as

$$\psi_t(\omega) = \tan^{-1}\{t(\omega)/q(\omega)\} \tag{13}$$

with $t(\omega) = \beta_1(\omega)\sin\theta_1$ and $q(\omega) = s(\omega)[\alpha_2(\omega)\sin\zeta(\omega) + \beta_2(\omega)\cos\zeta(\omega)]$.

From (13) it is clear that the true refraction angle is also frequency dependent in nature, which means that for different frequency components of the UWB signal, the true real angles of refraction are different. Thus, a single UWB ray incident on a lossy dielectric material actually splits into a beam of rays after refraction, corresponding to all the frequency components comprising the bandwidth of the signal. It means that the different frequency components of the transmitted signal follow different paths after refraction up to Rx. However, we will show later that for low-loss dielectric obstacles (i.e. $\sigma/\omega\varepsilon \ll 1$), for UWB signals, the different true refracted angles reduce to an effective, constant real angle. So during the TD analysis for low-loss cases we assume the refracted angle to be a constant value to simplify the development of the TD formulations and to obtain the effective single path travelled by the TD transmitted field as shown in the propagation profile of Sect. 3. The accuracy of such an assumption is established through the comparison between the obtained TD transmitted field and the actual IFFT-FD transmitted field.

4.2 The TD Model

We employ inverse Laplace transform, like [11], to the FD formulation obtained after applying the low-loss approximation to the original FD solution, discussed in the previous section, to obtain the TD formulation for the transmitted field. The proposed TD solution is accurate

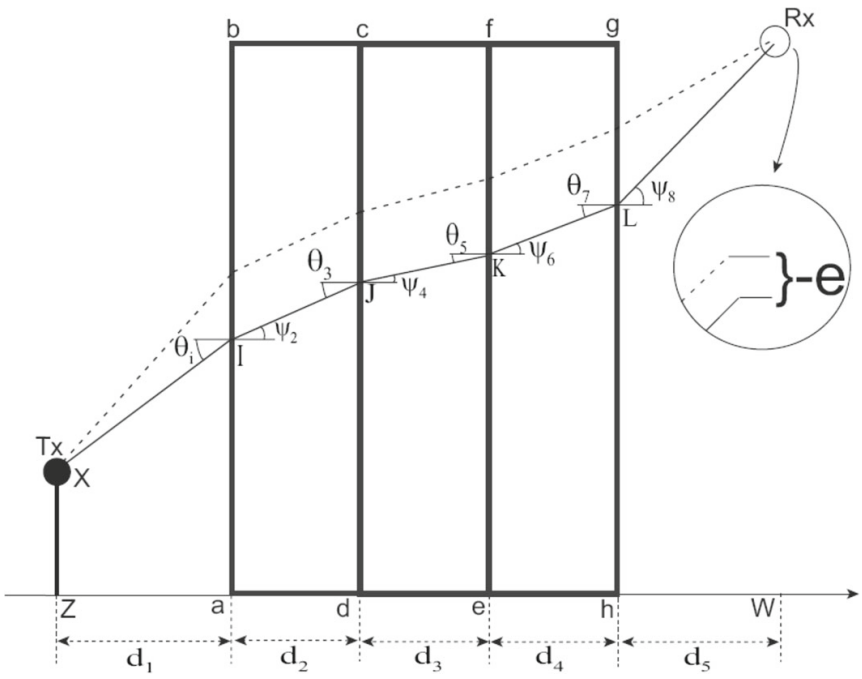

Fig. 3 Illustration of the actual transmitted path (*dotted*) and the ray-traced path (*solid*) with zoom on error e

for low loss dielectric obstacles with the possibility of interface having different dielectric mediums on each side. In TD,

$$e_{RX}(t) = [e_i(t)/r_{total}] * \Gamma_{total,s,h}(t) * l_{total,s,h}(t) \tag{14}$$

with '$*$' representing the convolution operator, $\Gamma_{total,s,h}(t)$ is the TD counterpart of term $T_{total,s,h}(\omega)$ of (3), $l_{total,s,h}(t)$ [31,32] is the TD counterpart of the term $L_{total,s,h}(\omega)$.

Now, before applying the FD or TD model to a given scenario, we first need to determine the path followed by the field in that particular situation. The algorithm to trace the path of the transmitted field for the scenario shown in Fig. 1 is presented next. Figure 3 shows the error between actual transmitted path (dotted) and ray traced path (solid) for the propagation scenario discussed in Fig. 1.

4.3 Proposed Algorithm to Determine the Transmission Path Through a Single Multilayer Wall

- Load the coordinates of Tx, Rx and all layers of the wall with Tx located at the position with coordinates $x = 0$, $y = h_t$, where h_t is the height of the transmitting antenna.
- Considering the left side of the first layer of the wall, choose an arbitrary point with incident angle θ_i of the incident ray from Tx, with respect to normal at first layer. For each of the chosen point, compute the angles θ_3, θ_5, θ_7 and true refracted angles ψ_2, ψ_4, ψ_6, ψ_8 (using Eq. 13) shown in Fig. 3 using the procedure discussed above.
- Also compute the coordinates of points I, J, K, L (intersection points of transmitted path with different layers of the wall).
- Next compute the y coordinate of the transmitted path at a distance of $d_1 + d_2 + d_3 + d_4 + d_5$ (see Fig. 3) from the Tx. Let this value be $h_{estimate}$. The difference $\Delta h = (h_r - h_{estimate})$ is stored in a vector $\overline{error}$ (h_r is the height of receiving antenna).
- Repeat this process for each sample point of the incident angle on the left side of first layer of the wall and store the error value in vector $\overline{error}$.

Table 1 Accuracy of proposed ray-tracing algorithm

Step size $\Delta\theta_i$ (in degree)	1	0.6	0.1	0.05	0.01
Min. absolute error, e	15×10^{-3}	85×10^{-4}	13×10^{-4}	3.16×10^{-4}	1.43×10^{-5}

- Find the minimum error from the vector $\overline{error}$. If this minimum error is less than the desired threshold, then the transmission path corresponding to that error's value is the desired path otherwise the step size $\Delta\theta_i$ is reduced till the minimum error is less than the set threshold error.

This way, the best appropriate transmitted path is obtained. Table 1 present the accuracy of the proposed path tracing algorithm for single multilayer wall structure of Fig. 1.

4.4 TD Transmission and Reflection Coefficients

Here we derive the general expression for TD transmission coefficients corresponding to (4) and (5), for both hard and soft polarizations. The TD analytical expressions of reflection coefficient and transmission coefficient, mentioned in Barnes and Tesche [11] and Yang et al. [31] respectively, are valid only for a finitely conducting slab, i.e. parallel wall type structure where the incident angle at the second surface of the obstacle is equal to the refracted angle at the first surface. If the finitely conducting slab is replaced by some canonical object like a finitely conducting wedge where the incident angle at the second surface is not equal to the refracted angle at the first surface, then the TD analytical expression for reflection coefficient at the second surface (propagation from dielectric medium to free space) of the dielectric obstacle and the corresponding TD transmission coefficient cannot be derived using the approximations considered in Barnes and Tesche [11]. On the other hand, our proposed TD analytical expressions of reflection coefficient and transmission coefficient are applicable for any kind of dielectric obstacles and that also at both surfaces of the obstacles. Also our proposed TD analytical expressions of reflection coefficient and transmission coefficient cover the cases like wave propagating from a dielectric medium to another dielectric medium while considering the low-loss assumption for both dielectric mediums.

For a non-magnetic medium, like drywall, plywood, wooden-door etc., relative magnetic permeability is approximately one ($\mu_r \approx 1$), thus in such cases $\mu \approx \mu_0$. The dielectric obstacles considered in this work have low-loss characteristics i.e. their loss-tangent value ($\sigma/\omega\varepsilon$) is very much less than unity, within the UWB frequency range. In such a condition the true refracted angle is almost independent of frequency for the entire UWB frequency range, and it is approximately equal to

$$\psi_t \simeq \sin^{-1}(\sin\theta_i/\sqrt{\varepsilon_r}) \tag{15}$$

Thus here in this section we treat the real refracted angle ψ_t as constant and frequency independent, to obtain the approximate analytical TD transmission coefficients. Starting with the hard polarization case, for the wave propagating form one low-loss dielectric medium to another low loss dielectric medium from (4) and [37, Examples 5–8] we obtain

$$T_h(\omega) \simeq \frac{2\eta_2 \cos\theta_i}{\eta_2 \cos\theta_i + \eta_1 \cos\psi_t} \tag{16}$$

where η_1 and η_2 are the characteristic impedances of first and second mediums respectively. Now from (16) we get

$$T_h(\omega) \simeq \frac{2\cos\theta_i}{\cos\theta_i + \left(\sqrt{\frac{\varepsilon_0\varepsilon_{r2}+\sigma_2/j\omega}{\varepsilon_0\varepsilon_{r1}+\sigma_1/j\omega}}\right)\cos\psi_t} \tag{17}$$

After further manipulation and doing the replacement $s \to j\omega$ in (17) we obtain

$$T_h(s) \simeq 1 - \left\{\frac{\sqrt{s+\tau_2} - k_h\sqrt{s+\tau_1}}{\sqrt{s+\tau_2} + k_h\sqrt{s+\tau_1}}\right\} \tag{18}$$

where

$$\tau_1 = (\sigma_1/\varepsilon_1),\ \tau_2 = (\sigma_2/\varepsilon_2) \quad \text{and} \quad k_h = (\cos\theta_i/\cos\psi_t)(\sqrt{\varepsilon_{r1}}/\sqrt{\varepsilon_{r2}}).$$

Now using the inverse Laplace technique we get

$$\gamma_h(t) = L^{-1}[T_h(s)] \simeq L^{-1}\left[1 - \left\{\frac{\sqrt{s+\tau_2} - k_h\sqrt{s+\tau_1}}{\sqrt{s+\tau_2} + k_h\sqrt{s+\tau_1}}\right\}\right] \tag{19}$$

Finally the TD transmission coefficient for this case is given by

$$\gamma_h(t) \simeq \delta(t) - r_h(t) \tag{20}$$

with,

$$r_h(t) = L^{-1}[r_h(s)] = L^{-1}\left[\left\{\frac{\sqrt{s+\tau_2} - k_h\sqrt{s+\tau_1}}{\sqrt{s+\tau_2} + k_h\sqrt{s+\tau_1}}\right\}\right].$$

For solving $r_h(t)$, put $s + \tau_1 = s_1$ which gives

$$r_h(s_1) = \frac{\sqrt{s_1+\tau_2-\tau_1} - k_h\sqrt{s_1}}{\sqrt{s_1+\tau_2-\tau_1} + k_h\sqrt{s_1}} = \frac{\sqrt{s_1+\tau} - k_h\sqrt{s_1}}{\sqrt{s_1+\tau} + k_h\sqrt{s_1}} \text{with, } \tau = \tau_2 - \tau_1 \tag{21}$$

$r_h(s_1)$ is of the form, [11,42]. So using the result from Barnes and Tesche [11] and the frequency shifting property of Laplace transform gives

$$r_h(t) = [K_h\delta(t)] + \frac{4k_h}{(1-k_h^2)}e^{-pt}e^{\tau_1 t}\left[\frac{K_h}{2}X_h + \frac{(1-X_h)}{2K_h} - \frac{(pt)\,X_h}{4}\right] \tag{22}$$

with, $X_h = e^{-\left(\frac{K_h pt}{2}\right)}$, $K_h = \left(\frac{1-k_h}{1+k_h}\right)$ and $p = \frac{\tau_2-\tau_1}{2}$.

From (4) and (20) we get '$-r_h(t)$' as the TD reflection coefficient for hard polarization. Next, we obtain the TD transmission coefficient for a soft polarized wave propagating from one dielectric medium to another dielectric medium under the condition of low loss assumption. Similar to the analysis for hard polarization case, from (5) and (15) we get

$$T_s(\omega) = \frac{2\eta_2\cos\theta_i}{\eta_2\cos\psi_t + \eta_1\cos\theta_i} \tag{23}$$

After manipulating (23) we obtain

$$\gamma_s(t) \simeq L^{-1}\left[1 - \left\{\frac{\sqrt{s+\tau_2} - k_s\sqrt{s+\tau_1}}{\sqrt{s+\tau_2} + k_s\sqrt{s+\tau_1}}\right\}\right]\left(\frac{\cos\theta_i}{\cos\psi_t}\right) \tag{24}$$

where $k_s = (\cos\psi_t/\cos\theta_i)\,(\sqrt{\varepsilon_{r1}}/\sqrt{\varepsilon_{r2}})$. Thus finally we get

$$\gamma_s(t) \simeq [\delta(t) - r_s(t)]\left(\frac{\cos\theta_i}{\cos\psi_t}\right) \tag{25}$$

where

$$r_s(t) = K_s\delta(t) + \frac{4k_s}{\left(1-k_s^2\right)}e^{-pt}e^{\tau_1 t}\left[\frac{K_s}{2}X_s + \frac{(1-X_s)}{2K_s} - \frac{(pt)\,X_s}{4}\right] \tag{26}$$

with, $X_s = e^{-\left(\frac{K_s pt}{2}\right)}$, $K_s = \left(\frac{1-k_s}{1+k_s}\right)$ and $p = \frac{\tau_2-\tau_1}{2}$.

From (5), and (25) we get '$-r_s(t)$' as the TD reflection coefficient for soft polarization.

4.5 Transmitted Field Through a Single Multilayer Wall Structure

According to (3), the FD expression for the transmitted field at Rx through the single multilayer wall structure as shown in Fig. 1, is given by

$$E_{RX}(\omega) = (E_i(\omega)/r_{total}(\omega))\left(\prod_{i=1}^{4} T_{i,s,h}(\omega)\right) \times \left(\exp(-jk_0r_1)\prod_{j=2}^{5}\exp\left\{-\left(\alpha_{ej}(\omega)+j\beta_{ej}(\omega)\right)\right\}\right) \tag{27}$$

with $r_{total} = r_1 + r_2 + r_3 + r_4 + r_5$ and $T_{total,s,h}(\omega) = T_{1,s,h}(\omega)T_{2,s,h}(\omega)T_{3,s,h}(\omega)T_{4,s,h}(\omega)$ where $T_{1,s,h}(\omega)$, $T_{2,s,h}(\omega)$, $T_{3,s,h}(\omega)$, $T_{4,s,h}(\omega)$ are the FD transmission coefficients with respect to points 'I', 'J', 'K', 'L' (See Fig. 1). The above equation is obtained by extending the formulation presented in [37, Section 5.4.2, Eqs. 5-53 to 5-61]. Here it is important to note that (27) is to be calculated for each frequency component of the UWB signal that is contributing to the total transmitted field at Rx. On comparing (3) and (27) we get the following actual FD path loss expression for the single multilayer wall structure

$$L(\omega) = \left(\exp(-jk_0r_1)\prod_{j=2}^{5}\exp\left\{-\left(\alpha_{ej}(\omega)+j\beta_{ej}(\omega)\right)\right\}\right) \tag{28}$$

The terms $\alpha_{ej}(\omega)$ and $\beta_{ej}(\omega)$ in (28) can be derived from Eqs. (6–13) discussed in Sect. 4.1. From Fig. 1 and Eqs. (6–13), we get

$$\alpha_{e2}(\omega) = [x_2(\omega) - x_1]\,s_1(\omega)[\alpha_2(\omega)\cos\{\zeta_1(\omega)\} - \beta_2(\omega)\sin\{\zeta_1(\omega)\}] \tag{29}$$

Here (x_1, y_1) are the coordinates of point 'I' and $(x_2(\omega), y_2(\omega))$ are the coordinates of point 'J' in Fig. 1. The term $\alpha_{e2}(\omega)$ is the total effective attenuation constant at point 'I' during propagation of the refracted wave from medium 1 (free space) to medium 2 (dielectric medium). The corresponding total effective phase constant is given as

$$\beta_{e2}(\omega) = \beta_{2e}(\omega)\left([x_2(\omega) - x_1]\cos[\psi_2(\omega)] + [y_2(\omega) - y_1]\sin[\psi_2(\omega)]\right) \tag{30}$$

The expressions for the effective frequency dependent phase constants $\beta_{2e}(\omega)$ as mentioned in (30) is given by

$$\beta_{2e}(\omega) = \sqrt{t_1^2(\omega) + q_1^2(\omega)} \tag{31}$$

where $t_1(\omega) = \beta_1(\omega)\sin\theta_1$ and $q_1(\omega) = s_1(\omega)[\alpha_2(\omega)\sin\{\zeta_1(\omega)\} + \beta_2(\omega)\cos\{\zeta_1(\omega)\}]$ with

$$\cos\{\theta_2(\omega)\} = \sqrt{1-\sin^2\{\theta_2(\omega)\}} = \sqrt{1-\sin^2(\theta_1)[\gamma_1(\omega)/\gamma_2(\omega)]} = s_1(\omega)\exp[j\zeta_1(\omega)] \tag{32}$$

The true angle of refraction corresponding to the point of refraction 'I' as per (13) [37], is given by $\psi_2(\omega) = \tan^{-1}\{t_1(\omega)/q_1(\omega)\}$.

At point 'J' (from one dielectric medium to another dielectric medium as shown in Fig. 1), the total effective attenuation constant is given by

$$\alpha_{e3}(\omega) = [\alpha_2(\omega)\sin\{\theta_3(\omega)\}[y_3(\omega) - y_2(\omega)] - s_2(\omega)\sin\{\zeta_2(\omega)\}\beta_3(\omega)[x_3(\omega) - x_2(\omega)] + s_2(\omega)\cos\{\zeta_2(\omega)\}\alpha_3(\omega)[x_3(\omega) - x_2(\omega)]] \quad (33)$$

Here $(x_3(\omega), y_3(\omega))$ are the coordinates of point 'K' in Fig. 1. The corresponding total effective phase constant is given as

$$\beta_{e3}(\omega) = \beta_{3e}(\omega)\,([x_3(\omega) - x_2(\omega)]\cos[\psi_4(\omega)] + [y_3(\omega) - y_2(\omega)]\sin[\psi_4(\omega)]) \quad (34)$$

The expressions for the effective frequency dependent phase constants $\beta_{3e}(\omega)$ as mentioned in (34) is given by

$$\beta_{3e}(\omega) = \sqrt{t_2^2(\omega) + q_2^2(\omega)} \quad (35)$$

where $t_2(\omega) = \beta_2(\omega)\sin\theta_3(\omega)$ and $q_2(\omega) = s_2(\omega)[\alpha_3(\omega)\sin\{\zeta_2(\omega)\} + \beta_3(\omega)\cos\{\zeta_2(\omega)\}]$ with

$$\cos\{\theta_4(\omega)\} = \sqrt{1 - \sin^2\{\theta_4(\omega)\}} = \sqrt{1 - \sin^2\{\theta_3(\omega)\}[\gamma_2(\omega)/\gamma_3(\omega)]} = s_2(\omega)\exp[j\zeta_2(\omega)] \quad (36)$$

The true angle of refraction corresponding to the point of refraction 'J' as per (13) [37], is given by $\psi_4(\omega) = \tan^{-1}\{t_2(\omega)/q_2(\omega)\}$.

At point 'K', the analysis can be done similar to the analysis done at point 'J'.

Finally at point 'L' (from dielectric medium to free space as shown in Fig. 1), the total effective attenuation constant is given by

$$\alpha_{e5}(\omega) = [\alpha_4(\omega)\sin\{\theta_7(\omega)\}[y_5(\omega) - y_4(\omega)] - s_4(\omega)\sin\{\zeta_4(\omega)\}\beta_1(\omega)[x_5(\omega) - x_4(\omega)]] \quad (37)$$

Here $(x_4(\omega), y_4(\omega))$ are the coordinates of point 'L' and $(x_5(\omega), y_5(\omega))$ are the coordinates of point 'Y' in Fig. 1. The corresponding total effective phase constant is given as

$$\beta_{e5}(\omega) = \beta_{5e}(\omega)\,([x_5(\omega) - x_4(\omega)]\cos[\psi_8(\omega)] + [y_5(\omega) - y_4(\omega)]\sin[\psi_8(\omega)]) \quad (38)$$

The expressions for the effective frequency dependent phase constants $\beta_{5e}(\omega)$ as mentioned in (38) is given by

$$\beta_{5e}(\omega) = \sqrt{t_4^2(\omega) + q_4^2(\omega)} \quad (39)$$

where $t_4(\omega) = \beta_4(\omega)\sin\theta_7(\omega)$ and $q_4(\omega) = s_4(\omega)[\beta_1(\omega)\cos\{\zeta_4(\omega)\}]$ with

$$\cos\{\theta_8(\omega)\} = \sqrt{1 - \sin^2\{\theta_8(\omega)\}} = \sqrt{1 - \sin^2\{\theta_7(\omega)\}[\gamma_4(\omega)/\gamma_1(\omega)]} = s_4(\omega)\exp[j\zeta_4(\omega)] \quad (40)$$

The true angle of refraction corresponding to the point of refraction 'L' as per (13) [37], is given by $\psi_8(\omega) = \tan^{-1}\{t_4(\omega)/q_4(\omega)\}$.

These expressions for the true angles of refractions are to be used in place of the complex refracted angles along each transmission path during the calculation of the total transmitted field at Rx.

Now the TD expression for the received field at Rx is as follows

$$e_{RX}(t) \simeq \left(\frac{e_i(t)}{r_{total}}\right) * \Gamma_{1,s,h}(t) * \Gamma_{2,s,h}(t) * \Gamma_{3,s,h}(t) * \Gamma_{4,s,h}(t) * l_{total,s,h}(t) \quad (41)$$

where $\Gamma_{1,s,h}(t) * \Gamma_{2,s,h}(t) * \Gamma_{3,s,h}(t) * \Gamma_{4,s,h}(t) = \Gamma_{total,s,h}(t)$ with $\Gamma_{1,s,h}, \Gamma_{2,s,h}, \Gamma_{3,s,h}, \Gamma_{4,s,h}$ as the TD expressions for the transmission coefficients at points 'I', 'J', 'K' and

'L' in Fig. 1 and are obtained as per (15), (20) and (25). The term $l_{total,s,h}(t)$ in (41) is the TD propagation path-loss expression corresponding to the FD term $L_{total,s,h}(\omega)$ in (3).

For loss-tangent much less than unity ($\sigma/\omega\varepsilon \ll 1$), the FD path loss expression (28) reduces to the following approximate form with constant values of angles of refraction as in (15) and along a single effective path for transmission

$$\begin{aligned} L_{total,s,h}(\omega) \simeq & \exp\left[-j\omega d_2\sqrt{\mu_1\varepsilon_1}\left(1+\frac{\sigma_1}{2j\omega\varepsilon_1}\right)\sqrt{\frac{\varepsilon_{r1}}{\varepsilon_{r1}-\sin^2\theta_1}}\right] \\ & \times \exp\left[-j\omega d_3\sqrt{\mu_2\varepsilon_2}\left(1+\frac{\sigma_2}{2j\omega\varepsilon_2}\right)\sqrt{\frac{\varepsilon_{r2}}{\varepsilon_{r2}-\varepsilon_{r1}\sin^2\theta_3}}\right] \\ & \times \exp\left[-j\omega d_4\sqrt{\mu_3\varepsilon_3}\left(1+\frac{\sigma_3}{2j\omega\varepsilon_3}\right)\sqrt{\frac{\varepsilon_{r3}}{\varepsilon_{r3}-\varepsilon_{r2}\sin^2\theta_5}}\right] \\ & \times \exp\left(-jk_0(r_1+r_5)\right) \end{aligned} \tag{42}$$

Here $r_1 + r_5$ is the total distance travelled by the field in free space. The term $l_{total,s,h}(t)$ in (41) is given by

$$\begin{aligned} l_{total,s,h}(t) \simeq & \exp\left\{(-(\sigma_1 d_2)/2)\sqrt{\frac{\mu_1}{\varepsilon_1}}\sqrt{\frac{\varepsilon_{r1}}{\varepsilon_{r1}-\sin^2\theta_1}}\right\} \\ & \times \exp\left\{(-(\sigma_2 d_3)/2)\sqrt{\frac{\mu_2}{\varepsilon_2}}\sqrt{\frac{\varepsilon_{r2}}{\varepsilon_{r2}-\varepsilon_{r1}\sin^2\theta_3}}\right\} \\ & \times \exp\left\{(-(\sigma_3 d_4)/2)\sqrt{\frac{\mu_3}{\varepsilon_3}}\sqrt{\frac{\varepsilon_{r3}}{\varepsilon_{r3}-\varepsilon_{r2}\sin^2\theta_5}}\right\} \\ & * \delta\left(t-\frac{r_1+r_5}{c}\right) * \delta\left\{t-d_2\sqrt{\mu_1\varepsilon_1}\sqrt{\frac{\varepsilon_{r1}}{\varepsilon_{r1}-\sin^2\theta_1}}\right\} \\ & * \delta\left\{t-d_3\sqrt{\mu_2\varepsilon_2}\sqrt{\frac{\varepsilon_{r2}}{\varepsilon_{r2}-\varepsilon_{r1}\sin^2\theta_3}}\right\} * \delta\left\{t-d_4\sqrt{\mu_3\varepsilon_3}\sqrt{\frac{\varepsilon_{r3}}{\varepsilon_{r3}-\varepsilon_{r2}\sin^2\theta_5}}\right\} \end{aligned} \tag{43}$$

This approximated TD propagation path-loss expression will be used in (41) to compute the TD transmitted field through the wall and the accuracy will be proved by the comparison of TD transmitted field with the IFFT of the exact FD results, as shown in next section.

5 Results and Discussion

In this section the numerical simulation results, based on the aforementioned TD and FD solutions for the transmitted field are presented. The TD results are compared with the numerical IFFT of the corresponding exact FD results. First the exact analytic FD formulations representing CTFT of the transmitted field are used to calculate the transmitted field at the Rx. Then as discussed in Sect. 2, the obtained FD results are converted into TD through ICTFT integral. Numerical IFFT-FD method [39] is adopted to accurately approximate the ICTFT integral with the relationship between two given in Eq. (2). The FD transmitted field has to be calculated up to a frequency, which follows the Nyquist sampling rate in order to eliminate the effects of aliasing. Secondly the frequency step size Δf has to be sufficiently small such that IFFT of FD result accurately approximates ICTFT Integral [39].

In FD analysis first the frequency components contributing to the total transmitted field at Rx are identified. All the transmitted frequency components are considered as if received

Table 2 Electromagnetic properties of different materials

Material	Relative permittivity (ε_r)	Conductivity σ (S/m)
Brick [33]	4.4	0.018
Dry concrete [31]	5	0.016
Drywall [28]	2.4	0.004
Wood [31]	2	0.01

by the Rx. For all these frequencies the FD transmitted field is calculated as per (27), and then IFFT of this result is computed to obtain the reference transmitted field. In TD analysis first the single effective path of the transmitted field for the given scenario is traced using the path-tracing algorithm discussed in Sect. 4.3, based on low-loss approximation, and then the transmitted field along that path is calculated in TD through (41). The TD results are then compared with the reference IFFT-FD transmitted field for validation of the proposed solution. Throughout our work the Gaussian doublet pulse is used as the excitation UWB signal which is expressed in TD as [22]

$$s(t) = \left(\frac{1}{\tau}\right)\left(\sqrt{\frac{\tau}{3\sqrt{\pi/2}}}\right)\left(1 - \frac{2t^2}{\tau^2}\right)\exp\left(-\frac{t^2}{\tau^2}\right) \tag{44}$$

where τ is the full width half maximum pulse duration with a value of 0.1 ns. The Fourier transform of (44) is given as

$$S(f) = 2 \times \sqrt{\pi} \times \sqrt{\frac{\tau}{3\sqrt{\pi/2}}} \times \left(\pi^2\tau^2 f^2\right) \times e^{-\pi^2\tau^2 f^2} \tag{45}$$

Each layer of the multilayer wall is considered to be made up of low-loss dielectric material with relative magnetic permeability as unity. Indoor building materials are chosen with low loss-tangent values like drywall, wooden door, structure wood, plywood, glass, brick, concrete block (also called dry concrete) and office partition. In this work, we have taken the cases of both hard and soft polarizations under the condition of low loss assumption. In the first scenario, first and third layers of the wall are considered to be made up of drywall [30] and second layer is considered to be made up of wood [33]. In another scenario, first and third layers of the wall are considered to be made up of brick [35] and second layer is considered to be made up of dry concrete [33]. Table 2 shows the electromagnetic properties of the considered materials.

First, a case of transmission through the multilayer wall for both soft and hard polarizations is shown in Figs. 4 and 5 (for both the scenarios of building materials discussed above). Considering Fig. 1, transmitter height h_t and receiver height h_r are taken to be 2 and 3 m respectively. The height of the wall h_w is taken to be 4 m, distance d_1 and d_5 are 0.3 m and the thickness of each layer of the wall is 0.1 m. As it can be seen from Fig. 4 and 5, the transmitted field at Rx suffers no distortion in shape in comparison to the shape of the UWB pulse incident at the first layer of the wall.

The transmitted field is undistorted due to very small magnitude of the loss-tangent with respect to unity. However, the amplitude of the transmitted field is attenuated because of the transmission loss through the layers of the wall. It can be observed from Figs. 4 and 5, the signal field strength is stronger in the former case than in the latter case. This is because of very low loss-tangent value of drywall, used as dielectric material for the external layers of the wall. The soft polarized wave is less attenuated than the hard one, with a small difference between the transmitted fields for the two polarizations. The TD results for the transmitted field for both

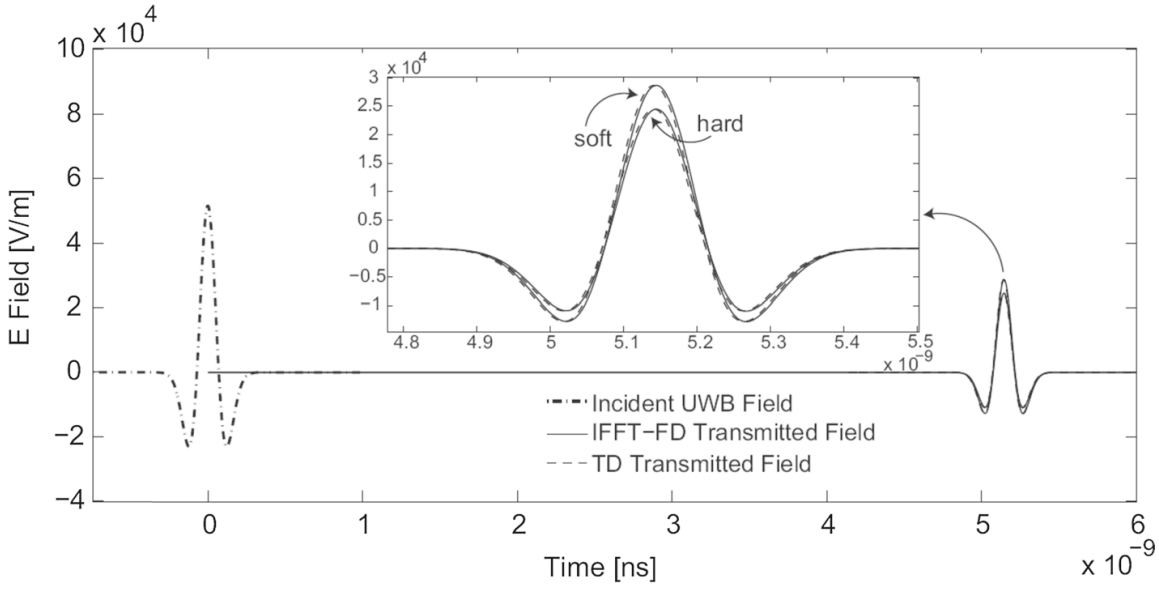

Fig. 4 Transmitted field through a low-loss multilayer wall compared with the reference Gaussian doublet pulse, with drywall [28] and wood [31]

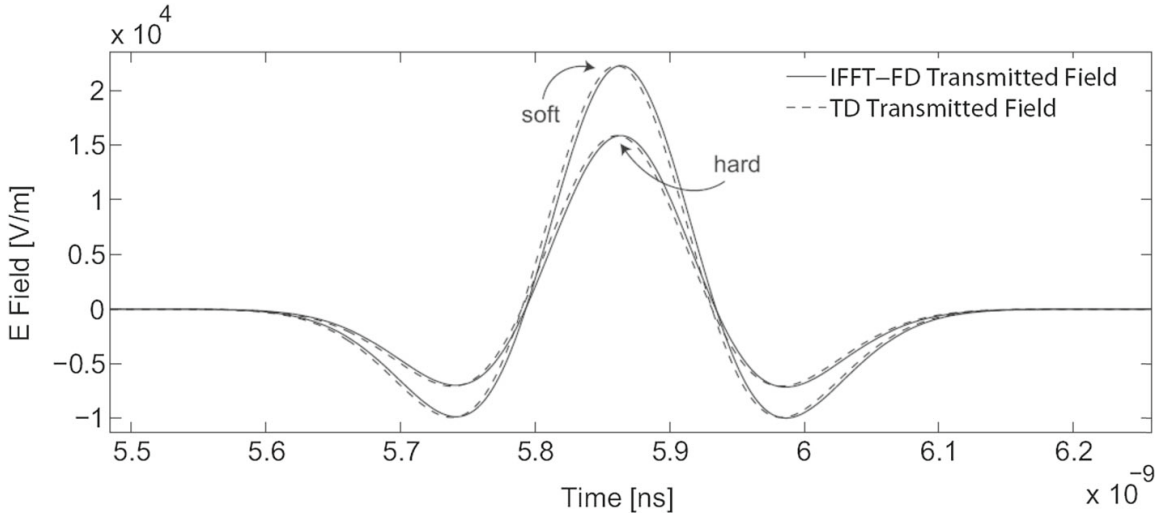

Fig. 5 Transmitted field through a low-loss multilayer wall with brick [33] and dry concrete [31]

the polarizations are in excellent agreement with corresponding IFFT of exact FD results, thus providing validation to the proposed TD solution. The Figs. 6 and 7 show transmitted field at the receiver for both the polarizations for different thickness of the multilayer wall with each layer having uniform thickness. The other dimensions such as height of the transmitter h_t, receiver height h_r, wall height h_w, distance of transmitter from the wall d_1 and distance of receiver from the wall d_5, are taken to be same as that for Figs. 4 and 5. It can be inferred that the results for soft and hard polarized fields come closer to each other as the thickness of the layers increases. Also the TD results match quite closely with the IFFT-FD results.

In all the results produced above, we have chosen the time step dt as 0.002 ns for the TD analysis and in case of IFFT-FD calculations, we used frequency step df as 0.0001 GHz. Corresponding to the chosen dt we took 5×10^6 frequency sample points to calculate the IFFT-FD transmitted field [39,40]. The software tool MATLAB 7.1 was used and all the cases were run on an Intel Core-i5 2.5 GHz computer, with 8 GB of RAM.

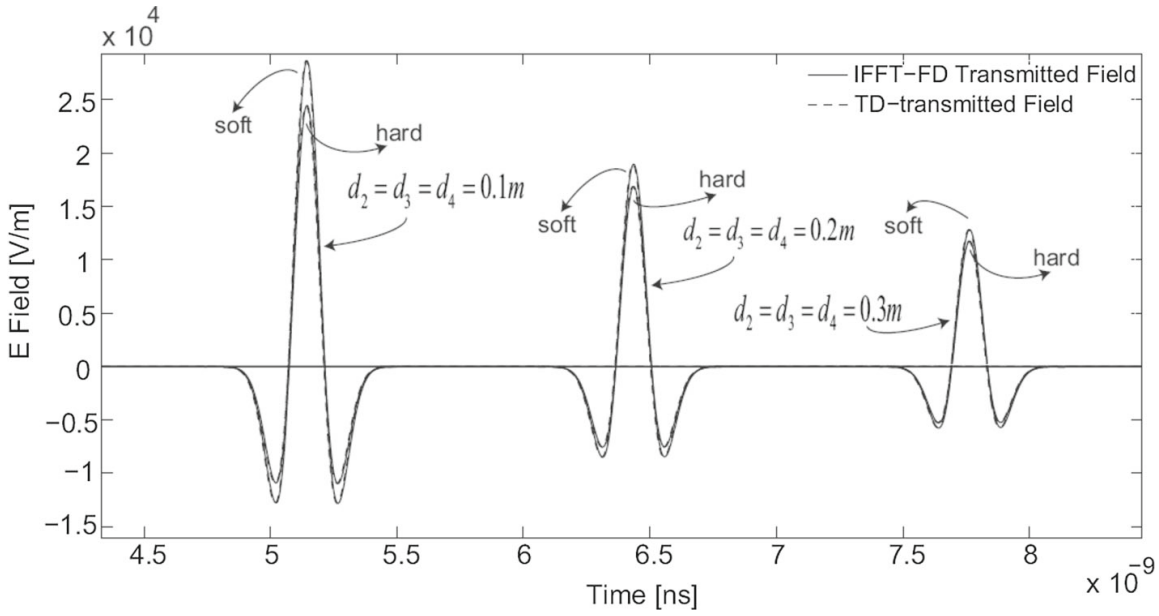

Fig. 6 Comparison of the transmitted field through a multilayer wall of different thickness, with first and third layers as drywall [28] and second layer as wood [31]

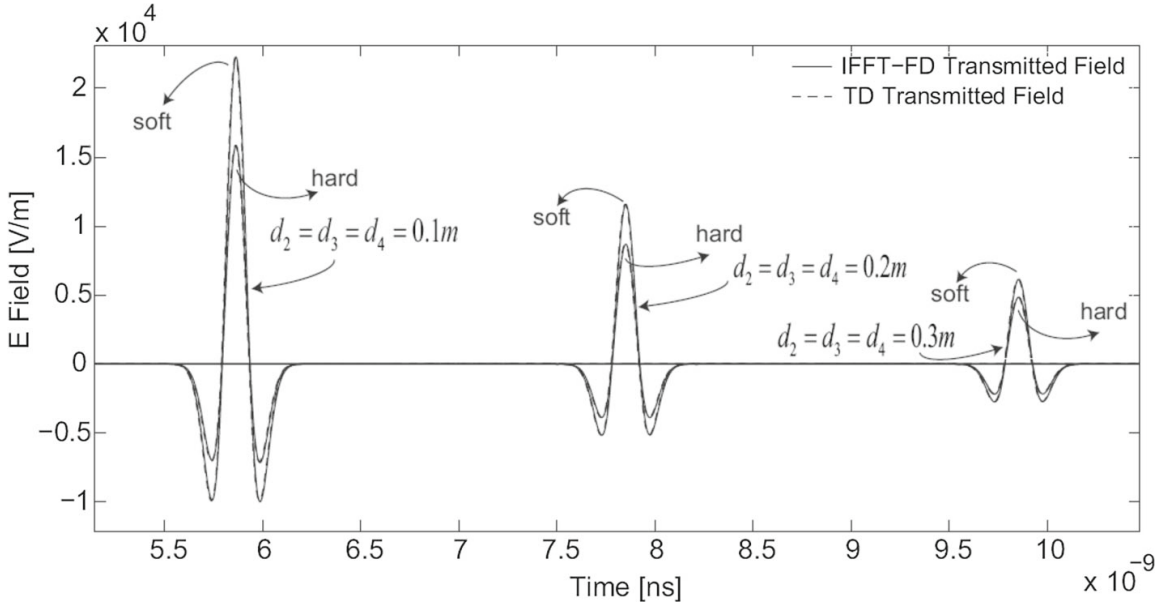

Fig. 7 Comparison of the transmitted field through a multilayer wall of different thickness, with first and third layers as brick [33] and second layer as dry concrete [31]

A comparison between the computation times of the IFFT-FD method and the proposed TD solution for Figs. 4 and 5 is presented in Table 3. The presented results in Table 3 establish that the proposed TD analysis is computationally very efficient in comparison to the IFFT-FD solution.

The two main reasons for such a significant reduction in the computational time in TD are: (i) the efficient convolution technique [39, Section 10.1, Fig. 10.1 and 10.2] due to which few number of time samples suffice to provide accurate results. (ii) Approximation of the multiple transmission paths in FD by a single effective path for low-loss dielectric case.

Given the excellent agreement between proposed TD solution and IFFT of FD solution, we can say that the proposed method is accurate for low loss-tangent values in the UWB

Table 3 Average ratios of the computation time of the two methods

Propagation profile	$T_{IFFT\text{-}FD}/T_{TD}$
Drywall–Wood–Drywall hard polarization	238.90
Drywall–Wood–Drywall soft polarization	244.71
Brick–Dry concrete–Brick hard polarization	250.09
Brick–Dry concrete–Brick soft polarization	229.12

bandwidth. Thus it is clear that for accurate prediction of the total received field past dielectric obstacles, for UWB signals, transmitted field is necessary to be accounted. The presented work also establishes that the proposed TD solution is computationally more efficient in determination of the transmitted field than the conventional IFFT-FD method.

6 Conclusion

An analytical TD solution has been presented for the transmitted field through the multi-layer wall structure made up of low-loss dielectric materials. Novel ray tracing algorithm is presented with error of an order of 10^{-5}. An analytical TD transmission and reflection coefficients are derived for soft and hard polarizations, for transmission through an interface between two low-loss dielectric mediums with different electrical properties. A deeper insight, based on the analytical FD formulations, obtained by extension of the established FD formulations from technical literature, is presented to explain the physical propagation mechanism of the transmitted field through the low-loss dielectric wall. The results of the proposed TD solution are validated against the corresponding IFFT-FD results. The proposed TD solution outperforms the IFFT-FD analysis in terms of the computational complexity and efficiency. The proposed TD solution and the in depth analysis of the underlying physical propagation mechanism during transmission of the UWB signals through walls of different dielectric materials, are supposed to be vital in the analysis of UWB communication as they provide a fast and accurate prediction of the total transmitted field in microcellular and indoor propagation scenarios.

References

1. Ghavami, M., Michael, L. B., & Kohno, R. (2004). *Ultra wideband signals and systems in communication engineering*. Chichester, UK: Wiley.
2. Yang, L., & Giannakis, G. B. (2004). Ultra-wideband communications: An idea whose time has come. *IEEE Signal Processing Magazine*, *21*(6), 26–54.
3. Hirt, W. (2003). Ultra-wideband radio technology: Overview and future research. *Computer Communications*, *26*(1), 46–52.
4. Muqaibel, A., Safaai-Jazi, A., Attiya, A., Woerner, B., & Riad, S. (2006). Path-loss and time dispersion parameters for indoor UWB propagation. *IEEE Transactions on Wireless Communications*, *5*(3), 550–559.
5. Karousos, A., & Tzaras, C. (2008). Multiple time-domain diffraction for UWB signals. *IEEE Transactions on Antennas and Propagation*, *56*(5), 1420–1427.
6. Porcino, D., & Hirt, W. (2003). Ultra-wideband radio technology: Potential and challenges ahead. *IEEE Communications Magazine*, *41*(7), 66–74.
7. Molisch, A. F. (2005). Ultrawideband propagation channels-theory, measurement, and modelling. *IEEE Transactions on Vehicular Technology*, *54*(5), 1528–1545.
8. Qiu, R. C., Zhou, C., & Liu, Q. (2005). Physics-based pulse distortion for ultra-wideband signals. *IEEE Transactions on Vehicular Technology*, *54*(5), 1546–1555.

9. Liu, P., Guo, J., Liu, J., Wang, J., & Long, Y. (2010). Multiple time-domain diffraction of plane waves by an array of perfectly conducting wedges for UWB signals. In *Proceedings of the IEEE international conference on microwave and millimeter wave technology, Chengdu* (pp. 1173–1176).
10. Attiya, A. M., & Safaai-Jazi, A. (2004). Simulation of ultra-wideband indoor propagation. *Microwave and Optical Technology Letters*, *42*(2), 103–108.
11. Barnes, P. R., & Tesche, F. M. (1991). On the direct calculation of a transient plane wave reflected from a finitely conducting half space. *IEEE Transactions on Electromagnetic Compatibility*, *33*(2), 90–96.
12. Kouyoumjian, R. G., & Pathak, P. H. (1974). A uniform geometrical theory of diffraction for an edge in a perfectly conducting surface. *Proceedings of the IEEE*, *62*(11), 1448–1461.
13. Veruttipong, T. W. (1990). Time domain version of the uniform GTD. *IEEE Transactions on Antennas and Propagation*, *38*(11), 1757–1764.
14. Rousseau, P. R., & Pathak, P. H. (1995). Time-domain uniform geometrical theory of diffraction for a curved wedge. *IEEE Transactions on Antennas and Propagation*, *43*(12), 1375–1382.
15. Zhou, C., & Qiu, R. C. (2007). Pulse distortion caused by cylinder diffraction and its impact on UWB communications. *IEEE Transactions on Vehicular Technology*, *56*(4), 2385–2391.
16. Capolino, F., & Albani, M. (2005). Time domain Double diffraction at a pair of coplanar skew edges. *IEEE Transactions on Antennas and Propagation*, *53*(4), 1455–1469.
17. Górniak, P., & Banduriski, W. (2008). Direct time domain analysis of an UWB pulse distortion by convex objects with the slope diffraction included. *IEEE Transaction on Antennas and Propagation*, *56*(9), 3036–3044.
18. Rousseau, P. R., Pathak, P. H., & Chou, H. T. (2007). A time domain formulation of the uniform geometrical theory of diffraction for scattering from a smooth convex surface. *IEEE Transactions on Antennas and Propagation*, *55*(6), 1522–1534.
19. Karousos, A., & Tzaras, C. (2007). Time-domain diffraction for a double wedge obstruction. In *IEEE antennas and propagation society international symposium, Honolulu, HI* (pp. 4581–4584).
20. Liu, P., & Long, Y. (2009). Time domain UTD-PO solution for multiple building diffraction for UWB signals. *IEEE Electronics Letters*, *45*(18), 924–926.
21. Han, T., & Long, Y. (2010). Time-domain UTD-PO analysis of a UWB pulse distortion by multiple-building diffraction. *IEEE Antennas and Wireless Propagation Letters*, *9*, 795–798.
22. Liu, P., Tan, J., & Long, Y. (2011). Time domain UTD-PO solution for the multiple diffraction of spherical waves for UWB signals. *IEEE Transactions on Antennas and Propagation*, *59*(4), 1420–1424.
23. Jong, Y. L. C. D., Koelen, M. H. J. L., & Herben, M. H. A. J. (2004). A building-transmission model for improved propagation prediction in urban microcells. *IEEE Transactions on Vehicular Technology*, *53*(2), 490–502.
24. Soni, S., & Bhattacharya, A. (2011). An analytical characterization of transmission through a building for deterministic propagation modelling. *Microwave and Optical Technology Letters*, *53*(8), 1875–1879.
25. Chen, Z., Yao, R., & Guo, Z. (2004). The characteristics of UWB signal transmitting through a lossy dielectric slab. In *Proceedings of the IEEE 60th vehicular technology conference, VTC 2004-Fall, 1, Los Angeles, CA, USA* (pp. 134–138).
26. Yao, R., Chen, Z., & Guo, Z. (2004). An efficient multipath channel model for UWB home networking. In *Proceedings of the IEEE radio and wireless conference* (pp. 511–516).
27. Qiu, R. C. (2004). A generalized time domain multipath channel and its application in ultra-wideband (UWB) wireless optimal receiver design–part II: physics-based system analysis. *IEEE Transactions on Wireless Communications*, *3*(6), 2312–2324.
28. Muqaibel, A., Safaai-Jazi, A., Bayram, A., Attiya, A. M., & Riad, S. M. (2005). Ultrawideband through-the-wall propagation. *IEE Proceedings-Microwaves, Antennas and Propagation*, *152*(6), 581–588.
29. Muqaibel, A., & Safaai-Jazi, A. (2008). Characterization of wall dispersive and attenuative effects on UWB radar signals. *Journal of the Franklin Institute*, *345*(6), 640–658.
30. Yun, Z., & Iskander, M. F. (2005). UWB pulse propagation through complex walls in indoor wireless communications environments. In *Proceedings of the IEEE international conference on wireless networks, communications and mobile computing* (Vol. 2, pp. 1358–1361).
31. Yang, W., Qinyu, Z., Naitong, Z., & Peipei, C. (2007). Transmission characteristics of ultra-wide band impulse signals. In *Proceedings of the IEEE international conference on wireless communications networking and mobile computing, Shanghai* (pp. 550–553).
32. Yang, W., Naitong, Z., Qinyu, Z., & Zhongzhao, Z. (2008). Simplified calculation of UWB signal transmitting through a finitely conducting slab. *Journal of Systems Engineering and Electronics*, *19*(6), 1070–1075.
33. Karousos, A., Koutitas, G., & Tzaras, C. (2008). Transmission and reflection coefficients in time-domain for a dielectric slab for UWB signals. In *Proceedings of the IEEE vehicular technology conference, Singapore* (pp. 455–458)

34. Tewari, P., & Soni, S. (2014). Time-domain solution for transmitted field through low-loss dielectric obstacles in a microcellular and indoor scenario for UWB signals. *IEEE Transactions on Vehicular Technology* (accepted).
35. Yahalom, A., Pinhasi, Y., Shifman, E., & Petnev, S. (2010). Transmission through single and multiple layers in the 3–10 GHz band and the implications for communications of frequency varying material dielectric constants. *WSEAS Transactions on Communications*, *9*(12), 759–772.
36. Remcom. (2008). Wireless insite, Site-specific radio propagation prediction software user's manual version 2.3.
37. Balanis, C. A. (1989). *Advanced engineering electromagnetic*. New York: Wiley.
38. Jing, M., & Nai-tong, Z. (2009). Transmission characteristics analysis of IR-UWB signal. In *Proceedings of the IEEE international conference on wireless and optical communication networks, Cairo* (pp. 1–5).
39. Brigham, E. O. (1988). *The fast fourier transform and its applications*. Englewood Cliffs, New Jersey: Prentice Hall.
40. Sevgi, L. (2007). Numerical fourier transforms: DFT and FFT. *IEEE Antennas and Propagation Magazine*, *49*(3), 238–243.
41. Grubisic, S., Carpes, W. P, Jr, Lima, C. B., & Kuo-Peng, P. (2006). Ray-tracing propagation model using image theory with a new accurate approximation for transmitted rays through walls. *IEEE Transactions on Magnetics*, *42*(4), 835–838.
42. Erdelyi, A., Magnus, W., Oberhettinger, F., & Tricomi, F. G. (1954). *Tables of integral transforms*. New York: McGraw-Hill, Bateman Manuscript Project.

Bajrang Bansal was born in Haryana, India. He received the B.E., degree in Electronics and Communication from Institute of Technology and Management, Gurgaon, India in 2005 and the M.Tech., degree in VLSI Design and CAD from the Thapar University, Punjab, India in 2008. Currently he is working toward the Ph.D. degree at Delhi Technological University, Delhi, India. His research interests include wireless channel modeling and UWB technology.

Sanjay Soni was born in UP, India on March, 1975. He received his Bachelor of Engineering in electronics engineering from Madan Mohan Malviya Engineering College, Gorakhpur in 1997, the M.Tech., degree in communication engineering from IIT Kanpur in 2004, and Ph.D. in wireless Communication Engineering from IIT Kharagpur in 2011. From 1998 to 2007 he was Assistant Professor in the department of Electronics and Communication engineering, G. B. Pant Engineering college, Pauri. From 2007 he joined IIT kharagpur as a Research Scholar to pursue his Ph.D. In 2010 he joined back to the same institute at the post of Associate Professor. At present, He is an Associate Professor in the department of Electronics and Communication in Delhi Technological University (Formerly Delhi College of Engineering). Currently, he is involved in teaching and research in the area of wireless communication. His research interest includes propagation modeling and characterization of wireless channel, time-domain analysis of propagation channel for UWB signals.

Case Study of the Nisarguna Based Biogas Plant Installed at Delhi Technological University

Mohit Gupta[*1], Aadish Jain[*2], P.K Jain[*3]

[*]Department of Mechanical Engineering, Delhi Technological University, Bawana Road, Delhi-110042

[1]mohitgupta2809@gmail.com(corresponding author)

[2]aadish.friend@gmail.com

[3]pdcej@yahoo.co.in

Abstract

The present study talks about the conversion of organic solid waste into useful biogas through the processes namely hydrolysis, acidogenesis, acetogenesis, methanogenesis and aerobic enrichment. Nisarguna technology enjoys an advantage of converting almost any type of organic solid waste over the conventional cowdung/ animal faeces based biogas plants. The reduction in the size of the plant has attracted many institutions to erect it in a rather confined space with less setup time and enhanced output. A similar plant has been installed at Delhi Technological University which handles 500 kg of organic solid waste per day aimed to supply the biogas to the university's canteen and research purposes. The output of the plant is nearly 60-65% biogas along with a high quality manure which is completely organic in nature. This paper talks about the technological aspects of such a plant and also stated the future scope through which the quality of biogas can be further improved and make the plant a multi-utility plant.

Keywords: Renewable Technology; Biomass; Organic solid waste; Green House gas; Compressed natural gas; Nisarguna Technology

Introduction

A Sensible renewable technology must be simple to understand, reliable in functioning and economical in production. Along with these properties if it helps in addressing some major problems of the urban areas of developing world then the technology becomes lucrative and can be more easily accepted.[1] The search for promising and renewable sources of carbohydrates for the production of biofuels and other bio-renewables has been stimulated by an increase in global energy demand in the face of growing concern

over greenhouse gas emissions, solid waste management and fuel security. In particular, interest has focused on lingo-cellulosic biomass as a potential source of abundant and sustainable feedstock for bio-refineries. Further, Solid waste management for the same biomass is a serious problem in the urban areas of a fast developing nation like India. With the rapid increase in urban population the problem is becoming more severe with every passing day. However the solution to the problem on the same scale is still at large.

It is believed that substituting various biofuels for fossil based fuels will reduce production of greenhouse gases as biofuels sequester carbon through the growth of the feedstock. The studies supporting this belief may have omitted the amount of carbon emissions that occur as farmers worldwide change cropland to replace the grain and divert to biofuels (estimate emissions from land-use change pattern) various studies found that corn-based ethanol, instead of producing a 20% savings, nearly doubles greenhouse emissions over 30 years and increases greenhouse gases for 167 years. Biofuels from switch-grass, if grown on U.S. corn lands, increase emissions by 50%. This result raises concerns about large biofuel mandates and highlights the value of using waste products.[5]

Converting forests, peatlands or grasslands to produce food crop–based biofuels creates a "biofuel carbon debt" by releasing 17 to 420 times more CO2 than the annual greenhouse gas (GHG) reductions that these biofuels would provide by displacing fossil fuels. Whereas, biofuels derived from waste biomass incur little or no carbon debt and can offer immediate and sustained GHG advantages.[4]

Biomass such as cattle dung, agriculture wastes and other organic wastes provide a vast scope to convert these sources into biogas. Biogas production is a clean low carbon chain technology which converts fermentable organic wastes into cheap, versatile as well as clean fuel and organic soil conditioner. Biogas produced by anaerobic digestion of mentioned organic matters and biomass wastes can be used as an energy source for various applications such as cooking, heating, space cooling/ refrigeration, electricity generation and gaseous fuel for vehicular application[6].

India is implementing one of the World's largest programme in renewable energy.

The country ranks second in biogas utilization. Unlike Solar energy Biogas can be generated and supplied round the clock and is immune to the problem of intermittent availability if planned adequately. Biogas plants provide one solution for concerns such as fuel, organic soil conditioner and waste management.

Bio-methanation process of converting waste biomass into gaseous fuel is superior and a sustainable process in comparison to general practice of burning waste which produces pollutant, ash and hence needs to be preferred for such biomass materials that can be processed in biogas plants.

Vipul and Shivangi of Delhi Technological University[7] have already conducted a study for feasibility of a Biogas plant in Campus and proposed 3 digesters of 1000 liters each to cater to the food waste at the campus. They suggested digesters to be placed near kitchen as food waste can be directly used as feedstock and calculated a potential of 650 lit of biogas daily in 1000 lit reactor, under ideal conditions [7](like maintaining pH, VFA, Alkalinity, etc.) and also concluded that biogas from food waste can save at least 50 % of the LPG(9-10 cylinders/day) gas consumption of the campus and also provide substantial amount of manure for gardening purposes in the campus.

Functional principal:

A Biogas plant based on this Nisargruna technology digest all kinds of organic solid wastes comprises mainly of long organic polymer chains such as carbohydrates, fats and proteins in presence of Biocatalysts. First of all the waste is separated to make sure that no non-biodegradable material is left and processed to make slurry. The waste is then passed through the aerobic and anaerobic processes. The end products consist of biogas, carbon dioxide, water vapour and very good quality weed free manure. Recovery of nearly 70% of water can be made by recycling at the end of the process[8].

Description

The whole process of converting biomass to biogas is through 5 steps namely

1. **Hydrolysis**
2. **Acidogenesis**
3. **Acetogenesis**
4. **Methanogenesis and**
5. **Aerobic Enrichment.**

1. **Hydrolysis:** As we feed the digester at first the mass has to go through hydrolysis. During this

process long organic polymer chains breaks down to smaller parts such as simple Sugars, Amino and fatty acids. Molecules such as volatile fatty acid are first catabolized to smaller compounds.

2. **Acidogenesis :** Fermentation of the remaining components by Fermentative Acidogenic Bacteria occurs and fatty acids, ammonia and carbon di oxide are produced along with some other by-products. This biological breakdown towards smaller chains is also known as Acidogenesis.

3. **Acetogenesis:** The third stage anaerobic digestion. Here simple molecules created through the Acidogenesis phase are further digested by acetogens to produce largely acetic acid as well as carbon dioxide and hydrogen.

4. **Methanogenesis :** The final stage is Methanogenesis, during this stage Methanogenic bacteria (methanogens) utilizes the products formed in the earlier stages to give Methane, Carbon di oxide and some water-vapour which is mainly the Bio Gas. These methanogens act between a certain range of pH only i.e. pH level should be maintained from 6.5 to 8 for the process to occur.

5. **Aerobic Enrichment :** The treated non-digestible overflow from this digester tank which is not digested by the bacteria is aerobically enriched and is converted to high quality manure.

The earlier Biogas plants conventionally used cow dung/ animal focus as primary or only fuel and required regular supply of feed stock and water for longer durations which made biogas plants unattractive for investment. But recent developments and introduction of Nisarguna, the plants can run on nearly all type of solid bio waste such as Kitchen waste, spoiled or left over food, all kinds of bio oils, used cooking oil, extracted tea powder, used flowers or leaves, gardening waste etc. and the whole process can be completed in time period of as low as 1 day for small scale plants. With introduction of this technology minimum required size of the plant is greatly reduced. This has given freedom of selection of size of the plant required and has also attracted many institutions to invest in biogas as size is the main economic factor for such kinds of plants.

Some important components of the system:

1. **Receiving / Sorting /Mixing platform:** Steel platform prefabricated & installed at some height. It holds mixer.

2. **Mixer:** Motor driven mixer is specially fabricated in M.S. and S.S. top for loading of waste and is connected to control panel with necessary electrical wiring and fixers

3. **Thermophilic Aerobic Bioreactor**: Digester with manholes , inlet and outlet holes working with compressor and solar water heater, constructed in mild steel with acid proof & rust proof two coats of red oxide and two coats of oil paint, connected to main digester with coated pipe (Total effective Capacity). Major amount of carbon-di-oxide is released in this tank. And the contents are tranfrered to Anaerobic Digestor.

4. **Anaerobic Bioreactor:** Has a dome on top for coaction of released methane gas, constructed in mild steel with acid proof & rust proof two coats of red oxide and two coats of oil paint coating, connected to slurry handling system with coated pipes. Accessories such as pressure control valves, partition walls along with methane recycling grids and various other smaller components with equal importance are also connected to this tank.

5. **Gas Holder :** Thick Mild Steel dome with necessary supports of angles and brackets surface finished with rust proof Coating & two coats of red oxide and two coats of oil paint and Gas outlet.

6. Water pump, Compressor, Air and Water Injection, non-return valves and fittings, Control panel, Gas meter, Gas measuring equipment, Dome Balance system for balancing dome are also part of the standard equipment.

Output of the plant:

Description	**Quantity**
Capacity of Digester	**500 kg / Day**
Biogas Produced	**40-60 m^3 / Day**
CO_2 Produced	**50-60 m^3 / Day**
Manure Produced	**40 – 80 kg / Day**

1. Primary output is Bio gas (i.e. around 60-65% biogas 35-30% carbon di oxide along with some water vapors and H_2S gas), can be directly used as cooking gas which burns with clear blue flame and gives out high energy.
2. Although secondary but the digester waste or spent slurry is very good quality manure which is 100% organic in nature. This 100% organic manure has good concentration of stable carbon which will help soil in improving microbial activity, nitrogen fixation, water retention and soil fertility and can be used in gardens or potted plants.

Benefits from the plant:

1. 100% recycling of organic / bio waste: with the freedom of putting any organic matter to the digester and get organic manure and high grade biogas and no other by product.
2. Treatment of waste locally at source reduces the load on Municipal corporations.
3. This type of system can be installed on individual or cooperative basis by hotels, chains or restaurants, malls, group of small eateries in a region and can get cooking gas without having to worry about the waste disposal.
4. Reduced dependence on petroleum based resources.
5. Highly environment friendly as the waste will eventually degrade on landfill site and release the products to the environment and water may seep and pollute underground water is now being channelized to produce energy and other resources.
6. Reduction in Green House Gas emissions can help government to earn carbon credits.

Conclusion:

The process of composting, biogas generation has been know from very early times. NISARGRUNA biogas technology has accelerated the Biomethanation process which has reduced the time taken for the biodegradation of the bio mass and could be a potentially a good solution for the problem of solid waste management. Methane on one hand has high calorific value is also very lethal as Green House Gas (i.e. nearly 21 times more than CO_2) which is generally released in the environment if waste goes to land filling sites along with carbon dioxide

Future Scope:

Biogas may serve as fuel for India as India is an agricultural economy and large amount of biomass as waste is available. This certainly gives biogas an edge to become the fuel for the cause of economic growth and Energy Security. Technologies must be established for production, Bottling / storage, transporting of biogas in a decentralized manner.

Further, Biogas has nearly 65% of methane and enrichment processes can be applied to make it equivalent to Compressed Natural Gas (CNG) and the infrastructure for CNG is already well established and thus will not incur any new cost in this regard and Bio-methane could replace CNG as fuel for transportation etc.

References:

[1.]M. Samer, Biogas Plant Constructions, Cairo University, Faculty of Agriculture, Department of Agricultural Engineering, Egypt

[2.]Interim Technical Report, AFBI Hillsborough ,27 Months Performance Summary For Anaerobic Digestion Of Dairy Cow Slurry, Peter Frost And Stephen Gilkinson June, 2011

[3.]Christian Müller, Anaerobic Digestion of Biodegradable Solid Waste in Low- and Middle-Income Countries Overview over existing technologies and relevant case studies Dübendorf, 2007

[4.]Joseph Fargione, Jason Hill, David Tilman, Stephen Polasky, Peter Hawthorne, Land Clearing and the Biofuel Carbon Debt, 2008

[5.]Timothy Searchinger, Ralph Heimlich, R. A. Houghton, Fengxia Dong, Amani Elobeid, Jacinto Fabiosa, Simla Tokgoz, Dermot Hayes, Tun-Hsiang Yu, Use of U.S. Croplands for Biofuels, Increases Greenhouse Gases Through Emissions from Land-Use Change, 2008

[6.]Biogas Generation, Purification And Bottling Development In India – A case study

[7.]Vipul Vaid and Shivangi Garg, Food as Fuel : Prospects of Biogas Generation from Food Waste, IJAFST,ISSN No. 2249-3050, Volume 4 No. 2 (2013) 68.

[8.]http://www.barc.gov.in/technologies/kitchen/kitchen_br.html

CONCEPT OF HEAT EXCHANGER INSIDE ROOF OF BUILDINGS: AN APPROACH TO SAVE WASTED ENERGY

Sandeep Tripathi

Department of Aeronautical Engineering, Feroze Gandhi Institute of Engg. and Tech., Raebareli, Uttar Pradesh, (India)

ABSTRACT

To decrease the expenditure of non - renewable resources we have to approach towards a renewable energy system which utilizes the energy wasted by us. To utilize the solar energy accumulated during the daytime, this concept is introduced. This implementation of Heat Exchanger will provide an added advantage to the other conventional solar radiation collectors. These heat exchangers will be in the form of metallic pipes embedded inside the roof during its construction. They will be distributed in a regular pattern such that we get maximum rate of heat transfer. The proposed work is concerned with the procedures for the setup of this system and to analyze its performance. In the technical section heat transfer rates are calculated which determine the temperature upto which water will be heated in this system. Many previous researchers have proposed equivalent concept but most of them have done experiments on a particular portion of the roof by using metal reinforced concrete collectors. This renewable energy system will expand and apply their concept to the entire roof.

Keywords: Heat Exchanger, Metallic Pipes, Renewable Energy System, Roof, Water.

I. INTRODUCTION

With recent advancements in science and technology, we have got better ways to utilize solar energy. Devices like solar panel, solar cooker, solar water heater etc. have proved that we can save most of the non-renewable sources of energy by using a renewable energy system. My paper deals with the concept of heat exchangers inside the roof of buildings. These heat exchangers are basically metallic pipes which will be used for solar water heating. At noon , the temperature of upper surface of the roof is around 55°C, which can be used to heat water upto that temperature and can save LPG's or coal required for the same purpose. The heat exchangers we use are a kind of solar water heater where the metallic pipes are spread through the roof in a regular manner. This raises the temperature of water which flows in the pipe. The main aim is to save those resources which are non-renewable and apply a renewable energy system for a particular purpose. For example, we mostly use LPGs to boil water for household purposes which could be saved and energy which goes waste can be utilized in an optimized way. In this research the objective is to explain how to use this system, advantages and applications of this system. The technical analysis is performed considering some assumptions and includes the heat transfer method and whole description of material, dimensions of roof and pipe, and temperature details at any particular phase.

II. THEORY AND PROCEDURE

This analysis involves all three processes of heat flow which are conduction, convection and radiation. All aspects of heat flow contribute in saving the wasted energy. The result is determined by finding the final temperature of water at the outlet. This temperature also determines how much this system is economically stable.

It will be done in four stages:

- Above the roof
- Through the roof
- Between roof and pipe
- Between pipe and water

The sectional view of roof with pipes is given in Fig 1. The inlet and outlet of pipe is shown along with cross section of roof. The inside pattern is the proposed design of pipe to act as heat exchanger. More number of curves in the pipe will increase its surface area and more heat transfer will take place.

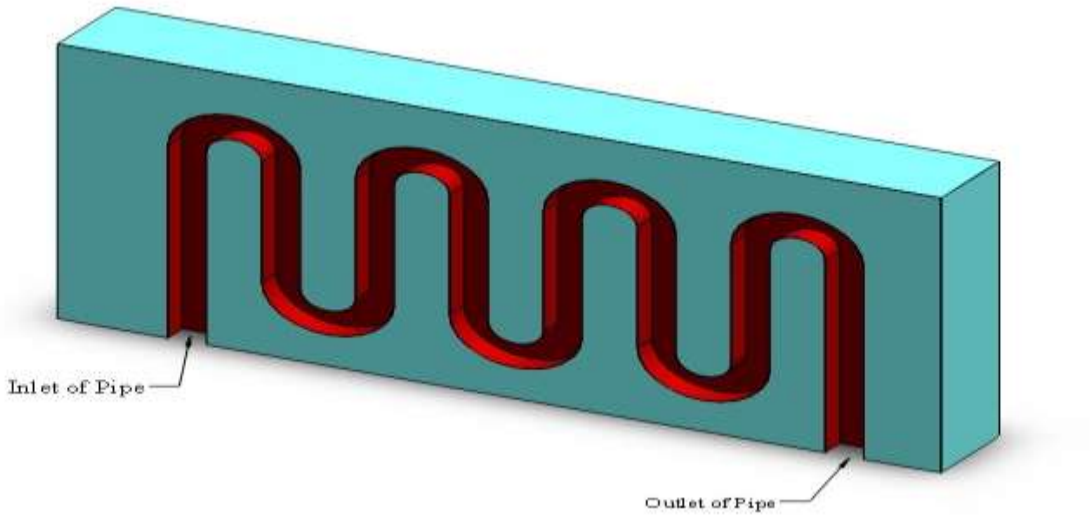

Fig 1. Sectional view of roof with pipe

Each stage is studied separately with some assumptions:

- The flow of heat is unidirectional.
- Steady state heat flow.
- No other internal heat generated source.
- No external equipment is used.
- Constant temperature all over the roof.

The study of stages of heat flow is given below:

2.1 Above the Roof

This is part of the system which is under direct exposure to sun. The phenomenon of heat flow over the surface of roof is only due to solar radiation. Since there is atmosphere between sun and roof so temperature of upper surface can't be determined directly. This temperature will be determined by considering a suitable atmospheric model. In this section we will determine the rate of heat flow Q which will lead the analysis to further stages.

2.2 Through the Roof

This phase considers conduction as the phenomenon of heat flow. If $T1$ and $T2$ are temperatures of upper and inner surface then by using Fourier's Heat conduction equation, $T2$ is calculated.

$$Q = \frac{k \times A \times (T1 - T2)}{t1} \quad (1)$$

where Q is rate of heat flow in watts, k is thermal conductivity of concrete in watts per meter per °C and $t1$ is thickness of upper slab over the pipe.

2.3 Between Roof and Pipe

Since the pipe is fully covered with concrete all around so we can neglect air resistance caused due to voids. It can be assumed that temperature of lower surface of roof will be approximately equal to temperature of upper surface of pipe.

Let $T3$ = temperature of upper surface of pipe

The heat flow through pipe from upper to inner surface will be through conduction. If $T4$ is temperature of inner surface of pipe then it can be calculated by using Fourier's Heat conduction equation for a cylinder which is:

$$Q = \frac{2\pi . k . L_c (T3 - T4)}{\ln \frac{r2}{r1}} \quad (2)$$

where Q is heat flow through cylinder in watts, k is thermal conductivity of metallic pipe in watts per meter per °C, $r1$ and $r2$ are inner and outer radius of pipe and L is length of pipe.

The temperature of inner surface of pipe plays an important role as this surface is in direct contact with water.

2.4 Between Pipe and Water

Since water is flowing inside the pipe so the heat flow from pipe to water is a mixed phenomenon of conduction as well as convection. So Nusselt's number is calculated to find convective heat transfer coefficient of water. This will include formation of boundary layer (both hydrodynamic and thermal) on inner surface of pipe.

Firstly, Reynolds number will be calculated which will help to determine type of flow of water. Then prandtl number is calculated at $T4$, temperature of inner surface of pipe.

Now it depends on flow that how Nusselt's number will be calculated and what kind of analysis will be performed. But convective heat transfer coefficient will be calculated from

$$Nu = \frac{h \times Lc}{k} \quad (3)$$

where Nu is Nusselt's number, h is convective heat transfer coefficient, k is thermal conductivity of water and Lc is characteristic length.

The final temperature of water is calculated by applying the theory of heat exchanger. If $T5$ is temperature of inlet of water and $T6$ is temperature of outlet of water then Fig 2 depicts the flow diagram of hot and cold fluid.

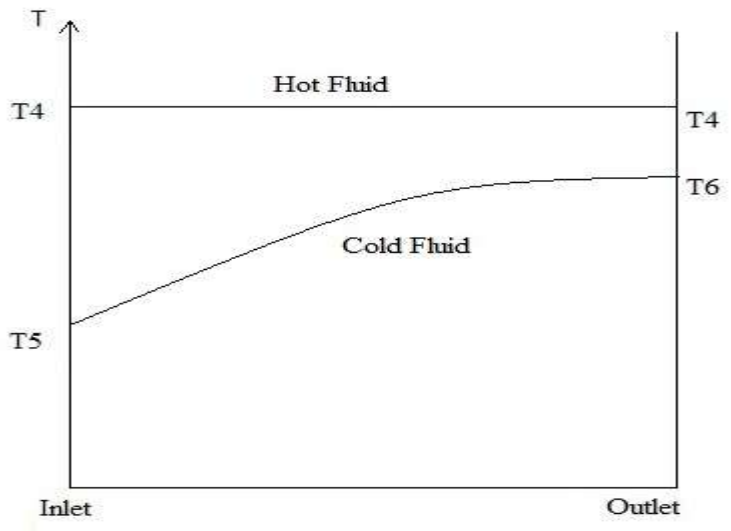

Fig 2. Flow Diagram of Hot and Cold fluid

Here we use LMTD (Logarithmic Mean Temperature Difference) method to calculate final temperature of water.

$Q = h \times A \times \theta m$ (4)

where $\theta m = \frac{\theta 1 - \theta 2}{\ln \frac{\theta 1}{\theta 2}}$ (5)

$\theta 1 = T4 - T5$ (6)

$\theta 2 = T4 - T6$ (7)

From these methods we will calculate $T6$ and finally calculate profit gained and try to maximize it by changes in system and methods to calculate this temperature.

III. DISCUSSION AND RESULTS

The above procedures are based on some assumptions. These assumptions helped to break the analysis into three simple heat transfer modes which were then sequentially analyzed. Without the assumptions the analysis would require numerical computation. In real we have to make a thermal model with these stages and solve them to produce results that can benefit the society from this system. If this system works then we can save most of money spent on non- renewable resources.

IV. ADVANTAGES AND DISADVANTAGES

All systems have some advantages and disadvantages. The advantages of this system are given below:

a) This system has a higher degree of reliability and durability.

b) Due to use of non- corrosive metallic pipes the chances of corrosion are reduced.

c) By using this system, convection of heat in the room just below the roof could be avoided and as a result the internal room temperature will drop.

The disadvantages of this system are:

a) This system is not very efficient in the days of winter or cloudy days.

b) The profit gained by installation of this system varies according to dimension of roof and quantity of water boiled by this system.

V. CONCLUSION

In the age of globalization, there is demand of inexpensive systems with better performance and the above given system meets this criteria. Further studies regarding flow of water inside pipe, concentration of heat can be done to produce a more efficient and optimized system. If analysis is performed regarding variation in material of pipe used, arrangement of pipe inside the roof, and dimensions of pipe, then better results could be produced which can be compared for efficiency and helps consumer to choose a system according to his/her choice. The main aim is to utilize as much solar energy as possible and save the environment from global warming. This system helps in reduction of global warming by absorbing heat on roofs in such a way that radiation of heat back in the atmosphere reduces.

VI. ACKNOWLEDGEMENT

I am grateful to Mr Vivek Dwivedi and Mr Anikesh Tripathi both professors of Department of Mechanical Engineering, Uttar Pradesh Technical University for their early discussions regarding this topic. I am also thankful to my colleague Priyam Srivastava who provided his contribution towards the analysis of this research paper. Mr Afraz Khan and Mr Shivom Gupta assisted me to think creatively and kept me motivated throughout this endeavour.

REFERENCES

[1] Yunus A. Cengel **"**Heat Transfer: A Practical Approach**" 2nd Edition, Published 2002**

[2] R.H. Turner, Concrete Slabs as winter solar collectors, *ASME solar energy conference, page no. 9-13.*

[3] S. V. Bopshetty, J. K. Nayak, S. P. Sukatme, Performance Analysis of Solar Concrete Collector, *Energy Converse. Manage, 33(11), 1007-1016.*

[4] P. B. Chaurasia, Solar water heaters based on concrete collectors, *Energy, 33(11),1007-1016*

[5] M. Sokholof and M. Reshef, Performance Simulation of Solar Collectors made of concrete with embedded Conduit Lattice, *Solar Energy,48(6),403-417.*

[6] M. Hazami, Performance of Solar storage Collector, *Desalination, 183,167-172.*

[7] Kore S.S & Sane N.K,Experimental Investigations Of Heat Transfer Enhancement From Dimpled Surface In A Channel, *International Journal Of Engineering Science & Technology, 6227-6334.*

[8] D. Antoni M, Saro O Massive Solar-Thermal collectors-A critical literature review Renewable and Sustainable Energy Reviews, 16, 2012.

[9] R. Sarachitti Thermal performance analysis and economic evaluation of roof integrated solar concrete collector Energy and buildings, 43 (2011).

[10] B.A.Jubran, M.A.Al-saad, N.A.AbuFaris Computational evaluation of solar heating systems using concrete collectors Energy conversion and management. 35, (12), 1994.

DESIGNING A CAPACITIVE MICROMACHINED ULTRASONIC TRANSDUCER CELL FOR HIGH FREQUENCY APPLICATIONS

Sunita Malik[1], Manoj Duhan[2], Archana Chhikara[3]

[1, 2, 3] *Electronics and Communication Department,*

Deenbandhu Chhotu Ram University of Science & Technology, Murthal (Sonepat), Haryana, (India)

ABSTRACT

This paper highlights the design of a high fill factor Capacitive Micro machined Ultrasonic Transducer (CMUT) cell having a high resonance frequency. Two models of CMUT are simulated simultaneously; one with circular membrane and other with a hexagonal membrane. These two models are analyzed for four parameters namely resonance frequency, collapse voltage, capacitance change and fill factor. Hexagonal membrane cell have a high fill factor for similar dimensions as the circular membrane. The other three parameters of the two models differ with in an acceptable range. This paper establishes that hexagonal membrane cells can replace the existing CMUT cells due to their high fill factor. It will serve as a basis for designing CMUT arrays with hexagonal membrane in near future.

Keywords: CMUT, Collapse Voltage, Fill Factor, Hexagonal Membrane, Resonance Frequency.

I. INTRODUCTION

Ultrasonic technology is a powerful tool with application in medical diagnostic, industrial process control, environment control, non destructive testing etc. While piezoelectric transducers are dominant, capacitive micromachined Ultrasonic transducers are being explored as a complementary technology. CMUT is based on electrostatic principle for its working and have a large number of advantages like impedance matching with surrounding, larger bandwidth, good capability to make high frequency arrays, ability to integrate with electronics, low cost for mass production, high pressure sensitivity, rapid response to changing pressure, can withstand lot of vibrations and low temperature sensitivity [7]. It is basically a parallel plate capacitor, voltage applied on one electrodes and other is grounded. Movement of the plates generates ultrasonic waves during transmission and change in capacitance is detected during reception.

II. DEVICE DESCRIPTION

CMUT consists of two plates; ground plate being fixed while voltage is applied on the movable plate. The vibrations in the movable plate will surround medium and conversely ultrasonic wave's causes a change in capacitance by displacing the movable plate [6].

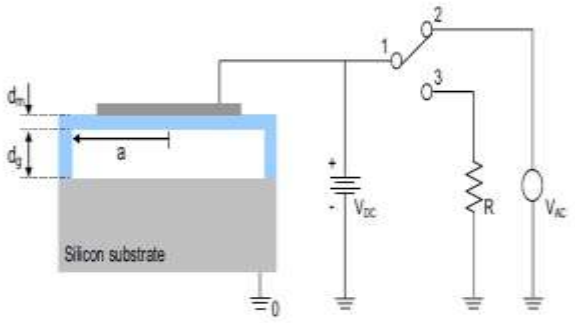

Fig.1 CMUT Schematic

When switch is at position 2, AC voltage is superimposed on the DC voltage which makes the membrane to vibrate and generate an ultrasonic wave and device works as a transmitter and at switch position 3, DC voltage is only applied to the device and device works as a receiver [8]. Ultrasonic waves cause a change in capacitance between the plates which is detected at the output.

The CMUT cell can work both in the collapse mode and the conventional but for better results it is operated in the collapse mode [5]. A complete ultrasonic transducer consists of many single cells of CMUT connected in parallel to achieve desirable acoustic pressure during transmission and high sensitivity during reception [6].

III. PARAMETERS DISCRIPTION

3.1 Resonance Frequency

CMUT needs to work at resonance frequency to get best possible ultrasound output during transmission and high sensitivity during reception and therefore it become an important design parameter.

For a circular membrane of radius 'a' and thickness 'd_m' it is given by [8]:

$$f_r = \frac{0.47\, d_m}{a^2}\sqrt{\frac{E}{\rho(1-\sigma^2)}} \qquad (1)$$

Where, E is young's modulus, ρ is density and σ is Poisson ratio of membrane material.

Here in (1) internal stresses are not considered only membrane dimensions and material properties determines the resonance frequency.

3.2 Collapse Voltage

At collapse voltage electrostatic force overcomes the internal restoring force of the membrane and membrane collapses to the bottom electrode [3].

For a membrane, collapse voltage is given by:

$$V_{collapse} = \sqrt{\frac{8k\,d_0^3}{27A\epsilon_0}} \qquad (2)$$

Where, k is spring constant of membrane, d_0 is original cavity gap, ϵ_0 is permittivity of free space and A is overlapping area of CMUT parallel plates.

CMUT membrane collapses when displacement of upper plate is equal to $d_0/3$ [9] and applied voltage must always be less than collapse voltage of the membrane.

3.3 Capacitance Change

The capacitance of CMUT varies to the parallel plate arrangement and is given by [3]:

$$C_0 = \frac{\epsilon_0 A}{[d_0 - x(t)]} \qquad (3)$$

Where, A is overlapping area of parallel plates, is permittivity of free space, d_0 is original cavity gap and x t) s displacement of membrane of CMUT.

3.4 Fill Factor

CMUT basically consists of a number of individual cells. These cells need to be arranged on a wafer and this arrangement creates dead or inactive areas which reduces the power of ultrasonic transducer [2]. This area coverage is defined by the fill factor which in turn is determined by the area coverage of support walls and geometry of CMUT cell [4].

For circular membrane cell, fill factor is given by:

$$FF = \frac{\pi a^2}{p^2 \sin 60} \qquad (4)$$

Where a and p are respectively radius and pitch of the CMUT membrane.

Similarly for hexagonal membrane, it is given by:

$$FF = \frac{6a^2 \tan 30}{p^2 \cos 30} \qquad (5)$$

Where a and p are respectively side and pitch of hexagonal membrane.

IV. DESIGN PARAMETERS

Designing of any device starts with the choice of material. Here during simulation silicon nitride is used as membrane material due to its advantages like excellent ionic and water barrier, highly selective etch rate, high tensile strength etc and gold as electrode material due to its number of advantages like good electrochemical inertness, ease of fabrication in different forms etc [1], [11]. Using these materials two models of CMUT were simulated, one with circular and other with hexagonal membrane; dimensions of these are given below in table I.

TABLE I DESIGN PARAMETERS

	Model 1	**Model 2**
Membrane Shape	Circular	Hexagonal
Electrode Shape	Circular	Circular
Membrane radius/side (µm)	10	10
Membrane Thickness (µm)	1	1
Electrode radius (µm)	5	5
Electrode Thickness (µm)	0.25	0.25
Cavity gap (µm)	1	1

V. RESULTS

Two models were simulated using finite element analysis (FEA) tool. 13940 elements are generated for finite element analysis. Resonance frequency for model 1 is 99.6 MHz and for model 2, it is 100.8 MHz; which is only

1.4% greater than the other. This difference in resonance frequency is due to their shapes, which differs the loading of these two membranes.

The collapse voltage of the membrane is calculated by plotting a graph of applied voltage vs. membrane displacement and using the fact that a membrane collapses when its displacement is $d_0/3$ [9]; d_0 being the initial cavity gap i.e. gap between the two electrodes of CMUT.

The collapse voltage for model 1 is 10500 V while for model 2 it is 10510 V. This difference is due to different values of von Mises stress developed in two membranes. Collapse Voltage of two membranes is shown in figure 2 below.

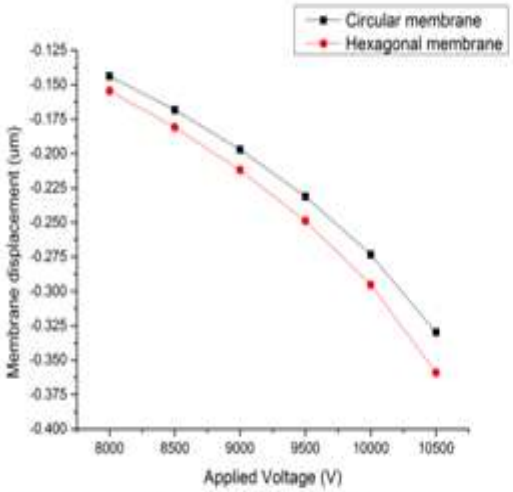

Fig. 2. Collapse Voltage of Two Membranes

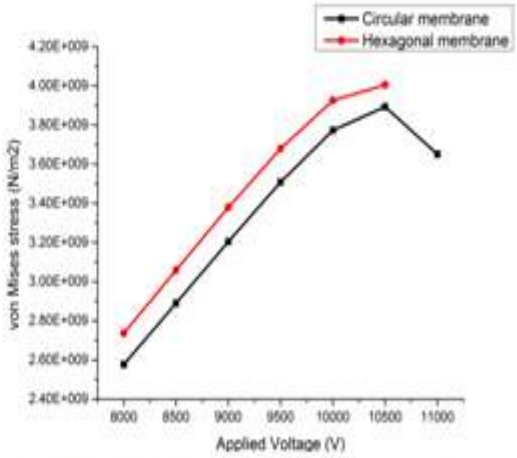

Fig. 3 Von Mises Stress Developed In Two

The variation of the von Mises stress with applied voltage is shown in figure 3. The stress developed in hexagonal membrane is more which decreases its collapse voltage. Stress achieves a maximum value at collapse voltage and then decreases.

The capacitance change at collapse voltage for model 1 is 3.788 E-15 and 3.212 E-15 for model 2. Fill factor calculated for circular membrane using equation 4 is 0.87 and for hexagonal membrane it is 0.96 as per equation 5. Hexagonal membrane cells have a better fill factor by almost 10% than circular membrane cells.

All these parameters are summarized in table II below.

Table II CMUT Cell Parameters

	Model 1	**Model 2**
Membrane Shape	Circular	Hexagonal
Resonance Frequency (MHz)	99.6	100.8
Collapse Voltage (V)	10500	10100
Capacitance Change (F)	3.788 E-15	3.212 E-15
Fill Factor	0.87	0.96

VI. CONCLUSION

Two models of CMUT with a circular and hexagonal membrane are characterized successfully. Hexagonal membrane CMUT cell have a high fill factor of 0.96. A high resonance frequency of almost 100MHz is achieved

for both the membranes. These CMUT cells can be fabricated using surface micro machining or wafer bonding technique. Wafer bonding technique is preferred due to its less process steps, which makes the device time and cost effective. Further a hexagonal cell CMUT array can be built and analyzed; which can be fabricated further.

REFERENCES

[1] Tai-Ran Hsu, "MEMS and Microsystem: design, manufacture and nanoscale engineering", 2nd edition, John Wiley and Sons, 2008, pp. 245-281.

[2] P. M. Morse and K. U. Ingard, "Theoretical Acoustic",. New Jersey, McGraw-Hill Inc.

[3] Archana Chhikara and Sunita Malik, "Parameters affecting performance of Capacitive Micro machined Ultrasonic Transducer (CMUT)," International Journal of Applied Science and Engineering Research, vol. 3(2), April 2014, pp 333-338, Doi: 10.6088/ijaser.030200003.

[4] Ahmet Murat Cetin and Baris Bayram, "Diamond-Based Capacitive Micromachined Ultrasonic Transducers in Immersion", IEEE Transactions on Ultrasonics, Ferroelectrics, and Fr 414 equency Control, vol. 60, no. 2, February 2013.

[5] Kwan Kyu Park, Omer Oralkan and Butrus T. Khuri-Yakub, "A Comparison Between Conventional and Collapse Mode Capacitive Micromachined Ultrasonic Transducers in 10-MHz 1-D Arrays," IEEE Transactions on Ultrasonics, Ferroelectrics, and Frequency Control, vol. 60, June 2013.

[6] Robert Wodnicki, Charles G. Woychik, Albert T. Byun, Rayette Fisher, Kai Thomenius, Der-Song Lin et. al., "Multi-Row Linear CMUT Array Using CMUT and Multiplexing Electronics," in IEEE International Ultrasonics Symposium Proceedings, 2009.

[7] Anil Arora, Ram Gopal, V. K. Dwivedi, Chandra Shekhar, Babar Ahmad, P.J George et. al. "Fabricating Capacitive Micromachined Ultrasonic Transducers with Wafer Bonding Technique," Sensors & Transducers Journal, vol. 93, pp. 15-20, 2008.

[8] Serena H. Wong, Mario Kupnik, Kim Butts-Pauly, and Butrus T. Khuri-Yakub, "Advantages of Capacitive Micromachined Ultrasonics Transducers (CMUTs) for High Intensity Focused Ultrasound (HIFU)", IEEE Ultrasonics Symposium, 2007.

[9] M.F. Teng and A. J. Hariz, "Characterisation and Modelling of MEMS Ultrasonic Transducers," Institute of Physics Publishing, vol. 34, pp. 949-954, 2006.

[10] Arif S. Ergun Goksen G. Yaralioglu and Butrus T. Khuri-Yakub, "Capacitive Micromachined Ultrasonic Transducers:Theory and Technology", Journal of Aerospace Engineering, April 2003.

[11] Kurt E. Petersen, "Silicon as a Mechanical Material", Proceedings of the IEEE, Vol.70 (5), May 1982.

EFFECTS OF PARAMETERS ON PERFORMANCE OF EARTH AIR HEAT EXCHANGER SYSTEM (EAHE): A REVIEW

Dheeraj Sardana[1], Rishi kumar[2], Snehal S Patel[3], Gaurav Saini[4]

[1, 2, 3] *Department Of Mechanical Engineering, SRPEC, Unjha, (India)*

[4]*Research Scholar, Department of Mechanical Engineering, YMCA, Faridabad (India)*

ABSTRACT

Earth air heat exchanger or earth tube heat exchanger is a device used to produce heating effects in winter and cooling effects in summer using the ground or soil as a source or sink. Till date many researchers have implemented numerous ideas, conducted experiments on EAHE with different parameters depending on the location and found optimum values of parameters for better performance. The present study reviews the previously conducted studies in terms of performance assessment with effects of various parameters like material of construction, depth from earth surface, velocity of air and length of pipe etc.

Keywords: Eahe-Earth Air Heat Exchanger

I. INTRODUCTION

It is found that the soil at some depth from earth surface has a property of remaining cold during summer and relatively hotter during winter days from the atmospheric temperature. This strikes the researchers to use the temperature gradient of soil for cooling in summer and heating in winter [1]. As we have limited source of energy it is important to find alternatives sources to save conventional fuel for future to save exergy of universe. These days air conditioning is widely employed in industries and for the comfort purpose in livestock buildings and hospitals etc. It is employed efficiently by vapour compression cycle in which we are using high grade electrical energy which also affects atmosphere by CFC so to reduce the use of high grade energy number of methods are explored[2,3]. EAHE is one of such techniques. It uses heat source from underground soil and heat is transferred to air through conduction and convection which results increased air temperature than that of ambient temperature at outlet of earth-air-pipes.and this outlet air directly can be used for space heating purposes [4].

Till date a lot of research work on EAHE has been carried out. Vikas Bansal et al. [2,3] developed the model inside the FLUENT simulation program and validated against experimental investigations on an experimental set-up in Ajmer (Western India) during summer, and found 23.42m long EAHE system gave cooling in the range of 8.0–12.7˚C for the flow velocities 2–5 m/s. M.K. Ghosal et al. [5] developed a simplified analytical model to study the year round effectiveness of a recirculation type EAHE coupled with a greenhouse located in IIT Delhi, India, and found Temperatures of greenhouse air to be on an average 6–7 ˚C more in winter and 3–4 ˚C less in summer than the same greenhouse when operating without EAHE. Fabrizio Ascione et al. [6] studied the energy performances achievable using an EAHE for an air-conditioned building for both winter and summer

by means of dynamic building energy performance simulation codes, and analyzed the energy requirements of the systems for different Italian climates. . Trilok Singh Bisoniya et al. [4] presented experimental and analytical analysis of EAHE systems in India. Rohit Misra et al. [7] experimented transient analysis based on determination of derating factor for EAHE in summer. Joaquim Vaz et al. [8] conducted an experiment in southern Brazil in the city of Viamao, and its results were used to validate the computational modeling of EAHE, the variation of air temperature inside the ducts, to an annual cycle, was investigated. The numerical solution of the conservation equations of the problem is performed with a commercial code (FLUENT) which is based on the Finite Volume Method (FVM).

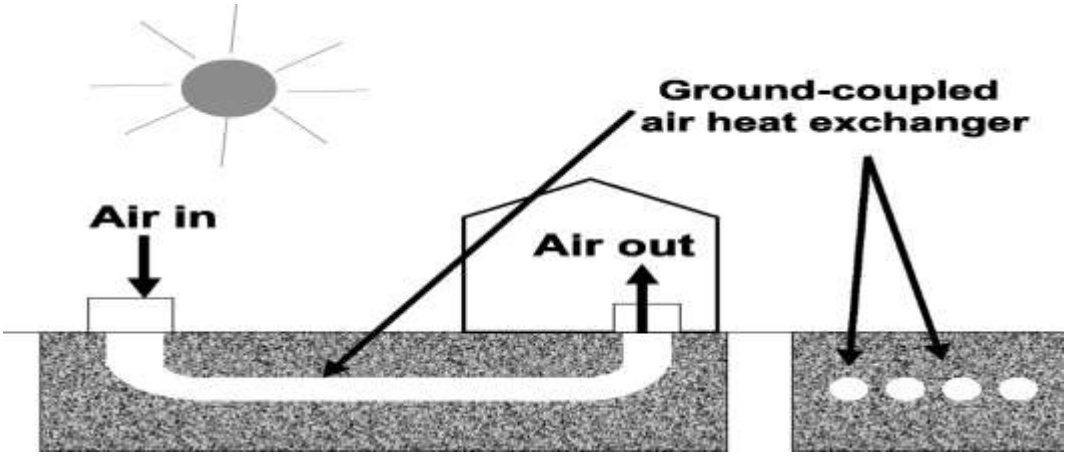

Fig.1 Ground Coupled Heat Exchanger [10]

II. A BRIEF OF HISTORICAL BACKGROUND EAHE SYSTEMS IN THE WORLD

If air from buildings is blown through the heat exchanger for heat recovery ventilation, they are called earth tubes (also known as earth cooling tubes or earth warming tubes) in Europe or earth–air heat exchangers (EAHE or EAHX) in North America. The idea of using earth as a heat sink was known in ancient times.[9] In about 3000 B.C., Iranian architects used wind towers and underground air tunnels for passive cooling.[10,11] EAHE is a passive climate control technique that has application in residential as well as agricultural building utilizes the underground soil temperature that stays fairly constant at a depth of about 2.5–3 m [6]. In agricultural facilities (animal buildings) and horticultural facilities (greenhouses) Earth–air heat exchangers have been used over the past several decades and have been used in conjunction with solar chimneys in hot arid areas for thousands of years, probably beginning in the Persian Empire Earth–air heat exchangers are one of the fastest growing applications of renewable energy in the world, with an annual increase in the number of installations with 10% in about 30 countries over the last 10 years [12]. With the exception of Sweden and Switzerland, the market penetration is still modest throughout Europe but is likely to grow with further improvements in the technology and the increasing need for energy savings. From the middle of the 20th century, a number of investigators have studied the cooling potential of buried pipes. South Algeria is typical of a dry desert climate with the highest air temperature being recorded in July and August with an afternoon average maximum of 45°C. Summer starts at the beginning of May and continues until the end of September, with a mean air temperature of 37 °C. In addition, the air is generally dry [11]. In winter, the weather is comfortably cool, generally mild, with a monthly mean temperature of 10°C, and a minimum temperature recorded being occasionally below 1°C. The EAHE

system alone cannot maintain indoor thermal comfort, but it could be used to reduce energy demand in domestic building in south Algeria if used in conjunction with an air conditioning system.

III. METHODOLOGY

Earth air heat exchanger (EAHE) systems. EAHE systems are long metallic, plastic or concrete pipes that are laid underground and are connected to the air intake of buildings, particularly houses. From inlet the atmosphere air is forced by using blower in the pipe during the movement heat gets transferred from hot soil to cold air in winter and cold soil to hot air in summer and it changes the air temperature accordingly. The pipe outlet is given where the space needs to be air conditioned in industrial or livestock buildings etc. By taking benefits of this costless energy we can reduce our energy consumption for air conditioning of space hence a very useful technique it is.

3.1 Open Loop Systems and Closed Loop Systems

In an open loop system air is directly supplied to the building and this system provides the ventilation while closed loop circulates the interior air and is more efficient than open loop [9]

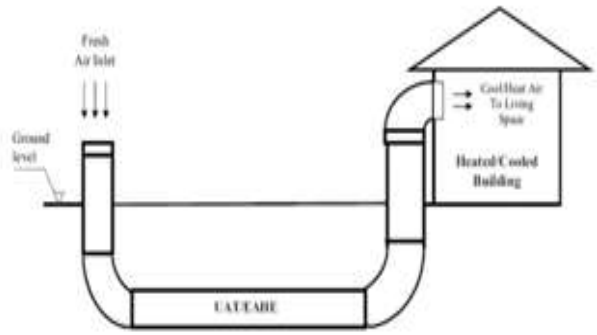

Fig.2 Open Loop for Space Heating/Cooling System [9]

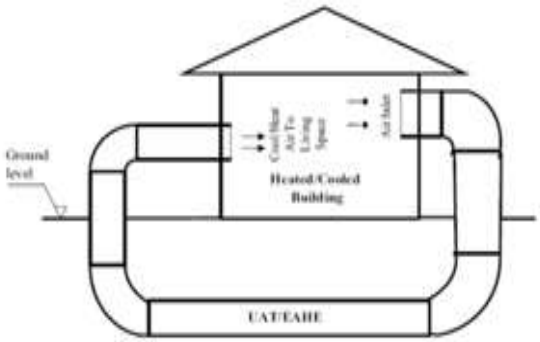

Fig.3 Closed Loop for Space Heating/Cooling System [9]

3.2 Effects of Various Parameters on ETHE

3.2.1 Effect of Material

Initially steel pipes were used for the construction of ETHE but then experiments were conducted for different materials. Researcher [2, 3] studied the effects and they found that PVC material also give the similar performance hence we can use cheaper material like PVC instead also there life is more. Though steel has higher conductivity than that of PVC yet the variation in temperature of the air at the outlet of pipe between steel and PVC is very small. Therefore, it can be concluded that in EAHE system, convective heat transfer plays a more important role than conductive heat transfer.

3.2.2 Effect of Velocity of Air inside Pipe

Researchers studied [2,3] the effects and concluded the reduction in temperature of the air at the exit of pipe due to increment in air velocity occurs because when the air velocity is increased from 2.0 to 5.0 m/s, the convective heat transfer coefficient is increased by 2.3 times, while the duration to which the air remains in contact with the ground is reduced by a factor of 2.5. Thus the later effect is dominant and therefore, less rise in temperature is

obtained at air velocity 5.0 m/s than the 2.0 m/s. At high speeds due to reduction in time of contact the performance gets reduce.

3.2.3 Effect of Tube Length

It can be concluded that up to some extent length matters after a certain length no improvement in the performance is found however large its length may be. It can be inferred that, for all the considered climates, lengths of about 10 m are unsatisfactory, while significant advantages do not occur for lengths over 70 m, according to *Lee KH, Strand RK[13]*.

3.2.4 Effect of Tube Depth

The ground temperature is affected by the external climate and soil composition its thermal properties and water content. The temperature of soil fluctuates but become stable after some depth. This temperature remains same throughout the year. And it is concluded that after a depth of 1.5 meters this temperature becomes stable so the depth taken should be more than that. According to the (EREC2002) more than 3.5 meters depth is also not justifiable [15].

3.2.5 Effects of Tube Length, Diameter and Air Flow Rate

Cooling capacity depends on the overall surface area which is a keyway in designing it. This can be affected in two ways by changing length and diameter of the pipe. On increasing the diameter the mass flow rate gets reduced and more length increases pressure drop and increases the blower input. According to (EPEC2002) the optimum solution is the parallel tube of proper length and diameter are used. The air quickly reached the soil temperature so larger tubes are not needed. Generally 150 to 450 mm tubes are used. (IEA1999)

REFERENCE

[1] M. Santamouris, A. Argiriou, M. Vallindras, Design and operation of a low energy consumption passive solar agricultural greenhouse, Solar Energy 52 (1994) 371–378

[2] BansalVikas,Misra Rohit, Agrawal Ghanshyam Das,Mathur Jyotirmay. Performance analysis of earth–pipe air heat exchanger for winter heating. Energy andBuildings2009; 41:1151–4.

[3] BansalVikas, MisraRohit, AgrawalGhanshyamDas,MathurJyotirmay. Performance analysis of earth pipe air heat exchanger for summer cooling. Energy and Buildings 2010;42:645

[4] Trilok Singh Bisoniya, Anil Kumar, Prashant Baredar. Experimental and analytical studies of earth–air heat exchanger (EAHE) systems in India: A review. Renewable and Sustainable Energy Reviews 19 (2013) 238–246.

[5] M.K. Ghosal, G.N. Tiwari, N.S.L. Srivastava. Thermal modeling of a greenhouse with an integrated earth to air heat exchanger: an experimental validation. Energy and Buildings 36 (2004) 219–227.

[6] Fabrizio Ascione, Laura Bellia, Francesco Minichiello. Earth-to-air heat exchangers for Italian climates. Renewable Energy 36 (2011) 2177-2188

[7] Rohit Misra, Vikas Bansal, Ghanshyam Das Agrawal, Jyotirmay Mathura, Tarun Aseric. Transient analysis based determination of derating factor for Earth Air Tunnel Heat Ex

[8] Joaquim Vaza, Miguel A. Sattler, Elizaldo D. dos Santosa, Liércio A. Isoldi. Experimental and numerical analysis of an earth–air heat exchanger. Energy and Buildings 43 (2011) 2476–2482.changer in winter. Energy and Buildings 58 (2013) 76–85.

[9] Leyla Ozgener. A review on the experimental and analytical analysis of earth to air heat exchanger (EAHE) systems in Turkey. Renewable and Sustainable Energy Reviews 15 (2011) 4483– 4490

[10] M. De Paepe, A. Jannsens. Thermo-hydraulic design earth-air heat exchangers. Energy and Buildings 35 (2003) 389-397

[11] Abdelkrim.Sehli, Abdelhafid.Hasni, Mohammed. Tamali. The potential of earth-air heat exchangers for low energy cooling of buildings in South Algeria. Energy Procedia 18 (2012) 496 – 506.

[12] Sanner B.Current status of ground source heat pumps in Europe, Futurstock, Warsaw, 2003.

[13] Lee KH, Strand RK. The cooling and heating potential of an earth tube system in buildings. Energy and Buildings 2008;40:486e94

[14] Environmental Protection Agency. (2009). Heat and Cool Efficiently. Washington DC: Energy Star. Available at http://www.energystar.gov/index. cfm?c=heat_cool. pr_hvac [Accessed on 18 Feb 2009].

[15] EREC, reference brief 'Earth cooling tubes' US Department of Energy 2002.

AN ANALYSIS OF REACTION TO GREEN PRODUCT INITIATIVES

[1]Gaurav Dawar, [2]Dr. Seema Singh

[1]Research Scholar, [2]Associate Professor, Department of Humanities,

Delhi Technological University (India)

ABSTRACT

The purpose of this paper is to investigate the reaction of consumer towards green product initiatives of the companies and impact of Household Income on Consumer's Green consumption decision. The study conducted is exploratory in nature with four levels of income. The survey of 300 respondents has been conducted and responses gathered have been analyzed on the basis of descriptive statistics. It was found from the study that the consumers in the region have high awareness about recycle, organic and energy efficient product but their utility is limited due to higher pricing by companies. The study is one of the first to focus on the consumption decision of females in relation to the green products offered by the companies.

Keywords: Sustainable Development, Green Marketing, Environmental, Ecological, Green Product, Green Products.

I INTRODUCTION

Sustainability has become the mantra for companies seekingto create a competitive advantage in the global marketplace.Recent interviews with over 750 CEOs from around the worldrevealed that 93 percent feel that implementing sustainabilityprograms that mesh with their corebusinesses would becritical to the future success of those businesses (UN GlobalCompact, 2010). These programs range from developingtotally new green products, developing recycled orrefurbished products to engaging in greener processes.

Thenewly produced goods that result are made of reclaimed/recycled/refurbished components. We propose that consumersevaluate these types of products differently than new greenproducts. Third, strategies for developing green processes canbe developed from firms' everyday business activities. Thesemethods may include reducing water usage, plant/manufacturing emissions, energy consumption, solid wastes,and acid rain emissions (sulfur dioxide, nitrogen oxide, and ammonia).

The challenge of healthier communities begins with environmental concern and collective adoption of Green behaviors, because the choices consumers make with regard to the environment influence thehealth and quality of

life for both current and future generations. Ingeneral terms, environmental concern is a "concept that can refer tofeelings [consumers have] about many different green issues" (Zimmer,Stafford, and Stafford 1994, p. 64). The topic became an important one in1962 when Rachel Carson's Silent Spring was published and has recentlybecome even more critical with today's concerns about creating a sustainableand healthy environment.

Economic world is now thinking in favor of the fairer sex. Now-a-days women are not only playing role of hardcore 'housewives', they are also playing a different role of 'chief purchasing officer' & controlling 85% of buying decisions. In today's world, they are working as multi-tasker by playing a role of house maker as well as professional women with their hard work. With their new role as a professional, there has been a gradual evolution in the status of women & now they are called as marketers. As a professional India, women hold 25% of jobs in different sectors, although in 1980 it was only 10%. An Indian woman today has a greater sense of empowerment and economic freedom, which indicates that their consumption pattern has changed.

Gender has been studied as a predictor of attitudes for many years based on the notion that males and females possess distinct characteristics, and green research has suggested that females might be more environmentally concerned than males (Lee 2009; Mostafa 2007; Schwartz and Miller 1991).

II REVIEW OF LITERATURE

Pacific Gas and Electric has admitted that CompactFlorescent Light bulbs are not as long lasting as hadoriginally claimed and their green advantages in terms ofenergy and hazardous waste may not be as significant asanticipated (Smith, 2011). Nissan's electric car, the Leaf, willonly achieve its promised 100-mile range under idealconditions; any use of heater, air conditioner, or otherenergy-drawing device can significantly reduce the Leaf'srange (Ramsey, 2010).

MiglaniSurinder (1997) has investigated the buying behavior of Indian women by using a well-structured questionnaire with 500 respondents fromDelhi-NCR region. His findings were that there is change in the role of Indian women and they now fit in the role of a facilitator than purchasing on family needs and wants. She also considers the importance of corporate social responsibility while making a buying decision.

Irawan Ronnie (1998) has investigated the factors influencing green purchasing behavior of university students in Jakarta. The findings of the research were Environmental Concern, Perceived Seriousness of Environmental Problems, and Perceived Environmental Responsibility-were significantly affecting green purchasing behavior and there was no gender differences on these significant variables. The researcher concluded that there are different variable that can influence the green purchasing behavior but independently only three variable environmental concerns, perceived seriousness of environmental problem and perceived environmental responsibility had the significant influence.

Dennis Charles (2000) has researched on shoppers, particularly women, and factors influencing them. The researcher has used comparison experiment, semi-structured questionnaire and focus group to compare a traditional e-shopping website with a social e-shopping one. The findings of the research were young women prefer social e-

shopping sites. Both utilitarian and hedonic young adult female shoppers found social e-shopping enjoyable and useful. However, although many participants found the social e-shopping site more difficult to use, this was outweighed by their enjoyment of the site and its usefulness. The study demonstrated the potential value of the concept of social e-shopping for future research. The researcher concluded social e-shopping can be a valuable strategy for e-retailers wanting to gain competitive advantage and to positively increase the e-shopping behavior intentions of young women.

Fowler (2002) reported that 42 percent of people will not buy green products, fearing that the products will not work as well as conventional products. A 2007 Gfk Roper study found that 61 percent of consumers believe that green products performed less effectively than non-green (Gfk Custom Research North America, 2009). More recently, however, Manget et al., 2009 discovered that almost half of the respondents in a multi-country survey indicated that green products offer comparable or superior quality over conventional alternatives.

Collins M. Christy (2007) has investigated customer's values, beliefs on sustainable corporate performance and their buying behavior. To achieve the research objectives a well-structured questionnaire was used where in total 300 respondents from Aldi and Albert Heijn supermarkets in the city of Groningen, Netherlands. The research explored values, beliefs about the importance of SCP, and buying behaviors of supermarket customers from within a stakeholder framework. Beliefs about the importance of SCP (both social and environmental, but not economic) were found to be related to values. Also, it was found that customers' environmentally responsible buying behaviors were related to their beliefs about the importance of environmental SCP. However their socially responsible buying was not related to their beliefs about the importance of social SCP. The researcher concluded that Marketing professionals have a central role to play in moving towards a greater level of corporate transparency and sustainability.

Veisten (2007) determined that willingness to pay forecologically labeled tables ranged from 2-16 percent abovethose of unlabeled products. Laroche et al. (2001) found that13.1 percent of respondents were willing to pay a higher pricefor green products. Sammer and Wustenhagen (2006) foundthat consumers were willing to pay a 50 percent pricepremium for a washing machine labeled as energy efficient.Vlosky et al. (1999) analyzed the effects of environmentalattitudes on a consumer's willingness to pay, concluding thatconsumers with higher levels of environmental consciousnessare willing to pay more for environmentally friendly products,and D'Souza et al. (2006) found that quality is moreimportant than price to consumers.

Laroche Michel (2008) has investigated aboutconsumers' willingness to pay more for environmentally friendly products. Awell-structured questionnaire was used where in total 500 respondents were sampled. Concerns related to the environment are evident in the increasingly ecologically conscious marketplace. Using various statistical analyses, investigated the demographic, psychological and behavioral profiles of consumers who are willing to pay more for environmentally friendly products. The findings of the research were that this segment of consumers were more likely to be females, married and with at least one child living at home. They reported that today's ecological

problems are severe, that corporations do not act responsibly toward the environment and that behaving in an ecologically favorable fashion is important and not inconvenient. The researcher concluded They place a high importance on security and warm relationships with others, and they often consider ecological issues when making a purchase.

Chatterjee (2009) examined consumer reaction to green category (or line) extensions of well-known brands. Their primary findings relevant to the current project are that consumers have significantly positive reactions to green extensions if the category has high environmental impact (e.g. paper towels, detergents), and that for existing customers, line extensions are preferred over category extensions.

Essoussi and Linton (2010) investigated consumers' willingness to pay for recycled products. They found that though consumers were willing to pay a price premium, this premium narrowed as the functional risk of the product category rose. The price premium represented the additional value consumers place on recycled versus non-recycled products. Extending this line of thought presents the possibility that, for certain product categories, recycled products may be perceived less positively than new green products.

Flannery Tim (2010) has investigated the gap between the consumer attitude and purchase behavior of green products.He surveyeda total of 2000 Australian consumers completed an online survey using structured questionnaire for one of four product categories, namely: televisions, digital cameras, air conditioners and washing machines. The findings were Respondents who cared about the environment tended to be guided by self-transcendence values of equality, helpfulness, forgiveness and loving. Unexpectedly, even those respondents who were more concerned about how their purchases affected their own individual situation still had positive attitudes towards purchasing green products.

Gan Christopher (2010) has investigated Consumers' purchasing behavior towards green products in New Zealand. A survey of total 500 respondents were done using structured questionnaire. He found thatpeople engage in environmental behavior as a result of their desire to solve environmental problem, to become role models and a belief that they can help to preserve the environment. However, consumers' indications of positive attitude towards environmental issues do not necessarily lead to actual environmentally friendly purchasing behavior. Majority of consumers do not purchase products based on the environmental concern alone and there will not trade-off other product attributes for a better environment.

Bjork Peter (2013) has investigated the value of green labels- consumers perceptive.A survey of 200 respondents was done. The value-attitude-behavior model was tested in this study, and the effects of greenlabels on the consumer decision making processes were assessed. The findings of the research were that Finnish consumers have a positive attitude toward green labels and are willing to pay a higher price for productsmarked with a green label. Attitudes have a direct effect on consumer behavior, but values correlate only with the variable willingness- to-pay.

Past research has found that a company and its products areconsidered as non-separate entities (Brown and Dacin, 1997),and therefore the image of a company's practices can have asignificant impact on consumers. Research also shows that 79percent of US consumers feel that a company's environmentalpractices influence decisions about which products andservices they recommend to others (Gfk Custom ResearchNorth America, 2009). Of the consumers, 53 percent preferto purchase products and services from a company with astrong environmental reputation. D'Souza et al. (2006) statethat "consumer's perception of the firm's corporate strategiestoward environmental issues is expected to contribute to theformation of the overall perception about green products."Brown and Dacin (1997) reported that a company's corporatesocial responsibility (CSR) activities have a positive impact onproduct preference, though the impact is not direct. PositiveCSR activities have a positive impact on the evaluation of thecompany, which, in turn, has a positive impact on theproduct.

An attempt has been made to examine the different elements of buying behavior of females towardsgreen product in Delhi and NCR and are they willing to pay more for an green product.

To examine the different elements of environmental concern, we utilize different dimensions identified by Zimmer, Stafford, and Stafford (1994). This allowed us to determine whether the level of importance of certain types of environmental concern is significantly related to the willingness to spend more on an green product.

Thus we test the following hypothesis:

H1: There is a significance difference between the attitudes of respondent of different house hold income towards different environmental friendly practices.

III RESEARCH METHODOLOGY

The present study conducted is exploratory in nature and survey method has been used for data collection. The data is collected from 300 females from across Delhi and NCR from November 2014 to December 2014. The sampling of population is done on the basis of females pursuing their graduation and post-graduation, working women, professionals, entrepreneur & housewives and Convenience samplinghas been used for the study.The data collected has been tabulated and analyzed systematically with the help of Descriptive Statistics.Cron batch Alpha has been applied to test the reliability of the questionnaire.

The questionnaire has 10 questions with multiple choice options and 5 point likert scale. The result of Cron batch Alpha is .80 (Table 1) which is greater than 0.7, therefore the data is considered to be reliable.

The demographic profile of 300 females who has completed the survey is 63% of females are single; 43% of females are graduate, 39% are postgraduate and 12 % are Doctorate; 28% of females are organizational employees, 14% are students, 11% are housewives and 8% are entrepreneur and 3% are retired females.The age group of females in survey is 57% of females are of age group 20 to less than 30, 30% of females are of the age group30 to less than 40, 7% of the age group of 40 to less than 50, 5% of the age group more than 50.

The females of different income group is 27% females have total household income of 5 to less than 10 lakhs, 17% are of 15 to less than 20 lakhs and 24% are of 10 to less than 15 and 24% are of the income group of 20 lakhs and above.

In our survey we have also tried to identify the area of origin of our respondents as Delhi being a cosmopolitan city. 41% of our respondents have originated from North India, 18% are from South India, 17% are from East India, 11% from Central India.

IV DATA ANALYSIS

In our survey of green products 63% of the females are single, 43% are post graduate, 28% are organizational employees. From the survey we can conclude that 90% of the respondents in our survey are energy efficient including the respondents who sometimes act energy efficient. And also around 50% of the respondents consider them environmental friendly including the respondents who sometimes act environmental friendly. Also from the survey it is clear that only 45% female consider buying products which are labeled as green. Also the survey showed that 40% out of the sample population is affected by friends/relatives/colleagues opinion while making decision when they are shopping for green products, 29% is affected by T.V, newspaper and magazine ads and 19% are affected by point of purchase.

The data of females from Delhi & NCRshows that 45% of total females consider themselves energy efficient (chart 1), 50% considers themselves as environmental friendly (Chart 2), 45% buy the product which are labeledas environmentally safe (Chart 3). 42% of the respondent's mentions relative or friends' influence the decision to buy green product (Chart 4).

Chart 5 shows that about 60% of the women respondents have heard about organic products and 30% of them have actually used it. This shows that there is enough awareness about ecofriendly products among females as their responses have been collected from different demographics. Chat 6 no shows that 29% of the female respondents have heard about recycled product and 19% have actually used it.

Char 7 highlights the reasons of less usage of organic products. Our respondent's awareness of organic products is quite high. It is about 60% and usability rate among respondents is 30%. They highlighted various factors for less usage of these products. Survey shows that 35% of respondents feel that organic products are not used as it does not fulfill the respondents' expected performance level and 17% considers that the appearance of the organic product unattractive and 12% find organic products expensive.Chart 8 shows 23% of Respondents with medium awareness level of recyclable products feels that reason for less usage of recyclable products is product appearance not appealing and 15% feels that product is too expensive to buy.

Chat 9 shows that 70% of respondents says that it is very important for a product to be energy efficient. Whereas 47% of the respondents say it is important to be environmental friendly. While almost the same majority also consider products possessing the trait of being environment friendly is not that important.Chart 10 shows 60% of Respondents said that they consider Ozone depletion and greenhouse effect of the product on environment very

important while buying the product. Internet based advertisement and out-door ads has very less impact.In case of organic products out of the total sample 60% of the respondents have heard about the product and 32% have actually used the product. The major reason for not using the organic product is reduced performance possibility according to the survey. While In case of recyclable products out of the total sample 10% of the respondents have heard about the product and 19% have actually used the product. In case of energy efficient products out of the total sample only 1% of the respondents have heard about the product and 16% have actually used the product. On the other hand in case of wastage reduction products out of the total sample only 5% of the respondents have heard about the product and 10% have actually used the product. In case of solar power products out of the total sample only 3% of the respondents have heard about the product and 6% have actually used the product. In case of green construction material out of the total sample only 1% of the respondents have heard about the product and 4% have actually used the product. The major reason for not using the wastage reduction product, solar power product and green construction material is that it too expensive and the reason for not using the recyclable product and energy efficient products is that the product appearance is not appealing according to the survey.The level of the importance the respondents attach with the energy efficient product is very high than the other aspects in the survey and on the other hand wastage reduction product are not considered important related to environment protection.According to the survey generally 40% of the people think that green products are of same quality versus similar products but not green and 39% of the respondents think that green products are of higher quality versus similar products but not green and 10% consider the quality as inferior. If a product is available for Rs.100 then the maximum amount the respondent is ready to pay is Rs.131 for another product which is almost similar except that it is also green. This shows the willingness of people who are ready to pay more for green products.Also there is no significance difference between the attitudes of respondent of different house hold income towards different environmental friendly practices. In this case we can say that female respondents with different house hold income have similar attitude and buying behavior towards different green products and they try to convince friends, relatives and colleagues not to buy products which are harmful to the environment.

V CONCLUSION & SUGGESTIONS

Our findings do offer insight into perceptions of environmental concern and willingness to pay forgreen product. These findings suggest that educational messages should be targeted toward people to encourage purchase of such products. The findings also suggest that respondents who are particularly concerned with waste may be more likely to spend more money on an environmentally friendly product. Therefore, a reduced usage of energy via simpler packaging and recycling innovations may be supported by a group of consumers. Educating consumers on why green products cost more as well as the benefits of using green products, particularly where health benefits are concerned (i.e., reduced factory emissions, pesticide-free agriculture, reduce ozone depletion), may be helpful in closing the gap between consumers merely possessing a pro-environmental attitude and extending that attitude to

intentions to adopt pro-environmental behaviors—in the case here, spending more money on an environmentally friendly product. However, because our research only examined willingness to pay forgreen product and not behavior, this speculation needs to be examined in future research.Although a movement toward reducing the costs of these environmentally friendly products might be helpful, it may not be realistic. Another alternative is increased government subsidies for companies developing green products so that the cost to the consumer can be reduced. If the ultimate universal goal is a sustainable environment with long-term health benefits for all consumers, then collective effort among consumers and businesses is critical.In short, the research begins to understand who is willing to pay more for an environmentally friendly product and it showed that one should allow for the development of effective communications to different groups of consumers to educate them on the benefits of purchasing these products. Addressing salient needs is critical in moving from environmental concern to action, and consumers need to play an active role in maintaining their environment to protect their own community and personal health.

VI LIMITATIONS

- Sample size of the study was 300, we can increase the sample size and replicate the research for more accurate results.
- Environment concern is huge issue nowadays so many more sections and issues can be targeted and the report can be replicated to get the result.
- Time was one of the limitations.
- The questionnaire can be replicated by involving many other factors of buying behavior and attitude.
- The study is focused only on female consumer; male consumer can be also targeted to get more effective result.

REFERENCES

- Aaker, David A. and Richard P. Bagozzi. 1982. Attitudes toward Public Policy Alternatives to Reduce Air Pollution. Journal of Public Policy & Marketing, 1: 85–94.
- Abdul-Muhmin, Alhassan G. 2007. Explaining Consumers' Willingness to be Environmentally Friendly. International Journal of Consumer Studies, 31 (May): 237–247.
- Allen, Jeff, Duane Davis, and Mark Soskin. 1993. Using Coupon Incentives in Recycling Aluminum:A Market Approach to Energy Conservation Policy. Journal of Consumer Affairs, 27 (winter):300–319.
- American Public Health Association. 2007. Addressing the Urgent Threat of Global Climate Change to Public Health and the Environment.

- Anderson Jr., Thomas W. and William Cunningham. 1972. The Socially Conscious Consumer. Journal of Marketing, 36 (July): 23–31.
- Antil, John. 1984. Socially Responsible Consumers: Profile and Implications for Public Policy. Journal of Micromarketing, 4 (December): 18–39.
- Baugh, Joyce A. 1991. African-Americans and the Environment: A Review Essay. Policy Studies Journal, 19 (Spring): 182–191.
- Bone, Paula Fitzgerald, Karen Russo France, and Kathryn J. Aikin. 2009. On Break-up Cliches Guiding Health Literacy's Future. Journal of Consumer Affairs, 43 (summer): 185–198.
- Chang, N. and Fong, C. (2010), "Green product quality,green corporate image, green customer satisfaction, andgreen customer loyalty", African Journal of BusinessManagement, Vol. 4 No. 13, pp. 2836-44.
- Chatterjee, P. (2009), "Green brand extension strategy andonline communities", Journal of Systems and InformationTechnology, Vol. 11 No. 4, pp. 367-84.
- D'Souza, C., Taghian, M. and Khosla, R. (2007),"Examination of environmental beliefs and its impact onthe influence of price, quality and demographiccharacteristics with respect to green purchase intention",Journal of Targeting, Measurement and Analysis for Marketing,Vol. 15 No. 2, pp. 69-78.
- Diamantopoulos, Adamantios, Bodo B. Schlegelmilch, Rudolf R. Sinkovics, and Greg M. Bohlen. 2003. Can Socio-Demographics Still Play a Role in Profiling Green Consumers? A Review of the Evidence and an Empirical Investigation. Journal of Business Research, 56 (June): 465–480.
- Do Paco, Arminda and Mario Raposa. 2009. "Green" Segmentation: An Application to thePortuguese Consumer Market. Marketing Intelligence & Planning, 27 (3): 364–379.
- Drumwright, Minette. 1994. Socially Responsible Organizational Buying: Environmental Concern as a Noneconomic Buying Criterion. Journal of Marketing, 58 (July): 1–19.
- D'Souza, Clare, Mehdi Taghian, Peter Lamb, and Roman Peretiatko. 2007. Green Decisions:Demographics and Consumer Understanding of Environmental Labels. International Journalof Consumer Studies, 31 (July): 371–376.
- Ebi, Kristie L., David M. Mills, Joel B. Smith, and Anne Grambsch. 2006. Climate Change and Health Impacts in the United States: An Update on the Results of the U.S. National Assessment. Environmental Health Perspectives, 114 (September): 1318–1324.
- Ellen, Pam Scholder, Joshua Lyle Wiener and Cathy Cobb-Walgren. 1991. The Role of Perceived Consumer Effectiveness in Motivating Environmentally Conscious Behaviors. Journal of PublicPolicy & Marketing, 10 (Fall): 102–117.
- Fuller, R.A. Graduate Environmental Sciences. International Graduate (Accessed April 16, 2010)
- Gallup Poll. 2009. Water Pollution Americans' Top Green Concern. 117079.

- Grantham, Susan. 2007. But What Do They Really Think? Identifying Consumers' Values Relevant to Adopting Biotechnologically Produced Foods. Journal of Public Affairs, 7 (November):372–382.
- Hartman Group (2007), Hartman Report on Sustainability:Understanding the Consumer Perspective, Hartman Group,Bellevue, WA
- Hansman, Harrie and Veronique Schutjens. 1993. Dynamics in Market Segmentation: A Demographic Perspective on Age-specific Consumption. Marketing and Research Today, 21 (3):139–147.
- Harrell, Gilbert and Diane M. McConocha. 1992. Personal Factors Related to Consumer Product Disposal Tendencies. Journal of Consumer Affairs, 26 (winter): 397–417.
- Jones, Robert E. and Lewis F. Carter. 1994. Concern for the Environment Among Black Americans: An Assessment of Common Assumptions. Social Science Quarterly, 75 (September): 560–579.
- Martha Barlett, CEO of Trendsight Group, a marketing Consultancy firm "Marketing to Women" – Advertising express – ICFAI[2]
- Philips, Hugh, How customers actually shop, Journal of Market Research Society, January 1993,Vol 35 Issue 1, pp 51 – 62.
- Simintiras, Pre-purchase satisfaction and first time buying behavior, European Journal of Marketing, 1997,Vol 31 issue 11/12, pp 737 – 872.
- Shainesh, Understanding buying behavior, International Journal of Technology Management, 2004, Vol 28 issue 1, pp 118 – 127.
- Vandermerwe, S. and Oliff, M.D 1990." Customers drive corporations green", Long Range Planning", vol. 23, no. 6, pp. 10-16.
- Veisten, K. (2007), "Willingness to pay for eco-labeled woodfurniture: choice-based conjoint analysis versus open-endedcontingent valuation", Journal of Forest Economics, Vol. 13No. 1, pp. 29-48.
- Yeung, S.P 2005." Teaching approaches in geography and students‟environmental attitudes‟, The Environmentalist", vol 24, no. 1, pp 101-17.
- Zelenym L., Chua, P. and Alrich, C 2000." Elaborating on gender differences in environmentalism, Journal of Social Issues", vol. 56, no. 3, pp 443-57.

APPENDIX

Table 1 Reliability Statistics

Cronbach's Alpha	Cronbach's Alpha Based on Standardized Items	N of Items
.704	.800	10

Chart 1

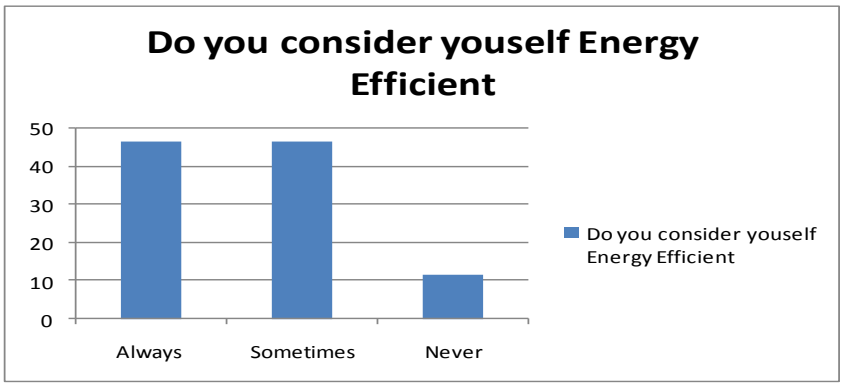

Chart 2

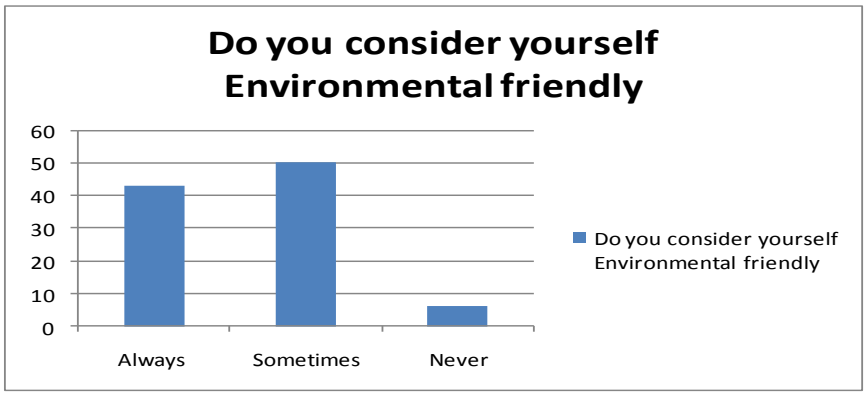

Chart 3

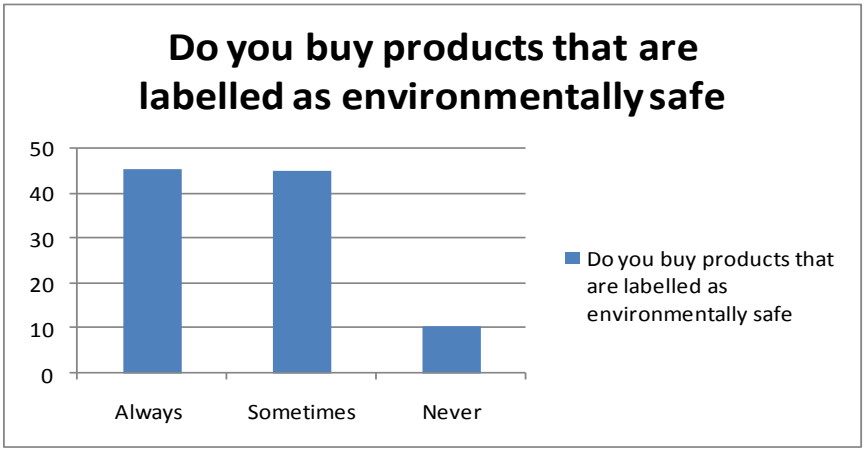

Chart 4

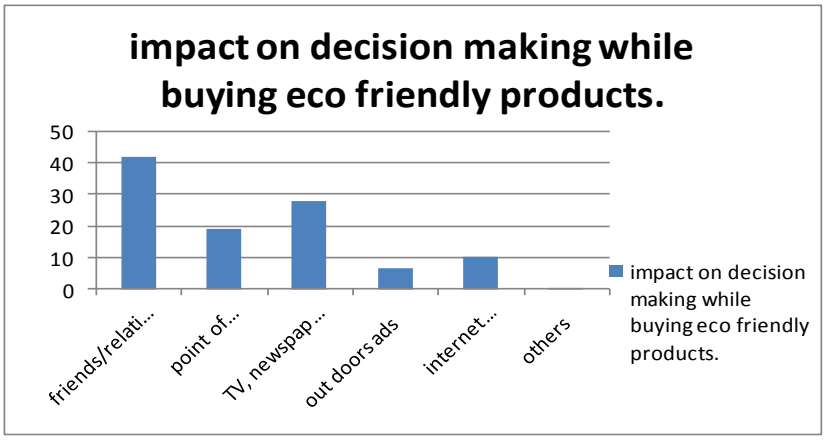

Chart 5

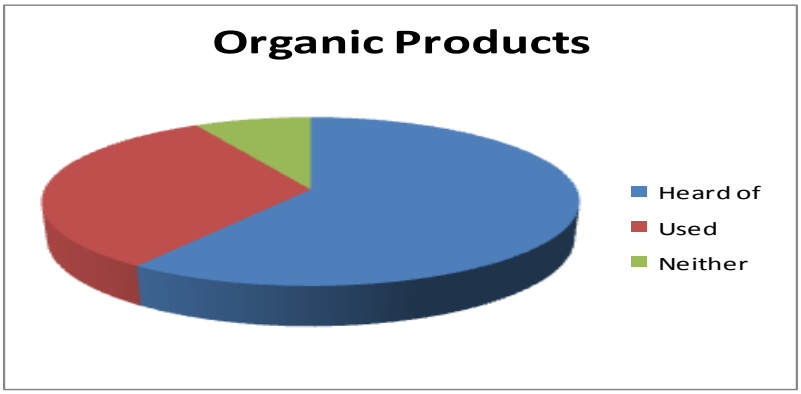

Chart 6

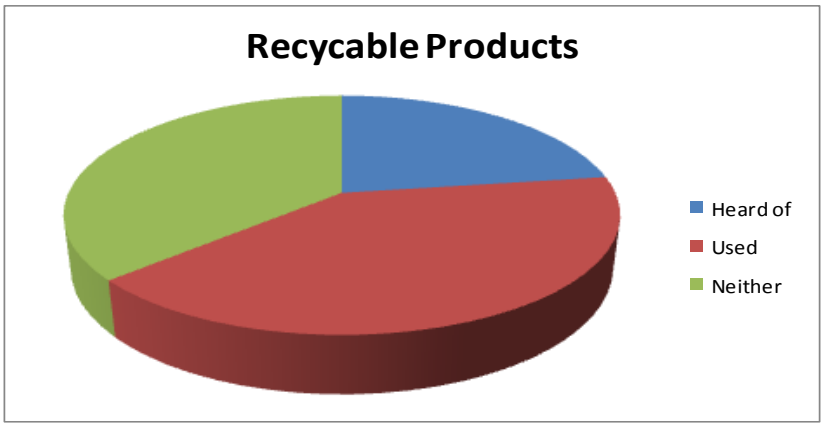

Chart 7

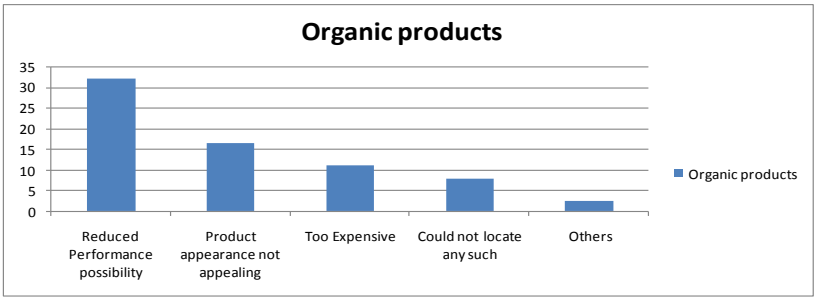

Chart 8

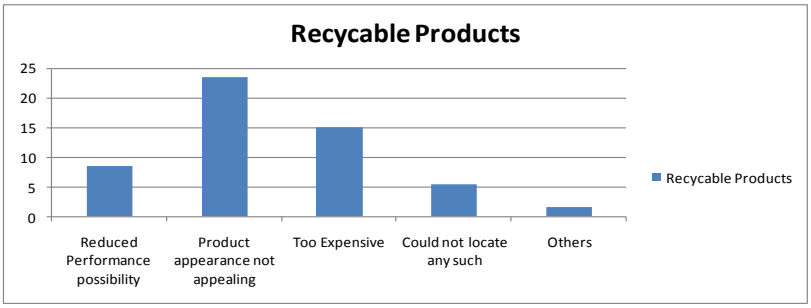

Chart 9

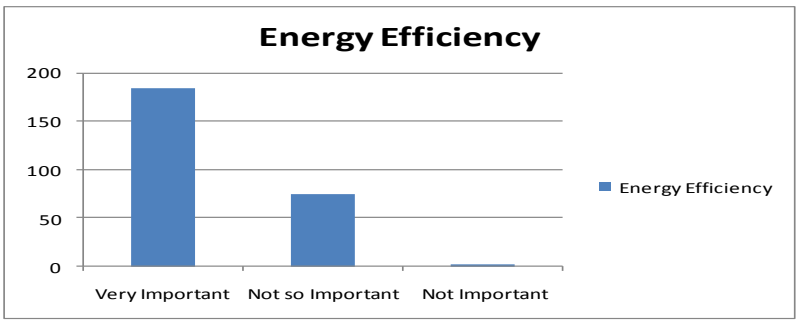
Energy Efficiency
200
150
100
50
0
Very Important
Not so Important
Not Important
Energy Efficiency

Chart 10

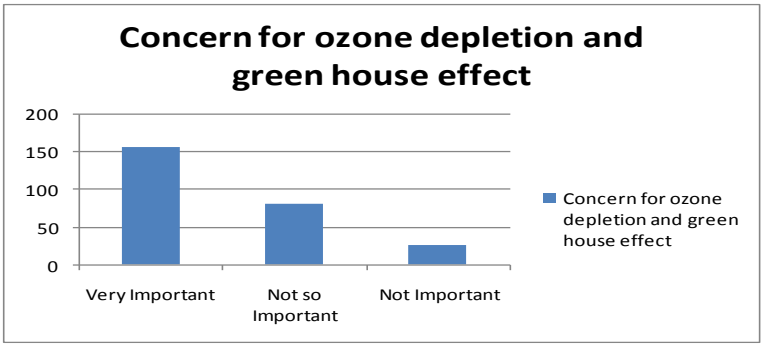
Concern for ozone depletion and green house effect
200
150
100
50
0
Very Important
Not so Important
Not Important
Concern for ozone depletion and green house effect

SIGNIFICANCE OF BODILY MOVEMENT FOR DETECTION AND ANALYSIS OF EMOTIONS: A REVIEW

Saurabh Singh[1], Nidhi Sethi[2], Vishal Sharma[3]

[1]*Department of Computer Science and Engineering, DIT University, Dehradun, India*
[2,3]*Assistant Professor in Computer Science Department , DIT University, Dehradun, India*

ABSTRACT

Through this paper we are trying to convey that there is a need of unified body language framework so that we can infer and reveal the underlying emotions. We can apply a verity of psychology inspired body language features to describe bodily emotion through posture. With the advancement in Affective Computing there is progress in the field of facial, vocal and physiological emotion detection. Humans communicate primarily through bodily movements. But the detection of emotion through the body is limited and the development in this field is comparatively down because of the absence of the proper equipments and coding scheme's, dedicatedly designed and prepared for bodily movement expression. A lot of researchers criticize to work on body expressions. However, work-done by the psychologist's provide knowledge and shows the bright side by presenting that the emotions shown by the body are as accurate as we get them from face. Recent researches in automatic bodily emotion detection have also shown promising results. The primary purpose of this review is to provide positive view and prepare a platform for emotion detection using bodily emotions. We will look at Laban Movement Analysis as a prominent and a promising method for movement representation in this field.

Keywords: ***Affective Computing Unified Body Language Framework, Gesture Recognition, Facial Action Coding System, Gestures.***

I INTRODUCTION

Communication is an important aspect of daily life; it helps us to connect with others as individuals or as groups. Without communication life would be non-existent, we communicate to others verbally and non-verbally. It helps us in the development of relationships, education and work. But when we communicate, our communication is less than 20% verbally; percentage is ranging from 55% to 80% when we communicate through non-verbal behavior.

First ever research done on human emotion, was done by W. James [1] in the year 1884. From that time and till now a lot work has been done by the psychologist and provided us with the knowledge about the origin[2,3] and categorization[4,5,6,3] of emotion. The study of emotion has moved from psychology to computing, remarked by the book of Picard[7], which created a new field called Affective Computing. This book provides us with standards and ideology to create smart and intelligent emotion detecting system. The influence of emotion detection covered a

wide range including medicine[8], education[9], health[8] and at a grater extent in Human Computer Interaction[10,11]. Usually emotion detection system takes input either in the form of audio, image or visual and then provides appropriate results produced according to the input given. Visual emotion detection was established by the classical study of Darwin[12]. Using the visual detection, Darwin gave us an idea of how emotions can be recognized from face and body; it created two broad fields for detecting emotions: facial and bodily emotions. Scientists and researchers have shown a keen interest to work on facial expression[13]. Detection using facial expression has a successful history due to the work done by Ekman and Friesen who introduced us to Facial Action Coding System (FACS)[14]. This system has provided us with the standard and outlines for facial emotion detection[15], and using this system a lot of face recognition and facial emotion detection system have been evolved. As compared to the facial expressions bodily expression were not addressed by the researchers. Ekman stated that bodily emotions could not indicate the emotions of a person whereas facial expressions can be read and understand by most of the people, most of the scientists agreed with him[16,17]. Most researchers have a notion that emotion is only the secondary signatures. Most of the work done in emotion detection, facial expression covers the major proportion while the bodily expression has only a minute proportion. Most of the researchers don't even consider bodily expression.

Whereas psychology support the bodily expressions by providing evidences [18] and nonverbal communication gestures[19]. Bodily expressions are important as inferred from the evidences [20,13] and they are as important as facial expressions. The evidences provided but the psychology made scientist and researchers to ponder over it again and work in this area of emotion detection. This survey will cover two primary purposes. Firstly, we will re-view evidences that support the importance of human body, in opposing with face for emotion recognition. Secondly to study the existing emotion detection system that works on bodily emotions. Finally, the paper will give some discussions and suggestions about how to effectively use bodily expression as a signal for building emotion recognition systems.

II AFFECTING BODY EXPRESSION

The human body plays a significant and an important role in expressing the emotions felt by the person, which can be used for emotion detection. There has been a lot of study and work-done on non-verbal communication and human behavior. The detection of emotions felt by a person can be studied in two ways either by the facial expression (a lot of work-done) or by the bodily movements and gestures. According to Darwin[12], his studies inferred that along with the facial expression, human body movements and the gestures made also represent the state of mind and the emotions of a person. Both facial and bodily gestures can be taken into account for affect detection.

Body gestures include hand movements, shoulder position, torso alignment, head position and leg movements. Working alone on the body posture (hiding hand and face) we can predict the emotions of a person accurately, the results found are accurate as we get it form the analysis of facial expression as stated by Walter and Walk[18]. Meeren et al.[21] stated that the facial expression and the body movements are related and their affect on each other.

Similarly, if we work on each body part individually we will get to know about the emotions felt by the person not exact but almost correct and each body part is somehow connected to some or the other emotion[13,22]. According to the fact that the body parts have a posture that's static or our body has a static configuration. Posture is usually defined by the position and orientation of specific body parts. Orientation can be relative. Mehrabian [20] et al. he used a few global descriptors such as relative orientation of a partner during a conversation, closeness or openness and symmetry of body limb. Harrigan et al. reported that human body posture can be decoded using the following common descriptors: trunk lean (upright, forward or backward), trunk orientation (facing, turned), arms and leg positions and configurations.

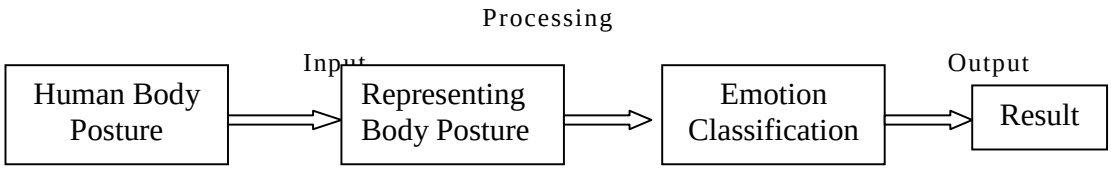

Fig. 1 Phases of bodily emotion detection system

As compared to the static gesture detection as lot of work and research has been done in the field of dynamic configuration. According to the primitive research done we have found that every motion and position of human body can express the emotions felt by the person for example: interested/bored, agreed/disagreed, defensive etc Bull[24]. Lagerlof worked on recognizing the emotions felt by kids and he did experiments on 4-year-old children, and he found that children too show emotions according to their likes and dislikes and revealed that, children can distinguish four emotions: anger, fear, joy and sadness[25].

III GESTURE REPRESENTATION AND DETECTION

Fig.2 (a) Defensive standing position; (b) Closed body and closed attitude; (c) Open body and open attitude

Every movement is not a gesture but every gesture is a movement. While communicating or interacting with a person either a face to face or telephony a person shows gestures and movements which represents his/her mind state and emotional level. Gestures can be intentional or fake. A lot of research suggests that in a verbal communication a person uses hand and arm to express his thoughts. These gestures can be can be categorized as the following: emblems, illustrators and adaptors[26,27].

Emblems are gestures that help the speaker used to express their meaning to the listener. They are conventional symbols that convey the meaning i.e. folding hands – defensive, showing palm – stop etc[28].

Illustrators are the gestures that a person uses or they are just accompanied in the verbal communication. It includes simple and repetitive movements; these movements might be related to the communication. It can be further divided into: deictic, iconic and metaphoric gestures. Deictic includes pointing towards an object and expressing themselves to the listener. Iconic and metaphoric are gestures that represent inherited qualities of an object or action such as representing the object and mimicking etc[29].

Fig. 3 (a) Raised steeple; (b) Lowered steeple.

According to the recent work done by Dael [30], a new system has been proposed that would provide the coding of body and body-parts positions, movement and communicative intent of gestures. The Body Action and Posture Coding System (BAP), it includes wide range of coding approaches to study emotions by using a multilevel coding.

The anatomical level is used to specify which body parts are concerned by a movement. Available articulators are the neck, the trunk (including spine and chest), the upper and lower-arms (including shoulders, elbow, wrist and fingers) and the legs. The form level describes the form of the movement of a set of articulators.

Scientifically gestures can be divided into two broad fields static and dynamic gestures. Gesture recognition and detection is a process of recognizing and interpretation of the input (static and dynamic gestures) provided which is evaluated over the time.

IV BODY POSTURE EMOTION DETECTION

Due to insufficient knowledge of body posture very little work is done in the field of postural emotion detection. Schindler et al.[9], stated that according to his study he found that emotions shown by the body posture can be

understood using the low-level visual data, without using the posture representation method. They took images of body posture, and then turned the problem into object recognition. This approach of considering the body posture as an object and then decoding the emotions is reliable. Using this method which included low level processing alone the system still had a recognition rate of 81.6%. They stated that there model can be extended further by using motion analysis which can be taken from the model of action perception [31]. To the best of my knowledge, to present, this is the only work that detects emotion directly from postural images.

In contrast, Kleinsmith et al. [32,33] suggested an approach that detects postural emotion by building a complicated representation of human body parts. This approach captures exact position of different body parts and therefore, can produces richer feature set. 24 features were generated directly from distances and angles between body parts (e.g. head, shoulder, and elbow). The results were accurate, 70% of affective postures were correctly classified. Unfortunately, this work did not include an automatic process for generate these features. This study is more valuable than the work of Schindler et al. [9].

TABLE 1
Expressive elements of posture.

Emotion	Body Posture
Anger	Head backward, no chest backward, no abdominal twist, arms raised forwards and upwards, shoulders lifted.
Joy	Head backward, no chest forward, arms raised above shoulder and straight at the elbow, shoulders lifted.
Sadness	Head forward, chest forward, no abdominal twist, arms at the side of the trunk, collapsed posture.
Surprise	Head backward, chest backward, abdominal twist, arms raised with straight forearms.
Pride	Head backward or lightly tilt, expanded posture, hands on the hips or raised above the head.
Fear	Head backward, no abdominal twist, arms are raised forwards, shoulders forwards.
Disgust	Shoulders forwards, head downwards.
Boredom	Collapsed posture, head backwards not facing the interlocutor.

4.1 Method for Detecting Body Expressions

Emotion detection looks familiar to the gesture recognition if we are not using the motion representation methods and this approach is similar to the approach of Schindler [9]. A lot of work and research has been done on gesture recognition but we haven't used automatic gesture recognition techniques. Researchers have directly process each segment of bodily motions alone instead of mapping emotions with the gestures. By using the motion capture equipment's the study on bodily movements has reached to new platform which provide better, reliable and efficient results [34]. The most widely used equipment is the VICON system, it uses magnetic markers on the joints and on the body to get and create a 3d image of the body. Using this device, Bernhardt and Robinson [35] developed a model for emotion detection from day today life. Complex motions were classified primitively into motion primitives. Feature representations were done with the help of the motion primitives and then this output serves as

the input for SVM-based classifier. The system gave classification result at 81% .Using the artificial neural network in this classification will provide classification results above 90%. Kapur and Virji-Babul [36] used the VICON system with only 14 markers in place of standard number of markers (the standard system regularly has more than 30 markers) that made the problem more sophisticated and hard. This experiment was done on 40 acted videos that constitute the recognition of emotion: joy, anger, sad and fear. Even though they have used only 14 markers but the results were promising and provided results with 93%.

Motion emotion representation is an issue which was raised a long time back i.e. even before when the computers came into existence. Methodology used for coding on movement are: the Bernese system [37,38], Laban Movement Analysis (LMA) and Labanotation [39,40]. LMA is the best methodology used for bodily emotion detection.

4.2 Expressing Emotions through Movement and its Analysis

The study of nonverbal movements is called as Kinesics. It argues that the body movement is enough to reveal the underlying emotional state. Both objective (using motion-capture data) and subjective studies showed that velocity, acceleration and jerk are movement variable that are particularly affected by an emotional state. Kinesics has a-lot of focus on the orientation and movement of the whole body. Angry movements tend to be large, fast and relatively jerky, while fearful and sad movements are less energetic, smaller and slower, so it's easy to understand the underlying emotional state of a person. Kipp and Martin (2009) [41] et al. stated that there is a correlation between the handedness and emotion: for two hand-righted actors, the right hand was more used when experiencing anger and the left hand when experiencing relaxed and positive feelings.

LMA is used by most of the scientists to work on the unified representation method to analyze bodily movements. LMA is a method used to observe, describe and notating the human movement. LMA consists of four components: Body, Effort, Shape and Space. Body: it focuses on the structural states of human body, movement of body parts. Space: it focuses on the movement the pathway used by the person. Effort: it focuses on the dynamic attribute of the body and attitude of movement i.e. swift, fast, jerky or slow. Shape: describes the changing forms that body. A significant characteristic of LMA is that it captures emotional state of a human according to his/her movements. Camurri [42,43] and the Info Mus Lab et al. worked on the emotion detection from dance and music performers, using a regular 2-D camera [22,10,12]. They used a four-level framework to work on and focused on Effort component. Experimental results revealed that the framework provided the same results as they got from the spectators [44]. In contrast, to the best of my knowledge, there has not been any work dealing with Body component. LMA still shows it's great possibly to be extended to use in emotion detection.

V CONCLUSION

In this paper, through evidences from psychology, we got an idea that tells us that there is a significant role of human body expression in emotion detection. We have discussed about the existing approaches that are used for automatic emotion detection which provided us with a new notion that we should have a unified framework for

motion representation so that we can infer and reveal the underlying emotions. There is a need to work a-lot in the field of bodily emotion as we are lacking if compared to facial emotion detection. In fact, according to a general overview we have not worked on the human body in emotion detection, regardless evidences from psychology. As we have a framework for facial emotion detection FACS[14], we need to have a similar framework that provide us with all necessary tools so that we can get a unified bodily movement representation framework. However, recent approaches in applying Laban Movement Analysis (LMA) for emotion detection are promising, although only a part of LMA is implemented.

According to our survey we have found that, the emotion detection was done in two ways: Firstly, we used image to detect emotions, using the low-level visual data [9] and by building a complicated representation of human body parts [32,33] the results were satisfactory 81.6% and 70% respectively. The results found by Kleinsmith [32,33] were more important as the affective postures were correctly classified. Secondly, we used the motion capture equipment to create a new platform to get reliable and accurate results. We used classifiers [34] and artificial neural networks [35] to get more efficient results, 81% and 90%

Using the psychological studies and the research done till now, we will be working on multimodal interaction so that we can infer the emotion of the people while they interact or work. The work will be based on bodily movements excluding the facial expression, as we have inferred from the above discussion that the body movements also reveal the underlying emotions.

REFERENCES

[1] James, W. “What is an Emotion?”. “Mind” 9, 34 (1884),188–205.

[2] Rauterberg, M. “Emotions: the voice of the unconscious.” Entertainment Computing-ICEC 2010 ,205–215.

[3] Russell, J. “A circumplex model of affect”. “Journal of Personality and Social Psychology” 39, 6 (1980), 1161.

[4] Ortony, A., and Turner, T. J. “What’s Basic About Basic Emotions?”, “Psychological Review” 97 , 3 (1990),315–331.

[5] Ekman, P. “An argument for basic emotions”. “Cognition and Emotion 6” (1992), 169–200.

[6] Gunes, H., Schuller, B., Pantic, M., and Cowie, R. “Emotion representation, analysis and synthesis in continuous space: A survey”. “In Automatic Face &Gesture Recognition and Workshops (FG 2011), 2011 IEEE International Conference on, IEEE” (2011), 827–834.

[7] Picard, R. “Affective Computing”, “1st ed. The MIT Press”, 2000.

[8] Wright, B., Clarke, N., Jordan, J., and Young, A. “Emotion recognition in faces and the use of visual context Vo in young people with high-functioning autism spectrum disorders”. “Autism the international journal of research and practice” 12 , 6 (2008), 607–626.

[9] Schindler, K., Van Gool, L., and de Gelder, B. “Recognizing emotions expressed by body pose: a biologically inspired neural model”. “Neural networks: the official journal of the International Neural Network Society” 21, 9 (Nov. 2008), 1238–1246.

[10] Cowie, R., Douglas-Cowie, E., Tsapatsoulis, N., Votsis,G., Kollias, S., Fellenz, W., and Taylor, J. "Emotion Recognition in Human-Computer Interaction". "IEEE Signal Processing Magazine" 18 , 1 (Jan. 2001), 32–80.

[11] Hudlicka, E. "To feel or not to feel: The role of affect in human computer interaction". "International Journal of Human-Computer Studies" 59, 1-2 (July 2003), 1–32.

[12] Darwin, C. "The expression of the emotions in man and animals", 2nd ed. London, 1980.

[13] Wallbott, H. "Bodily expression of emotion. European journal of social psychology" 28 , 6 (1998), 879–896.

[14] Ekman, P., and Friesen, W. "Facial Action Coding System: A Technique for the Measurement of Facial Movement". "Consulting Psychologists Press", 1978.

[15] Fasel, B., and Luettin, J. "Automatic facial expression analysis: a survey". "Pattern Recognition" 36 , 1 (2003),259–275.

[16] Ekman, P. "Differential communication of affect by headand body cues.Journal of Personality and Social Psychology" 2, 5 (1965), 726–735.

[17] Ekman, P., and Friesen, W. "Detecting deception from the body or face". "Journal of Personality and Social Psychology" 29, 3 (1974), 288–298.

[18] Walters, K., and Walk, R. "Perception of emotion from body posture". "Bulletin of the Psychonomic Society" 24, 5(1986), 329–329.

[19] Dittman, A. T. "The Role of Body Movement in Communication. In Nonverbal Behavior and Communication", "2nd ed. Lawrence Erlbaum Associates", Publishers, 1987, 37–64.

[20] van Heijnsbergen, C. C. R. J., Meeren, H. K. M.,Gr`ezes, J., and de Gelder, B. "Rapid detection of fear in body expressions, an ERP study". "Brain research" 1186 (Dec. 2007), 233–41.

[21] Meeren, H. K. M., van Heijnsbergen, C. C. R. J., and de Gelder, B. "Rapid perceptual integration of facial expression and emotional body language". "Proceedings of the National Academy of Sciences of the United States of America" 102, 45 (Nov. 2005), 16518–23.

[22] Coulson, M. "Attributing emotion to static body postures: Recognition accuracy, confusions, and view point dependence". "Journal of Nonverbal Behavior" 28 , 2 (2004), 117–139.

[23] Mehrabian, Albert. 1972. "Nonverbal Communication". Transaction Publishers.

[24] Bull, P. "Posture and Gesture", volume 16 ed. Pergam on Press, 1987.

[25] Lagerl¨ of, I., and Djerf, M. "Children's understanding of emotion in dance". "European Journal of Developmental Psychology" 6 , 4 (July 2009), 409–431.

[26] Kendon, Adam. 1983. "Gesture and Speech: How They Interact." Nonverbal Interaction: 13–45.

[27] Ekman, P., and W. V. Friesen. 1969. "The Repertoire of Nonverbal Behavior: Categories, Origins, Usage, and Coding." Semiotica 1: 49–98.

[28] Efron, David. 1941. "Gesture and Environment." 1972. Gesture, Race and Culture. Mouton The Hague.

[29] David McNeill 1987. "The Role of Body Movement in Communication".

[30] Dael, Nele, Marcello Mortillaro, and Klaus R. Scherer. 2011. "Emotion Expression in Body Action and Posture."

[31] Giese, M. A., and Poggio, T. "Neural mechanisms for the recognition of biological movements". "Nature Neuroscience" 4 (2003), 179–192.

[32] Kleinsmith, A., and Bianchi-Berthouze, N. "Recognizing affective dimensions from body posture. Affective Computing and Intelligent" (2007), 48–58.

[33] Kleinsmith, A., Fushimi, T., and Bianchi-Berthouze, N. "An incremental and interactive affective posture recognition system". In Context (2005), 1–13.

[34] Shen, L., Wang, M., and Shen, R. "Affective e-Learning: Using Emotional Data to Improve Learning in Pervasive Learning Environment Related Work and the Pervasive e-Learning Platform". "Learning" 12, 2 (2009),176–189.

[35] Bernhardt, D., and Robinson, P. "Detecting affect from non-stylised body motions". "Affective Computing and Intelligent Interaction" 4738 (2007), 59–70.

[36] Kapur, A., and Virji-Babul, N. "Gesture-based affective computing on motion capture data". "Affective Computing" (2005), 1–7.

[37] Frey, S., and von Cranach, M. "A method for the assessment of body movement variability". "Social communication and movement" (1973), 389–418.

[38] Rosenfeld, H. "Measurement of body motion a and orientation". "In Handbook of methods in non verbal behavior research", K. Scherer and P. Ekman, Eds. Cambridge University Press, 1982, 199–286.

[39] Laban, R., and Lawrence, F. Effort . Macdonald & EvansLtd., London, 1947.

[40] Hutchinson, "A. Labanotation: The System of Analyzing and Recording Movement". "New Directions", 1954.

[41] Kipp, Michael, and J.-C. Martin. 2009. "Gesture and Emotion: Can Basic Gestural Form Features Discriminate Emotions?" "In Affective Computing and Intelligent Interaction and Workshops", 2009. ACII 2009. "3rd International Conference", 1–8.

[42] Camurri, A. "Recognizing emotion from dance movement: comparison of spectator recognition and automated techniques". "International Journal of Human-Computer" 59 (2003), 213–225.

[43] Camurri, A., Hashimoto, S., Ricchetti, M., Ricci, A.,Suzuki, K., Trocca, R., and Volpe, G. "Eyes web: Toward gesture and affect recognition in interactive dance and music systems". "Computer Music Journal" 24 , 1 (2000),57–69.

[44] Camurri A., Mazzarino, B., Trocca, R., and Volpe, G."Real-time analysis of expressive cues in human movement". Proc. CAST01, GMD, St. Augustin-Bonn (2001), 63–68.

[45] Scherer, K. "What are emotions? And how can they be measured?". "Social science information" 44, 4 (2005),695–729.

[46] Siegman, A. W., and Feldstein, S. "Nonverbal behavior and Communication", "Second ed. Psychology Press", 1987.

STATISTICAL INVESTIGATION OF MAGNETO-HYDRODYNAMIC TURBULENCE DESCRIBED BY SPACE-TIME FUNCTIONAL FORMALISM- II

Kirti Sahu

Department of Mathematics, St. Vincent Pallotti College of Engineering and Technology, Nagpur-441108(India)

ABSTRACT

Joshi N. E. and Meshram M. C. derived the equations describing the dynamics of the kinetic energy spectrum density function and the magnetic energy spectrum density function on using the Lewis–Kraichnan space–time version of the Hopf functional formalism and the multiple-scale-cumulant expansion method for their investigation of Magnetohydrodynamic turbulence . Meshram M.C. and Sahu K. have written these equations in dimensionless form with respect to a representative wavenumber k_0 and a representative value of the energy spectrum E_0 and then integrated these equations numerically. The statistical quantities which were not included there (namely skewness, enstropy and Taylor's micro-scale of both the velocity field and the magnetic field for the representative value of Reynolds number R=20 and R=1600) are evaluated in the present work. We also discover the laws governing these statistical quantities. Further, we discuss the merits and scope of the present closure scheme for studying similar types of turbulent flows.

Keywords* : *Closure Method , Energy Specturm Function, MHD Turbulence, Statistical Quantities

I INTRODUCTION

Turbulence is a ubiquitous phenomenon. Turbulent fluid flows are experienced in daily life. When the fluid is electrically conducting, the turbulent motions are accompanied by magnetic field fluctuations and give rise to magnetohydrodynamic turbulence. G.K. Batchelor[1] and S. Chandrasekhar[2,3,4] have shown that the phenomenological theory of turbulence in magnetohydrodynamics can be developed to same extent as the corresponding theories in ordinary hydrodynamic turbulence developed by Taylor[5], Von Karman and Howarth[6], Robertson[7], Kolmogoroff[8], Batchelor[1] and Heisenberg[9]. Hence, concepts and techniques that have evolved in fully developed hydrodynamical turbulence can be extended to other strongly non-linear problems. Functional calculus for the theory of hydrodynamic turbulence was first introduced by E Hopf[10]. K. Goto[11] extended this theory to the magnetohydrodynamic turbulence. R.M. Lewis and R.H. Kraichnan[12] gave the space-time functional formalism of Hopf equation. N.E.Joshi and S.V. Krishna[13] translated this functional formalism for magnetohydrodynamic turbulence and obtained two equations for characteristic functional of the joint probability distribution of the velocity and magnetic fields. G.Ahmadi[14] offered

approximate methods for Burger's model of hydrodynamic turbulence based on series expansion of the natural logarithm of characteristic functional. N.E. Joshi and M.C. Meshram[15] extended Ahmadi's version to magnetohydrodynamic turbulence and obtained a closed set of cumulant equations in real space using zero-fourth-order-cumulant approximation. N.N. Bogoliubov[16] originated a method of multiple time scale expansion. W.M.P Malfliet[17] was first to apply this method of multiple time scales to Burgers hydrodynamic turbulence. T. Tatsumi, S. Kida and J. Mizushima[18] applied multiple-scale-cumulant-expansion method to an incompressible isotropic turbulence and obtained positive definite energy spectrum at all Reynolds numbers. N.E. Joshi and M.C. Meshram[15] have raised the domain to space-time functional which indeed is essential in order to extend this concept to hydromagnetic turbulence.

In section 2 a close set of equations for the energy spectrum functions for MHD turbulence in dimensionless form are considered from M.C.Meshram and K.Sahu[19]. The equations for energy spectrum functions are integrated numerically and the statistical quantities describing the MHD turbulence such as the energy transfer function, energy dissipation function, enstrophy , Taylor's micro-scale and the skewness are evaluated from the numerical values of energy spectrum function of velocity field and magnetic field and a detail analysis of these quantities is presented in section 3. In section 4 we write the summary and discuss the merit of results obtained which is followed by the scope of the method for conducting further research.

II EQUATIONS FOR THE ENERGY SPECTRUM FUNCTIONS IN DIMENSIONLESS FORM

M.C. Meshram and K.Sahu[19] obtained the following equations describing the dynamics of the kinetic energy spectrum density function and the magnetic energy spectrum density function in dimensionless form with respect to a representative wavenumber k_0 and a representative value of the energy spectrum E_0 :

$$\left(\frac{\partial}{\partial\tau}+\frac{\kappa^2}{R}\right)\phi^V(\kappa,\tau)=4\pi R\int_{-\infty}^{\infty}d\kappa'\int_{-1}^{1}\frac{1-e^{-\left(\kappa^2+\kappa'^2+\kappa''^2\right)\tau/R}}{\left(\kappa^2+\kappa'^2+\kappa''^2\right)}\kappa\kappa'^3\left(\frac{\kappa\kappa'}{\kappa''^2}+\mu\right)\left(1-\mu^2\right)$$
$$\left\{\left(\phi^V(\kappa',\tau)-\phi^V(\kappa,\tau)\right)\phi^V(\kappa'',\tau)-\left(\phi^M(\kappa',\tau)-\phi^M(\kappa,\tau)\right)\phi^M(\kappa'',\tau)\right\}d\mu \quad (2.1a)$$

$$\left(\frac{\partial}{\partial\tau}+\frac{\kappa^2}{R}\right)\phi^M(\kappa,\tau)=4\pi R\int_{-\infty}^{\infty}d\kappa'\int_{-1}^{1}\frac{1-e^{-\left(\kappa^2+\kappa'^2\right)\tau/R}}{\left(\kappa^2+\kappa'^2\right)}$$
$$\left\{\kappa(\kappa+\kappa'\mu^3)\phi^V(\kappa',t)\phi^M(\kappa,\tau)-\kappa'(\kappa'+\kappa\mu^3)\phi^V(\kappa,\tau)\phi^M(\kappa',\tau)\right.$$
$$\left.-\kappa^2\left(1+\frac{\kappa'}{\kappa''^2}(\kappa+\kappa'\mu)(1-\mu^2)\right)\left(\phi^V(\kappa',\tau)-\phi^V(\kappa,\tau)\right)\phi^M(\kappa'',\tau)\right\}d\mu$$

(2.1b)

Where $\kappa''^2=\kappa^2+\kappa'^2+2\mu\kappa\kappa'$

They solved these equations numerically by using the following initial conditions for energy density functions

$$\phi^V(\kappa,0)=\frac{1}{4*pi}\exp(-\kappa^2) \text{ and } \phi^M(\kappa,0)=\frac{1}{400*pi}\exp(-\kappa^2) \quad (2.2)$$

Also, they selected the following initial conditions for energy spectrum functions $E^V(k,t)$ *and* $E^M(k,t)$:

$$E^V(k,0)=E_0^V\left(k/k_0\right)^2\exp\left[-\left(k/k_0\right)^2\right] \quad \text{and} \quad E^M(k,0)=E_0^M\left(k/k_0\right)^2\exp\left[-\left(k/k_0\right)^2\right] \quad (2.3)$$

The integrals on the right –hand side of (2.1a) and (2.1b) are calculated numerically by using appropriate sum rules at discrete values of κ' and μ and terminating the infinite integrals with respect to κ' at a sufficiently large value of κ'. At very large Reynolds number the integrand changes rapidly at small κ' and does not vanish even at large κ'. In order to evaluate such an integral accurately and efficiently we employ a non–uniform mesh for κ' whose size is an increasing function of κ'.

The following variables are introduced for this purpose:

$$\xi=\log(10\kappa) \qquad \eta=0.01R\tau \qquad \phi(\xi,\eta)=0.1\phi(\kappa,\tau) \quad (2.4)$$

In terms of these new variables equations (2.1a) and (2.1b)

$$\left(\frac{\partial}{\partial\eta}+\frac{e^{2\xi}}{R^2}\right)\phi^V(\xi,\eta)$$

$$=3\pi\int_{-\infty}^{\infty}e^{3\xi'}d\xi'\int_{-1}^{1}\left(\frac{1-\exp\left[-2e^{\xi+\xi'}\left(e^{\xi-\xi'}+e^{\xi'-\xi}+\mu\right)\eta/R^2\right]}{e^{\xi-\xi'}+e^{\xi'-\xi}+\mu}\right)\left(\frac{1}{e^{\xi-\xi'}+e^{\xi'-\xi}+2\mu}+\mu\right)\left(1-\mu^2\right)$$

$$\times\left\{\left(\phi^V(\xi',\eta)-\phi^V(\xi,\eta)\right)\phi^V(\xi'',\eta)-\left(\phi^M(\xi',\eta)-\phi^M(\xi,\eta)\right)\phi^M(\xi'',\eta)\right\}d\mu \quad (2.5a)$$

$$\left(\frac{\partial}{\partial\tau}+\frac{e^{2\xi}}{R^2}\right)\phi^M(\xi,\eta)=3\pi\int_{-\infty}^{\infty}d\xi'\int_{-1}^{1}\left(\frac{1-\exp\left[-e^{\xi+\xi'}\left(e^{\xi-\xi'}+e^{\xi'-\xi}\right)\eta/R^2\right]}{e^{\xi-\xi'}+e^{\xi'-\xi}}\right)\times$$

$$\left\{(e^{\xi}+e^{\xi'}\mu^3)\phi^V(\xi',\eta)\phi^M(\xi,\eta)-(e^{\xi'}+e^{\xi}\mu^3)\phi^M(\xi',\eta)\phi^V(\xi,\eta)\right.$$

$$\left.-e^{\xi}\left(1+\frac{(1+e^{\xi'-\xi}\mu)(1-\mu^2)}{e^{\xi-\xi'}+e^{\xi'-\xi}+2\mu}\right)\left(\phi^V(\xi',\eta)-\phi^V(\xi,\eta)\right)\phi^M(\xi'',\eta)\right\}d\mu$$

(2.5b)

III EVALUATION OF STATISTICAL QUANTITIES AND GOVERNING LAWS

The infinite integral with respect to ξ' is terminated at $\xi' = \Sigma + \log 2 \quad (\kappa' = 0.2)$ and calculated by Simpsons rule in the region $-\Sigma < \xi' \le \Sigma$ with a mesh size $\Delta\xi' = 0.01$. The following values have been chosen for Σ :

$$\Sigma = \begin{cases} 30 & R = 5,10,20,100 \\ 40 \quad for & R = 200,400 \\ 45 & R = 800,1600 \end{cases}$$

These values of Σ have been confirmed to be sufficiently large by numerical results .The integration with respect to μ is carried out by Simpson rule with a mesh size $\Delta\mu = 0.1$.The derivative $\frac{\partial}{\partial\eta}$ is replaced by the forward–difference quotient with mesh size $\Delta\eta = 0.0002R$.Thus, the equations (2.5a) and (2.5b) are solved numerically for the initial conditions(2.2) ; the Reynolds number R=20 and R=1600; and the energy spectrum functions $E^V(k,t)\ and\ E^M(k,t)$ are obtained as functions of the wavenumber k and time t. Important statistical quantities characterizing magneto-hydrodynamic turbulence are derived from numerical results for energy spectrum functions for velocity field and magnetic field are as defined below:

Energy spectrum function: $E^V(k,t) = 4\pi k^2 \phi^V(k,t)$ and $E^M(k,t) = 4\pi k^2 \phi^M(k,t)$

Ratio of magnetic to kinetic energy spectrum function: $\psi(k,t) = \frac{E^M(k,t)}{E^V(k,t)}$

Energy transfer functions:

$$T^V(k,t) = 4\pi k^2 \left(\frac{\partial}{\partial t} + 2\gamma k^2 \right) \phi^V(k,t) \text{ and } T^M(k,t) = 4\pi k^2 \left(\frac{\partial}{\partial t} + 2\gamma k^2 \right) \phi^M(k,t)$$

Enstropy : $\varepsilon^V(t) = 4\pi \int_0^\infty k^2 \phi^V(k,t) dk$ and $\varepsilon^M(t) = 4\pi \int_0^\infty k^2 \phi^M(k,t) dk$

Energy dissipation function: $D^V(k,t) = 2\nu k^2 E^V(k,t)$ and $D^M(k,t) = 2\nu k^2 E^M(k,t)$

Skewness: $S^V(t) = \frac{3\sqrt{30}}{14} \frac{5\int_0^\infty k^2 T^V(k,t)\, dk}{\left[\int_0^\infty k^2 E^V(k,t)\, dk\right]^{3/2}}$ and $S^M(t) = \frac{3\sqrt{30}}{14} \frac{5\int_0^\infty k^2 T^M(k,t)\, dk}{\left[\int_0^\infty k^2 E^M(k,t)\, dk\right]^{3/2}}$

Taylor's Microscale: $\lambda^V(t) = \frac{5\int_0^\infty E^V(k,t) dk}{\int_0^\infty k^2 E^V(k,t) dk}$ and $\lambda^M(t) = \frac{5\int_0^\infty E^M(k,t) dk}{\int_0^\infty k^2 E^M(k,t) dk}$

The numerical integration of (2.5a)–(2.5b) uncovers following laws for the magnetohydrodynamic turbulence.

In the lowest subrange of the universal wavenumber range, the kinetic energy spectrum function and magnetic energy spectrum function both are proportional to -5/3 power of the wave number in the inertial range.

These laws are symbolically written as follows:

$$E^V(k,t) \propto k^{-\frac{5}{3}} ; E^M(k,t) \propto k^{-\frac{5}{3}} \quad (3.1)$$

These energy spectrum function has exactly the same power as Kolomogorov's inertial- subrange spectrum. Next to previous subrange, there exists a subrange in which the energy spectrum functions of both the velocity field and magnetic field are inversely proportional to a wavenumber. These laws are symbolically written as follows:

$$E^V(k,t) \propto k^{-1} ; E^M(k,t) \propto k^{-1} \quad (3.2)$$

At still higher wave number, both the spectrum functions take the exponential form. Thus, the results obtained by the application of multiple–scale–cumulant–expansion method support the asymptotic decay of the spectrum functions for very high wavenumber irrespective of Reynolds numbers considered. The function $\psi(k,t)$ which is the ratio of magnetic energy to kinetic energy is shown in fig 3. From figure 3 it is clear that $\psi(k,t)$ grows monotonically to a value of 4 by t=1.2.The variation of $\psi(k,t)$ with time is linked to the magnetic Reynolds number of the flow. The enstropy of velocity field , $\varepsilon^V(t)$ and magnetic field , $\varepsilon^M(t)$ are plotted in figure 4 and figure 5 respectively. We infer from these graphs of enstropy that they are analogous to each other. The shape of each of these graphs can be divided into three parts depending upon their behaviour with respect to time. For R=20, the first part being from t = 0 to t =7, the second part from t =7 to t=15 and third part t=15 onwards. The enstropy for both the fields, $\varepsilon^V(t)$ and $\varepsilon^M(t)$ increase monotonically with respect to time in the initial period.

Thereafter, in the second period the curves attain the Gaussian shape. In the final period corresponding to t >15 the enstropy of both the velocity and magnetic field increases monotonically. We also observe from these figures that as the Reynolds number increases there is decrease in the time taken to attain the maximum enstropy in case of both the fields.

In the initial period before attaining the maximum value the enstropy of the velocity field is proportional to 2.2 power of time and analogues to this enstropy of the magnetic field are proportional to 2.27 power of time.

These laws symbolically are written as follows:

$$\varepsilon^V(t) \ \alpha \ t^{2.2} ; \varepsilon^M(t) \ \alpha \ t^{2.27} \quad (3.3)$$

Next to previous period just after attaining the maximum value for R=20 and R=1600 the value of enstropy of both the fields decreases and this decrease is governed by the following laws:

The enstropy of the velocity field is proportional to the negative 2.2 power of time and the enstropy of the magnetic field is proportional to the negative 2.25 power of time. These laws symbolically are written as follows

$$\varepsilon^V(t) \propto t^{-2.2} \; ; \varepsilon^M(t) \propto t^{-2.25} \tag{3.4}$$

These laws agree quite well with the experimental results. In the last period enstropy of the velocity field and magnetic field varies with respect to time as per the following laws:

The enstropy of the velocity field is proportional to the 1.03 power of time whereas the enstropy of the magnetic field is proportional to the 1.13 power of time. These laws symbolically are written as follows:

$$\varepsilon^V(t) \propto t^{1.03} \; ; \; \varepsilon^M(t) \propto t^{1.13} \tag{3.5}$$

The enstropy of magnetic field clearly grows more than enstropy of velocity field. From figure 6 and figure 7 showing the skewness of velocity field and magnetic field we infer that they are analogous to each other. The shape of each of these graphs can be divided into three parts depending upon their behaviour with respect to time. For R=20, the first part being from t = 0 to t =7, the second part from t =7 to t=15 and third part t=15 onwards. The skewness for both the fields, $S^V(t)$ and $S^M(t)$ increases monotonically with respect to time in the initial period .Thereafter in the second period the curves attain the Gaussian shape. In the final period corresponding to t >15 the skewness of both the velocity and magnetic field increases monotonically. We also observe from these figures that as the Reynolds number increases there is decrease in the time taken to attain the maximum skewness in case of both the fields.

For both the velocity and magnetic field their skewness grows very rapidly in the initial period and attains a quite large maximum value 0.37 for R=20 and 2.8 corresponding to R=1600 by velocity field. Similarly the corresponding maximum values for the magnetic field are 0.21 and 2.4 respectively. This reveals that there is a increase in the maximum value of skewness with rise in the Reynolds number.

In the initial period before attaining the maximum value the skewness of the velocity field is proportional to 2.2 power of time and an analogue to this skewness of the magnetic field is proportional to 2.27 power of time.

These laws symbolically are written as follows:

$$S^V(t) \propto t^{2.2} \; ; S^V(t) \propto t^{2.27} \tag{3.6}$$

Next to previous period just after attaining the maximum value for R=20 and R=1600 the value of skewness of both the field decreases and this decrease is governed by the following laws:

The skewness of the velocity field is proportional to the negative 2.2 power of time and the skewness of the magnetic field is proportional to the negative 2.25 power of time. These laws are symbolically written as follows:

$$S^V(t) \propto t^{-2.2} \; ; \; S^V(t) \propto t^{-2.25} \tag{3.7}$$

These laws agree quite well with the experimental results. In the last period skewness of the velocity field and magnetic field varies with respect to time as per the following laws:

The skewness of the velocity field is proportional to the 1.03 power of time whereas the skewness of the magnetic field is proportional to the 1.13 power of time. These laws are symbolically written as follows:

$$S^V(t) \ \alpha \ t^{1.03} \ ; \ S^V(t) \ \alpha \ t^{1.13} \tag{3.8}$$

From figure 6 and 7 we also notice that these skewness are a measure of the departure from Gaussianity , and indicate how transfer functions vary with the time at high wavenumber. They decrease substantially after having reached their sharp maximum and before stabilizing.

The energy dissipation function for kinetic energy and magnetic energy clearly exhibit the characteristic of energy spectra as shown in figure 8 and figure 9.

The transfer spectra of magnetic energy and kinetic energy depict in figure 10 and figure 11 behave differently. Both transfer spectra are positive in the first shell, indicating that an inverse transfer of magnetic energy is occurring at low wavenumber.

It is observed that for large Reynolds number, the energy containing range and the inertial subrange the energy dissipation is much smaller in magnitude than the energy transfer. For a given Reynolds number, in the neighbourhood of the wavenumber both the energy transfer functions change their sign satisfying the condition:

$$\int_0^\infty T^V(k,t)dk = 0 \quad ; \int_0^\infty T^M(k,t)dk = 0 \tag{3.9}$$

as per the present closure scheme employed. Finally it is observed that the exponential spectrum occurs in the wavenumber range in which energy transfer is nearly balanced by the energy dissipation. A.Pouquet and G.S.Patterson[20] have investigated MHD turbulence numerically by restricting to magnetic Prandtl number of one and obtained results for Reynolds number 40 based on Taylor micro scale. The predictions of present closure scheme for magnetic Prandtl number one and Reynolds number as large as 1600 are in good agreement with those of the former.

The Taylor's microscale of the velocity field, $\lambda^V(t)$ and for the magnetic field, $\lambda^M(t)$ are plotted in figure 12 and figure 13. At large Reynolds numbers the micro-scale for the velocity field and that of the magnetic field decreases rapidly from its initial value to a minimum and then increases almost proportionally with time. The minimum value of the Taylor's micro-scale of the velocity field and that of the magnetic field is t=0.5 and t=0.6 for R=20 respectively and these values for R=1600 respectively are t=0.55 and t=0.65.

The decrease of the Taylor's micro-scale of the velocity field and that of the magnetic field with time is governed by the laws that the microscale of both the velocity field and magnetic field vary proportional to negative 0.5 power of the time. Symbolically these laws are

$$\lambda^V(t) \ \alpha \ t^{-0.5} \ ; \lambda^M(t) \ \alpha \ t^{-0.5} \tag{3.10}$$

The variation of the Taylor's micro-scale of the velocity field and that of the magnetic field with time confirms the asymptotic decrease of Taylor's micro-scale with time. Similarly the increase of the Taylor's micro-scale of the velocity field and that of the magnetic field with time is governed by the laws that the microscale of both the velocity field and magnetic field vary proportional to 0.5 power of the time. Symbolically these laws are

$$\varepsilon^{M}(t) \qquad \lambda^{V}(t) \alpha\ t^{0.5}\ ; \lambda^{M}(t) \alpha\ t^{0.5} \tag{3.11}$$

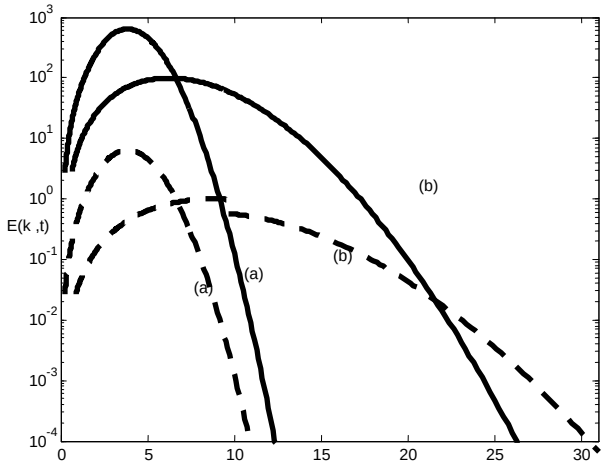

Figure 1. Kinetic (solid lines) and Magnetic (Dashed lines) energy spectrum function for R=20 at (a) t =0 and (b) t =3

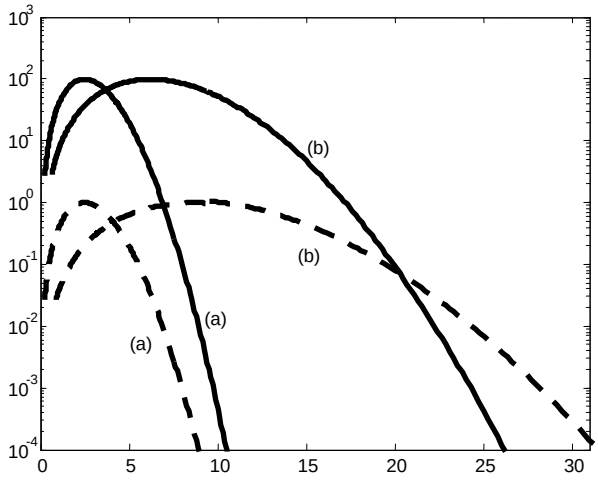

Figure 2. Kinetic (solid lines) and Magnetic (Dashed lines) energy spectrum function for R=1600 at (a) t =0 and (b) t =3

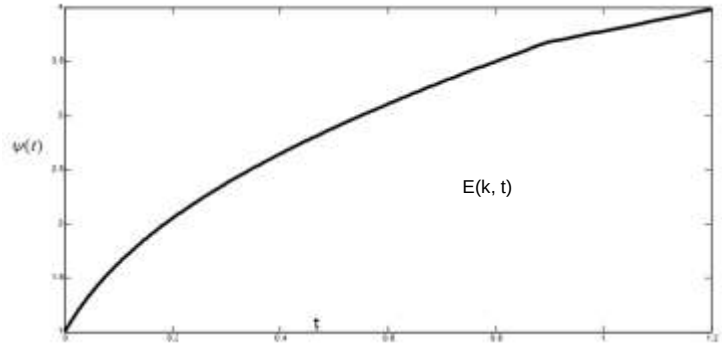

Figure 3. $\psi(t)$ ***verses time***

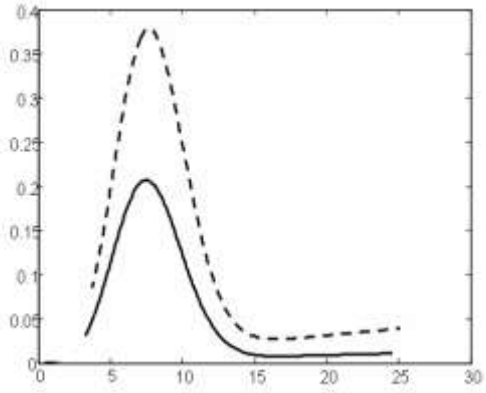

Figure 4. Enstropy for Velocity field (solid lines) *and Magnetic field (Dashed lines) at R=20*

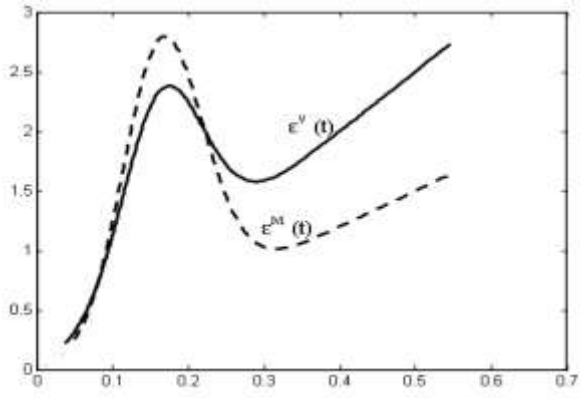

Figure 5. Enstropy for Velocity field (solid lines) *and Magnetic field (Dashed lines)at R=1600*

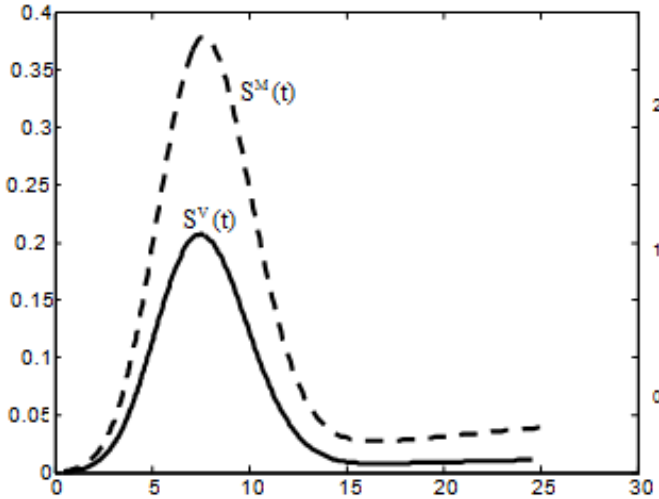

Figure 6. Skewness for for Velocity field (solid lines) Magnetic field (Dashed lines) at R=20

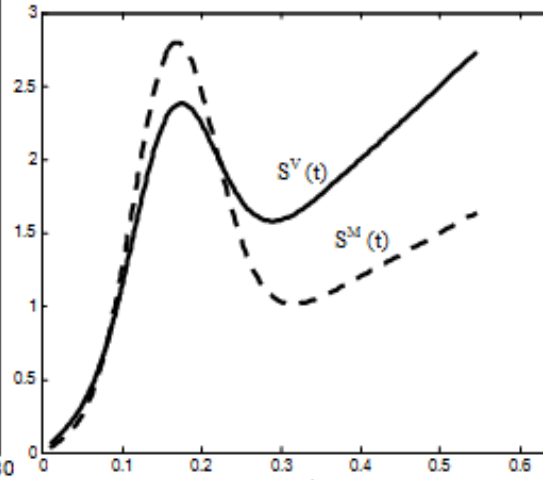

Figure 7. Skewness for Velocity fie(solid and Magnetic field (Dashed lines) at R=1600

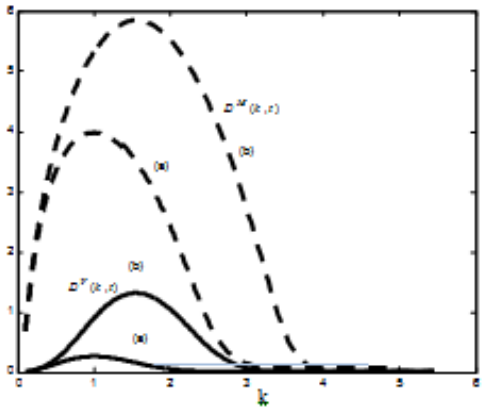

Figure 8. Energy dissipation function for R=20 at (a) t=0 and (b) t=3 ,

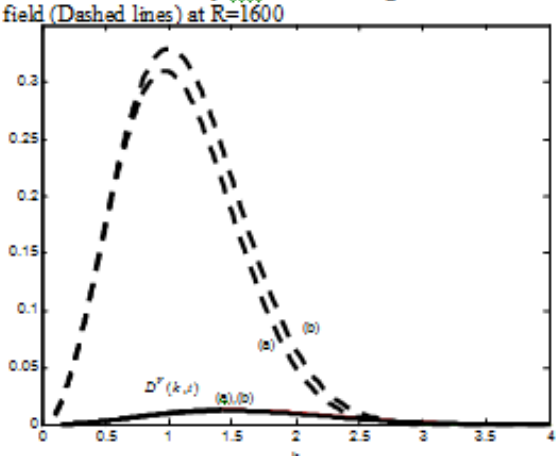

Figure 9. Energy dissipation function for R=1600 at (a) t=0 and (b) t=3

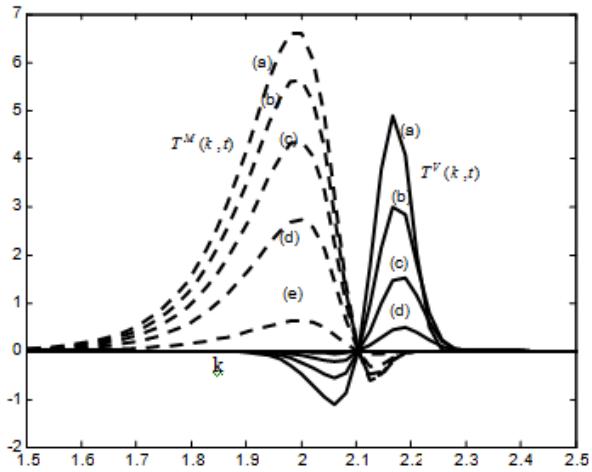

Figure 10. Kinetic (Solid lines) and Magnetic (dashed lines) energy transfer function for R=20 at (a) t =0 , (b) t=1 , (c) t=2 , (d) t=3 and (e) t=4

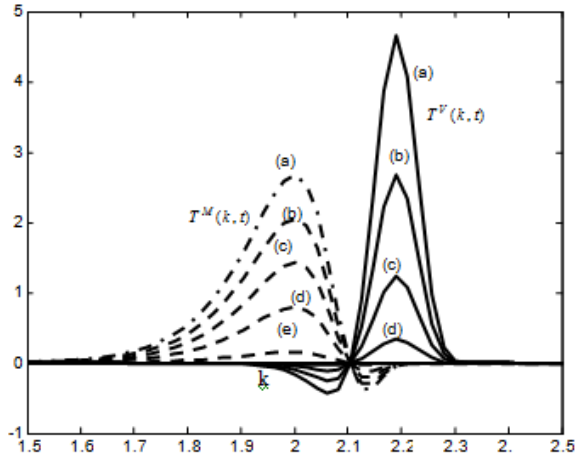

Figure 11. Kinetic (Solid lines) and Magnetic (dashed lines) energy transfer function for R=1600 at (a) t =0 , (b) t=1

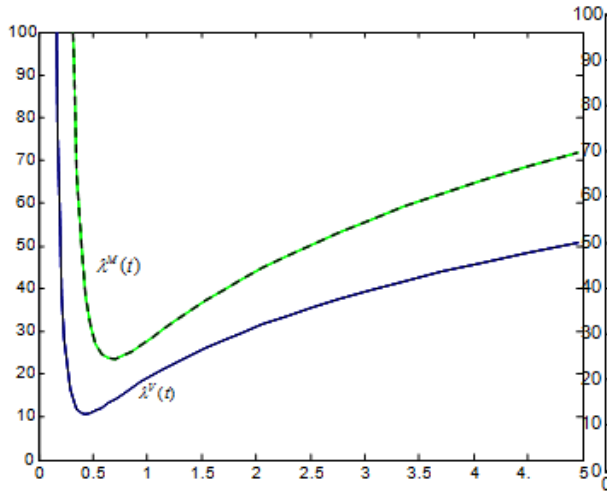

Figure 12. Kinetic (Solid lines) and Magnetic (dashed lines) energy transfer function for R=20 at (a) t =0, (b) t=1 , (c) t=2 , (d) t=3 and (e) t=4

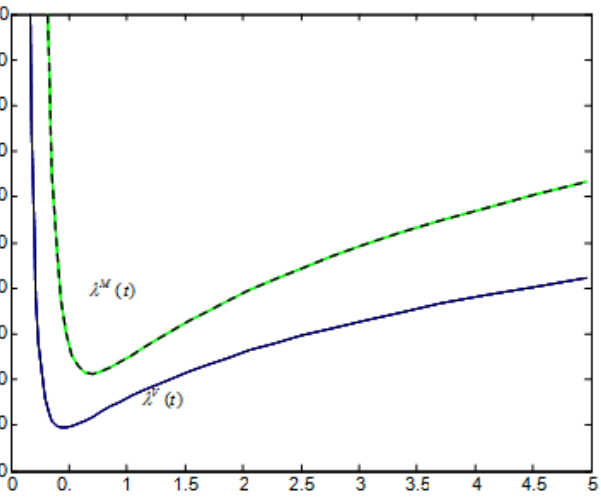

Figure 13. Kinetic (Solid lines) and Magnetic (dashed lines) energy transfer function for R=1600 at (a) t =0 , (b) t=1 (c) t=2 , (d) t=3 and (e) t=4

IV RESULTS

1. Both the kinetic energy spectrum function and the magnetic energy spectrum function are found to be positive definite for all values of Reynolds numbers R=20 and R=1600.

2. At large Reynolds numbers both the kinetic energy spectrum function and magnetic energy spectrum function take the form of Kolmogorov's -5/3 power spectrum in the inertial subrange , whose extent increases indefinitely with Reynolds number .In the higher wavenumber region beyond the inertial subrange the spectrum takes a universal form which is independent of its structure at lower wavenumbers.

3. The universal spectrums are composed of three different subspectra, which are in order of increasing wavenumber, the $k^{-5/3}$ spectrum, the k^{-1} spectrum and the exponential spectrum.

4. The ratio of magnetic energy to kinetic energy $\psi(t)$ which initially was 10^{-2}, is found as a monotonically growing function with respect to time. The variation of $\psi(t)$ with time is related to Reynolds number.

5. As Reynolds number increases the time required to attain the maximum value of enstropy also increases. For both the velocity and magnetic field their enstrophy grows very rapidly in the initial period and the velocity field attains a quite large maximum value. This reveals that there is an increase in the maximum value of enstropy with rise in the Reynolds number. In the initial period the enstropy of the velocity field is proportional to 2.2 power of time and analogues to this enstropy of the magnetic field is proportional to 2.27 power of time.In the intermediate period the enstropy of both the velocity and magnetic fields assumes the Gaussian shape and the enstropy of the velocity field is proportional to the negative 2.2 power of time and the enstropy of the magnetic field is proportional to the negative 2.25 power of time whereas in the third period the enstropy increases with time and enstropy of the velocity field is proportional to the 1.03 power of time and the enstropy of the magnetic field is proportional to the 1.13 power of time. The enstropy of magnetic field grows more than the enstropy of velocity field.

6. The initial value of skeness is identically zero for both the reactants. In the initial period the the skewness of the velocity field is proportional to 2.2 power of time and analogues to this skewness of the magnetic field is proportional to 2.27 power of time. In the intermediate period the skewness of both the velocity and magnetic fields assumes the Gaussian shape and the skewness of the velocity field is proportional to the negative 2.2 power of time and the skewness of the magnetic field is proportional to the negative 2.25 power of time whereas in the third period the skewness increases with time .The skewness of the velocity field is proportional to the 1.03 power of time and the skewness of the magnetic field is proportional to the 1.13 power of time.

7. As Reynolds number increases the energy dissipation decreases in magnitude than the energy transfer. The transfer spectra of magnetic energy and kinetic energy behave differently. As the Reynolds number takes the larger value the wavenumber at which energy transfer function of both the field vanish is shifted to the lower wavenumber.

8. The Taylor's microscale of both the velocity field and magnetic field varies proportionally to 0.5 power of the time.

REFERENCES

[1] Batchelor G K 1950 *Proc. Roy. Soc.* A 201 405

[2] Chandrasekhar S 1951 *Proc. Roy. Soc.* A 204 435

[3] Chandrasekhar S 1951 *Proc. Roy. Soc.* A 207 301

[4] Chandrasekhar S 1955 *Proc. Roy. Soc.* A 233 322

[5] Taylor G I 1935 *Proc. Roy. Soc.* A 151 1

[6] Von Karman T and Howarth L 1938 *Proc. Roy. Soc.* A 164 192

[7] Robertson H P 1940 *Proc. Camb. Phil. Soc.* 36 209

[8] Kolmogoroff A N 1941 *Dokl. Akad. Nauk. SSSR* 32 16

[9] Heisenberg W 1948 *Proc. Roy. Soc.* A 195 402

[10] Hopf E 1962 *Symp. Appl. Math.* 13 157

[11] K. Goto. 1961 Prog. of Theoretical Phys. 25(4) 603

[12] Lewis R M and Kraichan R H 1962 *Commun. Pure Appl. Math.* 15 397

[13] Krishna S. V. and Joshi N. E. 1967 J. Math and Phys.Sci. 1(3) 207

[14] G.Ahmadi 1976 Appl. Sci. Res. 32 207

[15] Joshi N E and Meshram M C 1985 *30th Congress of ISTAM (New Delhi)* 167

[16] N. N. Bogoliubov 1962 Studies in Statistical Mechanics North Holand

[17] W.P.M. Malfliet 1969 Physics. 45 257

[18] T.Tatsumi, S.Kida and J.Mizushima 1977 J. fliud Mech. 31 97

[19] Meshram M.C. and Sahu K. 2013 Phys. Scr. T155 014044 1

[20] Pouquet A and Paterson G S 1978 *J. Fluid Mech.* 85 305

SAAS INTERFACE LAYER VULNERABILITIES IN CLOUD COMPUTING

John Jeya Singh.T[1], Dr E.Baburaj[2]

[1]Research Scholar, Dept of CS ,Bharathiar University, Coimbatore ,Tamilnadu, (India).

[2]Professor and Head, Dept of Computer Science & Engineering,

Narayanaguru College of Engineering, Majalumoodu, Tamilnadu, (India)

ABSTRACT

Cloud computing is gaining remarkable popularity in the recent year. During the past few years cloud computing is fastest growing parts of the IT industry. Cloud computing can offer a verity of services including hosted service over internet. We can use third party facilities and resources as a service to perform out computing needs. The risks of compromised security and privacy may be lower overall. One of the must be very careful to understand the security risk and challenges posed in utilizing these technologies. In this paper we summarize Cloud computing SaaS Interface layer vulnerabilities. We have suggested feasible and available solutions for the same.

Keywords: Cloud Computing, Interface, Middleware, Security, Virtualization.

I INTRODUCTION

Cloud computing is seen as a trend in the present day scenario with almost all the organizations trying to make on entry into it. The main advantages of cloud computing are cost saving, high availability and easy scalability [1]. One must be very careful to understand the security risks and challenges posed in utilizing these technologies. Network security technology needed in service of Cloud computing. The Cloud computing model [2][3] is enabled by the ongoing standardization of underlying technologies like virtualization, service oriented Architecture (SOA) and Web 2.0 In this paper we discuss in detail cloud computing its types and cloud computing security issues.

The remainder of this paper is organized as follows. Section 2 described Cloud service models. Section 3 described Cloud developments modal Section 4 discusses characteristics of Cloud. Section 5 discusses SaaS Interface layer middleware's. Section 6 discusses middleware services. Section 7 analyses SaaS Interface layer security threats. Section 8 we given suggested feasible and available solution. Section 9 will conclude the paper.

II CLOUD SERVICE MODELS

In this section we describe cloud service model

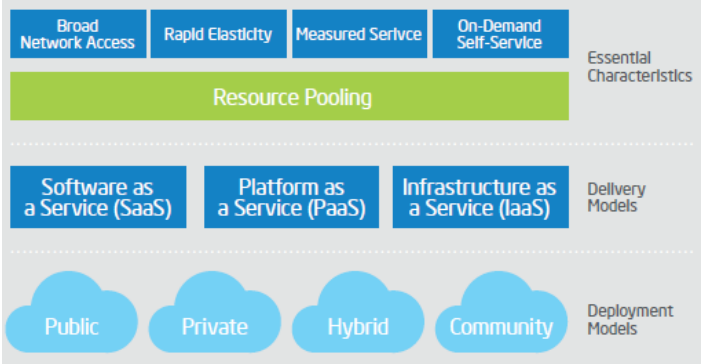

Fig 1:National Institute of Standards and Technology (NIST) Cloud Computing Model [4]

2.1 Software as a Service (SaaS)

It employs the provider's applications running on a cloud infrastructure. The applications are accessible from various client devices through either a thin client interface, such as a web browser (e.g., web based email), or a program interface. Example SalesForce CRM is an example of the SaaS provider, Google apps and Zoho.

2.2 Platform as a Service (PaaS)

It is Consumer created or acquired applications supported by the provider are deployed onto the cloud infrastructure. It is managed or controlled by the providers.

Example: Force.Com, Microsoft Azure and Google App Engine.

2.3 Infrastructure as a Service (IaaS)

It is consumer provisions processing it include storage, networks, and other fundamental computing resources. In this the consumer is able to deploy and run arbitrary software, which can include operating systems and applications.

Example: Amazon EC2 and S3, Rackspace, AT&T and Verizon.

III CLOUD DEPLOYMENT MODELS

3.1 Community Cloud

It shares infrastructure between several organizations from a specific community with common concerns (e.g., security, compliance, jurisdiction), deployment models. It can also be defined as multiple cloud systems that are connected in a way that allows programs and data to be moved easily from one deployment system to another. It is either managed internally or by a third party and can be hosted internally or externally.

3.2 Public Cloud

This cloud infrastructure is provisioned by the cloud provider for open use by the general public. It may be owned, managed, and operated by a business, academic, or government organization, or some combination of them.

3.3 Private Cloud

Infrastructure provisioned solely for a single organization. It is either managed internally or by a third party and can be hosted internally or externally.

3.4 Hybrid Cloud

A composition of two or more clouds (private, community, or public) those remain unique entities but are bound together, offering the benefits of multiple deployment models. It can also be defined as multiple cloud systems that are connected in a way that allows programs and data to be moved easily from one deployment system to another.

IV CHARACTERISTICS OF CLOUD

The National Institute of Standards and Technology and also the Information Technology Laboratory (NIST) given five essential characteristics of Cloud [5].

4.1 On demand self service

Resources should be always available when you need them, and you have control over turning them on or off to ensure there's no lack of resource or wastage happen.

4.2 Broad network access

Capabilities are available over the network and accessed through standard mechanisms that promote use by heterogeneous thin or thick client platforms (e.g. mobile phones, tablets, laptops, and workstations).

4.3 Resource pooling

The provider's computing resources are pooled to serve multiple consumers using a multi tenant model, with different physical and virtual resources dynamically assigned and reassigned according to consumer demand.

4.4 Rapid elasticity

Capabilities can be elastically provisioned and released, in some cases automatically, to scale rapidly outward and inward commensurate with demand. To the consumer, the capabilities available for provisioning often appear to be unlimited and can be appropriated in any quantity at any time.

4.5 Measured service

Cloud systems automatically control and optimize resource use by leveraging a metering capability at some level of abstraction appropriate to the type of service .e.g. storage, processing, bandwidth, and active user accounts.

V SaaS INTERFACE LAYER AND MIDDLEWARE

The SaaS interface Layer is the most important and Utilized Layer of cloud computing. This layer includes software applications targeted at end users or programs application functionality via the internet. This is responsible for the layer management of the software and databases including installation, updating and removal etc. This layer support Java Script, XML and Perl languages as well as back end infrastructure applications like Apache, Tomcat and SQL.

Cloud SaaS interface middleware service provides business independent. Cloud provides basic function for hosting cloud application [6].The middleware is the natural place to monitor and secure communication between various system components. The middleware is as follows

5.1 Virtual Layer Middleware

This middleware communicate between physical layer and SaaS interface layer. This middleware provide transparent infrastructure management service.

5.2 SaaS Interface Layer Middleware

This layer provides a transport management service to server applications. This middleware have two parts a) Server Middle tier Middleware b) server Backend Middleware.

a) Server Middle tier Middleware

This Middleware supports server middle tier applications like Apache, Tomcat, Web logic, Oracle Application Server and etc.

b) Server Backend Middleware

This middleware coordinate server middle tier application and server Backend application. This includes the server backend middleware application like Oracle, DBMS, Microsoft SQL Server, Debby and etc.

5. 3 Client Fonted Middleware

This middleware coordinate server middle tier middleware and client middle tier middleware.

VI MIDDLEWARE SERVICES

This services support application availability, reliability, scalability, resilience and adoptability (fig 2) that consider user requirement of security and privacy by design.

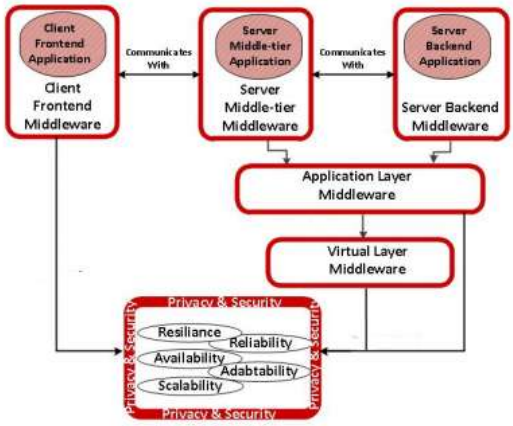

Fig 2 : SaaS Interface Layrer Middleware Service

6.1 Adaptability

The adaptability is managing and coordinating services in the same layer or other layer. The adaptability service in turn performs Action based on the Event and changes.

6.2 Resilience

The resilience service communicates with other devices to collaborate for providing end-to-end resilient cloud.

6.3 Scalability

Scalability is providing quick and efficient adapts to the addition and removal of the virtual resources.

6.4 Availability

If a resource is down or if it is relatively overloaded the availability of the service should be stopped diverting traffic immediately to that resource, and redirects traffic to other active resources until the adaptability service fixed the problem or until the overloaded resource returns to normal processing capacity.

6.5 Reliability

Reliability is of higher priority than the availability of the service. It is very important; it ensures that the end to end service integrity is maintained.

VII SaaS INTERFACE LAYER SECURITY THREATS

SaaS Interface layer security threats are described as bellow.

7.1 Interfaces and APIs

Cloud computing provides number of interfaces and APIs to interact with the services provided to the user organizations and third parties. It is often build upon these interfaces to offer value added services to their customers. This introduces the complexity of the new layered API, it also increase risk, as the organizations may be required to relinquish their credentials to third parties in order to enable their agency [7].

7.2 Cross Site Scripting

It is a type of attack in which user enters right URL of a website and hacker on the other site redirect the user to its own website and hack its credentials. [8]

7.3 Denial of service attacks

The biggest security threat to the Cloud is SasS Interface layer distributed denial of service (DDoS) attacks. Hackers have found and are actively exploiting weaknesses in Cloud defenses, utilizing cheap, easily accessible tools to launch SaaS interface layer attacks. A major reason they have been successful is that enterprise data centers and Cloud operators are not well prepared to defend against them. The DDoS attack is an attempt to make the service unable to use which is assigned to the authorized users. [9]

7.4 Data Loss

Cloud computing service providers handling high volumes of data, it's almost inevitable that some data loss will occur. This could be especially damaging if the client is relaying sensitive (not easy to recover) information over your cloud computing services network. In the summer of 2012, attacker broke into Mat's Apple, Gmail and Twitter accounts [10]. Through that access they erased personal data of the clients of those providers. The cloud lost data due to that reasons other than malicious attackers.

7.5 Account or Service Hijacking

Cloud solutions add a new threat to the landscape. If an attacker gains access to your credentials, they can eavesdrop on your activities and transactions, manipulate data, return falsified information, and redirect your clients to illegitimate sites.

VIII SOLUTIONS FOR THE SECURITY PROBLEMS IN THE CLOUD SaaS INTERFACE LAYER

Developers should develop the application using encrypted data which is provided by the providers for the security purpose. Developers should analyze the data for protection both at the time of design and run.

Developers should take care of the following:

- Strong key generation, storage and management and destruction practices should be implemented.
- Provider backup and retention strategies should be specified contractually
- Cloud provider security policies and SLAs should be understood clearly
- Data backup should be carried out in regular intervals
- Install trusted Antivirus and spyware Antivirus and Updates must be done without fail
- Never download on unknown antispyware program never be downloaded
- Freeware downloads must be avoided [11]
- Buy and use intrusion detection system [12]
- Regulate device description downloads based on Router Hops. [13]

IX CONCLUSION

The past few years cloud computing become very popular in the promising and competitive business world. It is one of the fastest growing fields in the IT industry. There are various issues that need to be dealt with respect to security and privacy in a cloud computing environment. Cloud service providers must ensure that all the SLA is meeting the human errors. In this paper we discussed various security risks at SaaS Interface layer and also suggested solution for the same.

REFERENCES

[1] M.Rajendra Prasad et Al, "*Cloud Computing: Research Issues and Implications*", International Journal of Cloud Computing and Services Science (IJ-CLOSER), Vol.2, No.2, pp. 134-140, April 2013.

[2] Anthony T Velte,Toby J Velte,Robert Elsenpeter, "*Cloud Computing A Practical Approach*",McGraq Hill Publications, pp 135-144,2010.

[3] Linda Xu,Miklos Sandorfi and Tanya Loughlin," *Cloud Storage for Dummies*", Wiley Publishing, pp 5-24,2010.

[4] Available from http://csrc.nist.gov/publications/nistpubs/800-145/SP800-145.pdf

[5] Peter Mell and Timothy Grance,The NIST Definition of Cloud Computing,SNational Institute of Standards and Technology Special Publication 800-145, pp 1-7 ,September 2011

[6] Qingpeng Zeng and Shuixiu Wu," *A SaaS Development Platform Based on Cloud Computing*",TELKOMNIKA, Vol.11, No.3, pp. 1646 - 1651, March 2013.

[7] CSA (Cloud Security Alliance), "*Top threats to cloud computing 2013*" ,pp 1-21, February 2013.

[8] Kangchan Lee "*Security Threats in Cloud computing Environments*", International Journal of Security and it applications, Vol 6, No 4,October 2012.

[9] Software Engineering Institute Carnegie Mellon, denial of service attacks. ww.cert.org/tech_tips/denial_of_service.html

[10] MAT HONAN, "*Hacked: Passwords have failed and it's time for something new*",17 JANUARY 13, http://www.wired.co.uk/magazine/archive/2013/01/features/hacked/viewall

[11] Tips to stop or Reduce Threats Posted by DDoS,9/14/2011http://brighthub.com/computing/enterprise-security/articles/106930.aspx

[12] Problems Faced by Cloud Computing, Lord CrusAd3r, dl.packetstormsecurity.net/ .../ProblemsFacedby CloudComputing.pdf

[13] Available from http://support.microsoft.com/kb/315056.aspx

PERFORMANCE ANALYSIS OF OPTICAL WIRELESS CHANNELS AT VARIOUS MODULATION TECHNIQUES

JavedAshraf [1], Prof. M .T. Beg [2], Prof. Mainuddin[3]

[1,2] *Deptt. of Electronics & Comm. Jamia Millia Islamia,New-Delhi-25,*

[3]*Deptt. of Electronics & Comm. (Head of the Dept.),Jamia Millia Islamia, New-Delhi 25.*

ABSTRACT

There are many modulation techniques which are used for optical wireless communication. For getting high average-power-efficiency, OOK and PPM are implemented extensively in optical wireless communication. In optical wireless communication, DPPM, DPIM and DH-PIM are three new modulation techniques which may become the replacement of PPM because of their better results in bandwidth efficiency and power efficiency. In this paper, the bandwidth efficiency, transmission capacity, power efficiency and slot error rate of the typical modulation techniques such as OOK, PPM, DPPM, DPIM and DH-PIM are analyzed in combination of the features of the atmospheric optical wireless channel. Theoretical analysis and simulation results by matlab shows that DPPM, DPIM and DH-PIM are more applicable for the future optical wireless communication. When bit resolutions increases in OOK, PPM, DPPM, DPIM and DH-PIM modulation techniques, corresponding symbol length also increases. Hence the average optical power requirement decreases but the bandwidth requirement increases.

Keywords: DH-PIM, DPIM, OOK , Optical Wireless Communication, PPM, Slot Error Rate.

I. INTRODUCTION

Extension of network bandwidth resources and improvement of communication streams are the two important issues with the ever-increase of information communication. Currently, microwave and fiber are the main means of transmission of communication. In comparison with wire communication, microwave communication saves a lot of non-ferrous metals and complex topography can be crossed by using microwave. As a new communication technology, optical wireless communications have the advantages of optical fiber communication and mobile communications, with wide bandwidth and without the need for application of frequency. Therefore, in recent years, the research on wireless optical communication is getting more noticed. But the wireless optical communication leads to signal attenuation as it is influenced by atmospheric absorption, scattering and turbulence in the atmosphere. The average transmission power is limited owing to the requirements for safety of human eye [1],[2].Thus higher necessity of modulation is proposed.

II. CLASSIFICATION OF WIRELESS OPTICAL MODULATION

2.1 On-Off Keying Modulation

The On-Off Keying Modulation is based on intensity modulation with direct detection [3]. When sending information "1", the light pulses are sent; when sending information "0", the laser is shut down completely. In this way the optical pulses are generated by opening and breaking of lasers [4].

2.2 Single-Pulse Position Modulation (L-PPM)

Single-pulse position modulation at a particular time slot in time segment converts a binary M-bit data group to a single pulse signal. Time segments are composed by $L=2^M$ time slots and each time slot is called chip. Where L symbol length and M represent the bit resolution.

2.3 Differential Pulse Position Modulation (DPPM)

Differential Pulse Position Modulation improves the power and bandwidth efficiency as well as throughput also. In DPPM, modulation techniques removing all empty slots and follow a pulse in a PPM symbol [5,6]. Average number of slots per symbol in DPPM $\bar{L}_{DPPM} = \left(\frac{L+1}{2}\right)$ is approximately half of the PPM, which improves the bandwidth efficiency and possibility of the data throughput [5].Where L symbol length and $\bar{L}$ average number of slots per symbol. For the given channel and for any symbol length L, DPPM slightly requires higher power but a much lower bandwidth requirement as compare to PPM. Performance of DPPM, using a combination of Marker and Solomon coding, is used to correct insertion and deletion errors as shown in [7].

2.4 Digital Pulse Interval Modulation (DPIM)

The symbol length of DPIM can be divided into unprotected slots and protected slots as in DPPM. The symbol length is not fixed. For decreasing the impact of Inter-Symbol Interference (ISI) effectively, one protected slot is mostly adopted by protected DPIM modulation. The modulation symbols S_k (k is the decimal number expressed by the symbol) contain k+2 time slots; After each starting time slot L, the pulse adds a protected empty slot and k empty slots for expressing information. When demodulation in the receiver, after determining the pulse time slot, is received, it only needs to count the empty time slot and subtract one of them. Implementation of the system is efficiently simplified since DPIM only needs clock synchronization without symbol synchronization.

2.5 Double Header-Pulse Interval Modulation (DH-PIM)

DH-PIM is more complex as the symbol adopts two kinds of starting pulse. The time slot included by each symbol is also mutative. The symbol S_k is formed by a head slot and m empty time slots followed .The head time slot is

included by α+1 time slots (α is integer). Considering two forms of head H_1 and H_2, the H1 initial pulse width is α/2 time slot, followed by (α /2) +1 protected time slots; H_2 pulse width is a time slots, followed by one time slot. When k<2M-1, the head time slot of symbol S_k is, otherwise it is H_2 .Where M I is the bit resolution.

III. COMPARISONS OF DIFFERENT MODULATION SCHEMES

Different modulation schemes are differentiated, with respect to power efficiency and bandwidth requirements. (Power requirement is defined as the average optical power required by an ideal system in the presence of AWGN channel to achieve error probability and a certain bit rate.)

3.1 Requirements of optical power and efficiency of different modulation schemes:

3.1.1Average power required for OOK system

The average power required for OOK system is

$$P_{avg_OOK} = \sqrt{\frac{N_0 R_b}{2R^2}} Q^{-1}\left(P_{e_bit_OOK}\right).....(1)$$

where

N_0 = Noise Spectral density

R_b = Bit Rate

R = Responsivity of the Photodetector

P_e = Probability of Error

3.1.2Average power required for PPM system

Average power required for PPM system is

$$P_{avg_PPM} = \sqrt{\frac{2N_0 R_b}{R^2 L \log_2 L}} Q^{-1}\left(P_{sle_PPM_H}\right).....(2)$$

P_{sle}_PPM_H= Probability of slot error for the hard decoding for PPM

where

L = Symbol Length

Hence the power efficiency of PPM is

$$\eta_{P-PPM} = \sqrt{\frac{4}{L\log_2 L}} \quad \text{.....(3)}$$

3.1.3Average power required for soft decision decoding PPM system:

Average power required for soft decision decoding PPM system is

$$\eta_{P-PPM} = \sqrt{\frac{2}{L\log_2 L}} \quad \text{.....(4)}$$

3.1.4Average optical power and power efficiency requirements for DPIM system:

Average optical power and power efficiency requirements for DPIM system is

$$P_{avg_DPIM} = \sqrt{\frac{2N_0R_b}{R^2\bar{L}_{DPIM}\log_2 L}}Q^{-1}\left(P_{se_DPIM}\right) \text{....(5)}$$

where

$\bar{L}$ = Average Symbol Length

P_{se} = Probability of slot error

$$\eta_{P-DPIM} = \sqrt{\frac{8}{(L+1)\log_2 L}} \quad \text{.....(6)}$$

3.1.5 Average optical power and power efficiency requirements for DH-PIM system:

Average optical power and power efficiency requirements for DPIM system is

$$P_{avgDH-PIM} = \sqrt{\frac{9\alpha^2 2N_0R_b}{16R^2M\bar{L}_{DH-PIM}}}Q^{-1}\left(P_{seDH-PIM}\right) \text{.....(7)}$$

where

M = Bit resolution

α = Integer

$$\eta_{p-DPIM} = \sqrt{\frac{9\alpha^2}{2M\left(2^{M-1}+2\alpha+1\right)}} \quad \text{.....(8)}$$

3.1.6 Requirements of bandwidth for different modulation schemes:

Bandwidth requirement of the baseband modulation schemes is defined by the minimum slot duration $\tau_{\min}$ given by the following relation.

$$B_{req} = \frac{1}{\tau_{\min}}$$

The bandwidth requirements for OOK, PPM, DPIM and DH-PIM are given as:

$$B_{req_OOK} = R_b$$

$$B_{req_PPM} = \frac{L}{M} R_b$$

$$B_{req_DPIM} = \frac{L+1}{2M} R_b$$

$$B_{req_Dh_PIM} = \frac{\left(2^{M-1} + 2\alpha + 1\right)R_b}{\alpha M} R_b$$

IV-EXPERIMENTAL RESULTS

Simulated results clearly shows that when bit resolution increases, so corresponding symbol length also increases and the average optical power requirement decreases but the bandwidth requirements increases.

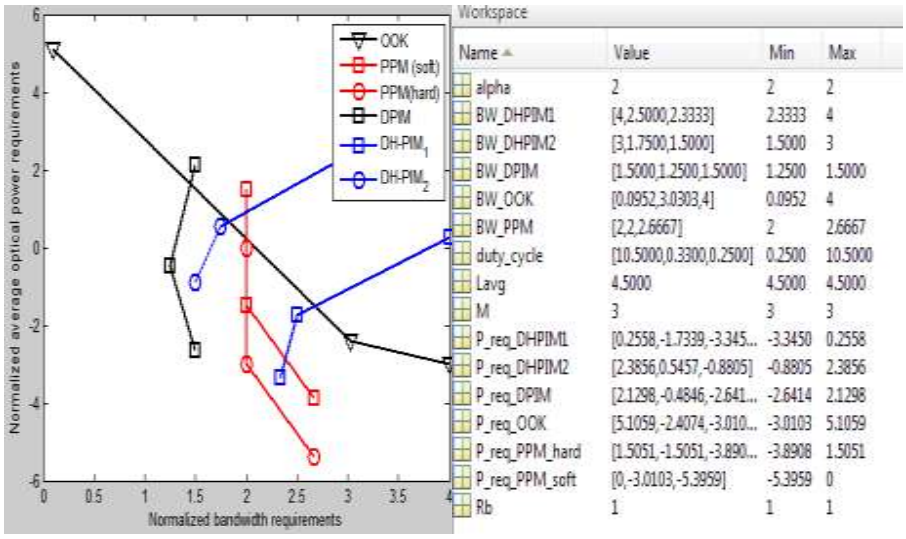

Performance of optical power and bandwidth requirements at bit resolution M=1:3

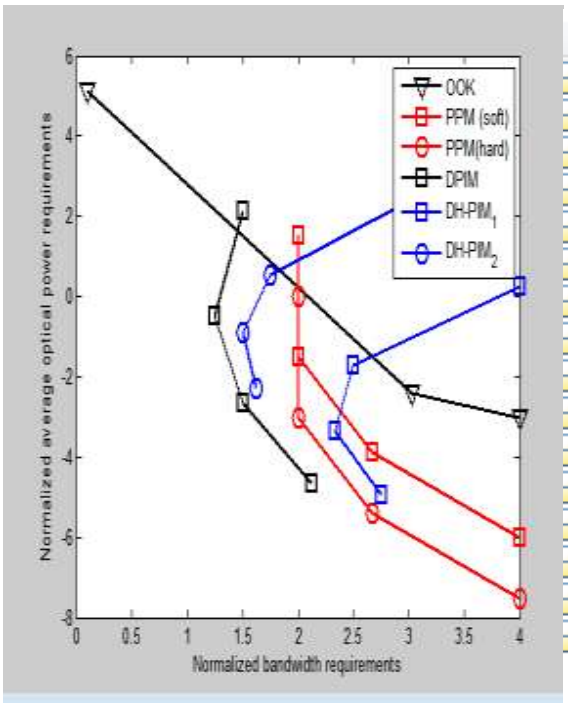

Name	Value	Min	Max
alpha	2	2	2
BW_DHPIM1	[4,2.5000,2.3333,2.7500]	2.3333	4
BW_DHPIM2	[3,1.7500,1.5000,1.6250]	1.5000	3
BW_DPIM	[1.5000,1.2500,1.5000,...	1.2500	2.1250
BW_OOK	[0.0952,3.0303,4]	0.0952	4
BW_PPM	[2,2,2.6667,4]	2	4
duty_cycle	[10.5000,0.3300,0.2500]	0.2500	10.5000
Lavg	6.5000	6.5000	6.5000
M	4	4	4
P_req_DHPIM1	[0.2558,-1.7339,-3.345...	-4.9512	0.2558
P_req_DHPIM2	[2.3856,0.5457,-0.880...	-2.3037	2.3856
P_req_DPIM	[2.1298,-0.4846,-2.641...	-4.6471	2.1298
P_req_OOK	[5.1059,-2.4074,-3.010...	-3.0103	5.1059
P_req_PPM_hard	[1.5051,-1.5051,-3.890...	-6.0206	1.5051
P_req_PPM_soft	[0,-3.0103,-5.3959,-7....	-7.5257	0
Rb	1	1	1

Performance of optical power and bandwidth requirements at bit resolution M=1:4

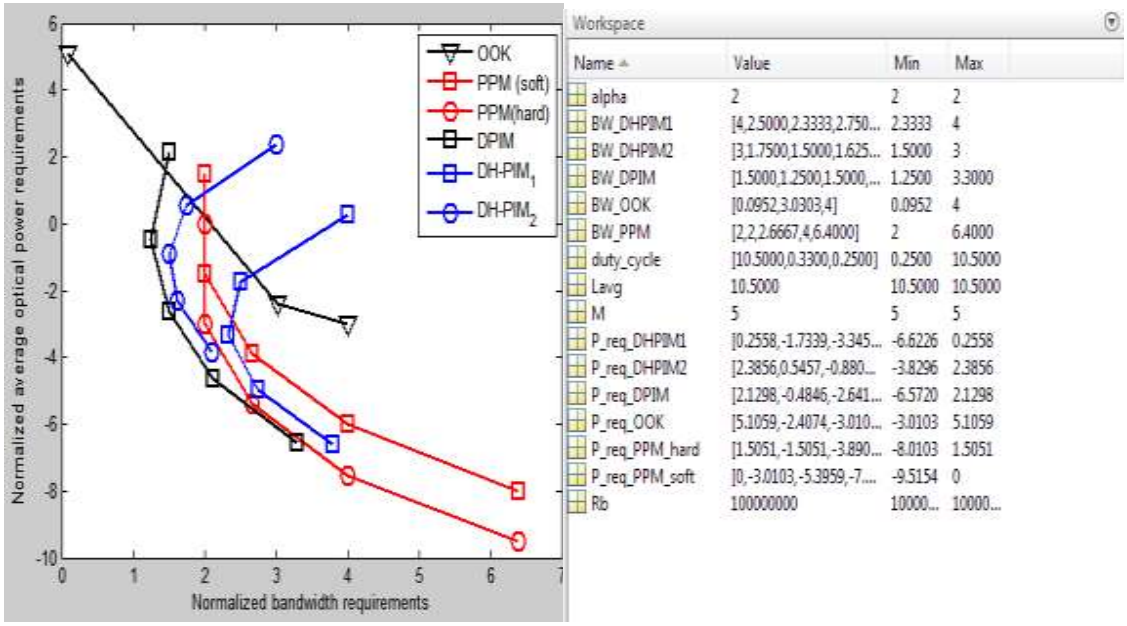

Name	Value	Min	Max
alpha	2	2	2
BW_DHPIM1	[4,2.5000,2.3333,2.750...	2.3333	4
BW_DHPIM2	[3,1.7500,1.5000,1.625...	1.5000	3
BW_DPIM	[1.5000,1.2500,1.5000,...	1.2500	3.3000
BW_OOK	[0.0952,3.0303,4]	0.0952	4
BW_PPM	[2,2,2.6667,4,6.4000]	2	6.4000
duty_cycle	[10.5000,0.3300,0.2500]	0.2500	10.5000
Lavg	10.5000	10.5000	10.5000
M	5	5	5
P_req_DHPIM1	[0.2558,-1.7339,-3.345...	-6.6226	0.2558
P_req_DHPIM2	[2.3856,0.5457,-0.880...	-3.8296	2.3856
P_req_DPIM	[2.1298,-0.4846,-2.641...	-6.5720	2.1298
P_req_OOK	[5.1059,-2.4074,-3.010...	-3.0103	5.1059
P_req_PPM_hard	[1.5051,-1.5051,-3.890...	-8.0103	1.5051
P_req_PPM_soft	[0,-3.0103,-5.3959,-7....	-9.5154	0
Rb	100000000	10000...	10000...

Performance of optical power and bandwidth requirements at bit resolution M=1:5

V CONCLUSION

In this paper, we have compared the bandwidth requirement and the power requirement of different popular modulation techniques in optical wireless communication systems; OOK ,PPM, DPIM and DH-PIM in order to give a wide view about the modulation techniques that are suitable for optical wireless communication systems.

PPM is the most efficient technique in terms of power performance. But as both slot and symbol synchronizations are required at the receiver in PPM so it has a poor clock recovery and resynchronization characteristics. However, this would increase the power requirement by a factor of two. In DPIM, receiver structure is much simplified because each symbol is initiated with a pulse. Therefore, DPIM does not require symbol synchronization. Furthermore, DPIM removes all the unused time slots from within each symbol, thus giving a higher transmission capacity. It is concluded that the main advantages of DPIM, DH-PIM modulation techniques is the symbol synchronization ability and these are the most efficient techniques in terms of optical power and band width requirements. For OOK-RZ the power requirements decreases with duty cycle but the bandwidth increases accordingly. For PPM,DPIM and DH-PIM average optical power requirement decreases when the value of bit resolution M is increases because corresponding value of L increases; however the bandwidth requirements increases with M or the value of L increases.

REFERENCES

[1]Sun Yi, Wu Lei. Simulink Communication Simulation Development Manual [M]. Beijing: National Defence Industry Press, 2006.10.

[2]Hu Zongmin, Tang Junxiong. Atmospheric optical wireless communications systems in the digital pulse interval modulation [J]. Communications, 2005, 26 (3):75-79.

[3]Wang Hongxing, Zhang Tieying, Zhang Tieying, et al. Wireless Optical DH-PIM with DPIM modulation Performance Study [J]. Laser Technology, 2007, 31 (1):95-96.

[4]L. W. Couch, Digital and Analog Communication Systems, 6th ed. New Jersey: Prentice Hall, 200

[5]D. Shiu and J. M. Kahn, Differential pulse position modulation for power-efficient optical communication, IEEE Transactions on Communication, 47, 1201–1210, 1999.

[6]U. Sethakaset and T. A. Gulliver, MAP detectors for differential pulse-position modulation over indoor optical wireless communications, IEICE Transactions on Fundamentals of Electronics, Communications and Computer Sciences, E89-A, 3148–3151, 2006.

[7]U. Sethakaset and T. A. Gulliver, Performance of differential pulse-position modulation(DPPM) with concatenated coding over optical wireless communications, *IET Communications*, 2, 45–52, 2008.

[8] Ke Xizheng, Xi Xiaoli. The Survey of Wireless Laser. Communication [M]. Beijing: Beijing University of Posts and Telecommunications Press, 2004:148-157.

[9] Li jianxin, Liu naian. Analysis and Simulation of Modern Communication System [M]. Xian: Xi Dian University Press, 2004:48-58.

[10] Z. Ghassemlooy, W.Popoola, S. Rajbhandari- Optical Wireless Communications System and Channel Modelling with MATLAB.

[11] Mohamed D.A.Mohamed. Steve Hranilovic .”Optical Impulse Modulation for Indoor Diffuse Wireless Communication”. IEEE Transaction on Communications. Vol- 57,No.2,Februrary-2009.

[12] Xiaoming Jiang,Na Zhu.”Analysis of Power Request and Multiple-Site Techniques for Indoor Wireless Visible-Light Communication System Using LED Lights”978-1-4244-3709- 2/10/$25.00,2010 IEEE.

[13] Daniel J.F.Barros,Sarah K.Wilson,Joseph M. Kahn.”Comparison of Orthogonal Frequency- Division Multiplexing and Pulse-Amplitude Modulation In Indoor Optical Wireless Links”,0090-6778/11$26.00-2011 IEEE.

MOLECULAR MODELLING, STRUCTURAL AND CYTOTOXIC STUDY OF 1-[1-OXO-3-PHENYL-(-2-BENZOSULFONAMIDE-)-PROPYL AMIDO] – ANTHRACENE-9, 10-DIONE

Pamita Awasthi[1], Manu Vatsal[2], Shamsher S. Kanwar[3]

[1, 2] Department of Chemistry, NIT, Hamirpur, (India)

[3]Department of Biotechnology, HPU, Shimla, (India)

ABSTRACT

The family of anthracenediones, has been extensively used for treatment of advanced breast and prostate cancer, lymphoma, acute leukemia and non-Hodgkin's lymphoma. The anthracycline class of antibiotics used in various cancer hospitals are- daunomycin, adriamycin, epiadriamycin and mitoxantrone. One of the important antibiotic, Mitoxantrone, an anticancer drug, used in chemotherapy has been the subject of intense chemical research. This has prompted us to synthesize series of anthraquinone based compounds in our laboratory. The structure of one of the analog of synthesized series, 1-[1-oxo-3-phenyl-(-2-benzosulfonamide-)-propyl amido] – anthracene-9,10-dione has been confirmed by FT-IR, [1]H-NMR, mass spectrometry tools. The unit cell parameters of the compound were calculated using the powder XRD tool which confirms the monoclinic unit system and P lattice type of the compound. Further the structural and electronic parameters of the compound 1-[1-oxo-3-phenyl-(-2-benzosulfonamide-)-propyl amido] – anthracene-9,10-dione have been studied extensively using Gaussian 98. Cytotoxic studies of the compound is carried out on Hep2C cancer cell lines in comparison to mitoxantrone.

Keywords: Anticancer, Anthraquinone, Gaussian, Mitoxantrone.

I. INTRODUCTION

Mitoxantrone (MTX)-1, 4-dihydroxy-5, 8-bis [[2-[2-hydroxyethyl) amino] amino]-9, 10-anthracenedione, is marketed under the name Novantrone. The compound derived from anthracycline class of antibiotic group [1,2]. It is cytotoxic and has major clinical value in treatment of leukemias as well as solid tumors such as advanced breast cancer and non-Hodgkin lymphoma etc. [3]. The biochemical evidences suggest that it inhibit DNA and RNA synthesis by intercalating between base pairs of the DNA and RNA strand, thus preventing the replication of rapidly growing cancer cells [4-7]. Major drawback associated with the drug is non-specific inaction. In order to better understand the cytotoxicity of anthraquinone based compounds, we have to design an analog by varying the functional group and its position on anthraquinone ring. Structure of the compound was confirmed by Fourier transform infrared spectroscopy, ^{1}H-NMR,^{13}C NMR and mass spectroscopic tools. Electronic properties of the molecule has been studied in comparison to mitoxantrone using computational study on Gaussian software tool. Further cytotoxic studies confirm the anticancer action of the analog.

II. MATERIAL AND METHODS

IR spectra in cm-^{1} was recorded on PERKIN ELMER spectrum version. ^{1}HNMR, spectra were recorded in DMSO on a BRUKER AVANCEII 400. XRD analysis was performed on Philips PAN alytical X'Pert PRO 1710 X-ray diffractometer with standard input parameter. Melting point in^{0} C were measured in open capillary tubes on Digital Melting/Boiling apparatus. The geometries of the 1-[1-oxo-3-phenyl-(-2-benzosulfonamide-)-propyl amido] – anthracene-9,10-dione and mitoxantrone were fully optimized using Hartree Fock Method on Gaussiansoftware98Wversion. Cytotoxic studies of the compounds were carried out on P155 Hep2C cell lines in comparison to mitoxantrone. The cell lines were grown in culture Dulbecco's modified Eagle's medium supplemented with 10% fetel calf serum, penicillin and streptomycin at 37 ^{0}C under a CO_2 –humidified atmosphere. Cell lines in coster wells were incubated with various amounts of the test compound and mitoxantrone for 72h growth period with Trypan blue staining.

III. RESULTS AND DISCUSSION

3.1 FTIR- Spectrum

The FTIR spectrum was recorded in the frequency region 500- 4000cm^{-1} to identify the functional groups present in the compound using KBr pellet in comparison to starting compound i.e, 2-benzosulfonamide-3-phenyl propanoic acid. IR (υcm^{-1}): υ_{N-H} 3341.66, $\upsilon c_{=}o$1734.52, υ $o_{=}s_{=}o$ 1375.62,1170.48 υ_{C-N} (aliphatic)1093 cm^{-1}. 1-[1-oxo-3-phenyl-(-2-benzosulfonamide-)-propyl amido] – anthracene-9,10-dione IR(υcm^{-1}): υ_{N-H} 3261.87, $\upsilon c_{=}o$1702.57cm,υ $o_{=}s_{=}o$ 1335.45,1163.42cm υ_{C-N} (aromatic)1269,1288, υ_{C-N} (aliphatic)1074,1091 table I. The formation of peaks at 1269 and 1288 cm^{-1} and shifting of $\upsilon c_{=}o$ peak from 1734.52 to 1702 cm^{-1} confirms the formation of final compound(Fig 1).

3.2 X-Ray Data Collection and Structure Determination

The powder X-ray diffraction study was performed to understand lattice structure of the compound $C_{29}H_{22}N_2O_5S$. The diffractometer is equipped with a copper rotating anode. Diffracted beam monochromator tuned to 1.542-A^{0} Cu X-ray tube providing a Kα_1 and scintillation detector. Data were collected over a range of 10-50 degrees 2θ as a continuous scan of 2 degrees2θ min^{-1}. The crystal size determined by measuring the line width at half maximum (B) and employing the same value of B in Debye- Scherrer's equation i.e. D=(λ X 0.94) / β cos θ. In equation, D as a crystallite size of (h, k, l) planes and λ as wavelength of incident radiation while β act as full width half maxima (FWHM). θ is incident angle for X-rays. The crystallite size for compound came out to be 3.04nm. The unit cell parameters of the compound have been calculated using powderX software [8] and result are summarized as in tableII. Further with decrease in crystallite size, peaks becomes more broader (Fig 2).

3.3 Cytotoxicity Assay

Cytotoxic studies of the compound were carried out on P155 Hep 2C cell lines. IC_{50} values of mitoxantrone and test compound came out to be 2.5µg/ml and 9µg/ml respectively table III. Inhibitory concentration of test compound is higher than the currently in use drug mitoxantrone.

3.4 Computational Details

In order to correlate the electronic properties of mitoxantrone and synthesized analogs which can have relevance towards the biological properties of synthesized analog, we have carried out extensive computational studies using Hartree Fock employing 6-311+G(2d, p) *ab initio* calculations [9] . The optimized strucuture given in Fig 3 for analog and mitoxantrone is entirely different. Although, the conformation of aromatic NH is same in both the cases but difference in structure of functional groups on side chain makes the difference. Mitoxantrone came out to be symmetrical while analog is not, due to presence of heavy phenyl group at the centre and O_2S-NH_2- group with phenyl group stabilize the conformation of side chain and affect the effective intercalation of anthraquinone chromophore. Since it is only 1 substituted and can further make a difference. The side arm of analog is not coplanar with the chromophore like that of mitoxantrone. Total energy, degree of freedom and electric dipole moment calculated for mitoxantrone and analog is tabulated in table IV. Interestingly the calculated dipole moment of the analog and mitoxantrone might explain the difference in biological action. First of all difference in dipole moment and secondly in direction (x, y, z) of dipole moment. Due to difference in functional groups on side chain direction of dipole is totally changed. This behavior might be important parameter for molecular recognition of receptor by the molecule/drug (Fig 4). Hence we are observing difference in IC_{50} value of analog with mitoxantrone.

IV. FIGURES AND TABLES

Table I. The assignment of IR spectrum of the title compound

Wavenumbers,cm^{-1}	Cause
3261	N-H stretching
1702	C=O stretching
1335,1163	S=O stretching
1269,1288	C-N (aromatic)
1074,1091.	C-N (aliphatic)

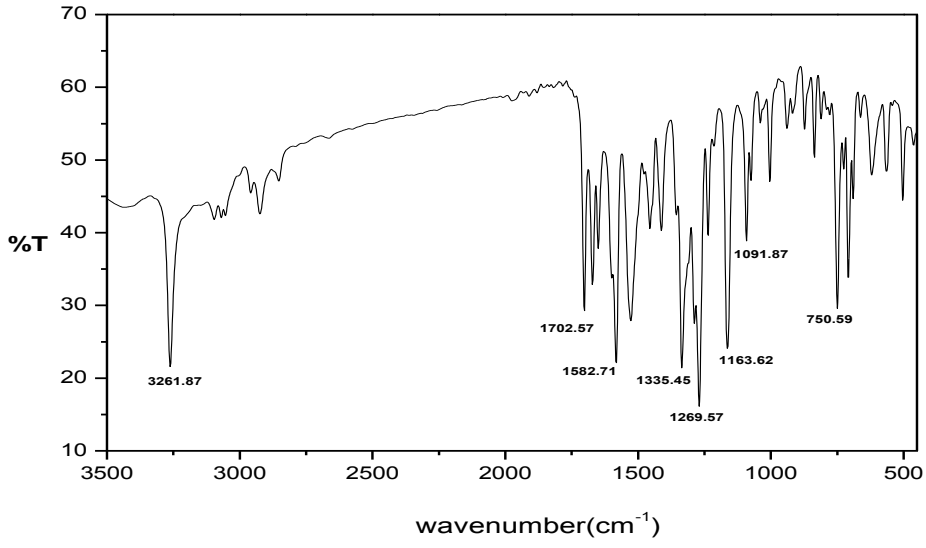

Fig.1.IR Spectrum of the Titled Compound

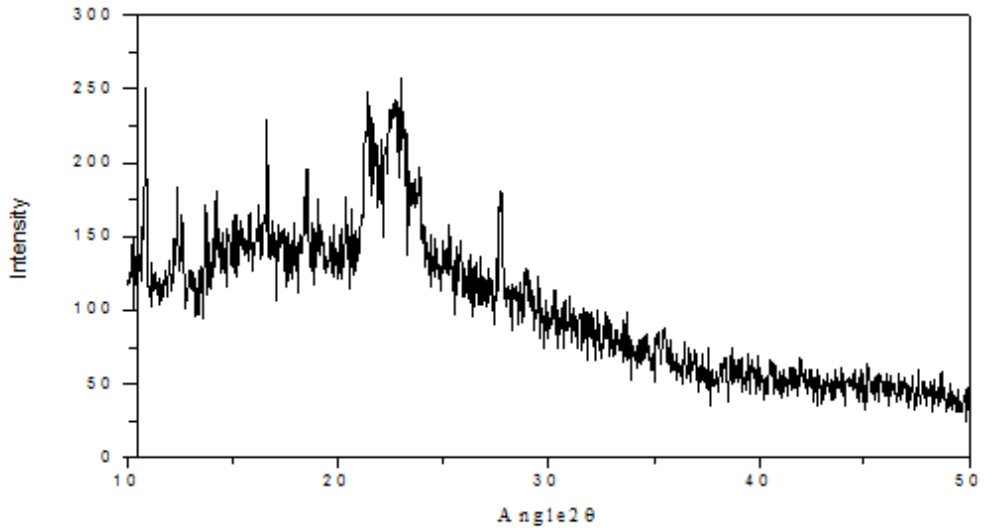

Fig.2.Powder XRD pattern of 1-[1-oxo-3-phenyl-(-2-benzosulfonamide-)-propylamido-anthracene-9,10, Dione

Table II. Crystallographic characteristics and the X-ray data collection and structure –refinement parameter for -[1-oxo-3-phenyl-(-2-benzosulfonamide-)-propylamido-anthracene-9,10,dione

Empirical formula	$C_{29}H_{22}N_2O_5S$
Formula weight	510
Crystal system	Monoclinic
Lattice type	P
a (A^0)	8.84
b (A^0)	6.21
c(A^0)	31.18
V, ($A^{0\,3}$)	1711.66
A	90
β	90
γ	120
Radiation	Cu K_α
Wavelengthλ, A^0	1.5
Crystallite size,nm	3.76nm
Diffractometer	X'PERT-PRO
Scan mode	2θ
2θ start	10
2θ end	50

TableIII Cytotoxic studies on Hep2C cell lines using by MTT assay (15µg).

Compound	IC_{50} value
MTX	2.5 µg/ml
Analog	9 µg/ml

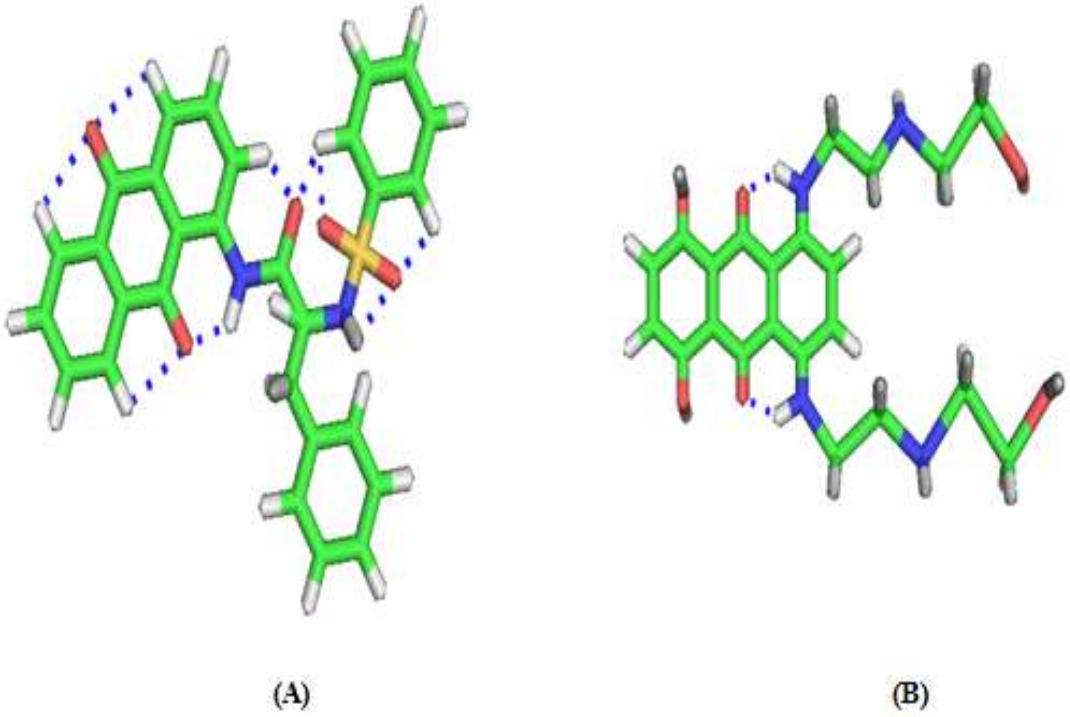

Fig.4. *Ab initio* HF Optimized structure of 1-[1-oxo-3-phenyl-(-2-benzosulfonamide-)-propylamido-anthracene-9,10, dione(A) and (MTX)-1, 4-dihydroxy-5, 8-bis [[2-[2-hydroxyethyl) amino] amino]-9, 10-anthracenedione.

Table IV Total energies, degrees of freedom and electric dipole moments for MTX and its analog(see figure 3)

Compound	HF/6-311+g(2d,p)	Degrees of freedom	Dipole moment(Debye)
MTX	-1516.49411887	174	1.4657(x= -0.9607, y= -0.2368, z= -1.0814)
Analog	-1990.46064134	171	7.7670(x= -2.4509, y= 6.9667, z= -22.4049)

V. CONCLUSION

Synthesis, structural and computational study of 1-[1-oxo-3-phenyl-(-2-benzosulfonamide-)-propylamido-anthracene-9,10,dione has been carried out. Comparative biological and computational study predicts the difference in behaviour due to position and type of functionalities on the molecule. By keeping the basic skelton i.e, anthraquinone chromophore same does not gurantee the effective biological activity. Its the functional groups act as a side arms further dictate the mechanism of action.

VI. ACKNOWLEDGEMENT

The facilities provided by the centre for material science and engineering at National Institute of Technology, Hamirpur, India for the access to the X-ray diffractometer are gratefully acknowledged. We are pleased to thank Sukhdev Singh for skillful technical help in cytotoxic study and Sumit Bhardwaj for valuable support of XRD studies. We are indebted to Department of Biotechnology, Himachal Pradesh University, Shimla for carrying out in vitro cytotoxic studies.

REFERENCES

[1] C.Murdock, R.G Child, P.F Fabio, R.B Angier, Antitumor agents. 1. 1,4-Bis [(aminoalkyl)amino]-9,10-anthracenediones, *Journal of Medicinal Chemistry, 22 (9),* 1979, 1029.

[2] D.A.Collier, and S.Neidle, Syntheis, molecular modelling, DNA binding and antitumor properties of some substituted amidoanthraquinone, *Journal of Medicinal Chemistry, 31,* 1988, 847-857.

[3] I.E Smith, R,S.Harris, N. Pavlidis, T. Bozek, Mitoxantrone (Novantrone) as single agent and in combination chemotherapy in the treatment of advanced breast cancer, *Cancer Treatment Reviews, 10,* 1983, 103-115.

[4] B.S Parker, C.Cullinane, and D.R.Phillips, Formation of DNA adducts by formaldehyde-activated mitoxantrone, *Nucleic Acids Research, 27,* 1999, 2918-2923.

[5] B.S Parker,S.M.Cutts, C.Cullinane and D.R Phillips, Formaldehyde activation of mitoxantrone yields CpG and CpA specific DNA adducts, *Nucleic Acids Research, 28,* 2000, 983-989.

[6] Cheng-Zee, R.K-Y.Podrebarac, C.C Cheng, Structural modification study of bis(substituted aminoalkylamino) anthraquinones. An evaluation of the relationship of the [2-[(2-hydroxyethyl)amino]ethyl]amino side chain with antineoplastic activity, *Journal of Medicinal Chemistry, 21,* 1978, 291-294.

[7] B.S Parker, T.Buley, B.Evinson, S.M Cutts, G.M Neumann, M.N Iskander and D.R.Phillips, A Molecular Understanding of Mitoxantrone-DNA Adduct Formation, *Journal of Biological Chemistry, 279,* 2004, 18814-18823.

[8] R. Kaushal, N. Kumar, P.Awasthi, K. Nehra, Synthesis, characterization, and antibacterial study of titanium complexes, *Turkish Journal of Chemistry*, 37, 2013, 936 -945

[9] G. Zagotto, S. Moro, E.Uriarte, E.Ferrazi, G.Palu, M.Palumbo, Amido analogs of mitoxantrone: physic-chemical properties, molecular modelling, cellular effects and antineoplastic potential, *Anti-Cancer Drug Design,* 12, 1997, 99-112.

RAINFALL RUNOFF REGRESSION MODEL FOR GALWA CATCHMENT IN BANAS RIVER BASIN

Sunil Kumar Vyas[1], Gunwant Sharma[2], Y.P. Mathur[3]

[1] Research Scholar, Department of Civil Engineering, MNIT & Executive Engineer, Water Resources Department, Govt. of Rajasthan, Jaipur, Rajasthan,(India.)

[2,3] Professor, Department of Civil Engineering, Malviya National Institute of Technology, JLN Marg, Jaipur,302017, Rajasthan

ABSTRACT

For proper planning designing and maintaining of a water resource project previous hydrological and meteorological data of the concerned area are required. Galwa dam is constructed across river Galwa, a tributary of river Banas which is situated in Rajasthan in India. The total monthly and monsoon rainfall over the catchment of the Galwa is taken as the rainfall measured at the Nainwa rain-gauge station which is influencing maximum to the catchment. Runoff generated from the catchment is measured at the Galwa dam site. Statistical analysis on the rainfall for different periods in the catchment & runoff data is carried out. Rainfall Runoff relations between the total rainfall and corresponding runoff for different months i.e. July, August & September and Monsoon period were developed. Three types of empirical relations i.e. linear, polynomial & logarithmic were developed and the corresponding correlation factors were also calculated. These relations can be used for the computation of inflow from catchment and further planning for new projects.

Index Terms*: *Rainfall, Runoff, Catchment, Total rainfall, Statistical Analysis, Coefficient of variation, Skewness, Regression Analysis, Correlation Coefficient, Determination Coefficient.

I INTRODUCTION

The rainfall which is clearly a natural hydrological phenomenon depends on various parameters. The knowledge of rainfall occurred and runoff generated from a specified area in a particular period is very important for planning designing and optimum utilization of water resources project. Local physiographic, climatic and biotic factors influence very much the rainfall and the corresponding surface runoff generated in a particular catchment. Developmental activities required for human development is increasing and changing with time which are ultimately changing the local physiographic biotic and abiotic factors. The local climate is changing due to change in the local physiographic and biotic factors and vice versa due to which the behavior of rainfall and corresponding runoff is also changing. There may be some empirical relations i.e. linear, polynomial, logarithmic and exponential between the rainfall and corresponding runoff, which can be used for computing water inflow generated from the catchment.

II LITERATURE REVIEW

M. Afzal Ali Baig and P Mallikarjuna (1) developed empirical relations between rainfall and runoff for the Bahuda river basin in Andra Pradesh by multiple correlation and regression analysis carried out for forecasting empirical relationships between the rainfall and corresponding runoff generated in particular period.

Gunwant Sharma et.al (2) have developed rainfall-runoff relation for Meja Catchment and also studied the trends in annual rainfall and runoff. It was found that the trend on occurrence of rainfall in the past thirty four years i.e. from 1979 to 2012 is roughly equal while the observed runoff is reducing in the previous thirty four years in the Meja Catchment.

John F. Joseph and Earnest Falcon (3) studied the hydrologic trends and correlations in South Texas River Basin and found the majority of trends and correlations were found to be statistically significant at the level 0.05 and all relationships were positive or increasing.

Hamed (4) reviewed trends in U.S. rivers and found three to have increasing trends, one to have a decreasing trend, and the remaining to not have a trend statistically significant at the level of 0.05.

The Intergovernmental Panel on Climate Change (5) indicates that extreme weather (including heavy rainfall and prolonged dry periods) is likely becoming more common in some regions of the world due to global warming.

Krishnegowda et al (6) have developed rainfall runoff relationship for Malathi river basin.

Mallikarjuna and Vishnu Vardhan (7) generated monthly rainfall sequences independently for the four raingauge stations of Kalangi basin located in Andhra Pradesh and concluded that the Thomas-Fiering model for the independent generation of synthetic sequences of rainfall may be used in the design of water resources system of Kalangi Basin.

Sudhisri et al. (8) developed the rainfall-runoff models for annual, pre-monsoon, monsoon and post-monsoon seasons and found to have high correlation coefficient.

Mallikarjuna and Prabhakara Rao (9) developed a relationship between rainfall and other meteorological parameters such as relative humidity, wind velocity; temperature and sunshine hours for the Tirupati area of the drought prone Rayalaseema region through multiple correlation and regression analysis.

Gorantiwar and Majumdar (10) analysed the streamflow sequences of some west Bengal streams and modeled the streamflow using autoregressive model of first order.

Mirza et al (11) have reported the trends and persistence in precipitation in Ganga, Bramhaputra and Meghna river basin.

Srinivasan and Thandaveshwara (12) fitted lower order periodic autoregressive/ autoregressive moving average (PAR/PARMA) models to the monsoon-dependent river flows of Southern India measured at Chunchanakatte (Cavery river), Akkihebbal (Hemavathy river) and Unduwadi (Lakshmanathirtha river) and showed that the above models do not seem to perform satisfactorily in modeling highly variable monsoon dependent river flows.

Verma and Haque (13) developed a stochastic model for generation of daily rainfall sequences by analyzing rainfall data at Mokhada rain guage station.

Reddy and Vedula (14) compared the applicability of different streamflow generating models using the same historic data of monthly streamflows into upper Cauvery river basin and found that the Thomas- Fiering model

was found best to preserve the mean, standard deviation and lag one correlation of historic streamflows. Koteshwaram and Alva (15) and Bhargava and Bansal (16) studied the secular trends and periodicities in the monsoon and annual rainfall of selected stations in India.

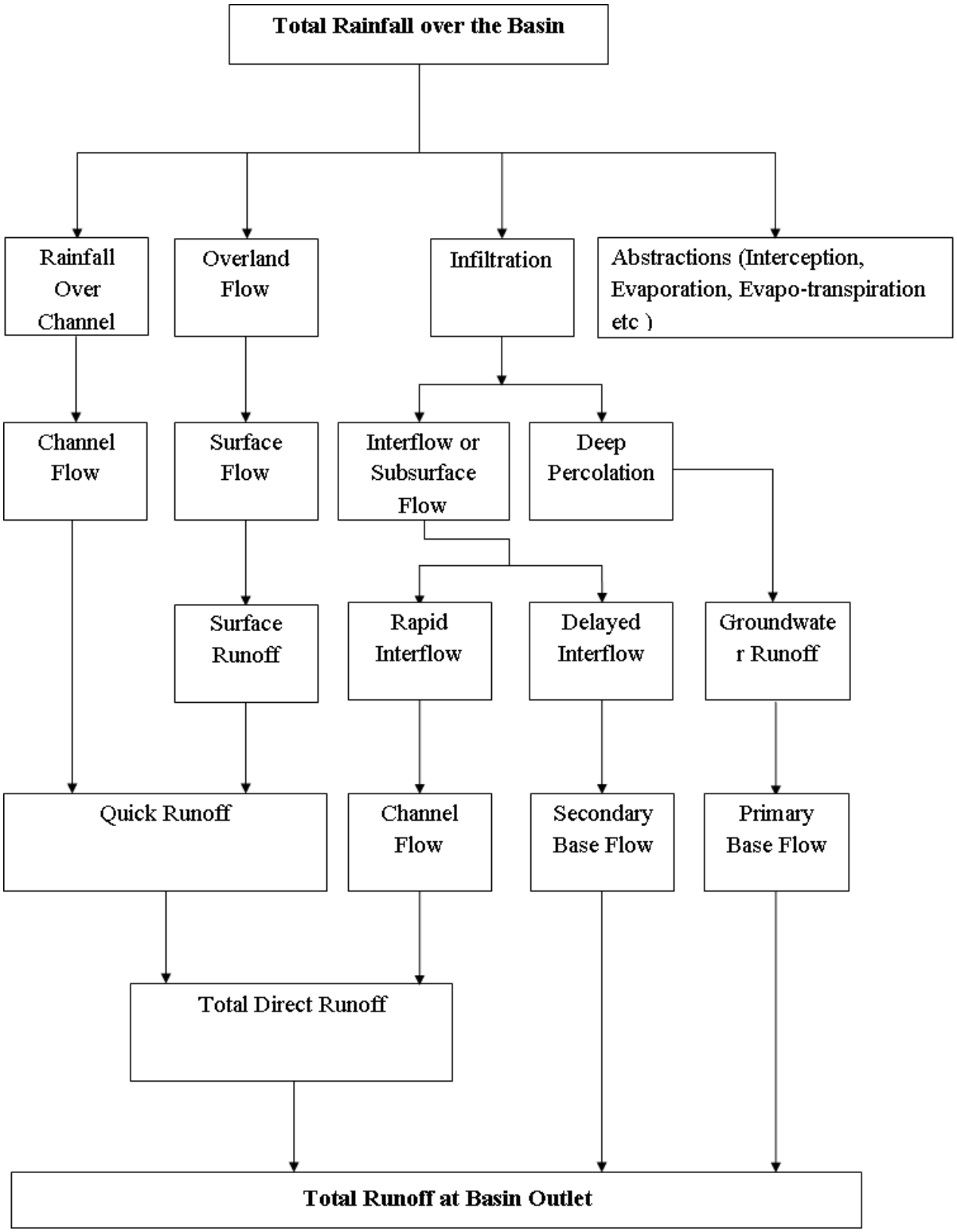

Figure-1 Flow Chart for generated runoff in a basin

III. STUDY AREA

The Galwa catchment area is up to the Galwa Dam. The dam site is located 7 Km. from Uniara town in Tonk district in Rajasthan in India at latitude 25°53' N and longitude 76°02' E. Galwa dam is constructed across river Galwa, a tributary of river Banas for providing irrigation facilities in 43 villages in Uniara and Sawai Madhopur tehsils. The total catchment area is 405.1 Square Km. The rain gauge station influencing the maximum is Nainwa. This dam was constructed in 1960 as an earth cum masonry type with spillway of length 244m; gross storage is 48.7 MCM, live storage 47.22 MCM.

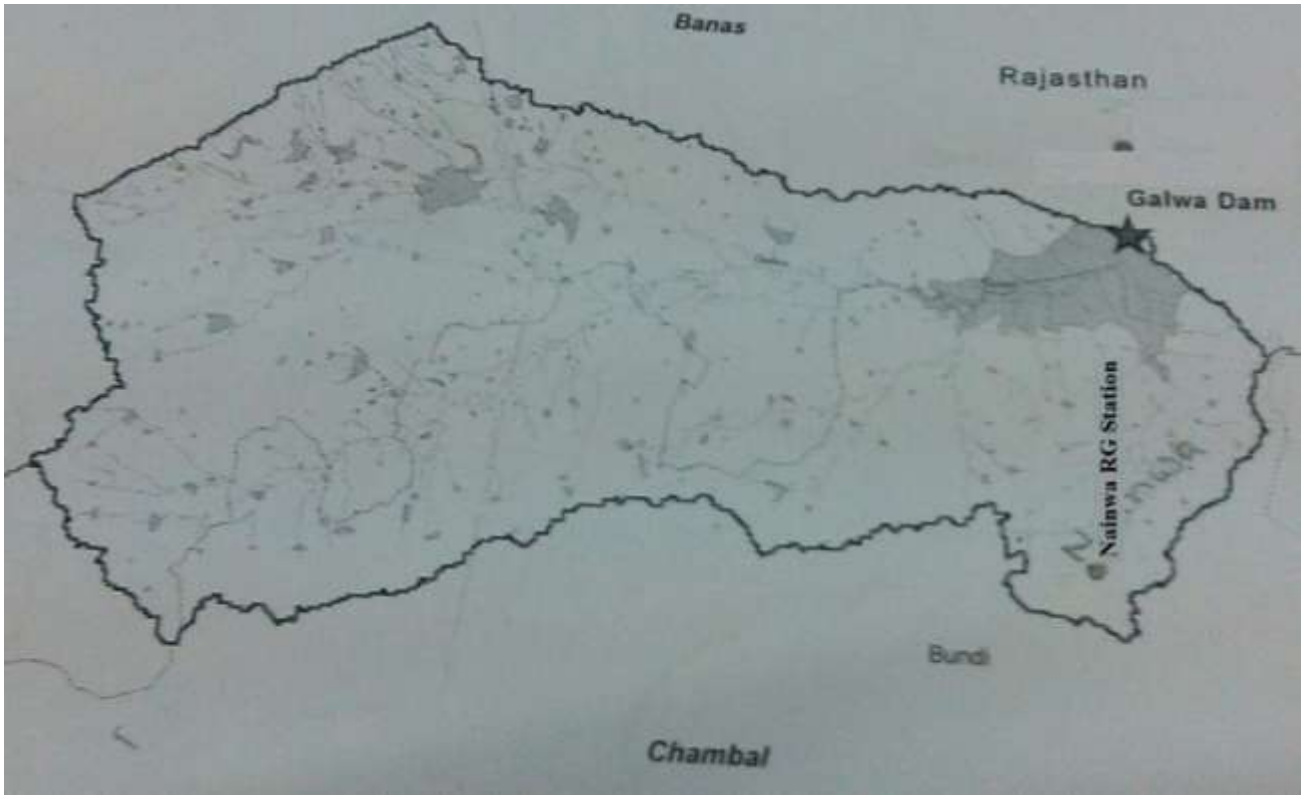

Figure-2 Catchment area plan with the location of raingauge station and dam site for Galwa Catchment

IV. DATA USED

Monthly rainfall data for the month July, August and September in the period 1996 to 2010 at Nainwa raingauge station which is in the Galwa catchment and the water inflow in the dam measured in the months July, August and September coming from the Galwa catchment observed by IMD and Water Resources Department Rajasthan are used in the study. The analysis is done on monthly and monsoon period basis. Since only one rain-gauge station is influencing the catchment, so the necessity of Thiessen polygon is not required. The inflow coming in the Galwa dam in the different months or monsoon period is used as runoff is computed in the depth form by dividing the total inflow in the particular period by the catchment area. The total weighted average

monthly and monsoon rainfall and runoff depths in mm are shown in Table-1.

V METHODOLOGY

Location of raingauge stations are marked on the catchment area. Thiessen polygon is drawn and the influence area with the influence factors of the various raingauge stations are determined by measuring the individual effected area. Total weighted rainfall in mm occurring in the catchment is computed using the influence factors. Here only one rain-gauge station at Nainwa is available so the Thiessen polygon is not required. The inflow coming from the catchment up to the Galwa dam in the month is determined, than the runoff in mm in the depth form is computed by dividing the volume of water inflow with the catchment area. Graphs between the rainfall in mm taking on X axis and corresponding runoff in mm on Y axis are plotted. Regression equations /graphs in various forms i.e. linear, polynomial, exponential and logarithmic assuming the rainfall as independent variable and the runoff as dependent variable can be plotted. The reliability/ performance of the relation/ graph can be checked by computing the various statistical parameters i.e. Correlation Coeff. (R), Determination Coeff. (R^2). Statistical parameter R represents about the strength of the relationship between observed rainfall and the runoff. R value between 0.6 to 1.0 indicates that there is a good relation and parameter R^2 provides information about the percentage of variation of runoff on rainfall.

VI. STATISTICAL AND REGRESSION ANALYSIS

The computed monthly and monsoon rainfall in mm and the corresponding water inflow depth computed in mm are statistically analyzed. Various statistical parameters are obtained which are shown in the Table-2. Parabolic, Linear and Logarithmic relation with their correlation and determination coefficients between the rainfall in mm and corresponding runoff in mm are obtained by the regression analysis.

Table 1:- Computed Total Rainfall and Corresponding Runoff Generated

	Total Rainfall (in mm)				Corresponding Runoff Generated (in mm)			
Year	July	Aug	Sept.	Monsoon	July	August	Sept.	Monsoon
1996	145.90	217.00	100.40	463.30	8.29	82.25	26.64	117.18
1997	238.80	151.60	65.00	455.40	28.68	19.65	1.83	50.16
1998	143.00	61.00	76.00	280.00	60.60	8.00	0.00	68.60
1999	278.80	152.20	59.20	490.20	87.16	48.95	0.00	136.11
2000	455.60	124.60	28.40	608.60	64.48	29.65	0.00	94.12
2001	321.10	141.10	0.00	462.20	59.39	8.74	0.00	68.13
2002	12.00	94.80	61.00	167.80	0.00	7.23	0.00	7.23
2003	97.20	141.40	80.00	318.60	28.68	10.17	13.70	52.55
2004	41.00	419.00	18.00	478.00	0.79	92.00	0.00	92.79
2005	239.00	18.00	153.00	410.00	28.17	0.00	0.00	28.17
2006	240.00	136.00	10.50	386.50	17.63	14.24	0.00	31.87
2007	99.00	176.00	91.00	366.00	17.18	0.00	0.99	18.17
2008	105.00	88.00	114.00	307.00	8.64	1.04	6.22	15.90
2009	73.00	102.00	19.00	194.00	7.36	1.38	0.00	8.74
2010	116.00	271.00	95.00	482.00	6.99	47.86	16.07	70.92

Table 2:- Statistical Parameters for Total Rainfall and Corresponding Runoff Generated

Sr. No.	Statistical Parameter	Total Rainfall (in mm)				Runoff Generated (in mm)			
		July	August	September	Monsoon	July	August	September	Monsoon
1	Max	455.6	419.0	153.0	608.6	87.2	92.0	26.6	136.1
2	Min	12.0	18.0	0.0	167.8	0.0	0.0	0.0	7.2
3	Range	443.6	401.0	153.0	440.8	87.2	92.0	26.6	128.9
4	Average	173.7	152.9	64.7	391.3	28.3	24.7	4.4	57.4
5	Median	143.0	141.1	65.0	410.0	17.6	10.2	0.0	52.6
6	Variance	14302.2	9113.0	1873.4	14409.7	732.8	892.8	65.2	1608.8
7	St. Dev.	119.6	95.5	43.3	120.0	27.1	29.9	8.1	40.1
8	Var. Coeff.	0.7	0.6	0.7	0.3	1.0	1.2	1.9	0.7
9	Skewness	0.9	1.6	0.2	-0.4	1.0	1.4	2.0	0.5

Table 3:- Various Empirical Relations between Rainfall and Runoff

Sr. No.	Month	Type of Relation	Relationship	Correlation Coeff.	Determination Coeff.
1	July	Parabolic	Y= -0.00016 (x2) + 0.23793 (x) - 6.105	0.747	0.558
		Linear	Y= 0.1676 (x) - 0.8413	0.740	0.548
		Logarithmic	Y= 20.02 log (x) - 69.098	0.677	0.458
2	August	Parabolic	Y= 0.00007 (x2) + 0.2276 (x) - 12.17696	0.820	0.673
		Linear	Y= 0.2567 (x) - 14.507	0.820	0.673
		Logarithmic	Y= 28.07 log (x) - 111.01	0.669	0.448
3	September	Parabolic	Y= -0.00109 (x2) + 0.2258 (x) - 3.79	0.490	0.24
		Linear	Y= 0.0755 (x) - 0.5231	0.405	0.164
4	Monsoon	Parabolic	Y= 0.00012 (x2) + 0.1551 (x) - 22.554	0.723	0.523
		Linear	Y= 0.2411 (x) - 36.98	0.721	0.52
		Logarithmic	Y= 78.071 log (x) - 404.5	0.697	0.486
		Exponential	Y= 3.644 $e^{0.006\ x}$	0.807	0.652

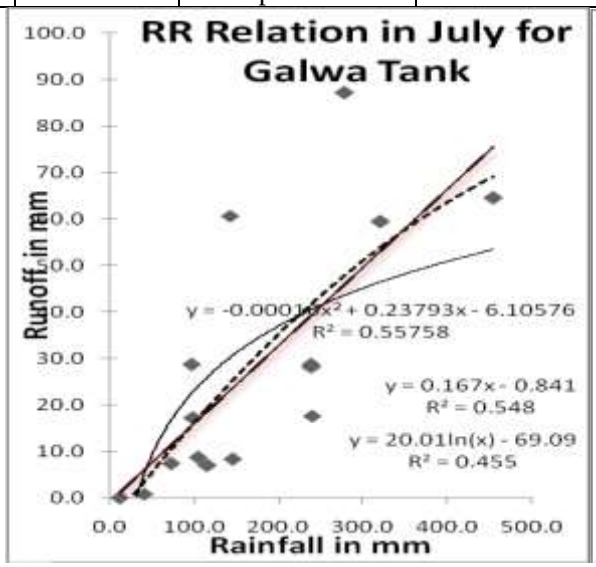

Figure-3 Rainfall Runoff Relation for July

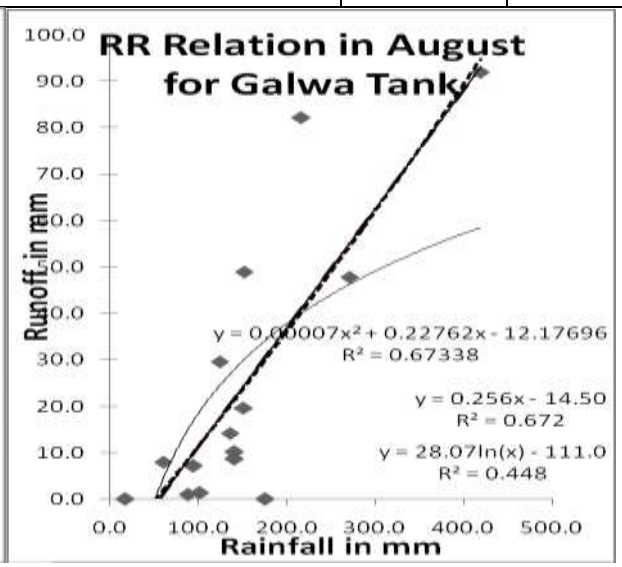

Figure-4 Rainfall Runoff Relation for August

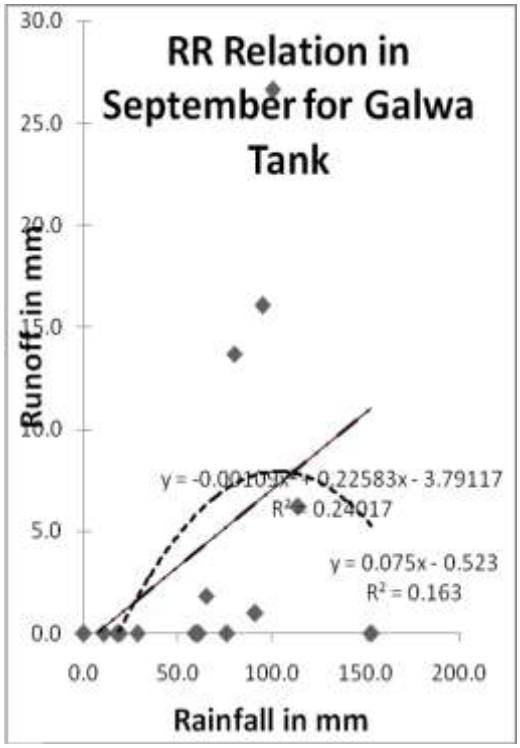

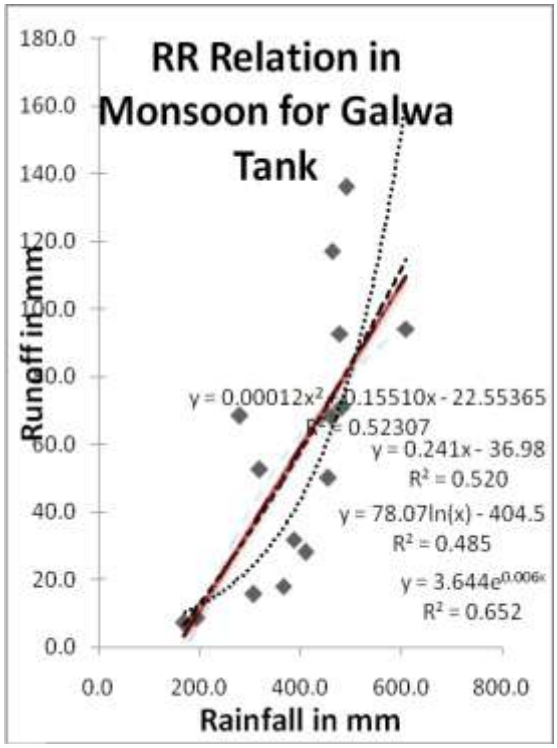

Figure-5 Rainfall Runoff Relation for September **Figure-6 Rainfall Runoff Relation for Monsoon**

VII. RESULTS AND DISCUSSIONS

Rainfall Contribution in the Galwa Catchment is maximum from Nainwa rain-gauge station. Variation of the total rainfall from the mean rainfall is minimum in September and maximum in July. The variation in total runoff is minimum in September and maximum in August. Rainfall and corresponding Runoff generated from the catchment are positively skewed in each month while the monsoon rainfall is skewed negatively. The parabolic, linear and logarithmic correlations between the rainfall and corresponding runoff with their correlation coefficients has been developed using regression analysis, results are shown in the Figure-3 to Figure-6.

Parabolic rainfall-runoff empirical relation gives highest coefficient of correlation and determination in each time period, secondly linear and then logarithmic as tabulated in Table-3.

Exponential rainfall-runoff empirical relation could not be achieved in the catchment except for monsoon period.

VIII CONCLUSION

Only three types of regressions i.e. Parabolic, Linear or Logarithmic can be developed in Galwa Catchment. Parabolic Rainfall-Runoff Regression Model is most suitable in the Galwa Catchment for different time periods, which can be used for computing runoff generated from the catchment or its part in the rainy days.

REFERENCES

[1] M. Afzal Ali Baig,, P. Mallikarjuna and T.V. Krishna Reddy," Rainfall Runoff Modeling – A Case Study

on Bahuda River Basin in Karnataka(India)", ISH, Journal of Hydrolic Engineering, Volume- 14, 2008, No.2

[2] Gunwant Sharma, Y.P. Mathur and S.K. Vyas "Rainfall-Runoff Regression Model for Meja Catchment", International Journal of Inventions in Research, Engineering, Science and Technology (IJIREST), Vol. I, No. I, April 2014, P. 58-62.

[3] John F. Joseph, H. Earnest Falcon and Hatim O. Sharif, "Hydrologic Trends and Correlations in South Texas River Basin", ASCE, Journal of Hydrologic Engineering.

[4] Hamed, K.H. 2008, "Trend detection in hydrologic data" The Mann-Kandell trend test under the scaling hypothesis, Journal of Hydrology, 349,350-363.

[5] Intergovernmental Panel on Climate Change 2007: Synthesis Report. Contribution of Working Group I, II and III to the Fourth Assessment Report of the Intergovernmental Panel on Clima5te Change [Core Writing Team, Panchauri, R.K. and Reisinger, A. (Eds.)]. IPCC, Geneva, Switzerland, 104 pp.

[6] K. Krishna Gowda, K. Manjunatha, R.Yadupathyputty and B.M. Manjunatha, " Rainfall Analysis of Bhadra Command Area (Karnataka, India)", Hydrology General Volume-34, Issue- 1and 2 January-June, 2011

[7] Mallikarjuna, P. and Vishnuvardhan, G. (2002)." Stochastic Modellling of Monthly Rainfall- A case study". ISH Journal of Hydraulic Engineering, vol8, No. 2 Sept.pp 60-72.

[8] Sudhisri, S., Pattnaik, V.S. and Mohapatra, N. (2002)." Rainfall Runoff Modelling for upper Kolab Catchment of Orissa". Journal of applied Hydrology, Vol.XVI, No.3,pp. 5-

[9] Mallikarjuna, P. and Prabhakara Rao. A. (2001)." Multiple Correlation Analysis of seasonal rainfall- A Case Study". Journal of Indian water works association, vol.33, No.4, Oct-Dec.pp.347-351.

[10] Gorantiwar, S.D. and Manjumdar, M. (1988). 'Application of Autoregressive Model of First Order to Annual Flow of Some West Bangal streams".Journal of the Institute of Engineers (India), Vol.169, Nov., pp 156-159.

[11] Mirza M.Q., Warrick R.A., Ericksen N.J. and Kenney G.J. (1998). Trends and Persistence in Precipitation in Ganga, Brahmaputra and Meghna River Basin, Hydrology journal 43 (6), 845-858.

[12] Srinivasan, K. and Thandaveswara, B.S. (1995). "Stochastic Modelling of monsoon dependent Flows of south Indian rivers" Journal of Institution of Engineers 9 India), Vol.75, Feb., pp.220-227.

[13] Varma, H.K. and Haque, M.E. (1991). "A Stochastic Model for Generation of Daily Rainfall Data at a station". Journal of Institution of Engineers (India), Vol. 72, Nov., pp 150-155.

[14] Reddy, D.V. and Vedula, S. (19810. "Stochastic Modelling for Monthly streamflows- A comparision by Case Study. Journal of Institution of Engineers, Vol. 61, March, pp. 271-276.

[15] Koteshwaram, P. and Alwa, S.M.A. (1969) Secular Trends and Periodicities in Rainfall at West Coastal station in India.

[16] Bhargava, B. N. and Bansal, K. 1973," A Quasi-biennial oscillation in precipitation at some Indian stations". Indian Journal of metrology and Geophysics, 20(2), 127-128.

[17] "Irrigation and Water Power Engineering" by Punmia B.C., Lal, B.B. etc., Laxmi Publications (P) Ltd.

[18] "Research Methodology" by C.R. Kothari.

[19] "Research Methodology by Ranjit Kumar.

[20] "Thesis submitted by Fekadu Moreda for the degree of Ph.D. in Brussels, July 1999 "Conceptual rainfall-runoff models for different time steps special consideration for semi-arid and arid catchments.

Environmental Geotechnics

Consolidation of clayey gouge amid permeating rock masses
Trivedi, Banik, Sukumar *et al*.

Environmental Geotechnics
http://dx.doi.org/10.1680/envgeo.13.00043
Paper 13.00043
Received 20/05/2013; accepted 08/01/2014
Keywords: geoenvironment/geohydrology

ICE Publishing: All rights reserved

ice Institution of Civil Engineers
publishing

Consolidation of clayey gouge amid permeating rock masses

1 **Ashutosh Trivedi** PhD
Professor and Head, Department of Civil Engineering, Delhi Technological University, Delhi, India

2 **Tanmay Banik** BEng
GET, Triune Energy Services Pvt Ltd, New Delhi, India

3 **Tanay Sukumar** BEng
Fellow, Teach for India, Green Park Extn, New Delhi, India

4 **Naresh Kumar** MTech
Associate Professor, Department of Civil Engineering, Delhi Technological University, Delhi, India

5 **Akshay Jain** BEng
Sales Officer, Indian Oil Corporation Ltd, Ranchi, Jharkhand, India

6 **Amit Kumar** BEng
Officer Trainee, Indian Oil Corporation Ltd, Vijayawada, Andhra Pradesh, India

There are numerous occurrences of soil–rock–water interaction in the natural geo-environment involving saturated clayey gouge consolidating amid permeating rock masses and draining laterally through a network of joints. In this paper, the concept of two-dimensional drainage for consolidation along the vertical direction for saturated clay has been applied to a layer of gouge amid rock joints. Solutions for pore water pressure distribution and average degree of consolidation have been computed. The orthogonal directions along which the drainage has been assumed for the derivation of these expressions are vertical direction (as in Terzaghi's theory of one-dimensional consolidation) and lateral direction. Initially, such a case corresponds to a Dirichlet problem applied to a rectangular gouge lamina. The deformations appearing in the vertical direction are a result of the effects of drainage in the lateral and vertical directions together. An expression for the relationship of time factor with the average degree of consolidation as a function of dimensionless parameter relating rock mass characteristics has been proposed.

Notation

$a_v(x)$	coefficient of compressibility in x direction
$a_v(z)$	coefficient of compressibility in z direction
c''', c'', c'	coefficients of dimension less ratio r to obtain $\varphi(r)$
$C_h(x)$	coefficient of consolidation in x direction
$C_h(y)$	coefficient of consolidation in y direction
$C_h(z)$	coefficient of consolidation in z direction
E	deformation modulus of gouge material
E_{hv}	modulus ratio = E_h/E_v
E_h	deformation modulus in horizontal direction
E_v	deformation modulus in vertical direction
e	void ratio
e_0	initial void ratio
$2H$	descriptor of thickness of gouge
H_z, H_z	drainage path along vertical direction, thickness of gouge in z direction, and equivalent thickness of gouge amid a number of joints respectively
j	joints in rock mass
K	coefficient of permeability
K_{rm}	intrinsic permeability of rock masses
K_{uc}	intrinsic permeability of unconsolidated organic soils and clays
K_x	coefficient of permeability in x direction
K_y	coefficient of permeability in y direction
K_z	coefficient of permeability in z direction
k_h	coefficient of permeability along lateral direction
k_v	coefficient of permeability along vertical direction
$2L$	descriptor of lateral spread of gouge
L_x, L_y	drainage path along x direction and y direction respectively
n	porosity
r	dimension less ratio depending on r_c, r_k and r_s
r_c	ratio of coefficient of consolidation of clayey gouge to that of rock mass
r_k	ratio of intrinsic permeability of clayey gouge to that of rock mass
r_s	shape factor
T_f	final value of non-dimensional time factor at $U = 1$
T_{fs}	value of non-dimensional time factor where post primary consolidation offsets primary consolidation
T'_{fs}	variant of non-dimensional time factor T_{fs}
T_v	non-dimensional time factor
t_a	asperity height
U_{av}	average degree of consolidation

$U_{av}1$, $U_{av}2$, $U_{av}3$, $U_{av}4$	average degree of consolidation in Figure 3, at r = 0, 0·1, 1, 10 respectively
$U_{av}1$, $U_{av}2$	average degree of consolidation in Figure 4 for 1-D and 2-D drainage case, respectively
U_p	average degree of consolidation at the end of primary consolidation
U_s	average degree of consolidation at the end of post primary consolidation
U_z	degree of consolidation at depth 'z'
u	pore water pressure at time 't'
u_i	initial excess pore water pressure
v_x	component of velocity in x direction
v_z	component of velocity in z direction
β	joint inclination with the direction of loading
γ	bulk unit weight
γ_w	unit weight of water
γ_{xz}	shear strain in x–z plane
$\bar{\sigma}_x$	effective stress in x direction
$\bar{\sigma}_z$	effective stress in z direction
$\varphi(r)$	dimension less parameter depending on dimension less ratio, r

Introduction

Most of the rock masses in our planetary geo-environment are neither massive nor intact nearly to a hundred meters of earth crust. Several groups of interconnected discontinuities, under a set of geo-physical and geo-chemical forces, allow deposition of gouge and granular fragments. In a geo-mechanical stress environment, for a saturated ground water condition, the hydraulic and strain adjustment amid these formations is well anticipated. Therefore, the consolidation of randomised distribution of saturated clayey gouge is frequently encountered amid the permeating rock masses. The gouge material is defined as a fine hydro-geo-thermal deposit of clay and silt amid rock joints produced by soil–rock–water interaction and soil–rock–mineral alterations. Often, the fluid flow and deformability of the rock masses can be interpreted from in situ rock quality designation, number of joint (J), joint inclination (β), joint condition, gouge density, gouge thickness ($2H_z$) (Trivedi, 2010) and joint aperture ($2t_a$) (Hsu *et al.*, 2011; Klimczak *et al.*, 2010). The thickness of the gouge material ($2H_z$) and its lateral spread may vary in the range of several meters to a few millimetres with multiple drainage paths. In submerged conditions, these heterogeneous distributions of clayey gouge may be idealised as a lamina of variable permeability consolidating in the vertical direction and draining in plane strain conditions amid fractured rock masses. Figure 1 shows an example of a clayey gouge layer draining in the horizontal and vertical directions. The range of permeability of rock masses and that of silty–clayey gouge is shown in Table 1.

While the deformation of rock masses with gouge can be estimated reasonably well (Trivedi, 2010, 2013) from normal, shear stiffness (Zhang, 2010) and in situ rock mass characterisation, their time-dependent consolidation behaviour is yet to be computed by a physically idealised and numerically consistent method. Under varying salute and fluid transport conditions influenced by temperature, pressure and geo-environment, the saturated clayey gouge is expected to show a time-dependent volume change behaviour, which was ideally simplified in the seminal works of Terzaghi (1925, 1943) on one-dimensional (1-D) consolidation. Accordingly, the process of consolidation is defined as the decrease in pore fluid content of a saturated soil without its replacement by air. This definition attracted widespread interest in the scientific and engineering community, which had been involved in estimating the consolidation settlement of saturated clays for more than half a century using experimental and numerical techniques (Biot, 1941; Das, 2008; Di Francesco, 2011; Gibson *et al.*, 1967; Lambe and Whitman, 1969; Scott, 1963; Tewatia *et al.*, 2013; Wood, 2004).

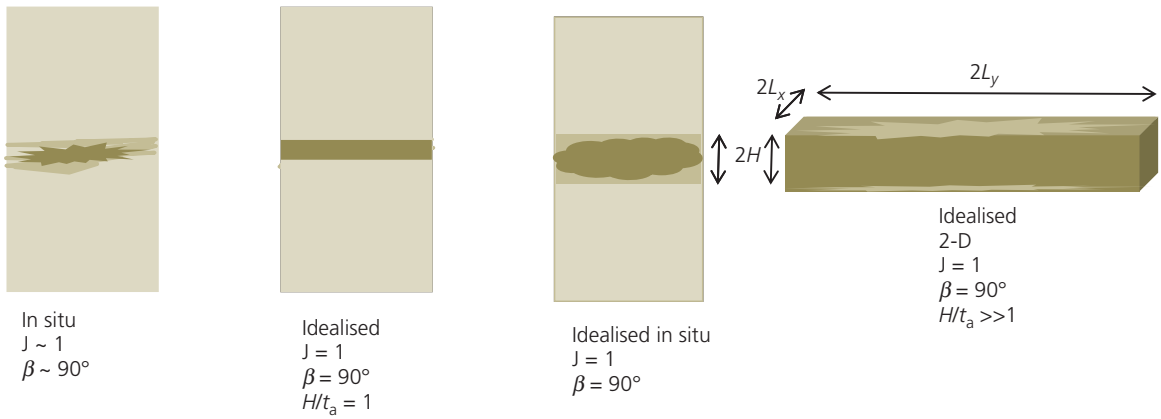

Figure 1. In situ and idealised saturated clay lamina amid permeating rock mass for single joint (J = 1) oriented normal to the direction of loading (β = 90°) at different asperity ratio (H/t_a); gouge thickness ($2H$) covers the asperity height ($2t_a$); the gouge is shown in dark shades

In situ profile	Coefficient of permeability: mm/sec	Physical effects
Well sorted gravels	>1	High permeability, pervious in nature
Sandy gouge	10^{-1}–10^{-4}	Medium to low permeability, semi-pervious
Highly fractured rock masses	10^{-2}–10^{-5}	Low permeability, pervious
Sand with silt and clay gouge	10^{-4}–10^{-6}	Low permeability, semi-pervious
Poorly weathered rock masses	10^{-5}–10^{-10}	Very low permeability, semi-pervious in nature, drainage is poor
Clayey gouge and organic soils	10^{-6}–10^{-11}	Very low permeability, impervious
Un-weathered rock mass	10^{-11}–10^{-13}	Impervious in nature

Interpreted from Bear (1972).

Table 1. Range of permeability as per soil and rock mass profile

In a classical work on consolidation theory, Biot (1941) assumed isotropy of the material, reversibility of stress–strain relations under final equilibrium conditions, linearity of stress–strain relations, small strain behaviour, incompressibility of pore water, possibility of air bubbles and that dissipation of pore water follows Darcy's law.

Biot (1941) agreed that among these basic assumptions, the isotropy and the reversibility of stress–strain are mostly subjected to serious criticism. However, he kept in mind that they also constitute the basis of Terzaghi's theory, which has been found quite satisfactory for the practical requirements of engineering. In fact, it can be imagined that the grains composing the soil are held together in a certain pattern by surface tension forces and tend to assume a configuration of minimum potential energy. This would especially be true for the colloidal particles constituting clay. It seems reasonable to assume that for small strains, when the grain pattern is not too much disturbed, the assumption of reversibility will be applicable. The assumption of isotropy is not essential, and anisotropy can easily be introduced by a mathematical induction in time factor due to the effects of 1-D and two-dimensional (2-D) drainage.

It might be of great importance to evaluate the influence of the state of initial stress in the soil before application of the load on the stress distribution and the settlement due to multi-draining systems. Such an influence may introduce an initial convexity in the time factor due to 1-D and 2-D drainage, which is captured in the present study by a non-dimensional ratio r and a parameter $\varphi(r)$. It is understood that this influence is significant for rock masses with high values of the parameter $\varphi(r)$.

As a consequence of the assumptions, there have been many estimates of 1-D, 2-D and three-dimensional (3-D) consolidation (McNamee and Gibson, 1960; Gibson *et al.*, 1970; Christian and Boehmer, 1970; Hansbo, 1981; Indraratna and Redana, 1997; Ai and Han, 2006; Ai and Cheng, 2009; Huang *et al.*, 2006; Zwanenburg, 2005; Sukumar *et al.*, 2013). Some of them based on Fourier transform became extensively popular owing to their natural simplicity. The consolidation scheme as that of saturated clayey gouge within permeable boundaries has rarely been considered in the past studies. Therefore, the solution to consolidation with permeable boundaries that originate amid rock masses has remained elusive. Therefore, it is proposed to derive a solution in the present study for 1-D consolidation with 2-D drainage for a clayey gouge layer sandwiched amid rock masses of higher permeability. The graphic representation of the degree of consolidation and time factor is shown using the software Mathematica (Wolform, 2013).

Based on discrete Fourier transform, Terzaghi (1943) proposed a solution for 1-D consolidation. Hansbo (1981) and Al-Tabbaa and Wood (1991) derived a relationship for the average degree of consolidation (U_{av}) and time factor (T_v) by assuming 2-D radial consolidation (Indraratna and Redana, 1997). The authors derived the 1-D consolidation with 2-D drainage equations for a layer of saturated clayey gouge of low permeability compared to the boundaries. The results obtained by 1-D consolidation 2-D drainage are significantly different from the case of radial consolidation (Hansbo, 1981; Al-Tabbaa and Wood, 1991). It is observed that there are innate similarities in the numerical representation of 1-D consolidation with 2-D drainage with that obtained by 1-D solutions, but at lower and moderately lower degree of consolidation, there appeared significant departures. The 1-D consolidation with 2-D drainage showed more realistic pore pressure distribution in the lateral and vertical directions for the sandwiched layer of saturated clayey gouge, where the rock masses are characterised by a non-dimensional parameter identified in the present text.

General theory for 1-D consolidation with 2-D drainage

It is assumed that a layer of clayey gouge is confined amid permeating rock masses. When a surcharge of load intensity $\Delta\sigma$ is transferred over this clay layer, the entire stress increase contributes to an increase in pore water pressure only and none to the stresses in the soil skeleton itself. This increase in pore water pressure equivalent to $\Delta\sigma$ appears at all depths of the saturated clay and dissipates gradually by 'squeezing out' through the relatively permeable sand stone layers and through the lateral sides, as shown in Figure 1. Normally, the thickness and spread of the gouge material ($2H_z$ and $2L_x$ respectively) should be larger than the asperity height ($2t_a$) such that ($H_z/t_a > 1$ and $L_x/t_a > 1$) while $L_y >> L_x$. The equivalent of joint fractures, gouge thickness and inclination of the gouge is considered in the z direction as

represented by $2H(= 2H_z)$. The gradual dissipation of pore water pressure causes an increase in the effective stresses at every depth of the layer, and a subsequent time-dependent settlement occurs in that layer.

The 3-D consolidation is given by the following differential equation:

$$\frac{\partial u}{\partial t} = c^2 \nabla^2 u \qquad 1.$$

where $\nabla^2 u = \frac{\partial^2 u}{\partial x^2} + \frac{\partial^2 u}{\partial y^2} + \frac{\partial^2 u}{\partial z^2}$.

Here, u represents the pore water pressure in vector space (x, y, z) in the soil sample at time t, after the application of surcharge. The ∇^2 is a Laplace operator in 3-D vector space. Like any other great work of science, the double integrands of Equation 1 provide an opening to a myriad of numerical, analytical and empirical interpretations. It allows a constant in the solution, which itself may be deduced as a function of time and space. Induction of such a function is often avoided deliberately as an input parameter in the differential equation for the purpose of simplicity in the solution. However, as an appearance due to the complementarity of observations, the effects become apparent in the post primary phase of consolidation and hence in time factor, where there are effects of particulate rotation, shear and compression. De Josselin de Jong and Virujit (1965) showed that the double integrand of Equation 1 with a constant in the solution reduces to only a function of time alone when deformations occur in the absence of rotations (Zwanenburg, 2005). These considerations allowed convergence of Biot's analytical solutions with that proposed by Terzaghi as also used in the present context.

In a simple initial form of 2-D vector space, if $\frac{\partial u}{\partial t} = 0$, Equation 1 may be represented as Dirichlet's problem as

$$c^2 \left(\frac{\partial^2 u}{\partial x^2} + \frac{\partial^2 u}{\partial z^2} \right) = 0 \qquad 2.$$

Here, c^2 is fully described on pore pressure u.

The effects of hydraulic and deformation anisotropy may be conveniently considered through C_{vz} and C_{hx} as $\frac{\partial u}{\partial t} \neq 0$

$$C_{hx} \frac{\partial^2 u}{\partial x^2} + C_{vz} \frac{\partial^2 u}{\partial z^2} = \frac{\partial u}{\partial t} \qquad 3.$$

If $C_{hx} = C_{vz} = c^2$, and $\frac{\partial u}{\partial t} = 0$, Equation 3 is converted into Dirichlet's problem, which permits induction of geometric anisotropy in 2-D space similar to Equation 2.

Incidentally, the 1-D consolidation problem can be solved with the same ease as is possible for the 2-D seepage problem. Terzaghi's model has a spring constant that is comparable to the deformation modulus for an elastic body; similarly, gouge lamina has orthogonal springs for isotropic elastic body. It retains Terzaghi's model of one constant for primary and a different constant for post-primary range. It is a model material with a hardening–softening character. These difficulties get resolved from the 2-D pore pressure dissipation model, similar to the solution of problems of transient heat transfer in two dimensions (Carslaw and Jaegar, 1986). Scott (1963) intuitively provided a simple solution for the average degree of consolidation of an infinitely long square prism that is shown to be a special case of the present study. Moreover, some approximate solution for the problem of transient flow in two dimensions is provided with reference to what is known of 1-D transient flow as per Terzaghi's theory of 1-D consolidation and 1-D drainage.

The surcharge applied has a value $\Delta\sigma$, which is initially equal to u_i (the initial value of pore pressure at time $t = 0$). The quantity c^2 is equal to the coefficients of consolidation c_v, and have the dimensions of L^2T^{-1}. The layer of clay is bounded at the sides (x direction) by permeable joints, top and bottom (z direction), by permeable rock mass. The extent of space in the y- direction is assumed infinite so as to have 1-D consolidation with 2-D drainage.

Equation 1 is reduced to the case of 1-D consolidation with 1-D drainage if the pore water pressure changes in the x- and y-directions are zero. Fourier analysis of the partial differential equation given by Equation 1 provided the following solutions for the case of 1-D consolidation with 1-D drainage:

$$u = \sum_{n=1}^{n\to\infty} \left(\frac{1}{H} \int_0^{2H} u_i \sin \frac{n\pi z}{2H} \mathrm{d}z \right) \sin \frac{n\pi z}{2H} \exp\left(\frac{-n^2 \pi^2 T_v}{4} \right) \qquad 4.$$

The degree of consolidation at a given depth and time is a quantity defined as

$$U_z = \frac{u_i(z) - u_t(z)}{u_i(z)} \qquad 5.$$

In Equations 4 and 5, H represents the thickness of the longest drainage path in the layer (a two-way vertical drainage condition has been assumed; thus, H is half the thickness of the layer), and $u_t(z)$ is the pore water pressure at depth z at a given time t, and $u_i(z)$ is the initial pore water pressure at depth z. T_v is the non-dimensional time factor such that $T_v = c_v t/H^2$, where c_v is coefficient of consolidation, and $c_v = kE/\gamma_w$.

In isotropic condition, the coefficient of consolidation varies according to the isotropic hydraulic conductivity k. Here, the deformation modulus E, which is the inverse of the coefficient

of volume compressibility, and the unit weight of pore fluid γ_w are considered constant during the process of consolidation. The coefficient of volume compressibility is defined as the ratio of change in volume per unit volume of soil corresponding to the unit change in pressure.

While defining non-dimensional time factor T_v, c_v is induced such that c^2 is fully described over time t and descriptor of space H. Since the description of c_v is numerically holomorphic, therefore a fully described c_v in space entails $U_z = U_p$, where U_p is the limiting magnitude of primary consolidation such that the behaviour is poro-elastic. In the range of primary consolidation, according to Terzaghi (1925), there is a unique relation of T_v and U_z such that $T_v = (\pi/4)U_z^2$. Alternatively, the relationship of time factor with degree of consolidation is presumed nearly parabolic $T_v = (3/4)U_z^2$ (Schofield and Wroth, 1968; Wood, 2004). If the degree of consolidation is such that $U_z > U_p$, the consolidation is presumed to be in the post-primary range. As the magnitude of $U_z > U_p$, the deformation may not remain poro-elastic; therefore, the coefficient of consolidation is alternatively described over space and time.

Since the consolidation amid rock masses gradually proceed from primary to post primary and reach finality (U_z = 1), the modified convexities in the time factor either in primary, post primary or later range of consolidation should be captured using the concepts of 1-D consolidation with 2-D drainage. Because of the fact that the clay lamina amid rock masses have an apparent similarity (Figure 1) to drainage through a plane frame and secondly for simplicity of assumptions, a solution for 1-D consolidation with 2-D drainage is obtained numerically using a non-dimensional parameter, depending on shape factor, modulus and intrinsic permeability ratio.

Application of consolidation with 2-D drainage

The solutions obtained by Terzaghi (1925) remain valid for the situation where drainage takes place along the vertical direction. There are varied practical situations where drainage may take place along two directions as in the case of clay lamina sandwiched amid permeating rock masses (Figure 1). For consolidation settlement to occur, the thickness of the lamina must be greater than the asperity height of the rock joints. The gouge material is often deposited as a sheet of clay amid the rock joints, which show a diffusivity pattern for pore fluid similar to consolidation with 2-D drainage. Similarities may also be observed in the thermal conductivity through a metal sheet, which shows a 2-D diffusion pattern. Starting from the continuity equation for fluid flow and Darcy's law, the authors derived an expression that describes the dissipation of pore water pressure along more than one direction.

The expressions were derived for the case where dissipation takes place along the z direction and one of the two lateral directions, say, the x direction. The starting point for the derivation remains the same as for the expressions for consolidation as per Equation 1, that is, the continuity equation for fluid flow. Finally, the expressions are used to plot a relationship between pore pressure and space coordinates, which provide an interpretation to the 1-D consolidation 2-D drainage of a clay layer. The authors in proviso studied the relationship between the degree of consolidation and the time factor.

Terzaghi's theory of 1-D consolidation is meant for applications to the ideal case of excess pore pressure dissipation occurring along the vertical direction. In real-life situations, such cases are encountered where only lateral drainage is possible, yet vertical deformations are visible due to lateral dissipation of pore pressure, as shown in Figure 1. During the geotechnical investigation for several projects, the saturated clay layer is found to be sandwiched between relatively pervious rock masses. While movement of water is possible through the lateral direction, the settlement is a result of 1-D consolidation with 2-D drainage.

Theoretical descriptors for consolidation of gouge

Equation for consolidation with 2-D drainage

There are solutions available for 1-D consolidation by Terzaghi (1925), 2-D consolidation by Ai and Wu (2009) and Di Francesco (2011) and 3-D consolidation by Biot (1941), with varied assumptions. Further, there are numerous natural occurrences of varied structural shapes of gouge material amid rock masses with one of the relatively longer dimensions. Alternatively, the no-flow conditions may also exist due to the locking of gouge amid rock mass in one of the directions. It corresponds to the presence of 1-D consolidation with 2-D drainage of clay layers amid rock masses with all possible randomness in length and thickness. The presence of such a varied and random distribution of shapes of clay lamina amid rock masses induces variation in permeability in the orthogonal directions. Since there may be natural variation in the compressibility of rock masses along these directions, the ratio of coefficient of consolidation and shape factor provides a guiding parameter $\varphi(r)$ to evaluate the consolidation of clayey gouge. The authors assume the continuity equation for fluid flow, which is applicable to all flow situations.

At this stage, the following assumptions are considered to simplify the problem:

(*a*) The nature of the problem allows conceiving the quantity $\left[\frac{\partial^2 u}{\partial y^2}\right]$ in Equation 1 as zero, such that the drainage along one of the two lateral directions is negligible due to its extent, which is assumed infinite. At time $t = 0$, there is no compression and no flow along the y direction. There is a vertical surcharge (along z direction) and a confining stress along the x direction. Also, $c_{hx} = c_h$ and $c_{vz} = c_v$.

(*b*) Darcy's law is valid along both drainage directions on which stresses are applied, that is, $v_z = k_z \frac{\partial h}{\partial z}, v_x = k_x \frac{\partial h}{\partial x}$

(*c*) The gouge layer is completely saturated.

(*d*) The gouge layer is homogeneous.

(*e*) The gouge grains and water are isotropic and incompressible

(*f*) The primary consolidation controls deformation as long as the degree of consolidation is fully described by c_v and a dimensionless ratio r.
(*g*) The post-primary consolidation is said to control deformation as the degree of consolidation is alternatively described by c_v, r and a non-dimensional parameter $\varphi(r)$.

The consolidation with 2-D drainage equation is a particular case of the expression for consolidation given by Equation 3. It can be derived by applying the above assumptions to the continuity. The equations of static equilibrium in a x–z plane as per Ai and Wu (2009) and Ai and Cheng (2009) may be expressed as

$$\frac{\partial \sigma_x}{\partial x} + \frac{\partial \tau_{zx}}{\partial z} = 0 \quad \text{6a.}$$

$$\frac{\partial \tau_{xz}}{\partial x} + \frac{\partial \sigma_z}{\partial z} = 0 \quad \text{6b.}$$

where σ_x and σ_z are the total stresses in the x and z directions, respectively, and τ_{xz} is the shear stress. The relationships for strain and displacement can be expressed for an elastic media as

$$\varepsilon_x = \left[\frac{1-v^2}{E}\right]\left[\sigma_x + u - \left\{\frac{v}{1-v}(\sigma_z + u)\right\}\right] \quad \text{6c.}$$

$$\varepsilon_z = \left[\frac{1-v^2}{E}\right]\left[\sigma_z + u - \left\{\frac{v}{1-v}(\sigma_x + u)\right\}\right] \quad \text{6d.}$$

$$\gamma_{xz} = 2(1+v)\tau_{xz}/E \quad \text{6e.}$$

where E is the deformation modulus, and ν is Poisson's ratio. The permeability of gouge is anisotropic because of their directional drainage restrain. Therefore, to consider the anisotropy of permeability in the consolidation calculation, the continuity equation for a plane strain medium with anisotropic permeability can be expressed as

$$\frac{1}{1+e_0}\frac{\partial e}{\partial t} = (1/\gamma_w)\left(k_h \frac{\partial^2 u}{\partial x^2} + k_v \frac{\partial^2 u}{\partial z^2}\right) \quad \text{6f.}$$

where $\varepsilon_v = \varepsilon_x + \varepsilon_z$ is the volumetric strain, resulting in a change in void ratio ∂e. γ_w is the unit weight of water, and k_h and k_v are the permeability coefficients in the horizontal and vertical directions, respectively. As conceived in Equation 3, the continuity Equation 6f may be represented as

$$c_h \frac{\partial^2 u}{\partial x^2} + c_v \frac{\partial^2 u}{\partial z^2} = \frac{\partial u}{\partial t} \quad \text{7a.}$$

$$c_v = \frac{k_z(1+e_0)}{a_{v(z)}\gamma_w},\ c_h = \frac{k_x(1+e_0)}{a_{v(x)}\gamma_w} \quad \text{7b.}$$

For no changes in total stresses,

$$a_{v(z)} = a_{v(x)} \quad \text{7c.}$$

It implies that the changes in void ratio in the vertical and horizontal directions are complimentary to the global changes in scalar product of change in stresses and compressibility.

Similarly, for the 1-D consolidation with 1-D drainage case

$$\partial e \rightarrow f(\partial e_{(z)}) \rightarrow a_v \partial \bar{\sigma}_z \quad \text{7d.}$$

Solution for the 1-D consolidation with 2-D drainage

To solve Equation 7a, the pore pressure is assumed as $u(x, z, t)$ to be the product of three functions as

$$u(x, z, t) = F(x) \cdot F(z) \cdot G(t) \quad \text{8.}$$

In differential form, it is represented as

$$\frac{\partial u}{\partial t} = F(x) \cdot F(z) \cdot G'(t) \quad \text{9.}$$

$$\frac{\partial^2 u}{\partial x^2} = F''(x) \cdot F(z) \cdot G(t) \quad \text{10.}$$

$$\frac{\partial^2 u}{\partial z^2} = F(x) \cdot F''(z) \cdot G(t) \quad \text{11.}$$

Substituting Equations 9, 10 and 11 in Equation 8

$$F(x) \cdot F(z) \cdot G'(t) = c_h F''(x) \cdot F(z) \cdot G(t) + c_v F(x) \cdot F''(z) \cdot G(t)$$

Dividing this equation by $F(x) \cdot F(z) \cdot G(t)$,

$$\frac{G'(t)}{G(t)} = c_h \frac{F''(x)}{F(x)} + c_v \frac{F''(z)}{F(z)}$$

The left-hand side of this equation is dependent only on time t. Similarly, on the right-hand side of the equation, one expression is a

function of x only, whereas the other is a function of z only. Hence, for the equation to be true, both sides must be individually equal to a constant, say, $-B^2$. So

12. $G'(t) = -B^2 G(t)$

13. $$c_h \frac{F''(x)}{F(x)} + c_v \frac{F''(z)}{F(z)} = -B^2$$

The solution to Equation 12 is

14. $G(t) = A_1 e^{-B^2 t}$

where A_1 is a constant. Solving Equation 13

15. $$\frac{F''(x)}{F(x)} = -C^2, \frac{F''(z)}{F(z)} = -D^2$$

The values of C and D are such that

16. $c_h C^2 + c_v D^2 = B^2$

The solutions to Equation 15 are

17. $$F(x) = A_2 \cos Cx + A_3 \sin Cx,$$
$$F(z) = A_4 \cos Dz + A_5 \sin Dz$$

where A_2, A_3, A_4 and A_5 are constants.

Now substituting Equations 14 and 17 in Equation 8

18. $u = (A_2 \cos Cx + A_3 \sin Cx)(A_4 \cos Dz + A_5 \sin Dz) A_1 e^{-B^2 t}$

To obtain the particular solution, the constant terms in Equation 18 need to be evaluated, which is obtained by using Initial Value Condition (i) and Boundary Value Conditions (ii)–(v):

Initial Value Condition:

(*i*) $t = 0$, $u = u_i$

Boundary Value Conditions:

(*ii*) $u = 0$ at $z = 0$
(*iii*) $u = 0$ at $z = 2H$
(*iv*) $u = 0$ at $x = 0$
(*v*) $u = 0$ at $x = 2L$

Conditions (ii) and (iv) give $A_4 = 0$ and $A_2 = 0$ respectively. Conditions (iii) and (v) give $C = \frac{m\pi}{2L}$ and $D = \frac{n\pi}{2H}$, where m and n are integers. From the above relations, a general solution can be given in the form

19. $$u = \sum_{m=1}^{\infty} \sum_{n=1}^{\infty} A_{mn} \sin \frac{m\pi x}{2L} \sin \frac{n\pi z}{2H} e^{-B^2 t}$$

Substituting the obtained values of C and D in Equation 16

20. $$c_h \frac{m^2\pi^2}{4L^2} + c_v \frac{n^2\pi^2}{4H^2} = B^2$$

Substituting B^2 in Equation 19

21. $$u = \sum_{m=1}^{\infty} \sum_{n=1}^{\infty} A_{mn} \sin \frac{m\pi x}{2L} \sin \frac{n\pi z}{2H} \times \exp\left[-\left(c_h \frac{m^2\pi^2}{4L^2} + c_v \frac{n^2\pi^2}{4H^2} \right) t \right]$$

According to boundary condition (i), at $t = 0$, and $u = u_i$

22. $$u_i = \sum_{m=1}^{\infty} \sum_{n=1}^{\infty} A_{mn} \sin \frac{m\pi x}{2L} \sin \frac{n\pi z}{2H}$$

The solution for this equation is given by the double integral

23. $$A_{mn} = \frac{1}{L \cdot H} \int_0^{2H} \int_0^{2L} u_i \sin \frac{m\pi x}{2L} \sin \frac{n\pi z}{2H} \, dx dz$$

Therefore, the general expression that is a solution to Equation (7a) is

24. $$u = \sum_{m=1}^{\infty} \sum_{n=1}^{\infty} A_{mn} \sin \frac{m\pi x}{2L} \sin \frac{n\pi z}{2H} \times \exp\left[-\left(c_h \frac{m^2\pi^2}{4L^2} + c_v \frac{n^2\pi^2}{4H^2} \right) t \right]$$

with A_{mn} as defined in Equation 23.

Particular expression for the case when u_i is constant with depth

For this case, initially the pore pressure

25. $u_i = u_0$

Taking u_i outside and evaluating the double integral, Equation 23 is expressed as

$$\int_0^{2H}\int_0^{2L} \sin\frac{m\pi x}{2L}\sin\frac{n\pi z}{2H}\,dx\,dz = \frac{4LH}{mn\pi^2}(1-\cos m\pi)(1-\cos n\pi) \quad (26)$$

Using Equation 23 and 26, A_{mn} is derived as

$$A_{mn} = \frac{4u_0}{mn\pi^2}(1-\cos m\pi)(1-\cos n\pi) \quad (27)$$

Therefore, the solution for this case is given by substituting A_{mn} from Equation 27 into Equation 24. Since the terms $(1 - \cos n\pi)$ and $(1 - \cos m\pi)$ vanish for even values of m and n, the solution is given by

$$u = \sum_{k=0}^{\infty}\sum_{l=0}^{\infty}\frac{16u_0}{mn\pi^2}\sin\frac{m\pi x}{2L}\sin\frac{n\pi z}{2H} \times\exp\left[-\left(c_h\frac{m^2\pi^2}{4L^2}+c_v\frac{n^2\pi^2}{4H^2}\right)t\right] \quad (28)$$

where $m = 2k + 1$, $n = 2l + 1$.

Expression for degree of consolidation for a particular depth

At a given time and depth, the degree of consolidation is as given in Equation 3. Using Equation 28 for the particular case as described by Equations 25 to 28, the degree of consolidation is computed as

$$U_z = 1-\sum_{k=0}^{\infty}\sum_{l=0}^{\infty}\frac{16}{mn\pi^2}\sin\frac{m\pi x}{2L}\sin\frac{n\pi z}{2H} \times\exp\left[-\left(c_h\frac{m^2\pi^2}{4L^2}+c_v\frac{n^2\pi^2}{4H^2}\right)t\right] \quad (29)$$

where $m = 2k + 1$, $n = 2l + 1$.

Through a few basic operations, Equation 29 is expressed in terms of the time factor T_v, as defined in Equations 2 and 3 as

$$\left(c_h\frac{m^2\pi^2}{4L^2}+c_v\frac{n^2\pi^2}{4H^2}\right)t = \frac{c_v t}{H^2}\left(\frac{c_h}{c_v}\cdot\frac{H^2}{L^2}\cdot\frac{m^2\pi^2}{4}+\frac{n^2\pi^2}{4}\right) = T_v\left(r\cdot\frac{m^2\pi^2}{4}+\frac{n^2\pi^2}{4}\right) \quad (30)$$

where $r = \frac{c_h}{c_v}\cdot\frac{(2H)^2}{(2L)^2}$.

Therefore, Equation 29 may be rewritten as

$$U_z = 1-\sum_{k=0}^{\infty}\sum_{l=0}^{\infty}\frac{16}{mn\pi^2}\sin\frac{m\pi x}{2L}\sin\frac{n\pi z}{2H} \times\exp\left[-T_v\left(r\cdot\frac{m^2\pi^2}{4}+\frac{n^2\pi^2}{4}\right)\right] \quad (31)$$

where $m = 2k + 1$, $n = 2l + 1$ and $r = \frac{c_h}{c_v}\cdot\frac{(2H)^2}{(2L)^2}$.

Relationship between average degree of consolidation and time factor

This section computes the relationship for the particular case as described by Equations 25 to 28.

The degree of consolidation for every layer, as given in Equation 3, when averaged over all layers in the case of 1-D consolidation with 2-D drainage, provides following expression as

$$U_{av} = 1-\frac{\frac{1}{4L\cdot H}\int_0^{2H}\int_0^{2L}u\,dx\,dz}{\frac{1}{4L\cdot H}\int_0^{2H}\int_0^{2L}u_i\,dx\,dz} \quad (32)$$

To compute the value of U_{av}, the initial pore pressure is integrated over the two directions as

$$\int_0^{2H}\int_0^{2L}u_i\,dx\,dz = 4u_0L\cdot H \quad (33)$$

Further, from Equation 28

$$\int_0^{2H}\int_0^{2L}u\,dx\,dz = \int_0^{2H}\int_0^{2L}\sum_{k=0}^{\infty}\sum_{l=0}^{\infty}\frac{16u_0}{mn\pi^2}\sin\frac{m\pi x}{2L}\sin\frac{n\pi x}{2H} \times\exp\left[-\left(c_h\frac{m^2\pi^2}{4L^2}+c_v\frac{n^2\pi^2}{4H^2}\right)t\right]dx\,dz \quad (34)$$

where $m = 2k + 1$, $n = 2l + 1$. The double integral above is evaluated to give

$$\int_0^{2H}\int_0^{2L}u\,dx\,dz = L\cdot H\sum_{k=0}^{\infty}\sum_{l=0}^{\infty}\frac{256u_0}{(mn\pi^2)^2} \times\exp\left[-\left(c_h\frac{m^2\pi^2}{4L^2}+c_v\frac{n^2\pi^2}{4H^2}\right)t\right] \quad (35)$$

Finally, using the evaluated integrals from Equations 33 and 35 in Equation 32, the expression for the average degree of consolidation is expressed as

$$36.\quad U_{av} = 1 - \sum_{k=0}^{\infty}\sum_{l=0}^{\infty} \frac{64}{(mn\pi^2)^2} \exp\left[-\left(c_h \frac{m^2\pi^2}{4L^2} + c_v \frac{n^2\pi^2}{4H^2}\right)t\right]$$

where $m = 2k + 1$, $n = 2l + 1$.

Expressing in terms of T_v, as described in Equation 30, average degree of consolidation is expressed as

$$37.\quad U_{av} = 1 - \sum_{k=0}^{\infty}\sum_{l=0}^{\infty} \frac{64}{(mn\pi^2)^2} \exp\left[-T_v\left(r \cdot \frac{m^2\pi^2}{4} + \frac{n^2\pi^2}{4}\right)\right]$$

where $m = 2k + 1$, $n = 2l + 1$, $r = \frac{c_h}{c_v} \cdot \frac{(2H)^2}{(2L)^2}$.

Evolution of approximate expressions

It is evident that the relationship shown in Equation 37 involves two infinite steps of summation, and hence, a handy alternate relationship is required. Further, observation of test data reveals that the deformations in the post primary phase of consolidation are not necessarily poro-elastic. Hence, two sets of approximate relationship between U_{av} and T_v are proposed.

The following approximate equations may be used for the case of constant u_i with depth:

$$38.\quad U_{av} = 1 - \left(1 - \sqrt{\frac{4T_v}{\pi}}\right)\left(1 - \sqrt{\frac{4rT_v}{\pi}}\right) \text{ for } U_{av} < U_p$$

$$39.\quad T_v = T_f - \frac{T_{fs}}{r+1}\{\log(1 - U_{av}) + 2\varphi(r)\} \text{ for } U_{av} > U_p$$

Equation 38 represents a relation among the average degree of consolidation, time factor and non-dimensional ratio (r) as used in Equation 37. The non-dimensional ratio (r) introduces varied levels of convexities in the $U_{av} - T_v$ relationship. It emphatically establishes a gradual numerical departure by way of non-dimensional ratio (r) in $U_{av} - T_v$ relationship obtained so far in the works of Terzaghi (1925, 1943) and Scott (1963). Equation 39 has an initial intercept for time space evolution for post-primary consolidation. Ideally, the final value of time factor T_f is undefined, yet some terminal values derived from experimental observations of 1-D consolidation are more frequently used in practice. T_{fs} represents an empirical observation of time factor where post primary consolidation offsets primary consolidation. This transformation corresponds to a granular adjustment at particulate level when the proximity of the grains is promoted by lateral drainage and implies convergence influenced by material characteristics.

As Equation 39 draws meaning similar to consolidation theory as per Terzaghi (1925), $T_f = 1{\cdot}781$ and $T_{fs} = 0{\cdot}933$. In the present study, the terminal value of T_f is rounded off for simplicity to 1·782, whereas the terminal value of T_{fs} is acceded by trials among the values 0·930 to 0·860 respectively. The non-dimensional parameter $\varphi(r)$ is a function of the dimensionless ratio r. For limiting values of dimensionless ratio r, the non-dimensional parameter $\varphi(r)$ is a second-degree polynomial function of the form

$$40.\quad \varphi(r) = c'''r^2 + c''r^1 + c'r^0$$

The coefficients of Equation 40, namely, c''', c'' and c', take values in the present range of analysis as -3×10^{-6}, 0·9574 and 1·0497 respectivly. The variation of the non-dimensional parameter $\varphi(r)$ with the dimensionless ratio r is given in Table 2.

r	$\varphi(r)$	r	$\varphi(r)$	r	$\varphi(r)$
0·0	1·000	0·8	1·807	7·0	7·720
0·1	1·127	0·9	1·902	8·0	8·670
0·2	1·228	1·0	2·000	9·0	9·625
0·3	1·324	2·0	2·950	12·0	12·480
0·4	1·421	3·0	3·900	15·0	15·344
0·5	1·520	4·0	4·850	39·0	39·196
0·6	1·617	5·0	5·810	100·0	96·455
0·7	1·712	6·0	6·765	1000·0	955·455

Table 2. Variation of non-dimensional parameter $\varphi(r)$ with dimensionless ratio r

Results and discussion

In Equation 31, the authors have derived the expression for 1-D consolidation with 2-D drainage. The plot among U, x and z are shown in Figures 2(a) and 2(b). The plots have been drawn using Mathematica Wolfram (2013). An observation of the 3-D plot provides an understanding into the manner in which pore water pressure is dissipated at different time factors in the consolidating layer. The wavy lines appear in the plots because only a limited number of terms of the Fourier expansion have been used to evaluate the relationship. Using the code, the authors have also plotted the relationship between the average degrees of consolidation with respect to time factor according to Equation 37, in Figure 3.

In Equation 37, the dimensionless ratio (r) is equal to $\frac{c_h}{c_v} \cdot \frac{(2H)^2}{(2L)^2}$. If $r = 1$, the situation corresponds to isotropy, which further consists of geometric isotropy and consolidation isotropy defied by a shape factor (r_s) and a consolidation factor (r_c) respectively. Therefore, the dimensionless ratio ($r = r_s * r_s$) is resolved into a function of the shape (a shape factor, $r_s = \frac{(2H)^2}{(2L)^2}$) and a consolidation ratio r_c, depending on the ratio of coefficient of consolidation of gouge in the horizontal and vertical directions such that $r_c = \frac{c_h}{c_v}$. The consolidation ratio r_c is equivalent to the scalar product of

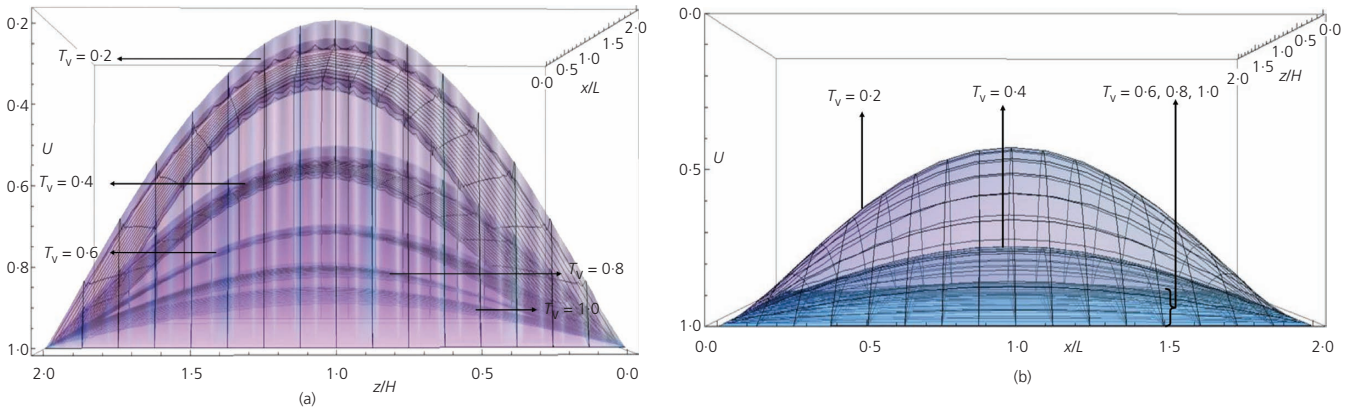

Figure 2. (a) Variation of U, x/L and z/H for $r = 0$, i.e., the case of one-dimensional consolidation, showing plots for five different values of T_v (T_v = 0·2, 0·4, 0·6, 0·8, 1·0); (b) variation of U, x/L and z/H for $r = 1$, showing plots for five different values of T_v (T_v = 0·2, 0·4, 0·6, 0·8, 1·0)

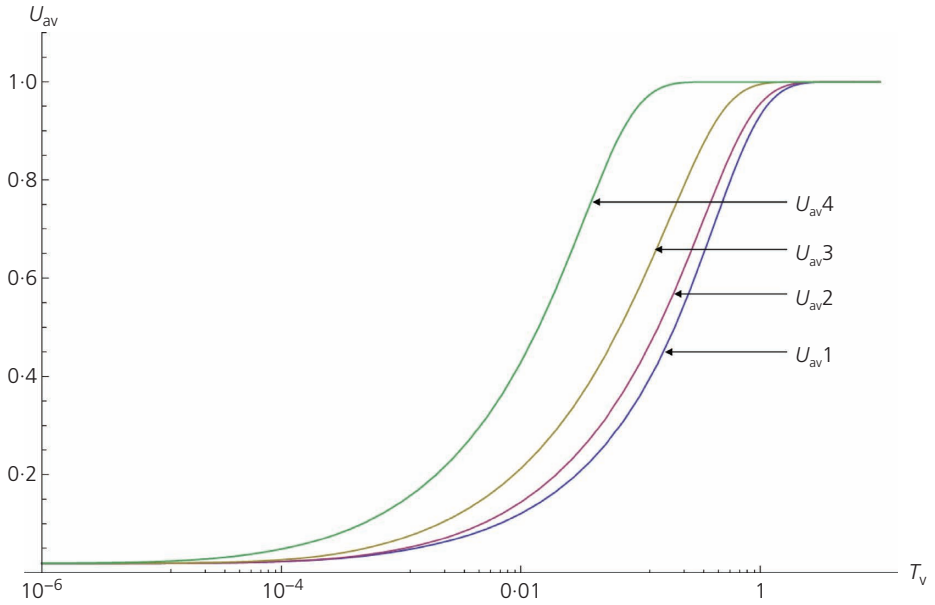

Figure 3. Variation of U_{av} and T_v for different values of r as $U_{av}1(T_v)$, $U_{av}2(T_v)$, $U_{av}3(T_v)$ and $U_{av}4(T_v)$, refer to r = 0, 0·1, 1, 10, respectively

modulus ratio and intrinsic permeability ratio $\left(E_{hv}\frac{k_{uc}}{k_{rm}}\right)$ under the same range of pressures. k_{rm} and k_{uc} are the intrinsic permeabilities of rock mass and that of clayey gouge respectively. The intrinsic permeability depends on the area of the fracture network and takes the dimensions of surface of contact (L^2T^0). The intrinsic permeability does not depend on the properties of pore fluid.

The deformation isotropy depends on the modulus ratio ($E_{hv} = E_h/E_v$), which is considered equal to unity for the case of isotropic deformation. The modulus ratio is defined as a ratio of deformation modulus of rock masses consisting of clay gouge in the horizontal and vertical directions. The variance in the values of modulus ratio and intrinsic permeability brings tortuosity in the consolidating clayey gouge.

The value of modulus ratio and intrinsic permeability can be readily estimated from rock mass investigations (Hsu *et al.*, 2011; Jiang *et al.*, 2009; Klimczak *et al.*, 2010; Liu *et al.*, 1999) and characterisation. The rock masses are typically characterised to

obtain modulus using rock quality designation (RQD). The RQD is empirically related to the joint condition and gouge thickness (Trivedi, 2013).

The typical values of effective porosity, intrinsic permeability of intact rocks, rock masses, gouge materials and consolidation anisotropy (O'Kelly, 2005) of clays are given in Tables 3, 4, 5 and 6 respectively for ready reference. Therefore, selectively the value of r is picked up in a practical range as $r = 0$ to 10. For higher values of $r \geq 10$, the dissipation pattern is free draining. The variation of average degree of consolidation with time factor is shown in Figure 3, where $U_{av}1(T_v)$, $U_{av}2(T_v)$, $U_{av}3(T_v)$ and $U_{av}4(T_v)$, refer to the function U_{av}, for $r = 0$, 0·1, 1, 10 respectively.

In situ profile	Effective porosity[a]: %	Physical effects
Unconsolidated clays, silt, sand and gravel	Up to 25	Pervious
Consolidated clastic rocks	5–15	Semi-pervious
Hard massive rocks	1–2	Impervious

[a] Interpreted from Franciss (2010).

Table 3. Effective porosity of massive rocks and gouge

Relationship with Terzaghi's expression for 1-D consolidation

Terzaghi's equation for 1-D consolidation gives this expression for U_{av} and T_v:

$$U_{av} = 1 - \sum_{k=0}^{\infty} \frac{8}{m^2\pi^2} \exp\left[-T_v \frac{n^2\pi^2}{4}\right] \quad 41.$$

where $m = 2k + 1$.

The expression proposed in Equation 37, albeit for 1-D consolidation with 2-D drainage, may be reduced to the case of 1-D consolidation with 1-D drainage by putting $r = 0$ (since $c_h = 0$ for this case). Equation 37 reduces to

$$U_{av} = 1 - \sum_{k=0}^{\infty} \sum_{l=0}^{\infty} \frac{64}{(mn\pi^2)^2} \exp\left[-T_v \frac{n^2\pi^2}{4}\right] \quad 42.$$

Although Equations 41 and 42 appear different, the plots for the degree of consolidation against time factor for both equations were

In situ profile	Intrinsic permeability[a]: mm^2	Physical effects	Range of intrinsic permeability ratio[b]
Highly fractured rock masses	10^{-1}–10^{-4}	Pervious	10^{-3}–10^{3}
Oil reservoir rocks	10^{-5}–10^{-7}	Semi-pervious	10^{-2}–10^{2}
Fresh sand stone	10^{-8}–10^{-9}	Semi-pervious	10^{-1}–10^{1}
Fresh lime stone, dolomite	10^{-10}–10^{-11}	Impervious	10^{-1}–10^{1}
Un-weathered rock mass, fresh granite	10^{-12}–10^{-13}	Impervious	10^{-1}–10^{1}

[a] Interpreted from Bear (1972).
[b] Ratio used for consideration of numerical inputs in the present study.

Table 4. Intrinsic permeability of rock masses (k_{rm})

In situ profile	Intrinsic permeability[a]: mm^2	Physical effects	r[b]
Peat	10^{-5}–10^{-6}	Semi-pervious	0·1–10
Layered clay	10^{-7}–10^{-9}	Semi-pervious	0·1–10
Un-weathered clay	10^{-10}–10^{-13}	Impervious	0·01–10

[a] Interpreted from Bear (1972).
[b] Ratio used for numerical inputs in the present study.

Table 5. Intrinsic permeability of unconsolidated organic soils and clays (k_{uc})

In situ profile	Permeability ratio	Physical effects	r[a]
Organic silt with peat	1·2 to 1·7[b]	Semi-pervious	1–2
Boston blue clay	0·7 to 3·3[c]	Semi-pervious	0·1–5
Singapore marine clay	2·0 to 3·0[d]	Semi-pervious	1–5

[a] Representative range for numerical input in the present study.
[b] Tsien (1955).
[c] Haley and Aldrich (1969).
[d] Chu *et al*. (2002).

Table 6. Horizontal and vertical permeability ratio

found to be nearly coinciding beyond 10% of consolidation, as shown in Figure 4, drawn using Mathematica, but, in fact, they originate differently. Therefore, the expression derived in Equation 37 has a solution extendible as 1-D consolidation. The present solution appears close to Terzaghi's solution, as shown in Figure 4.

Convergence of 1-D consolidation with 2-D drainage and 1-D drainage

Using $r = 0$ in Equations 38 and 39

$$43.\quad \text{For } U_{av} < U_p,\ U_{av} = 1 - \left(1 - \sqrt{\frac{4T_v}{\pi}}\right) = \sqrt{\frac{4T_v}{\pi}} \Rightarrow T_v = \frac{\pi}{4}U^2$$

According to Terzaghi (1925), for 1-D consolidation, $U_p = 0{\cdot}526$.

Also

$$44.\quad \text{For } U_{av} > U_p,\ T_v = T_f - T_{fs}\{\log(1-U) + 2\}$$

According to Terzaghi (1925), for 1-D consolidation, $T_f = 1{\cdot}781$ and $T_{fs} = 0{\cdot}933$.

T_f and T_{fs} are limiting values of time factor corresponding to $U_{av} = 1$ and degree of consolidation in the range of post primary consolidation (Tables 7 and 8). Equations 43 and 44 are similar to the approximate relations proposed by Terzaghi for 1-D consolidation.

Figures 5(a) and 5(b) show the convexity in time factor due to the effect of $r = 0$ and $0{\cdot}1$, respectively. The effect of 2-D drainage indicates convergence with the plot of primary consolidation with the post primary effect at U_{av} as early as 30% and 2% for $r = 0$ (for $T_{fs} = 0{\cdot}880$) and $r = 0{\cdot}1$ (for $T_{fs} = 0{\cdot}86$), respectively.

Application of 1-D consolidation with 2-D drainage for the special case for rock masses, $r = 1$

Using $r = 1$ in Equations 38 and 39

$$45.\quad \left(1 - \sqrt{\frac{4T_v}{\pi}}\right)\left(1 - \sqrt{\frac{4T_v}{\pi}}\right) = 1 - U \text{ for } U_{av} < U_p$$

$$46.\quad T_v = T_f - T'_{fs}\{\log(1-U) + 4\} \text{ for } U_{av} > U_p$$

Equation 45 is similar to the results proposed by Scott (1963) for 1-D consolidation and 2-D drainage. Incidentally, it corresponds to the solutions proposed by the present study for $r = 1$. Additionally, Equation 46 provides a solution for the time factor in the post primary phase of consolidation settlements with $T'_{fs} = \frac{T_{fs}}{r+1} = 0{\cdot}4665$.

Equations 45 and 46 show the relation of time factor and average degree of consolidation for the 2-D drainage case at $r = 1$. There can be varied applications of Equation 37 in petroleum engineering,

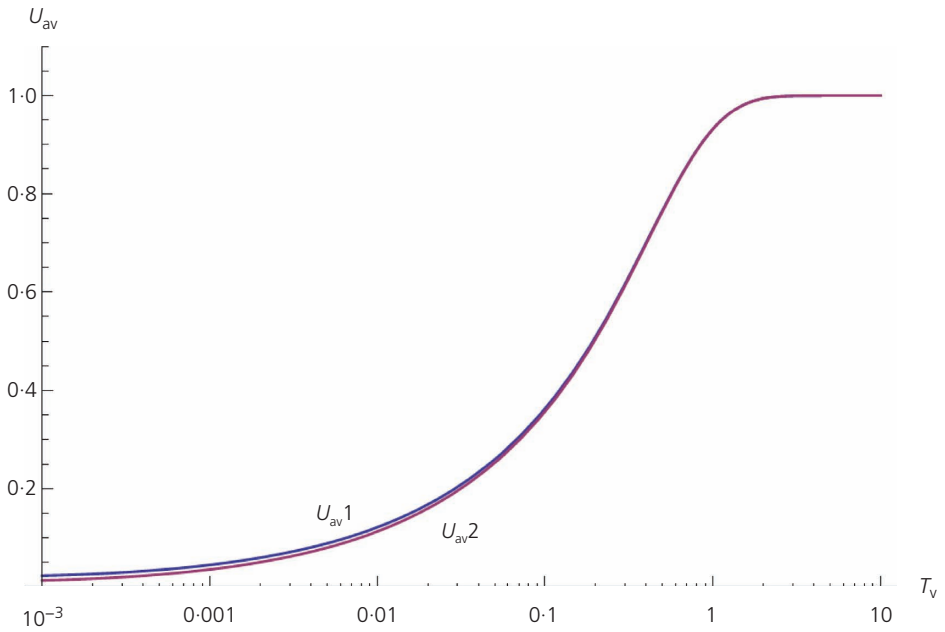

Figure 4. Plot for degree of consolidation U_{av} and time factor T_v for $r = 0$ ($U_{av}1$ from Equation 41 for 1-D consolidation nearly superimposes over $U_{av}2$ from Equation 42, the plot for 1-D consolidation with 2-D drainage)

r	U_{av}
0[a,b]	$1-\left(1-\sqrt{\frac{4T_v}{\pi}}\right)$
0·1[a]	$1-\left(1-\sqrt{\frac{4T_v}{\pi}}\right)\left(1-\sqrt{\frac{0{\cdot}4T_v}{\pi}}\right)$
1[a,c]	$1-\left(1-\sqrt{\frac{4T_v}{\pi}}\right)^2$
10[a]	$1-\left(1-\sqrt{\frac{4T_v}{\pi}}\right)\left(1-\sqrt{\frac{40T_v}{\pi}}\right)$

[a] Present work.
[b] Terzaghi (1925) for 1-D drainage $U_{av}=1-\left(1-\sqrt{\frac{4T_v}{\pi}}\right)$.

[c] Scott (1963) for 2-D drainage $U_{av}=1-\left(1-\sqrt{\frac{4T_v}{\pi}}\right)^2$.

Table 7. Variation of degree of consolidation of clayey gouge ($U_{av} < U_p$) amid rock masses with variation of time factor and dimensionless ratio (r)

r	T'_{fs}	T_{fs}	T_v
0·0[a, b]	0·9330[a], 0·8800[b]	0·840–0·930	$T_f-T'_{fs}\{\log(1-U)+2\}$[a, b]
0·1[b]	0·8481	0·860–0·940	$T_f-T'_{fs}\{\log(1-U)+2{\cdot}254\}$[b]
1·0[b]	0·4665	0·890–0·950	$T_f-T'_{fs}\{\log(1-U)+4\}$[b]
10·0[b]	0·0848	0·923–0·960	$T_f-T'_{fs}\{\log(1-U)+21{\cdot}246\}$[b]

[a] Terzaghi (1925), T_f = 1·781 for 1-D consolidation with 1-D drainage.
[b] Representative expressions in the present study, for 1-D consolidation with 2-D drainage.

Table 8. Approximation of time factor for post primary consolidation of clayey gouge ($U_{av} > U_p$) amid rock masses with variation of dimensionless ratio r using Equation 46

soil and rock mechanics, with a few typical examples shown in Equations 38 to 46. Tables 7 and 8 show the relationship between time factor and dimensionless ratio (r) for the degree of consolidation of clayey gouge using 1-D consolidation 2-D drainage equation. The dimensionless ratio (r) is a function of the shape of saturated clay lamina, deformation modulus of mass material and intrinsic permeability ratio.

Figures 5(c) and 5(d) show the convexity in time factor due to the effect of using r = 1 and 10, respectively. The effect of 2-D drainage indicates convergence with the plot of primary consolidation with the post primary effect at U_{av} as early as less than 1% for r = 1 (T_{fs} among 0·90 and 0·88) and 10 (T_{fs} among 0·924 and 0·923), respectively.

The effect of the variation of dimensionless ratio (r) relative to the rock mass characteristics is shown in Table 9.

Steps for implementation of present technique to obtain the time factor

The steps followed to find out the consolidation of clayey gouge amid rock mass using 1-D consolidation 2-D drainage equation are the following:

- Prepare the bore log sheet containing important information, namely, area and depth of sampling at requisite interval, unit weight, overburden pressure, number of joints, orientation of joints, maximum, minimum and mean thickness of gouge, void ratio of gouge, water table and *RQD*.
- Assign values of thickness and spread of gouge material ($2H_z$ and $2L_x$, respectively) to obtain the shape factor. It should be larger than the asperity height ($2t_a$) such that ($H_z/t_a > 1$ and $L_x/t_a > 1$) while $L_y >> L_x$.
- Evaluate the overburden, confining pressure and consider modulus ratio E_{hv} according to the values of *RQD*, number of joints, joint inclination, gouge spread and thickness and asperity height.
- Evaluate the intrinsic permeability ratio for clay gouge and rock material.
- According to the values of $2H_z$ and $2L_x$ respectively, find out the final value of dimension less ratio (r) from the shape factor, modulus ratio, E_{hv} and intrinsic permeability ratio.
- Estimate values of non-dimensional parameter $\varphi(r)$ (use Equation 40) for an appropriate value of dimensionless ratio (r).
- Operate the dimensionless ratio (r) and non-dimensional parameter $\varphi(r)$ in Equations 38 and 39 to get the time factor corresponding to any degree of consolidation at any value of intermediate dimension less ratio (r) obtained from rock mass and gouge characteristics shown in Table 9.
- Using approximate analysis consequent to the value of non-dimensional parameter $\varphi(r)$, use the corresponding plots for the primary or post primary consolidation to obtain the time factor.

Comments on the applicability of the present study

The present study for the evaluation of consolidation of clayey gouge amid rock masses should be applied to the field conditions carefully owing to the following reasons:

- This study neither intends to make any comment on the merits of either 1-D, 2-D or 3-D consolidation nor provides any resolve to the extent of elastic, plastic or elasto-plastic deformation during the process of consolidation. It has no scope to offer any resolve to time impending discussions on the scientific relevance of the proposed solutions by either Terzaghi's or Biot's or any other great work. Rather, it provides a simple numerical tool to estimate consolidation settlement with frequently encountered 2-D drainage condition for gouge amid permeating rock masses from rock mass characteristic and drainage features.

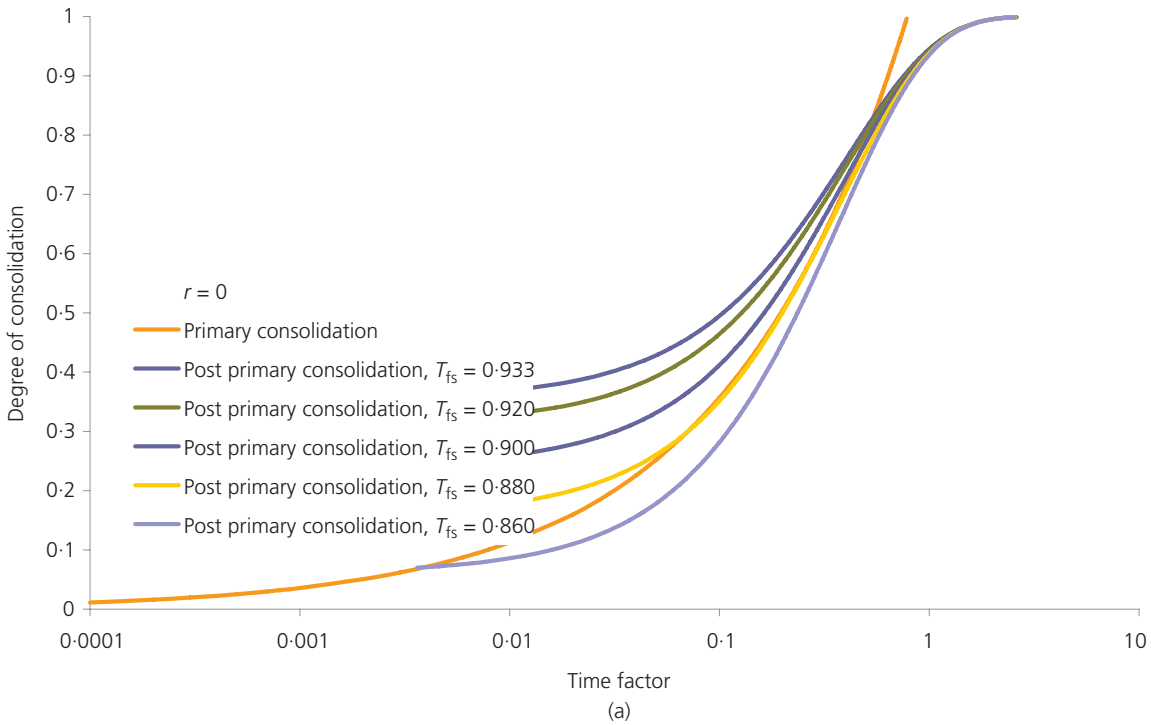

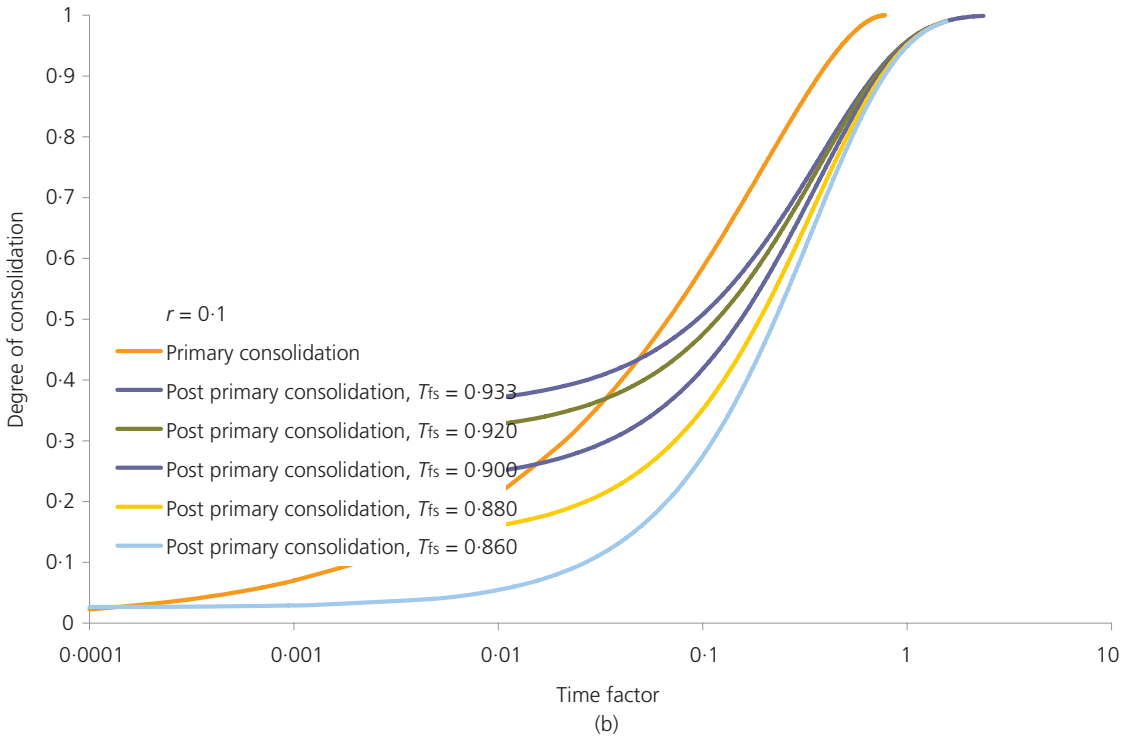

Figure 5. (a) Convexities in time factor due to primary and post primary consolidation at $r = 0$; (b) convexities in time factor due to primary and post primary consolidation at $r = 0{\cdot}1$; (c) convexities in time factor due to primary and post primary consolidation at $r = 1$; (d) convexities in time factor due to primary and post primary consolidation at $r = 10$ (continued overleaf)

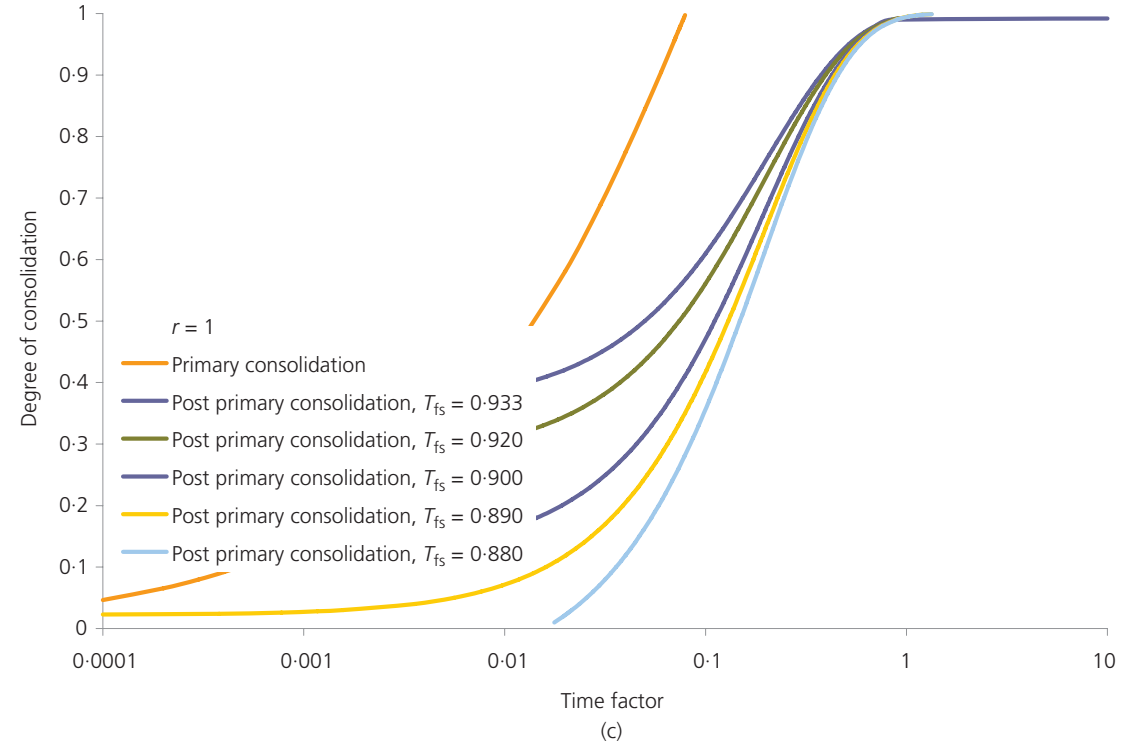

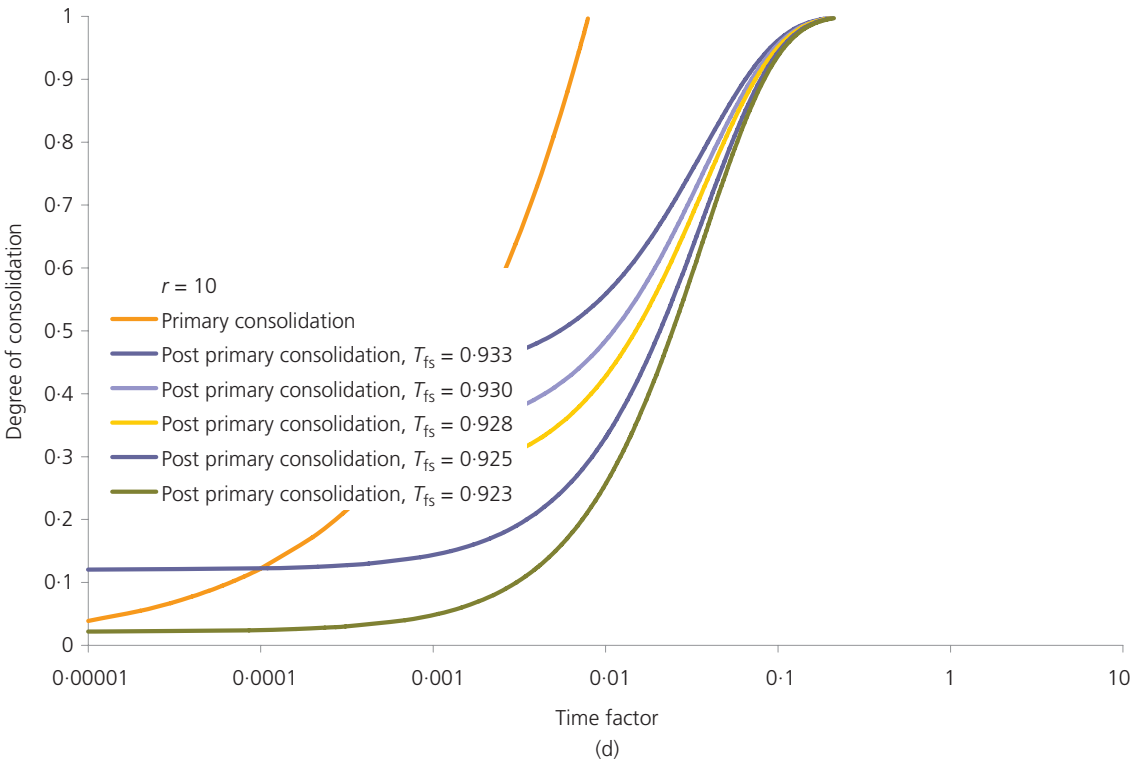

Figure 5. (continued)

r	Rock mass characteristic parameters		
	Shape of clay lamina	Deformation modulus	Intrinsic permeability
$r << 1$	Disturbed geometric isotropy. Thickness of gouge layer is significantly lower compared to the lateral spread, i.e., $2H_z << 2L_x$, and $2L_x << 2L_y$.	Anisotropy in deformation modulus may exist as $E_v >> E_h$ for 2-D consolidation. For 1-D consolidation and 2-D drainage, $E_v = E_h$.	Hydraulic anisotropy possible, intrinsic permeability of adjoining rock mass and intrinsic permeability of gouge material may be such that $K_V >> K_H$.
	$C_v/H_z^2 > C_h/L_x^2$		
$r = 1$	Geometric isotropy for a self-limiting, spherically consolidating element with permeable boundary may exist. Thickness of gouge layer is comparable to the lateral spreads, i.e., $2H_z = 2L_x$, and $2L_x = 2L_y$.	Possible initial isotropy in deformation modulus. The horizontal and vertical deformation modulus may be such that $E_v = E_h$.	Hydraulic isotropy possible, intrinsic permeability of clay gouge nearly equal to that of adjoining rock mass.
	$C_v/H_z^2 = C_h/L_x^2$		
$r >> 1$	Disturbed geometric isotropy. Thickness of gouge layer is significantly higher compared to the lateral spread, i.e., $2H_z >> 2L_x$, and $2L_x << 2L_y$.	Anisotropy in deformation modulus may exist as $E_v << E_h$ for 2-D consolidation. For 1-D consolidation and 2-D drainage, $E_v = E_h$.	Hydraulic anisotropy possible, intrinsic permeability of adjoining rock mass and intrinsic permeability of gouge material may be such that $K_V << K_H$.
	$C_v/H_z^2 < C_h/L_x^2$		

Table 9. Rock mass characteristic parameters controlling consolidation of clayey gouge

- The main aim of this study is to propose a solution for the consolidation of gouge material amid rock masses based on three variable systems, namely, degree of consolidation, time factor and dimensionless ratio r, which is interpreted from rock mass characteristics. The dimensionless ratio r in itself has features of rock mass, gouge and contact characteristics.
- Taking a cue from Terzaghi's work, the consolidation settlement is divided into primary and post primary phases where the time factor may be evaluated using dimensionless ratio r and a non-dimensional parameter $\varphi(r)$ respectively, which are related to the rock mass, gouge and contact characteristics.
- The present study further considers the single horizontal gouge layer draining vertically through the rock mass and laterally through the vertical joints while the in situ gouge may be draining through the oriented joints and through a number of layers of uneven thickness. The presence of thick asperities may significantly undermine the actual thickness of gouge participating in the consolidation process.
- The lateral protrusion of the gouge material is assumed to be restricted by the lateral pressure exerted by the adjoining block; while in practice, such protrusion may happen, which may lead to additional settlements.
- The horizontal gouge layer may be draining vertically through open joints and laterally through the rock mass opposed to the assumption. In these circumstances, the non-dimensional parameter must be selected carefully.
- The non-dimensional parameter is assumed to remain constant throughout the consolidation process, which may not remain so in the actual case while the deformations are progressive and mutual adjustment of rock mass and gouge material leads to redistribution of pressure.
- The modulus ratio estimated from rock mass investigations needs to be considered on the scale of horizontal and vertical strength ratios, which may vary due to gouge thickness, and joint orientation.
- There may be significant variation in the estimate of intrinsic permeability ratio within the rock mass itself and extent of contact.
- The length of drainage path is considered a straight line in the direction of drainage in the orthogonal directions while in situ conditions may co-generate orthogonal equipotential and flow paths.

One or many situations as listed in the comments on the applicability of the present study frequently appear in the geo-mechanical environment. They may call for suitable adjustments in the numerical parameters proposed in this study or a separate numerical scheme.

Conclusions

Solutions to the partial differential equation for pore water pressure distribution and average degree of consolidation have been obtained for consolidation of saturated clayey gouge amid permeating rock masses. The clay lamina amid rock masses have an apparent similarity to 2-D drainage; therefore, a solution for the 1-D consolidation with 2-D drainage is obtained numerically using a dimensionless ratio (r) and a non-dimensional parameter $\varphi(r)$, depending on shape factor, modulus and intrinsic permeability ratio. An expression for the time factor with average degree of consolidation in 1-D and 2-D drainage cases has been shown to be a consistent numeric sub-set of the proposed solutions in relation to the newly proposed dimensionless ratio (r) and non-dimensional parameter $\varphi(r)$. It is shown that with higher values of dimensionless ratio (r), the dominance of primary consolidation becomes apparent. The increasing values of dimension less ratio (r) are essentially associated with decreasing time factor and hence reduced time taken for completion of primary consolidation as captured numerically by the present study.

Acknowledgements

The authors sincerely compliment the reviewers, assessors and editors for their savant inputs, comments and questions, which improved the presentation of this paper. The authors thankfully acknowledge the support of Delhi Technological University in conducting this study.

REFERENCES

Ai ZY and Cheng ZY (2009) Transfer matrix solutions to plane-strain and three-dimensional Biot's consolidation of multi-layered soils. *Mechanics of Materials* **41(3)**: 244–251.

Ai ZY and Han J (2006) A solution to plane strain consolidation of multi-layered soils. Soil and Rock Behavior and Modeling, ASCE Geotech. Sp. Pub., *Proceedings of the Geo-Shanghai International Conference, Shanghai, China*, June 6–8, pp. 276–283.

Ai Z and Wu C (2009) Plane strain consolidation of soil layer with anisotropic permeability. *Applied Mathematics and Mechanics* **30(11)**: 1437–1444.

Al-Tabbaa A and Wood DM (1991) Horizontal drainage during consolidation: insights gained from analyses of a simple problem. *Geotechnique* **41(4)**: 571–585.

Bear J (1972) *Dynamics of Fluids in Porous Media.* Dover, ISBN 0-486-65675-6.

Biot M (1941) General theory of three-dimensional consolidation. *Journal of Applied Physics* **12(2)**: 155–164.

Carslaw HS and Jaeger JJC (1986) *Conduction of Heat in Solids*. Clarendo Press, Oxford, UK.

Christian JT and Boehmer JW (1970) Plane strain consolidation by finite elements. *Journal of the Soil Mechanics and Foundations Division, ASCE* **96**: 1435–1457.

Chu J, Bo MW, Chang MF and Choa V (2002) Consolidation and permeability properties of Singapore marine clay. *Journal of Geotechnical and Geoenvironmental Engineering, ASCE* **128(9)**: 724–732.

Das BM (2008) *Advanced Soil Mechanics*. Routledge, Oxford, UK.

De Josselin de Jong G and Verruijt A (1965) Primary and secondary consolidation of a spherical clay sample. *Proceedings of the 6th International Conference on Soil Mechanics and Foundations Engineering*, Montreal Vol. 1, pp. 254–258.

Di Francesco R (2011) Exact solutions of two-dimensional and tri-dimensional consolidation equations. *Physics.Geo.Ph arXiv:1103.6084*, **(1)**: 1–8.

Franciss FO (2010). *Fractured Rock Hydraulics.* CRC Press, London.

Gibson RE, England GL and Hussey MJL (1967) The theory of one dimensional consolidation of saturated clays. *Geotechnique* **17**: 261–273.

Gibson RE, Schiffman RL and Pu SL (1970) Plane strain and axially symmetric consolidation of a clay layer on a smooth impervious base. *Quarterly Journal of Mechanics and Applied Mathematics* **23**: 505–520.

Haley X and Aldrich X (1969) Engineering properties of foundation soils at Long Creek-Fore River areas and Black Cove. *Report to Maine State Highway Company*. Report no. 1.

Hansbo S (1981) Consolidation of fine-grained soils by prefabricated drains. *Proceedings of the 10th International Conference on Soil Mechanics and Foundations Engineering* (Balkema AA (ed)). Publications Committee of ICSMFE, Rotterdam, The Netherlands, pp. 677–682.

Hsu S, Lo H, Chi S and Ku C (2011) Rock mass hydraulic conductivity estimated by two empirical models. *Developments in Hydraulic Conductivity Research* (Dikinya O (ed)). InTech Europe, pp. 1–27.

Huang W, Fityus S and Bishop D (2006) Finite-element parametric study of the consolidation behavior of a trial embankment on soft clay. *International Journal of Geomechanics, ASCE* **6(5)**: 328–341.

Indraratna B and Redana IW (1997) Plane-strain modelling of smear effects associated with vertical drains. *Journal of Geotechnical and Geoenvironmental Engineering, ASCE* **123(5)**: 474–478.

Jiang X-W, Wan L, Wang X-S, Wu X and Zhang X (2009) Estimation of rock mass deformation modulus using variations in transmissivity and RQD with depth. *International Journal of Rock Mechanics and Mining Sciences* **46(8)**: 1370–1377.

Klimczak C, Schultz RA, Parashar R and Reeves DM (2010) Cubic law with aperture-length correlation: implications for network scale fluid flow. *Hydrogeology Journal* **18(4)**: 851–862.

Lambe TW and Whitman RV (1969) *Soil Mechanics*. John Wiley & Sons, NY, USA.

Liu J, Elsworth D and Brady B (1999) Linking stress-dependent effective porosity and hydraulic conductivity fields to RMR. *International Journal of Rock Mechanics and Mining Sciences* **36**: 581–596.

McNamee J and Gibson RE (1960) Plane strain and axially symmetric problem of the consolidation of a semi-infinite clay stratum. *Quarterly Journal of Mechanics and Applied Mathematics* **13**: 210–227.

O'Kelly BC (2005) Consolidation anisotropy of some natural soft soils. *Proceedings of the International Conference on Problematic Soils, Cyprus*, Vol. 3, pp. 1183–1192.

Schofield A and Wroth P (1968). *Critical State Soil Mechanics.* McGraw Hill, London.

Scott RF (1963). *Principles of Soil Mechanics*. Addison-Wesley, London.

Sukumar T, Jain A, Kumar A and Banik T (2013) *Evaluation of settlement in 2-D consolidation*. BE-Major Project, Department of Civil Engineering, University of Delhi, New Delhi, India.

Terzaghi K (1925) *Erdbaumechanik auf Bodenphysikalischer Grundlage*. F. Deuticke, Vienna.

Terzaghi K (1943) *Theoretical Soil Mechanics*. John Wiley & Sons, NY, USA.

Tewatia S, Bose P and Sridharan A (2013) Fastest rapid loading methods of vertical and radial consolidations. *International Journal of Geomechanics, ASCE* **13(4)**: 332–339.

Trivedi A (2010) Strength and dilatancy of jointed rocks with granular fill. *Acta Geotechnica* **5(1)**: 15–31.

Trivedi A (2013) Estimating in situ deformation of rock masses using a hardening parameter and RQD. *International Journal of Geomechanics, ASCE* **13(4)**: 348–364.

Tsien SI (1955) Stability of marsh deposits. *Highway Research Bulletin* **15**: 15–43.

Wolfram S (2013) *The Mathematica Book*, Version 9. Cambridge University Press, Cambridge, UK.

Wood DM (2004) *Geotechnical Modelling.* Spoon Press, London.

Zhang L (2010) Method for estimating the deformability of heavily jointed rock masses. *Journal of Geotechnical and Geoenvironmental Engineering, ASCE* **136(9)**: 1242–1250.

Zwanenburg C (2005) *The influence of anisotropy on the consolidation behaviour of peat*. PhD thesis, Delft University of Technology, Delft University Press, Delft, the Netherlands.

WHAT DO YOU THINK?

To discuss this paper, please submit up to 500 words to the editor at journals@ice.org.uk. Your contribution will be forwarded to the author(s) for a reply and, if considered appropriate by the editorial panel, will be published as a discussion in a future issue of the journal.

Author's Accepted Manuscript

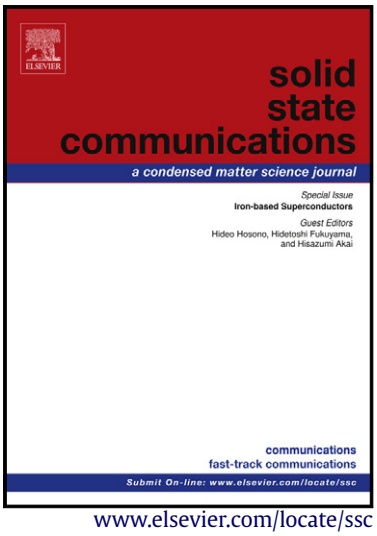

www.elsevier.com/locate/ssc

Crystal structure and mechanical properties of spark plasma sintered Cu_2Se: An efficient photovoltaic and thermoelectric material

Kriti Tyagi, Bhasker Gahtori, Sivaiah Bathula, M. Jayasimhadri, Sakshi Sharma, Niraj Kumar Singh, D. Haranath, A.K. Srivastava, Ajay Dhar

PII: S0038-1098(15)00047-2
DOI: http://dx.doi.org/10.1016/j.ssc.2015.02.004
Reference: SSC12618

To appear in: *Solid State Communications*

Received date: 13 December 2014
Revised date: 23 December 2014
Accepted date: 5 February 2015

Cite this article as: Kriti Tyagi, Bhasker Gahtori, Sivaiah Bathula, M. Jayasimhadri, Sakshi Sharma, Niraj Kumar Singh, D. Haranath, A.K. Srivastava, Ajay Dhar, Crystal structure and mechanical properties of spark plasma sintered Cu_2Se: An efficient photovoltaic and thermoelectric material, *Solid State Communications,* http://dx.doi.org/10.1016/j.ssc.2015.02.004

This is a PDF file of an unedited manuscript that has been accepted for publication. As a service to our customers we are providing this early version of the manuscript. The manuscript will undergo copyediting, typesetting, and review of the resulting galley proof before it is published in its final citable form. Please note that during the production process errors may be discovered which could affect the content, and all legal disclaimers that apply to the journal pertain.

ACCEPTED MANUSCRIPT

Crystal structure and mechanical properties of spark plasma sintered Cu_2Se: An efficient photovoltaic and thermoelectric material

Kriti Tyagi,[a] Bhasker Gahtori,[a] Sivaiah Bathula,[a,b] M. Jayasimhadri,[b] Sakshi Sharma,[a] Niraj Kumar Singh,[a] D. Haranath,[a] A. K. Srivastava,[a] Ajay Dhar[a,1]

[a]*CSIR-Network of Institutes for Solar Energy, CSIR-National Physical Laboratory, Dr. K. S. Krishnan Road, New Delhi 110012, India*
[b]*Department of Applied Physics, Delhi Technological University, Delhi, India*

Abstract

Copper Selenide (Cu_2Se) based materials are currently being investigated globally for efficient photovoltaic and thermoelectric (TE) device applications. Despite having enormous device potential its crystal structure and mechanical properties is still not fully explored owing to its complex behavior. Stereographic projection is one of such useful tool to estimate the crystallography of the material conclusively. In the current study, the crystal structure of α and β-phases of Cu_2Se was determined by its stereographic projections in reciprocal space. Further, mechanical properties of Cu_2Se are highly important to avoid catastrophic failure and ensure longevity of the TE devices made out of these materials. Cu_2Se exhibited the compressive strength of ~45 MPa with ~3% of plastic strain and a fracture toughness value of ~2±0.02 MPa√m, the latter being significantly higher than that of the other known TE materials. Finally, thermal shock resistance, which is one of the crucial parameters for the stability and longevity of the device applications, was calculated to be ~281±12 Wm^{-1}. Superior mechanical properties coupled with highly reported thermoelectric behavior makes Cu_2Se as a potential candidate for green energy generation.

Accepted manuscript

Keywords: A. Semiconductor, C. Scanning and transmission electron microscopy, D. mechanical properties, D. Phase transitions, D. Crystal and ligand fields

[1]Corresponding author email: adhar@nplindia.org
Tel.: +91 11 4560 9455/9456; Fax: +91 11 4560 9310

ACCEPTED MANUSCRIPT

Crystal structure and mechanical properties of spark plasma sintered Cu_2Se: An efficient photovoltaic and thermoelectric material

Kriti Tyagi,[a] Bhasker Gahtori,[a] Sivaiah Bathula,[a,b] M. Jayasimhadri,[b] Sakshi Sharma,[a] Niraj Kumar Singh,[a] D. Haranath,[a] A. K. Srivastava,[a] Ajay Dhar[a,2]

[a]*CSIR-Network of Institutes for Solar Energy, CSIR-National Physical Laboratory, Dr. K. S. Krishnan Road, New Delhi 110012, India*
[b]*Department of Applied Physics, Delhi Technological University, Delhi, India*

Abstract

Copper Selenide (Cu_2Se) based materials are currently being investigated globally for efficient photovoltaic and thermoelectric (TE) device applications. Despite having enormous device potential its crystal structure and mechanical properties is still not fully explored owing to its complex behavior. Stereographic projection is one of such useful tool to estimate the crystallography of the material conclusively. In the current study, the crystal structure of α and β-phases of Cu_2Se was determined by its stereographic projections in reciprocal space. Further, mechanical properties of Cu_2Se are highly important to avoid catastrophic failure and ensure longevity of the TE devices made out of these materials. Cu_2Se exhibited the compressive strength of ~45 MPa with ~3% of plastic strain and a fracture toughness value of ~2±0.02 MPa√m, the latter being significantly higher than that of the other known TE materials. Finally, thermal shock resistance, which is one of the crucial parameters for the stability and longevity of the device applications, was calculated to be ~281±12 Wm^{-1}. Superior mechanical properties coupled with highly reported thermoelectric behavior makes Cu_2Se as a potential candidate for green energy generation.

Keywords: A. Semiconductor, C. Scanning and transmission electron microscopy, D. mechanical properties, D. Phase transitions, D. Crystal and ligand fields

[2]Corresponding author email: adhar@nplindia.org
Tel.: +91 11 4560 9455/9456; Fax: +91 11 4560 9310

Accepted manuscript

ACCEPTED MANUSCRIPT

1. Introduction

The development of promising power generation methods that are eco-friendly in nature require special attention to meet the global needs of large power usage [1]. The direct conversion of heat into electrical energy based on thermoelectric (TE) effect without moving parts in the device is an attractive alternative for power generation [2]. The performance of a thermoelectric device depends on its *figure-of-merit (ZT)*, a dimensionless quantity of the material defined as $ZT = (\alpha^2\sigma T/\kappa)$, where α, σ, T and κ are Seebeck coefficient, electrical conductivity, temperature and thermal conductivity, respectively. The optimization of ZT clearly demands high TE power and electrical conductivity but having low thermal conductivity values. It is known that these three physical quantities (α, σ and T) of materials are correlated in such a way that the optimization of one adversely affects the other. Among several other available TE materials, Cu_2Se has been designated as one of the most promising material for TE power generation, due to its high ZT value [2-8] in spite of its complex crystal structure. Further, it has been reported in literature that phase transition in Cu_2Se occurs from monoclinic (α) → cubic (β) at ~413 K [2, 9]. But, all the available literature on Cu_2Se unanimously confirms that the high temperature phase exists as β [3, 9, 10], while quandary still exists over the low temperature α-phase of Cu_2Se. Various groups[2, 3, 9] have already reported different crystal structures for Cu_2Se predicting that the low temperature phase is either monoclinic, orthorhombic or tetragonal at room temperature (~25°C). But still there are many debates unresolved over the crystal structure of Cu_2Se. Hence, there is a need to address the existence of α-phase in Cu_2Se at low temperature with suitable supporting characterization techniques. Moreover, in the β – phase of Cu_2Se, the surface migration of Cu ions as well as evaporation of elemental Se limits the precise control over the final composition.

Accepted manuscript

ACCEPTED MANUSCRIPT

Furthermore, it is desired to have complete crystallographic information of state-of-art TE materials prior to device fabrication to ensure that these materials are strong enough to operate in the temperature range 500 - 600 K useful for automobiles. Consequently, these materials have to withstand high internal thermal stresses created due to rapid temperature cycling gradients of two ends of the same TE element. Many of the existing TE materials are strong enough in thermoelectric performance, but poor at their mechanical strength. Hence, the mechanical facets of these TE materials are also to be addressed properly. Very few reports are available on mechanical properties of other state-of-the art TE materials, such as, n-type nanostructured SiGe alloys [11], Co_4Sb_{12} [12], $In_{0.1}Co_4Sb_{12}$ [12] and Bi_2Te_3+0.1vol% SiC [13]. But for Cu_2Se, there is no comprehensive study available in the literature either on stereographic microstructural interpretations of its crystal structure or mechanical properties. Therefore, in the current study, we report the crystal structure determination employing stereographic projections in reciprocal space for Cu_2Se with respect to temperature dependent $\alpha \rightarrow \beta$ phase transformations. The current study will surely be a guideline for other researchers in the photovoltaic and thermoelectric fields to interpret the crystallographic information for other novel TE materials. Additionally, mechanical properties, such as, fracture toughness; thermal shock resistance and compressive strength have also been investigated in the context of TE device fabrication.

Accepted manuscript

ACCEPTED MANUSCRIPT

2. Experimental Details

Cu_2Se samples were synthesized by thorough grinding of Copper (Cu, 99.99%, Alfa Aesar) and Selenium (Se, 99.99%, Alfa Aesar) powders in respective chemical stoichiometric ratio in a glove box, under a high-purity argon atmosphere and these powders were subsequently pelletized and vacuum-sealed (10^{-5} Torr) in quartz tubes. The sealed quartz ampoules were heat-treated at 1000°C for 24 hours, and then naturally cooled to room temperature. The powder samples of Cu_2Se were subsequently consolidated and sintered under vacuum (~ 4 Pa) using spark plasma sintering (SPS Syntex, 725) technique at identical optimized process parameters of pressure 60 MPa and temperature 600°C for 3 minutes (soaking time) at a heating rate of 400°C/minute using graphite die and punches. Mechanical properties such as fracture toughness measurements were carried out employing the indentation-crack technique using Vickers micro-hardness tester (FM-e7) with a load of 4.9 N for 10 s of indentation time. Also, compression tests at room temperature were performed as per ASTM standard (ASTM: E9-09) with an aspect ratio of ~2.5 under uniaxial loading with a strain rate of 2×10^{-5} s^{-1} (INSTRON 4204).

3. Results and Discussion

3.1. Crystal structure determination by stereographic projections

The microscopy results in conjunction with x-ray diffraction patterns clearly shown in Fig. 1(a&b). It is evident from the Fig.1(a) $\alpha \rightarrow \beta$ transition takes place as the system loses its monoclinic structure and begins to behave as cubic after ~ 413 K, which is supported by disappearance of (090) peak in the XRD pattern Fig.1(b). It has been reported in literature [3] that

Accepted manuscript

ACCEPTED MANUSCRIPT

α → β phase transition is reversible in Cu_2Se around 413 K. In the current study, we have observed that Cu_2Se has a structural metamorphosis at about 400 (±10) K. Moreover, it could be noted that, this is a reversible phase transformation. There are several reports on different crystal structures of Cu_2Se [9, 14, 15]. A review on literature pertaining to various crystalline phases delineates that presumably the composition and also the processing conditions influence the final crystal symmetry of the product. A few crystalline phases, including the current investigation, are summarized in *Table 1*. However, it is to be noted that there exists no evidence about the formation of different crystalline phases and their phase transformations. Hence, we have employed stereographic interpretations in reciprocal space to determine the structural transitions. With these stereographic projections, the α-phase (monoclinic) and β-phase (cubic) have been drawn to understand the important zone axes of two different crystal structures in reciprocal space. This methodology has been opted to give an idea of movement of atoms (crystallographic planes) during reversible transformation between α → β and vice versa in case of Cu_2Se. For this symmetry elements and lattice constants for α-phase (space group: C2/c, lattice constants: a = 7.14 Å, b = 12.39 Å, c = 27.33 Å, β = 94.40°) and β-phase (space group: $Fm\bar{3}m$, a = 5.787 Å) are recalled from the literature[15]. The stereographic projection along (010) for monoclinic (α-phase) crystal with space group C2/c has been displayed in Fig. 2. The stereogram shows the presence of important planes in the structure located with respect to the angular distances between the two planes. It is important to mention that a section of 45° (as marked with a white dotted line) is sufficient to exhibit the entire crystal symmetry of a given structure. Keeping this in view the repeatability of 45° section of the stereogram, a zone axes map has been plotted and the reciprocal space calculated diffraction patterns are appended with stereographic projection as

Accepted manuscript

ACCEPTED MANUSCRIPT

shown in Fig. 3. In a similar way stereographic projection along (010) for cubic (β-phase) crystal with space group $Fm\bar{3}m$ has been displayed in Fig. 4. Further, the stereogram of β-phase (lattice constants: a = 5.787 Å) has been calculated and plotted for a 45° section along 010 zone axis of face centred cubic lattice. Correspondingly the reciprocal space calculated diffraction patterns are appended with stereographic projection as shown in Fig. 5. The idea of putting the important diffraction patterns of both α and β- phases together to realize about the important planes that are probably involved in thermally reversible transformations during cyclic low to high between these crystalline structures. The structure of Cu_2Se makes a reversible phase transformation around 413 K. Based on the understanding of crystal structure employing stereographic interpretations and XRD experiments [2, 3], the final structure is classified in terms of the sub-lattice of selenium, for the reason that copper sub-lattice turns into a super-ionic state at high temperature. However, the structure of copper in the low temperature regime has ever been considered to be random [2, 3].

3.2 Mechanical Properties

3.2.1 Fracture toughness analysis

It is well known that, most of the research has been focused on thermal and electrical transport properties of Cu_2Se, primarily aimed towards enhancing their thermoelectric performance and efficiencies of state-of-art novel TE materials [1, 16-19]. However, their mechanical properties are equally important for the long term reliability of TE modules, as these materials are known to be brittle with low fracture toughness. Further, there is no comprehensive report available for the mechanical properties of this material, which is equally important, for the in-service application

Accepted manuscript

ACCEPTED MANUSCRIPT

of TE modules to avoid catastrophic failure. Hence, in the current study, we report some of the mechanical properties of Cu_2Se samples.

Fracture toughness (K_{IC}) of TE materials is often estimated using Vicker's indentation-Crack (VIF) technique as this method was outlined by Antis *et al.* [20] for brittle solids for radial mean crack systems, as described below:

$$K_{IC} = 0.016\left(\frac{E}{H}\right)^{1/2} \times \frac{P}{c^{3/2}} \quad (1)$$

where, P is the load in Newton's, a is the half-diagonal of Vicker's indentation mark in meters, E is Young's modulus in GPa [21] and H is Vickers hardness ~ 0.43 GPa. As sintered Cu_2Se samples exhibited near theoretical density and these samples were indented with a Vicker's diamond shaped indenter at a load of 4.9 N with a dwell time of 10 seconds, enough to generate cracks without any spill out of material, as shown in Fig. 6. Subsequently, the observed cracks were in radial mean type cracks as it was reported for other brittle solids [22]. Crack lengths were measured using field emission scanning electron microscope (FESEM) for estimating the fracture strength. The radial mean crack length (c) on the material surface has been measured to be ~46 μm after removal of indenter. The calculated fracture toughness of Cu_2Se alloy after spark plasma sintering (SPS) was found to be ~2.0±0.02 MPa√m by VIF method employing equation (1). It has been reported that low temperature (<500 K) operating applications of Bi_2Te_3+0.1vol% SiC exhibited a fracture toughness of 1.35 MPa√m [13]. Where as Co_4Sb_{12}, and $In_{0.1}Co_4Sb_{12}$ at high operating temperatures (>500 K) exhibited a fracture toughness of 0.82 ± 0.11, 0.46 ± 0.13 and 1 ± 0.02 MPa√m, respectively [12]. Recently, for nanostructured SiGe alloys a fracture toughness

Accepted manuscript

value of 1.6±0.05 MPa√m has been reported by our group [11]. However, these SiGe materials can be operated only at high (≥1173 K) temperature. In the current study, Cu_2Se sample finds applications in the temperature range of 500 - 600 K and most of the automobile exhaust systems fall in this category. Further from the literature, it is to be noted that the fine grain size in nanostructured alloys help to minimize the dislocation pile-up stresses resulting in improvement in fracture toughness [23, 24]. Moreover, nanostructured materials containing low crystallite size is expected to enhance the localized fracture processes [25], which generally occur during crack extension [26, 27]. On the other hand, the fine nanocrystallites in nanostructured materials would certainly enhance the fracture toughness [28] because during the steady state of crack initiation [29, 30], work done by an applied stress is considered to be dissipated as heat by specific rotational deformation, grain boundary sliding and diffusion process [28, 31, 32]. Hence, the fracture toughness of Cu_2Se could be improved by nanostructuring the Cu_2Se sample.

Accepted manuscript

3.2.2 Compressive strength analysis

Compressive strength test of as-sintered Cu_2Se (α-phase) has been conducted at room temperature (25ºC) under uniaxial compressive loading and a typical stress-strain curve is plotted as shown in Fig. 7. Further, it has been observed that compressive strength of the p-type Cu_2Se found to be 45 MPa with almost 3% of plastic strain, which is significantly higher than other reported values of nearly similar alloy composition [33]. Micro-hardness of the bulk Cu_2Se measured to be 0.43 GPa and these values are comparable with the existing state-of-the art materials, such as Bi_2Te_3 and PbTe, which have the hardness values of 0.62 and 0.23 GPa, respectively [34]. Also, it has been reported in literature that high temperature β-phase (cubic) of Cu_2Se shows the super plastic

ACCEPTED MANUSCRIPT

deformation behavior after α → β phase transition at 413 K, which in turn resulted a lower (0.0325 GPa) values of compressive strength [33]. However, higher compressive strength values associating with moderate ductility of the Cu_2Se assumes that this could be a reliable TE candidate material in the temperature range of 500–800 K, where as this material also possesses highest ZT among all the available polycrystalline bulk TE materials [3]. It is also to be noted that, strength and ductility of these alloys could also be improved further by nanostructuring approach, where dislocation pinning for slip movement and grain boundary strengthening result the enhancement of compressive strength [35-37].

3.2.3 Thermal shock resistance

Many of the novel TE materials are sensitive to thermal shock in-service TE devices applications [38-40]. Thermal shock resistance parameter can be defined as a sudden temperature change between hot and cold ends of the TE device legs that can lead to failure due to internal mechanical stress induced by temperature gradients [41-43]. Moreover, structural reliability of TE modules become important and should possess high thermal shock resistance in order to seize resistance to different kinds of thermal stresses under actual operating conditions [23, 44-46]. The thermal shock resistance parameter (R_T), is given by the expression [41],

$$R_T = \frac{\sigma(1-\nu)\kappa}{\alpha E} \tag{2}$$

where, ν is Poisson's ratio, κ is thermal conductivity and α is the coefficient of thermal expansion. The value of R_T for Cu_2Se has been calculated using equation (2) with experimentally determined values of σ = 0.045 GPa, κ=2.6 W/mK and α [2], ν [47] and E [21] from the literature. Thermal shock resistance of current Cu_2Se sample was found to be ~ 281±12 Wm^{-1}. This value a bit higher

Accepted manuscript

ACCEPTED MANUSCRIPT

than the other state-of-art TE materials such as, PbTe alloy, which exhibited a value of 140 Wm^{-1} [48]. This suggests that Cu_2Se sample prepared in the current study has a very high resistance to thermal shock without compromising their thermoelectric performance. Also, the high value of R_T is attributed to high compressive strength and thermal conductivities for Cu_2Se sample. In general, many of the known TE materials represent high ZT due to their low thermal conductivities [49-51]. But, for higher R_T, the materials should have high thermal conductivity to reduce sudden failure in practical applications. Hence, there is need to optimize these transport properties and R_T to get longer life periods for TE materials in device applications. Further, substantial improvement in R_T may be realized through better control and understanding of the microstructure at high temperatures. Also, temperature dependence of the mechanical properties of TE materials has to be evaluated thoroughly since these materials are highly prone to changes in their microstructure with change in temperature.

4. Conclusions

In summary, we have successfully demonstrated the crystal structure determination for both α and β-phases of spark plasma sintered Cu_2Se in reciprocal space by stereographic projections. Further, fracture toughness of Cu_2Se exhibited a value of ~2±0.02 MPa√m, which is significantly higher than that of other existing thermoelectric materials at similar operating temperature. Consequently, the compressive strength was found to be 45 MPa with ~3% of plastic strain. Moreover, thermal shock resistance of Cu_2Se was found to be ~281±12 Wm^{-1} and we take the credit of reporting for the first time for Cu_2Se system. Mechanical properties of Cu_2Se could be improved further by nanostructuring methodology. Superior mechanical properties coupled with

Accepted manuscript

ACCEPTED MANUSCRIPT

high photovoltaic and thermoelectric performances of Cu_2Se makes it as a potential candidate material for green energy generation.

Acknowledgments

This work was supported by CSIR-TAPSUN (CSIR-NWP 54) programme entitled *"Novel approaches for solar energy conversion under technologies and products for solar energy utilization through networking"*. The authors are grateful to the Director, Prof. R.C. Budhani, for his constant mentoring and support for this project. The technical support rendered by Mr. Radhey Shyam and Mr. Naval Kishor Upadhyay is also gratefully acknowledged.

Accepted manuscript

ACCEPTED MANUSCRIPT

References

[1] M. Martín-González, O. Caballero-Calero, P. Díaz-Chao, Renewable and Sustainable Energy Reviews, 24 (2013) 288-305.
[2] H. Liu, X. Shi, F. Xu, L. Zhang, W. Zhang, L. Chen, Q. Li, C. Uher, T. Day, G.J. Snyder, Nature materials, 11 (2012) 422-425.
[3] B. Yu, W. Liu, S. Chen, H. Wang, H. Wang, G. Chen, Z. Ren, Nano Energy, 1 (2012) 472-478.
[4] S. Ballikaya, H. Chi, J.R. Salvador, C. Uher, Journal of Materials Chemistry A, 1 (2013) 12478-12484.
[5] C. Wadia, A.P. Alivisatos, D.M. Kammen, Environmental Science & Technology, 43 (2009) 2072-2077.
[6] S. Deka, A. Genovese, Y. Zhang, K. Miszta, G. Bertoni, R. Krahne, C. Giannini, L. Manna, Journal of the American Chemical Society, 132 (2010) 8912-8914.
[7] Q. Guo, G.M. Ford, H.W. Hillhouse, R. Agrawal, Nano letters, 9 (2009) 3060-3065.
[8] D. Lu, B. Sang, Y. Deng, B.J. Stanbery, L. Eldada, in: Photovoltaic Specialists Conference (PVSC), 2010 35th IEEE, IEEE, 2010, pp. 000175-000178.
[9] L. Gulay, M. Daszkiewicz, O. Strok, A. Pietraszko, Chem. Mater. Alloy, 4 (2011) 200-205.
[10] H. Liu, X. Yuan, P. Lu, X. Shi, F. Xu, Y. He, Y. Tang, S. Bai, W. Zhang, L. Chen, Advanced Materials, 25 (2013) 6607-6612.
[11] S. Bathula, B. Gahtori, M. Jayasimhadri, S.K. Tripathy, K. Tyagi, A.K. Srivastava, A. Dhar, Applied Physics Letters, 105 (2014) -.
[12] J. Eilertsen, M. Subramanian, J. Kruzic, Journal of Alloys and Compounds, 552 (2013) 492-498.
[13] L.-D. Zhao, B.-P. Zhang, J.-F. Li, M. Zhou, W.-S. Liu, J. Liu, Journal of Alloys and Compounds, 455 (2008) 259-264.
[14] R.M. Murray, R.D. Heyding, Canadian Journal of Chemistry, 53 (1975) 878-887.
[15] O. Milat, Z. Vučić, B. Ruščić, Solid State Ionics, 23 (1987) 37-47.
[16] D.M. Rowe, CRC handbook of thermoelectrics, CRC press, 1995.
[17] A. Minnich, M. Dresselhaus, Z. Ren, G. Chen, Energy & Environmental Science, 2 (2009) 466-479.
[18] P.H. Ngan, D.V. Christensen, G.J. Snyder, L.T. Hung, S. Linderoth, N.V. Nong, N. Pryds, physica status solidi (a), 211 (2014) 9-17.
[19] A.P. Gonçalves, C. Godart, The European Physical Journal B, 87 (2014) 1-29.
[20] G. Anstis, P. Chantikul, B.R. Lawn, D. Marshall, Journal of the American Ceramic Society, 64 (1981) 533-538.
[21] O.L. Anderson, Journal of Physics and Chemistry of Solids, 24 (1963) 909-917.
[22] C.-M. Lin, C.-M. Chang, J.-H. Chen, W. Wu, Materials Science and Engineering: A, 527 (2010) 5038-5043.
[23] A. Kallel, G. Roux, C. Martin, Materials Science and Engineering: A, 564 (2013) 65-70.
[24] J.-F. Li, W.-S. Liu, L.-D. Zhao, M. Zhou, NPG Asia Materials, 2 (2010) 152-158.
[25] M. Ke, S. Hackney, W. Milligan, E. Aifantis, Nanostructured Materials, 5 (1995) 689-697.

Accepted manuscript

ACCEPTED MANUSCRIPT

[26] J.R. Sootsman, J. He, V.P. Dravid, S. Ballikaya, D. Vermeulen, C. Uher, M.G. Kanatzidis, Chemistry of Materials, 22 (2009) 869-875.
[27] T. Zhu, J. Li, Progress in Materials Science, 55 (2010) 710-757.
[28] E. Lavernia, B. Han, J. Schoenung, Materials Science and Engineering: A, 493 (2008) 207-214.
[29] Y. Wang, M. Chen, F. Zhou, E. Ma, Nature, 419 (2002) 912-915.
[30] K. Kumar, H. Van Swygenhoven, S. Suresh, Acta Materialia, 51 (2003) 5743-5774.
[31] D. Hasselman, Journal of the American Ceramic Society, 52 (1969) 600-604.
[32] L. Freund, J. Hutchinson, Journal of the Mechanics and Physics of Solids, 33 (1985) 169-191.
[33] M. Korzhuev, V. Bankina, I. Korolkova, G. Sheina, E. Obraztsova, physica status solidi (a), 123 (1991) 131-137.
[34] F. Ren, E. Case, E. Timm, H. Schock, Journal of Alloys and Compounds, 455 (2008) 340-345.
[35] J. Wang, I. Beyerlein, C. Tomé, International Journal of Plasticity, 56 (2014) 156-172.
[36] B. Murty, P. Shankar, B. Raj, B. Rath, J. Murday, Nanostructured Materials with High Application Potential, in: Textbook of Nanoscience and Nanotechnology, Springer, 2013, pp. 176-213.
[37] C.A. Handwerker, T.M. Pollock, JOM, 1-21.
[38] K. Masumoto, I. Nishida, in, Google Patents, 1986.
[39] X. Huang, Y. Miyazaki, T. Kajitani, Solid State Communications, 145 (2008) 132-136.
[40] M. Estili, W.-W. Wu, M. Khazaei, Y. Sakka, Science and Technology of Advanced Materials, 15 (2014) 014201.
[41] J.R. Salvador, J. Yang, A.A. Wereszczak, H. Wang, J.Y. Cho, Science of Advanced Materials, 3 (2011) 577-586.
[42] K. Bartholomé, B. Balke, D. Zuckermann, M. Köhne, M. Müller, K. Tarantik, J. König, Journal of Electronic Materials, 43 (2014) 1775-1781.
[43] F. Ren, H. Wang, P.A. Menchhofer, J.O. Kiggans, Applied Physics Letters, 103 (2013) 221907.
[44] J. Gladden, G. Li, R. Adebisi, S. Firdosy, T. Caillat, V. Ravi, Physical Review B, 82 (2010) 045209.
[45] V. Ravi, S. Firdosy, T. Caillat, E. Brandon, K. Van Der Walde, L. Maricic, A. Sayir, Journal of electronic materials, 38 (2009) 1433-1442.
[46] T.-J. Ha, M.-H. Hong, C.-S. Park, H.-H. Park, Sensors and Actuators B: Chemical, 181 (2013) 874-879.
[47] J.B. Goodenough, A. Hamnett, G. Huber, F. Hullinger, M. Leiß, S. Ramasesha, H. Werheit, Physics of Non-Tetrahedrally Bonded Binary Compounds III/Physik Der Nicht-tetraedrisch Gebundenen Binären Verbindungen III, Springer, 1984.
[48] J. Salvador, J. Yang, X. Shi, H. Wang, A. Wereszczak, H. Kong, C. Uher, Philosophical Magazine, 89 (2009) 1517-1534.
[49] L.-D. Zhao, S.-H. Lo, Y. Zhang, H. Sun, G. Tan, C. Uher, C. Wolverton, V.P. Dravid, M.G. Kanatzidis, Nature, 508 (2014) 373-377.
[50] G. JeffreyáSnyder, Journal of Materials Chemistry A, 2 (2014) 3169-3174.
[51] H. Alam, S. Ramakrishna, Nano Energy, 2 (2013) 190-212.

Accepted manuscript

ACCEPTED MANUSCRIPT

Figure captions

Figure 1: X-ray diffraction pattern for (a) low temperature monoclinic (α) phase and (b) high temperature cubic (β) phase.

Figure 2: Stereographic projection along 010 for a monoclinic crystal with space group C2/c.

Figure 3: Reciprocal space along different UVW for a monoclinic crystal structure.

Figure 4: Stereographic projection along 010 for a face centred cubic crystal structure with space group $Fm\bar{3}m$.

Figure 5: Reciprocal space along different UVW for a face centred cubic crystal structure.

Figure 6: SEM image of Vicker's-indentation cracks developed at a load of 4.9 N (a) c, the radial-median crack length on the material surface after indenter removal.

Figure 7: Stress - Strain curve of bulk p-type Cu_2Se tested under uniaxial compression mode with a strain rate of 2×10^{-5} s^{-1}.

Accepted manuscript

Figure-1

ACCEPTED MANUSCRIPT

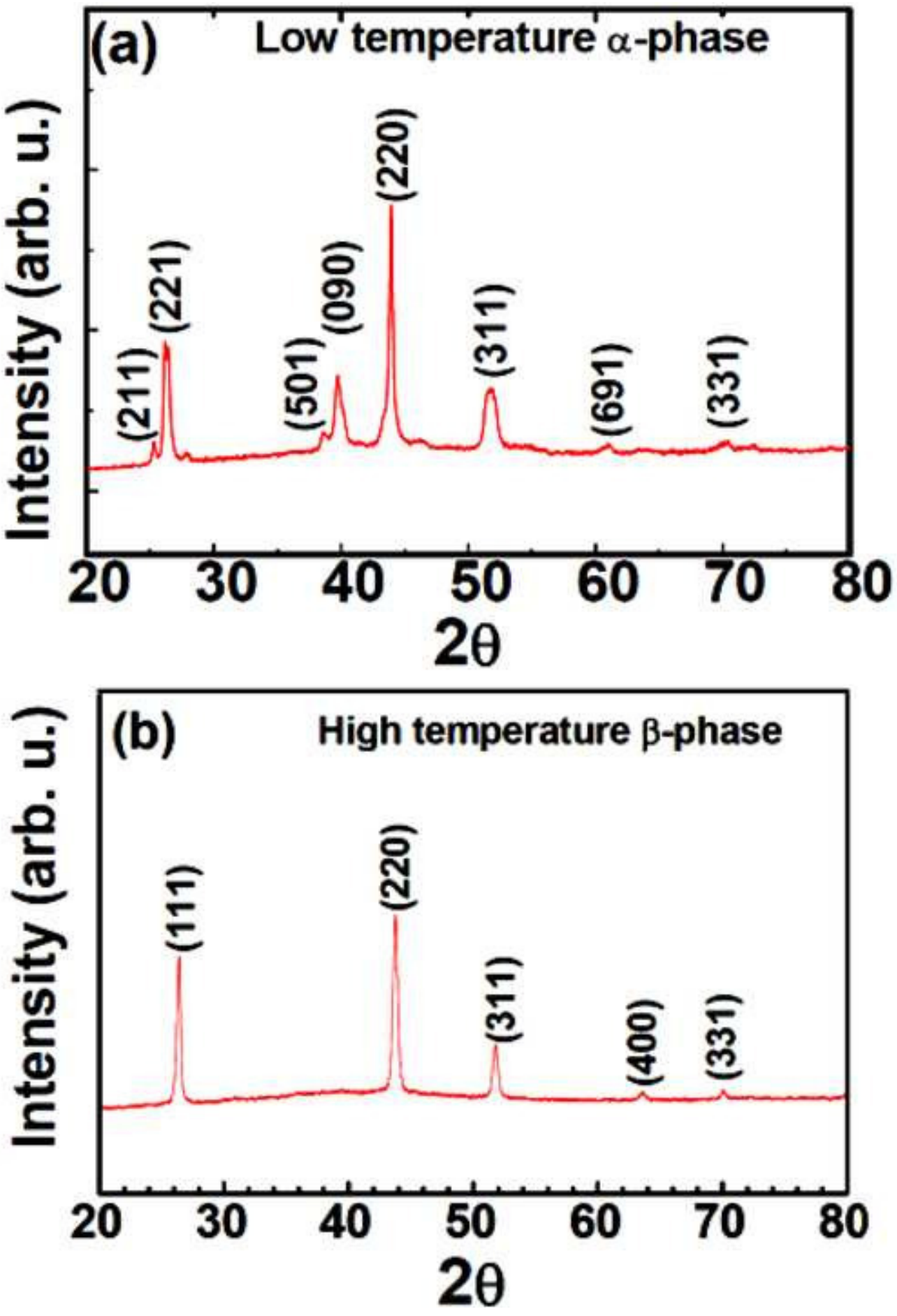

Figure-2

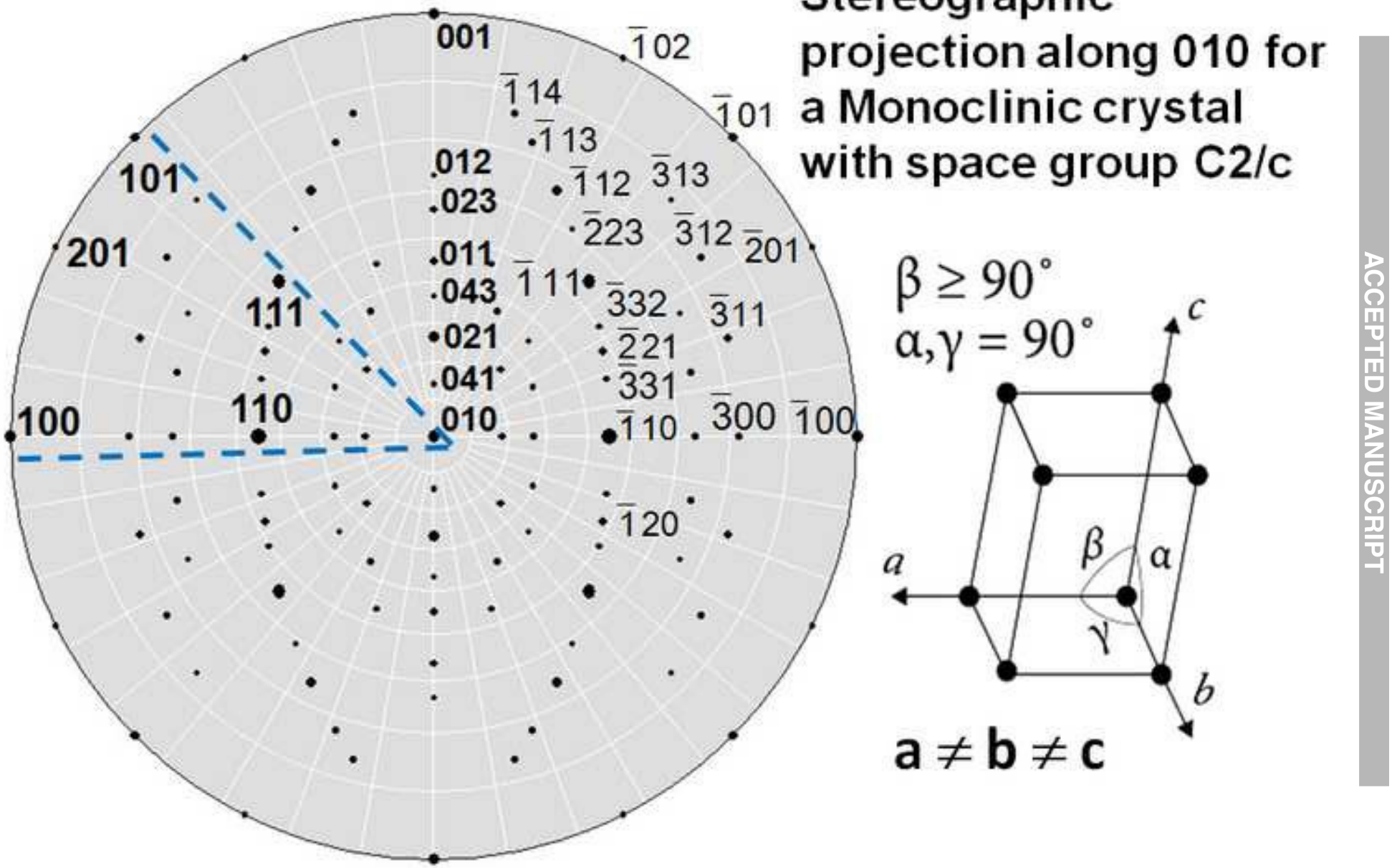

ACCEPTED MANUSCRIPT

Figure-3

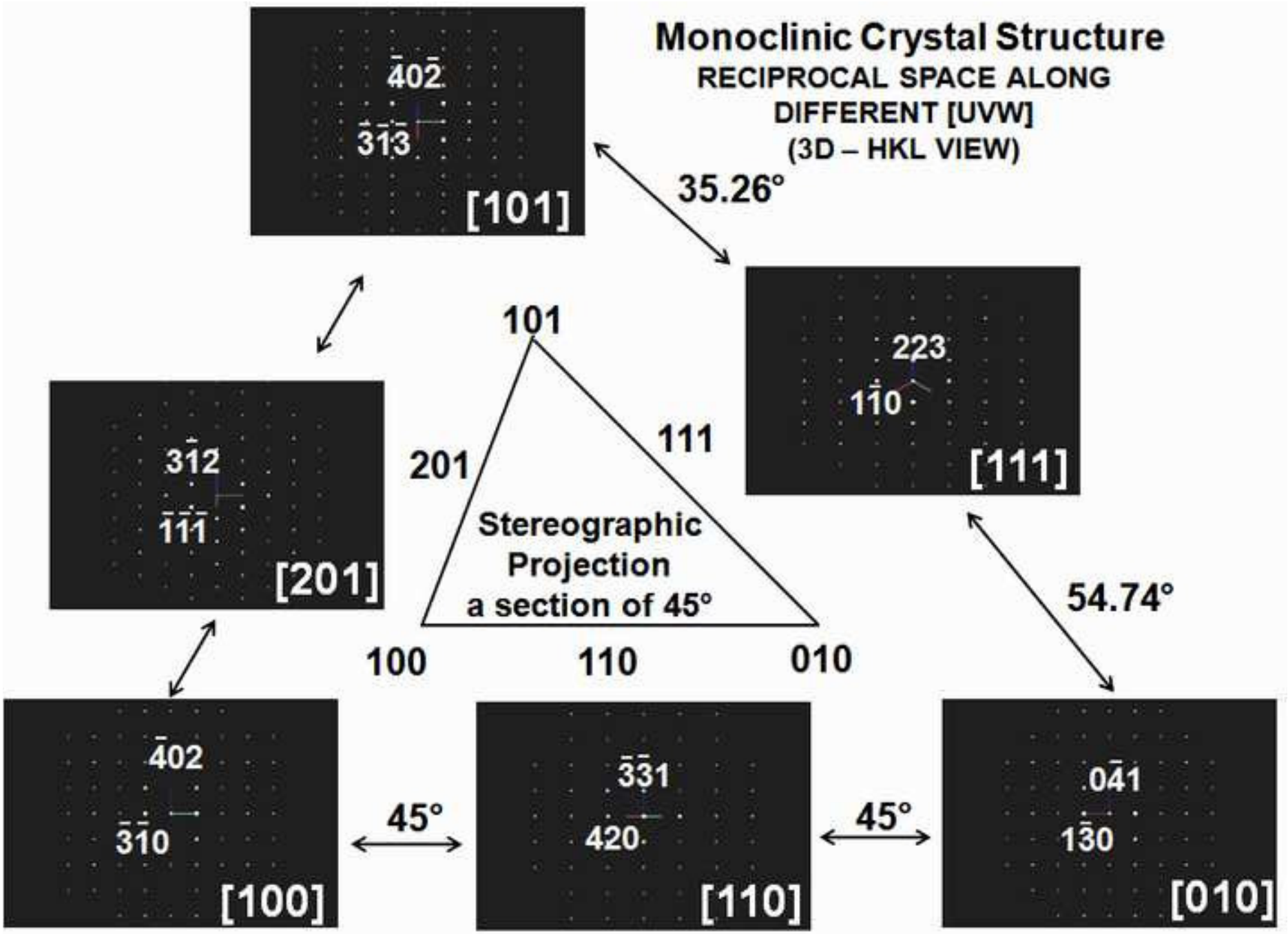

ACCEPTED MANUSCRIPT

Figure-4

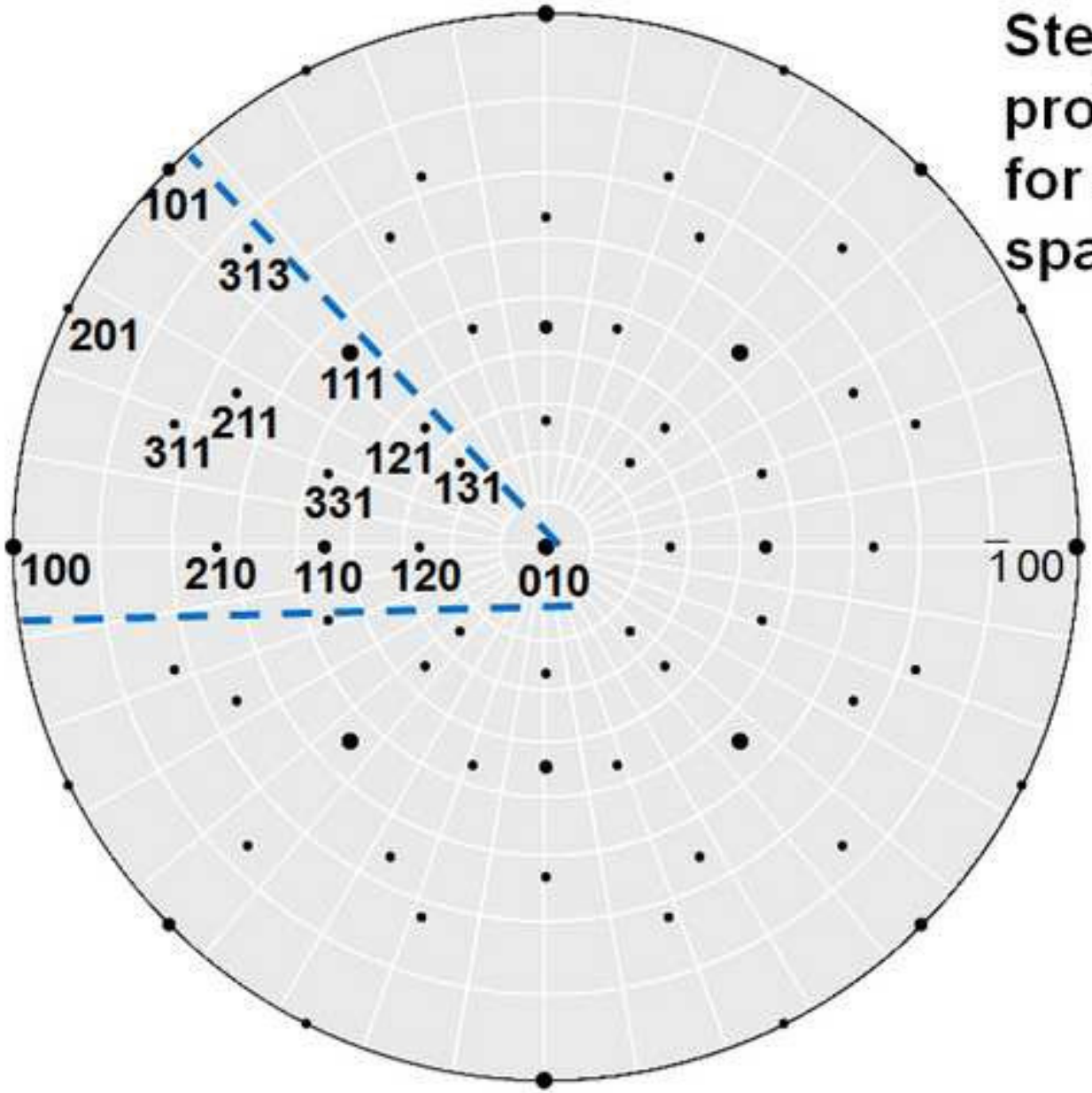

Stereographic projection along 010 for a FCC crystal with space group $Fm\bar{3}m$

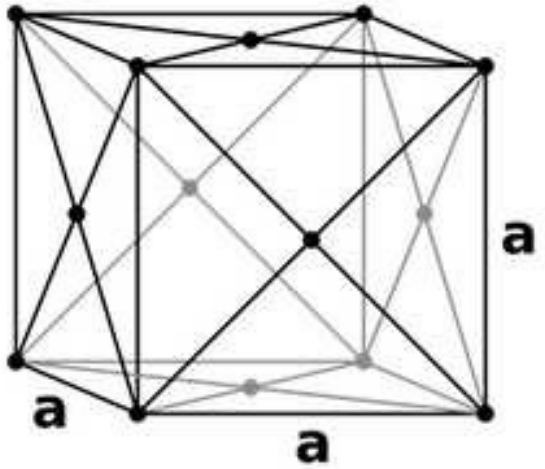

$a = b = c$

$\alpha = \beta = \gamma = 90°$

ACCEPTED MANUSCRIPT

Figure-5

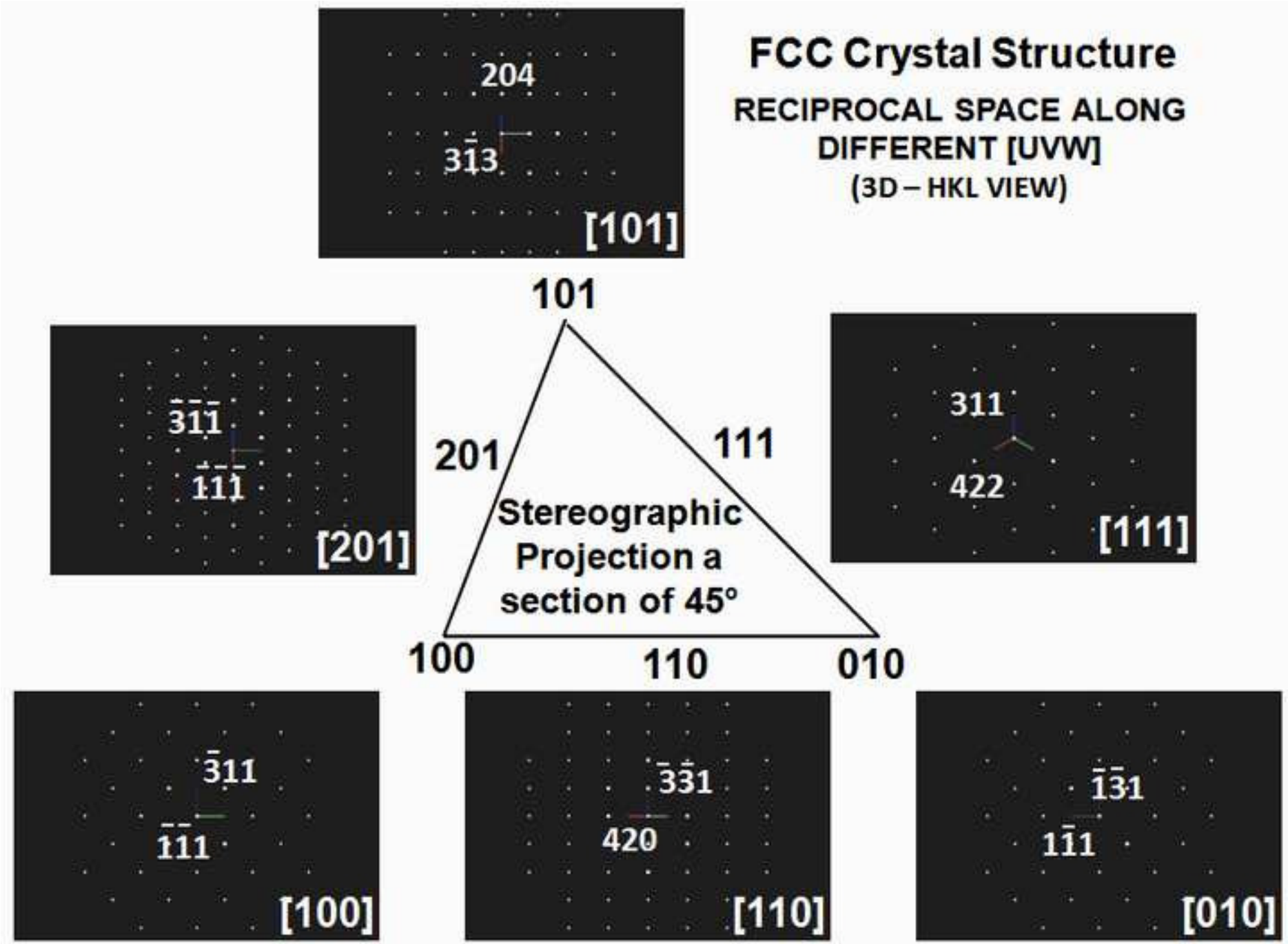

ACCEPTED MANUSCRIPT

Figure-6

ACCEPTED MANUSCRIPT

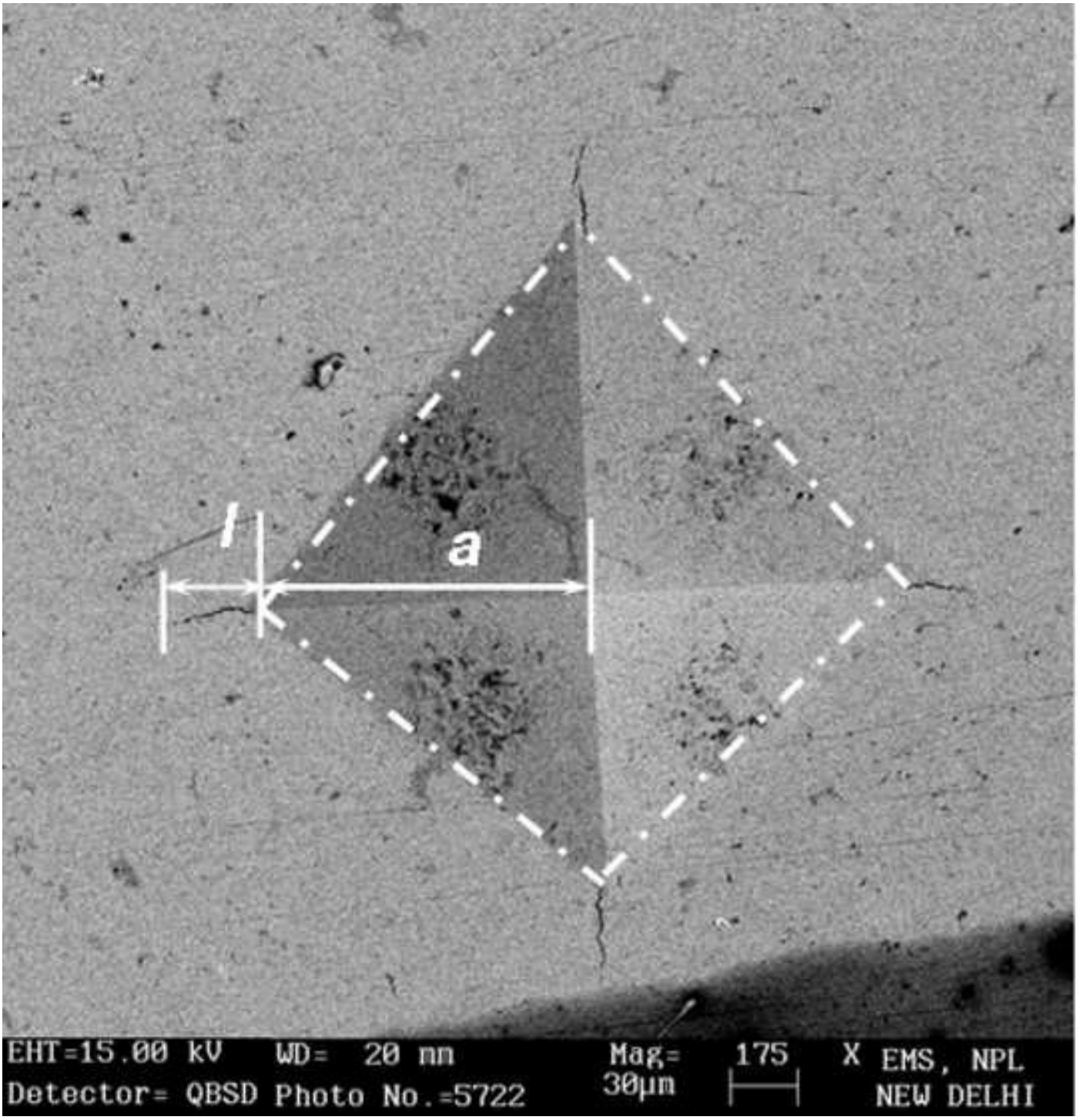

ACCEPTED MANUSCRIPT

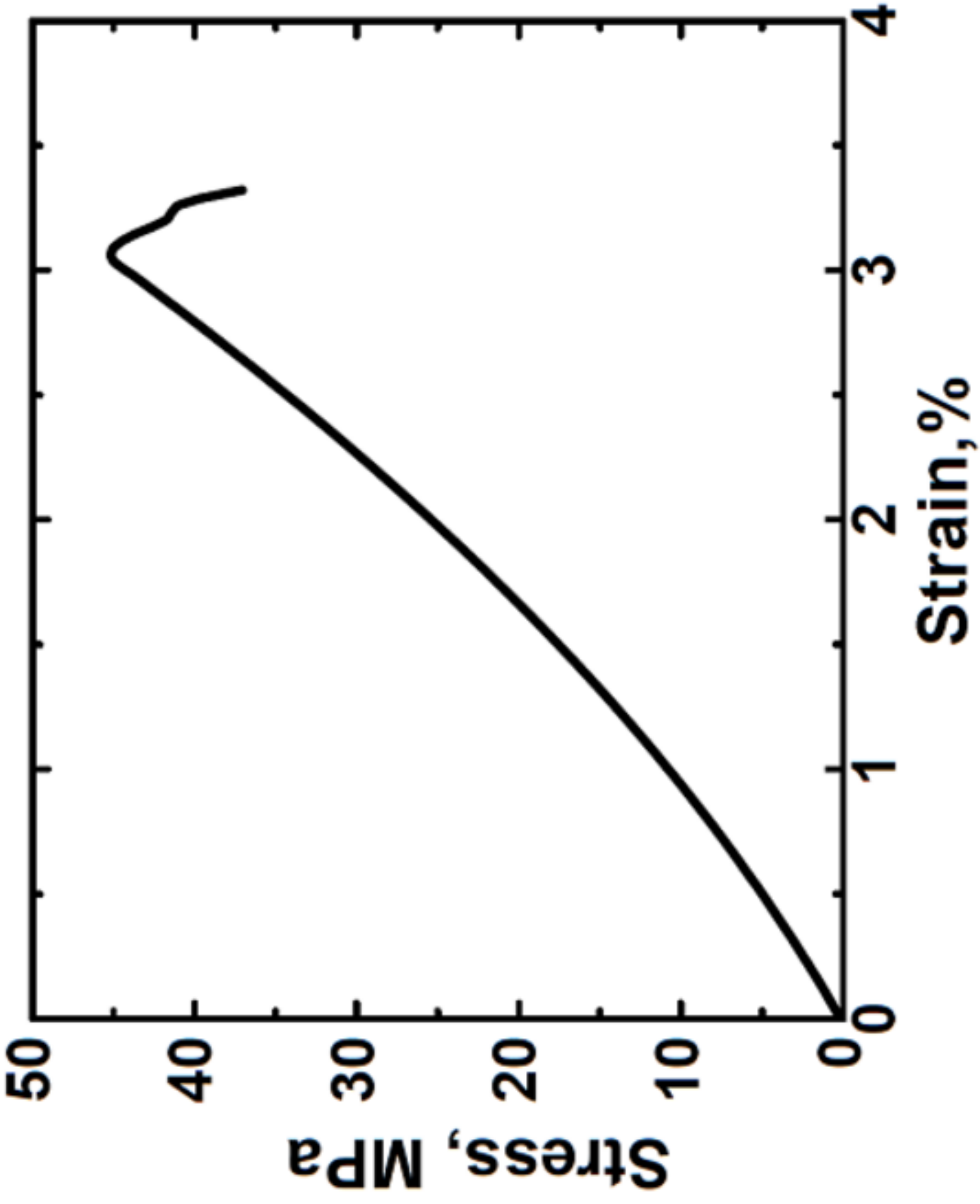

Figure-7

ACCEPTED MANUSCRIPT

Table 1: Lattice parameters and space groups of Cu_2Se available in literature are compared to the current study.

Materials	Phase	Space Group	Unit cell details	Reference
Cu_2Se	Monoclinic (low temperature)	C2/c	a = 14.087 Å, b = 20.481 Å, c = 4.145 Å, β = 90.38º	Murray *et al*. [14]
Cu_2Se	Cubic (high temperature)	Fm-3m	a = 5.787 Å	Milat *et al*. [15]
Cu_2Se	Monoclinic	C2/c	a = 7.1379 Å, b = 12.3823 Å, c = 27.3904 Å, β = 94.308º	Gulay *et al.* [9]
Cu_2Se	**Monoclinic**	**C2/c**	**a = 7.14 Å, b = 12.39 Å, c = 27.33 Å, β = 94.40º**	**This work**

Accepted manuscript

ACCEPTED MANUSCRIPT

Highlights

- Crystal structure determination by stereographic projections for Cu_2Se.
- Superior mechanical properties coupled with high thermoelectric performance.
- Improved fracture toughness, compressive strength and thermal shock resistance.

Accepted manuscript

Electrical Power and Energy Systems 69 (2015) 264–272

Contents lists available at ScienceDirect

Electrical Power and Energy Systems

journal homepage: www.elsevier.com/locate/ijepes

Design and control of LCL filter interfaced grid connected solar photovoltaic (SPV) system using power balance theory

Ravi Nath Tripathi [a,*], Alka Singh [b], Tsuyoshi Hanamoto [a]

[a] Graduate School of Life Science and Systems Engineering, Green Electronics Division, Kyushu Institute of Technology, Kitakyushu 808-0196, Japan
[b] Electrical Engineering Department, Delhi Technological University (formerly DCE), Delhi 110042, India

ARTICLE INFO

Article history:
Received 31 May 2014
Received in revised form 13 December 2014
Accepted 14 January 2015

Keywords:
Solar photovoltaic (SPV)
Maximum power point tracking (MPPT)
Voltage source converter (VSC)
Unity power factor (UPF)
LCL filter
Electromagnetic interference (EMI)

ABSTRACT

In this paper solar photovoltaic (SPV) system connected to the utility grid is designed and simulated. The utility grid and SPV system are coupled with current controlled voltage source converter (VSC) and LCL filter. The design of LCL filter, MPPT algorithm and power quality improvements are discussed and simulation results are shown for the performance analysis of grid-coupled PV system under different load condition. The system is controlled through power balance theory method. The principle behind the control implementation is to evacuate the solar power generated during the daytime and the reactive power demand for the load should be supplied by the PV. The grid coupled system consists of SPV system, dc–dc boost converter, maximum power point tracking (MPPT), voltage source converter (VSC), LCL filter, different loads and three phase utility grid. This system is capable of eliminating harmonic and load balancing by supplying unbalanced current from the PV as a compensator. The system is simulated with 10 kW SPV array using indirect current control scheme.

© 2015 Elsevier Ltd. All rights reserved.

Introduction

The advent of the new technologies in the different area of science and engineering gives rise in the power consumption level due to the use of various equipments which require energy to operate. But, it also provides the aspects of new energy generation technologies. In the newer aspects of energy, solar energy is one of the prominent sources. The advantage of solar energy is the possibility of uses in variety of forms and application. It can be used as solar thermal energy, solar photovoltaic system and various applications as stand-alone mode and grid connected mode. The aspects of energy generation are also related to make the individual houses, offices and societies self-sufficient in terms of energy by distributed generation. The one of the most dominant areas of distributed generation deals with the photovoltaic (PV) power generating system connected to utility grid. PV system has different characteristics with conventional power generation by fossil fuel. Therefore, the new topologies and control algorithms are implemented to couple the PV sources with utility grid [1]. Solar power generating system is a good choice for power generation because of its direct conversion capability into electrical power [2].

The solar power production is growing at very fast rate in India and world also. In India approximately 1.5 GW grid connected solar power is produced presently [3]. To cater the power demand with the increasing rate of consumption, the distributed generation in grid connected mode is mostly desirable with grid following power export control [4,5] and also it lowers the possibility of energy storage problems. The PV system can be coupled to the grid using inverter to convert the dc into ac as power generated by PV system is dc in nature. This system requires power conditioning unit for smooth operation and control algorithm for grid synchronization and power control. The LC filter can be used for reduction of ripples as power conditioner but it is expensive for medium and high power application due to the inclusion of high value inductance [6]. The LC filter is substituted by the LCL filter. The design of LCL filter is having one of the important roles in the entire system and plays vital role for stability of the system. By taking care of cost problems, the LCL filter design is used in a way that using lower value of inductance which is expensive and bulky too, higher value of capacitance which is cheaper [7]. The grid impedance is also having impact on the stability of the system and special care required in the design of LCL filter. The resonance frequency of LCL filter varies as the grid impedance varies i.e. stiffness of the grid [8]. The PV system is coupled with the grid, and the synchronization and power control strategy is required for the operation. The various control strategy is mentioned in the literature and researches based on

* Corresponding author.
E-mail addresses: ravi1989tripathi@gmail.com (R.N. Tripathi), alkasingh.dr@gmail.com (A. Singh).

http://dx.doi.org/10.1016/j.ijepes.2015.01.018
0142-0615/© 2015 Elsevier Ltd. All rights reserved.

Nomenclature

N	diode ideality factor	L_g	grid side inductance of LCL filter
e or q	electronic charge (1.6×10^{-19} C)	C_f	capacitance of LCL filter
k	Boltzmann's constant (1.38×10^{-38} J/K)	Z_{base}	base value of grid impedance
I_{ph}	photocurrent, function of irradiation level	V_{dc}	DC link voltage
I_s	reverse saturation current of diode	V_{sa}, V_{sb}, V_{sc}	phase voltages of grid
V_t	thermal voltage (kT/q)	u_{sa}, u_{sb}, u_{sc}	in-phase templates for phases a, b, c
R_{se}	series resistance of cell	w_{sa}, w_{sb}, w_{sc}	quadrature templates for phases a, b, c
R_{sh}	shunt resistance of cell	V_{PCC}	voltage at point of common coupling
N_s	number of series connected cells	$V_{PCC,t}/V_t$	magnitude of PCC voltage
N_p	number of parallel connected cells	p_L, q_L	load active and reactive power
P	solar PV power	i_{Lp}, i_{Lq}	active and reactive component of load current
V	solar PV voltage	I^*_{sp}	grid reference current for active power
ΔI	change in solar PV current	I^*_{sq}	grid reference current for reactive power
ΔV	change in solar PV voltage	I^*_s	grid reference current
L_i	inverter side inductance of LCL filter	V_{LL}	line to line grid voltage

the power control algorithms and synchronization. The synchronous reference frame (SRF) theory is implemented for control in [9–13]. The SRF based control is implementing using phased locked loop (PLL) for frequency synchronization. In [14,15] the instantaneous power based control for integration of PV system to grid. Earlier, the power balance theory (PBT) is applied to implement the active power filters in [16,17]. This theory does not require PLL for grid synchronization, and power compensation and synchronization principle is simple and is achieved by templates.

In this paper the LCL filter interfaced grid connected system is proposed and simulated with the design consideration for filter. The power balance theory is applied for the control of system with inherent capability of grid synchronization. The principle behind this algorithm implementation is to generate the templates using the source/grid voltage as the reference. The exact mathematical equation required for the generation of different templates and compensation under different operating condition is considered and investigated by the simulation results. The PV system configuration, design is illustrated and incremental conductance based maximum power point tracking (MPPT) algorithm is considered for simplified implementation of the system.

Design of grid coupled system

Design of photovoltaic array

The solar photovoltaic array (SPVA) system is designed for the 9.65 kW (≈10 kW). Reference of different designs and models of PVA system suggests that the open circuit voltage of single solar cell is in between 0.5 and 0.7 V depending upon the material of solar cell. PV array module consists of number of series and parallel connected cells as per the required rating of PV array. The following are the equations [2,18–20] based up-on that PV array is designed in MATLAB/Simulink environment.

$$I = N_p I_{ph} - N_p I_s \left[e^{(V+IR_{se})/NV_t N_s} - 1 \right] - \frac{V + IR_{se}}{R_{sh}} \tag{1}$$

$$R_{se} = R_{se}\left(\frac{N_s}{N_p}\right), \quad R_{sh} = R_{sh}\left(\frac{N_s}{N_p}\right) \tag{2}$$

Maximum power point tracking

Two different schemes are used to couple the solar PV system to grid. First one is single stage and the other one is two stages. In single stage, there is only dc–ac inverter used which deals with MPPT and synchronization. The two stage scheme includes a dc–dc converter for tracking MPPT [21,22] and inverter for the conversion of dc to ac. Both schemes have its own advantages and disadvantages. In this paper, the two stage scheme used for the coupling of PV system to grid. As the characteristics of PV system in Figs. 2 and 3 are exponential in nature and depend upon weather conditions it is necessary to track the maximum power point (MPP) to improve the efficiency of entire system. The tracking of MPP requires implementation of maximum power point tracking algorithm with dc–dc converter. Voltage and current values for MPP are tracked by using different MPPT algorithms. Incremental conductance MPPT algorithm is implemented and is based on (3) and given as

$$\frac{dP}{dV} = I + V\frac{dI}{dV} \approx I + V\frac{\Delta I}{\Delta V} \tag{3}$$

According to (3) the conditions in (4) are derived for MPP as

$$\begin{aligned} &\Delta I/\Delta V = -I/V \quad \text{at MPP} \\ &\Delta I/\Delta V > -I/V \quad \text{left of MPP} \\ &\Delta I/\Delta V < -I/V \quad \text{right of MPP} \end{aligned} \tag{4}$$

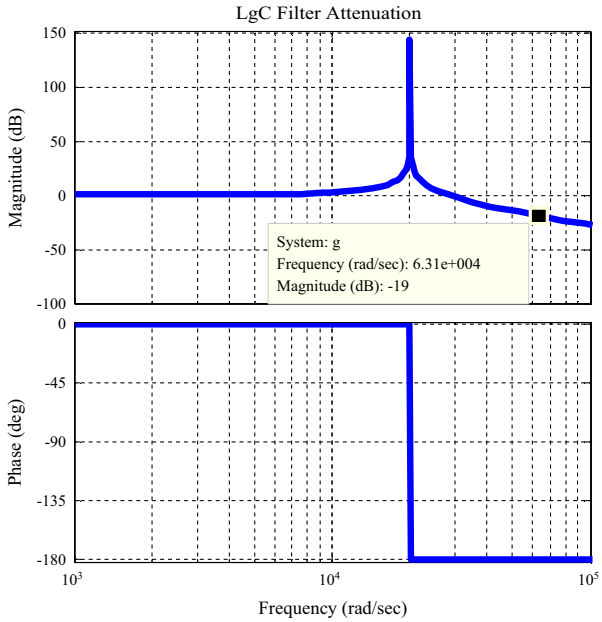

Fig. 1. Bode plot of L_gC_f component of LCL filter.

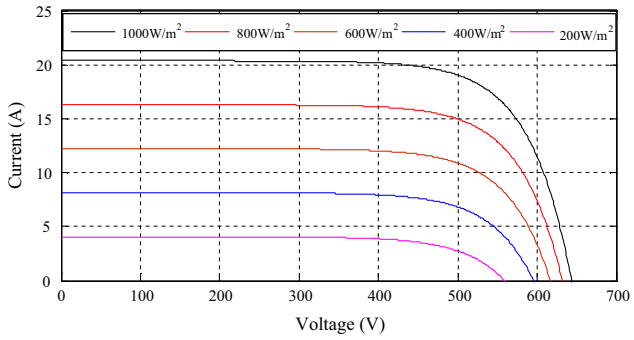

Fig. 2. *I–V* characteristic of PV system.

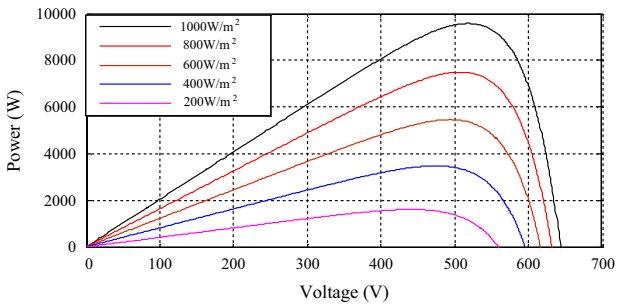

Fig. 3. *P–V* characteristic of PV system.

Hence the power delivered by the SPV array will automatically be tracked through MPPT algorithm using dc–dc boost converter.

Design of LCL filter

The LCL filter designing is categorized into two parts. First part deals with the design of inverter side inductance (L_i) and the second part deals with the design of grid side inductance (L_g) and capacitance (C_f) which is considered as L_gC_f second order low pass filter. The grid side inductance design is having relation with inverter side inductance and the ratio between grid side inductance and converter side inductance depends upon the ripple current attenuation [23]. The simplified equations are used for the designing of LCL filter [6] and in this paper the ratio between grid side inductance and converter side inductance is decided as unity based on the design assumption for ripple current attenuation.

$$L_i = \frac{V_s}{2\sqrt{6} f_s i_{ripple,peak}} \tag{5}$$

$$C_f = \frac{0.05}{\omega_n Z_{base}} \tag{6}$$

$$Z_{base} = \frac{V_{sLL}^2}{P_n} \tag{7}$$

$$L_g = L_i \tag{8}$$

where V_g is grid r.m.s. phase voltage, f_s inverter switching frequency, $i_{ripple,peak}$ 15% 0f peak value of rated output current, L_g grid side inductance, L_i inverter side inductance, C_f capacitance of LCL filter, P_n inverter rated power and ω_n operating frequency.

The electromagnetic interference filter (EMI) attenuates the high frequency current harmonics due to switching of inverter. For normal cases, the filter for grid coupled PV system includes only an inductance or an LC filter. The value of inductance for above mentioned cases is very high, bulky and costly [24]. The LCL filter worked as an EMI filter having common mode inductance and differential mode inductance.

For the case of 10 kW PV system coupled to the grid, LCL filter having resonance frequency of 4.7 kHz has been designed using (5)–(8). The low pass second order filter (L_gC_f) was designed to get the attenuation of −20 dB of the inverter current at switching frequency. The stability analysis of L_gC_f filter and attenuation at the switching frequency is calculated by plotting bode plot shown in Fig. 1 and −19 dB attenuation is achieved at the switching frequency.

DC link capacitor voltage

The DC link capacitor voltage of VSC is given by [25] (9) significantly related to the grid voltage based on the principle related to power flow from high potential to low potential.

$$V_{dc} = \frac{\left(2\sqrt{2}V_{LL}\right)}{\sqrt{3}m} \tag{9}$$

It means the dc link voltage should be greater than twice of the peak of the phase voltage of the system. For the system designed for investigation DC link voltage (V_{dc}) is selected as 800 for modulation index (m) taken as 0.9 and V_{LL} is 415 V.

Control strategy implementation

The control strategy implementation is based upon the generation of templates. The templates are generated and categorized upon their phase orientation with grid voltage. The active and reactive power control is achieved by the generation of in phase templates and quadrature templates. In this control algorithm the templates are responsible for the grid frequency synchronization with converter and power compensation control.

In phase unit templates generation

This template is having phase orientation in phase with the grid voltage. The magnitude of templates is normalized and is equal to unity. The in phase unit templates are generated by using (10) and (11)

$$u_{sa} = \frac{V_{sa}}{V_t}, \quad u_{sb} = \frac{V_{sb}}{V_t}, \quad u_{sc} = \frac{V_{sc}}{V_t} \tag{10}$$

where V_t is amplitude of three phase point of common coupling (PCC) voltage and calculated as

$$V_{PCC,t} = \left(\frac{2}{3}\right)^{\frac{1}{2}} \left(v_{sa}^2 + v_{sb}^2 + v_{sc}^2\right)^{1/2} \tag{11}$$

The in phase templates are used for the grid frequency synchronization and active power control in the system. For the active power control the unit templates are multiplied with direct axis component of the currents.

Quadrature unit templates generation

The phase orientation of this type of unit templates is at 90° to the in phase unit templates i.e. the phase is in quadrature to the grid voltage. The quadrature unit templates are generated by the in phase unit templates and are responsible for the control of reactive power compensation. The quadrature unit templates are generated as

$$\frac{u_c - u_b}{\sqrt{3}} = w_a \tag{12}$$

$$\frac{u_a}{\sqrt{2}} + \frac{u_b - u_c}{\sqrt{6}} = w_b \tag{13}$$

$$\frac{u_b - u_c}{\sqrt{6}} - \frac{u_a}{\sqrt{2}} = w_c \tag{14}$$

Current component of active power and reactive power of load

The active power and reactive power can be calculated using (15), (16) and correspondingly the current component of active and reactive power can be calculated using the (17) and (18). The active power and reactive power can also be computed by using (21) but it requires transformation from three phase to two phase i.e. abc to αβ.

The load current and PCC voltage are transformed from abc to αβ using the Clark's transformation matrix [26] as shown in (18) and (19). The active and reactive power is calculated using (21). The active and reactive component of current is calculated from the active and reactive power by (24). The active and reactive components of current are having two parts, one is along the α-axis and other one is along the β-axis. The components of current in (22) and (23) are converted into matrix form in (24)

$$p_L = v_{PCC,a} * i_{L,a} + v_{PCC,b} * i_{L,b} + v_{PCC,c} * i_{L,c} \tag{15}$$

$$q_L = (v_{PCC,a} - v_{PCC,b}) * i_{L,a} + (v_{PCC,b} - v_{PCC,c}) * i_{L,b} + (v_{PCC,c} - v_{PCC,a}) * i_{L,c} \tag{16}$$

$$i_{Lp} = \frac{2}{3}\frac{p_L}{V_t} \tag{17}$$

$$q_{Lp} = \frac{2}{3}\frac{q_L}{V_t} \tag{18}$$

$$\begin{bmatrix} i_{L\alpha} \\ i_{L\beta} \end{bmatrix} = \sqrt{\frac{2}{3}}\begin{bmatrix} 1 & -1/2 & -1/2 \\ 0 & -\sqrt{3}/2 & \sqrt{3}/2 \end{bmatrix}\begin{bmatrix} i_{La} \\ i_{Lb} \\ i_{Lc} \end{bmatrix} \tag{19}$$

$$\begin{bmatrix} v_{L\alpha} \\ v_{L\beta} \end{bmatrix} = \sqrt{\frac{2}{3}}\begin{bmatrix} 1 & -1/2 & -1/2 \\ 0 & -\sqrt{3}/2 & \sqrt{3}/2 \end{bmatrix}\begin{bmatrix} v_{PCC,a} \\ v_{PCC,b} \\ v_{PCC,c} \end{bmatrix} \tag{20}$$

$$\begin{bmatrix} p_L \\ q_L \end{bmatrix} = \begin{bmatrix} v_{L\alpha} & v_{L\beta} \\ -v_{L\beta} & v_{L\alpha} \end{bmatrix}\begin{bmatrix} i_{L\alpha} \\ i_{L\beta} \end{bmatrix} \tag{21}$$

$$i_{Lp} = \frac{v_{L\alpha}}{v_{L\alpha}^2 + v_{L\beta}^2}p_L + \frac{v_{L\beta}}{v_{L\alpha}^2 + v_{L\beta}^2}p_L \tag{22}$$

$$i_{Lq} = \frac{v_{L\beta}}{v_{L\alpha}^2 + v_{L\beta}^2}q_L + \frac{-v_{L\alpha}}{v_{L\alpha}^2 + v_{L\beta}^2}q_L \tag{23}$$

$$\begin{bmatrix} i_{Lp} \\ i_{Lq} \end{bmatrix} = \frac{1}{v_{L\alpha}^2 + v_{L\beta}^2}\begin{bmatrix} v_{L\alpha} & v_{L\beta} \\ v_{L\beta} & -v_{L\alpha} \end{bmatrix}\begin{bmatrix} p_L \\ q_L \end{bmatrix} \tag{24}$$

Reference current for active power control and unity power factor operation

For the operation of grid connected system in unity power factor mode, the control algorithm considers that utility grid must supply direct axis component of load current as well as active power component of current required to regulate the DC bus voltage to the reference level and to feed VSC losses (i_{loss}) as shown in (25). The dedicated dc voltage PI controller regulates the dc bus voltage to desired reference level and provides the active power transfer for compensation of VSC losses.

The reference current generated for 'd' component of grid current is given as

$$i_{Lp}^* = i_p + i_{d,loss} \tag{25}$$

Active power components of reference grid currents are

$$i_{Lq}^* = i_q - i_{qPCC,t} \tag{26}$$

Reference current for reactive power control and zero voltage regulation

Zero voltage regulation at point of common coupling (PCC) of the proposed system, considers that ac mains grid must deliver the quadrature axis current component (i_q) which will be responsible to regulate the voltage at PCC with direct axis current component (i_d). PI controller is used to regulate the voltage at the point of PCC. The quadrature component of current is zero for unity power factor operation and for zero voltage regulation condition it is computed as the difference of the output of PI controller (for voltage regulation at PCC) and the fundamental component of load reactive power. The input for the controller is the error signal generated by the difference of measured voltage at PCC (V_s) and the reference voltage (V_s^*). The PCC voltage amplitude is computed by (10).

The reference current generated in terms of q components in (27) is given as

$$i_q^* = i_q - i_{qPCC,t} \tag{27}$$

Reactive power components of reference grid currents are

$$I_{sqa}^* = I_{Lq}^* * w_{sa}, \quad I_{sqb}^* = I_{Lq}^* * w_{sb}, \quad I_{sqc}^* = I_{Lq}^* * w_{sc} \tag{28}$$

Grid references

The combination of references generated for active power control and reactive power control will generate the reference for grid current. According to the basic methodology of the control grid current should follow the reference current generated by the active and reactive current components of the load. The reference current is given by (29)

$$I_{sa}^* = I_{spa}^* + I_{sqa}^*, \quad I_{sb}^* = I_{spb}^* + I_{sqb}^*, \quad I_{sc}^* = I_{spc}^* + I_{sqc}^* \tag{29}$$

Hysteresis current controller is used to control the output current of the converter. The reference current generated is compared with the grid current and it will force the converter current to remain within the zone decided by the hysteresis current controller.

Results and discussions

The simulation model of the grid connected solar system with control strategy in Fig. 4 is developed in MATLAB/Simulink. The simulation is performed for the linear and non-linear type of loads under the transition from balanced load condition to unbalanced load condition and irradiance effect on solar system. The simulation results are represented on the basis of following terms: DC link voltage (V_{dc}), PCC voltage (V_{PCC}), grid voltage (V_s), grid current (I_s), compensation/inverter/PV current (I_{PCC}), PV voltage (V_{pv}), PV current (I_{pv}), load current (I_{load}, I_a, I_b, I_c), active power from grid (P), reactive power from grid (Q). The results are investigated and analyzed based on the mentioned terms. The solar PV system parameters and grid connection system parameters with LCL filter are mentioned in Tables 1 and 2. The in phase and quadrature phase templates generated during the simulation for the phases 'a', 'b' and 'c' are shown in Figs. 5a–5c respectively. Fig. 6 illustrates the behavior of the system under the change in solar irradiation

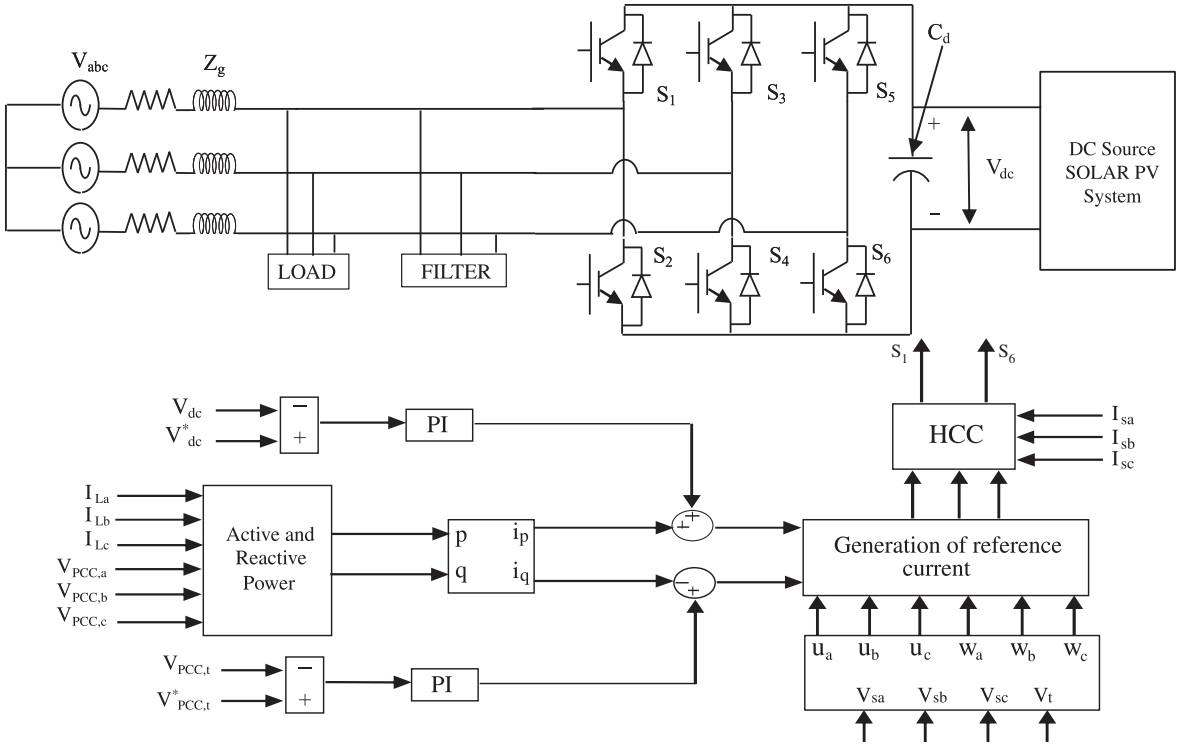

Fig. 4. Grid connected solar PV system with control strategy.

Table 1
Parameters of the solar PV CS5P-225 M and boost converter.

Description	Parameter
Number of parallel connected PV module	4
Number of series connected PV module	11
Open circuit voltage of module (V_{OC})	59 V
Short circuit current of module (I_{SC})	5.09 A
Voltage at MPP (V_{MPP})	47.4
Current at MPP (I_{MPP})	4.74
Voltage coefficient (k_v)	−0.35%/°C
Current coefficient (k_v)	0.060%/°C
Inductance (boost converter)	1.5 mH
Capacitance (boost converter)	250 μF
Switching frequency	10 kHz

Table 2
Parameters of the electrical utility grid system.

Description	Parameter
Line impedance (Z_s)	R_s = 0.05 Ω, L_s = 1 mH
Grid voltage	V_{LL} = 415 V
LCL filter	L_i = 1.4 mH, L_g = 1.4 mH, C_f = 5 μF
DC bus voltage	V_{dc} = 800 V
DC bus capacitance	1500 μF
Loads	(i) 15–20 kV A, 0.8 pf lagging (ii) 10 Ω and 100 mH
Frequency	50 Hz
Switching frequency	10 kHz

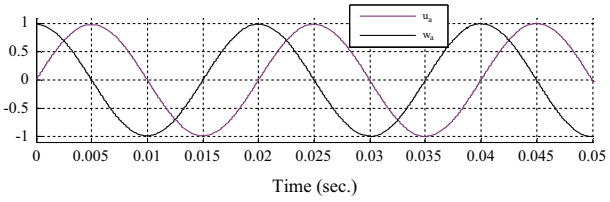

Fig. 5a. In-phase and quadrature template for phase 'a'.

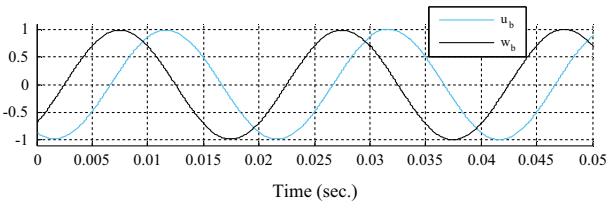

Fig. 5b. In-phase and quadrature template for phase 'b'.

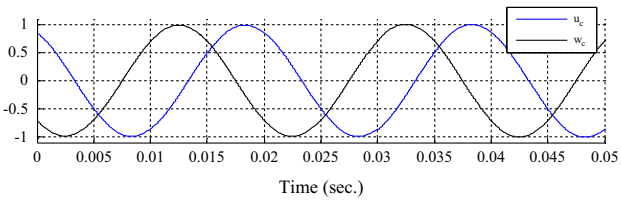

Fig. 5c. In-phase and quadrature template for phase 'c'.

level. This change in irradiance is considered for the little worst condition. t = 0.45 s is the reference irradiance condition and at t = 0.5 s the irradiance is changed from the 1000 W/m^2 (reference condition) to 200 W/m^2. The MPP point for PV current shifts and reduced suddenly. As the solar current reduced, the current (I_s) and therefore active power (P) from the grid are increased to fulfill the load demand. The change in irradiance has small effect on solar PV voltage (V_{PV}) and dc link voltage (V_{dc}) is maintained. The system is switched to the initial condition at t = 0.7. The system is normally operating at unity power factor i.e. the grid voltage and grid current are in same phase and the reactive power demand by the load is supplied by the PV power. There is a possibility that

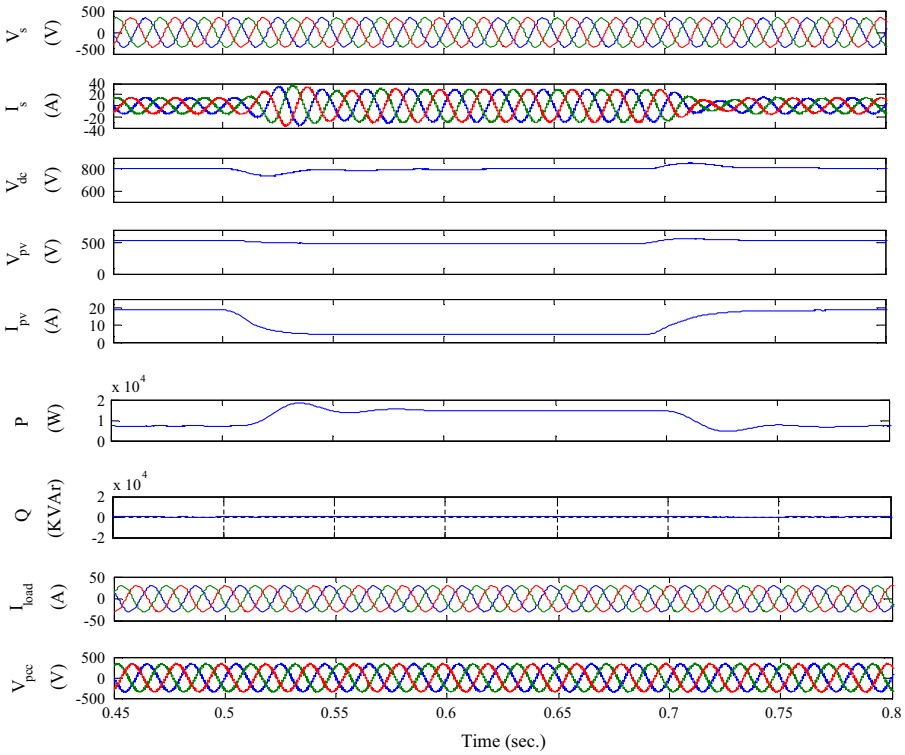

Fig. 6. Performance of the system under changed irradiance condition.

under the low irradiance condition, some part of the reactive power is supplied by the grid as the PV may not be able to produce sufficient power under low irradiance. The solar PV parameters for CANADIAN SOLAR CS5P-225M are mentioned in Table 1.

Fig. 7 shows the increase in the linear load from 15 kV A to 20 kV A. The transition for the change in the load occurs at $t = 0.3$ s. and the load current (I_{load}) increases. As load power demand increases the grid current is changed to meet the demand required by the load. Alongside the increase in the active power supplied by the grid is observed in Fig. 7. During this transition the dc link voltage (V_{dc}) is maintained at the reference value. The system is working under the unity power factor operation as the reactive power demand of the load is supplied by the PV power and the grid reactive power supply (Q) is observed as zero. Therefore, the grid voltage and grid current are in the same phase. By using power balance theory control strategy, the generation of references for active power and reactive power is easily obtained. The in phase templates multiplication is responsible for the active

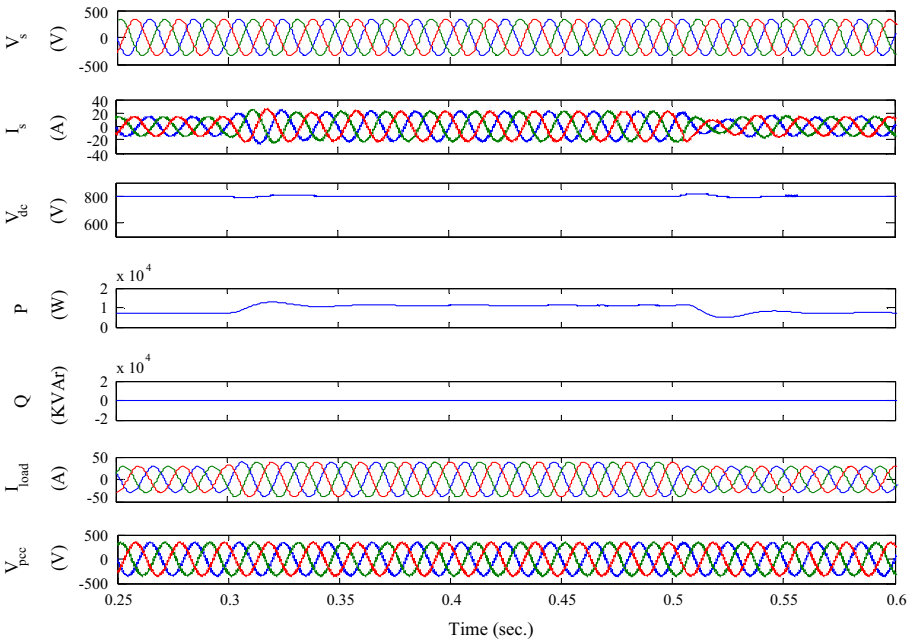

Fig. 7. Performance of the system under linear load changing condition.

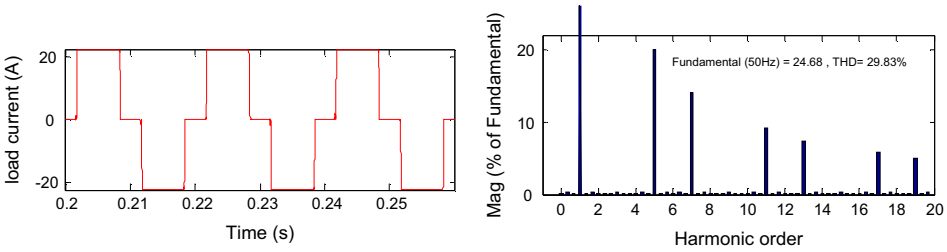

Fig. 8a. Waveform and harmonic spectrum for I_{load} under non-linear condition.

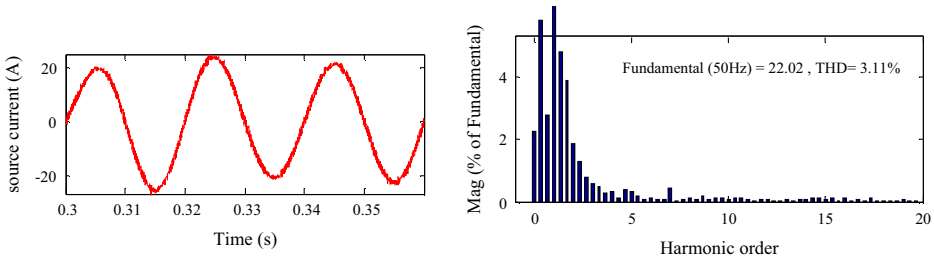

Fig. 8b. Waveform and harmonic spectrum for I_s under unbalanced linear load.

power component/reference and quadrature template multiplication is responsible for the reactive power component/reference.

Fig. 9 shows the unbalanced linear load condition operation. In this case the unbalanced is created by changing the load for one of the phases. In a three phase balanced system the load for all the phases should be same. For the case of load unbalancing, at $t = 0.3$ s. the load in phase 'b' switched to half of the normal operating condition. As the load is decreased, the power demand of the load is decreased; therefore, the decrease in the active power (P) supply from the grid is observed. Alongside the grid current is also reduced during low power demand period. But the current from the PV/inverter (I_{PCC}) behaves as a compensating current and maintains the source current (I_s). The source current is balanced by unbalancing the inverter current. During this transition

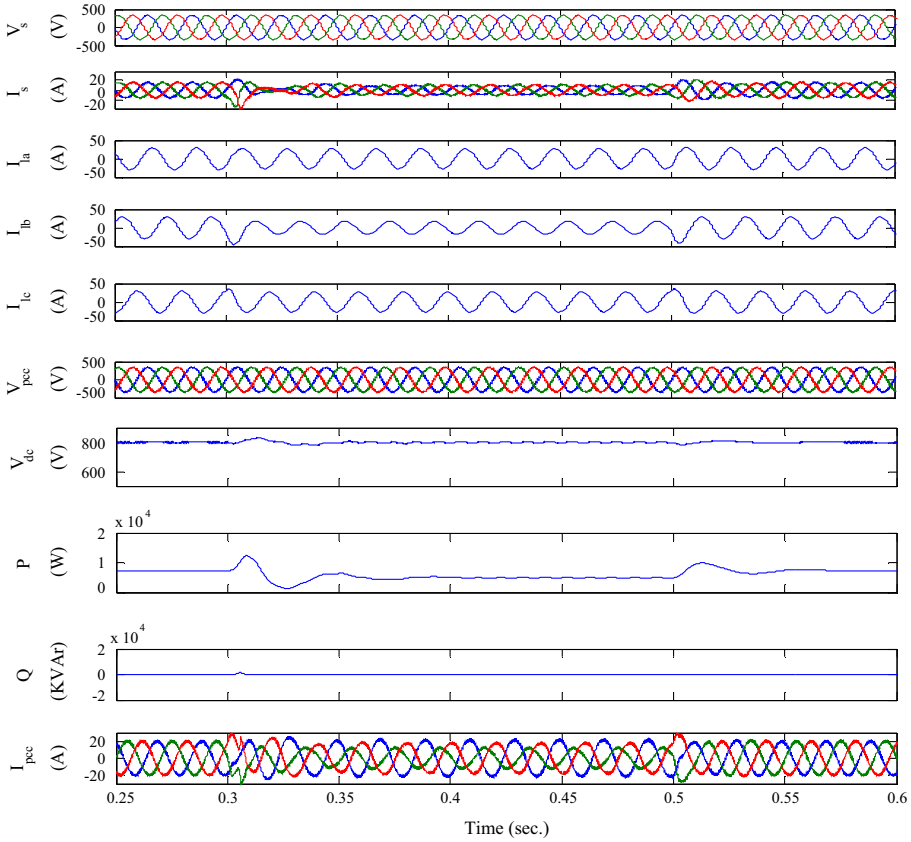

Fig. 9. Performance of the system under unbalanced linear load condition.

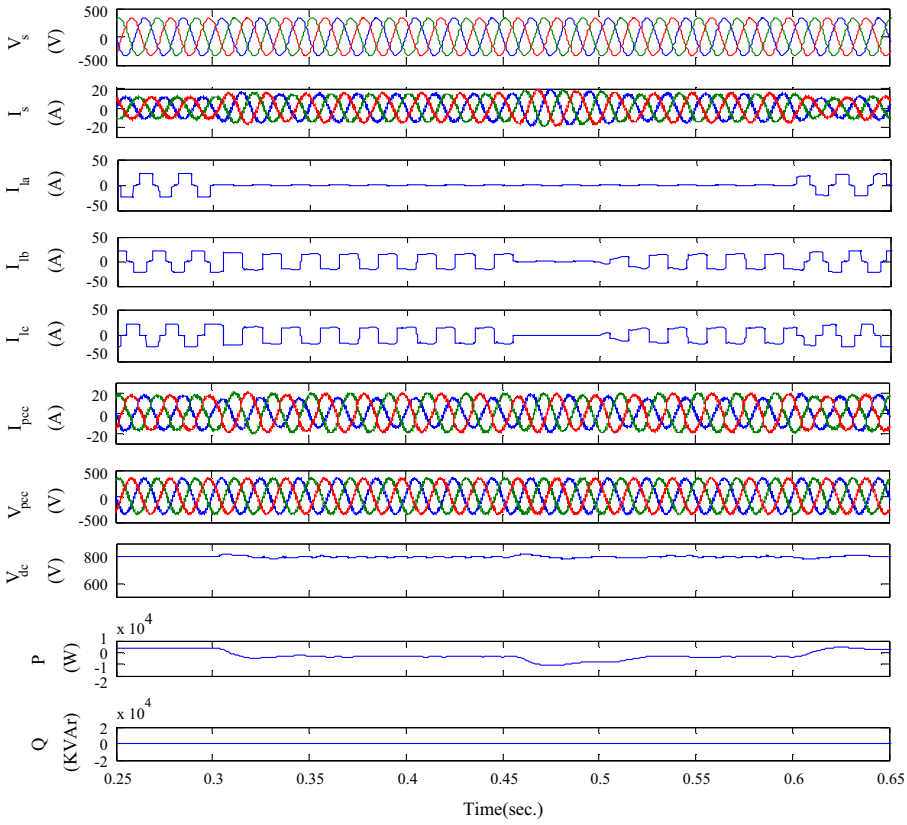

Fig. 10. Performance of the system under unbalanced non-linear load condition.

the dc link voltage (V_{dc}) is maintained at the reference value. For the unbalanced condition the unbalanced and reactive component of current is supplied by the inverter current (I_{PCC}); therefore, the grid is maintained under the unity power factor operation. So, the grid current (I_s) and grid voltage (V_s) are in same phase and the reactive power supplied by the grid (Q) is observed as zero.

Fig. 10 illustrated the operation under the unbalanced non-linear load condition. For the non-linear load case unbalanced is created by disconnecting the phases of the load. The phase 'a' is disconnected at $t = 0.3$ s. and the decrease in the active power supply by the grid (Q) is observed. As in the case of unbalanced linear load condition the grid current (I_s) is maintained at balanced condition by unbalancing the inverter current (I_{PCC}). In this case also the inverter current (I_{PCC}) becomes unbalanced to maintain the source current (I_s) in balanced condition and the dc link voltage (V_{dc}) is maintained at the reference level. The total harmonic distortion (THD) for the different operating conditions is maintained well within the limit according to the IEEE-519 standards [27]. The THD of the load current under non-linear load condition and source current is shown in Figs. 8a and 8b At $t = 0.45$ s. all three phases of the load are disconnected and at $t = 0.6$ it is changed to the balanced condition.

Conclusion

The LCL interfaced solar photovoltaic (PV) system is designed and simulated successfully using power balance theory algorithm. The desired results for evacuation of PV power are achieved and by providing compensating reactive power from PV system, grid is operated under unity power factor. It improves the power factor of the system. The grid connected system is investigated and analyzed under changed irradiance and load condition.

The grid active and reactive power current references are generated by in phase and quadrature phase templates generation using the power balance theory. The system is investigated and analyzed for unbalanced load and non-linear load condition also. The performance of the system is maintained according to IEEE-519 standards for THD and under unbalanced and non-linear load conditions as the PV inverter generates the compensating current. This system does not require PLL as the synchronization is achieved through templates.

References

[1] Sun Kai, Zhang Li, Xing Yan, Guerrero JM. A distributed control strategy based on DC bus signaling for modular photovoltaic generation system with battery energy. IEEE Trans Power Electron 2011;26(10).
[2] Tripathi Ravi Nath, Singh Alka, Badoni Manoj. A MATLAB-Simulink-based solar photovoltaic array (SPVA) module with MPPT. In: IEEE International conference on communication, control, signal processing and computing application (C2SPCA), 10–11, ISBN 978-1-4799-1085-4, October, 2013.
[3] Grid connected solar power in India. Ministry of New and Renewable Energy (MNRE). Government of India (GoI), Feb-March 2013.
[4] Katiraei Farid, Iravani Reza, Hatziargyriou Nikos, Dimeas Aris. Microgrid management control and operation aspect of microgrids. IEEE Power Energy Mag 2008.
[5] Tripathi Ravi Nath, Singh Alka. Design and control of grid interconnected solar photovoltaic (SPV) system with improvement in power quality. In: Fifth international conference on power and energy systems, Kathmandu, Nepal, 28–30 October, 2013.
[6] Zue Aslain Ovano, Chandra Ambrish. Simulation and stability analysis of a 100 kW grid connected LCL photovoltaic inverter for industry. In: IEEE power engineering society general meeting, ISBN 1-4244-0493-2, Montreal, Que.; 2006.
[7] Enslin JHR, Heskes PJM. Harmonic interaction between a large number of distributed power inverters and the distributed network. PESC 2003:1742–7.
[8] Liserre Marco, Blaabjerg Frede, Hansen Steffan. Design and control of an LCL-filter-based three-phase active rectifier. IEEE Trans Ind Appl 2005;41(5).
[9] Sha D, Wu D, Liao X. Analysis of hybrid controlled three-phase grid-connected inverter with harmonics compensation in synchronous reference frame. IET Power Electron 2011;4(7):743–51.

[10] Monfared M, Golestan S, Guerrero JM. Analysis, design and experimental verification of a synchronous reference frame voltage control for single phase inverters. IEEE Trans Industr Electron 2013;61(1):258–69.
[11] Busada CA, Blanca Bahia, Gomez Jorge S, Leon AE, Solsona JA. Current controller based on reduced order generalized integrators for distributed generation systems. IEEE Trans Industr Electron 2012;59(7):2898–909.
[12] Hwang Seon-Hwan, Liu Liming, Li Hui, Kim Jang-Mok. DC offset error compensation for synchronous reference frame PLL in single-phase grid-connected converters. IEEE Trans Power Electron 2012;27(8):3467–71.
[13] Adda R, Ray O, Mishra SK, Joshi A. Synchronous-reference-frame-based control of switched boost inverter for standalone DC nanogrid applications. IEEE Trans Power Electron 2012;28(3):1219–33.
[14] Tsengenes Georgios, Adamidis Georgios. Investigation of the behavior of a three phase grid-connected photovoltaic system to control active and reactive power. Electr Power Syst Res 2011;81:177–84. Elsevier.
[15] Herrera RS, Salmeron P. Present point of view about the instantaneous reactive power theory. IET Power Electron 2009;2(5):484–95.
[16] Singh BN, Rastgoufard P, Singh B, Chandra A, Haddad KA. Design, simulation and implementation of three pole/four pole topologies for active filters. Inst Electr Eng Proc Electr Power Appl Jul. 2004;151(4):467–76.
[17] Singh BN, Singh B, Chandra A, Haddad KA. Design, digital implementation of active filters with power balance theory. Inst Electr Eng Proc Electr Power Appl Oct. 2005;152(5):1149–60.
[18] Ding Kun, Bian XinGao, Liu HaiHao, Peng Tao. A MATLAB-Simulink-based PV module and its application under conditions of non-uniform irradiance. IEEE Trans Energy Convers 2012;27(4).
[19] Altas IH, Sharaf AM. A photovoltaic array simulation model for Matlab-Simulink GUI environment. In: International conference on clean power; 2007. p. 341–5.
[20] Villalva MG, Gazoli JR, Ruppert F E. Modelling and circuit-based simulation of photovoltaic arrays. Braz J Power Electron 2009;14(1):35–45. ISSN 1414-8862.
[21] Eshram Trishan, Chapman Patrick L. Comparison of photovoltaic array maximum power point techniques. IEEE Trans Energy Convers June 2007;22(2):439–49.
[22] Tey Kok Soon, Mekhilef Saad. Modified incremental conductance MPPT algorithm to mitigate inaccurate responses under fast-changing solar irradiance level. Solar Energy 2014;101:333–42. Elsevier.
[23] Liserre Marco, Blaabjerg Frede, Dell'Aquila Antanio. Step-by-step design procedure for grid-connected three phase PWM voltage source converter. Int J Electron 2004;91(8).
[24] Teodorescu R, Blaabjerg F, Borup U, Liserre M. A new control structure for grid-connected LCL PV inverters with zero steady-state error and selective harmonic compensation. In: Applied power electronics conference and exposition (APEC), ISBN 0-7803-8269-2; 2004.
[25] Mohan Ned, Undeland Tore M, Robbins William P. Power electronics converters, applications, and design. Wiley India Press Pvt. Ltd.; 2009. Third Edition, Reprint.
[26] Akagi Hirofumi, Watanabe Edson H, Aredes M. Instantaneous power theory and applications to power conditioning. IEEE Press-Wiley Press Pvt. Ltd.; 2007.
[27] IEEE Recommended Practices and Requirements for Harmonics Control in Electric Power Systems. IEEE Standard 519; 1992.

Appl Biochem Biotechnol (2014) 174:1092–1103
DOI 10.1007/s12010-014-0940-0

Effect of Nickel–Cobaltite Nanoparticles on Production and Thermostability of Cellulases from Newly Isolated Thermotolerant *Aspergillus fumigatus* NS (Class: Eurotiomycetes)

Neha Srivastava · Rekha Rawat · Reetika Sharma · Harinder Singh Oberoi · Manish Srivastava · Jay Singh

Received: 31 January 2014 / Accepted: 21 April 2014 /
Published online: 7 May 2014
© Springer Science+Business Media New York 2014

Abstract In the present study, effect of nickel–cobaltite ($NiCo_2O_4$) nanoparticles (NPs) was investigated on production and thermostability of the cellulase enzyme system using newly isolated thermotolerant *Aspergillus fumigatus* NS belonging to the class Euratiomycetes. The $NiCo_2O_4$ NPs were synthesized via hydrothermal method assisted by post-annealing treatment and characterized through X-ray diffraction (XRD) and transmission electron microscopy (TEM) techniques. In the absence of NPs in the growth medium, filter paper cellulase (FP) activity of 18 IU/gds was achieved after 96 h, whereas 40 % higher FP activity in 72 h was observed with the addition of 1 mM concentration of NPs in the growth medium. Maximum production of endoglucanase (211 IU/gds), β-glucosidase (301 IU/gds), and xylanase (803 IU/gds) was achieved after 72 h without NPs (control), while in the presence of 1 mM concentration of NPs, endoglucanase, β-glucosidase, and xylanase activity increased by about 49, 53, and 19.8 %, respectively, after 48 h of incubation, against control, indicating a substantial increase in cellulase productivity with the addition of $NiCo_2O_4$ NPs in the growth medium. Crude enzyme was thermally stable for 7 h at 80 °C in presence of NPs, as against 4 h at the same temperature for control samples. Significant increase in the activity and improved thermal stability of cellulases in the presence of the $NiCo_2O_4$ NPs holds potential for use of $NiCo_2O_4$ NPs during enzyme production as well as hydrolysis. From the standpoint of biofuel production, these results hold enormous significance.

N. Srivastava · R. Rawat · R. Sharma · H. S. Oberoi (✉)
Central Institute of Post-Harvest Engineering and Technology, P.O. PAU, Ludhiana 141 004 Punjab, India
e-mail: hari_manu@yahoo.com

M. Srivastava
Department of Biotechnology, Delhi Technological University, Shahabad Daulatpur, Main Bawana Road, Delhi 110042, India

J. Singh
Department of Applied Chemistry, Delhi Technological University, Shahbad Daulatpur, Main Bawana Road, Delhi 110042, India

Keywords *Aspergillus fumigatus* NS · Cellulases · Enzyme productivity · Eurotiomycetes · Nickel–cobalt oxide nanoparticles · Thermostability

Introduction

Cellulases find wide application in various fields, such as biofuel, detergent, and paper industries. Cellulases that bring about hydrolysis of cellulose comprise of three enzymes, namely endo-1,4-β-glucanase (also referred to as carboxymethylcellulase or CMCase; EC 3.2.1.4), exo-1,4-β-glucanase or cellobiohydrolases (EC 3.2.1.91), and β-glucosidase (EC 3.2.1.21) that synergistically convert cellulose into soluble sugars and glucose [1]. Thermostable cellulases can be used at high temperatures leading to increased substrate solubility and higher reaction rates resulting in high conversion of lignocellulosic biomass into fermentable sugars, essentially required for production of biofuels. Thermostable enzymes are stable at temperatures considerably higher than their optimum temperatures [2–4]. An enzyme or protein may be considered as thermostable if it maintains its half life at relatively higher temperatures for a longer time [5].

Fungi and bacteria are the most extensively studied microorganisms for the production of cellulolytic enzymes and degradation of cellulose. However, fungi are preferred over bacteria because of their high production potential and good penetrating ability [6]. Fungi belonging to the class Eurotiomycetes are well known for the production of useful secondary metabolites and enzymes [7]. Eurotiomycetes include morphologically and ecologically diverse group of fungi, and because of their broad importance in basic research, industry, and public health, several studies have started focusing on this fungal species [8]. However, to the best of our knowledge, fungi belonging to the class Eurotiomycetes have not yet been studied or exploited for the production of cellulolytic enzymes.

Presently, cellulases contribute to about 20 % of the world's enzymes market [9] and account for about 40 % of the total cost during ethanol production from cellulosic biomass [10]. High production cost and low production yields are the major bottlenecks for industrial applications of these enzymes [11]. Protein adsorption on nanomaterials can lead to enhanced activity and significant improvements in thermal stabilities of the enzymes [12, 13]. Nanoparticles have many properties which include large surface-to-volume ratio, high surface reaction activity, and high catalytic efficiency as well as strong adsorption capacity [14, 15]. Enzyme stability can be improved with support of nanoscaled and feasible modulation of the catalytic specificity [16]. Nickel–cobaltite ($NiCo_2O_4$) nanoparticles (NPs) are compounds which can be prepared in a nano-form that is apparently nontoxic. Among the various available metal oxides, $NiCo_2O_4$ is known as a low-cost environment-friendly transition metal oxide [17]. The electronic conductivity of $NiCo_2O_4$ is comparatively higher than those of nickel oxide and cobalt oxide. Nickel and cobalt ions are the important components of microbial media and play a crucial role in growth and production of microbial enzymes [18]. Therefore, the current study was focused on the synthesis of nickel–cobaltite ($NiCo_2O_4$) NPs, their characterization, and evaluating the effect of these NPs on cellulase production and thermostability of cellulase enzyme for its potential applications in different industries.

Materials and Methods

Materials

All the analytical chemicals, media components, and reagents used in the present study were purchased from Fisher Scientific (Mumbai, India) and HiMedia Laboratories Pvt Ltd (Mumbai, India). Aqueous ammonia solutions, cobalt nitrate (II) hex-hydrate [$Co(NO_3)_26H_2O$] and nickel nitrate (III) hexahydrate [Ni $(NO_3)_2{\cdot}6H_2O$], were procured from Sigma-Aldrich (St. Louis, MO, USA.). Rice straw of variety PR-127 was procured from the research fields of Punjab Agricultural University (PAU), Ludhiana, Punjab, India. Rice straw was dried, cut into small pieces with chaff cutter, and ground into smaller particles of about 2 mm each and used as substrate for solid-state fermentation. Wheat bran was procured from the local flour mill.

Synthesis of Nickel–Cobaltite Nanoparticles

Nickel–cobaltite ($NiCo_2O_4$) NPs were synthesized by hydrothermal-assisted post-calcination process. The synthesis procedure involved the following steps: 1 mmol of Ni $(NO_3)_2{\cdot}6H_2O$ and 2 mmol of Co $(NO_3)_2{\cdot}6H_2O$ were prepared by mixing solution of distilled water (H_2O) and ethanol [H_2O: ethanol (1:1)]. The solutions of metal precursors were mixed together and stirred vigorously. Subsequently, 25 % aqueous solution of ammonia was gradually mixed to maintain the pH ~10 of the solution. The prepared solution was transferred to a 50-ml Teflon vessel for hydrothermal treatment. The reaction was carried out at 160 °C for 30 h. After the completion of reaction, the hydrothermal reactor was allowed to cool down to room temperature. The product was filtered and washed several times with deionized (DI) water and ethanol was dried at 60 °C under vacuum. The product thus obtained was further calcined at 400 °C for 2 h to obtain $NiCo_2O_4$ NPs.

Characterizations of the $NiCo_2O_4$ Nanoparticles

Phase formation and crystalline feature of the synthesized sample was investigated by powder X-ray diffraction (XRD) using a Philips X'Pert Pro-diffractometer, consisting of CuKa radiation (λ=1.54060 Å). The surface morphology of the sample was probed through the field emission scanning electron microscope (FE-SEM) SIRIDN 2000, whereas the size and shape of the synthesized nanoparticles were studied by high-resolution transmission electron microscope (HR-TEM) Tecnai F30.

Isolation and Screening of the Fungal Isolates

Compost sample was collected from PAU, Ludhiana, India. The sample was aseptically transferred to the 250-ml Erlenmeyer flask containing 50 ml sterile distilled water. The flask was vortexed vigorously for 15 min on a vortex shaker. Fungi were isolated by serial dilution method using sterilized Rose-Bengal Chloramphenicol (RBC) agar medium plates. As the major objective of this study was to isolate thermotolerant/thermophilic fungal strains, the plates were incubated at 45 °C in an environment chamber having controls for temperature and relative humidity (RH) for 4 to 6 days and were observed regularly for colony development. Different colonies based on their morphological features, color of spores, and colony characteristics were picked, and pure fungal isolates were obtained by successive subculturing of

these colonies on the fresh potato dextrose agar (PDA) medium plates. Stock cultures were preserved at 4 °C on PDA slants in a refrigerator for further identification and characterization. Further, inoculum from the culture tubes of each of the isolate was transferred to carboxymethycellulose (CMC) agar medium. The plates were incubated at 45 °C for 48 h and were flooded with Gram's iodine for 5 min. Production of extracellular cellulase by the organisms was indicated by the zone of clearance around the colony [19]. Cellulolytic index (CI) was determined and expressed as the ratio between the diameter of the degradation halo and the diameter of the colony.

Effect of $NiCo_2O_4$ Nanoparticles on Cellulase Production

Solid-state fermentation was carried out in 250-ml Erlenmeyer flasks using rice straw and wheat bran (4:1) as substrate. In order to determine the effect of NPs on cellulase production, the medium was supplemented with different concentrations (0.5–3.0 mM) of $NiCo_2O_4$ NPs. The medium without NPs was treated as control. Moisture content of 70 % was made up with the Mandel Weber (MW) medium. Initial pH of the medium was adjusted to 4.8. Flasks were autoclave-sterilized, cooled, and subsequently inoculated with 10 % of spore suspension containing 10^7 spores/ml and incubated at 45 °C for 120 h. After cultivation of the fungal isolate in the fermentation medium, 50 ml sodium citrate buffer (pH 4.8) was added and the cultures were shaken for 30 min on a vortex shaker and subsequently centrifuged at 5,000 rpm for 10 min at 4 °C. The culture supernatant thus obtained after centrifugation was directly used for enzyme assays.

Molecular Identification of the Screened Fungal Isolate

For molecular identification of the selected fungal strain, genomic DNA was extracted and used as a template for PCR amplification of the 28S rRNA gene. The PCR amplified products were then purified and subjected to sequence analysis. The similarity search for the sequence was carried out using the BLAST program of the National Center of Biotechnology Information (NCBI). Phylogenetic analysis was carried out by neighbor-joining method using MEGA software program [20].

Enzyme Assays

Filter paper cellulase (FP) and endoglucanase (EG) activity were determined by the method described previously [21]. β-Glucosidase (BGL) was assayed by the procedure reported previously [22], while xylanase activity was determined by the method of Saratale et al. [23]. Reducing sugar concentration was determined by using the dinitrosalicylic acid (DNS) method [24]. One unit (IU) of EG or FP activity was defined as the quantity of enzyme required to liberate 1 μmol of glucose per milliliter per minute from CMC and filter paper, respectively, under standard assay conditions. In case of xylanase activity, one unit of xylanase was defined as the amount of enzyme needed to liberate 1 μmol of xylose per milliliter per minute from birchwood xylan under standard assay condition. One unit of BGL was defined as the amount of enzyme liberating 1 μmol of *p*-nitrophenol (pNP) per milliliter per minute from *p*-nitrophenyl glucopyranoside. Protein concentration was estimated by Bradford method using bovine serum albumin (BSA) as a standard [25]. Specific activity was computed as the concentration of enzyme in the protein and reported as IU per milligram of protein.

Thermal Stability of Cellulases in Presence of Nanoparticles

In the present investigation, thermal stability evaluation was done on the basis of FP activity, as it measures the overall activity of multi-component enzyme complex for cellulose hydrolysis [26]. Effect of NPs on thermostability of enzyme was determined by incubating the crude enzyme at 60 to 80 °C for 2 h in presence of different concentrations (0.5 to 3.0 mM) of $NiCo_2O_4$ NPs. On the basis of results of these experiments, it was decided to conduct thermostability studies at 1.0 mM concentration of NPs for 0–8 h at 80 °C, discussed elsewhere in this paper. Crude enzyme solution without the NPs was treated as control. The control samples as well as the samples having NPs were evaluated for FP activity.

Statistical Analysis

All the experiments were carried out in triplicate, and the mean and standard deviation (SD) values were calculated using the Microsoft Excel program. The significance for the treatment means was determined with JMP 9.0 software (Statease Inc., MN, USA).

Results and Discussion

XRD Analysis of $NiCo_2O_4$ Nanoparticles

XRD pattern of the synthesized product is shown in Fig. 1. The XRD pattern showed six diffraction peaks corresponding to (220), (311), (400), (422), (511), and (440) planes of face-centered cubic spinal type structure of $NiCo_2O_4$ crystal. These diffraction peaks were well matched with (JCPDS-73-1702) [27]. The crystallite size of $NiCo_2O_4$ was calculated using the Debye–Scherrer equation and found to be ~30 nm [28].

FE-SEM and TEM Analysis of $NiCo_2O_4$ Nanoparticles

Figure 2a shows the FE-SEM image of the $NiCo_2O_4$ nanoparticles. It can be seen that that particles are well distributed over the entire region of the micrograph and possess the grain size

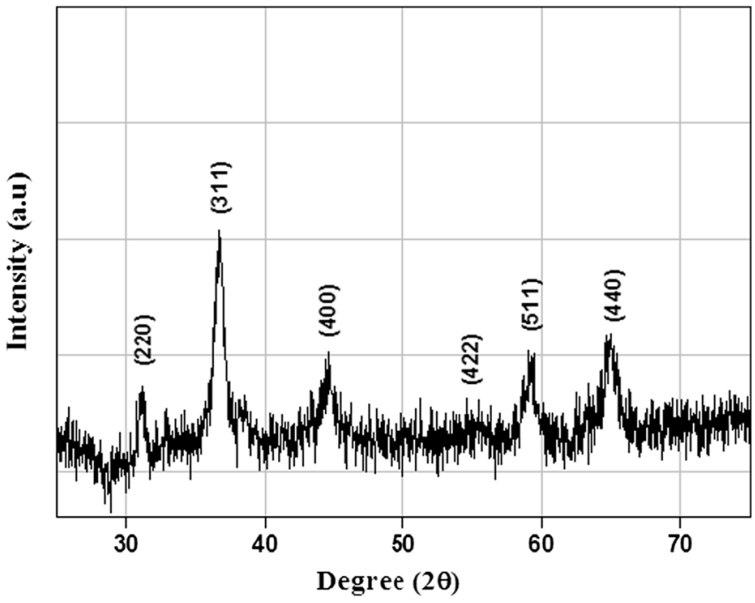

Fig. 1 XRD pattern of the synthesized nickel–cobaltite ($NiCo_2O_4$) NPs

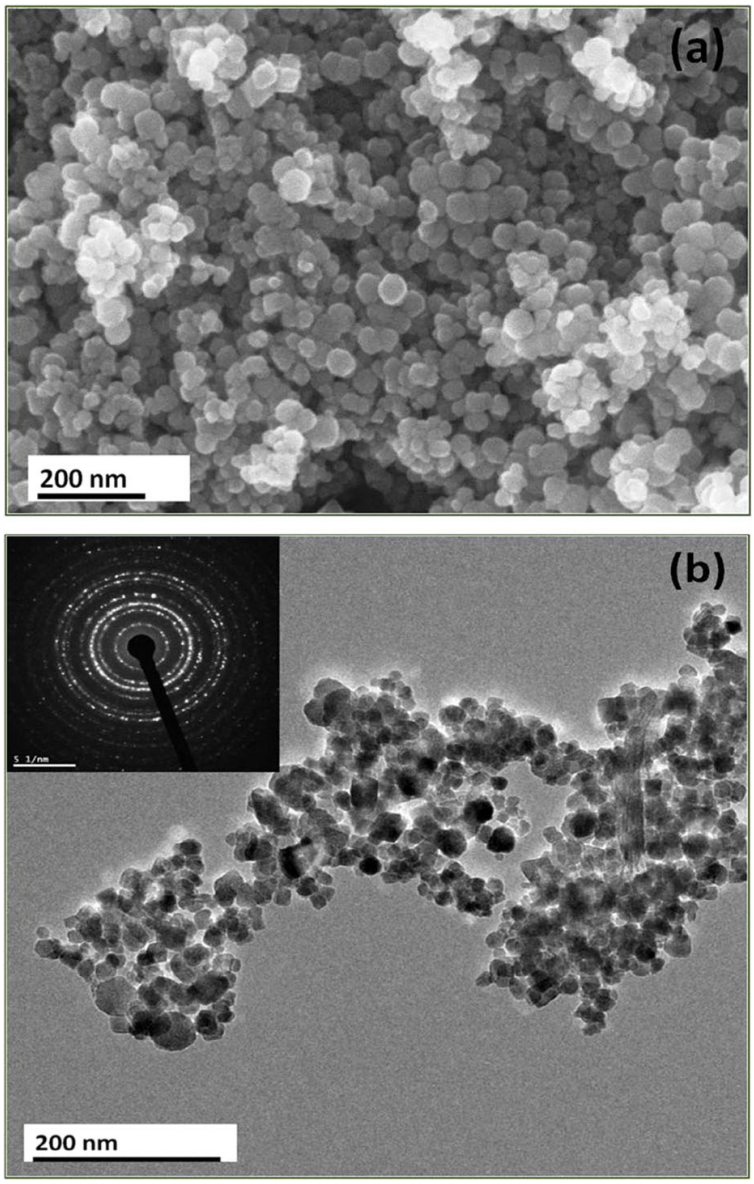

Fig. 2 FE-SEM micrograph of **a** $NiCo_2O_4$ and **b** TEM micrograph of $NiCo_2O_4$ [*inset* shows selected area electron diffraction pattern]

in the range of 20–35 nm. The particle size of $NiCo_2O_4$ was further investigated through transmission electron microscope (TEM). Figure 2b shows TEM image of the $NiCo_2O_4$ nanoparticles which indicates that the nanoparticles were spherically shaped. The size of the nanoparticles was found to be in the range of 10–35 nm. In addition, the selected area electron diffraction (SAED) pattern [inset of Fig. 2b] shows a series of diffraction rings suggesting polycrystalline nature of the $NiCo_2O_4$ NPs [29].

Isolation and Identification of Cellulolytic Strain

Among the various fungal strains isolated from compost sample, four isolates that showed cellulolytic index ≥2 were selected and further evaluated for their enzyme production potential through solid-state fermentation (SSF). Among the four isolates, the isolate NS showed significantly higher enzyme activities as compared to other strains, and therefore, it was selected for further studies. The identity of the isolate NS was confirmed through molecular characterization. The 28S ribosomal DNA (rDNA) sequence of isolate NS was obtained and submitted to GenBank under accession no. KF 359928. Phylogenetic analysis based on BLAST search using 28S rDNA sequence showed that the strain exhibited maximum homology (100 %) with

Aspergillus fumigatus strain LCF20 with accession no. FJ867935.1. On the basis of the cladistic analysis and homology assessment, it was inferred that the selected isolate could henceforth be considered as *A. fumigatus* NS belonging to the class Eurotiomycetes. The class Eurotiomycetes is further divided into two subcategories including classified Eurotiomycetes and the unclassified Eurotiomycetes (NCBI database). Eurotiomycetes includes species of *Aspergillus* for which a sexual phase of reproduction has been identified.

Effect of $NiCo_2O_4$ Nanoparticles on Production of Cellulases

In order to evaluate the effect of $NiCo_2O_4$ NPs on the production of cellulases, different concentrations of $NiCo_2O_4$ NPs were used in the production medium. Nickel–cobaltite NPs used in the present study were not stabilized with surfactants or any other protective coatings and were as such added in production medium. It is clear from Fig. 3 that FP activity increased in the presence of NPs in the medium as compared to control and the maximum FP production was obtained at 1.0 mM concentration of NPs. In the absence of NPs, *A. fumigatus* NS produced FP of 18 IU/gds after 96 h, whereas it produced 40 % higher FP after 72 h in the presence of 1.0 mM NPs in the growth medium. Specific activity of NP-treated cellulase was also found to be significantly higher than the control sample (Fig. 4). However, production of cellulases decreased as the concentration of NPs increased beyond 1.0 mM and the enzyme activity reduced by about 20 % at 3.0 mM concentration of NPs in the growth medium. A decrease in enzyme activity with further increase in the concentration of NPs could be due to the lethal effect of metals at higher concentration which might have a detrimental effect on the living cells. Therefore, it was decided to carry out the enzyme assays for EG, BGL, and xylanase in addition to FP for the enzyme produced in control samples as well as in the presence of 1.0 mM NPs in the growth medium. It was observed that maximum production of EG (211 IU/gds), BGL (301 IU/gds), and xylanase (803 IU/gds) was achieved after 72 h of incubation in the absence of NPs (Fig. 5). On the other hand, EG, BGL, and xylanase activities were higher by about 49, 53, and 19.8 %, respectively, in the presence of 1.0 mM NPs after 48 h of incubation against control. Fall in enzyme production after reaching its maximum level could be due to the organism entering stationary phase of growth, depletion of the nutrients,

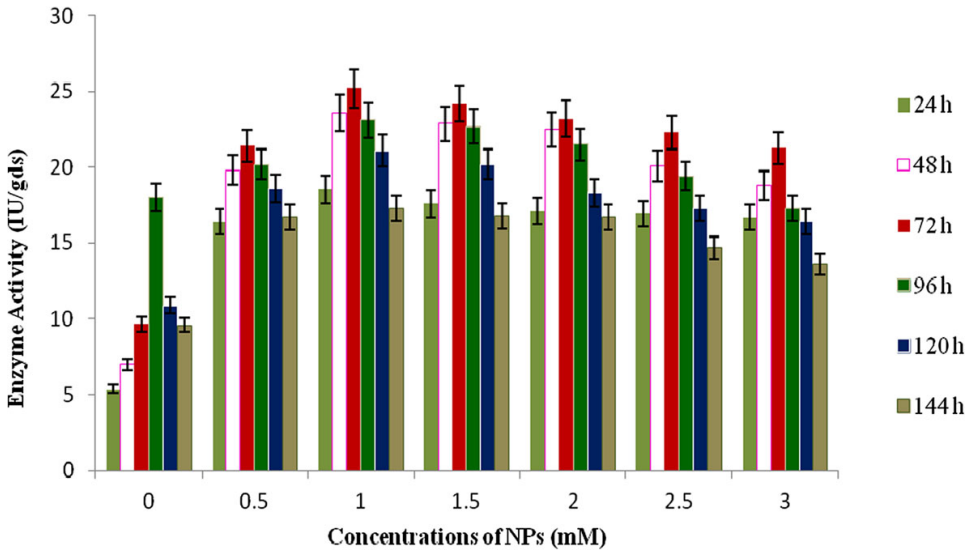

Fig. 3 Filter paper cellulase activity (FP) at different concentrations of $NiCo_2O_4$ NPs. LSD ($p<0.05$) value was 1.02, 1.01, 0.49, 0.70, 0.63, and 0.81 for FP activity at 0.5, 1.0, 1.5, 2.0, 2.5, and 3.0 mM concentration of NPs, respectively

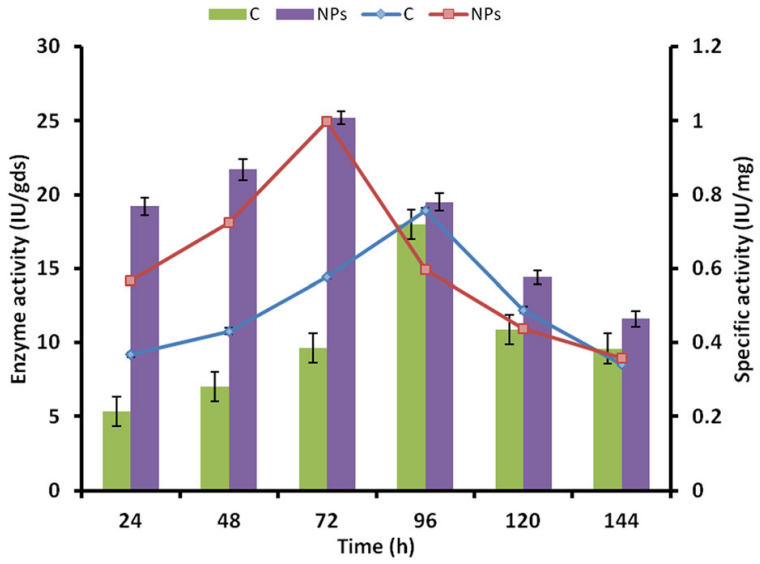

Fig. 4 Comparative evaluation of specific activity (IU/mg) and filter paper cellulase (FP) activity for the enzyme produced by *A. fumigatus* NS in the presence and absence of $NiCo_2O_4$ NPs in the growth medium. LSD ($p<0.05$) value was 0.012, 0.008, 1.002, and 1.000 for specific activity (control), specific activity (NPs), FP activity (control), and FP activity (NPs), respectively. *Bars* represent cellulase activity, while *lines* represent specific activity

and production of other by-products in the fermentation medium or combination of all of such factors. It is noteworthy to mention here that the incorporation of $NiCo_2O_4$ NPs in the medium not only led to higher cellulase production but also resulted in significant time saving, indicating a substantial increase in enzyme productivity as compared to control. As mentioned previously, large surface-to-volume ratio and high surface reaction activity associated with NPs could be the major reason for enhanced cellulase production and productivity in the

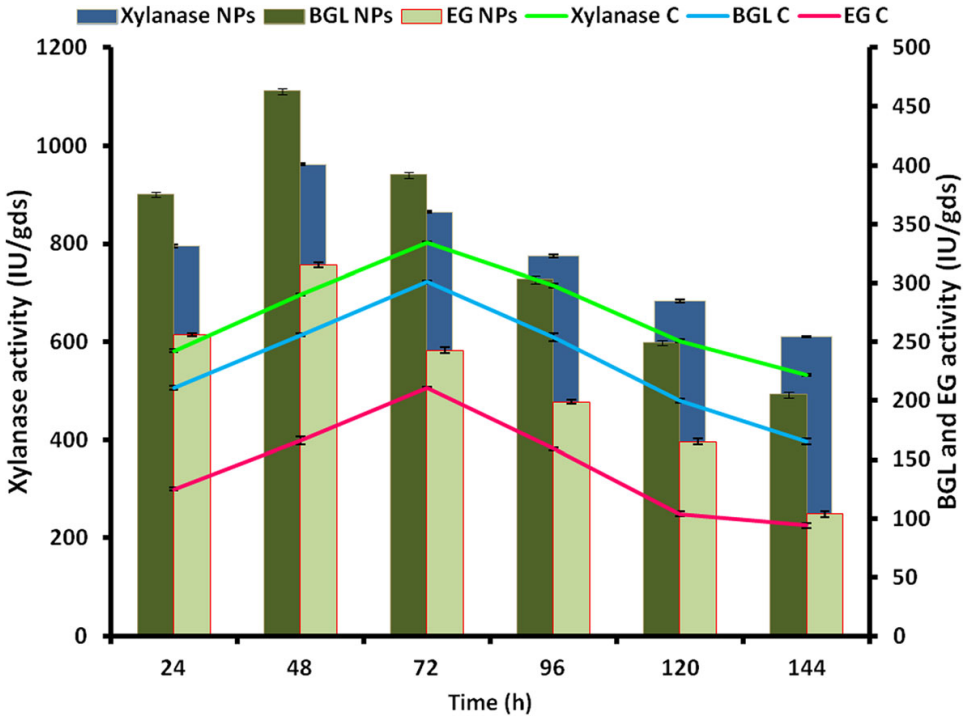

Fig. 5 Enzyme activities (IU/gds) for cellulase enzyme from *A. fumigatus* NS in the presence and absence of $NiCo_2O_4$ NPs. LSD ($p<0.05$) value was 3.68, 4.59, 3.68, 3.89, 4.19, and 4.21 for BGL (control), BGL (NPs), EG (control), EG (NPs), xylanase (control), and xylanase (NPs), respectively

presence of NPs. These results are significant as higher enzyme productivity is required for industrial biofuel production from cellulosic biomass.

Most of the cellulase-producing microorganisms show either inhibition or activation with different types of additives depending on the nature of the metals required [30]. Huang et al. [31] reported that supplementing specific metal ions in the medium increased the size and the amount of mycelium in white rot fungi, resulting in higher cellulase activity. Some other studies have also reported improved catalytic efficiency of cellulase when treated with nanoparticles [32, 33]. In a recent study, Mukhopadhyay et al. [34] reported that the production of pectate lyase enzyme increased by about 34.4 % in the presence of hydroxyapatite nanoparticles. In a study conducted by Shah et al. [35], production of BGL decreased in the presence of iron and copper nanoparticles, whereas in current investigation, enzyme activity significantly increased in the presence of $NiCo_2O_4$ NPs. In general, $NiCo_2O_4$ is regarded as a mixed metal oxide having spinal type crystal structure, where the nickel cation occupies octahedral sites, while the cobalt cations are distributed over the tetrahedral and octahedral sites in random order. The redox couples Ni^{+3}/Ni^{+2} and Co^{+3}/Co^{+2} found in the crystal structure provide effective electrocatalytic properties [36].

Effect of $NiCo_2O_4$ NPs on Thermostability of Cellulases

In the present study, thermostability characteristics of cellulases were tested at different temperatures in the presence of different concentrations of $NiCo_2O_4$ NPs up to 2 h. It is clear from Fig. 6 that the enzyme was stable at all the selected temperatures in the presence of 1.0 mM of $NiCo_2O_4$ NPs. At 60 °C, the enzyme retained about 74 % relative activity in control, while it could retain about 96 % activity in the presence of 1.0 mM NPs. However, further increase in concentration of NPs led to a fall in enzyme activity. Similar pattern was also obtained at temperatures of 70 and 80 °C, where enzyme stability increased from 69 to 87 % and 63 to 82 %, respectively, in the presence of 1 mM NPs, whereas in the presence of 3.0 mM NPs, the stability decreased to 53 and 42 %, respectively, as compared to control. The decrease in enzyme stability at higher concentration of NPs could be due to the nonsupportive interaction of NPs with the substrate. The stability of cellulase in presence of NPs at higher temperature could be because of the compositional differences in secondary structures (helix, sheet, and loop) of proteins which lead to differences in intramolecular interactions in a fold-dependent manner.

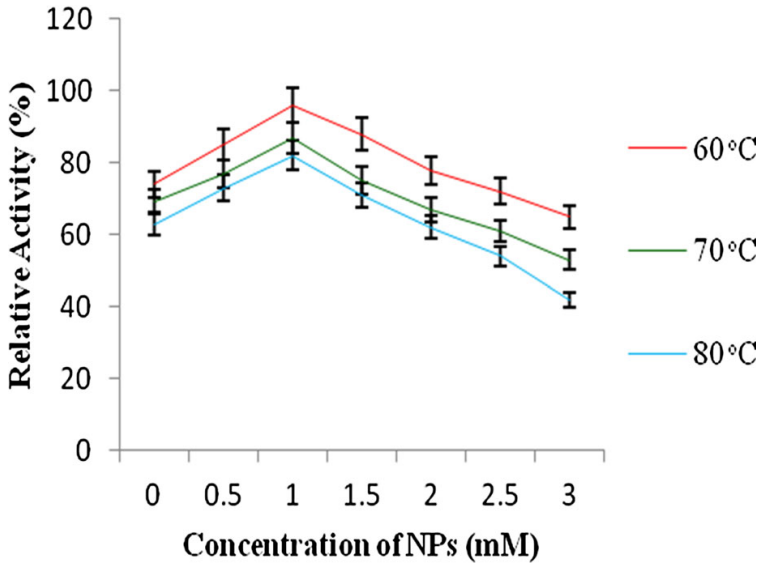

Fig. 6 Effect of temperature on thermostability of enzyme in presence of different concentrations of $NiCo_2O_4$ NPs (0.5–3.0 mM)

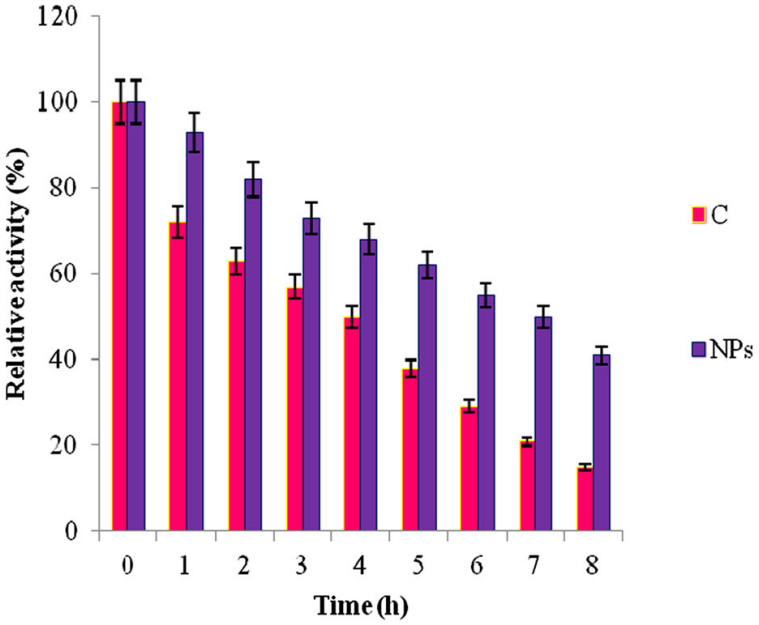

Fig. 7 Effect of temperature (80 °C) on thermostability of enzyme in the presence and absence of 1 mM $NiCo_2O_4$ NPs

Further, thermal stability of enzyme in the presence of 1.0 mM NPs and control samples were tested for 0–8 h at 80 °C. The results showed that at 80 °C, cellulase retained about 63 and 50 % of relative activity for 2 and 4 h, respectively, whereas the activity declined to 21 % after 7 h of incubation. On the other hand, cellulase in presence of NPs showed 68, 50, and 41 % higher stability after 4, 7, and 8 h of incubation, respectively, as compared to control at 80 °C (Fig. 7). These results clearly indicate that cellulase in presence of NPs showed enhanced stability at high temperatures compared to control. The use of enzymes for industrial purpose may require reactions to be conducted at high temperatures for a long time, such as in the case of processing of fibers in the textile industries [37]. It has been reported by Tao et al. [38] that under high temperatures, hydrolysis of cellulose occurs rapidly. Hegedus and Nagy [39] have also reported improved stability of cellulase in presence of NPs, as compared to control. Ang et al.[40] reported the half life of about 90 min for cellulase enzyme at 60 °C, while the cellulase used in current study showed a half life of 4 h which further increased to 7 h in the presence of $NiCo_2O_4$ NPs. In a study conducted by Mukhopadhyay et al. [34], effect of hydroxyapatite NPs on the thermal stability of pectate lyase was analyzed, but we are yet to come across any literature reporting the effect of $NiCo_2O_4$ NPs on thermostability of cellulases. These results clearly showed that cellulases in the presence of 1.0 mM $NiCo_2O_4$ NPs hold potential for efficient hydrolysis of cellulose at high temperatures. The nanoparticle-mediated retention of relative enzyme activity at elevated temperature indicates interaction of the nanoparticle with the enzyme active site. The rationale behind the effectiveness of $NiCo_2O_4$ NPs in stabilizing the activity as compared to the ionic Ni, Co metals needs further investigation at molecular levels. Additionally, catalytic activity can be enhanced by size reduction and uniform dispersion of the nanoparticles, which can provide high surface area, thereby resulting in an increase in the reaction rate of enzyme and substrate [17].

Conclusion

The results obtained in the current study illustrate that the presence of characterized $NiCo_2O_4$ NPs in the growth medium have a significant positive influence on cellulase production by newly isolated *A. fumigatus* NS. In addition, the enzyme in the presence of 1.0 mM $NiCo_2O_4$

NPs showed a much higher thermostability as compared to control (without NPs), in the buffer. This indicates a specific role of the $NiCo_2O_4$ NPs in promoting and maintaining the activation of both the catalytic and structural features of the enzyme in addition to the improved production of the enzyme. The cost-effective production of enzyme using inexpensive substrates along with improved thermostability indicates significant potential of these NPs and nanoparticles–cellulase system in production of sugars from the lignocellulosic biomass which could be subsequently fermented to bioethanol and biohydrogen.

Acknowledgments Authors Neha Srivastava, Rekha Rawat, Reetika Sharma, and Harinder Singh Oberoi thankfully acknowledge the financial assistance received from the AMAAS subproject funded by the Indian Council of Agricultural Research, Government of India for conducting this study. Author Jai Singh acknowledges the Department of Science & Technology, Government of India for awarding the DST-INSPIRE Fellowship [IFA-13 CH-105] 2013 and DST Young Scientist award (CS-393/2012).

References

1. Lynd, L. R., Weimer, P. J., Vanzyl, W. H., & Pretorious, I. S. (2002). *Microbiology and Molecular Biology Reviews, 66*, 506–577.
2. Saboto, D., Nucci, R., Rossi, M., Gryczynski, I., Gryczyniski, Z., & Lakowicz, J. (1999). *Biophyshysical Chemistry, 81*, 23–31.
3. Demirijan, D., Moris-Varas, F., & Cassidy, C. (2001). *Current Opinion in Chemical Biology, 5*, 144–151.
4. Haki, G. D., & Rakshit, S. K. (2003). *Bioresource Technology, 89*, 17–34.
5. Turner, P., Mamo, G., & Karlsson, E. N. (2007). *Microbial Cell Factories, 6*, 9. doi:10.1185/1475-2859-6-9.
6. Swaroopa, R. D., Thirumale, S., & Nand, K. (2004). *Biotechnology, 20*, 629–632.
7. Liu, Y. J., & Hall, B. D. (2004). *Proceedings of National Academy Sciences USA, 101*, 4507–4512.
8. Geiser, D. M., Gueiden, C., Miadlikowska, J., Lutzoni, F., Kauff, F., Hofstetter, V., et al. (2006). *Mycologia, 98*, 1053–1064.
9. Polizeli, M., Rizzatti, A., Monti, R., Terenzi, H., Jorge, J., & Amorim, D. (2005). *Applied and Microbiology Biotechnology, 67*, 577–5791.
10. Solomon, B. D., Barnes, J. R., & Halvorsen, K. E. (2007). *Biomass and Bioenergy, 6*, 416–425.
11. Kang, S., Park, Y., Lee, J., Hong, S., & Kim, S. (2004). *Bioresource Technology, 91*, 153–156.
12. Lynch, I., & Dawson, K. A. (2008). *Nanotoday, 3*, 40–47.
13. Chronopoulou, L., Kamel, G., Sparago, C., Bordi, F., Lupi, S., Diociaiutic, M., et al. (2011). *Soft Material, 7*, 2653–2662.
14. Pendry. (1999). *Science, 285*, 1687–1688.
15. Hudson, S. D., Jung, H. T., Percec, V., Johansson, W. D., Cho, G., & Balagurusamy, K. (1997). *Science, 278*, 449–452.
16. Konwarh, R., Karak, N., Rai, S. K., & Mukherjee, A. K. (2009). *Nanotechnology, 20*, 225107–225117.
17. Srivastava, M., Uddin, M. E., Singh, J., Kim, N. H., & Lee, J. E. (2014). *Journal of Alloys and Compounds, 590*, 266–276.
18. Mandels, M., & Weber, J. (1969). *Advances in Chemistry, 95*, 391–414.
19. Kasana, R. C., Salwan, R., Dhar, H., Dutt, S., & Gulati, A. (2008). *Current Microbiology, 57*, 503–507.
20. Tamura, K., Dudley, J., Nei, M., & Kumar, S. (2007). *Molecular Biology and Evolution, 24*, 1596–1599.
21. Ghosh, T. (1987). *Pure and Applied Chemistry, 59*, 257–268.
22. Kubicek, C. P. (1982). *Archives Microbiology, 132*, 349–354.
23. Saratale, G. D., Saratale, R. G., Lo, Y. C., & Chang, J. S. (2010). *Biotechnology Progress, 26*, 406–416.
24. Miller, G. L. (1959). *Analytical Chemistry, 31*, 426–428.
25. Bradford, M. M. (1976). *Analytical Biochemistry, 72*, 248–254.
26. Teeri, T. T. (1997). *Trends in Biotechnology, 15*, 160–167.
27. Ding, R., Qi, L., & Wang, H. (2012). *Journal of Solid State Electrochemistry, 16*, 3621–3633.
28. Monshi, A., Foroughi, M. R., & Monshi, M. R. (2012). *World Journal of Nano Science and Engineering, 2*, 154–160.
29. Srivastava, M., Ojha, A. K., Chaubey, S., & Singh, J. (2010). *Journal of Solid State Chemistry, 183*, 2669–2674.

30. Christakopoulos, P., Goodenough, P. W., Kekos, D., Macris, B. J., Claeyssens, M., & Bhat, M. K. (1994). *European Journal of Biochemistry, 224*, 379–385.
31. Huang, L. D., Zheng, G. M., Feng, C. L., Hu, S., Zhao, M. H., Lai, C., et al. (2010). *Journal of Chemosphere, 81*, 1091–1097.
32. Lupoi, J. S., & Smith, E. A. (2011). *Biotechnology Bioengineering, 108*, 2835–2843.
33. Blanchette, C., Lacayo, C. I., Fischer, N. O., Hwang, M., & Thelen, M. P. (2012). *Public Library of Science One, 7*, e42116. doi:10.1371/journal.pone.0042116.
34. Mukhopadhyay, A., Dasgupta, A. K., Chattopadhyay, D., & Chakrabarti, K. (2012). *Bioresource Technology, 116*, 348–354.
35. Shah, V., & Nerud, F. (2002). *Canadian Journal of Microbiology, 48*, 857–870.
36. Wei, T. Y., Chen, C. H., Chien, H. C., Lu, S. Y., & Hu, C. C. (2010). *Advanced Material, 22*, 347–351.
37. Rombouts, F. M., & Pilnik, W. (1986). *Symbiosis, 2*, 79–90.
38. Tao, M. Y., Xu, Q. X., Liang, S. M., Jaun, G., Bing, X. W., Long, M. N., et al. (2011). *Journal of Agriculture and Food Chemistry, 59*, 10971–10975.
39. Hegedus, I., & Nagy, E. (2009). *Hungarian Journal of Industrial Chemistry Veszprem, 37*, 123–130.
40. Ang, S. K., Shaza, E. M., Adibah, Y., Suraini, A., & Madihah, M. S. (2013). *Process Biochemistry, 48*, 1293–1302.

Int J Adv Manuf Technol
DOI 10.1007/s00170-015-6806-y

ORIGINAL ARTICLE

Electrochemical-aided abrasive flow machining (ECA^2FM) process: a hybrid machining process

B. S. Brar · R. S. Walia · V. P. Singh

Received: 5 March 2013 / Accepted: 18 January 2015
© Springer-Verlag London 2015

Abstract Abrasive flow machining is a fine finishing process, mainly for the finishing of complex internal/external surfaces of metallic parts. Like most of the finishing processes, this process is also a slow process due to low material removal rate. Hybridization of abrasive flow machining process (AFM) with other non-conventional machining (NCM) processes is being explored in the recent times, so as to overcome the main limitation of low material removal in the AFM process and to satisfy the stringent finish/functional requirements. The present study is about the development of a novel hybrid of electrochemical machining (ECM) and abrasive flow machining (AFM), for the fine finishing of internal holes or prismatic recesses. The new process has been termed as electrochemical-aided abrasive flow machining (ECA^2FM) process, and higher abrasion of the material was observed in this process due to the synergetic effect of ECM and AFM processes. Further in the present investigation, the various process parameters have been optimized for the response characteristic of material removal, based on Taguchi method and using standard L_{27} orthogonal array (OA) for the plan of experimentation. Overall, the ECA^2FM process has a very promising future in the industries in terms of its ability to finish fast even if the component is thin/delicate and made of hard alloys.

B. S. Brar · V. P. Singh
PEC University of Technology, Chandigarh, India

B. S. Brar
e-mail: brarbalraj@yahoo.com

V. P. Singh
e-mail: vps_pec@yahoo.co.in

R. S. Walia (✉)
Delhi Technological University, Delhi, India
e-mail: waliaravinder@yahoo.com

Keywords Abrasive flow machining (AFM) · Electrochemical machining (ECM) · Electrochemical-aided abrasive flow machining (ECA^2FM) · Hybrid machining process (HMP) · Optimization

1 Introduction

The modern world is more concerned about the quality of a product, so there are stringent requirements of developing fine finished products of complex shapes with varied operational functionalities. A fine finished part has better aesthetics, life, and functional performance due to its high polish, close dimensional controls and strength endurance. Finishing operations are labour intensive, least controllable and cost approximately 15 % of the total machining cost in the manufacture of precision parts [1]. The traditional finishing methods of grinding, lapping, honing and super finishing are good for the simple surface geometries but are found lacking in the fine finishing of intricate/hard surfaces. For the aforementioned finishing challenges, abrasive flow machining (AFM) process is a suitable candidate. This non-traditional polishing process is also termed as abrasive flow finishing (AFF) process [2], mainly due to a small quantity of material removal during the fine finishing of metallic components. AFM or AFF process was originally identified for deburring and finishing critical hydraulic and fuel system components of aircraft in aerospace industries. It can polish anywhere that air, liquid or fuel flows [2]. In this process, a self-deforming abrasive laden semi-liquid paste (made up of viscoelastic polymer, gel and abrasive particles) is extruded (by employing two vertically opposed hydraulic actuators) through a controlled passage over the surface to be polished. Machining action occurs due to the abrasion of the required surface by a large number of

Published online: 04 February 2015

randomly oriented cutting points of the abrasives during the extrusion of abrasive laden media through the restrictive passage formed by the work-piece and the tooling. This process is mainly suitable for the fine finishing of intricate/or internal cavities/holes/slots and is sometimes preferred for the simultaneous polishing of a number of fine slots.

Hybrid machining processes (HMPs) are in vogue in the latest manufacturing practices in order to meet the challenges of high surface quality and tolerance requirements, often coupled with high production rates of parts having complex shapes and contours [3] and for the finishing of hard materials. Towards the development of hybrid AFM processes, researchers have successfully integrated AFM with a number of non-conventional machining processes to achieve the higher material removal (low material removal is a limitation of the AFM process) and to produce better polished surfaces in a faster way.

Jones and Hull developed ultrasonic flow polishing (UFP) process and used an ultrasonically energized tool along with the abrasive laden media flow for the polishing of complex dies and moulds and observed 10 times improvement [4]. Magnetic-assisted abrasive flow machining (MAAFM) process was successfully developed by Singh and Shan [5] to achieve more number of active grains due to the magnetic assistance than in AFM alone. The magnetic action was attained by mixing the polymer base with ferromagnetic material, resulting in the desired rheology of the abrasive laden media along with magnetic forces on the iron particles. Walia et al. developed centrifugal force-assisted AFM (CFAAFM) process by simultaneously rotating the extruding AFM media employing different shaped rods and observed intensive abrasive action [1, 6–9]. Singh and Walia further optimized the various parameters to achieve polished surfaces [10]. Sankar et al. developed drill bit-guided abrasive flow finishing (DBG-AFF) process, and employed drill bit in place of prismatic rods, for the simultaneous rotation of abrasive laden media and observed better results due to a combination of abrasive laden media flows leading to better mixings of media and thus more number of active grains [11]. Sankar et al. also developed rotational abrasive flow finishing (R-AFF) process. In this process, the cylindrical work-piece was rotated and it resulted in better surface finish due to the shearing of more number of peaks during the extrusion and also due to additional shearing forces [12]. Yan et al. [13] and Chen et al. [14] employed spiral screws in the micro polishing of cylindrical pipes. Brar et al. developed helical abrasive flow machining (HLX-AFM) process for the finishing of internal cylindrical surfaces. An improvement in the material removal and surface finish was observed with the use of a coaxially fixed helical twist drill bit during the abrasive flow machining process [15, 16]. Cherian observed that surface finish and fatigue life of a part improves with the AFM process [17].

Rajurkar et al. published that electrochemical machining (ECM) has been successfully hybridized with a number of conventional/non-conventional machining methods viz. grinding, electro discharge machining, abrading process, ultrasonic machining, turning, etc. [18]. Dubey et al. observed in electrochemical honing (ECH) of internal cylinders that a distinct coupling of electrochemical machining and honing actions provides controlled functional surface generation and fast material removal capabilities in a single operation [3]. Qadri and Sharma also got polished surfaces with a hybrid of ECM employing suspended abrasive powders [19].

Dabrowski et al. successfully experimented on the integration of ECM with the AFM and developed electrochemical aided AFM (ECAFM). It employed polymeric electrolytes for the finishing of flat work-pieces only. More material removal was observed in this process due to anodic dissolution at an atomic level along with the abrasion due to mechanical cutting by the abrasives. Dabrowski et al. used a number of electrolytic pastes for these experiments and observed more material removal with cyanide-based electrolytic pastes [20, 21].

This paper discusses about a novel method of integrating ECM with AFM for the fine finishing of the internal cavities/slots/or holes. The indigenous process has been termed as electrochemical-aided abrasive flow machining (ECA^2FM) [22, 23]. Taguchi method has been used to study the effect of various process parameters on the material removal during the machining and for further parametric optimization. The Taguchi method helps in developing robust products and manufacturing systems that are insensitive to daily and seasonal variations of environment, machining wear, etc. and is widely used in engineering analysis to design high-quality systems [3, 24–26].

Like the general AFM, this process is suitable for the fine finishing of work-pieces with through internal holes/slots or cavities having the prismatic sections, for the faster finishing of hard alloys, removal of burrs and rounding of the slot edges and may find applications in medical technology, hydraulic and pneumatic components, automobile, space and aeronautics industry [23]. Large surface irregularities, such as deep scratches or bumps, cannot be removed by the AFM because the material is removed equally from all surfaces; so for the same reason, imperfections such as out-of-roundness, form errors and taper can be corrected by the developed ECA^2FM process. Moreover, heat damage in the laser/EDM machined parts can be removed and fragile parts can be finished at the low extrusion pressures due to additional ECM aid in this process. The developed process should also be able to improve the fatigue strength of the part as is usually achieved by AFM process [17].

2 Experimentation

2.1 ECA^{2}FM process

ECA^{2}FM process is a hybrid of ECM and AFM and is suitable for prismatic through holes or cavities. It is mentioned that Dabrowski et al. also studied the electrochemical aid along with the AFM for the fine finishing of flat surfaces only and achieved more material removal [20, 21]. Since the AFM finds its main applicability in the finishing of internal contours, so the developed ECA^{2}FM process is to address such finishing requirements. In this process, ECM action of anodic dissolution of the material is achieved in concurrence with the main action of abrasion of the work-piece material due to the cutting action of the abrasives while the electrolyte-abrasive laden media is being extruded back and forth through the gap between the prismatic cathode rod and the internal surface of anode work-piece. To achieve this, a low-voltage direct current (DC) potential is applied across the electrolyte-abrasive laden media flooded gap between the cathode prismatic rod and the hollow anodic work-piece. The gap between the cathode rod and the inner surface of the anodic work-piece governs the electrochemical machining process. A schematic diagram of the ECA^{2}FM process is shown in Fig. 1.

The schematic shows that a hollow cylindrical (or any hollow prismatic work-piece) is held with the necessary tooling made of nylon. The two halves of the nylon fixture hold the work-piece tightly, and the assembled nylon tooling acts as an interface between the two opposing media cylinders for the extrusion of the AFM media from one cylinder to the other as the abrasive laden media is abrading the internal surface of the work-piece. The necessary working pressure in the media is attained by maintaining a lower pressure (termed as the extrusion pressure in the AFM process) in the opposing cylinder while the active cylinder is pushing the media at a higher pressure. The improved fixture for ECA^{2}FM process is electrically insulating and has a provision of holding a copper cathode rod (of any prismatic shape in the corresponding shaped internal slot) along the axis of the work-piece. Further, the two electrodes are connected to the DC supply with copper connections while the suitable media is extruded by the hydraulic system. The fixture for the ECA^{2}FM process can be modified to hold the varied shaped prismatic work-pieces and corresponding electrodes for the finishing of internal as well as the external surfaces. The AFM media is suitably modified for the ECA^{2}FM process by adding electrolyte salts to it. The developed electrolyte-abrasive laden media has limited ECM action due to lower ion conductivity, less contact time between the electrolyte and electrodes, low ion diffusion ratio and no possibility of selecting between the anion and cation share in the charge transport process [21].

High-pressure extrusion of a viscous AFM media (in AFM process) through the constrictive cross-sections leads to a local elevation of the media temperature due to considerable changes in the condition of flow as a result of friction [20]. It further results in lower viscosity and productivity of the paste, and hence, AFM setup requires cooling mechanism for the cooling of the media whereas a low viscosity media is less effective in abrasive machining. In the ECA^{2}FM process, a low viscosity electrolyte-abrasive laden media can be extruded at low extrusion pressure so that there is no need to cool down the media. The presence of electrode in the passage of the media also helps in increasing the reduction ratio for a given work-piece geometry compared to conventional AFM process.

2.2 Experimental setup

The hybrid ECA^{2}FM process setup has been developed on the basic platform of an existing AFM setup in the Modern Manufacturing Laboratory at PEC University of Technology, Chandigarh, India [26] (Fig. 2). The AFM action part is achieved due to the back and forth

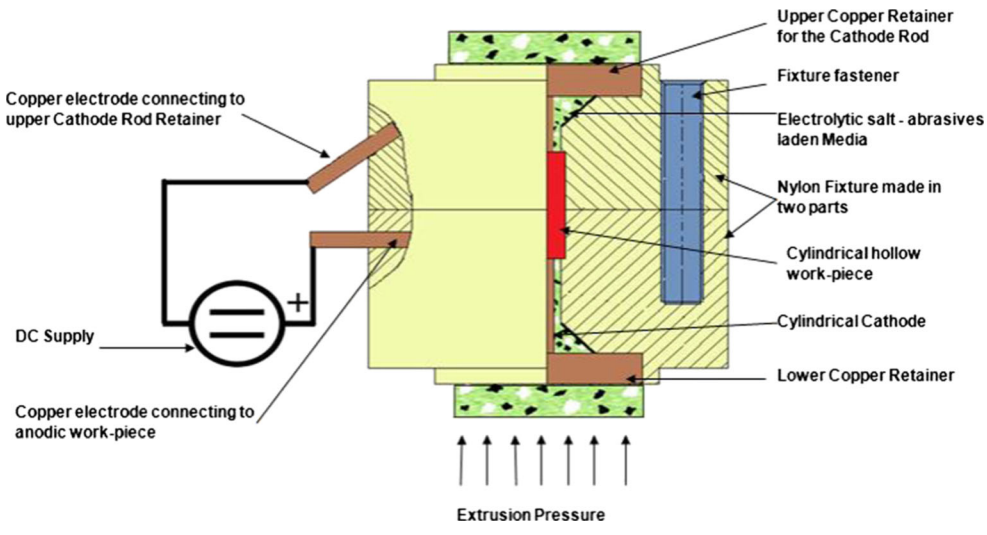

Fig. 1 Schematic of ECA^{2}FM process

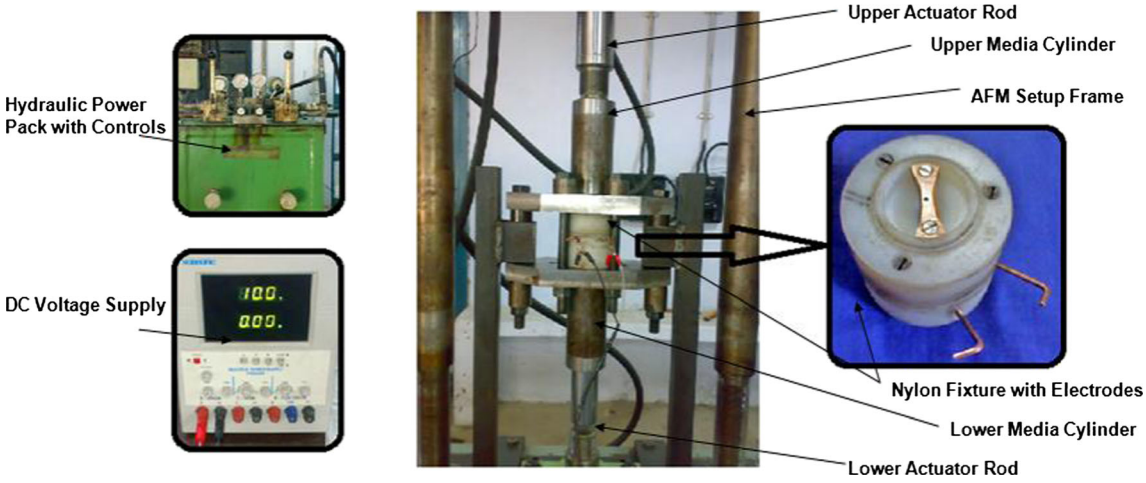

Fig. 2 Photograph of the ECA^{2}FM setup with the nylon fixture

extrusion of the electrolyte-abrasive laden media through the gap between the cathode rod and anode work-piece. This extrusion is controlled by a hydraulic system already developed for the basic AFM setup. A combination of one upward and downward stroke completes a cycle of AFM process. To achieve the electrolytic machining along with the abrasive cutting action, the necessary nylon fixture has been developed (Figs. 1 and 2). The modified nylon fixture is made in two parts and axially holds a cylindrical rod of copper inside the tightly held hollow cylindrical work-piece with the help of necessary retainers and fasteners. The axial cathode rod is supported at the two ends by two copper retainers in such a way that there is no hindrance in the media flow/sealing. In the nylon fixture, two copper electrodes are fitted in such a way that one electrode (cathode) is in contact with the axial copper rod through one of the rod retainers and is connected to the negative terminal of the DC power supply. The other electrode (anode) is in contact with the firmly seated work-piece and is connecting it to the positive terminal of the DC power supply. A Scientech DC power supply with voltage range 0–30 V has been used to supply the DC current to the electrodes. For the present study, the suitable electrolytic salt-abrasive laden polymeric media was made by adding NaI salt (a weak alkali) and Al_2O_3 (as abrasives) to a blend of a silicon-based polymer (polyborosiloxane) and hydrocarbon gel. As the electrolytic salt-abrasive laden medium passes through the annular space between the stationary cathode rod and work-piece under a DC potential, both electrolytic machining and abrasion due to the abrasive's cutting action take place.

This developed ECA^{2}FM setup has the provision to conduct the experiments at varied levels of process parameters of extrusion pressure, media flow rate, media flow volume, stroke length and number of cycles and also to operate it at different voltages and current flow rates and has provision for controlling the electrolytic gap by using different sizes of prismatic cathode rods. A number of electrolytic salt-abrasive laden media can be developed by using a wide variety of salts at different concentrations. Even the strong cyanide-based electrolytic salts can be added for more vigorous electrolytic action under a strictly controlled environment as these are very poisonous [20, 21].

Table 1 Process parameters and their levels

Sr. no.	Symbol	Process parameters	Unit	Level 1	Level 2	Level 3
1	V	Voltage	Volt	Nil	7	15
2	M	Salt molal concentration	Molal	0.75	1	1.25
3	R	Diameter of cathode rod	mm	3.3	4.2	5.2
4	P	Extrusion pressure	N/mm^2	3	5	7
5	G	Abrasives grain size	Mesh size	100	150	200

Polymer-to-gel ratio, 1:1; abrasives-to-media concentration, 1.0; NaI salt concentration, 0.75–1.25 M (mole/kg); work-piece material, brass; abrasive type, Al_2O_3; mesh size, 100–200 (150–75 μm); media flow volume, 300 cm^3; reduction ratio, 0.95; temperature, 32±2 °C; initial surface roughness of work-piece, 1.58–1.62 μm (Ra); number of cycles, 10; media viscosity, 810 Pa.s

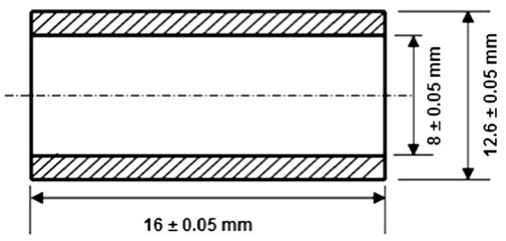

Fig. 3 Work-piece dimensions

2.3 Experimental details

The effect of various associated machining parameters on the machining characteristic of material removal (MR) was extensively investigated for ECA^{2}FM process.

2.3.1 Process parameters

Based on the parametric optimization of the developed basic AFM setup (using L_9 OA of Taguchi method) [26], pilot experimentation (using one-factor-at-a-time approach) [22, 23] for the developed ECA^{2}FM process setup and literature review [20, 21], five process parameters of voltage (*V*), salt molal concentration (*M*), diameter of cathode rod (*R*), extrusion pressure (*P*) and abrasives grain size (*G*) were selected for the experimentation. The three selected levels of the selected process parameters along with values of the fixed process parameters are given in Table 1.

2.3.2 Response parameter

Material removal (MR) had been selected as the response parameter. The material removal signifies the amount of material that has been removed (in mg) from a specimen in a specified number of process cycles. It was estimated by calculating the difference between initial weight of the specimen

Table 2 The L_{27} (3^{13}) OA (parameters assigned) with experimental results of response characteristic

Exp no.	Run order	Parameter trial conditions													Material removal (MR)			
		1	2	3	4	5	6	7	8	9	10	11	12	13	Raw data (mg)			*S*/*N* ratio (dB)
		V	*M*	VxM		*R*	VxR		MxR	*P*	*G*	MxR	*e*	*e*	R_1	R_2	R_3	
1	3	1	1	1	1	1	1	1	1	1	1	1	1	1	6.2	7.5	6	16.224
2	11	1	1	1	1	2	2	2	2	2	2	2	2	2	9.8	8.8	9.2	19.313
3	21	1	1	1	1	3	3	3	3	3	3	3	3	3	11.5	12.3	11	21.262
4	15	1	2	2	2	1	1	1	2	2	2	3	3	3	8.9	8.1	9.1	18.757
5	23	1	2	2	2	2	2	2	3	3	3	1	1	1	9.9	10.1	10.6	20.161
6	5	1	2	2	2	3	3	3	1	1	1	2	2	2	9.5	9	8.7	19.132
7	27	1	3	3	3	1	1	1	3	3	3	2	2	2	9.4	9.1	10.4	19.634
8	8	1	3	3	3	2	2	2	1	1	1	3	3	3	7.1	6.2	7.2	16.633
9	17	1	3	3	3	3	3	3	2	2	2	1	1	1	12.4	11.8	11.3	21.443
10	20	2	1	2	3	1	2	3	1	2	3	1	2	3	5.8	6.7	6	15.752
11	2	2	1	2	3	2	3	1	2	3	1	2	3	1	11.6	13.4	12.3	21.846
12	10	2	1	2	3	3	1	2	3	1	2	3	1	2	10.9	9.7	9.4	19.948
13	4	2	2	3	1	1	2	3	2	3	1	3	1	2	9.3	9.2	10.4	19.636
14	13	2	2	3	1	2	3	1	3	1	2	1	2	3	12.5	13.9	14.4	22.623
15	24	2	2	3	1	3	1	2	1	2	3	2	3	1	9.5	8.7	10.4	19.516
16	16	2	3	1	2	1	2	3	3	1	2	2	3	1	9.3	9.8	10	19.723
17	26	2	3	1	2	2	3	1	1	2	3	3	1	2	13.4	15.7	16.3	23.503
18	9	2	3	1	2	3	1	2	2	3	1	1	2	3	13.4	14.2	14.3	22.891
19	12	3	1	3	2	1	3	2	1	3	2	1	3	2	10.8	12.1	11.3	21.11
20	19	3	1	3	2	2	1	3	2	1	3	2	1	3	7.4	8.2	8.4	18.022
21	1	3	1	3	2	3	2	1	3	2	1	3	2	1	10.9	9.3	9	19.676
22	22	3	2	1	3	1	3	2	2	1	3	3	2	1	9.3	8.2	8.8	18.822
23	6	3	2	1	3	2	1	3	3	2	1	1	3	2	9.2	7.9	8.5	18.572
24	14	3	2	1	3	3	2	1	1	3	2	2	1	3	16.3	16.5	18.2	24.578
25	7	3	3	2	1	1	3	2	3	2	1	2	1	3	10.1	10.7	11.5	20.605
26	18	3	3	2	1	2	1	3	1	3	2	3	2	1	17.2	16.6	15.9	24.371
27	25	3	3	2	1	3	2	1	2	1	3	1	3	2	12.6	11.8	13.4	21.972
Total															$\overline{T_{MR}} = 10.638$mg			–

R_1, R_2, R_3 represent response value for three repetitions of each trial. *S*/*N* ratio is signal-to-noise ratio. *e* columns are left empty, $\overline{T_{MR}}$−overall mean of MR in mg

and final weight of the specimen after processing it at a specified set of conditions by the ECA^{2}FM process. The weight was measured by a precision electronic balance (CAS India CAY220) with a 0.1-mg resolution.

2.3.3 Experimental materials

A work-piece is a hollow cylindrical piece made up of yellow brass (65 % Cu, 35 % Zinc, 156 BHN hardness) and had been selected based on literature review [1, 5–8], past optimization of the developed basic AFM setup [26] and pilot experimentation [22, 23] (refer to Fig. 3). The internal cylindrical surface of the test specimen to be finished was prepared by drilling operation followed by boring to the required size by machining at a set of constant boring parameters like speed of spindle, depth of cut and longitudinal feed. From a big lot of specimens, the test specimens were selected so that the bore size and initial roughness of the bore was in a very narrow range so as to eliminate any effect of size variation and/or initial roughness of the work-piece. The specimens were selected from a large lot for an initial surface roughness value in the range of 1.58 to 1.62 μm.

2.3.4 Design of experiments

The effects of five key ECA^{2}FM process parameters of voltage (*V*), salt molal concentration (*M*), diameter of cathode rod (*R*), extrusion pressure (*P*) and abrasives grain size (*G*) and three prospective two-factor interactions, i.e. voltage and salt molal concentration (VxM), voltage and diameter of cathode rod (VxR) and salt molal concentration and diameter of cathode rod (MxR) on the response parameter of material removal (MR) were investigated. The experimental design was according to standard L_{27} (3^{13}) orthogonal array (OA) of the Taguchi method as the total degrees of freedom associated with the five parameters at three levels each (with three two-factor interactions was 22 [5×(3–1)+ 3(2×2)=22], which is less than 26, total degrees of freedom of L_{27} OA). The L_{27} orthogonal array has 13 columns and 27 rows; thus, five machining parameters were apportioned to the columns after indentifying the interacting columns using the linear graph for the standard L_{27} OA [25] leaving the 12th and 13th columns empty (refer to Table 2). The orthogonality is preserved, even if one or more columns of the array remain empty.

2.3.5 Experimentation

The work-piece was held in the setup with the help of the developed nylon fixture for the ECA^{2}FM setup. During the experimentation, the electrolyte-abrasive laden polymeric media was extruded through the recess between the copper cathode rod and the inner surface of the hollow cylindrical work-piece (anode). The internal cylindrical surface of the work-piece was finished due to the anodic dissolution and abrasive machining action after the developed media was extruded for the set process parameters. The required DC voltage potential across the electrolyte was switched on just before the start of extrusion and switched off in the middle of the last stroke of the experimentation so as to finally achieve a fine finishing due to abrasive flow machining only as the electrolytic machining may result in rough surfaces. Media used for the present investigation consist of silicon-based polymer, hydrocarbon gel and Al_2O_3 abrasive particles with NaI salt. The material removal (MR) values for the respective experiment were obtained after processing the work-piece at a specified

Table 3 Pooled ANOVA (raw data, material removal)

Source	SS	DOF	*V*	*F* ratio	SS'	*P*%
V	74.24	2	37.12	51.52*	72.8	11.28
M	79.94	2	39.97	55.48*	78.5	12.17
R	107.63	2	53.81	74.69*	106.19	16.46
P	142.68	2	71.34	99.02*	141.24	21.89
G	78.72	2	39.36	54.63*	77.28	11.98
VxM	31.39	4	7.85	10.89*	28.51	4.42
VxR	85.87	4	21.47	29.8*	82.99	12.86
MxR (pooled)	4.32	4	1.08	1.5	–	–
Error	44.67	62	0.72	–	57.63	8.93
Total (*T*)	645.15	80			645.14	100

*Significant at 95 % confidence level, Fcritical=*F* (0.05, 2, 62)=3.15, *F* (0.05, 4, 62)=2.52

SS sum of squares, *DOF* degree of freedom, *V* variance, *SS*' pure sum of squares, *P%* percentage contribution of a treatment

Table 4 Pooled ANOVA (*S*/*N* ratio, material removal)

Source	SS	DOF	*V*	*F* ratio	SS'	*P*%
V	14.86	2	7.43	10.67*	13.47	10.1
M	17.26	2	8.63	12.39*	15.86	11.89
R	24.21	2	12.1	17.38*	22.81	17.1
P	31.64	2	15.82	22.72*	30.25	22.68
G	17.18	2	8.59	12.34*	15.79	11.84
VxM (pooled)	6.5	4	1.62	2.33	–	–
VxR	19.89	4	4.97	7.14*	17.11	12.82
MxR (pooled)	0.44	4	0.11	0.16	–	–
Error	8.36	12	0.7	–	18.11	13.57
Total (*T*)	133.39	26			133.39	100

*Significant at 95 % confidence level, Fcritical=*F* (0.05, 2, 12)=3.89, *F* (0.05, 4, 12)=3.26

SS sum of squares, *DOF* degree of freedom, *V* variance, *SS*' pure sum of squares, *P%* percentage contribution of a treatment

Table 5 Average values and main effects: material removal, *MR* in mg (*S*/*N* ratio in dB)

Process parameter ↓	Level →	Level 1		Level 2		Level 3	
	Type of data →	Raw data	*S*/*N* ratio	Raw data	*S*/*N* ratio	Raw data	*S*/*N* ratio
Voltage, *V*		9.30	19.173	11.13	20.604	11.49	20.859
Salt molal concentration, *M*		9.46	19.239	10.56	20.200	11.89	21.197
Diameter of cathode rod, *R*		9.04	18.918	11.17	20.561	11.70	21.157
Extrusion pressure, *P*		9.46	19.233	9.96	19.682	12.49	21.721
Abrasives grain size, *G*		9.73	19.468	12.01	21.318	10.18	19.849

set of conditions by the ECA^{2}FM process. In order to minimize the effect of temperature on the viscosity of media, the entire set of experiments were carried out at an ambient temperature of 32±2 °C.

For the experimentation, the process parameters and run order were planned in accordance with the L_{27} OA as per Table 2, based on the Taguchi experimental method. Each experiment was repeated three times, and the response for the three observed values of MR for the respective experiment is also enlisted in the Table 2. The order of the trials was randomized to minimize the time error variations.

3 Analyses and discussions

The results were analysed based on the Taguchi method using the analysis of variance (ANOVA) and Fisher's test (*F* ratio) applied to both the raw and signal-to-noise (*S*/*N*) ratio data in order to identify the significant factors and quantify their effects on the process performance characteristic of MR. The response characteristic of material removal (MR) is of "higher-the-better" type of machining quality characteristics; hence, the *S*/*N* ratio for this is given below [25]:

$$\left(\frac{S}{N}\right)_{\mathrm{HB}} = -10\log\left[\frac{1}{R}\sum_{j=1}^{R}\left(\frac{1}{y_j^2}\right)\right] \tag{1}$$

Where y_j, j=1, 2, ..., R are the response values under the trial condition's repeated R times. The *S*/*N* ratio, which is a summary statistic measuring the sensitivity of the performance characteristic in a controlled manner to noise factors, is calculated based on data from all replications of a trial condition, and a high value of *S*/*N* ratio signifies a higher signal effect as compared to the random effects.

3.1 ANOVA calculations

The analysis of variance (ANOVA) of raw data and *S*/*N* ratio data are performed to identify the significant parameters and to quantify their effect on the response characteristic. Tables 3 and 4 represent the pooled ANOVA results for the material removal based on raw data and *S*/*N* ratio data, respectively. The pooling in the ANOVA increases the confidence level of the significant parameters by considering the pooled insignificant parameters as noise [25]. From the ANOVA based on raw data, it is observed that all the selected parameters/parametric interactions significantly affect the mean of MR, except the interaction of salt molal concentration and diameter of cathode rod (MxR). From the ANOVA based on the *S*/*N* ratio, it is observed that all selected parameters and only one interaction of voltage and diameter of cathode rod (VxR) significantly affect both the mean and variation of MR, and the two remaining interactions of voltage and salt molal concentration (VxM) and salt molal concentration and diameter of cathode rod (MxR) are not significant. According to the *S*/*N* ratio data, extrusion pressure (*P*, 22.68 %) has the maximum percentage contribution towards the MR followed by diameter of cathode rod (*R*, 17.1 %),

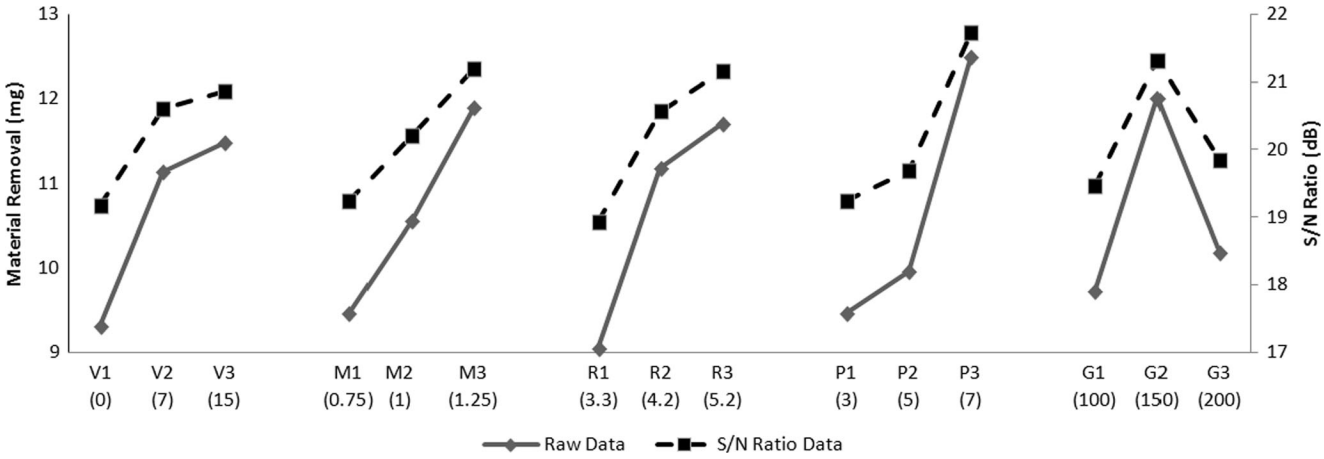

Fig. 4 Main effects for material removal in mg (*S*/*N* ratio in dB)

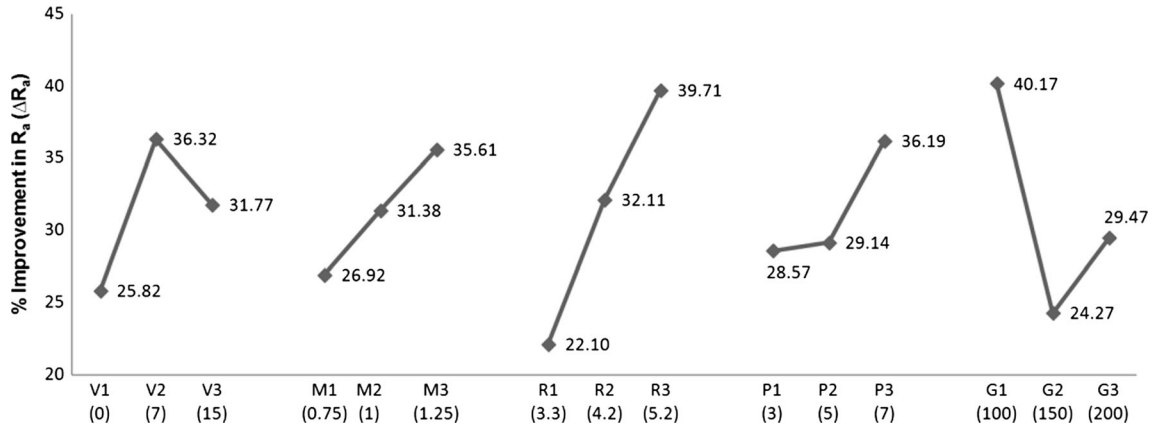

Fig. 5 Main effects for percentage improvement in surface roughness (%ΔR_a)

interaction of voltage and diameter of cathode rod (VxR, 12.82 %), salt molal concentration (*M*, 11.89 %), abrasives grain size (*G*, 11.84 %) and voltage (*V*, 10.1 %).

3.2 Parametric analysis (effect on MR)

3.2.1 Main effects

The main effects of process parameters for raw data and *S*/*N* ratio data for material removal are plotted by calculating the average values of response characteristics for each parameter at level one, level two and level three (L_1, L_2, L_3) (refer to Table 5 and Fig. 4).

The main effects show that the material removal (MR) increases with the increase in the applied Voltage (*V*), for the selected range of voltage potential (refer Fig. 4). The enhanced machining takes place due to the additional electrolytic dissolution of the material at the anodic work-piece along with the abrasion of materials due to the abrasives cutting action. Due to the electrochemical machining attack, the surface becomes soft as any oxide layer/hard surface is eroded [3] and now the surface is more susceptible to abrasion due to the abrasive's cutting action. Dabrowski et al. also observed similar results with a semi-liquid electrolytic paste with a 1-m concentration of NaI and Al_2O_3/SiC abrasives in the machining of flat surfaces made of steel [20, 21]. Bhattacharyya et al. [27] and Rajurkar et al. [28] also reported enhanced machining at higher inter-electrode gap current density. During the experimentation, a current of 0.01 A (amperage) was noted. During the screening experiments, the authors observed that at 10 V, an 87.43 % improvement in surface (%ΔR_a) was observed for a brass work-piece with an initial surface roughness of 4.02 μm leading to a final surface roughness value of 0.49 μm [23]. Since the AFM is a finishing process, so the main effects of the various process parameters on the response characteristic of percentage improvement in surface roughness have also been reported (refer to Fig. 5) (all factors are significantly affecting %ΔR_a, based on ANOVA). It is observed that %ΔR_a initially improves with the increase in the applied voltage to 7 V, and at the third level of 15 V, the surface quality deteriorates. At higher voltages, the deterioration in the surface quality is because of potentially more softening of work-piece, leading to a deeper abrasive cutting as has been observed by authors during the pilot experimentation too.

The increasing MR with the increasing salt molal concentration (*M*) corroborates the fact that the electrolytic action is the reason behind the increased MR, and as the concentration of salts is increasing, the enhanced electrochemical dissolution of material is observed at the anode work-piece due to more ionic reactions taking place at the

Table 6 Average values of material removal, *MR* in mg (*S*/*N* ratio in dB) for the interaction of VxM parameters

Levels of voltage ↓	Levels of salt molal → concentration	M_1		M_2		M_3	
	Type of data →	Raw data	*S*/*N* ratio	Raw data	*S*/*N* ratio	Raw data	*S*/*N* ratio
V_1		9.14	18.933	9.32	19.350	9.43	19.237
V_2		9.53	19.182	10.92	20.592	12.93	22.039
V_3		9.71	19.603	11.43	20.657	13.31	22.316

Table 7 Average values of material removal, *MR* in mg (*S*/*N* ratio in dB) for the interaction of VxR parameters

Levels of voltage ↓	Levels of diameter of → cathode rod	R_1		R_2		R_3	
	Type of data →	Raw data	*S*/*N* ratio	Raw data	*S*/*N* ratio	Raw data	*S*/*N* ratio
V_1		8.30	18.205	8.77	18.702	9.43	20.612
V_2		8.50	18.370	13.72	22.658	12.93	20.785
V_3		10.31	20.179	11.03	20.322	13.31	22.075

surface (refer to Fig. 4). From Fig. 5, an improvement in $\%\Delta R_a$ is also observed at a higher salt molal concentration. The parameter of diameter of cathode rod (*R*) governs the gap between the two electrodes, and with the increase in the diameter of cathode rod (*R*), the gap between the electrodes is decreasing. The increasing MR due to enhanced electrochemical action with the decrease in the electrode gap has been observed by other researchers too [20]. Additionally, the reduction ratio is also increasing with the decreasing gap between electrodes, which result in more MR due to the development of more pressures in the working zone resulting in more abrasives cutting forces. As enhancement in MR due to both the electrochemical dissolution of material and abrasion due to the cutting action of abrasives with the increase in the cathode rod size, these VxR interaction parameter dominate over the other factors/factor interactions in the present experimentation. The increase in MR due to the increasing cathode rod size is steep from the 1st level of rod diameter size (φ 3.3 mm) to the 2nd level of the rod diameter size (φ 4. 2 mm), and then onwards there is a relatively less increase in MR. This can be explained by the fact that with the very high reduction ratio, some critical higher media pressures in the working zone lead to lesser MR as the same abrasives (which are near to the surface) keep on abrading and lesser number of new abrasive particles are in action [1, 6, 7, 25]. A similar trend of improvement in $\%\Delta R_a$ is also observed with the decrease in the inter-electrode gap (refer to Fig. 5).

From Fig. 4, the MR is observed to increase with the increase in extrusion pressure for the selected extrusion pressure range (relatively low extrusion pressures had been selected). It is evident that the increasing MR with extrusion pressure in most of the AFM experimentations is due to more abrasive cutting forces as reported by Przyklenk [29] and Rajesha [30]. Similarly, the increase in $\%\Delta R_a$ is observed with the increase in the extrusion pressure as shown in Fig. 5.

From Fig. 4, it is noted that an initial increase in MR with the use of finer abrasive grain sizes (100–150 mesh) is due to the obvious reason that with the constant mass ratio of abrasives-to-media used, the more number of finer grains would make more number of cuts on the high spots on the work surface [6, 7]. With very fine abrasive grain sizes, though the number of cutting grains is more, but their cutting depths will be very less, and thus lesser material removal takes place in the set number of cycles. But from Fig. 5, it is observed that a relatively coarse grain size of 100 mesh results in the maximum finishing of the surface as large grain size results in a levelled surface, though very coarse grains will again result in poor surface finish with deep abrasives cutting marks. This is in line with the result of Siwert [31] and Jain and Adsul [32]. Intermediate size abrasive grains result in more MR, but the surface roughness increases due to relatively deep digging of abrasives. Very fine grains again result in improvement in surface finish due to shallow material cutting. So the proper grit size selection is very important to achieve higher MR and $\%\Delta R_a$.

The enhanced dissolution of the material from the ridges in the ECA^{2}FM process leads to faster polishing. Along with the micro-level material removal, this process would be able to make the macro-geometrical

Table 8 Average values of material removal, *MR* in mg (S/N ratio in dB) for the interaction of MxR parameters

Levels of salt molal conc. ↓	Levels of diameter of → cathode rod	R_1		R_2		R_3	
	Type of data →	Raw data	*S*/*N* ratio	Raw data	*S*/*N* ratio	Raw data	*S*/*N* ratio
M_1		8.04	17.695	9.90	19.727	10.44	20.295
M_2		9.03	19.072	10.78	20.452	11.87	21.075
M_3		10.03	19.987	12.84	21.502	12.80	22.102

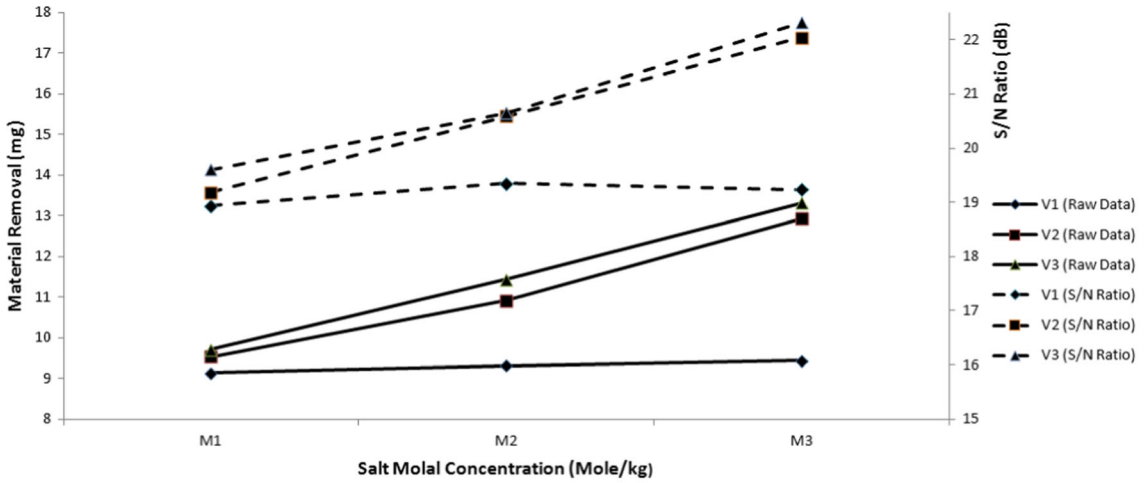

a - Interaction Plots for VxM (Material Removal in mg and S/N Ratio in dB).

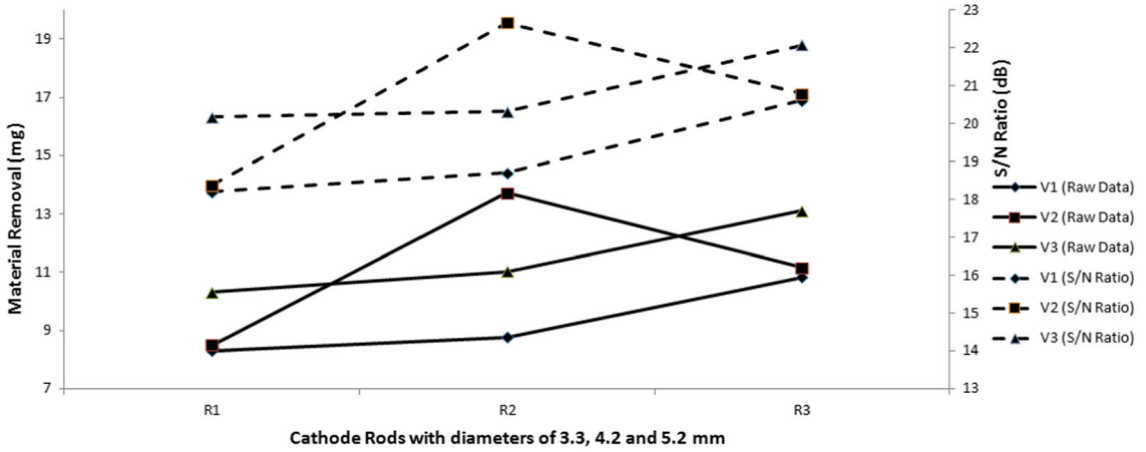

b - Interaction Plots for VxR (Material Removal in mg and S/N Ratio in dB).

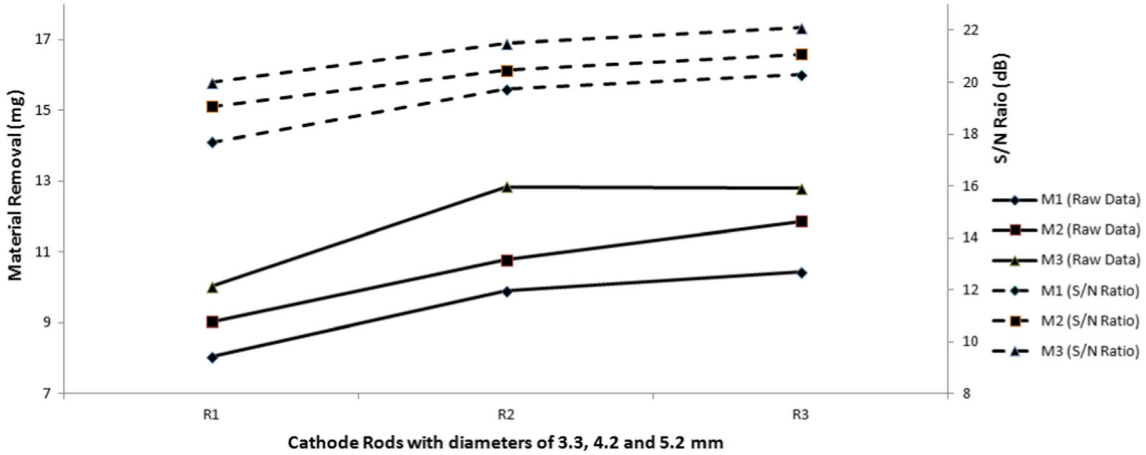

c - Interaction Plotsfor MxR (Material Removal in mg and S/N Ratio in dB).

Fig. 6 **a** Interaction plots for VxM (material removal in mg and *S*/*N* ratio in dB). **b** Interaction plots for VxR (material removal in mg and *S*/*N* ratio in dB). **c** Interaction plots for MxR (material removal in mg and *S*/*N* ratio in dB)

correction of the work surface profile as is observed by an almost similar process of electrochemical honing [3]. This is due to the presence of a shaped cathode electrode in conjunction with the work surface. Moreover,

with suitable electrolyte, this process should be able to finish even very hard materials with relatively less operating forces.

3.2.2 Effects of two-factor interactions

The ECA^{2}FM process is very interactive. The effects of three two-factor interactions, i.e. voltage and salt molal concentration (VxM), voltage and diameter of cathode rod (VxR) and salt molal concentration and diameter of cathode rod (MxR), on the response parameter of material removal (MR) are plotted by calculating average values of response characteristics for respective two-factor interaction at different level combinations (refer to Tables 6, 7, and 8 and Fig. 6a–c).

It is observed that the two-factor interaction of voltage and salt molal concentration (VxM) is significant based on ANOVA (raw data) and is insignificant based on ANOVA (*S*/*N* ratio data) (refer to Tables 3 and 4). Based on the raw data analysis too, it is the least significant parameter affecting the MR. The little observed effect of this interaction is explained by the fact that salt molal concentration (*M*) has a role to play in the MR only in the presence of some applied voltage (*V*). The interaction of voltage and diameter of cathode rod (VxR) is significantly affecting both mean and its variation for the response parameter of MR, and its effect is more than the independent effect of voltage (*V*). At the second levels of voltage (V_2) and diameter of electrode rod (R_2), the two factors are highly interactive resulting in higher electrochemical dissolution and abrasive cutting action. It seems that at R_2, the electrode gap is near to a critical gap leading to a compromise between lesser gap requirement for the electrochemical action and a reasonably high reduction ratio resulting in more abrasive cutting action. The third interaction of salt molal concentration and diameter of cathode rod (MxR) is not-significant in affecting the MR.

3.3 Optimal MR

Material removal (MR) is the "higher-the-better" type of quality characteristic. Therefore, higher values of MR are considered to be optimal. The optimum levels of the significant parameters have been selected based on the Taguchi method's *S*/*N* ratio analysis, and the optimum levels of various factors/factor interactions for the maximum MR are V_2xR_2, M_3, P_3 and G_2.

3.4 Estimation of optimum MR

The optimum values of the response characteristic MR along with their respective confidence intervals have been predicted using the Taguchi approach based on *S*/*N* ratio [25].

Predicted optimal MR:

The mean at the optimal MR (optimal value of the response characteristic) is estimated as follows:

$$MR = \overline{V_2 \times R_2} + \overline{M_3} + \overline{P_3} + \overline{G_2} - 3\overline{T} \quad (2)$$

$\overline{T}$ = overall mean of the response=10.638 mg (Table 2)

$\overline{V_2 \times R_2}$ = average value of MR for the interaction of Voltage (second level) and Diameter of Cathode rod (second level) parameters =13.72 mg (refer to Table 9)

$\overline{M_3}$ = average value of MR at the third level of salt molal concentration parameter = 11.89 mg (Table 5)

$\overline{P_3}$ = average value of MR at the third level of extrusion pressure parameter =12.49 mg (Table 5)

$\overline{G_2}$ = Average value of MR at the second level of abrasives grain size parameter = 12.01 mg (Table 5)

Substituting these values in the Eq. (1), MR=18.196 mg

Table 9 Predicted optimal values, confidence intervals and results of confirmation experiments

Response	Optimal process parameters	Predicted optimal value	Confidence interval 95 %	Actual value (avg of confirmation exp)
MR	$V_2xR_2M_3P_3G_2$	18.2 mg	CI_{CE}: 17.03<MR<19.36 CI_{POP}: 17.57<MR<18.82	18.02 mg (corresponding $\%\Delta R_a$ is 46.83 %)

CI_{CE} confidence interval for the mean of the confirmation experiments based on raw data

CI_{POP} confidence interval for the mean of the population based on raw data

V_2xR_2 average value of MR for the interaction of voltage (*second level*) and diameter of cathode rod (*second level*) parameters

M_3 average value of MR at the third level of salt molal concentration parameter

P_3 average value of MR at the third level of extrusion pressure parameter

G_2 average value of MR at the second level of abrasives grain size parameter

The confidence interval of confirmation experiments (CI_{CE}) and of population (CI_{POP}) is calculated by using the following equations [25]:

$$CI_{CE} = \sqrt{F_{\alpha}(1, f_e) V_e \left[\frac{1}{n_{eff}} + \frac{1}{R}\right]} \quad (3)$$

$$CI_{POP} = \sqrt{\frac{F_{\alpha}(1, f_e) V_e}{n_{eff}}} \quad (4)$$

where

$F_{\alpha}(1, f_e)$	the F ratio at the confidence level of $(1-\alpha)$ against DOF 1 and error degree of freedom f_e=4 [standard tabulated F ratio value, 25]
f_e	error DOF=62 (Table 3)
N	total number of result=81 (treatment=27, repetition=3)
R	sample size for confirmation experiments=3
V_e	error variance=0.72 (Table 3)
η_{eff}	effective number of replications

$$n_{eff} = \frac{N}{1 + [\text{DOF association in the estimate of mean response}]} = 7.36 \quad (5)$$

So, CI_{CE}=±1.162

and CI_{POP}=±0.625

The 95 % confirmation interval of predicted optimal range (for confirmation run of three experiments) is as follows:

Mean $MR - CI_{CE} < MR < MR + CI_{CE}$

$17.03 < MR < 19.36$

The 95 % confirmation interval of the predicted mean is as follows:

Mean $MR - CI_{POP} < MR < MR + CI_{POP}$

$17.57 < MR < 18.82$

3.5 Confirmation experimentation

In order to validate the results obtained, three confirmation experiments were conducted for response characteristics of MR at the optimal levels of V_2xR_2, M_3, P_3 and G_2 of process parameters based on S/N ratio (refer to Table 9). The average value of MR obtained through the confirmation experiments is 18.02 mg and is within 95 % of CI_{CE} and CI_{POP}. Corresponding $\%\Delta R_a$ is 46.83 % resulting in R_a value of 0.84 μm from an initial surface roughness value of 1.6 μm.

3.6 SEM micrographs and discussion

The influence of the presence of electrochemical dissolution and abrasion on the inner surface of the hollow cylindrical work-piece in the ECA^{2}FM process is evident from the set of representative SEM micrographs (corresponding to various experiments of L_{27} OA as per Table 2) as shown in Fig. 7. The micrograph in the Fig. 7a is corresponding to the experiment number 6 and had been finished without the electrochemical aid. The deep boring tool marks are still visible in this micrograph as finishing is only by abrasive cutting action. The micrographs in the Fig. 7b, c are corresponding to the experiment number 10 having ×250 and ×1000 magnifications, respectively, and the work-piece corresponding to these micrographs had been finished with electrochemical aid of 7 V with a lower size electrode rod. Boring tool marks are now shallow as more material had been removed from the ridges due to additional ECM action. In Fig. 7c, the characteristic spots typical to ECM surface are visible on the finished surface at a higher magnification. The micrograph in Fig. 7d is corresponding to the experiment number 18 and is having the best finish due to a synergy between the ECM and AFM mechanisms. The micrograph in Fig. 7e is corresponding to the experiment number 21 with electrochemical aid at 15 V. Boring tool marks have not been completely removed. Some long scratches on the surface signify that same abrasives were cutting the material for the longer distances. These are due to the higher reduction ratio at the third level of diameter of cathode rod parameter in this experiment. The micrograph in Fig. 7f is corresponding to the confirmation experiment, finished at the optimum process parameters, and almost all the traces of loosely held material and initial surface defects have been finished and the remaining boring tool marks are very shallow.

4 Conclusions

The important conclusions of this research work are the following:

- The developed electrochemical aided abrasive flow machining (ECA^{2}FM) is effective in enhancing the material removal (MR) in the abrasive flow finishing of internal cylindrical surfaces of brass work-pieces towards the generation of a polished surface.
- The abrasion of the material is intensified due to the co-operation of electrochemical dissolution along with the abrasive cutting in the electrochemical-aided abrasive flow machining (ECA^{2}FM) process, so a fast ECA^{2}FM process requiring lesser extrusion cycles can serve a finishing requirement.
- The various ECA^{2}FM process parameters like voltage, salt molal concentration, electrode rod size (for

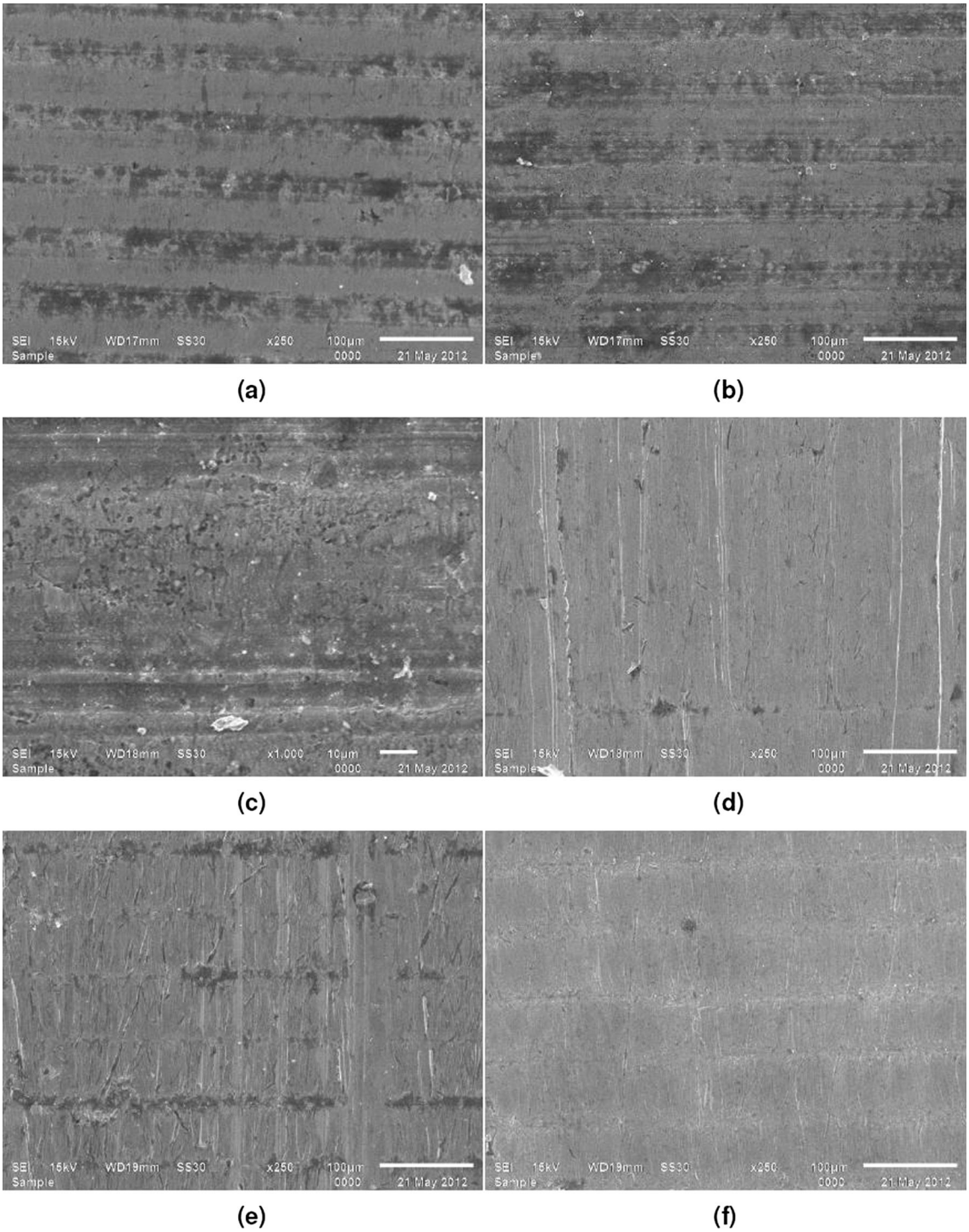

Fig. 7 SEM micrographs of ECA^{2}FM finished brass test pieces (×250): **a** without electrochemical aid, **b** and **c** (×1000) with the electrochemical aid at 7 V and finished with lower size electrode, **d** with best finish at electrochemical aid at 7 V, **e** with best finish at electrochemical aid at 15 V, **f** confirmation experiment for optimal MR

maintaining electrode gap), extrusion pressure and grain size etc. significantly affect the response parameter of material removal and need to be selected near to the optimal settings for a machine and work-piece combination. Along with the improvement in MR, an improvement in surface roughness is also observed. For the ECA^{2}FM finished specimens for the optimal MR of 18.02 mg, a corresponding $\%\Delta R_a$ of 46.83 % is noted which results in the final R_a value of 0.84 μm from an initial surface roughness value of 1.6 μm.

- The contributions of various ECM-based parameters is less but significant and can be further improved by using the strong cyanide-based or other electrolyte salts in the electrolyte-abrasive laden media. But experimentation with cyanide-based salts requires a very strictly controlled environment because of their poisonous nature.
- Unlike AFM process, the developed ECA^{2}FM process can be used for the prismatic geometries only, because of the cathode electrode requirement along with the anode work-piece.

Acknowledgments The authors wish to acknowledge the research grant-in-aid from The Institution of Engineers (India), Kolkata, India (Project Reference: SCK/RD2016830/2010-2011), for carrying out the R&D work on "Investigations of Hybrid Abrasive Flow Machining Process".

References

1. Walia RS, Shan HS, Kumar P (2009) Enhancing AFM process productivity through improved fixturing. Int J Adv Manuf Technol 44: 700–709. doi:10.1007/s00170-008-1893-7
2. Jain VK (2009) Magnetic field assisted abrasive based micro-/nano-finishing. J Mater Proc Technol 209:6022–6038. doi:10.1016/j.jmatprotec.2009.08.015
3. Dubey AK, Shan HS, Jain NK (2008) Analysis of surface roughness and out-of-roundness in the electro-chemical honing of internal cylinders. Int J Adv Manuf Technol 38:491–500. doi:10.1007/s00170-007-1180-z
4. Jones AR, Hull JB (1998) Ultrasonic flow polishing. Ultrasonics 36: 97–101
5. Singh S, Shan HS (2002) Development of magneto abrasive flow machining process. Int J Mach Tools Manuf 42:953–959. doi:10.1016/S0890-6955(02)00021-4
6. Walia RS, Shan HS, Kumar P (2006) Parametric optimization of centrifugal force-assisted abrasive flow machining (CFAAFM) by the Taguchi method. Mater Manuf Process 21(4):375–382. doi:10.1080/10426910500411645
7. Walia RS, Shan HS, Kumar P (2009) Modelling of centrifugal-force-assisted abrasive flow machining. Proc IMechE Part E J Proc Mech Eng 223:195–204. doi:10.1243/09544089JPME284
8. Walia RS, Shan HS, Kumar P (2008) Determining dynamically active abrasive particles in the media used in centrifugal force assisted abrasive flow machining process. Int J Adv Manuf Technol 38:1157–1164. doi:10.1007/s00170-007-1184-8
9. Walia RS, Shan HS, Kumar P (2008) Morphology and integrity of surfaces finished by centrifugal force assisted abrasive flow machining. Int J Adv Manuf Technol 39:1171–1179. doi:10.1007/s00170-007-1301-8
10. Singh R, Walia RS (2012) Study the effects of centrifugal force on abrasive flow machining process. IJRMET 2(1):34–39
11. Sankar MR, Mondal S, Ramkumar J, Jain VK (2009) Experimental investigations and modeling of drill bit-guided abrasive flow finishing (DBG-AFF) process. Int J Adv Manuf Technol 42:678–688. doi:10.1007/s00170-008-1642-y
12. Sankar MR, Jain VK, Ramkumar J (2009) Experimental investigations into rotating workpiece abrasive flow finishing. Wear 267:43–51. doi:10.1016/j.wear.2008.11.007
13. Yan BH, Tzeng HJ, Huang FY, Lin YC, Chow HM (2007) Finishing effects of spiral polishing method on micro lapping surface. Int J Mach Tools Manuf 47:920–926. doi:10.1016/j.ijmachtools.2006.07.009
14. Chen WC, Yan BH, Lee SM (2010) A study on the spiral polishing of the inner wall of stainless bores. Adv Mater Res 126–128:165–170. doi:10.4028/www.scientific.net/AMR. 126-128.165
15. Brar BS, Walia RS, Singh VP, Sharma M (2012) Helical abrasive flow machining (HLX-AFM) process. Int J Surf Engg and Mater Technol 2(2):48–52
16. Brar BS, Walia RS, Singh VP, Sharma M (2013) A robust helical abrasive flow machining (HLX-AFM) process. J Inst Eng (India) Series C 94(1):21–29. doi:10.1007/s40032-012-0054-9
17. Cherian J, Issac JM (2014) Fatigue performance in abrasive flow machining. Appl Mech Mater 592–594:354–362
18. Rajurkar KP, Zhu D, McGeough JA, Kozak J, De Silva A (1999) New developments in electro-chemical machining. Annals CIRP 48(2):567–579. doi:10.1016/S0007-8506(07)63235-1
19. Qadri SAH, Sharma SB (2011) Hybridisation of electrochemical machining using electrolyte with powder suspended abrasives. Int J Adv Engg Appl: 49–51
20. Dabrowski L, Marciniak M, Wieczarek W, Zygmunt A (2006) Advancement of abrasive flow machining using an anodic solution. J New Mater Electrochem Syst 9:439–445
21. Dabrowski L, Marciniak M, Szewczyk T (2006) Analysis of abrasive flow machining with an electrochemical process aid. Proc IMechE Part B J Eng Manuf 220:397–403. doi:10.1243/095440506X77571
22. Brar BS, Walia RS, Singh V (2012) Electro chemical machining in the aid of abrasive flow machining process. Int J Surf Eng Mater Technol 2(1):5–9
23. Brar BS, Walia RS, Singh VP (2012) Electro chemical aid to abrasive flow machining process: harnessed for improved surface finishing. Proc of Int Conf on AFTMME, PTU, Punjab, pp 527–532
24. Singh H, Kumar P (2006) Optimizing feed force for turned parts through the Taguchi technique. Sadhana 31(6):671–681
25. Ross PJ (1996) Taguchi techniques for quality engineering. McGraw Hill, New York
26. Brar BS, Walia RS, Singh VP, Singh M (2011) Development of a robust abrasive flow machining process setup. Int J Surf Eng Mater Technol 1(1):17–23
27. Bhattacharrya B, Munda J, Malapati M (2004) Advancement in electrochemical machining. Int J Mach Tools Manuf 44:1577–1589
28. Rajurkar KP, Sundaram MM, Malshe AP (2013) Review of electrochemical and electrodischarge machining. Procedia CIRP 6:13–26. doi:10.1016/j.procir.2013.03.002
29. Przyklenk K (1986) Abrasive flow machining—a process for surface finishing and deburring of work-pieces with a complicated shape by means of abrasive laden media. Adv Non Tradit Manuf PED ASME 22:101–110
30. Rajesha S, Venkatesh G, Sharma AK, Kumar P (2010) Performance study of a natural polymer based media for abrasive flow machining. Indian J Eng Mater Sci 17:407–413
31. Siwert DE (1974) Tooling for the extrude hone process. Proc. of EME Int. Engineering Conference. 302–311
32. Jain VK, Adsul SG (2000) Experimental investigations into abrasive flow machining (AFM). Int J Mach Tools Manuf 40:1003–1021

Author's Accepted Manuscript

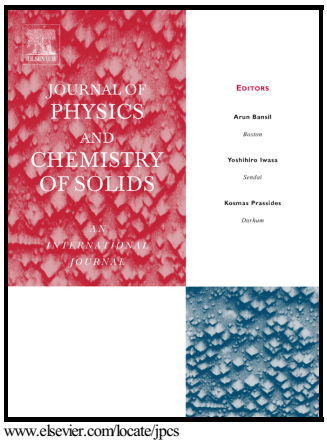

www.elsevier.com/locate/jpcs

Enhanced thermoelectric performance of spark plasma sintered copper deficient nanostructured copper selenide

Kriti Tyagi, Bhasker Gahtori, Sivaiah Bathula, M. Jayasimhadri, Niraj Kumar Singh, Sakshi Sharma, D. Haranath, A.K. Srivastava, Ajay Dhar

PII: S0022-3697(15)00029-3
DOI: http://dx.doi.org/10.1016/j.jpcs.2015.01.018
Reference: PCS7474

To appear in: *Journal of Physical and Chemistry of Solids*

Received date: 3 November 2014
Revised date: 23 January 2015
Accepted date: 31 January 2015

Cite this article as: Kriti Tyagi, Bhasker Gahtori, Sivaiah Bathula, M. Jayasimhadri, Niraj Kumar Singh, Sakshi Sharma, D. Haranath, A.K. Srivastava and Ajay Dhar, Enhanced thermoelectric performance of spark plasma sintered copper deficient nanostructured copper selenide, *Journal of Physical and Chemistry of Solids,* http://dx.doi.org/10.1016/j.jpcs.2015.01.018

This is a PDF file of an unedited manuscript that has been accepted for publication. As a service to our customers we are providing this early version of the manuscript. The manuscript will undergo copyediting, typesetting, and review of the resulting galley proof before it is published in its final citable form. Please note that during the production process errors may be discovered which could affect the content, and all legal disclaimers that apply to the journal pertain.

ACCEPTED MANUSCRIPT

Enhanced thermoelectric performance of spark plasma sintered copper deficient nanostructured copper selenide

Kriti Tyagi,[a] Bhasker Gahtori,[a] Sivaiah Bathula,[a,b] M. Jayasimhadri,[b]
Niraj Kumar Singh,[a] Sakshi Sharma,[a] D. Haranath,[a] A. K. Srivastava[a] and Ajay Dhar[a,1]

[a]CSIR-Network of Institutes for Solar Energy, CSIR-National Physical Laboratory,
Dr. K. S. Krishnan Road, New Delhi 110012, India
[b]Department of Applied Physics, Delhi Technological University, Delhi, India

Abstract

We report the thermoelectric properties of nanostructured Cu deficient Cu_2Se synthesized employing high energy ball milling followed by spark plasma sintering. Our methodology resulted in a significant enhancement in the thermoelectric figure of merit (ZT) ~1.4 at 973 K, which is ~30% higher than its bulk counterpart. This enhancement in thermoelectric performance was mainly due to a significant reduction in the lattice thermal conductivity which was attributed to the enhanced phonon scattering at various length scales by nanoscale defects and as well as by abundant nanograin boundaries. The nanoscale defects were characterized employing transmission electron microscopy of the nanostructured $Cu_{2-x}Se$ samples, based on which the enhancement of ZT has been discussed.

Keywords: C. electron microscopy, C. microstructure, C. thermal conductivity, C. electrical properties, C. specific heat

Accepted manuscript

1. Introduction

[1]Corresponding author email: adhar@nplindia.org
Tel.: +91 11 4560 9455/9456; Fax: +91 11 4560 9310

ACCEPTED MANUSCRIPT

Conversion of waste heat into electrical energy without involving any moving parts in an eco-friendly manner employing thermoelectric devices has been a subject of considerable attention in the recent past [1]. Since the last three decades, efforts have been concentrated to develop novel materials with high TE performances [2-4]. It is well-known that the performance of TE material is generally gauged by its dimensionless figure-of-merit (ZT) = $S^2\sigma T/\kappa$, where, S, σ, T, and κ are Seebeck coefficient, electrical conductivity, absolute temperature, and thermal conductivity, respectively [4]. Further, total thermal conductivity (κ) is the sum of the lattice thermal conductivity (κ_l) due to phonons and electronic thermal conductivity (κ_e) due to charge carriers [5, 6] travelling through the lattice. However, a simultaneous optimization of these physical parameters to obtain a high ZT is difficult because they are inter-dependent and a change in any one of these parameters adversely affects the others.

Although several strategies have been employed to enhance the ZT of TE materials which are focused on the optimization of the power factor ($S^2\sigma$) through controlled doping [7, 8], reduction of the thermal conductivity using solid-solution alloying [9], or employing the nanostructuring approach [10]. However, the remarkable progress in improving the ZT has been accomplished in several TE material adopting the latter approach [11, 12]. Quantum confinement effects induced on nanostructuring tend to enhance the Seebeck coefficient while numerous nanoscale interfaces tend to scatter phonons more effectively than charge carriers thereby significantly reducing thermal conductivity [13] leading to a considerable increase in ZT.

A variety of TE material nanostructures, such as, super-lattices [13-15], nanowires [16] and nanocomposites [17-20] have been developed with an appreciable improvement in their ZT. However, the high ZT in such nanostructures are not of much practical utility, due to their expensive fabrication processes coupled with their limited power handling capacity. On the other hand, a bulk

Accepted manuscript

nanostructured material [21], fabricated using a conventional powder metallurgical technique [22] has the advantage of being able to produce economically in large quantities and in a form that is compatible with the commercially available devices.

Out of several existing TE materials, Cu_2Se-based materials are the most intriguing compounds, as they exhibit a high TE performance resulting from the liquid-like behavior of Cu ions around the Se sub-lattice at high temperatures [23]. Stoichiometric and non-stoichiometric $Cu_{2-x}Se$ exists in different crystallographic forms, such as, like cubic [24], monoclinic [25], orthorhombic and tetragonal [26, 27]. However, it is well known that stoichiometric Cu_2Se becomes non-stoichiometric at high operating temperatures thus limiting its usage for actual device applications [23]. In the current study, we report the synthesis and transport properties of copper deficient Cu_2Se, which is stable up to its operating temperature (973 K), where its ZT exhibits a maximum value.

Liu et al. [23] have reported a ZT ~1.1 at 1000 K for bulk $Cu_{1.98}Se$. Later, Xiao et al. [28] reported the phase transition and TE properties of $Cu_{2-x}Se$ synthesized by melt-quenching and sintered using spark plasma sintering (SPS) technique, which resulted in a ZT value of ~0.38 at 750 K. However, there are no reports available in the literature on nanostructured $Cu_{2-x}Se$. In view of this, to optimize the electrical conductivity, by creating Cu vacancies, and thermal conductivity by nanostructuring of $Cu_{2-x}Se$, we prepared several $Cu_{2-x}Se$ samples with varying Cu concentration and achieved optimal TE properties in nanostructured $Cu_{1.98}Se$. It was observed that the enhancement in ZT is primarily due to a drastic reduction in κ resulting from nanostructuring leading to abundant grain boundaries and microstructural defects that act as scattering centers for various wavelength scales of phonons. As a

Accepted manuscript

ACCEPTED MANUSCRIPT

consequence, the current nanostructuring approach for the composition of $Cu_{1.98}Se$ resulted in a ZT value of ~1.4 at 973 K, which is ~30% higher than its bulk counterpart.

2. Experimental procedure

Cu (99.99%, Alfa Aesar) and Se (99.99%, Alfa Aesar) powders were milled in a ball mill set-up (Fritsch, Pulverisette-5) for an optimized time period of ~50 hours. The container of the ball-mill and the milling media were made of stainless steel. The ball-to-powder ratio was optimized at 20:1 by weight. The milling was carried out in an argon atmosphere with a speed of 400 rpm. In order to prevent re-welding and to promote fracturing of powder particles, 2 wt% of stearic acid was added as a process control agent. Prior to sintering, processing of the nanostructured alloy powders was carried out in a glove box (Mbraun, MB20) to avoid oxidation and other atmospheric contamination. Phase identification and crystallite size measurements were carried out by X-ray powder diffraction (XRD) (Rigaku, MiniFlexII). The stoichiometric bulk $Cu_{1.98}Se$ was synthesized by a vacuum melting process using high-purity Cu and Se powders and grinding them thoroughly in a glove box under a high-purity argon atmosphere. The powders were subsequently made into pellets and vacuum-sealed (10^{-4} Torr) in quartz tubes. The sealed quartz ampoules were placed in a box furnace, heat-treated at 800°C for 96 hours, and then naturally cooled to room temperature (~25^{o}C). The nanostructured and bulk alloy powders were subsequently consolidated and sintered under vacuum (~ 4 Pa) using spark plasma sintering (SPS Syntex, 725) at a pressure of 60 MPa at 600°C with a heating rate of 300°C/minute and soaking time of ~4 minutes, respectively, employing 12.7 mm diameter graphite die and punches. The actual composition of melt-processed bulk and nanostructured samples was determined using Flame atomic absorption spectrometry technique (Analytik Jena,Vario-6) and both the samples exhibited nearly the same stoichiometry as the starting composition i.e. $Cu_{1.96}Se$ for bulk and $Cu_{1.97}Se$

Accepted manuscript

for nanostructured sample. The density was measured using the conventional Archimedes principle. Electron microscopy experiments were performed using a (HRTEM model: Tecnai G2 F30 STWIN) operated at the electron accelerating voltage of 300 kV using the electron source as field emission gun. HRTEM was used to study the morphology, interfacial microstructural characteristics and crystallographic orientation of the as-sintered bulk and nanostructured samples. Specific heat measurements were performed using differential scanning calorimeter (DSC) (Mettler Toledo, DSC842). The thermal diffusivity was measured on polished sample discs of diameter 12.7 mm and thickness 3 mm using a laser flash system (Linseis, LFA 1023). The thermal conductivity was calculated as a product of thermal diffusivity, specific heat and volume density. The Seebeck coefficient and resistivity were measured using a commercial equipment (Ulvac, ZEM 3) employing polished sample bar of dimensions ~3 x 3 x 11 mm^3. The accuracies in transport measurement are: ± 6% for thermal diffusivity, ± 10% for electrical conductivity, ± 7% for Seebeck coefficient, ± 8% for specific heat and ±0.5% for density.

3. Results and Discussion

Phase transition and thermal stability studies of $Cu_{2-x}Se$ with different Cu composition were carried out using DSC measurement. It is clear from Figure 1 that the phase transition temperature shifts to lower temperatures as the Cu concentration in $Cu_{2-x}Se$ is decreased. A similar kind of behavior has been observed by other researchers on Cu deficient bulk $Cu_{1.98}Se$ material [28]. The XRD patterns of bulk and nanostructured $Cu_{1.98}Se$ samples, shown in Figure 2, suggest a significant peak broadening in nanostructured sample in comparison to its bulk counterpart, which is primarily due to its nanostructured grain features. The crystallite size has been evaluated from the XRD data after accounting for the instrumental broadening and using the Williamson-Hall method, which takes the

Accepted manuscript

lattice strain into account[29, 30]. The average crystallite size of the nanostructured $Cu_{1.98}Se$ sample after SPS was found to be ~12 nm. Current XRD patterns of $Cu_{1.98}Se$ sample are compared to the previously reported data on $Cu_{1.98}Se$ [23, 28] and confirmed the phase purity.

A detailed microstructural characterization on nanostructured and bulk samples of $Cu_{1.98}Se$ elucidated several interesting features in real and reciprocal space. In case of nanostructured alloy, a uniformly distributed ultra-fine microstructure has been observed at lower magnification as shown in Figure 3(a). One can easily see individual grains with the boundary length of about 3 to 6 nm (marked with dotted line between grains A and B, Figure 3(a)). The individual grains are sometime noticed with a mottled contrast due to strain in the microstructure (marked as A and B in Figure 3(a)). There was a significant presence of Moiré fringes in the matrix of the microstructure presumably due to the overlap of tiny nanocrystals. As an illustrative example, a region consisting of Moiré fringes has been marked as C in Figure 3(a). A magnified view of individual grain (A) as displayed in Figure 3(b) elucidates that the entire nanocrystal consists of planes hkl: 220, with the inter-planar spacing of 0.21 nm. At the interface (a region marked with the dotted line in Figure 3(a)) of grains A and B, it has been observed that the boundary is significantly distinct with interpenetrating planes, hkl indices 220 and 090 (inter-planar spacing: 0.23 nm) from the either side of the microstructure (Figure 3c). Interestingly, at higher magnifications, several regions of the microstructure such as region C of Figure 3(a) did show layered type of contrast due to certain types of modulations at the atomic scale (marked by a set of arrows in Figure 3(d)). It has been further noted that such modulated microstructure regions (Figure 3(d)) have inconsistency in their local periodic arrangement of the atomic sites (Figure 3(e)), although the overall microstructure exhibits crystalline state in the material. In reciprocal space, a fast Fourier transform (FFT, Figure 3(f)) shows the presence of the planes 220 and 090 with the inter-planar spacing of 0.21 and 0.23 nm, respectively. In general, several

Accepted manuscript

ACCEPTED MANUSCRIPT

nanocrystallites with ultra-fine size (2 to 10 nm) possessing random distribution in throughout the matrix-microstructure of the material have been observed (Figure 3(g)). The mottled contrast, as observed in some of the grains (as marked B in Figure 3(a)), further reveals a layered structure at the atomic scale (Figure 3h) due to the strain induced during processing of the material. Figure 3(i) elucidates another sharp interface evolved between the planes of 220 and 090 with an inter-planar spacing of 0.21 and 0.23 nm, respectively, at an atomic scale. The sizes of the nanocrystals were found to be between 6-10 nm. The microstructural engineering carried out while nanostructuring ((Figure 3(a-i)) leads to several types of interfaces and lattice scale modulations in the microstructure. These ultra-fine perturbations in an otherwise crystalline matrix influence the phonon-scattering to a great extent. Also, it has been proposed by Maier et al. [31] that strain field domains in TE materials generally cause some changes in their band structure that create shallow potential super-lattice structure which can scatter [15] acoustic phonons, which are the major carriers of heat in a material. Apart from the nanoscale defects, the nanostructured materials also have excess free volume at grain boundaries [32-34] due to severe plastic deformation associated with ball milling, which could also promote the phonon scattering. In the current study, similar kind of behavior could be the potential reason in reduction of lattice thermal conductivity in the nanostructured sample as compared to its bulk counterpart. The microstructural characterization of bulk $Cu_{1.98}Se$ (Figure 4) discerned a certain subtle difference when compared to its nanostructured counterpart (Figure 3). It has been noted that the bulk sample consists of an overall coarse-grained microstructure with the grain size between 20-50 nm (Figure 4(a)). A high magnification micrograph of a grain (marked as D in Figure 4(a)) clearly shows that the entire region is stacked with the planes, hkl: 090, with inter-planar spacing of ~0.23 nm (Figure 4(b)). Interestingly, no significant modulation in term of imperfection and strain at an atomic scale in this microstructure has been observed. A corresponding FFT further authenticates the presence

Accepted manuscript

ACCEPTED MANUSCRIPT

of 090 planes in the reciprocal space (inset in Figure 4(b)). Further investigations at the regions around boundary of these grains (marked as E in Figure 4(a)) exhibits the atomic planes of different hkl indices of 220, 090 and 311 (inter-planar spacing: 0.18 nm) with random orientations with respect to each other (Figure 4(c)). Some of these regions also show the existence of Moiré patterns that evolve due to the overlap of tiny crystals present in the material.

Temperature dependence of thermal and electronic transport properties of bulk and nanostructured $Cu_{1.98}Se$ samples is shown in Figure 5. The electrical resistivity of bulk and nanostructured $Cu_{1.98}Se$ has been displayed in Figure 5(a), which exhibits a behavior of typical a conducting material. An anomaly has been observed at 373 K, which corresponds to α to β transition in nanostructured $Cu_{1.98}Se$. A significant increase in the resistivity values for nanostructured $Cu_{1.98}Se$ sample with increasing temperature was noticed, which could be attributed to the enhanced charge carriers scattering due to density of interface boundaries. The electrical resistivity of nanostructured sample, shown in Figure 5(a), shows a value of 24.7 μΩm at 973 K, indicating a ~65% increase in electrical resistivity than that of bulk sample at 973 K. The Hall Effect measurement at room temperature was yielded a carrier concentration (n_e) of 8.5 x 10^{20}/cm^3 and 7.8 x 10^{20}/cm^3, mobility (μ) of 17cm^2/Vs and 14.6 cm^2/Vs for bulk and nanostructured samples, respectively. It is interesting to note that the resistivity of our bulk $Cu_{1.98}Se$ sample was observed to be lower whereas the resistivity of nanostructured sample was found higher than those reported by Liu et al. [23]. The carrier mobility (μ) is related to the carrier concentration (n) and electrical conductivity (σ) by the equation,

$$\sigma = ne\mu \qquad \text{..... (1)}$$

Accepted manuscript

ACCEPTED MANUSCRIPT

Where, e is the electronic charge, which is constant. Therefore, it can be attributed that variation in σ and μ are from the same origin. It is well known that mobility of carriers is related to the carrier effective mass (m*) and scattering relaxation time (τ) by an equation,

$$\mu = e\tau / m^* \quad \text{……(2)}$$

Using equation (1) & (2), σ can be given as,

$$\sigma = ne^2\tau / m^* \quad \text{……(3)}$$

Since the carrier concentration and also electronic charge are expected to be similar for both bulk and nanostructured samples, the difference in their electrical conductivity and mobility are related to the variations of the (τ/m^*) ratio. Further, according to the equation and based on assumptions of a single parabolic band model and energy independent relaxation time, Seebeck coefficient can be expressed as[4],

$$S = \frac{8\pi^2 k_B^2}{3eh^2} m^* T \left(\frac{\pi}{3n}\right)^{\frac{2}{3}} \quad \text{……(4)}$$

Where, k_B is the Boltzmann constant and h is the Planck's constant.

The above equation estimates the m* for nanostructured sample as 2.70m_e and for bulk sample m*= 2.68 m_e which are almost comparable. The nearly similar value of m* indicates that the variation in σ and μ of both samples is associated with the changes in τ. This could be possible due to the high density of defects, such as, grain boundaries and nanoscale imperfections introduced during mechanical milling. Thus, one can conclude from the above analysis that τ depends strongly on the processing methods which, in turn, affects the transport properties.

Accepted manuscript

ACCEPTED MANUSCRIPT

The temperature dependence of the Seebeck coefficient of both $Cu_{1.98}Se$ samples has been shown in Figure 5(b). Seebeck coefficient at room temperature is found to be ~46.2 μV/K and ~40.64 μV/K for bulk and nanostructured samples, respectively, which show a similar trend, especially at high temperature, although the magnitude for nanostructured sample is slightly higher. This slight enhancement in Seebeck coefficient could be attributed to a slight change in the density of states near the Fermi level for nanostructured sample. In the case of particle in the nano-regime, the allowed energies within continuous bands separate into discrete levels when the separation between levels approaches the thermal energy of the electrons. An anomaly, which corresponds to α to β phase transition can clearly be noticed at 373 K. The power factor ($S^2\sigma$) as shown in Figure 5(c) for bulk sample was calculated to be ~1.55 W/mK^2 compared to ~1.08 W/mK^2 at 973 K for the nanostructured sample, which is due to the high resistivity of the nanostructured sample.

The variation of thermal conductivity with temperature (Figure 5(d)) for nanostructured and bulk samples was found to be 0.76 $Wm^{-1}K^{-1}$ and 1.36 $Wm^{-1}K^{-1}$ respectively, at 973 K. These are quite lower than the values reported by Liu et al. for bulk sample [23]. The reduction in thermal conductivity for the nanostructured sample can be attributed to the enhanced phonon scattering by dense grain boundaries and other microstructural imperfections generated during ball milling. In order to get a quantitative idea of the effect of nanostructuring, the lattice thermal conductivity (κ_l) was obtained by subtracting the electron contribution (κ_e) from the total thermal conductivity. As the κ_e was calculated employing Wiedmann-Franz law. The lattice and electronic thermal conductivity plots for both bulk and nanostructured samples are shown in Figure 6(a). To calculate the electronic thermal conductivity Lorentz number is taken to be $L_o = 1.5 \times 10^{-8}$ V^2K^{-2} [28]. At room temperature, for the bulk sample, the values of κ_e and κ_l are found to be 1.06 $Wm^{-1}K^{-1}$ and 1.31 $Wm^{-1}K^{-1}$ respectively, whereas for the nanostructured these were estimated to be 0.84 $Wm^{-1}K^{-1}$ and 0.8 $Wm^{-1}K^{-}$

Accepted manuscript

ACCEPTED MANUSCRIPT

[1] respectively (Figure 6 (a)). After the phase transition at ~375 K, for bulk and nanostructured $Cu_{1.98}Se$ samples, the κ_l has been observed to be decreased significantly than κ_e as shown in Figure 6(a). But, it has also observed that the reduction in κ_e of bulk and nanostructured samples could be due to the charge carriers scattering with increasing temperature. Further, the lower values of κ_l of the nanostructured sample indicate the role of enhanced scattering of phonons with nanoscale defects and dense grain boundaries (HRTEM images shown in Figure 3). Based on the measured electrical and thermal transport properties, the temperature dependence of ZT for nanostructured $Cu_{1.98}Se$ exhibited a high ZT value of ~1.4 at 973 K, which is 30% higher than its bulk counterpart (see figure 6(b)). In order to confirm the reproducibility of our measurements, the temperature dependence of electrical and thermal transport properties was experimentally determined by repeated thermal cycling between room temperature and 973 K and the resulting ZT for three consecutive scans are plotted in Figure 6(c). This figure clearly suggests that the reproducibility in the ZT values is quite good, at all the temperatures and is within the experimental error of ZT.

4. Conclusions

In the current study, we have successfully synthesized nanostructured $Cu_{1.98}Se$ using high energy ball milling followed by spark plasma sintering technique. Rapid heating rates during SPS resulted in the retention of nanoscale features post sintering. HRTEM and XRD analysis of the nanostructured $Cu_{1.98}Se$ exhibited a very small crystallite size ~12 nm. The temperature dependent electrical resistivity of nanostructured $Cu_{1.98}Se$ sample was found to be higher than its bulk counterpart due to the scattering of charge carriers at the grain boundaries grain boundaries and atomic scale defects which were introduced during ball milling. As a result, the measured Seebeck coefficient of nanostructured sample was found to be slightly higher than its bulk counterpart. The enhanced phonon scattering due to low to high wavelength phonons by different kinds of nanoscale defects and abundant

Accepted manuscript

grain boundaries in a nanostructured matrix resulted in a lower thermal conductivity. As a consequence, nanostructured $Cu_{1.98}Se$ exhibited a ZT value ~1.4 at 973 K, which is ~30% higher than its bulk counterpart. This enhancement with better thermal stability suggests that Cu deficient Cu_2Se as a potential candidate for green energy generation.

Acknowledgments

This work was supported by CSIR-TAPSUN (CSIR-NWP 54) programme entitled "Novel approaches for solar energy conversion under technologies and products for solar energy utilization through networking". The authors are also grateful to Mr. Radhey Shyam and Mr. Naval Kishor Upadhyay for their technical support.

References

[1] G.J. Snyder, E.S. Toberer, Complex thermoelectric materials, Nature materials, 7 (2008) 105-114.
[2] S. Ballikaya, H. Chi, J.R. Salvador, C. Uher, Thermoelectric properties of Ag-doped Cu 2 Se and Cu 2 Te, Journal of Materials Chemistry A, 1 (2013) 12478-12484.
[3] J.R. Sootsman, D.Y. Chung, M.G. Kanatzidis, New and old concepts in thermoelectric materials, Angewandte Chemie International Edition, 48 (2009) 8616-8639.
[4] D.M. Rowe, CRC handbook of thermoelectrics, CRC press, 1995.
[5] M. Zebarjadi, K. Esfarjani, M. Dresselhaus, Z. Ren, G. Chen, Perspectives on thermoelectrics: from fundamentals to device applications, Energy & Environmental Science, 5 (2012) 5147-5162.
[6] T. Plirdpring, K. Kurosaki, A. Kosuga, T. Day, S. Firdosy, V. Ravi, G.J. Snyder, A. Harnwunggmoung, T. Sugahara, Y. Ohishi, Chalcopyrite CuGaTe2: A High-Efficiency Bulk Thermoelectric Material, Advanced Materials, 24 (2012) 3622-3626.
[7] Y. Pei, Z.M. Gibbs, B. Balke, W.G. Zeier, G.J. Snyder, Optimum Carrier Concentration in n-Type PbTe Thermoelectrics, Advanced Energy Materials, (2014).
[8] S. Muthiah, J. Pulikkotil, A. Srivastava, A. Kumar, B. Pathak, A. Dhar, R. Budhani, Conducting grain boundaries enhancing thermoelectric performance in doped Mg2Si, Applied Physics Letters, 103 (2013) 053901.
[9] G.-E. Lee, I.-H. Kim, Y.S. Lim, W.-S. Seo, B.-J. Choi, C.-W. Hwang, Preparation and Thermoelectric Properties of Doped Bi2Te3-Bi2Se3 Solid Solutions, Journal of Electronic Materials, 43 (2014) 1650-1655.
[10] L. Bulat, V. Bublik, I. Drabkin, V. Karataev, V. Osvenskii, Y.N. Parkhomenko, G. Pivovarov, D. Pshenai-Severin, N.Y. Tabachkova, Bulk nanostructured polycrystalline p-Bi-Sb-Te thermoelectrics obtained by mechanical activation method with hot pressing, Journal of Electronic Materials, 39 (2010) 1650-1653.

Accepted manuscript

ACCEPTED MANUSCRIPT

[11] A. Minnich, M. Dresselhaus, Z. Ren, G. Chen, Bulk nanostructured thermoelectric materials: current research and future prospects, Energy & Environmental Science, 2 (2009) 466-479.
[12] S. Bathula, M. Jayasimhadri, N. Singh, A. Srivastava, J. Pulikkotil, A. Dhar, R. Budhani, Enhanced thermoelectric figure-of-merit in spark plasma sintered nanostructured n-type SiGe alloys, Applied Physics Letters, 101 (2012) 213902.
[13] B. Yu, W. Liu, S. Chen, H. Wang, H. Wang, G. Chen, Z. Ren, Thermoelectric properties of copper selenide with ordered selenium layer and disordered copper layer, Nano Energy, 1 (2012) 472-478.
[14] L. Hicks, T. Harman, X. Sun, M. Dresselhaus, Experimental study of the effect of quantum-well structures on the thermoelectric figure of merit, Physical Review B, 53 (1996) R10493.
[15] R. Venkatasubramanian, E. Siivola, T. Colpitts, B. O'quinn, Thin-film thermoelectric devices with high room-temperature figures of merit, Nature, 413 (2001) 597-602.
[16] A.I. Boukai, Y. Bunimovich, J. Tahir-Kheli, J.-K. Yu, W.A. Goddard Iii, J.R. Heath, Silicon nanowires as efficient thermoelectric materials, Nature, 451 (2008) 168-171.
[17] B. Poudel, Q. Hao, Y. Ma, Y. Lan, A. Minnich, B. Yu, X. Yan, D. Wang, A. Muto, D. Vashaee, High-thermoelectric performance of nanostructured bismuth antimony telluride bulk alloys, Science, 320 (2008) 634-638.
[18] W. Xie, J. He, H.J. Kang, X. Tang, S. Zhu, M. Laver, S. Wang, J.R. Copley, C.M. Brown, Q. Zhang, Identifying the specific nanostructures responsible for the high thermoelectric performance of (Bi, Sb) 2Te3 nanocomposites, Nano letters, 10 (2010) 3283-3289.
[19] Y. Ma, Q. Hao, B. Poudel, Y. Lan, B. Yu, D. Wang, G. Chen, Z. Ren, Enhanced thermoelectric figure-of-merit in p-type nanostructured bismuth antimony tellurium alloys made from elemental chunks, Nano letters, 8 (2008) 2580-2584.
[20] X. Yan, B. Poudel, Y. Ma, W. Liu, G. Joshi, H. Wang, Y. Lan, D. Wang, G. Chen, Z. Ren, Experimental studies on anisotropic thermoelectric properties and structures of n-type Bi2Te2. 7Se0. 3, Nano letters, 10 (2010) 3373-3378.
[21] Y. Lan, B. Poudel, Y. Ma, D. Wang, M.S. Dresselhaus, G. Chen, Z. Ren, Structure study of bulk nanograined thermoelectric bismuth antimony telluride, Nano letters, 9 (2009) 1419-1422.
[22] W. Liu, X. Yan, G. Chen, Z. Ren, Recent advances in thermoelectric nanocomposites, Nano Energy, 1 (2012) 42-56.
[23] H. Liu, X. Shi, F. Xu, L. Zhang, W. Zhang, L. Chen, Q. Li, C. Uher, T. Day, G.J. Snyder, Copper ion liquid-like thermoelectrics, Nature materials, 11 (2012) 422-425.
[24] O. Milat, Z. Vučić, B. Ruščić, Superstructural ordering in low-temperature phase of superionic Cu_2Se, Solid State Ionics, 23 (1987) 37-47.
[25] R.M. Murray, R.D. Heyding, The copper-selenium system at temperatures to 850 K and pressures to 50 kbar, Canadian Journal of Chemistry, 53 (1975) 878-887.
[26] V. Bhuse, P. Hankare, K. Garadkar, A. Khomane, A simple, convenient, low temperature route to grow polycrystalline copper selenide thin films, Materials chemistry and physics, 80 (2003) 82-88.
[27] S.K. Haram, K. Santhanam, Electroless deposition of orthorhombic copper (I) selenide and its room temperature phase transformation to cubic structure, Thin Solid Films, 238 (1994) 21-26.
[28] X. Xing-Xing, X. Wen-Jie, T. Xin-Feng, Z. Qing-Jie, Phase transition and high temperature thermoelectric properties of copper selenide $Cu_{2-x}Se$ ($0 \leq x \leq 0.25$), Chinese Physics B, 20 (2011) 087201.
[29] A. Khorsand Zak, W. Abd Majid, M. Abrishami, R. Yousefi, X-ray analysis of ZnO nanoparticles by Williamson–Hall and size–strain plot methods, Solid State Sciences, 13 (2011) 251-256.

Accepted manuscript

ACCEPTED MANUSCRIPT

[30] S. Vives, E. Gaffet, C. Meunier, X-ray diffraction line profile analysis of iron ball milled powders, Materials Science and Engineering: A, 366 (2004) 229-238.
[31] D. Maier, Strain-field domain structure in Bi_2Te_3 thermoelectric materials, Solid state communications, 122 (2002) 565-568.
[32] Y. Kuru, M. Wohlschlögel, U. Welzel, E. Mittemeijer, Large excess volume in grain boundaries of stressed, nanocrystalline metallic thin films: Its effect on grain-growth kinetics, Applied Physics Letters, 95 (2009) 163112.
[33] G.K. Rane, U. Welzel, S.R. Meka, E.J. Mittemeijer, Non-monotonic lattice parameter variation with crystallite size in nanocrystalline solids, Acta Materialia, 61 (2013) 4524-4533.
[34] G. Rane, U. Welzel, E. Mittemeijer, Grain growth studies on nanocrystalline Ni powder, Acta Materialia, 60 (2012) 7011-7023.

Accepted manuscript

Figure captions:

Figure 1: The differential scanning calorimetry (DSC) measurement of different Cu compositions of nanostructured $Cu_{2-x}Se$

Figure 2: XRD patterns of $Cu_{1.98}Se$ nanostructured and bulk samples recorded at room temperature. Inset shows the significant peak broadening of nanostructured $Cu_{1.98}Se$ in comparison to bulk.

Figure 3: HRTEM images of nano-structured $Cu_{1.98}Se$, showing (a) uniform fine-grained densely packed microstructure, (b) atomic scale image of region A, (c) an interface between 020 and 090 planes, (d) magnified view of region C, (e) atomic scale image of region C, (f) FFT shows the planes 220 and 090, (h) strained microstructure of region B, and (i) two nano-crystals with planes 220 and 090 separated by a sharp interface between them.

Figure 4: HRTEM images of bulk-$Cu_{1.98}Se$, showing (a) coarse-grain microstructure, (b) atomic scale image of region D within an individual grain, and (c) atomic scale image of region E with different planes at the grain boundaries marked with dotted lines. Inset: (b) a corresponding FFT of the atomic scaled image.

Figure 5: Temperature dependence electrical and thermal transport properties (a) Electrical Resistivity, (b) Seebeck Coefficient, (c) Power Factor (d) Thermal conductivity (inset:

ACCEPTED MANUSCRIPT

shows the variation of thermal diffusivity with temperature) of samples bulk and nanostructured $Cu_{1.98}Se$.

Figure 6: Temperature dependence thermoelectric properties (a) Lattice and electronic thermal conductivity (b) ZT of bulk and nanostructured $Cu_{1.98}Se$ samples and (c) reproducibility data of ZT.

Highlights

1. Cu deficient Cu_2Se synthesized employing nanostructuring and spark plasma sintering.
2. Nanostructured $Cu_{1.98}Se$ resulted in a high ZT ~1.4 at 973 K.
3. Significant reduction in lattice thermal conductivity has been observed by nanostructuring.
4. Post sintering atomic/nanoscale features were characterized by HRTEM.

Accepted manuscript

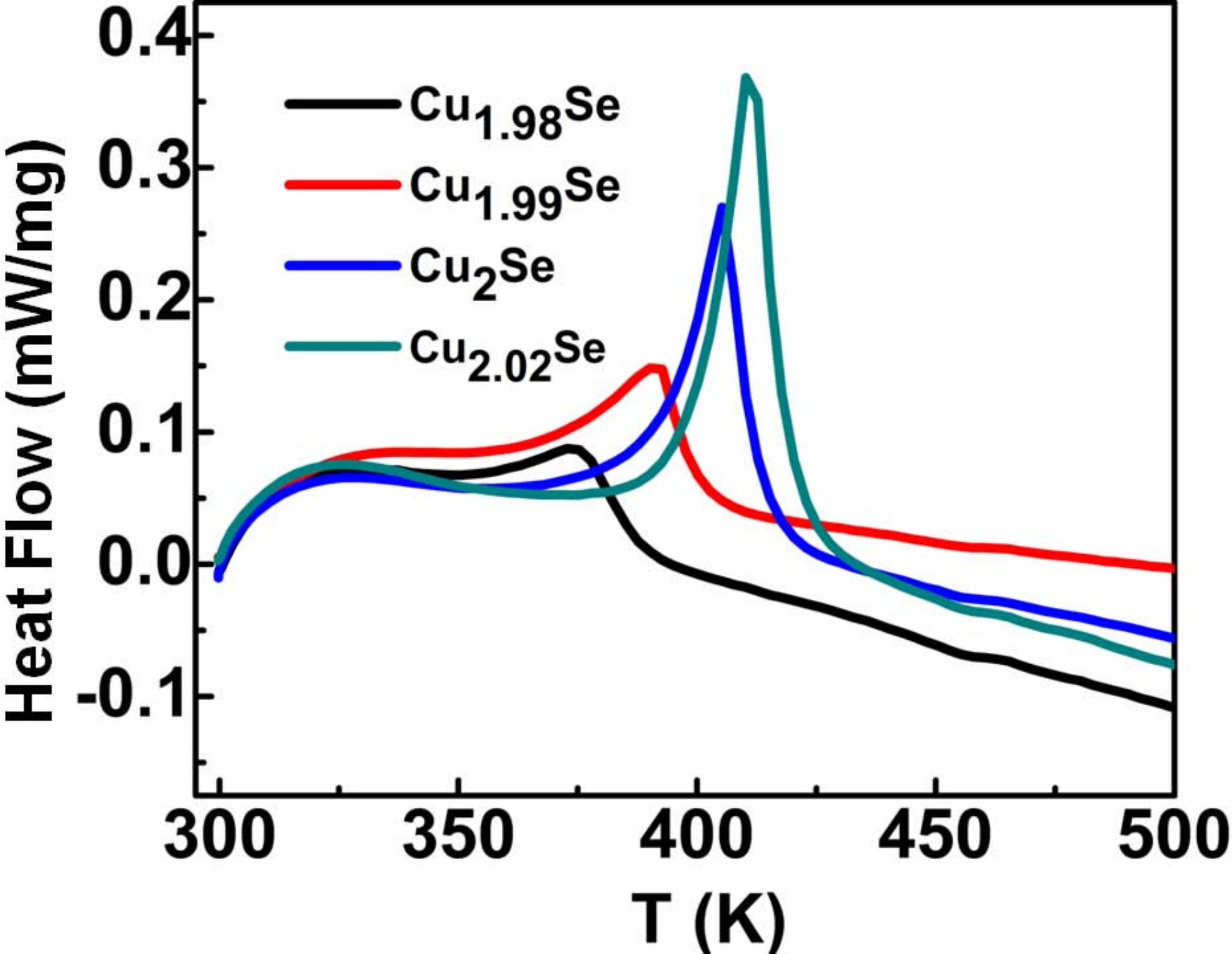
0.4
0.3
0.2
0.1
0.0
-0.1
Heat Flow (mW/mg)
Cu1.98Se
Cu1.99Se
Cu2Se
Cu2.02Se
300
350
400
450
500
T (K)

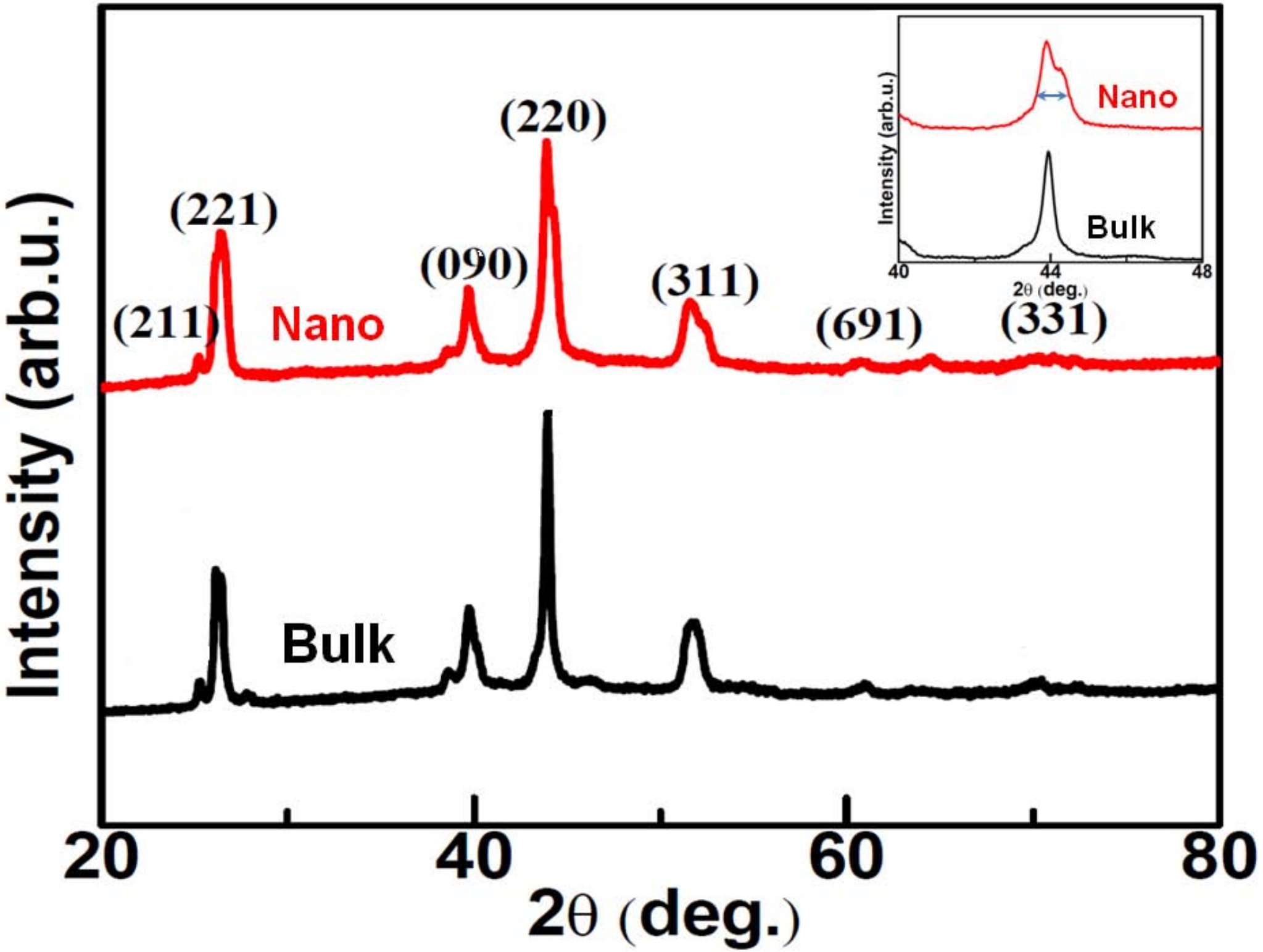
Intensity (arb.u.)
(221)
(211)
Nano
(090)
(220)
(311)
(691)
(331)
Bulk
20
40
60
80
2θ (deg.)
Intensity (arb.u.)
Nano
Bulk
40
44
48
2θ (deg.)

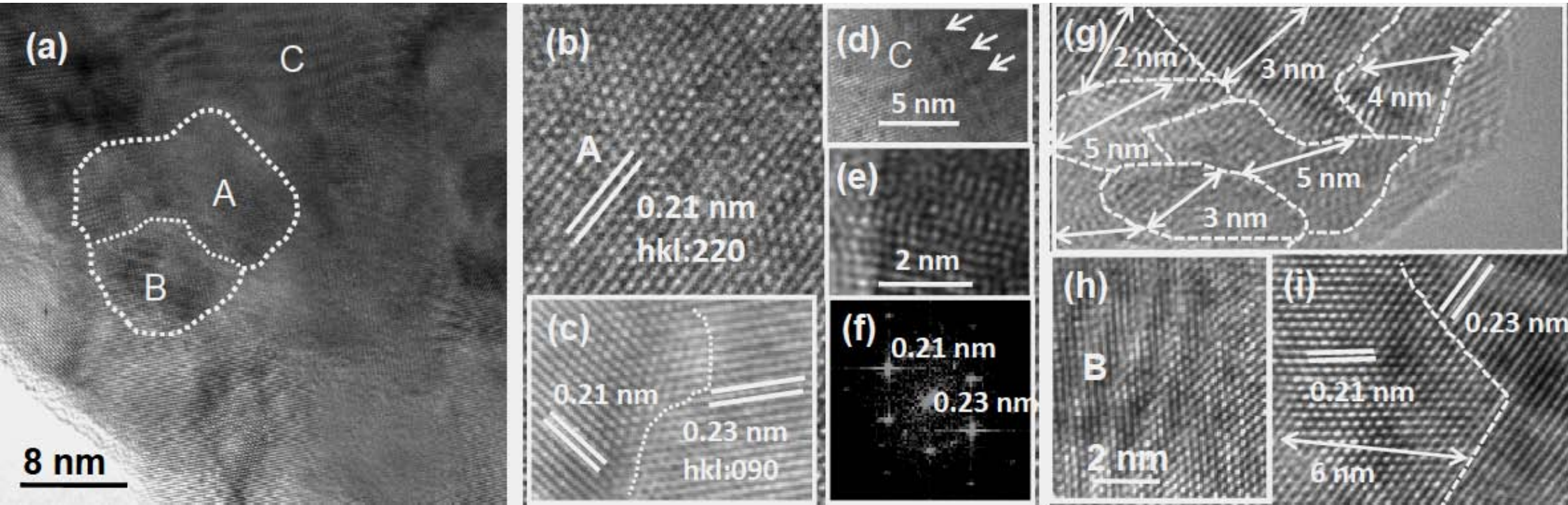
(a)
C
A
B
8 nm
(b)
A
0.21 nm
hkl:220
(c)
0.21 nm
0.23 nm
hkl:090
(d)
C
5 nm
(e)
2 nm
(f)
0.21 nm
0.23 nm
(g)
2 nm
3 nm
4 nm
5 nm
5 nm
3 nm
(h)
B
2 nm
(i)
0.23 nm
0.21 nm
6 nm

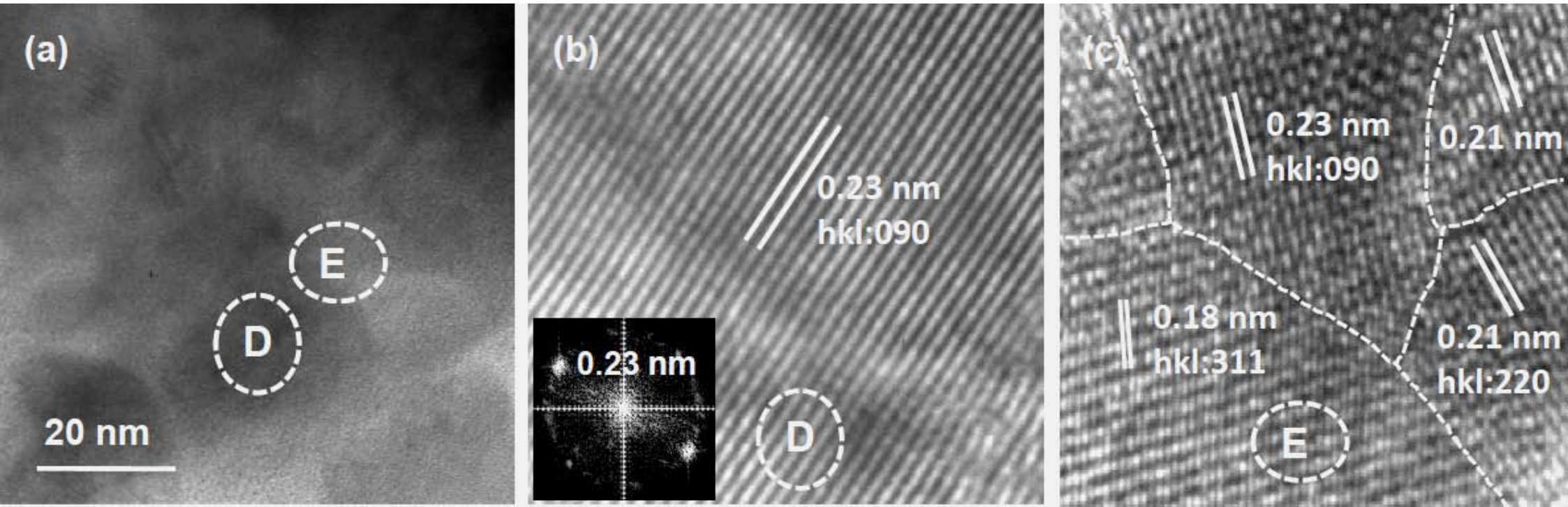
(a)
E
D
20 nm
(b)
0.23 nm
hkl:090
0.23 nm
D
(c)
0.23 nm
hkl:090
0.21 nm
0.18 nm
hkl:311
0.21 nm
hkl:220
E

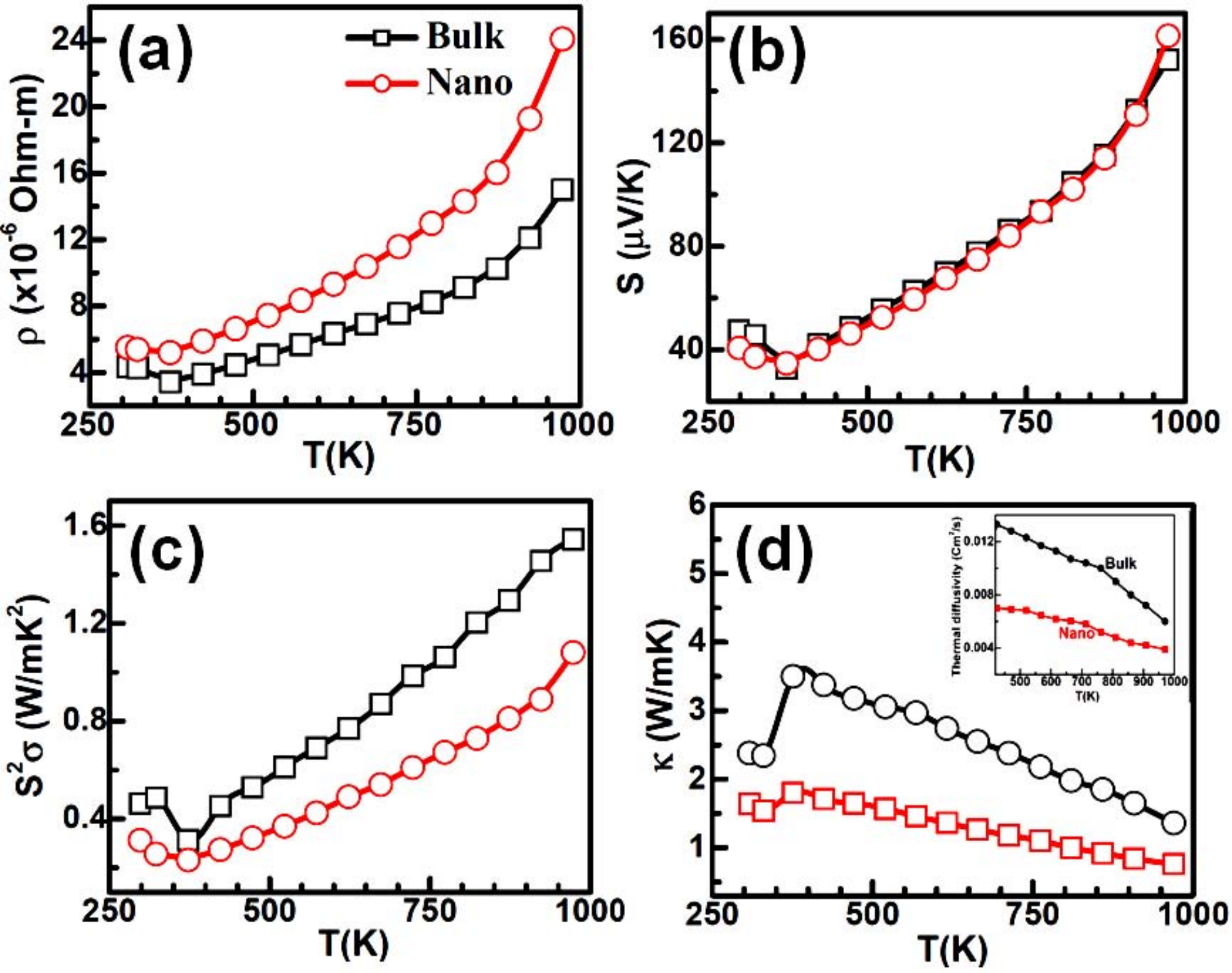
(a)
Bulk
Nano
ρ (x10^-6 Ohm-m)
T(K)
(b)
S (μV/K)
T(K)
(c)
S²σ (W/mK²)
T(K)
(d)
κ (W/mK)
T(K)
Thermal diffusivity (Cm²/s)
Bulk
Nano
T(K)

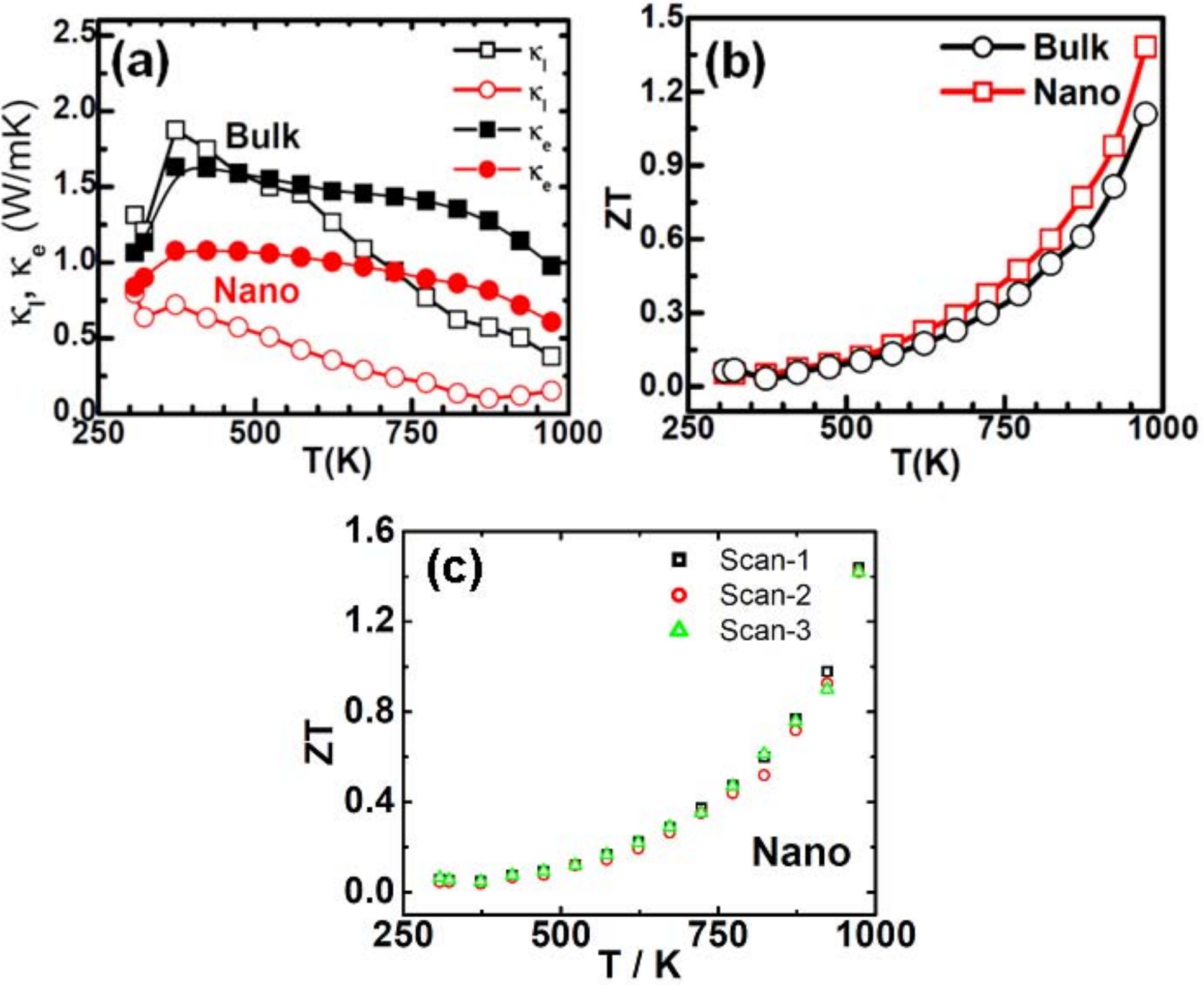
(a)
Bulk
Nano
κ_l
κ_l
κ_e
κ_e
κ_l, κ_e (W/mK)
T(K)
(b)
Bulk
Nano
ZT
T(K)
(c)
Scan-1
Scan-2
Scan-3
Nano
ZT
T / K

Appl Biochem Biotechnol (2014) 174:1174–1187
DOI 10.1007/s12010-014-0996-x

Enhancing Performance of Uricase Using Multiwalled Carbon Nanotube Doped Polyaniline

Kavita Arora · Meenakshi Choudhary · Bansi D. Malhotra

Received: 19 February 2014 / Accepted: 19 May 2014 /
Published online: 14 June 2014
© Springer Science+Business Media New York 2014

Abstract Multiwalled carbon nanotubes (CNT) doped polyaniline (Pani) nanocomposite has been electrochemically deposited onto indium tin oxide (ITO)-coated glass substrate for fabrication of uric acid biosensor. To achieve this, uricase (from *Bacillus fastidiosus*) has been covalently immobilized onto glutaraldehyde-modified CNT-Pani/ITO and characterized using cyclic voltammetry (CV), scanning electron microscopy (SEM), Fourier transform infrared (FTIR) spectroscopy, electrochemical impedance spectroscopy (EIS), etc. CV studies of CNT-Pani/ITO electrode reveals that the system obeys quasi-reversible electron transfer behavior with diffusion coefficient of 2.3346×10^{-8} cm s^{-1} in K_3FeCN_6. Fabricated uricase-CNT-Pani/ITO electrodes were tested for uric acid detection in buffer and spiked serum samples electrochemically. It was found that fabricated electrode was able to detect 0.01–1.0 mM uric acid using CV and 0.02–0.8 mM uric acid using differential pulse voltammetry (DPV). The enhanced electrochemical performance of this biosensor is due to the high enzyme loading synergistically connected to CNT-Pani nanocomposite leading to improved enzyme characteristics such as K_m value of 4.85×10^{-3} mM L^{-1} (about 70 times less than the free enzyme), sensitivity of 43.2 μA mM^{-1} for CV-based detection and 8.38 μA mM^{-1} for DPV-based detection within response time of 60 s. Fabricated electrodes were able to maintain their electrochemical activity with 60 times reusability and were stable up to 28 weeks when stored at 4 °C.

Keywords Carbon nanotubes · Polyaniline · Uric acid · Uricase · Biosensor

Introduction

Elevated urate levels in human are of major concern worldwide. Urate test or uric acid determination is a routinely performed to access existence of disease or its state in case of

K. Arora (✉) · M. Choudhary
Advanced Instrumentation Research Facility, Jawaharlal Nehru University, New Delhi 110067, India
e-mail:kavitaa@gmail.com, kavitaarora@jnu.ac.in

B. D. Malhotra
Department of Biotechnology, Delhi Technological University, Main Bawana Road, New Delhi 110042, India

gout/arthritis, kidney stone analysis/risk panel, effect of drugs/chemotherapy/radiation therapy leukemia, pneumonia, etc. Elevated uric acid levels from normal physiological range in human fluids (0.15–0.45 mM in serum and 1.4–4.4 mM in urine) are due to altered purine metabolism, and decreased levels are due to exposure of toxic compounds. Changing lifestyle pattern is witnessing rising hypertension cases, and it is being suspected to have relation with the elevated urate levels [1]. Consequently, uric acid measurement for diagnosis and treatment of these disorders is routinely required at a larger scale. In this context, a unique option lies in application of uricase enzyme for estimation of uric acid. Various uric acid biosensors have emerged in laboratories besides the available contemporary methods of uric acid determination to overcome their existing challenges [2, 3]. The available biosensors are providing immense opportunities to tune in various performances-related parameters through simple measurement, shorter response time, high sensitivity, and selectivity through application/integration of various "nano"-"bio" materials.

Biosensor fabrication process involves two important steps: selection of bio-element (here uricase for uric acid determination) along with immobilization surface to be interfaced and transduction of bio-recognition event to a measurable output. It has been noticed that most of the biosensors are amperometrically driven, and the measurements are being performed ≥0.5 V. This potential range is unfavorable towards the real-world measurements since most of the biological-electroactive molecules interfere in the analyte measurement. Interestingly, careful selection of immobilization support material in coherence to the bio-recognition event gives important key to resolve the challenges of this signal transduction. With the emergence of nanotechnology and available opportunities to tune in sensitivity, stability of bio-element and ease of fabrication, it is desired to design and choose a suitable functional material for enzyme immobilization [4]. Range of nanomaterials such as metal nanoparticles (gold, silver, zinc, etc.), carbon allotropes (carbon nanotubes, graphene, graphite, etc), nanostructured conducting polymers (polypyrrole, polyaniline, polyacrylate, etc.) are available to be integrated with the biological elements [5, 6]. Uses/applications of nanomaterials, conducting polymers (CPs) and their composites, towards fabrication in various biosensors are well cited. Carbon nanotubes ever since their discovery are most attractive due to their low cost, unique tunable mechanical and electric properties [7, 8]. Similarly, CPs also referred to as synthetic metals and their uniqueness lie in electrical and magnetic properties of a metal, while retaining the mechanical properties of a polymer. Here, polyaniline (Pani) is the second most widely studied member of intrinsically conducting organic polymers that has a rigid and planar backbone providing good conductivity and is insoluble in common organic solvents [5].

Yan Jiang et al. developed a selective uricase biosensor with electroactive intrinsic polyaniline synthesized in ionic liquid at high pH showing linear detection range from 1.0×10^{-3} to 1.0 m mol dm^{-3}. The value of the Michaelis–Menton constant (K_m) was found to be 7.83 m mol L^{-1} [9]. A polyaniline-uricase biosensor was developed by template process that uses generation of hydrogen peroxide and its consumption by peroxidase, subsequently measuring the dissolved oxygen concentration with shelf-life of about 75 days and the K_m as 2.31 mol dm^{-3} [10]. Polyaniline-poly-n-butyl-methacrylate composite film has been prepared for estimation of uric acid via measuring the change in electrical resistance as a function of concentration of the uric acid (5–12 mg dL^{-1}) [11]. Nanostructured polyaniline-uricase biosensor has been prepared that sensed uric acid in the range of 0.1–0.6 mM uric acid in 60 s response time, K_m value 5.1×10^{-3} mM L^{-1} reusability (more than 30 times) and stability (>16 weeks) [2]. Recently, self-assembled monolayers (SAMs) of thio-substituted nucleo-bases and their derivatives (mercaptopyrimidine (MPM), mercaptopurine (MPU), 4-amino-2-mercaptopyrimidine (AMP), 6-thioguanine (TG), 4,6-diamino-2-mercaptopyrimidine (DMP)) on gold (Au) electrode have been used for simultaneous electro analysis of NADH, ethanol, and uric acid (UA). Among them, Au-AMP electrode shows linear response for uric acid

concentration range (1–500 μM) with high sensitivity (0.78±0.007 $\mu A cm^{-2}$ μM^{-1}). However, the separation between the two broad peaks (uric acid and NADH) is small (80–100 mV) [12]. A reagent less uricase/MWCNTs–SnO_2 biosensor for uric acid determination has been reported in differential pulse voltammetry (DPV) measurements in 1.0×10^{-7}–5.0×10^{-4} mol L^{-1} range and detection limit of 5.0×10^{-8} mol L^{-1} which retained 79.5 % activity when stored at 5 °C and reused for about 10 successive uses with 4.5 % loss [13]. Uricase-thionine-single-walled carbon nanotube/glassy carbon has been developed with a low detection limit (0.5±0.05 μM), a wide linear range (0.002 to 2 mM), high sensitivity (~90 $\mu A mM^{-1} cm^{-2}$), as well as good stability and repeatability [14]. Uricase-polyacrylic acid-multiwalled carbon nanotube was used to detect uricase in 0.3–10 μM with LOD of 110 nM [15]. Gold nanoparticle-CNT composite has been used for uric acid in range of 0.01–0.8 mM with LOD of 0.01 mM [16]. PDDA-uricase-ZnO-MWNTs multilayer uricase biosensor showed a wide linear response range of 0.005 to 1 mM with a linear sensitivity of 393 mA cm^{-2} M^{-1}, a detection limit of 2.0 mM (3σ), and a long-term stability of 160 days can be obtained by using differential pulse voltammetry (DPV) [17]. Zinc oxide nanowires-based uric acid biosensor has been reported with sensitivity of 89.74 μA cm^{-1} mM^{-1} in the linear detection range of 0.1–0.59 mM [18].

In this work, we report immobilization of uricase to electrochemically prepared multiwalled carbon tube-polyaniline composite for its application towards detection of uric acid.

Methods

Chemicals and Reagents

Multiwalled carbon nanotubes (CNT), aniline (Ani), horse radish peroxidase (HRP, EC 1.11.1.7) having specific activity 200 U/mg, Tris buffer, indium tin oxide (ITO)-coated glass plates, o-dianisidine, uric acid, cholesterol, ascorbic acid, urea, and glucose were purchased from Sigma-Aldrich. Uricase was procured from Fluka as lyophilized powder having activity 16.2 U/mg (EC 1.7.3.3; from *Bacillus fastidiosus*). Aniline was distilled prior to being use. All other chemicals and solvents were of analytical grade and were used without any purification.

Preparation of CNT Doped Polyaniline onto Indium Tin Oxide (ITO)-Coated Glass Plates

In 1 M HCl, 1 mg ml^{-1} CNT was solubilized (chemical oxidation/carboxyl functionalization of CNT) through ultra-sonication for about 80 h [19, 20]. Thereafter, a monomer solution containing aniline (0.1 M) and 0.01 mg mL^{-1}CNT in 1 M HCl was subjected to constant current of about 150 μA for about 15 min to deposit carbon nanotubes-polyaniline (CNT-Pani) composite on ITO coated glass substrates (1 cm^2) using a three-electrode electrochemical cell consisting Ag/AgCl reference electrode and platinum counter electrode using chronopotentiometric technique with the intermittent washing steps using potentiostat-galvanostat (Autolab PGSTAT 302). It must be mentioned here that these CNT-Pani electrodes were prepared by controlling the chain length and morphology using two intermittent washing with 1 M HCl buffer after every 5 min of polymerization (i.e., total polymerization time of 15 min).

Immobilization of Uricase onto CNT-Pani Surface

Scheme 1 shows the enzyme interfacing with the CNT-Pani surface for fabrication of an electrochemical biosensor for uric acid. Five microliters (0.16 U) of uricase (1 mg/ml) was immobilized onto glutaraldehyde-activated CNT-Pani. The CNT-Pani was dipped in 0.5 %

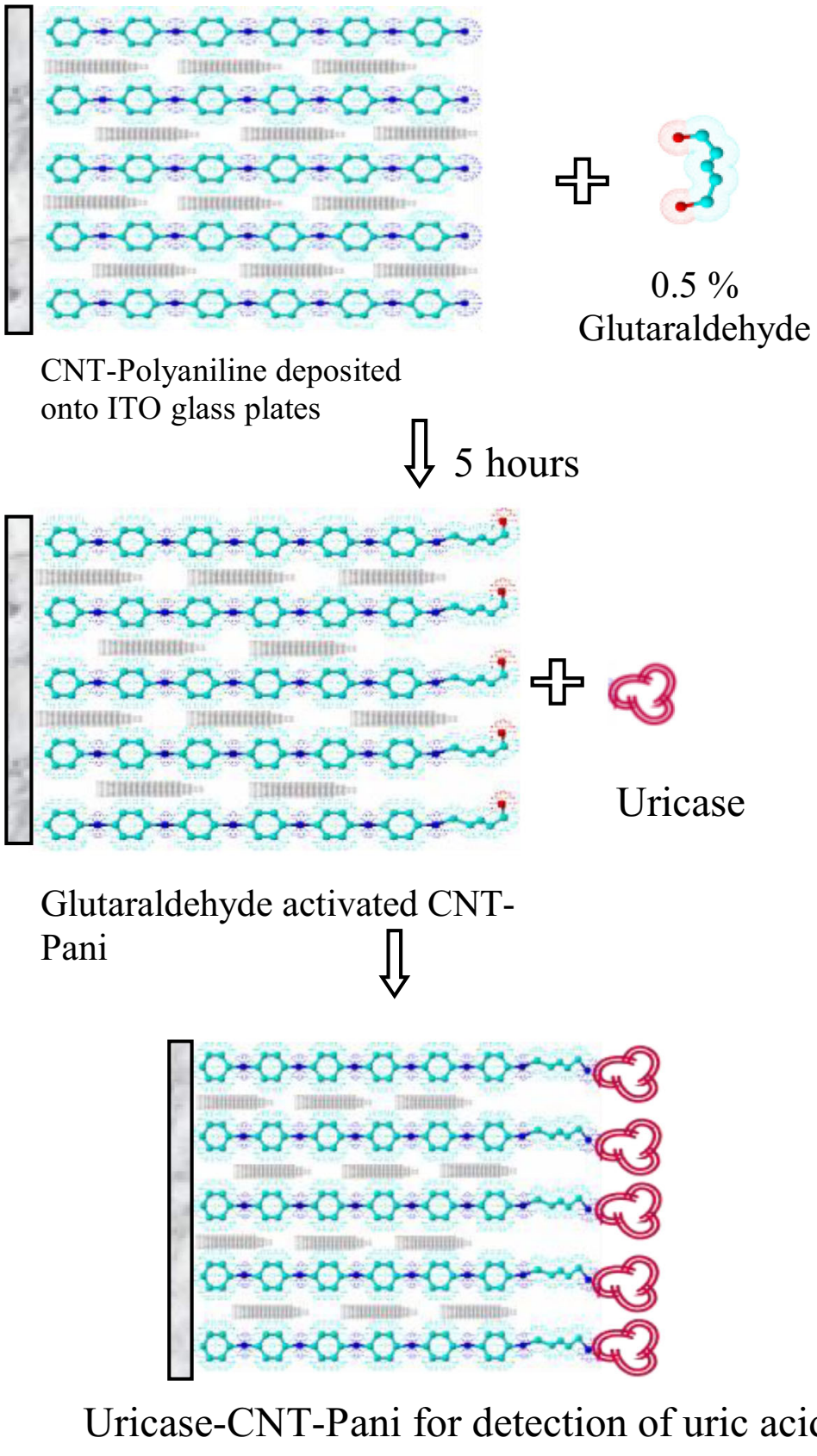

Scheme 1 Preparation of uricase-CNT-Pani/ITO electrode

glutaraldehyde solution for 5 h to covalently link "uricase" through its amino group. After the successful immobilization of the enzyme, the electrodes were washed with Tris-Cl buffer (50 mM at pH 6.5) to remove the non-covalently bound enzyme on polymer surface. UV-visible

measurements carried out to check presence of any unbound enzyme on "Tris-Cl buffer" collected after washing the electrode surface revealed that 98 % of uricase could be loaded onto CNT-Pani. The series of uricase-CNT-Pani electrodes were prepared and stored at 4 °C when not in use. The uricase-CNT-Pani electrodes were characterized using UV–VIS spectrometer (Shimadzu (model 160A), scanning electron microscopy (SEM, Leo 440), cyclic voltammetry (CV), differential pulse voltammetry (DPV), and impedance spectroscopy (Autolab Eco chemie, Netherlands)). Standard uric acid solutions were prepared in Tris-Cl buffer (50 mM at pH 6.5).

Uricase Measurements

UV-Visible Response Studies of Free Uricase and Uricase-CNT-Pani Electrodes

Uricase activity was studied for their UV visible response as a function substrate concentration (0.01–1.1 mM) at pH 6.5 and 10–50 °C temperature. These measurements were carried out with a UV–VIS spectrometer (Shimadzu 160A), and the entire process involves two-step biochemical reactions as indicated in Eqs. 1 and 2.

$$\text{Uric acid} + H_2O + O_2 \xrightarrow{\text{uricase}} \text{allantoin} + CO_2 + H_2O_2 \quad (1)$$

$$H_2O_2 \xrightarrow{\text{HRP}} 2H^+ + O_2 + 2e^- \xrightarrow{\text{diorthoanisidine}} \text{colored product} \quad (2)$$

UV visible response was recorded at 405 nm after 60 s. To stop the reaction process, uricase functionalized CNT-Pani electrode was removed from substrate containing reaction mix, and the reaction mix was kept in ice to immediately stop the enzyme action for in case free enzyme. Reaction mix consisted of 2 ml Tris-Cl buffer containing 0.025 mg/ml HRP (horse radish peroxidase), 0.01 % o-dianisidine dye, and desired concentration of substrate uric acid.

Characterization and Response Studies of Uricase-CNT-Pani Electrodes

The electrochemical behavior of CNT-Pani and uricase-CNT-Pani electrodes were studied by using CV, DPV, and impedance measurements using a three-electrode cell comprising Ag/AgCl as a reference electrode, platinum foil as a counter electrode, and uricase-CNT-Pani electrode as working electrode in 50 mM Tris-Cl buffer of pH 6.5. CV and DPV of uricase-CNT-Pani electrodes were recorded in 50 mM Tris-Cl buffer containing desired uric acid concentration (0.01–1.1 mM) at scan rate of 30 mV s^{-1} after 60 s reaction time at 35 °C. Fabricated uricase-CNT-Pani electrode was attested for its electrochemical performance in presence of various interferents such as ascorbic acid, urea, cholesterol, and glucose. Uric acid estimation was also performed in blood serum samples obtained from volunteers using uricase-CNT-Pani electrodes through photometric and electrochemical methods with reference to respective standard curves. The serum samples were kept at 4 °C before analysis.

Results and Discussion

Electrochemical investigations of Pani, CNT-Pani, and Uricase-CNT-Pani electrodes

Figure 1a shows CV and impedance studies (inset) of CNT-Pani deposited onto ITO-coated glass plates recorded in Tris buffer 50 m M, pH 6.5 at 30 mVs^{-1}. Where in CV of CNT-Pani

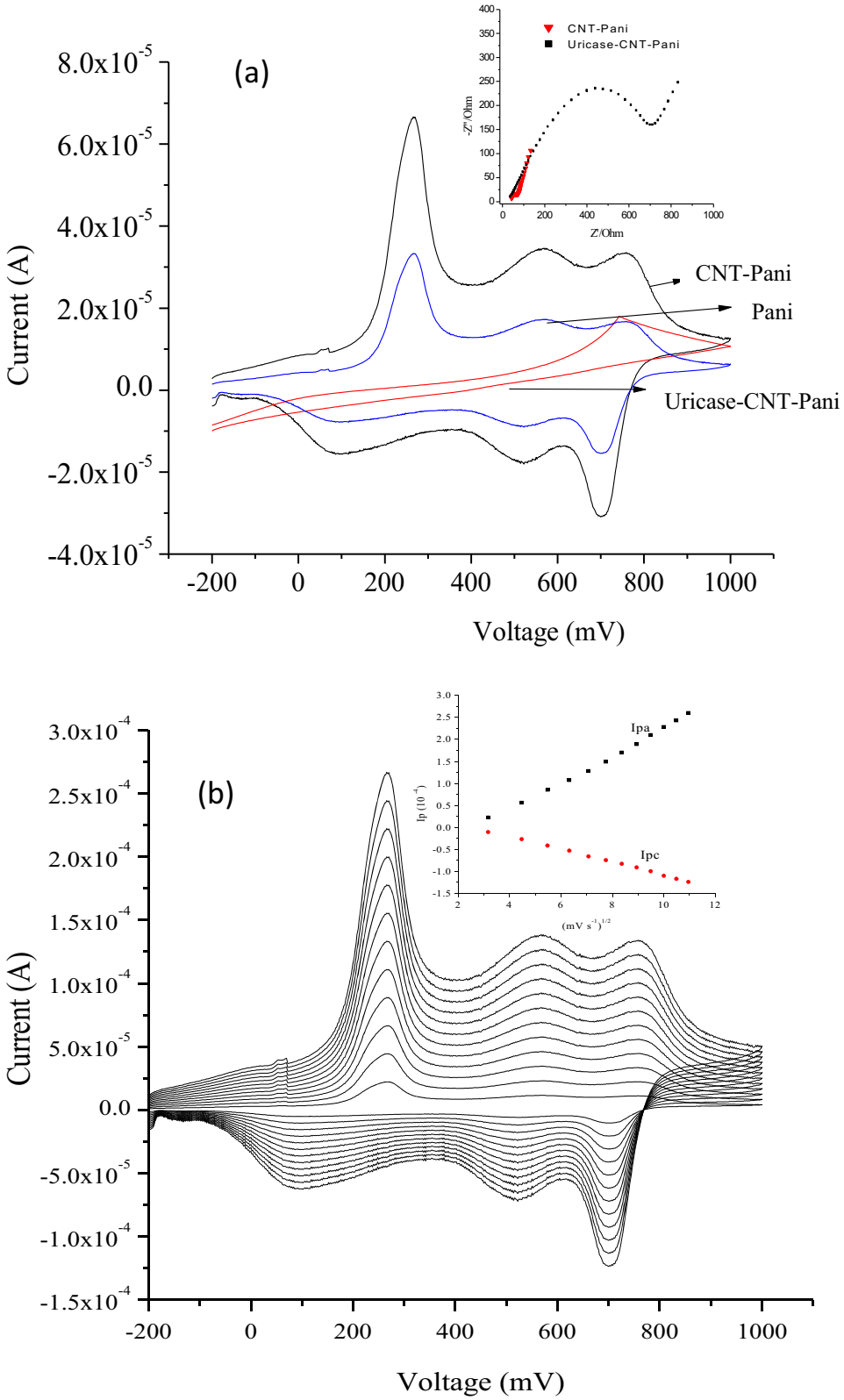

Fig. 1 **a** Cyclic voltammetry and impedance measurements (*inset*) of Pani, CNT-Pani, and uricase-CNT-Pani electrode in 50 mM Tris buffer pH 6.5 and 3 mM K_3FeCN_6, **b** CV studies of CNT-Pani at various scan rates (10–120 mV s^{-1}) in 50 mM Tris buffer pH 6.5

reveals three characteristic redox peaks at about 266 and 565 and 755 mV describing the first two peaks for oxidation of aniline to radical cation (leucoemeraldine) and then to radical dication (emeraldine). The third peak may be attributed to the formation of emeraldine to (per)

nigraniline [21]. These results indicate that negatively charged CNT is associated with the Pani as a dopant molecule. It is worth mentioning here that peak current of Pani-CNT is 6.8×10^{-5} A, which is higher than that of Pani electrode (3.2×10^{-5} A) [2]. Further to this, CV of uricase-CNT-Pani electrode indicates the successful immobilization of uricase due to absence of these oxidation peaks for CV. These results reveal the slow redox process occurring at the electrode surface due to slow electron transfer from the surface due to immobilization of uricase enzyme. Figure 1a inset contains the impedance spectroscopic studies of CNT-Pani and uricase-CNT-Pani electrodes in 50 mM Tris-Cl of pH 6.5 in the frequency range of 10 MHz to 10^5 Hz at a bias voltage of 0.13 V. In the Cole–Cole plot of dielectric spectroscopy, semicircle portion at higher frequency correspond to electrode transfer limited process whereas linear portion corresponds to diffusion. The value of electron transfer resistance depends on dielectric features at the electrode-electrolyte interface. Uricase-CNT-Pani electrode surface shows higher R_{CT} (732 Ω) as compared to CNT-Pani electrodes (37.5 Ω), which can be attributed to the presence of obstructing layer of enzyme uricase on the conducting polymer surface for ion exchange [2]. It may be noted that these results are in agreement with the CV studies.

Figure 1b exhibits CV studies of CNT-Pani at various scan rates (10–120 mV s^{-1}). It can be seen that anodic (I_{pa}) and cathodic peak (I_{pc}) current various linearly as a function of square root of scan rate $v^{1/2}$ (Fig. 1b inset, Eq. 3) suggesting that the electrochemical process follows quasi-reversible

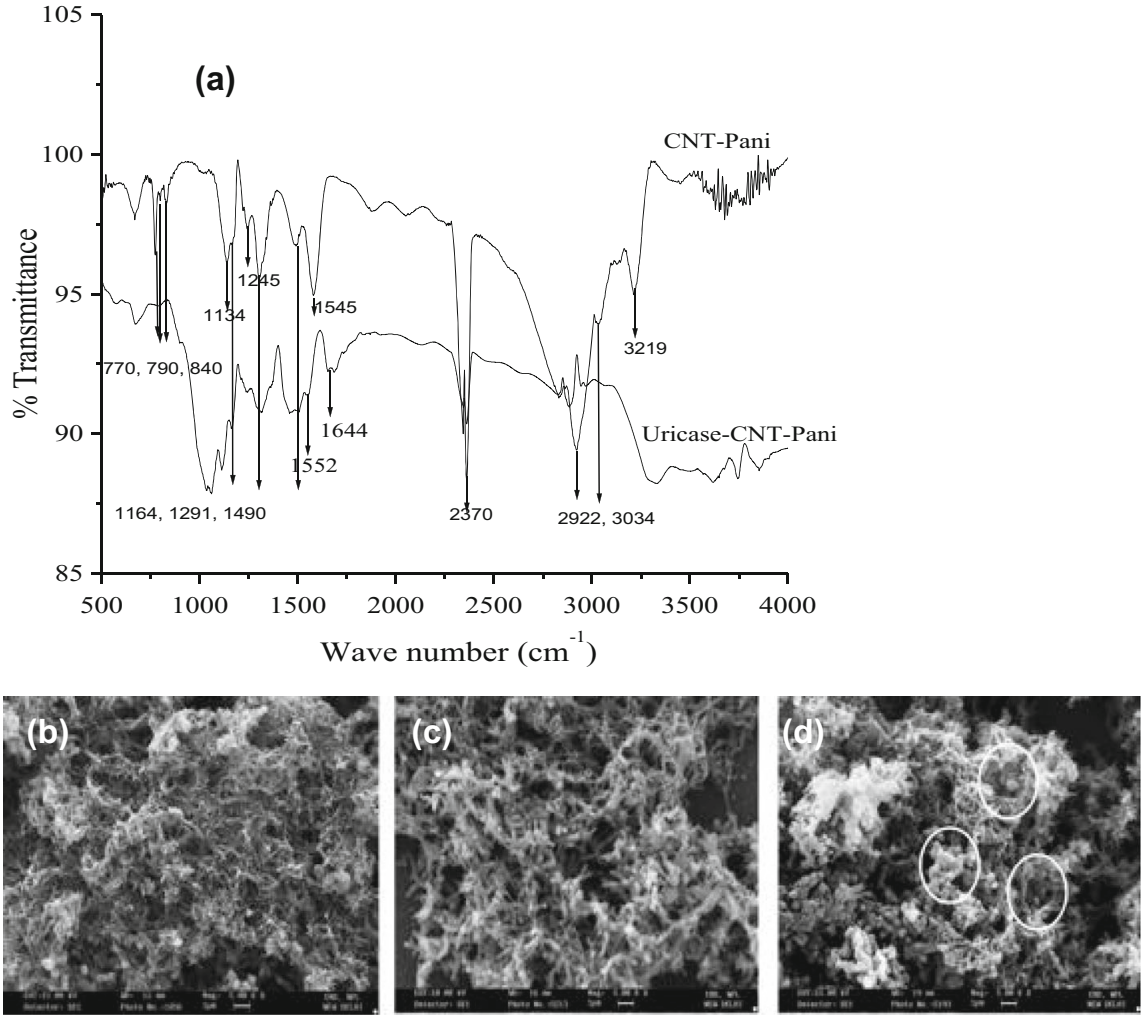

Fig. 2 **a** FTIR measurements and **b**–**d** SEM pictures of Pani, CNT-Pani, and uricase-CNT-Pani electrodes

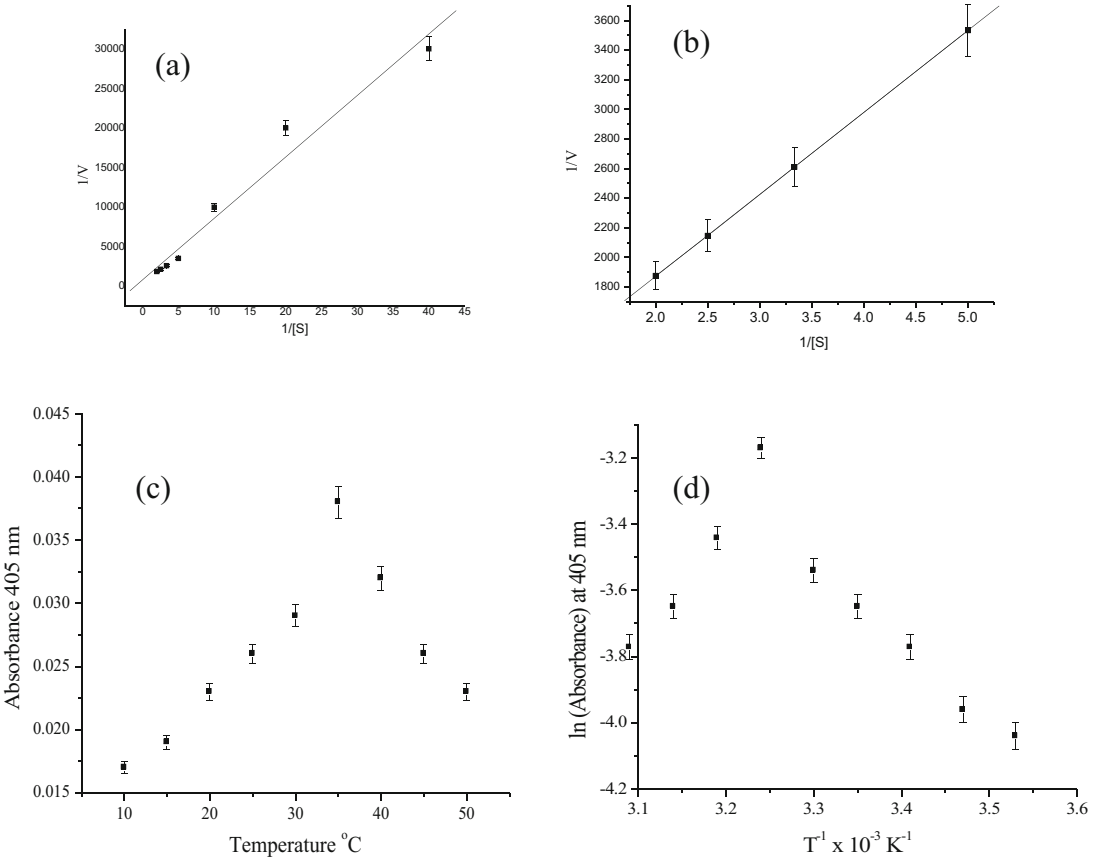

Fig. 3 Lineweaver–Burk plots: **a** free uricase and **b** uricase-CNT-Pani. **c** Activity of uricase-CNT-Pani electrode as a function of temperature (10–50 °C in 50 mM Tris-Cl of pH 6.5); **d** Arrhenius plot of ln (absorbance) as a function of reciprocal of absolute temperature (K^{-1})

electron transfer behavior (ΔE_p=1.44 V) and is diffusion controlled. The diffusion coefficient "*D*" has been calculated to be 2.3346×10^{-8} cm s^{-1} using Randal–Sevcik Eq. (4) [22].

$$I_p = 0.30787 \times 10^{-4} \pm 0.0062 \times v^{1/2} – 0.8335 \times 10^{-4} \pm 0.05 \left(R^2 = 0.9979\right) \quad (3)$$

$$I_p = \left(2.69 \times 10^5\right) n^{3/2} A D^{1/2} C v^{1/2} \quad (4)$$

[Where I_p is the peak current, v is scan rate in V s^{-1}, A is area of film in cm^2 (0.25 cm^2 in our case), C is the bulk concentration (5 mM for $FeCN_6^{-3}$), "*n*" is number of electron transfer per molecule in oxidation process (here n=1)]. The surface coverage/concentration (Γ) of electroactive species on CNT-Pani has been calculated using Brown-Anson model [23] and found to be 6.0517×10^{-7}molcm^{-2} using Eq. (5) as given below:

$$I_p = n^2 F^2 A \Gamma \times v/4RT \quad (5)$$

Where R is gas constant (8.314 J/mol/K), T is the absolute temperature of the system (=25 °C), F is Faraday's constant (96,584 C mol^{-1}), Γ is the surface concentration of the film in mol cm^{-2}.

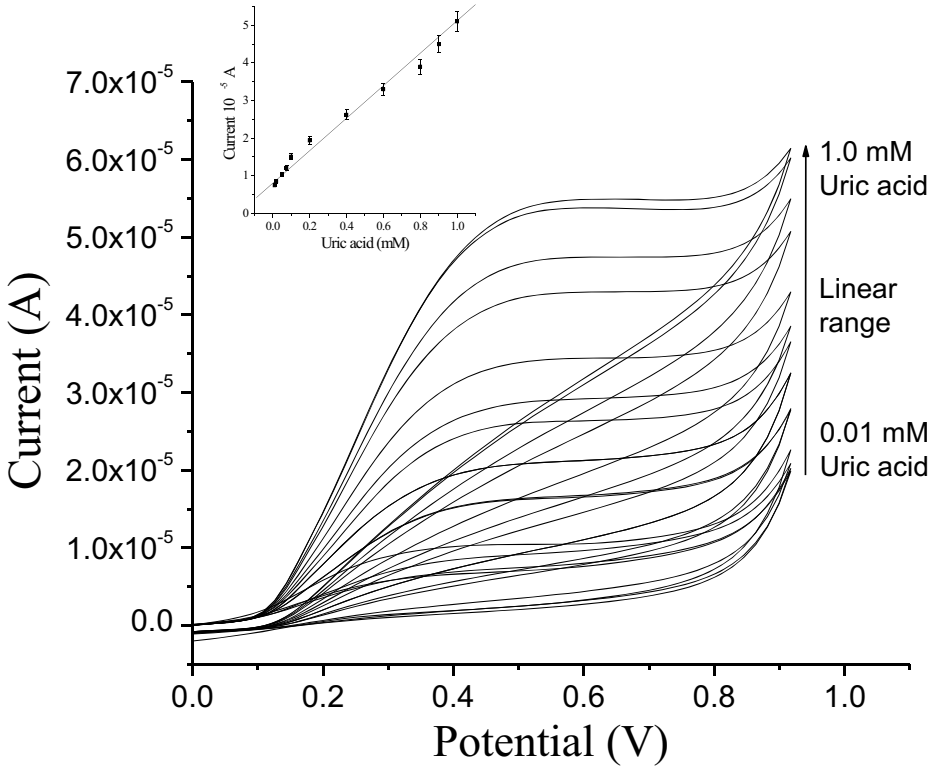

(a)

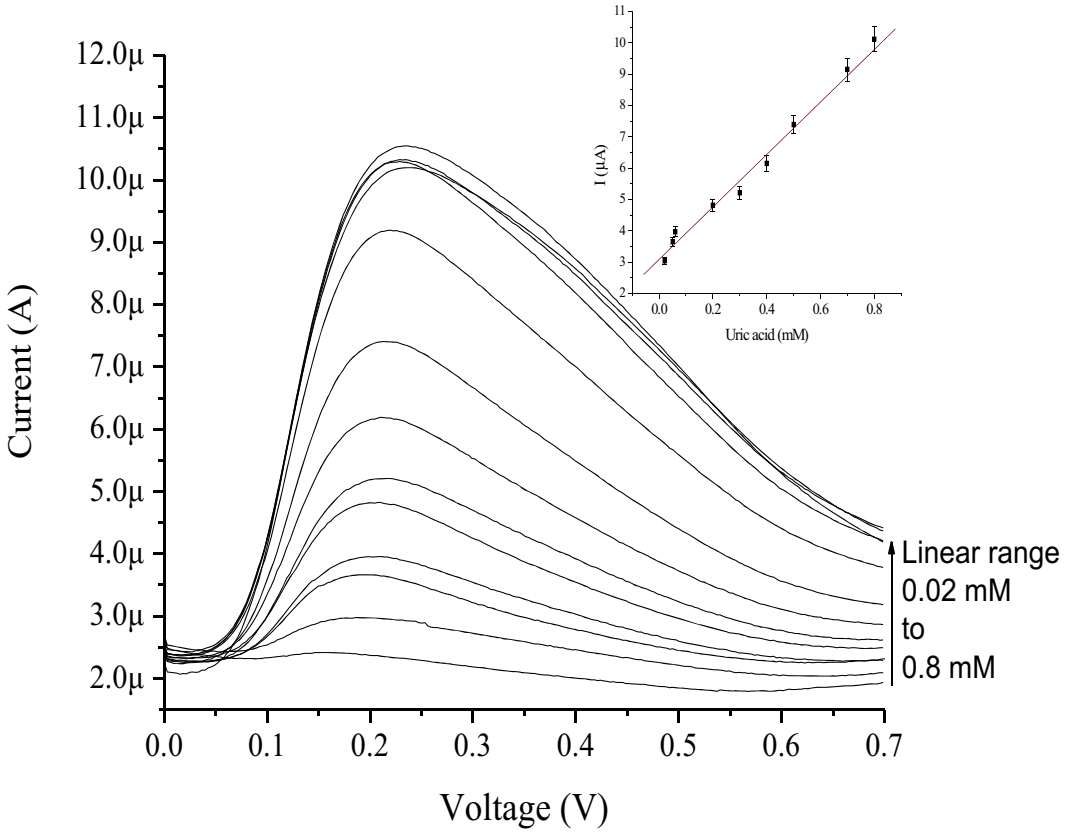

(b)

Fig. 4 **a** CV and **b** DPV (pulse height 50 mV and pulse width 70 ms) of uricase-CNT-Pani electrode in uric acid concentrations 0.01–1.1 mM in Tris–HCl, 50 mM, pH 6.5 and plot of uric acid concentration vs. peak height in mA in *inset*

FTIR and SEM Studies of CNT-Pani and Uricase-CNT-Pani Electrodes

The Fourier transform infrared (FTIR) spectrum and SEM pictures of Pani [2], CNT-Pani, and Uricase-CNT-Pani electrode are shown in Fig. 2a–d, respectively. FTIR spectra are shown in Fig. 2a where peaks at 770 (C-H bend), 790, and 840 $cm^{-1}$are for bending vibrations of C-H linkage in aniline in agreement to our earlier studies [2]. Dip seen at 1,291 cm^{-1} can be assigned to pyridine-type C-N bond representing presence of Pani [2, 24]. Peak at 1,490 cm^{-1} can be assigned to C=C of benzoid rings and 1,575 for aromatic and unsaturated structure of >C=C< bonds affirming presence of Pani [2, 25]. While peaks at 1,133 and 1,164 cm^{-1} for C-O bends and stretching vibrations in –carboxyl groups of CNT and polyaniline, respectively. Broad dip from 2,900–3,400 cm^{-1} is attributed to OH stretch present in CNT and 2,370 cm^{-1} peak is due to -OH stretch from strongly hydrogen bonded –COOH groups present on CNT [26]. Peak at 2,922 cm^{-1} is for asymmetric stretching of CH bond in Pani. However, peak at 3,034 and 3,219 cm^{-1} is due to OH asymmetric stretch in aromatic carbon. The additional peak observed in the spectra of uricase-CNT-Pani at 1,552 and 1,644 cm^{-1} are attributed to the primary and secondary amide linkages in enzyme molecules indicating the presence of uricase onto the CNT-Pani surface.

Figure 2b–d shows the scanning electron microscopic pictures of the Pani, CNT-Pani, and uricase-CNT-Pani electrodes, respectively. It can be seen that polyaniline exists as fibrous structure (Fig. 2b), which is colocated with brighter fibers of CNTs (Fig. 2c). It is worth noticing that presence of small globules structures present in uricase-CNT-Pani as shown in Fig. 2d confirms the immobilization of uricase onto CNT-Pani surface compared to CNT-Pani surface. It is introspected that negatively charged functional groups (-OH/-COOH) on CNT surface is providing sufficiently good doping to Pani that coexistence of both will be facilitating a promising immobilization support for electrochemical signal transduction.

Response Characteristics of free Uricase and Uricase-CNT-Pani Using Colorimetric Estimation

Colorimetric assay has been performed to assess enzyme activity of free uricase and uricase-CNT-Pani electrode at 405 nm using UV–VIS spectroscopy at varied pH of buffer, temperature, and uric acid concentration (0.01 to 1.1 mM). Uricase-CNT-Pani electrode was found to give maximum activity at pH 6.5 of Tris-Cl buffer (results not shown), and this is in agreement to a known trend that proteins generally work well at 1 pH strength higher than its pI (pI of uricase is 5.4) without any major change in confirmation. Besides this, the maximum activity of uricase at this pH may also be also assigned to use of positively charged matrix CNT-Pani that might be additionally buffering the surrounding negatively charged ions to sustain suitable microenvironment for uricase. Michaelis–Menton kinetic parameter (K_m) was calculated as the values of enzymatic reaction from Lineweaver–Burk plot (Fig. 3a, b). The K_m value of free and immobilized enzyme (uricase-CNT-Pani) were found to be 3.4×10^{-1} and 4.85×10^{-3} mM L^{-1}, respectively (Fig. 3a, b). The results indicate improved enzyme affinity towards the substrate (uric acid) leading to favorably improved activity of the immobilized uricase. It is significantly noticed that the K_m value of the immobilized uricase improved by about 70 times compared to free enzyme and 1.06 times compared to uricase-Pani [2]. This improved value can be assigned to CNT's role as dopant which is contributing towards improved signal transduction and bringing in favorable changes in enzyme affinity to substrate and its performance. Uricase-CNT-Pani electrode has been studied for their thermal stability by measuring the absorbance at 405 nm at

Table 1 Electrochemical response of uricase-CNT-Pani electrodes in presence of interferents for 0.2 mM uric acid in 0.05 M Tris, pH 6.5

Interferent	Concentration	Determination of uric acid (mM) without interferents		Determination of uric acid (mM) with interferents	
		CV	DPV	CV	DPV
Urea	2 mM	0.19±0.04	0.2±0.02	0.18±0.05	0.19±0.02
Glucose	5 mM	0.21±0.02	0.21±0.02	0.22±0.04	0.20±0.02
Ascorbic acid	2 mM	0.17±0.03	0.19±0.03	0.21±0.03	0.19±0.03
Cholesterol	150 mg/dl	0.19±0.04	0.19±0.03	0.19±0.04	0.2±0.02
All	Same as above	2.0±0.04	2.0±0.03	2.2±0.03	2.0±0.02

different temperatures ranging from 10 to 50 °C (Fig. 3c, d). It can be seen that the absorbance increased with the increase in the temperature up to 35 °C and started decreasing thereafter (Fig. 3c). This decrease in absorbance with increasing temperature beyond 40 °C can be due to the denaturation of enzyme through continuous heat denaturation that increases with rise in temperature. The activation energies in the lower and higher range were calculated (Fig. 3d) and found to be 13.9 and 34.65 kJ/mol, respectively, suggesting better activity of enzyme at lower temperature.

Electrochemical Estimation of Uric Acid Using Uricase-CNT-Pani Electrode

Figure 4a shows the cyclic voltammograms of uricase-CNT-Pani electrode for different uric acid concentrations (0.01–1.1 mM) wherein the oxidation peak observed at 0.45 V corresponding to the oxidation of hydrogen peroxide produced during the reaction between uricase enzyme and uric acid (Eq. 1).

The increase in the value of oxidation current with increase in urea concentration indicates the increase in the hydrogen peroxide concentration. Only single electrode was used to study the influence of different concentrations of uric acid on the electrochemical behavior. From the plot, it is clear that linear detection range of the uricase-CNT-Pani electrode has been found to be 0.01–1.0 mM of uric acid (Fig. 4a inset) with the sensitivity of 43.21 $\mu A\ mM^{-1}$. Improved performance of this biosensor may be due to the positively charged matrix of CNT-Pani which is facilitating inflow of negatively charged ions including substrate uric acid and is providing suitable microenvironment for immobilized uricase leading to enhanced biomolecule-analyte interaction. This might also include favorable confirmatory changes to enzyme uricase. Figure 4b contains similar studies of uricase-CNT-Pani using DPV indicating detection range of 0.2–0.8 mM uric acid and sensitivity of 8.38 $\mu A\ mM^{-1}$ at 0.227 V. These results indicate that measurement of uric acid is

Table 2 Estimation of uric acid concentration in serum samples

Serum sample	Uric acid (mM) using spectrophotometric measurement	Uric acid (mM) using electrochemical measurements	
		CV	DPV
S1	0.36±0.02	0.36±0.01	0.36±0.02
S2	0.43±0.02	0.38±0.01	0.42±0.02
S3	0.08±0.03	0.07±0.015	0.08±0.025

Table 3 Performance characteristics of Uricase-CNT-Pani/ITO electrodes as compared to uric acid biosensors reported in literature

Immobilization matrix	K_m value	Transducer used	Immobilization technique	Linearity	Interferents effect	Shelf life	Sensitivity	Response time	Detection limit	Reference
Screen printed electrodes-Prussian blue	Not reported	Chronoamperometry	Glutaraldehyde activation	0.03–0.3 mM	Not reported	15 days	6.67 mg dL^{-1}	2 min	0.01 mM	[29]
Gold/amino acid nanocomposite	1.78 mM	Amperometry	Not mentioned	0.02–2.5 mM	No	70 days	10.8 μA mM^{-1} cm^2	4 s	7.0 μM	[30]
PBNPs/cMWCNT/Pani/Au composite	0.058 mM	Cyclic voltammetry	Glutaraldehyde	0.005–0.8 mM	Yes	7 months	Not reported	4 s	5 μM	[31]
T-ZnO	Not reported	Amperometry	Electrostatic adsorbance	0.8 μM–3.49 mM	Not reported	72 h	80.0 μA cm^{-2} mM	9 s	0.8 μM	[32]
Polypyrrole	3.4×10^{-7} M	Electrochemiluminescence	Electropolymerization	7.5×10^{-11}–8.3×10^{-6} M	Yes	–		–	75 pM	[33]
Polyaniline uricase	5.1×10^{-3} (66 times less than free enzyme)	Amperometry	Glutaraldehyde activation	0.01–0.6 mM	No effect detected	>18 months	4.72 μA/mM	60 s	0.01 mM	[2]
Uricase-Pani-CNT/ITO	4.85×10^{-3} mM/L (70 times less than free enzyme)	Cyclic voltammetry	Glutaraldehyde activation	0.01–1.0 mM	No effect detected	>28 weeks	43.21 μA/mM	60 s	0.01 mM	Present work

possible at a relatively lower potential using DPV measurement, which is very useful to lower down the influence of interferents present in real-world samples.

Response of Uricase-CNT-Pani Electrode in Serum

Table 1 summarizes the effect of interferents (2 mM urea, 5 mM glucose, 2 mM ascorbic acid, 150 mg/dl cholesterol) in electrochemical response (CV and DPV) of the uricase-CNT-Pani electrodes on detection of 0.2 mM uric acid. These results indicate that there is little or no variation in the response current in the peak at 450 mV for CV and 0.227 V for DPV. These results indicate that developed uricase-CNT-Pani electrode reflects little or no influence of interferents especially in case of DPV. Table 2 describes the response studies of the uricase-CNT-Pani electrodes in serum samples. These results reveal that these designed electrodes can be used for clinical diagnostics since no significant influence of serum interferents has been observed.

Besides this, it may be noted that the uricase-CNT-Pani electrodes have been found to have response time of 60 s and can retain the enzyme activity by 95 % after 28 weeks of storage at 4 °C. The enzyme electrode was reused for about 60 times for electrochemical measurements while retaining the enzyme activity at about 90 %. These results are showing improvement over our previous studies [2]. Since polyaniline has been reported as good thermal insulator for various enzymes [27, 28], this CNT-Pani composite is providing improved, conducive, and favorable microenvironment contributing improved enzyme stability and affinity for substrate. The comparison of present work with performance characteristics various uric acid biosensors reported literature has been described in Table 3.

Conclusions

Uricase has been successfully integrated with CNT-Pani matrix for fabrication of uric acid biosensor. Interestingly, it was revealed using FTIR and SEM studies that CNTs and Pani fibers are colocated in a way that CNTs are substituting the Cl^- ions as dopants. Further studies of uricase-CNT-Pani electrodes have shown that value of the Michaelis–Menton constant (K_m=4.85×10^{-3} mM L^{-1}) decreased about 70 times compared to free enzyme. Negatively charged CNT dopant-fibers appear to facilitate increased interaction of uricase with uric acid. These uricase-CNT-Pani electrodes give promising and improved performance in terms of response time (60 s), sensitivity (43.2 μA mM^{-1} in 0.01–1.0 mM using CV and 8.38 μA mM^{-1} in 0.02–0.8 mM using DPV) and stability (>28 weeks). Attempts are being made to attest the efficacy of the Pani-uricase electrodes using urine samples.

Acknowledgments We are grateful to Prof. Sopory, Vice Chancellor, JNU, and Prof. Bhudhani, Director, NPL, New Delhi, India for their constant encouragement and infrastructural support. DST-PURSE, DBT sponsored projects IYBA-2008 (BT/B1/12/045/2008) andRGYI-2009 (BT/PR13127/GBD/27/195/2009) are duly acknowledged.

References

1. Poudel, B., Yadav, B. K., Kumar, A., Jha, B., & Raut, K. B. (2014). *Journal of Tropical Biomedicine, 4*, 59–64.
2. Arora, K., Sumana, G., Saxena, V., Gupta, R. K., Gupta, S. K., Yakhmi, J. V., et al. (2007). *Analytica Chimica Acta, 594*, 17–23.
3. Ali, S. M. U., Alvi, N. H., Ibupoto, Z., Nur, O., Willander, M., & Danielsson, B. (2011). *Sensors and Actuators B, 152*, 241–247.

4. Wanekaya, A. K., Chen, W., Myung, N. V., & Mulchandani, A. (2006). *Electroanalysis, 18*, 533–550.
5. Arora, K., Chand, S., & Malhotra, B. D. (2006). *Analytica Chimica Acta, 568*, 259–274.
6. Yang, D. S., Jung, D. J., & Choi, S. H. (2010). *Radiation Physics and Chemistry, 79*, 434–440.
7. Iiloma, S. (1991). *Nature, 354*, 56–58.
8. Heer, W. A., Charelain, A., & Ugarte, D. (1995). *Science, 270*, 1179–1180.
9. Jiang, Y., Wang, A., & Kan, J. (2007). *Sensors and Actuators B, 124*, 529–534.
10. Kan, J., Pan, X., & Chen, C. (2004). *Biosensors and Bioelectronics, 19*, 1635.
11. Castillo-Ortega, M. M., Rodríguez, D. E., Encinas, J. C., Plascencia, M., Mendez-Velarde, F. A., & Olayo, R. C. (2002). *Sensors and Actuators B, 85*, 19.
12. Behera, S., & Raj, C. R. (2007). *Sensors and Actuators B, 128*, 31–38.
13. Zhang, F. F., Xiao-Li Wang, X. L., Li, C. X., Li, X. H., Wan, Q., Xian, Y. Z., et al. (2005). *Analytical and Bioanalytical Chemistry, 382*, 1368–1373.
14. Chen, D., Wang, Q., Jin, J., Wu, P., Wang, H., Yu, S., et al. (2010). *Analytical Chemistry, 82*, 2448–2455.
15. Liu, A., Honma, I., & Zhou, H. (2007). *Biosensors and Bioelectronics, 23*, 74–80.
16. Chauhan, N., & Pundir, C. S. (2011). *Analytical Biochemistry, 413*, 97–103.
17. Yiting, W., Lei, Y., Ziqiang, Z., Jian, Z., & Jianzhong, Z. (2009). *Analytical Letters, 42*, 775–789.
18. Zhao, Y., Yan, X., Kang, Z., Lin, P., Fang, X., Lei, Y., et al. (2013). *Microchimica Acta, 180*, 759–766.
19. Jeykumari, D. R. S., Kumar, S. S., & Narayanan, S. S. (2005). *Pramana Journal of Physics, 65*, 731–738.
20. Datsyuk, V., Kalyva, M., Papagelis, K., Parthenios, J., Tasis, D., Siokou, A., et al. (2008). *Carbon, 46*, 833–840.
21. Pruneanu, S., Veress, E., Marian, I., & Oniciu, L. (1999). *Journal of Material Science, 34*, 2733–2739.
22. Randles, J. E. B. (1948). *Transactions of Faraday Society, 44*, 322–327.
23. Bard, A. J., & Faulkner, L. R. (2000). *Electrochemical Methods: fundamentals and applications* (2nd ed.). New York: Wiley.
24. Pengm, H., Mo, Z., Liao, S., Liang, H., Yang, L., Luo, F., et al. (2013). *Science Reports, 3*, 1765.
25. Silverstein, R. M., & Webster, F. X. (2002). *Spectrometric identification of organic compounds sixth edition*. India: Wiley. 165.
26. Saraf, R. (2013). *International Journal of Nano Devices, 2*, 1–6.
27. Gerard, M., Ramanathan, K., Chaubey, A., & Malhotra, B. D. (1999). *Electroanalysis, 11*, 450.
28. Stilwell, D. E., & Park, S. M. (1988). *Journal of the Electrochemical Society, 135*, 2491.
29. Piermarini, S., Migliorelli, D., Volpe, G., Massoud, R., Pierantozzi, A., Cortese, C., et al. (2013). *Sensors and Actuators B, 179*, 170–174.
30. Liu, Y., Yuan, M., Liu, L., & Guo, R. (2013). *Sensors and Actuators B, 176*, 592–597.
31. Rawal, R., Chawla, S., Chauhan, N., Dahiya, T., & Pundir, C. S. (2012). *International Journal of Biological Macromolecules, 50*, 112–118.
32. Lei, Y., Liu, X., Yan, X., Song, Y., Kang, Z., Luo, N., et al. (2012). *Journal of Nanoscience and Nanotechnology, 12*, 513–518.
33. Chu, H., Wei, X., Wu, M., Yan, J., & Tu, Y. (2012). *Sensors and Actuators B, 163*, 247–252.

Exergy analysis of a syngas fuelled cogeneration cycle for combined production of power and refrigeration

Mohd Parvez

Department of Mechanical Engineering,
Al-Falah School of Engineering & Technology,
Faridabad, Haryana 121004, India
E-mail: mparvezalig@rediffmail.com

Abdul Khaliq*

Department of Mechanical Engineering,
Delhi Technological University,
Bawana Road, Delhi 110042, India
E-mail: khaliqsb@gmail.com
*Corresponding author

Abstract: This communication presents a biomass fuelled cogeneration cycle for the combined production of power and refrigeration. The system is an integration of combined gas-steam cycle and absorption refrigeration cycle. A thermodynamic analysis through energy and exergy is employed, to investigate the effects of cycle pressure ratio, gas turbine inlet temperature and evaporator temperature on first-law efficiency and second-law efficiency of the proposed cogeneration cycle. The first and second-law efficiencies increases with the increase in gas turbine inlet temperature whilst decreases with the increase in pressure ratio. Exergy analysis indicates that maximum exergy is destroyed in the combustion chamber which is around 25% of the total exergy input to the cogeneration, followed by the Heat Recovery Steam Generator (HRSG) and gasifier, with the values of 21% and 9%, respectively. Solid waste fuelled cogeneration cycle provides better thermodynamic performance than its rice husk counterpart.

Keywords: biomass; gasification; exergy; syngas; cogeneration; combined power and cooling; rice husk; solid waste; HRSG; heat recovery steam generator.

Reference to this paper should be made as follows: Parvez, M. and Khaliq, A. (2014) 'Exergy analysis of a syngas fuelled cogeneration cycle for combined production of power and refrigeration', *Int. J. Exergy*, Vol. 14, No. 1, pp.1–21.

Biographical notes: Mohd Parvez is a Professor with the Department of Mechanical Engineering at Al-Falah School of Engineering & Technology Faridabad, Haryana, India. He has published numbers of papers in various national and international journals. He is also authors of many books in various subjects. He has delivered many papers in national conferences. He has supervised large number of M Tech dissertation.

Copyright © 2014 Inderscience Enterprises Ltd.

Abdul Khaliq is a Full Professor with the Department of Mechanical Engineering at Delhi Technological University (Formerly Delhi College of Engineering) Delhi, India. He has published large number of research papers in various international journals. He has delivered many keynotes and invited lectures. He is a recipient of BOYSCAST Fellowship of DST of the Government of India and Career Award for Young Teachers of AICTE of the Government of India. He has supervised large number of PhD thesis in the area of Thermal power generation, Alternate fuel combustion, Waste heat recovery and Multi effect Refrigeration.

1 Introduction

Biomass is usually considered as renewable energy source with low or zero life – cycle CO_2 emissions, since the carbon produced in the combustion can be balanced by the formation of new biomass (of course, this is true if the rate of biomass regeneration is equal to the rate of consumption). Therefore, in the future world energy scenario, biomass is expected to play a fundamental role for both greenhouse gas mitigation and traditional fossil – fuels replacement (Maniatis and Millich, 1998).

Biomass gasification has been proven in the past as an efficient mean to transform solid fuels into energy carriers. Activities worldwide are currently focused on demonstration of various technologies mainly for combined heat and power (CHP) production, aiming at proving the economical feasibility and to address the various technical risks associated with these technologies. Biomass integrated gasification combined cycles (BIGCCs) based on the gas turbine (GT) modified for the use of lower calorific values (LHV) gaseous fuels, can achieve higher efficiencies. The combination of the Brayton cycle with the Rankine cycle can result in overall thermal efficiencies of IGCC power plants in excess of 45% (Chuangzhi et al., 2008; Ferreira and Pilidis, 2001; Perez-Fortes et al., 2009).

Mark and Mike (2003) discussed the use of biomass gasification process as the key element in an advanced gas turbine combined cycle system. Savola (2005) simulated the possibilities to increase the power production and the power-to-heat ratio of 1–20 MW CHP plants using biomass fuels with optimisation tools. An analysis is carried out by Franco and Giannini (2005) for the use of biomass in combined cycle plants shows the opportunity of using biomass in plants with a thermodynamic efficiency higher than a minimum value. Their results show a thermodynamic analysis of combined plants using biomass to obtain exhaust gas after treatment with atmospheric post combustion (reheat). Prins et al. (2003) focused on the conversion of biomass with air and/or steam into gaseous components and char represented by solid carbon (graphite). Kilmantos et al. (2009) studied the IGCC based on the pressurised biomass gasification. They carried out a technical and economic assessment of alternative power plant concept with the aid of computer simulation tools. Based on their analysis they reported that estimated efficiency for BIGCCs (10–40 MWe) based on the current gas turbine technology is up to 40% (based on the future advanced gas turbine models it could be up to 45%). Bhattacharya et al. (2011) conducted a thermodynamic analysis of biomass IGCC considering the combustion of supplementary biomass fuel using the oxygen available in gas turbine exhaust. Their results show the plant efficiencies increase with the increase in both the pressure and the temperature ratios: however,

the latter has a stronger influence than the former. It was further shown that supplementary firing of the biomass increases the plant efficiencies of a BIGCC plant till the optimum level of degree of firing. They also evaluated the exergetic efficiencies of different plants equipments to localise the major thermodynamic irreversibilities in the plant.

Above-reported investigations on BIGCC show that about one-third of the fuel energy is rejected as waste enthalpy in the hot exhaust gases resulting in significant amount of exergy expelled from the system. Therefore, it is pertinent to recover some of the thermal energy of the exhaust gases in general and waste exergy in particular to develop more efficient environment friendly combined power cycles. In view of the same a cogeneration cycle for combined production of power and refrigeration has been explored for improving the overall energy conversion efficiency and decreasing the cost of energy per unit capital expense.

Colonna and Gabrielli (2004) worked on a combined system where a gas turbine or gas internal combustion engine drives an ammonia-water absorption refrigeration plant through a heat recovery exchanger. In contrast to the cycle configuration proposed by Erickson et al. (2004) this system drives the power and refrigeration cycle independently. Alexis (2007) proposed a combined system which is similar to Colonna and Gabrielli (2004) system, except that a steam ejector refrigeration cycle replaces the ammonia-water absorption system to produce refrigeration. This cycle utilises extraction steam from the steam turbine, for the conventional Rankine cycle, to heat up the working fluid in an independent steam ejector refrigeration cycle. A number of combined power/cooling cycles based on the Kalina cycle and the Goswami cycle have been proposed (Takeshita et al., 2005; Zheng et al., 2006; Liu and Zhang, 2007; Zhang and Lior, 2007; Phillppe et al., 2009). Takeshita et al. (2005) developed a trinary cycle using a gas turbine at the topping cycle, a steam Rankine cycle at the intermediate stage and an ammonia-water cycle at the bottoming stage. The bottoming stage is a combination of Kalina power cycle and ammonia refrigeration cycle. Their results indicate that the bottoming power-refrigeration cycle contributes to the overall efficiency which is about 7% in electric power.

Though ammonia is the most suitable refrigerant for cooling purposes but due to its toxicity and flammability it is unsafe and it also needs rectification which is an energy consuming process. Therefore, recently much is reported on exergy analysis of lithium bromide-water absorption refrigeration system which is neither toxic nor flammable and do not need any rectification (Lee and Sherif, 2001; Khaliq and Kumar, 2007; Arora and Kaushik, 2009). A very little information is available in the literature on exergy analysis of combined power and cooling cycle using lithium bromide-water as a working fluid. Khaliq et al. (2009) presented the exergy analysis results for waste heat-based combined power and cooling cycle using lithium bromide-water. They highlighted the effects of waste heat gas composition and pinch point temperature on energy and exergy efficiencies of the combined power and cooling cycle. Their results clearly show the benefits of waste heat recovery at the exit of heat recovery steam generator (HRSG) using lithium bromide-water absorption refrigeration system. To the best of our knowledge, no study has been carried out, to date, on exergy analysis of biomass fuelled combined power and cooling cycle using lithium bromide-water as a working fluid. Therefore, the objective of this paper is to construct a theoretical framework for the energy and exergy analyses of a biomass gasification fuelled combined power and

cooling thermodynamic cycle. Energy and entropy balance equations are applied to evaluate the energy and exergy losses in each component and in the overall proposed cycle. Change in some influencing parameters such as cycle pressure ratio, gas turbine inlet temperature and the evaporator temperature were also tested to evaluate their effects on the energy and exergy performance.

2 Problem formulation

The schematic diagram of biomass fuelled combined power and cooling cycle is shown in Figure 1. The biomass is fed to the gasifier at atmospheric conditions. The compressed air at 2 and pressurised steam at 4 enter the gasifier. The gas produced in the gasifier goes to combustion chamber after cleaning at 5. The synthetic gas burned in the combustion chamber in the presence of compressed air, and the combustion products at 6 goes to gas turbine where they expand and produce power. The gas turbine exhaust at 7 enters the HRSG where steam is generated. The superheat steam at 'a', goes to steam turbine for additional power production. A part of superheat steam is extracted at an intermediate stage of turbine at 'e' and goes back to gasifier for biomass gasification. Saturated steam at the exit of steam turbine at 'b' goes to condenser where its phase changes from vapour to liquid at 'c'. The water is then pumped to HRSG at 'd'. The stack gases coming out of the HRSG at state 8 fed to the generator of the vapour absorption system. The refrigerant (H_2O) is separated from LiBr–H_2O in the generator by means of the heat driven by the stack gas. The solution circulation ratio ($f = m_s/m_r$) depends on the temperature to which the solution is heated. After the refrigerant has reached the desired temperature it goes through the condenser at 10 and evaporator at 12 through the expansion valve at 11. The water vapour mixture that enters the evaporator at 12 is boiled and exits the evaporator in a saturated state at13. The saturated steam at 13 enters the absorber where it mixes with a weak solution at 19, generating heat that has to be dissipated to increase the efficiency of the mixing process. The heat released in the condenser and in the absorber is rejected to the cooling water. The mixing process results in a strong solution that exits the absorber at 14 and is pumped to the upper pressure of the cycle at 15. The high pressure strong solution at 15 is heated to a high temperature.

The following assumptions are made for the analysis of the cycle (Reddy and Mohamed, 2007; Khaliq and Rajesh, 2007).

1 Biomass fed to the gasifier at ambient conditions.

2 Air is admitted to the compressor at ambient conditions (p_0 = 1.013 bar, T_0 = 298 K).

3 The compression process is adiabatic and its isentropic efficiency is 85%.

4 The expansion process in the gas turbine is adiabatic with the isentropic efficiency of 85%.

5 The expansion process in the steam turbine is adiabatic with the isentropic efficiency of 85%.

6 Complete combustion takes place in combustion chamber.

7 Gasification of biomass occurs at high pressure under adiabatic condition.

8 Saturated steam extracted from the turbine enters to the gasifier at pressure equal to the compressed air pressure.

9 Steam fuel ratio (SFR) has been taken as unity.

10 Air fuel ratio (AFR) in the gasifier is assumed to be equal to 0.5.

11 System operates at steady state.

12 Pressure drop/losses in all the heat exchangers and the pipelines, as well as on the steam side, are neglected. Pressure drops on the gas side do not affect its temperature.

13 HRSG pressure and temperature at a point 'a' have been taken as 40 bar and 450°C, respectively. Condenser pressure at point 'b' is taken as 0.06 bar.

14 The value of gasifier temperature for selected biomass materials (solid waste and rice husk) at a given gasifier pressure has been taken from the graph reported by Srinivas et al. (2009).

15 Lithium bromide solutions in the generator and in the desorber are assumed to be in equilibrium at their respective temperatures and pressures.

16 Refrigerant (water) at the condenser and the evaporator exits in saturated states (liquid and vapour, respectively).

17 Strong solution of the refrigerant leaving the absorber and the weak solution of refrigerant leaving the generator are saturated.

18 To avoid crystallisation of the solution, the temperature of the solution entering the throttle valve should be the least (7–8°C) above-crystallisation temperature.

19 The system uses stack heat at state 8 to drive the generator, which produces chilled water in the evaporator.

20 Heat losses towards the surrounding air have not been taken into account, as they are generally a minute fraction of the other energy transfers.

3 Thermodynamic analysis of proposed combined power and cooling cycle

For gasification process the biomass is represented by a general formula as $C_{a_0}H_{a_1}O_{a_2}N_{a_3}$

The following will be the chemical reaction during biomass gasification

$$C_{a_0}H_{a_1}O_{a_2}N_{a_3} + wH_2O + a_4(O_2 + 3.76N_2) + a_5H_2O \rightarrow b_1CH_4 + b_2CO + b_3CO_2 + b_4H_2 + b_5H_2O + b_6N_2 \quad (1)$$

where C, H, O and N are the fuel mass fractions from the ultimate analysis on dry basis. For single-carbon-atom fuel ($a_0 = 1$), the coefficients a_2 and a_3 are determined from H/C, O/C and N/C mole ratios, respectively.

$$a_1 = \frac{(H/M_H)}{(C/M_C)} \tag{2}$$

$$a_2 = \frac{(O/M_O)}{(C/M_C)} \tag{3}$$

$$a_3 = \frac{(N/M_N)}{(C/M_C)} \tag{4}$$

Molecular weight of dry fuel

$$M_{\text{dry fuel}} = a_1 M_{CH} + a_2 M_O + a_3 M_N \tag{5}$$

then

$$w = \frac{M_{\text{dry fuel}} mc}{M_{\text{H}_2\text{O}}(100 - mc)} \tag{6}$$

Molecular weight of wet fuel

$$M_{\text{wet fuel}} = M_{\text{dry fuel}} + wM_{\text{H}_2\text{O}} \tag{7}$$

Stoichiometric air fuel ratio

$$\text{SAFR} = \frac{(a_1 + 0.25a_2 - 0.5a_3)M_A}{M_{\text{wet fuel}}} \tag{8}$$

where

$$M_A = M_{\text{O}_2} + 3.76M_{\text{N}_2}$$

$$a_4 = \frac{\text{SAFR} \times M_{\text{wet fuel}}}{M_A} \tag{9}$$

$$a_5 = \frac{\text{SFR} \times M_{\text{wet fuel}}}{M_{\text{H}_2\text{O}}(1 - 0.01 \times A)} \tag{10}$$

In equations (9) and (10), a_4 and a_5 are obtained. A numerical method is applied to solve the syngas coefficient in steam-air gasification by using Taylor's series method (Srinivas et al., 2010). After completion of numerical iteration at AFR = 0.5, SFR = 1 and gasifier pressure = 10 bar, the syngas composition is shown as follows:

Solid waste:

$$b_1(\text{CH}_4) = 0.16, \quad b_2(\text{CO}) = 0.52, \quad b_3(\text{CO}_2) = 0.32, \quad b_4(\text{H}_2) = 0.84,$$
$$b_5(\text{H}_2\text{O}) = 0.94, \quad b_6(\text{N}_2) = 0.44$$

Rice husk:

$$b_1(\text{CH}_4) = 0.06, \quad b_2(\text{CO}) = 0.62, \quad b_3(\text{CO}_2) = 0.31, \quad b_4(\text{H}_2) = 0.99,$$
$$b_5(\text{H}_2\text{O}) = 1.12, \quad b_6(\text{N}_2) = 0.39$$

Figure 1 Schematic diagram of the proposed cycle

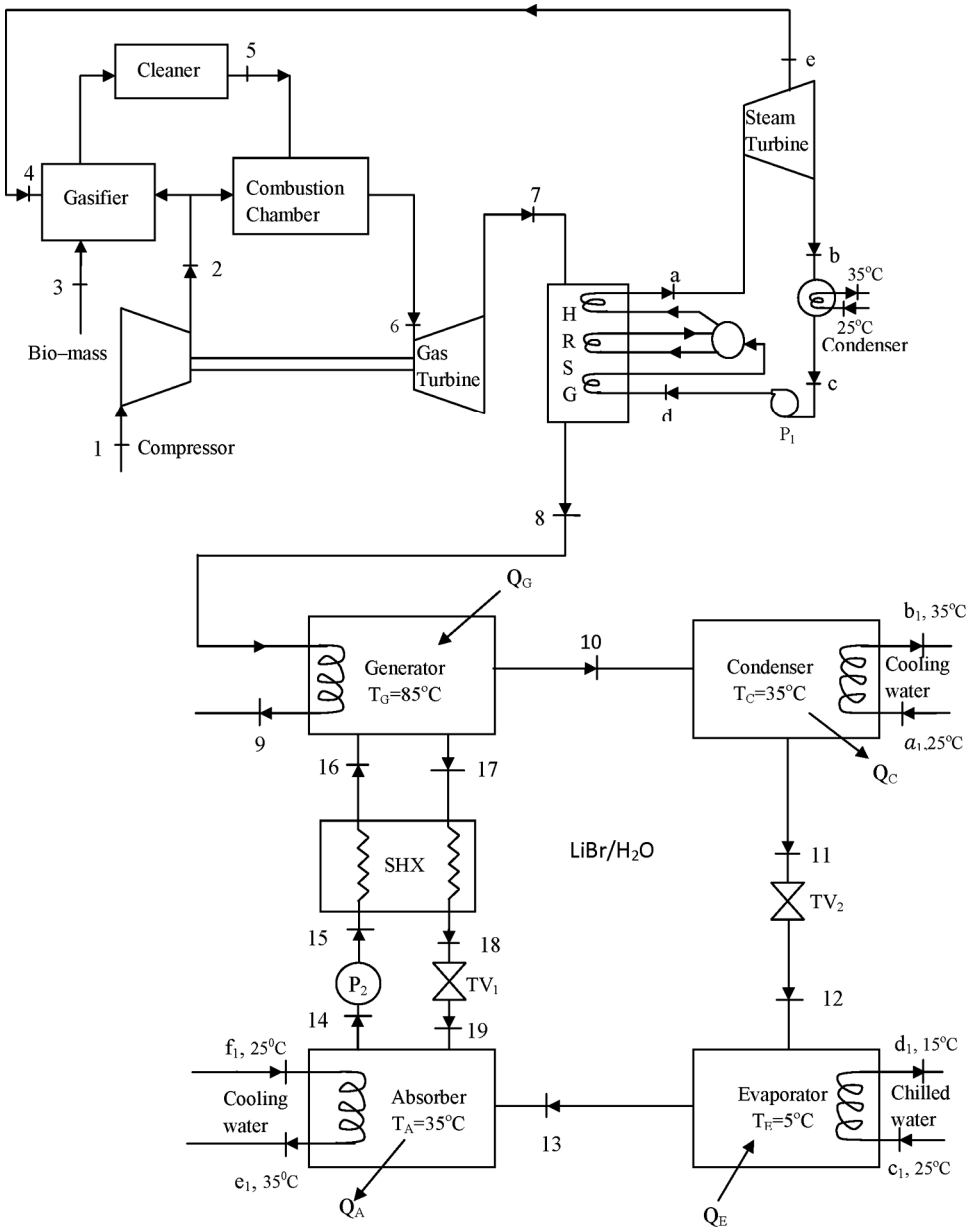

These are obtained at input data of

Solid waste:

$$a_0(\mathrm{C}) = 0.31, \quad a_1(\mathrm{H}) = 0.49, \quad a_2(\mathrm{O}) = 0.18, \quad a_3(\mathrm{N}) = 0.013$$
$$a_4(\mathrm{air}) = 0.111, \quad a_5(\mathrm{steam}) = 1.296 \text{ and } w(mc) = 0.15$$

Rice husk:

$$a_0(\mathrm{C}) = 0.29, \quad a_1(\mathrm{H}) = 0.48, \quad a_2(\mathrm{O}) = 0.22, \quad a_3(\mathrm{N}) = 0.004$$
$$a_4(\mathrm{air}) = 0.104, \quad a_5(\mathrm{steam}) = 1.416 \text{ and } w(mc) = 0.15$$

The complete combustion equation for the syngas in the gas turbine combustion chamber (GTCC) with the compressed air may be given as:

$$b_1\mathrm{CH_4} + b_2\mathrm{CO} + b_3\mathrm{CO_2} + b_4\mathrm{H_2} + b_5\mathrm{H_2O} + b_6\mathrm{N_2} + a_7(\mathrm{O_2} + 3.76\mathrm{N_2}) \rightarrow b_7\mathrm{CO_2} + b_8\mathrm{H_2O} + b_9\mathrm{N_2} \tag{11}$$

In equation (11) 'a_7' is the amount of air to be supplied in kg-mol (stoichiometric air for combustion) into the GTCC.

The amount of air required for combustion to obtain the required temperature (T) is determined from the energy balance of reactants and products.

Following are the products required in the GTCC at the above-mentioned conditions.

Solid waste:

$$b_7(\mathrm{CO_2}) = 1, \quad b_8(\mathrm{H_2O}) = 2.1, \quad b_9(\mathrm{N_2}) = 6.08, \quad (\mathrm{O_2}) = 0.5, \quad a_7 = 1.5$$

Rice husk:

$$b_7(\mathrm{CO_2}) = 1, \quad b_8(\mathrm{H_2O}) = 2.23, \quad b_9(\mathrm{N_2}) = 5.65, \quad (\mathrm{O_2}) = 0.47, \quad a_7 = 1.4$$

Application of second-law analysis to each component of the syngas fuelled combined power and cooling cycle results in the following equation which may be used to evaluate the exergy destruction in each component and they may be reported as:

3.1 Air compressor

The exergy balance of air-compressor yield exergy destruction which may be written as

$$E_{D,c} = W_c + m_a e_1 - m_a e_2 \tag{12}$$

where

$$e_1 - e_2 = (h_1 - h_2) - T_0\ (s_1 - s_2)$$

W_C is the work consumed by the compressor and $E_{D,C}$ is the exergy destruction during compression.

3.2 Gasifier

The exergy destruction in the gasifier is given by

$$E_{D,\text{gasifier}} = T_0 S_{\text{gen}} \tag{13}$$

where

$$S_{\text{gen}} = S_{\text{syenthatic gas}} - S_{\text{steam}} - S_{\text{biomass}} - S_{\text{air}}$$

3.3 Combustion chamber

The exergy destruction in the combustion chamber is given by

$$E_{D,CC} = T_0 S_{\text{gen}} \tag{14}$$

where

$$S_{\text{gen}} = S_q + S_{\text{comp}} - S_{\text{air}}$$

$$\text{and } S_q = \frac{Q_{CV}}{TIT_{\text{avg}}}$$

3.4 Gas turbine

With the change in gas turbine inlet temperature correspondingly the combustion of gases at exit of the gas turbine changes according to the relation

$$\frac{T_6}{T_7} = \left(\frac{p}{p_0}\right)^{\frac{\gamma-1}{\gamma}}$$

where γ is the ratio of the specific heats, i.e., $\gamma = C_p/C_v$ for air

The exergy balance yields the turbine work 'W_{GT}' and exergy balance for the turbine gives the exergy destruction

$$W_{GT} = m_{\text{mix}}(h_6 - h_7) \tag{15}$$

$$E_{D,GT} = m_{\text{mix}}(e_6 - e_7) - W_{GT} \tag{16}$$

3.5 Heat recovery steam generator (HRSG)

The exergy balance of HRSG yield exergy destruction and may be reported as

$$E_{D,\text{HRSG}} = m_{\text{mix}}(e_7 - e_8) + m_{\text{H}_2\text{O}}(e_d - e_a) \tag{17}$$

where m_{mix} is the mass of gas turbine exhaust.

3.6 Steam turbine

The exergy destruction in the steam turbine is given by

$$E_{D,ST} = m_a e_a - m_e e_e - m_b e_b - W_{ST} \tag{18}$$

3.7 Condenser 1

The exergy destruction in the condener 1 is given by

$$E_{D,SC} = m_b(e_b - e_c) \tag{19}$$

where *SC* = Steam Condenser.

3.8 Pump 1

The exergy destruction in the pump 1 is given by

$$E_{D,P1} = m_c(e_c - e_d) + W_{p1} \tag{20}$$

where $P1$ = Pump 1.

Second-law analysis applied to each component of the vapour absorption system results in the following equation which may be used to evaluate the exergy destruction in each component and they may be reported as:

3.9 Generator (Gen)

Energy and mass balances allow us to determine the heat transferred by the external fluid to the solution within the generator. The exergy destruction in the components of vapour absorption refrigeration part of the system used for cooling may be evaluated starting with energy balance on the generator

$$m_{s8}h_{16} + m_G h_{g8} - (m_{s8} - m_r)h_{17} - m_r h_{10} - m_G h_{\text{g,leaving GEN}} = 0 \tag{21}$$

The exergy of the fluids that enters the generator is

$$\sum m_{\text{in},G} e_{\text{in},G} = m_G[(h_8 - h_0) - T_0(s_8 - s_0)] + m_{s8}[(h_{16} - h_0) - T_0(s_{16} - s_0)] \tag{22}$$

The exergy of the outgoing mass is

$$\begin{aligned}\sum m_{\text{out},G} e_{\text{out},G} = {} & (m_{s8} - m_r)[(h_{17} - h_0) - T_0(s_{17} - s_0)] \\ & + m_G[(h_{\text{g,leaving GEN}} - h_0) - T_0(s_{\text{g,leaving GEN}} - s_0)] \\ & + m_r[(h_{10} - h_0) - T_0(s_{10} - s_0)]\end{aligned} \tag{23}$$

We obtained the exergy destruction because of the irreversibilities in the heat transfer between the external and the solution by applying equation (23).

$$E_{D,G} = T_0[m_r(s_{10} - s_{17}) + m_{s8}(s_{17} - s_{16})] + m_G T_0(s_{\text{g,leaving GEN}} - s_8) \tag{24}$$

The first two terms are positive whilst the third is negative. The overall destruction is positive. In the similar fashion, the exergy destruction in the solution heat exchanger (SHE), solution absorber, pump, condenser 2, evaporator and expansion valve can be obtained in the form of following equations. The exergy destruction in the SHE is given by

$$E_{D,\text{SHE}} = T_0[m_{s8}(s_{16} - s_{15}) + (m_{s8} - m_r)(s_{18} - s_{17})] \tag{25}$$

The pump transports the diluted solution in liquid state from the absorber to the generator, raising its pressure. The exergy destruction in the pump 2 is given by

$$E_{D,P2} = m_{s8} T_0(s_{15} - s_{14}) \tag{26}$$

The throttling valve reduces the pressure of the concentrated solution from the high pressure of the compressor (generator) towards the low pressure in the suction side of the compressor (absorber). The exergy destruction in the expansion valve may be given as

$$E_{D,TV} = (m_{s8} - m_r)T_0(s_{19} - s_{18}) \tag{27}$$

where $E_{D,TV}$ is higher than zero, since the difference is positive.

The absorber absorbs the refrigerant vapour at low pressure and low temperature, which condenses in the solution. By means of mass, energy and exergy balances, the exergy destruction in the absorber may be defined as

$$E_{D,A} = T_0[m_r(s_{19} - s_{13}) + m_s(s_{14} - s_{19}) + m_A(s_{f1} - s_{e1})] \tag{28}$$

The refrigerant vapour goes to condenser 2 from the generator. The exergy destruction in the condenser is given by

$$E_{D,\text{Cond2}} = T_0[m_r(s_{11} - s_{10}) + m_C(s_{b_1} - s_{a_1})] \tag{29}$$

The condensed refrigerant from the condenser goes to the throttling valve, and after throttling it goes to the evaporator. Therefore, the exergy destruction in the evaporator is given by

$$E_{D,\text{Evap}} = T_0[m_r(s_{13} - s_{12}) + m_E(s_{d_1} - s_{c_1})] \tag{30}$$

The condensed refrigerant from condenser 2 goes to the expansion valve where its pressure reduces to the evaporator pressure. The exergy destruction is given by

$$E_{D,EV} = m_r T_0(s_{12} - s_{11}) \tag{31}$$

3.10 Performance parameters

The relevant parameters required for the energetic and exergetic analyses of the combined production of power and cooling may be considered as follows.

3.10.1 First-law efficiency (η_I)

The energy measure of efficiency is simple a ratio of useful output energy to input energy. This quantity is normally referred to simply as efficiency, in the case of power cycles and as a coefficient of performance for refrigeration cycles. For the case of the cycle considered here, it may be defined as the ratio of all the useful energy extracted from the system (electric power and refrigeration) to the energy of exhaust (E_{in}) gas from the biomass. By definition it becomes

$$\eta_I = \frac{W_{GT} + W_{ST} - W_{AC} - W_P + Q_E}{E_{\text{in}}} \tag{32}$$

where Q_E is the amount of cooling produced at the evaporator and E_{in} the energy of fuel which is equal to m_f LHV.

3.10.2 Second-law efficiency (η_{II})

The energy fails to account for the quantity of energy. Therefore, energy efficiency does not reflect all the losses due to the irreversibilities in a system. Exergy efficiency measures the fraction of the exergy going into the cycle that comes out as a useful output. The remaining exergy is lost due to the irreversibilities in the components (Moran and Shapiro, 2008). The second-law efficiency is given by

$$\eta_{II} = \frac{W_{GT} + W_{ST} - W_{AC} - W_P + E_R}{E_{\text{ex, in}}} \tag{33}$$

where E_R is the exergy of refrigeration which is the refrigeration capacity Q_E divided the coefficient performance of a Carnot refrigeration cycle operating between the ambient and cycle low temperatures (Tamm et al., 2004).

$$E_R = \frac{Q_E(T_0 - T_{EV})}{T_{EV}}$$

where T_{EV} is temperature of evaporator and $E_{\text{ex,in}}$ is the exergy of the fuel.

4 Results and discussion

In order to have the numerical appreciation of the results obtained for biomass fuel combined power and cooling cycle, we have investigated the effect of cycle pressure ratio and gas turbine inlet temperature and evaporator temperature. The thermo-chemical properties of biomass materials are given in Table 1. The properties and operating variables for the analysis of proposed cycle is given in Table 2. The effect of each of these parameters has been examined whilst keeping the following as constant (TIT = 1010°C, r_p = 10 bar, T_{EV} = 5°C) and the discussion of results is given below.

Table 1 Thermo-chemical properties of biomass materials

Property	*Units*	*Solid waste*	*Rice husk*
C	Wt% daf	51.03	36.42
H	Wt% daf	6.77	4.91
O	Wt% daf	39.17	35.88
N	Wt% daf	2.64	0.59
Lower Heating Value	kJ/kg, daf	25021.51	22982.32
Moisture Content	Wt%	15.00	15.00
Ash	Wt%	5.00	22.20
Exergy ratio (φ)	–	1.037	1.133

4.1 Effect of gas turbine inlet temperature

Figure 2 shows the variation of first and second-law efficiencies of biomass fuelled combined power and cooling cycle with respect to gas turbine inlet temperature. It is seen

that increase in gas turbine inlet temperature results in a significant improvement of first and second-law efficiencies of combined cooling and power cycle for both the biomass fuels (rice husk and solid waste). For the closed range of gas turbine inlet temperature (970–1050°C), the variation in first-law efficiency is observed in the range between 40% to 46% for solid waste and 36% to 44% for rice husk. This deviation of first-law efficiency is observed due to the considerable difference in the energy content of solid waste and rice husk. This gradual increase in first-law efficiency of the proposed cycle is observed due to the lower amount of heat input required at higher gas turbine inlet temperature. In order to find out the true efficiency (second-law efficiency) of the proposed combined power and cooling cycle, exergy balance approach has been applied and the second-law efficiency is evaluated. It is shown that a second-law efficiency of 37% to 43% is observed in the range of gas turbine inlet temperature of 970°C to 1050°C for solid waste fuelled cycle and 30% to 37% for rice husk fuelled cycle. The reason for this deviation is again the considerable difference between the exergy values of solid waste and rice husk. It is interesting to note that second-law efficiency which is the ratio of net exergy output to the exergy input to the cycle is found to be lower than its first-law efficiency counterpart. This is due to the fact that exergy of both the biomass materials (rice husk and solid waste) is slightly higher than their energy content.

Table 2 Properties and operating variables for the analysis of the proposed cycle- cooling configuration

Properties of ambient air	
Pressure (bar)	1.013
Temperature (K)	298
Composition (*by volume*)	
Nitrogen	79%
Oxygen	21%
Equipment performance	
Isentropic efficiency of compressor ($\eta_{c,\text{isen}}$)	85%
Isentropic efficiency of gas turbine ($\eta_{gt,\text{isen}}$)	85%
Isentropic efficiency of steam turbine ($\eta_{st,\text{isen}}$)	85%
Pressure drop across the gasifier (ΔP_G)	5%
Pressure drop across the combustion chamber (ΔP_{CC})	3%
Pressure drop across the HRSG (ΔP_{HRSG})	2%
Operating parameters	
Compressor pressure ratio (r_p)	6–14 (range)
Turbine inlet temperature TIT (°C)	970–1050 (range)
Stack temperature after HRSG (K) at point 8	400
Mass of steam generated for a single mole of biomass (assumed in kg)	10

4.2 Effect of pressure ratio

The first and second-law efficiencies of combined power and cooling cycle have also been plotted with the increase in pressure ratio across the compressor of proposed combined power and cooling cycle as shown in Figure 3. A closed range of variation in first and second-law efficiencies of solid waste fuel combined power and cooling cycle is observed in the pressure ratio 6 to 14. The first-law efficiency varies from 44.64% to 42.11% and second-law efficiency varies from 41.56% to 39.12%. Whilst changing the fuel from solid waste to rice husk, a variation in the first and second-law efficiencies of the proposed cycle is also observed from 42.87% to 40.76% and 36.64% to 34.77%, respectively, in the same range of pressure ratio. The trend of decrease in first-law efficiency with the increase in pressure ratio is observed due to the reason that with the increase in pressure ratio the gas turbine output increases whilst the steam turbine output is decreases. But the decrease steam turbine output is much greater than the increase in gas turbine output, therefore, the net power output decreases with the increase in pressure ratio. The greater power consumed in the compressor to maintain higher pressure ratio also contribute towards the reduction of first-law efficiency. The magnitude of refrigeration output is much less as compared with the power output, therefore, the first-law efficiency of combined power and cooling cycle is greatly affected with the change in output. The second-law efficiency also shows the same trend of decreasing with the increase in pressure ratio due to the fact that net output which contributes 100% towards exergy is decreasing with the pressure ratio and the exergy of the fuel remain same. The second-law efficiency is found to be less than the first-law efficiency of combined power and cooling cycle due to the combined effects of exergy of both the fuels is greater than their energy content and the amount of exergy associated with the refrigerating capacity is less than the refrigerating capacity.

Figure 2 Variation of first and second law efficiencies with turbine inlet temperature (combined power and cooling cycle) at (r_p = 10) (see online version for colours)

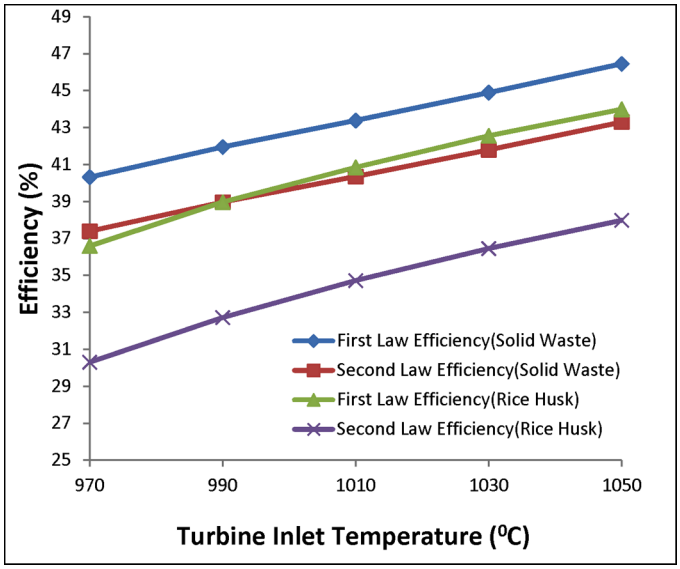

4.3 Effect of evaporator

In order to highlight the effect of employing the vapour absorption refrigeration system with biomass fuel combined power cycle, the effect of change in evaporator temperature of vapour absorption refrigeration is also observed on the first and second-law efficiencies of the proposed combined power and cooling cycle. It is shown in Figure 4, that there is marginal increase in first and second-law efficiencies of solid waste fuelled 43.37% to 43.41% and 40.355% to 40.359% at 2–10°C, respectively. In the same range of evaporator temperature, the first and second-law efficiencies for rice husk fuelled cycle varies in the range of 41.64–40.68% and 35.561–35.565%, respectively. This marginal variation in the efficiencies of both the biomass fuels combined power and cooling cycle is observed due to the fact that increase in the exergy of refrigeration output with the increase in evaporator temperature is increased but its magnitude relative to the magnitude of power output of gas turbine and steam turbine is quite insignificant. Since efficiency is the ratio of net output of energy and exergy to the input of energy and exergy, therefore, a negligible variation in the efficiencies is observed with the change in evaporator temperature.

An exergy analysis which is a field of research on energy systems devoted to the identification and quantification of the malfunction of the plant and component that results in a decrease of efficiency was performed to evaluate the exergy losses in the biomass fuelled combined power and cooling cycle as shown in Figure 5(a) and (b), respectively. This demonstrates well how the exergy is used and lost in all of the cycle components. For system improvement, an exergy analysis has also been performed to evaluate the exergy losses in the system and provide guidance for system improvement. Figure 5(a) and (b) demonstrates well how exergy is used, lost and reused in all the system components. It is found that the biggest exergy destruction occurs in combustion chamber and represents around 25% and 22.6% of the total exergy input to the cycle for both solid waste and rice husk, respectively. This is because combustion is highly irreversible phenomena where entropy is generated via: chemical reaction, heat transfer, viscous dissipation and mass diffusion. All this irreversibility process contributes towards the exergy destruction in combustion chamber. The second largest exergy destruction occurs in the HRSG which is around 21% for solid waste and 19.4% for rice husk as depicted in Figure 5(a) and (b). This is the largest due to the significant entropy generation due to the heat transfer at the finite temperature difference between the hot gas turbine exhaust stream and feed water. Since the two streams of opposite nature are interacting in the HRSG with a large temperature difference which leads to large entropy generation due to the heat transfer and hence the large exergy destruction. The third largest exergy destruction occurs in the gasifier with the values of 7.67% and 7.96% for solid waste and rice husk fuels, respectively. This is because in gasifier partial combustion takes place along with the simultaneous oxidation and reduction reaction occurs. Another reason for significant exergy destruction is the entropy generation due to the mixing of biomass steam and compressed air in the gasifier. A considerable amount of exergy destruction also occur in gas turbine due to the expansion of multi-component combustion product stream with larger temperature and pressure difference which results in a finite value of entropy generation due to the irreversibility in the gas turbine. Due to the expansion of superheated steam in the steam turbine to its saturated point causes a significant appearance of exergy destruction in the steam turbine. The amount of exergy destruction occurs in both gas turbine and steam turbine is around 4.68% in solid waste

and 4.91% in rice husk, respectively. The exergy destruction in rest of the components of combined power and cooling cycle appears to be negligible at the mean operating conditions.

Figure 3 Variation of first and second law efficiencies with pressure ratio (combined power and cooling cycle) at (TIT = 1010°C) (see online version for colours)

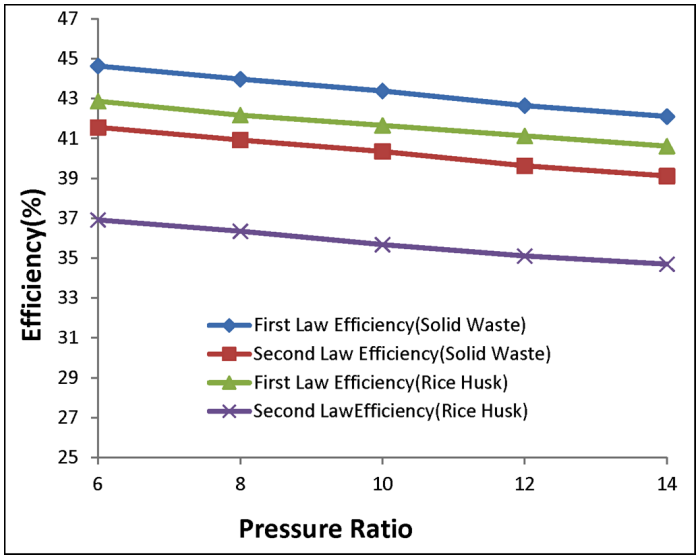

Figure 4 Variation of first and second-law efficiencies with evaporator temperature (see online version for colours)

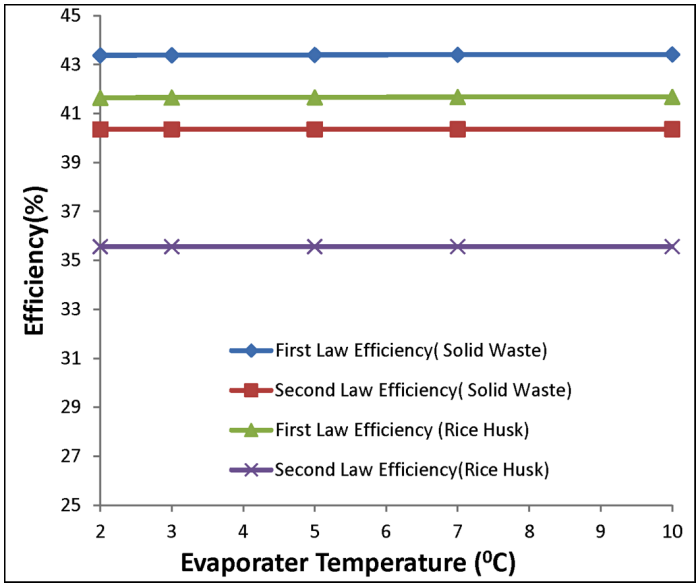

Figure 5 (a) Exergy destruction of solid waste in various component of cooling cycle and (b) exergy destruction of rice husk in various component of cooling cycle (see online version for colours)

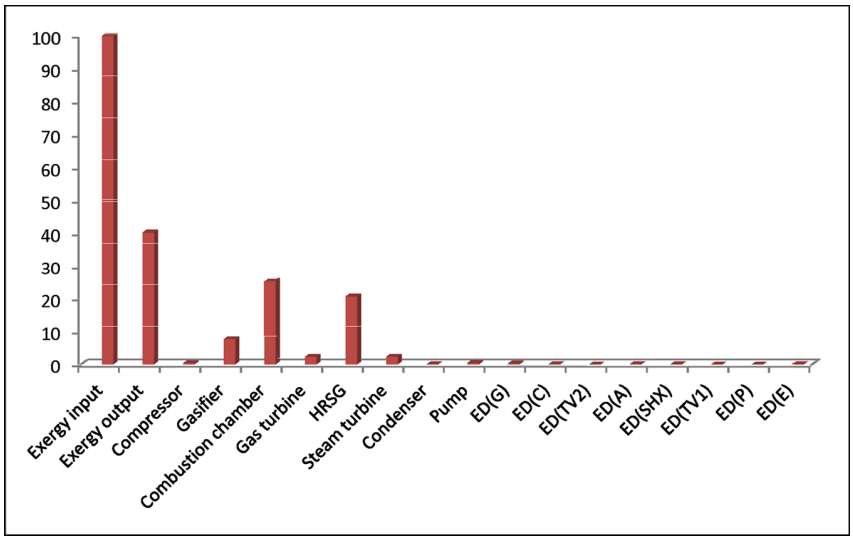

(a)

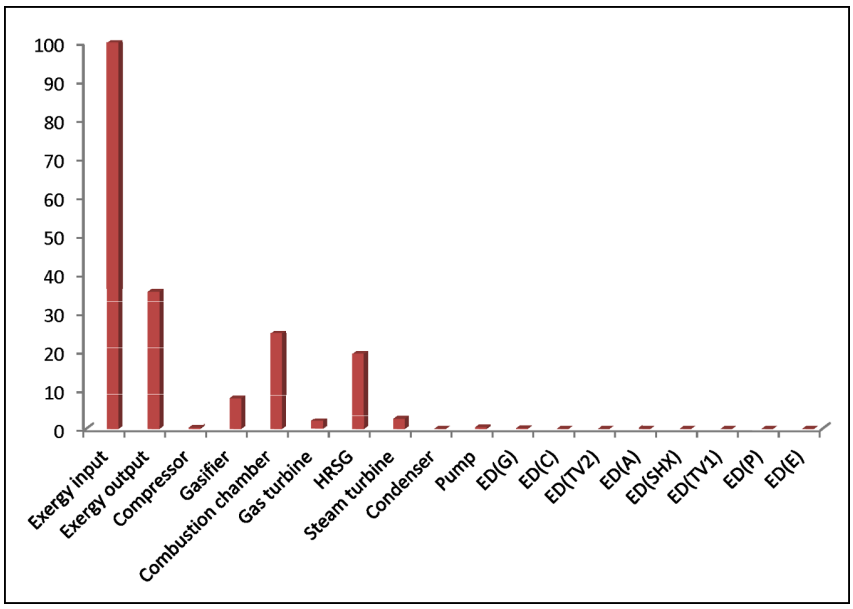

(b)

5 Conclusion

Based on the energy and exergy analyses of a proposed biomass fuelled cogeneration cycle, following concluding remarks may be reported:

- a close range of first-law efficiency from 44.64% to 42.11% for solid waste fuel and from 42.87% to 40.76% for rice husk is observed for the pressure ratio of 6 to 14
- the range of second-law efficiency for solid waste and rice husk fuelled for the pressure ratio of 6 to 14 are obtained as 41.56–39.12% and 36.64–34.77%, respectively
- both first and second-law efficiency of the cogeneration cycle decreases with the pressure ratio and increases with the gas turbine inlet temperature
- the effect of variation in evaporator temperature of absorption system seems to be marginal on the performance of cogeneration cycle
- a maximum destruction of exergy of 25% occurs in the combustion chamber followed by the HRSG and gasifier with the values of 21% and 9%, respectively
- solid waste fuelled cogeneration provides higher first and second-law efficiency than rice husk fuelled cycle due to the considerable difference in their energy content.

The energy and exergy analyses are important tools for measuring the performance by providing information on both first and second-law efficiencies, and the biomass energy content can be exploited for power and cooling production from quality point of view. The present study is expected to help researchers, engineers and designers for a better design, analysis and performance improvement of biomass IGCC.

References

Alexis, G.K. (2007) 'Performance parameters for the design of a combined refrigeration and electrical power cogeneration system', *International Journal of Refrigeration*, Vol. 30, No. 6, pp.1097–1103.

Arora, A. and Kaushik, S.C. (2009) 'Theoretical analysis of LiBr/H_2O absorption refrigeration systems', *International Journal of Energy Research*, Vol. 33, No. 15, pp.1321–1340.

Bhattacharya, A., Manna, D., Paul, B. and Data, A. (2011) 'Biomass integrated gasification combined cycle power generation with supplementary biomass firing: energy and exergy based performance analysis', *Energy*, Vol. 36, pp.2599–2610.

Chuangzhi, W., Xiuli, Y., Longlong, M., Zhaoqiu, Z. and Hanping, C. (2008) 'Design and operation of 5.5 MWe biomass integrated gasification combined cycle demonstration plant', *Energy &Fuels*, Vol. 22, pp.4259–4264.

Colonna, P. and Gabrielli, S. (2004) 'Industrial trigeneration using ammonia water absorption refrigeration systems', *Applied Thermal Engineering*, Vol. 23, No. 4, pp.381–396.

Erickson, D., Anand, G. and Kyung, I. (2004) 'Heat-activated dual function absorption cycle', *Transactions – American Society of Heating Refrigerating and Air Conditioning Engineers*, Vol. 110, No. 1, pp.515–524.

Ferreira, S.B. and Pilidis, P. (2001) 'Comparison of externally fired and internal combustion gas turbines using biomass fuel', *Journal of Energy Resources Technology*, Vol. 123, pp.291–296.

Franco, A. and Giannini, N. (2005) 'Perspectives for the use of biomass as fuel in combined cycle power plants', *International Journal of Thermal Sciences*, Vol. 44. pp.163–177.

Khaliq, A. and Kumar, R. (2007) 'Exergy analysis of solar powered absorption refrigeration system using LiBr-H_2O and NH_3-H_2O as working fluid', *International Journal of Exergy*, Vol. 4, No. 1, pp.1–18.

Khaliq, A., Kumar, R. and Dincer, I. (2009) 'Exergy analysis of an industrial waste heat recovery based cogeneration cycle for combined production of power and refrigeration', *Journal of Energy Resources Technology*, Vol. 131, pp.022402-1–022402-9.

Kilmantos, P., Koukouzas, N., Katsiadakis, A. and Kakaras, E. (2009) 'Air – blown biomass gasification combined cycle (BGCC): System analysis and economic assessment', *Energy*, Vol. 34, pp.708–714.

Lee, S-F. and Sherif, S.A. (2001) 'Thermodynamic analysis of a lithium bromide/water absorption system for cooling and heating application', *International Journal of Energy Research*, Vol. 25, No. 11, pp.1019–1031.

Liu, M. and Zhang, N. (2007) 'Proposal and analysis of a novel ammonia – water cycle for power and refrigeration cogeneration', *Energy*, Vol. 32, No. 6, pp.961–970.

Maniatis, K. and Millich, E. (1998) 'Energy from biomass and waste: the contribution of utility scale biomass gasification plant', *Biomass and Bioenergy*, Vol. 15, No. 3, pp.195–200.

Mark, A. and Mike, J.W. (2003) *Biomass Gasification Combined Cycle Opportunities Using the Future Energy Silvagas Gasifier Coupled to Alstom's Industrial Gas Turbines*, ASME paper No. GT2300-38294.

Moran, M.J. and Shapiro, H.N. (2008) *Fundamentals of Engineering Thermodynamics*, 6th ed., Wiley, New York.

Perez-Fortes, M., Bojarski, A.D., Velo, E., Nougues, J.M. and Puigjaner, L. (2009) 'Conceptual model and evaluation of generated power and emissions in an IGCC plant', *Energy*, Vol. 34, pp.1721–1732.

Phillppe, R., Desilets, M., Galanis, N., Nesreddine, H. and Cayer, E. (2009) 'Thermodynamic analysis of a power cycle using law – temperature source and a binary NH_3/H_2O mixture as working fluid', *International Journal of Thermal Sciences*, Vol. 49, pp.48–58.

Prins, M.J., Ptasinski, K.J. and Janssen, F.J.J.G. (2003) 'Thermodynamics of gas-char reactions: first and second law analyses', *Chem. Eng. Sci.*, Vol. 58, Nos. 3–6, pp.59–67.

Reddy, B.V. and Mohamed, K. (2007) 'Exergy analysis of a natural gas fired combined cycle power generation unit', *International Journal of Exergy*, Vol. 4, No. 2, pp.180–196.

Savola, T. (2005) *Simulation and Optimization of Power Production in Biomass – Fuelled Small Scale CHP Plants*, MS Thesis, Department of Mechanical Engineering, Helsinki University of Technology Energy, Engineering and Environmental Production Publications, Espoo, Finland Paper No TKK.ENY-23.

Srinivas, T., Gupta, A.V.S.S.K.S. and Reddy, B.V. (2009) 'Carbon dioxide emission reduction from combined cycle with partial oxidation of natural gas', *Energy for Sustainable Development, International Energy Initiative*, Vol. 13, No. 1, pp.33–37.

Srinivas, T., Reddy, B.V. and Gupta, A.V.S.S.K.S. (2010) 'Biomass – fuelled integrated power and refrigeration system', *Proc. IMech E*, Vol. 225, *Part: J. Power and Energy*, pp.249–258.

Takeshita, K., Amano, Y. and Hashizume, T. (2005) 'Experimental study of advanced cogeneration system with ammonia-water mixture cycles at bottoming', *Energy*, Vol. 30, Nos. 2–4, pp.247–260.

Tamm, G., Goswami, D.Y., Lu, S. and Hasan, A.A. (2004) 'Theoretical and experimental investigation of an ammonia-water power and refrigeration thermodynamic cycle', *Solar Energy*, Vol. 76, pp.217–228.

Zhang, N. and Lior, N. (2007) 'Development of a novel combined absorption cycle for power generation and refrigeration', *Journal of Energy Resources Technology*, Vol. 129, pp.254–265.

Zheng, D., Chen, B., Qi, Y. and Jin, H. (2006) 'Thermodynamic analysis of a novel absorption power/cooling combined-cycle', *Applied Energy*, Vol. 83, No. 4, pp.311–323.

Nomenclature

AFR	Air fuel ratio
BIGCC	Biomass integrated gasification combined cycle
C	Compressor
CC	Combustion chamber
CHP	Combined heat and power
COP	Coefficient of performance
Cond	Condenser
E	Exergy
E_D	Exergy destruction (kJ)
E_{in}	Energy of fuel (kJ)
E_{ex}	Exergy of the fuel (kJ)
E_R	Exergy of the refrigerant (kJ)
EV	Expansion valve
Evap	Evaporator
FP	Feed pump
G	Gibbs function (kJ)
Gen	Generator
GT	Gas turbine
HRSG	Heat recovery steam generator
LHV	Lower heating value (kJ/kg)
M	Molecular weight (kg/kmol)
m	Mass (kg)
mc	Moisture content
m_r	Mass of refrigerant
m_s	Mass of solution
m_{vapour}	Mass of refrigerant (kg)
N	Nitrogen
O	Oxygen
$P1$	Pump1
$P2$	Pump2
P	Product
p	Pressure (bar)
Q	Heat transfer interaction (kJ)
Q_{cv}	Calorific value (kJ/kmol-K)
Q_E	Amount of cooling produced at the evaporator (kJ)
R	Reactant
$\overline{R}$	Universal gas constant (kJ/kmol-K)
$r_{p,C}$	Pressure ratio across the compressor

$r_{p,\,GT}$	Pressure ratio across the gas turbine
S	Entropy (kJ/kg-K)
SAFR	Stoichiometric air-fuel ratio
SFR	Steam fuel ratio
SHE	Solution heat exchanger
ST	Steam turbine
s	Specific entropy (kJ/K)
S_q	Entropy associated with heat transfer during combustion (kJ/K)
S_{gen}	Entropy generation (kJ/K)
T	Absolute temperature (°C)
T_0	Atmospheric temperature (°C)
T_p	Saturated temperature at pressure of process steam (°C)
T_{Ev}	Evaporator temperature (°C)
TIT	Turbine inlet temperature (°C)
TV	Throttling valve
W	Work (kJ)
W_{AC}	Compressor work (kJ)
W_{GT}	Gas turbine work (kJ)
W_P	Pump work (kJ)
W_{ST}	Steam turbine work (kJ)
w	Number of moles of moisture in the biomass
Suffix	
a–e	State points of the steam cycle
a_1–f_1	State points of vapour absorption cycle
bmf	Biomass fuel
ch	Chemical
daf	Dry ash free
e	Specific exergy (kJ/kg)
f	Formation
h	Specific enthalpy (kJ/kg)
r	Refrigerant
s	Solution
0	Reference point
1–19	State points of the gas–steam cycle
η_I	First-law efficiency
η_{II}	Second-law efficiency

I.J. Modern Education and Computer Science, **2015, 2, 48-55**
Published Online February 2015 in MECS (http://www.mecs-press.org/)
DOI: 10.5815/ijmecs.2015.02.07

Experimental Analysis of SPF Based Secure Web Application

Nitish Pathak
Research Scholar and Corresponding Author, UTU, Dehradun (INDIA)
Email: nitish_pathak2004@yahoo.com

Dr. Girish Sharma and Dr. B. M. Singh
Departments of CS&E, BPIBS, Govt. of NCT, Delhi (INDIA)
Department of CS&E, College of Engineering Roorkee, Roorkee (INDIA)
Email: gkps123@gmail.com and bmsingh1981@gmail.com

Abstract—In this paper we will propose model driven software development and Security Performance Framework (SPF) Model to maintain the balance between security and performance for web applications.

We propose that all security in a Trusted Operating System is not necessary. Some non-essential security checks can be skipped to increase system performance. These non essential security checks can be identified in any web application.

For implementation of this Security Performance framework based trusted operating system, we propose object oriented based Code generation through forward engineering. This involves generating source code of web application from one or more Object oriented Rational Rose model. The novel integration of security engineering with model-driven software expansion approach has varied advantages.

To maintain security in various applications like E-commerce, Banking, Marketplace services, Advertising, Auctions, Comparison shopping, Mobile commerce Payment, Ticketing, Online insurance policy management, we have to use high secured operating systems. In this regard a number of trusted operating systems like Argus, Trusted Solaris, and Virtual Vault have been developed by various companies to handle the increasing need of security. Due to high security reason these operating systems are being used in defense. But still these secure operating systems have limited scope in commercial sector due to lower performance; actually this security will come at a cost. This paper analyzes UML-based software development solutions for SPF to manage the security, performance and modeling for web applications.

Index Terms—UML, Code generation, Model driven software development, OO Rose Mode-Object Oriented Rose Model, TOS -Trusted Operating System.

I. Introduction

Model-driven software development involves software system modeling and automatically code generation from these models. A system and software unit can be modeled at diverse levels of concept or from various viewpoints. The grammar of each model and replica is defined by a Meta model. Systems for Model-driven software development can be viewed as a novel generation of visual programming languages [1].

The Meta model defines the syntax of the UML modeling languages, a model plays the role of the source code, and the code generator replaces the compiler. Using this approach, it is possible to generate automatically huge amounts of source code and other artifacts, e.g. deployment descriptors. Files can also be created based on comparatively concise models. This improves the productivity and output of the development process as well as the quality and value of the resulting systems. It is also a great step towards the platform independent design of object oriented web application systems [2][3].

UML is well suited for designing secure systems. Therefore, Secure UML allows still developers without a strong security environment to develop secure and safe systems. With our prototype and trial product, we developed case studies for a product purchase system based web application. We also developed a scheduling application and code generator as discussed in this paper. UML has rapidly become the language of choice for developers who wish to visualize and model the system under development. The UML includes use cases to facilitate visualization of user requirements, class diagrams to visualize the design of the software and sequence diagrams to visualize the behavior of the objects in the system [4].

In the projected process, a web based e-commerce system is totally specified using object-oriented conceptual modeling techniques [5][6].Security and web application protection plays an innermost role in the development and functioning of several large-scale distributed software systems. On the other hand, an analysis of today's software design and development processes reveals that the careful engineering of security into the overall web system design is frequently neglected [2][7].

Security features are usually built into web application in an ad-hoc approach or are only integrated afterward during the system administration phase. There are several reasons for this. First, security and protection is a "horizontal" feature of software development that affects

Copyright © 2015 MECS

almost each component of an application and its incorporation into the software design and development process is not well understood.

Second, there is a lack of tools supporting security engineering. Third, the addition of security into a web application system by hand is complicated. Errors frequently arise due to the lack of experience and knowledge of the individual developers [2][3]. These developers are usually not security experts and they require actual guidelines for constructing secure on line web applications. In general, the post-hoc, low-level incorporation of security and protection has a negative impact on the quality and the worth of resulting web applications [5].

Due to gravity and importance of security in web applications; we should use trusted operating systems for the same [2][3].

High secure trusted operating systems recommend a number of safety mechanisms that can assist, defend information, make a system hard to break into, and detain attacks far better than conventional operating systems[8] [2].

Actually, this security will come at a charge, since it can humiliate the performance of an operating system. This performance defeat is one of the reasons why TOS have not become popular in web applications. UML can be applied in several areas like embedded systems, product purchase web applications, and social networking sites commercial applications etc. A number of UML tools generate program language code from UML in various object oriented programming languages. UML can be used for modeling and designing the entire system independent of platform/ language. Trusted operating systems can be designed by using UML based concepts [1][9].

While Trusted Operating Systems present an unbelievable quantity of security, observations about computing workloads recommend that only a few parts of the operating system security are really essential[6].

Web servers are the most excellent example. For various web servers, the greater part of the information on the server is freely legible and accessible on the Internet. So, if a Trusted Operating System is used on a web server, some security used to protect the privacy of the server's information is not needed. Any security used to protect and defend the confidentiality and privacy of web server data can be considered a waste and misuse of computational resources [1][10]. The security needed in online web servers is the security to guard the integrity of data, not the privacy of data. Based on this surveillance, this research article proposes the Security Performance Flexibility Model (SPF) of TOS to Web applications [6].

This paper will comprise four sections. Section I comprise introduction of SPF model, software design and development and its significance in Web applications, Section II comprise the related work for SPF based secure Web applications, Section III comprise the architecture of system SPF and object oriented development, Section IV comprise the description and object oriented experimental analysis of the problem and the last section comprise the references.

II. Related Work

According to SPF observation we feel that not all computing workloads need all the security in secure Operating Systems. SPF permits computer system administrators to selectively disable parts of the security protection in secure Operating Systems [9]. Whenever we disable some needless parts of the Trusted Operating System security, performance and efficiency of the computer system can potentially be increased [1].

System administrators can use the SPF framework to balance the security and performance needs in their particular web computing environment [11]. First we have to identify which part can be disabled to achieve the maximum performance in specific web application. We should identify various operations in product purchase web application to disable the undesirable operations to improve the performance in all respect. Based on Questionnaire and survey related to web applications like e-commerce sites, job portals, we can find trends, Hit rate, Max operations performed by users, Frequency of read, write, upload, share, comment, messaging operations, What is the chance that an event will occur?, Which patterns are significant?

After identifying the answer of above question we can identify the frequency of operations performed by web users and according to our desired requirement we can disable some security checks in trusted operating systems to improve performance of web applications [5][12]. As we know all security checks are not important in all web applications. Selection of these criteria will vary from one web application to another application.

III. Architecture

The design of Trusted Operating Systems is demonstrated under the Figure 1. As a prompt to the reader, the design of an online product purchase system is not the same as the execution. A mixture of implementations for trusted safety mechanisms can be followed for the web applications.

In secure operating systems, there is a larger amount of security and safety placed into the operating system. Figure 1.b indicates this security and safety with a much thicker coating of kernel security checks [13][10].What is inside the kernel security check layer of a Trusted Operating System depends on the design & implementation of web application.

We can see in figure 1.b, the kernel security layer in trusted operating system may comprise DAC, MAC, Least Privilege, auditing, or any more number of extra security features [6][14].

Copyright © 2015 MECS

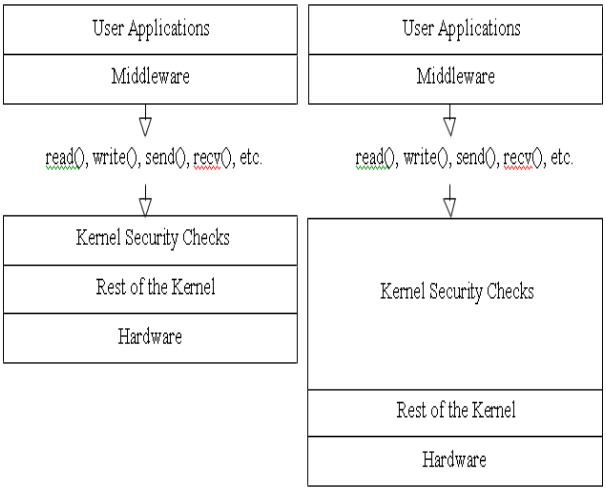

(a)Normal Operating Systems (b) Trusted or Secure Operating Systems

Fig.1. Security Framework of TOS

In figure 1.b the main point is that the kernel safety checks are a large amount in nature than conventional operating systems. This large layer of security and safety causes Trusted Operating Systems to bear performance degradation [8]. All system calls to the kernel of TOS must go through this thick layer of security checks before they can do any useful and valuable work [1][10].

IV. Problem Description And Solution

Design in Figure 1.b shows, the supplementary security checks in the kernel will cause Trusted Operating Systems to be slower than conventional operating systems [6]. If we implement the same trusted operating system for web applications like e-commerce sites, job portals, then we get lower performance but more security features as we are using the trusted operating system for the same. The main problem is to balance security and performance of secure operating system for web applications.

The incorporation of security engineering into a model-driven software development process has the following advantages. To start with, security and safety requirements can be formulated and integrated into software system design at a high level of abstraction for various web applications. In this way, it becomes probable to design and develop security aware web applications that are designed with the objective of preventing violations of a safety and security policy. For example, a database query can be designed so that users can only retrieve and access those data records that they are allowed to access. In addition, the model information can be used to notice and to accurate design errors or to confirm the correctness and rightness of the mapping between requirements and their understanding in a design process [10][11].

Unfortunately, many systems are constructed without the use of modeling and visualization artifacts, due to constraints imposed by deadlines, or a shortage of manpower. In this research paper we will suggest Object-oriented analysis based designing using forward engineering. This approach is accepted technical process to analyzing, designing a web application, TOS or business by applying the object-oriented paradigm and visual modeling throughout the development life cycles to promote better stakeholder communication and software product quality[6][1].

With a variety of diagrams from UML we can demonstrate clear views of system. If we model any problem before its progress there are less chances that our development sketch will go wrong, thus decreasing development costs. Modeling decreases the risk and danger of mistakes [15].

For better performance for specific computer system workloads, this research paper suggests the security performance flexibility (SPF) model for Trusted Operating Systems. The combination of SPF and forward engineering can help developers, designers, and analyst as well as web applications user. The architectural thought behind the SPF structure is illustrated in Figure 2. For example, a system manager can use SPF to turn off all read security and safety checks in a web server [16]. By turning off all the read security checks of a web server, it is probable the web server's throughput and efficiency can be increased and improved [1][17].

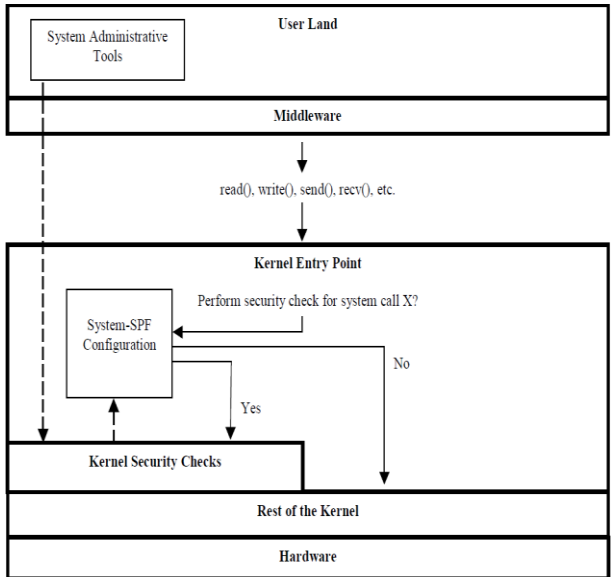

Fig.2. System-SPF Architecture for web applications

Taking the decision to adopt UML in the development process of web applications does not mean that all UML diagrams must be used. It is up to the modeller to decide, which diagrams to use in the development process. The decision is usually based on the nature of the system; the domain, the functionalities, as well as the preferences of the modeller, since some UML diagrams might in some cases replace each other [9].

We can implement the SPF and code generation in following case of web applications. Following requirements are for a product purchase system:

- The administrator runs inventory reports. Every time inventory reports are run, inventory data is loaded from disk.

Copyright © 2015 MECS

- The administrator updates the inventory stock. Every time inventory stock is updated, inventory data is loaded from disk. Also, every time inventory stock is updated, inventory data is saved to a disk.
- A (general) make-a-sale (hint: meant to be a verb-noun phrase) can be of two specialized kinds: (1) make-a phone order sale; and (2) make-a walk-in sale.
- A sales clerk records the make-a-walk-in sales.
- A telephone operator, a specialized kind of a sales clerk, handles and records all make-a phone orders.
- Whenever there is a make-a-sale, the inventory stock is updated.
- A sale may need to verify a credit card if the purchase is a credit card purchase.
- A sale may need to verify a check if the purchase is a check purchase.

First we have to design the use case diagram because Use cases are an influential method for the elicitation and documentation of blackbox functional requirements [17]. Use cases are printed in natural language, use cases are effortless to understand and provide an outstanding way for communicating with customers and users. Use cases diagram provide the groundwork on which to specify end-to-end timing requirements for real-time web applications. Use cases can assist control the complexity of huge projects by decomposing the complexity into most significant functions (i.e., use cases) and by specifying applications from the users' perspective [9][18].

The generic Use case diagram of above case study is as follows:–

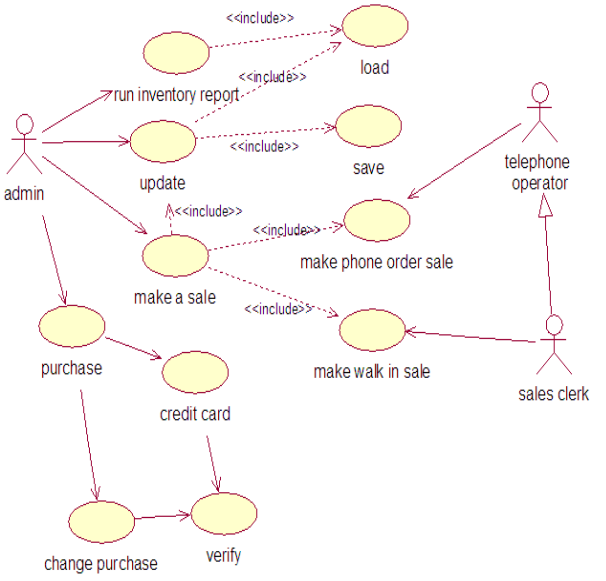

Fig.3. Use case diagram for a product purchase based web Application

For the above web application we can design and develop the class diagram with the help of above use case diagram and can perform forward engineering for the same application with the help of IBM Rational Rose Software [2][15]. We know a class diagram is "a diagram that shows a set of classes, interfaces, and collaborations and their relationships; class diagrams address the static design view of a system; a diagram that shows a collection of declarative (static) behavior"

Class diagrams are helpful in the development process from the very beginning, where they can be used for identifying system requirements and its entities [12]. For example, they construct the initial system architecture in the analysis phase, while in the design phase; they are refined and extended to represent the complete system specifications. In UML, a class is represented as a box with three vertical sections. The top section shows the name of the class [23]. The middle section displays the variables belonging to the class, with symbols representing the visibility (public, protected, or private) and properties (constant or static). The bottom section contains the member functions of the class [19]. Each method has a name, signature, and properties. On the basis of code and design we can implement the SPF model for trusted operating system i.e. well suited for various web applications [20].

The generic class diagram of online product purchase web application is as follows –

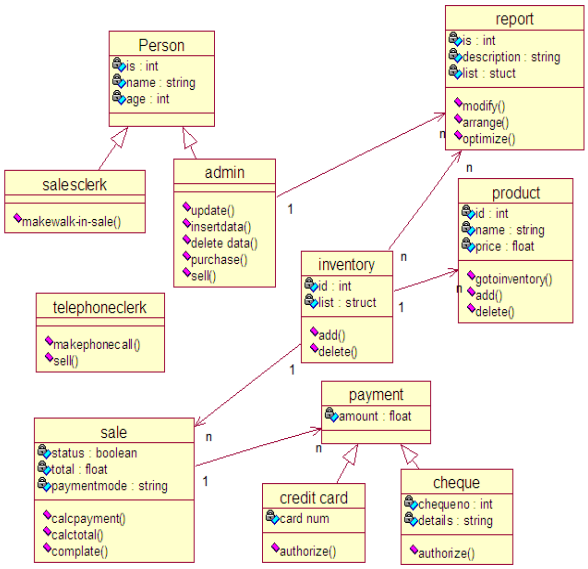

Fig.4. Generic Class Diagram for a product purchase web application

FORWARD ENGINEERING FOR PRODUCT PURCHACE BASED WEB APPLICATION

Forward engineering in Rose is component-centered. Class wise code i.e. component-based programming is given below, this code can help the designers, developers during the development process of web applications [21][22].The class wise corresponding sample code segment in C++ is as follows-

Code:

```
#include "admin.h"
//##ModelId=4F7AB819004E
admin::update ()
{
}
```

```
//##ModelId=4F7AB81B037A
admin::insertdata ()
{
}
//##ModelId=4F7AB81E0203
Admin::delete data ()
{
}
//##ModelId=4F7AB82101F4
admin::purchase ()
{
}
//##ModelId=4F7AB825037A
admin::sell ()
{
}
#ifndef ADMIN_H_HEADER_INCLUDED_B0853EE5
#define ADMIN_H_HEADER_INCLUDED_B0853EE5
//##ModelId=4F7AB8140222
class admin : public Person
{
  public:
    //##ModelId=4F7AB819004E
    update ();
    //##ModelId=4F7AB81B037A
    insertdata();
    //##ModelId=4F7AB81E0203
    delete data();
    //##ModelId=4F7AB82101F4
    purchase ();
    //##ModelId=4F7AB825037A
    sell ();
};
#endif /* ADMIN_H_HEADER_INCLUDED_B0853EE5 */
#include "cheque.h"
//##ModelId=4F7AB95302CE
cheque::authorize ()
{
}
#ifndef CHEQUE_H_HEADER_INCLUDED_B0857ACB
#define CHEQUE_H_HEADER_INCLUDED_B0857ACB
//##ModelId=4F7AB941003E
class cheque : public payment
{
  public:
    //##ModelId=4F7AB95302CE
    authorize ();
  private:
    //##ModelId=4F7AB947035B
    int chequeno;
    //##ModelId=4F7AB94C03C8
    string details;
};
#endif /* CHEQUE_H_HEADER_INCLUDED_B0857ACB */
#include "credit card.h"
//##ModelId=4F7AB93B0203
credit card::authorize()
{
}
#ifndef
CREDIT_CARD_H_HEADER_INCLUDED_B0850B00
#define
CREDIT_CARD_H_HEADER_INCLUDED_B0850B00
//##ModelId=4F7AB9300167
class credit card : public payment
{
  public:
    //##ModelId=4F7AB93B0203
    authorize();
  private:
    //##ModelId=4F7AB937000F
    card num;
};
#endif /*
CREDIT_CARD_H_HEADER_INCLUDED_B0850B00 */
#include "inventory.h"
//##ModelId=4F7AB8E50251
inventory::add()
{
}
//##ModelId=4F7AB8E6033C
inventory::delete()
{
}
#ifndef INVENTORY_H_HEADER_INCLUDED_B0856825
#define INVENTORY_H_HEADER_INCLUDED_B0856825
//##ModelId=4F7AB8D6037A
class inventory
{
  public:
    //##ModelId=4F7AB8E50251
    add();
    //##ModelId=4F7AB8E6033C
    delete();
  private:
    //##ModelId=4F7AB8DB0290
    int id;
    //##ModelId=4F7AB8DF0148
    struct list;
};
#endif /* INVENTORY_H_HEADER_INCLUDED_B0856825
*/
#ifndef PAYMENT_H_HEADER_INCLUDED_B0850957
#define PAYMENT_H_HEADER_INCLUDED_B0850957
//##ModelId=4F7AB922033C
class payment
{
    //##ModelId=4F7AB927032C
    float amount;
};
#endif /* PAYMENT_H_HEADER_INCLUDED_B0850957 */
#ifndef PERSON_H_HEADER_INCLUDED_B0851005
#define PERSON_H_HEADER_INCLUDED_B0851005
//##ModelId=4F7AB7FC02CE
class Person
{
   //##ModelId=4F7AB8040222
    int is;
    //##ModelId=4F7AB807007D
    string name;
    //##ModelId=4F7AB8090203
    int age;
};
#endif /* PERSON_H_HEADER_INCLUDED_B0851005 */
#include "product.h"
//##ModelId=4F7AB879032C
product::gotoinventory()
{
}
//##ModelId=4F7AB883009C
product::add()
{
}
//##ModelId=4F7AB884003E
```

```
product::delete()
{
}
#ifndef PRODUCT_H_HEADER_INCLUDED_B08533FA
#define PRODUCT_H_HEADER_INCLUDED_B08533FA
//##ModelId=4F7AB8630251
class product
{
  public:
    //##ModelId=4F7AB879032C
    gotoinventory();
    //##ModelId=4F7AB883009C
    add();
    //##ModelId=4F7AB884003E
    delete();
  private:
    //##ModelId=4F7AB8680261
    int id;
    //##ModelId=4F7AB86D008C
    string name;
    //##ModelId=4F7AB87102DE
    float price;
};
#endif /* PRODUCT_H_HEADER_INCLUDED_B08533FA
*/
#include "report.h"
//##ModelId=4F7AB8530251
report::modify()
{
}
//##ModelId=4F7AB8560261
report::arrange()
{
}
//##ModelId=4F7AB8590186
report::optimize()
{
}
#ifndef REPORT_H_HEADER_INCLUDED_B0851331
#define REPORT_H_HEADER_INCLUDED_B0851331
//##ModelId=4F7AB83D00CB
class report
{
  public:
    //##ModelId=4F7AB8530251
    modify();

    //##ModelId=4F7AB8560261
    arrange();
    //##ModelId=4F7AB8590186
    optimize();
  private:
    //##ModelId=4F7AB8420167
    int is;
    //##ModelId=4F7AB844034B
    string description;
    //##ModelId=4F7AB84A0148
    stuct list;
};
#endif /* REPORT_H_HEADER_INCLUDED_B0851331 */
#include "sale.h"
//##ModelId=4F7AB913035B
sale::calcpayment()
{
}
//##ModelId=4F7AB917031C
sale::calctotal()
{
}
//##ModelId=4F7AB91B0213
sale::complate()
{
}
#ifndef SALE_H_HEADER_INCLUDED_B085120D
#define SALE_H_HEADER_INCLUDED_B085120D
#include "payment.h"
//##ModelId=4F7AB8F500AB
class sale : public payment
{
  public:
    //##ModelId=4F7AB913035B
    calcpayment();
    //##ModelId=4F7AB917031C
    calctotal();
    //##ModelId=4F7AB91B0213
    complate();
  private:
    //##ModelId=4F7AB8F90167
    boolean status;
    //##ModelId=4F7AB8FD02DE
   float total;
    //##ModelId=4F7AB9010242
    string paymentmode;
};
#endif /* SALE_H_HEADER_INCLUDED_B085120D */
#include "salesclerk.h"
//##ModelId=4F7AB83302DE
salesclerk::makewalk-in-sale()
{
}
#ifndef SALESCLERK_H_HEADER_INCLUDED_B085310E
#define SALESCLERK_H_HEADER_INCLUDED_B085310E
#include "Person.h"
//##ModelId=4F7AB82A0280
class salesclerk : public Person
{
  public:
    //##ModelId=4F7AB83302DE
    makewalk-in-sale();
};
#endif /*
SALESCLERK_H_HEADER_INCLUDED_B085310E */
#include "telephoneclerk.h"
//##ModelId=4F7AB8CF01F4
telephoneclerk::makephonecall()
{
}
//##ModelId=4F7AB8D201A5
telephoneclerk::sell()
{
}
#ifndef
TELEPHONECLERK_H_HEADER_INCLUDED_B0852E98
#define
TELEPHONECLERK_H_HEADER_INCLUDED_B0852E98
//##ModelId=4F7AB8C6007D
class telephoneclerk
{
  public:
    //##ModelId=4F7AB8CF01F4
    makephonecall();
    //##ModelId=4F7AB8D201A5
    sell();
};
```

```
#endif /*
TELEPHONECLERK_H_HEADER_INCLUDED_B0852E98
*/
```

Here we have converted the object oriented model into the target language (e.g. C++, Visual Basic, COBOL, and Java).in above example we generated code in C++. In this approach main benefit is higher flexibility that the developer is not afraid to repeat the process several times and is therefore more adventurous.

V. Conclusion And Future Scope

In this paper, we have analyzed the integration of security engineering into a model-driven software development approach. We specifically focused on UML and component-based programming for forward engineering for web applications in trusted operating systems.

In this research, we have presented a SPF based software development process for web applications. This is based on object-oriented and SPF based conceptual modeling techniques applied to the development of online web applications. Then, we clarify how these primitives can be mapped in a web solution for automating the software development process through forward engineering using UML.

Presently our design focuses on static and fixed design models, which are comparatively close to the implementation. It is significance considering whether the efficiency and effectiveness of the development process of secure web applications can be improved by annotating models at a higher level of abstraction (e.g. analysis, Design etc) or by annotating dynamic models, e.g. state machines.

Furthermore, a number of critical questions concerning the development process are still open, e.g. how are roles and permissions identified?

Future research work will focus on modeling security requirements and design information using dynamic UML models. Additionally, the development process for secure web systems starting with the preliminary analysis up to the complete secure web system design will be investigated. In this perspective, we will study and examine the possibility of propagating security requirements between analysis and design models and ways to prove the compatibility of requirements and design information given at different levels during web based software development.

References

[1] Booch G., Jacobson I., Rumbaugh J. The UML Language Users Guide. Addison-Wesley, ACM Press, 1999.

[2] J. Jürjens. Towards development of secure systems using UMLsec. In H. Hussmann, editor, Fundamental Approaches to Software Engineering, 4th International Conference, Proceedings, LNCS, pages 187–200. Springer, 2001.

[3] P. Epstein and R. Sandhu. Towards a UML based approach to role engineering. In Proceedings of the fourth ACM Workshop on Role-based access control, pages 135–143. ACM Press, 1999.

[4] http://en.wikipedia.org/wiki/Applications_of_UML.

[5] Roy A, Karforma S, A Survey on E-Governance Security, International Journal of Computer Engineering and Computer Applications (IJCECA). Fall Edition 2011, Vol 08 Issue No. 01, Pp: 50-62, ISSN 0974-4983.

[6] Baresi L., Garzotto F., Paolini P. From Web Sites to Web Applications: New Issues for Conceptual Modeling. ER'2000 Workshop on Conceptual Modeling and the Web, LNCS 1921. Springer-Verlag, 2000, pp. 89-100.

[7] K. Koskimies, T. M¨annist¨o, T. Syst¨a, and J. Tuomi, "Automated Support for Modeling OO Software", IEEE Software, 15, 1, January/February 1998, pp. 87–94.

[8] Mark Aldrich. Secured Systems and Ada: A Trusted System Software Architecture. Proceedings of TRI-Ada, 2001.

[9] P. Epstein and R. Sandhu. Towards a UML based approach to role engineering. In Proceedings of the fourth ACM workshop on Role-based access control, pages 135–143. ACM Press, 1999.

[10] Gómez J., Cachero C., Pastor O. Extending a Conceptual Modeling Approach to Web Application Design. In Proc. Conference on Advanced Information Systems Engineering (CAiSE), LNCS 1789, Springer- Verlag, 2000, pp. 79-93.

[11] J. Jürjens. Towards development of secure systems using UMLsec. In H. Hussmann, editor, Fundamental Approaches to Software Engineering, 4th International Conference, Proceedings, LNCS, pages 187–200. Springer, 2001.

[12] Gómez J., Cachero C., Pastor O. Extending a Conceptual Modeling Approach to Web Application Design. In Proc. Conference on Advanced Information Systems Engineering (CAiSE), LNCS 1789, Springer- Verlag, 2000, pp. 79-93.

[13] http://www.ijric.org/volumes/Vol8/Vol8No8.pdf.

[14] http://cairo.cs.uiuc.edu/publications/papers/thesis-achu.pdf.

[15] James B.D. Joshi, Walid G. Aref, Arif Ghafoor, and Eugene H. Spafford. Security Models for Web-Based Applications, 2001.

[16] Christian Friberg and Achim Held. Support for Discretionary Role-Based Access Control in ACL-oriented Operating Systems. Proceedings of the Second ACM Role-Based Access Control Workshop, 2005.

[17] http://www.ksc.com/articles/usecases.htm.

[18] Ivar Jacobson, Magnus Christerson, Patrik Jonsson, and Gunnar Övergaard, Object-Oriented Software Engineering: A Use Case Driven Approach, Addison-Wesley, Wokingham, England, 1992. David Ferraiolo and Richard Kuhn. Role-Based Access Control. Proceedings of the 15th National Computer Security Conference, 2004.

[19] Power, J. F. & Malloy, B. A. (2000), an approach for modeling the name lookup problem in the C + + programming language, in `ACM Symposium on Applied Computing', Como, Italy.

[20] Tamar Richner and St éphane Ducasse. Recovering high-level views of object-oriented applications from static and dynamic information. In Hongji Yang and Lee White, editors, Proceedings ICSM'99 (International Conference on Software Maintenance). IEEE, September 1999.

[21] Vishal Jain, Dr. Mayank "Singh Ontology Based Information Retrieval in Semantic Web: A Survey, I.J. Information Technology and Computer Science", 2013/10, 62-69, http://www.mecs-press.org.

[22] Nan Nie, Suzhi Zhang, Quality Test Template toward Multi-user Access Control of Internet-Based System, International Journal of Information Engineering and Electronic Business (IJIEEB). Vol.3, No.3, June 2011, PP.30-36, ISSN: 2074-9031 (Online) http://www.mecs-press.org.

[23] Nitish Pathak, Dr. Girish Sharma and Dr. B. M. Singh " Forward Engineering based Implementation of TOS in Social Networking" International Journal of Computer Applications, USA, Volume 102 – No.11, September 2014,PP.33-38, ISSN: 0975 – 8887.

Authors' Profiles

Dr. Girish Sharma is currently working as Associate Professor& Head of BPIBS, GNCT OF DELHI. He has More than 19 Years of academic / research and administrative experiences in reputed organizations like Hindu College, Sonepat, ABES Engineering College, Ghaziabad, and College of Engineering Roorkee. He completed his PhD (2005) in Mathematics (Inter Disciplinary) at Department of Mathematics, Gurukul Kangri University, Haridwar. He completed his M.Tech in Computer Technology and Application (2003) from Delhi College of Engineering (DCE), Delhi University, Completed his MCA and M.Sc (Physics) in 1993 and 1996 respectively from Gurukul kangri University, Haridwar. His current research interests include different aspects of Distributed systems, trusted operating Systems; Object oriented based Forward Engineering and Data Mining.

He is a life time member of various professional bodies like IEEE, CSI and ISTE etc.

He has published more than 55 research papers in various reputed national / international journals.

Dr.Brijmohan Singh is currently working as Associate Professor& Head of computer science and engineering department at COER, Roorkee. He has More than 12 Years of academic/research and administrative experiences in reputed organizations. He completed his PhD (2012) in Computer science and Engineering from Uttrakhand Technical University, Dehradun, UK. He completed his Master of Technology (Computer Science) with First Class (76.8%, Grade 'A') from Rajasthan Vidhya peeth Deemed University, Udaipur Rajasthan, in the session 2005 to 2007. He did his Bachelor of Engineering (Computer Science & Engineering) with First Class (74.89%) from College of Engineering Roorkee. He is a life time member of various professional bodies like IEEE, CSI and ISTE etc.

His current research interests include different aspects of Digital Image Processing, Mobile Computing, Artificial Intelligence, Pattern Recognition; Multimedia Systems etc.He has published more than 30 research papers in various reputed national / international journals.

Nitish Pathak received his M.Tech in Computer Science and Engineering (2010) from SIET, Meerut. He did his MCA in 2005 from UPTU, Lucknow and completed M.Phil. (Computer Science) in 2007 from Madurai Kamraj University, Madurai, Tamilnadu, India. Now he is Assistant Professor of Computer Science department in BVICAM, GGSIPU, Delhi (INDIA).He has More than Nine Years of extensive Corporate as well as Professional Teaching Experience at Graduate and Post Graduate level. He got Directorate Award (Three times on teacher's Day) for best teaching performance since 2007 to 2009, at ABES Engineering College, Ghaziabad, India.

His current research interests include different aspects of trusted operating Systems; Object oriented based Forward Engineering and Data Mining. He is a life time member of various professional bodies like IEEE, CSI and ISTE etc.

He has published more than 15 research papers in various reputed national / international journals.

Copyright © 2015 MECS

Author's Accepted Manuscript

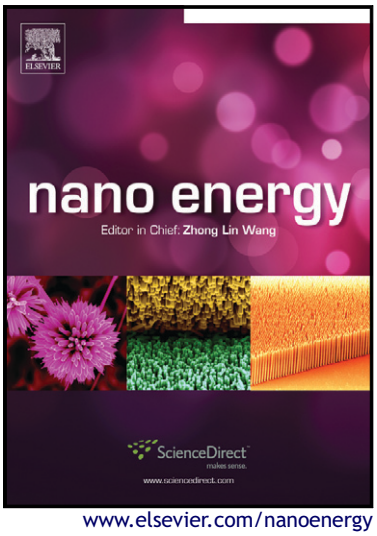

www.elsevier.com/nanoenergy

Giant enhancement in thermoelectric performance of copper selenide by incorporation of different nanoscale dimensional defect features

Bhasker Gahtori, Sivaiah Bathula, Kriti Tyagi, M. Jayasimhadri, A.K. Srivastava, Sukhvir Singh, R. C. Budhani, Ajay Dhar

PII: S2211-2855(15)00066-X
DOI: http://dx.doi.org/10.1016/j.nanoen.2015.02.008
Reference: NANOEN718

To appear in: *Nano Energy*

Received date: 28 November 2014
Revised date: 24 January 2015
Accepted date: 5 February 2015

Cite this article as: Bhasker Gahtori, Sivaiah Bathula, Kriti Tyagi, M. Jayasimhadri, A.K. Srivastava, Sukhvir Singh, R.C. Budhani, Ajay Dhar, Giant enhancement in thermoelectric performance of copper selenide by incorporation of different nanoscale dimensional defect features, *Nano Energy,* http://dx.doi.org/10.1016/j.nanoen.2015.02.008

This is a PDF file of an unedited manuscript that has been accepted for publication. As a service to our customers we are providing this early version of the manuscript. The manuscript will undergo copyediting, typesetting, and review of the resulting galley proof before it is published in its final citable form. Please note that during the production process errors may be discovered which could affect the content, and all legal disclaimers that apply to the journal pertain.

ACCEPTED MANUSCRIPT

Giant Enhancement in Thermoelectric Performance of Copper Selenide by incorporation of different Nanoscale Dimensional Defect Features

Bhasker Gahtori[a], Sivaiah Bathula[a,b], Kriti Tyagi[a], M. Jayasimhadri[b], A. K. Srivastava[a], Sukhvir Singh[a] , R. C. Budhani[a] and Ajay Dhar[a,1]

[a]*CSIR-Network of Institutes for Solar Energy, Materials Physics and Engineering Division, CSIR-National Physical Laboratory, Dr. K. S. Krishnan Road, New Delhi 110012, India*
[b]*Department of Applied Physics, Delhi Technological University, Delhi, India*

Abstract

We report a simple experimental strategy for enhancing the figure-of-merit (ZT) of thermoelectric materials by introducing different kinds of defect features, including nano-porosity, in a range of nano to meso-scale dimensions, employing spark plasma assisted (SPS) reaction sintering of mechanically alloyed nanopowders. This strategy has been experimentally demonstrated in a well known thermoelectric compound, Cu_2Se, which is shown to yield a high ZT of 2.1 at 973 K, which is among the highest reported value for this material and shows a ~ 40% increase over its bulk melt-processed counterpart. The main contribution to the enhanced ZT, despite moderate values of power factor, primarily originates from a very small value of thermal conductivity of 0.34 $Wm^{-1}K^{-1}$. This low thermal conductivity owes its origin primarily to the enhanced low-to-high wavelength phonon scattering by different kinds of defects, in a wide spectrum of nano to meso-scale dimensions, involving microstructural defects generated during high-energy ball milling, abundant nanocrystalline grain boundaries due to very low crystallite size, and more importantly the nano-to-meso scale residual porosity created due to SPS at optimized process parameters. The role of SPS in enhancing the ZT has been discussed and this strategy can also be applied to other thermoelectric materials.

Keywords: Thermoelectrics, nanoporosity, thermoelectric performance, copper selenide, spark plasma sintering, figure-of-merit.

[1]Corresponding author email: adhar@nplindia.org
Tel.: +91 11 4560 9456; Fax: +91 11 4560 9310

Accepted manuscript

ACCEPTED MANUSCRIPT

Introduction

Thermoelectric devices permit a direct conversion of heat into electrical energy and vice-versa. Owing to its green technology, vigorous efforts are being made to realize thermoelectric based waste heat recovery devices for energy generation. However, currently the main impediment in this direction is their limited conversion efficiency [1]. The efficiency of power conversion of a thermoelectric device depends mainly on the material's thermoelectric figure-of-merit (ZT), and the commercial realization of efficient thermoelectric devices [2] for power generation is currently hampered by the lack of thermoelectric materials with high ZT [3-7].

In the recent past, Cu_2Se and its derivative compounds has been a subject of keen interest for development of thermoelectric materials with high ZT [8-14]. The earliest report on thermoelectric bulk Cu_2Se is by Xiao et al. [8] who reported a peak ZT of 0.38 at 750°C. Later, Liu et al. [9] reported the thermoelectric behavior of Cu_2Se and they inferred a *'liquid-like'* behavior of Cu ions around the crystalline sub-lattice of Se, resulted in an intrinsically low lattice thermal conductivity culminating in an enhanced ZT of 1.5 at 1000 K in bulk Cu_2Se synthesized employing vacuum melting followed by consolidation using spark plasma sintering (SPS). Recently, ZT of 1.6 at 973 K has been achieved [9] in Cu_2Se synthesized by ball milling followed by hot pressing. After the initial report of Liu et al. [9] on Cu_2Se as a high ZT thermoelectric material, several other Cu_2Se based materials with relatively high ZT have been reported. Ballikaya et al. [12] have reported a ZT ~1 at 900 K in Ag doped Cu_2Se synthesized by melting, annealing followed by SPS. Although, recently a high ZT of 2.3 has been reported for iodine doped Cu_2Se [13], but it is at a much lower temperature (~ 400 K), where a second order monoclinic to cubic phase transition takes place in this material, which results in favorably altering the thermal and electrical transport parameters, leading to a high ZT.

Accepted manuscript

ACCEPTED MANUSCRIPT

Cu_2Se based TE devices have been a subject of discussion [15, 16] due to several constraints, including Se evaporation at high temperatures and more importantly the electro-migration of Cu. However, the focus of the present study is only to demonstrate a substantial enhancement in ZT by incorporation of different nano to meso-scale dimensional defect features, including residual porosity. Cu_2Se has been selected for experimental proof-of-concept study of our proposed strategy as it is a well established binary thermoelectric compound.

The dimensionless ZT [17] is defined as $ZT = S^2\sigma T/(\kappa_e + \kappa_L)$, where S, σ, and T are the Seebeck coefficient, electrical conductivity, and absolute temperature, respectively and κ_e and κ_L are electronic and lattice contribution to the thermal conductivity. Reducing κ_L has been an important strategy to improve ZT [18] as κ_e is coupled to σ through the Wiedmann-Franz law. Since both σ and κ are intimately related to the microstructure of the material, one way to improve ZT is *via* nanostructuring [19-23], which allows improvement in the power factor ($S^2\sigma$) and a simultaneous reduction in κ_L leading to an enhancement in ZT. This strategy has been earlier successfully demonstrated on several nanostructured thermoelectric alloys and compounds [20, 24-30] and the enhancement in ZT in some cases has been reported to be as high as 3.5 [24] to 6 [30] fold, over their bulk counterparts.

Kanatzidis's group has recently proposed a panoscopic approach [28, 31, 32] for the enhancement of ZT in thermoelectric materials by introduction of different dimensional atomic (point defects), nano (line and interfacial defects) and meso-scale (nano-precipitate grain boundaries) features, which contribute to the scattering in a large spectrum of short-to-long wavelength heat-carrying phonons. It is well known that in thermoelectrics most of the heat is transported by mid-to-long wavelength phonons [3, 17, 33, 34], thus the meso-scale defect features are expected to play a dominant role in controlling the thermal conductivity. Employing this all length-scale hierarchical structuring approach, Kanatzidis et al. [32] have reported a high ZT ~ 2.3 in PbTe with 4 mol% SrTe nanoprecipitates. On the other hand, there are several theoretical [28, 35-38] and experimental [39-41] studies in the literature, reporting a

Accepted manuscript

ACCEPTED MANUSCRIPT

considerable enhancement in ZT due to nanoporosity, owing to the reduction in thermal conductivity. These results show that the degradation of electrical conductivity due to the inclusion of nanopores is more than compensated by a large reduction in the phonon thermal conductivity and an increase in Seebeck coefficient, resulting in a significantly enhanced ZT. In the present study, we have employed a similar panoscopic all length-scale hierarchical structuring approach for enhancing ZT in Cu_2Se, except that we have introduced controlled nanoporosity as the nano to meso-scale defect feature in the nanostructured material matrix, and these nanoscale pores act as additional scattering centers for heat-carrying phonons. This approach for obvious reasons is simple, as the size and distribution of nano to meso-scale porosity in the thermoelectric material matrix can be engineered experimentally by optimizing the process parameters of SPS [40, 42] and the volume fraction of process control agent added during high energy ball milling (HEBM) [27, 43], to match the wavelength range of the phonons to be scattered. Further, apart from residual porosity, the other nano-scale defect features like, dislocations and nanoscale grain boundaries in Cu_2Se nanostructured matrix are introduced during its powder metallurgy processing [19, 43, 44] employing high energy ball milling followed by SPS at optimized process parameters. SPS, apart from retaining these nanoscale defect features [27, 45] also aids in the creation of a distributed nano to meso-scale residual porosity [40, 42] in the Cu_2Se nanostructured matrix. The overall effect of these nano to meso-scale defect features leads to an abundant scattering of low-to-high wavelength phonons resulting in a very small value of thermal conductivity ~ 0.34 $Wm^{-1}K^{-1}$ (at 973 K) thereby in turn enhancing the ZT.

Accepted manuscript

In the present studies, we describe a simple way of nanostructuring Cu_2Se, which allows realization of a ZT ~ 2.1 at 973K, which is higher by ~30-40% than the highest reported for this material [9, 10]. This value of ZT, which is ~ 40% higher than its melt-processed bulk counterpart, is among the highest reported for thermoelectric materials and is primarily due to an exceptional reduction in thermal conductivity (~65%) on nanostructuring, which introduces

various types of defects, in a wide spectrum of nano to meso-scale dimensions and these can scatter low-to-high wavelength heat-carrying phonons. Our approach involves controlled HEBM to produce Cu_2Se nanopowders followed by their consolidation employing SPS at optimized process parameters. To compare our results with the earlier reports in the literature [9, 10], bulk Cu_2Se samples were also synthesized employing the conventional vacuum melting process followed by their consolidation sintering using SPS. In both the cases, highly dense samples were obtained, which were extensively characterized employing high temperature X-ray diffraction (XRD), Field Emission Scanning Electron Microscopy (FESEM), High Resolution Scanning Electron Microscopy (HRTEM) and Differential Scanning Caloriemetry (DSC) measurements.

Sample Preparation

Powders of Cu (99.99%, Alfa Aesar) and Se (99.99%, Alfa Aesar) mixed in stoichiometric ratio were milled in a high energy ball-mill (Fritsch, Pulverisette-5) for an optimized time period of 50 hours. The grinding jars and balls of the high energy ball-mill were made of hardened stainless steel. The ball-to-powder weight ratio was varied between 10:1 to 20:1 during the grinding process, which was carried out in argon atmosphere with a speed of 400 rpm. In order to prevent re-welding and to promote fracturing of powder particles during milling, 2 wt. % of stearic acid was added as a process control agent. Prior to sintering, the processing of the nanostructured alloy powders was carried out in glove box (Mbraun, MB20) to avoid oxidation and other atmospheric contamination. We have also synthesized bulk Cu_2Se employing the conventional vacuum melting process. In this case Cu and Se powders in chemical stoichiometric ratio were ground thoroughly in a glove box under a high-purity argon atmosphere and these powders were

Accepted manuscript

ACCEPTED MANUSCRIPT

subsequently pelletized and vacuum-sealed (10^{-5} Torr) in quartz tubes. The sealed quartz ampoules were heat-treated at 1273 K for 24 hrs, and then naturally cooled to room temperature. The powders of bulk and nanostructured Cu_2Se were subsequently consolidated and sintered under vacuum (~ 4 Pa) using spark plasma sintering (SPS Syntex, 725) at identical optimized process parameters of pressure 80 MPa and temperature 873 K for 3 minutes (soaking time) at a heating rate of 400°C/minute using graphite die and punches. The actual composition of melt-processed bulk and nanostructured sintered Cu_2Se samples was determined using Flame atomic absorption spectrometry technique (Analytik Jena, Vario-6) and both the samples exhibited almost the same stoichiometry as the starting composition. The density of both, the nanostructured and bulk Cu_2Se samples, was measured using the conventional Archimedes principle and was found to be ~ 99.2% of their theoretical density. Phase identification and crystallite size measurements were carried out using Rigaku powder XRD (40kV and 30 mA) and the data was acquired at a scanning speed of 0.5°/min with a step width of 0.05° in conjunction with the use of Williamson-Hall method. HRTEM measurements were carried out using FEI, Tecnai G2 F30 STWIN microscope with field emission electron gun source and operated at 300 kV electron accelerating voltage. The thermal diffusivity was measured on polished sample discs of diameter 12.7 mm and thickness 3 mm using a laser flash system (Linseis, LFA 1023). Specific heat was determined by DSC (Netzsch, DSC 404 F3). The Seebeck coefficient and resistivity were measured using a commercial equipment (Ulvac, ZEM 3) employing polished sample bar of about 3 x 3 x 11 mm^3. The accuracies in transport measurement are: ± 6% for thermal diffusivity, ± 10% for electrical conductivity, ± 7% for Seebeck coefficient, ± 8% for specific heat and ±0.5% for density. The thermal conductivity was calculated as a product of thermal diffusivity, specific heat, and volume density. The transport

Accepted manuscript

ACCEPTED MANUSCRIPT

data of nanostructured Cu_2Se was found to be reproducible within ~ ± 7% for different experiments with identical synthesis processing parameters.

Results and Discussion

Microstructural characterization

Figure 1 depicts the XRD patterns of nanostructured Cu_2Se for a series of temperatures ranging from room temperature to 533 K. It is evident from the Figure 1(a) that a phase transition takes place as the system loses its monoclinic structure and begins to behave as cubic after ~ 413 K, which is supported by disappearance of (090) peak in the XRD pattern and is in accordance with our DSC results on same sample *(Figure S5, Supplementary Content)*. Figures 1(b) and (c) show the Reitveld refinement of Cu_2Se nanostructured samples with their Bragg's positions, carried out at room temperature (α-phase) and 413 K (β-phase), respectively (*Table 1S & 2S: Supplementary Content)*. Further, a comparison of room temperature XRD patterns of bulk and nanostructured Cu_2Se (*Figure S1, Supplementary Content*) indicated a slight shift of the XRD peaks towards higher Bragg angles in the nanostructured samples, thereby suggesting the presence of defects in this sample [46, 47]. Figure 1(d) shows the crystal structure of β-Cu_2Se, as obtained in present study, wherein the blue spheres represent Cu atoms at tetrahedral positions and green spheres indicate the Se atoms. The structure clearly shows Se atoms arranged in FCC lattice pattern.

The average crystallite size of high energy ball milled nanopowders and SPS consolidated nanostructured Cu_2Se samples, determined from the Williamson-Hall method [48] was found to be ~11nm and ~14 nm, respectively, which suggests that the fine nanoscale features introduced during the ball milling are retained post sintering.

Accepted manuscript

ACCEPTED MANUSCRIPT

A detailed microstructural characterization of nanostructured Cu_2Se sample employing HRTEM revealed several significant features in real and reciprocal space. In general, it was noted that the microstructure was nano-grained with individual grains abutting each other (Figure 2(a)). A few nano-grains, marked as region 'A' and displayed as an inset A at a higher magnification, show nano-sized individual crystallites of varied dimensions. The extent of overlap between the neighboring grains in some regions is such that the interference Moiré fringes are also noticeable (region B marked in Figure 2(a)) due to the overlap of crystallographic planes of individual crystallites. Inset B (Figure 2(a)), showing the magnified image of region B, delineates a set of crystallographic planes with inter-planar spacing of 0.22 nm (hkl : 090) of monoclinic crystal structure. Inset B clearly shows the appearance of Moiré fringes, as a sequential array of dark and white-bands, with an inter-band spacing of $\delta \sim 2$ nm. Such modulation in the microstructure, at an atomic scale, may be due to the rapid sintering rates, to which the nanostructured Cu_2Se sample is subjected under high pressure, during SPS. Further, atomic scale images and reciprocal space analyses have been carried out to resolve fine intricacies in the microstructure. Figure 2(b) typically exhibits a few randomly oriented nanocrystallites with inter-planar spacing's of 0.36 nm (hkl:211), 0.33 nm (hkl:221) and 0.19 nm (hkl:411) of a monoclinic crystal structure. The inset of Figure 1(b), which shows a corresponding Fast Fourier Transform (FFT) recorded from the same region, reveals that these are orientated randomly with respect to each other as manifested by the formation of Debye rings in reciprocal space.

It was noted that although most of these nanocrystallites have a clear boundary at the interfaces, but, regions with perturbed atomic scale arrangement are also clearly evident in the lattice-scale image (marked by a solid line in Figure 2(c)) due to complete random coordination of the atoms in this region leading to microstructural defects in a regular lattice structure with an appearance of an amorphous phase

Accepted manuscript

ACCEPTED MANUSCRIPT

(marked in the figure) at the grain boundaries. A corresponding FFT pattern which shows a diffused background in the centre corroborates the presence of microstructural defects, generated due to extended duration of HEBM and also due to sintering of these nanopowders at very high sintering rates during SPS. This has also been observed earlier for several materials processed using HEBM [20, 23, 24]. Figure 2(d), which presents an atomic scale image of nanostructured Cu_2Se sample, at relatively low magnification, exhibits the presence of several interfaces due to large number of nanocrystallites of varying dimensions. This micrograph clearly exhibits that the interfaces are generally well defined and the nanocrystallites are randomly oriented *(Supplementary Content, Figure S2 and S3)* with respect to one another although some atomic scale dislocations and amorphous regions are also clearly evident and some of them are highlighted in Fig. 2d. A statistical crystallite size distribution of nanostructured Cu_2Se, by estimating the dimensions of various crystallites in several regions of the specimen, revealed the size of the nanocrystallites in the range 5 to 30 nm *(Supplementary Content, Figure S4)* with an average crystallite size ~ 15 nm, which is reasonably well supported by our XRD analysis on the same sample. *In-situ* heating experiments were also conducted in real space employing HRTEM to observe the microstructural changes of the reversible phase transformation $\alpha \rightarrow \beta$ in nanostructured Cu_2Se. The sample was heated at the rate of 10 K/min and the HRTEM atomic scale images were recorded at 413 K and again after cooling at room temperature. As shown in Fig. 3(a), it was observed that at 413 K, the set of atomic planes are organized in such a way that the inter-planar spacing (0.34 nm) between them is close to that of (111) planes of face centered cubic (FCC) β-phase of Cu_2Se. An arrow demonstrating the growth direction of (111) plane is also depicted in this micrograph. This observation of visualizing the array of (111) planes at high temperature in a FCC phase is commensurate with the cubic symmetry, where (111) planes are considered to be atomically most dense. Fig. 3(b) shows the atomic scale image of the same area of the sample at room temperature after cooling from 413 K. The prominent planes with inter-planar spacing of 0.33 nm (hkl : 221) of monoclinic crystal suggests that Cu_2Se reverts back to its monoclinic α-phase at room temperature without any significant distortion.

Accepted manuscript

ACCEPTED MANUSCRIPT

The FESEM image analysis of our nanostructured Cu_2Se sample, exhibited a uniform microstructure with nanocrystalline aggregates of granular morphology and regions with residual porosity of varying nano-to-meso scale dimensions (~ 20 to 200 nm) distributed throughout the sample and Figure 4 (a) and (b) shows typical FESEM images of this nanostructured sample from different regions. Owing to spark plasma sintering of the Cu_2Se nanopowders at optimized parameters, we attained a density of 99.2% of the theoretical density and the remaining porosity manifests itself as the residual porosity in the form of nanopores in the range of ~ 20-200 nm uniformly distributed in the Cu_2Se nanostructured matrix. Similar nanoporosity has also been earlier reported in several thermoelectric [35-37, 41, 49-51] and other nanostructured materials [27] sintered employing SPS. The size and distribution of these nano-pores can be controlled by the SPS processing parameters, mainly, pressure [52, 53] and the volume fraction of the stearic acid [54],which is used as a process control agent during HEBM, which evaporates at high temperatures during SPS leaving behind nanopores. These processing parameters were optimized to introduce controlled nano-to-meso scale porosity in the nanostructured Cu_2Se sample, which is dimensionally comparable to mid-to-long wavelength phonons responsible for maximum heat-transport [20, 23]. The inset in Figure 4(b), which shows the energy dispersive spectrometry (EDS) point area analysis, exhibited an average chemical composition very close to stoichiometric Cu_2Se.

Role of SPS in enhancing ZT

In order to truly exploit the potential of nanostructuring in enhancing the ZT, the synthesized nanopowders have to be consolidated to near-theoretical density while simultaneously retaining their nanoscale features. However, in practice this is rather difficult because densification during sintering is always accompanied by microstructural coarsening. In order to achieve this, a rapid sintering rate is applied to the nano-powdered green compact under pressure so that the sample spends little time in the low-temperature regime, where non-densifying mechanisms, such as, surface diffusion are active, and proceeds quickly to higher temperatures where densifying mechanisms, such as, grain boundary or volume diffusion are dominant. Since grain growth occurs in both these regimes, it is believed that the

Accepted manuscript

ACCEPTED MANUSCRIPT

use of rapid sintering rates can greatly improve the final sintered density while retaining the initial nanostructure [28, 29]. High sintering rates over large volumes can be realized using SPS since it a pressure-assisted sintering process in which high amperage pulsed direct current is employed to sinter the samples under pressure. The SPS process makes it possible to sinter at lower temperatures and in shorter times because the particles are heated rapid by the spark plasma, which has a surface activating and cleaning effect on the particles being sintered [41, 49, 50]. The main advantage of SPS over its rival sintering techniques is that it leads to near-theoretical density (~ 99%) in the SPS product while retaining the nanoscale features of the starting nanopowders post-sintering [15,16,27,43]. These nanoscale features subsequently contribute significantly towards increasing the phonon scattering by high density of nanoscale grain boundaries and thus lowering the lattice thermal conductivity. Furthermore, the high density of the SPS product on one hand enhances the electrical conductivity and on the other hand it leads to residual nanoscale porosity in the SPS product and the resulting nano-pores can act as additional centers for phonon scattering, leading to further reduction in lattice thermal conductivity [26, 30, 35-37, 41, 49-51]. The resultant effect of these microstructural modifications culminates in a significant enhancement of ZT as exemplified earlier for several thermoelectric alloys and compounds [20, 24-30].

Accepted manuscript

Electrical transport measurements

The temperature dependent electrical transport properties of bulk and nanostructured Cu_2Se samples are shown in Figure 5 (a & b). A structural transformation from α to β phase of Cu_2Se at ~ 413 K appears quite prominently in all these measurements. Figure 5(a) shows that the electrical resistivity (ρ) of nanostructured sample is higher than its bulk counterpart, throughout the temperature range of measurement. Further, in contrast to the bulk sample, the nanostructured samples exhibit a rapid increase in ρ with temperature and at the highest temperature (973 K) it is ~ 60% higher than the value for our bulk samples. This increase in ρ, due to nanostructuring, could be attributed to the atomic sized defect features in our nanostructured samples, as indicated by HRTEM analysis (Fig. 2), which may result in

ACCEPTED MANUSCRIPT

electron scattering, especially due to atomic or nano defects of sizes comparable to the electron wavelength. Although the ionic conductivity is expected to increase owing to nanostructuring [6, 55, 56], but this increase is more than compensated by the decrease in the electronic conductivity due to enhanced scattering of electrons by atomic scale defect features, thus leading to an overall increase in ρ of nanostructured Cu_2Se as compared to its bulk counterpart. Furthermore, the ρ of our melt-processed bulk Cu_2Se sample is lower than the value reported earlier by Liu et al. [9] and Yu et al. [10] for material with the same composition and synthesized using similar technique. This could be attributed to the higher density (~ 99.2% of the theoretical density) of our samples achieved by consolidation sintering of nanopowders using SPS at temperatures and pressures much higher than those employed by earlier researchers [10]. Further, our measurements of Hall effect at ambient temperature show a carrier concentration of 9.1 x $10^{20}/cm^3$ and 6.3 x $10^{20}/cm^3$ for melt-processed bulk and nanostructured samples, respectively, which are higher than reported by Liu et al. [9] for melt-processed bulk Cu_2Se, which would also contribute the lower values of ρ.

Figure 5(b) shows the temperature dependence of Seebeck coefficient (S) for melt-processed bulk as well as the nanostructured Cu_2Se samples. The positive sign of S indicates holes as majority charge carrier's thereby suggesting p-type conduction in this material. The nearly linear temperature dependence of S in the cubic phase is consistent with the picture of a degenerate semiconductor where carrier mean free path is nearly equal to inter-atomic distance. Further, as is evident from Figure 5(b), the S of nanostructured Cu_2Se sample is higher than its bulk counterpart, in entire temperature range. This increase has been attributed to nanostructuring, which can enhance the density of states near the Fermi level due to quantum confinement, resulting in an increase in thermopower [19-22]. The power factor (S^2/ρ) deduced from the measured ρ and S was found to be 14.2 and 7.5 $\mu Wcm^{-1}K^{-1}$ for nanostructured and melt-processed bulk Cu_2Se, respectively, in the β-phase (973 K). The value of power factor for bulk Cu_2Se is lower than that reported earlier by other researchers [9, 10], which is primarily due to the higher ρ in our bulk samples.

Accepted manuscript

ACCEPTED MANUSCRIPT

Thermal Transport measurements

The variation of thermal conductivity (κ) with temperature for both, bulk and nanostructured Cu_2Se samples, has been shown in Figure 5(c). A large discontinuity in κ at ~ 413 K marks the α → β phase transition *(Supplementary Content, Figure S5)*. Expectedly, the κ of Cu_2Se in nanostructured sample is much lower than its value for its bulk counterpart, over the entire temperature range. Specifically, the value of κ for nanostructured Cu_2Se at the highest temperature of 973 K is 0.34 W/mK, which is ~ 65 % lower as compared to its bulk counterpart at the same temperature. This value of κ of our nanostructured Cu_2Se sample is not only the lowest obtained thus far for this material [8-10] but also among the lowest value for any state-of-the-art (ZT >1) thermoelectric material [4, 20-29] in the intermediate temperature range (β-phase of Cu_2Se). It is well known that heat-carrying phonons in thermoelectric semiconductors lie in a wide band of wavelengths, although most of the heat is carried by mid-to-high wavelength phonons [33, 34, 57]. In the present case, the presence of disorder in terms of nanocrystallite boundaries, microstructural defects (dislocations and amorphous regions) and nanoporosity in our nanostructured Cu_2Se sample, covers a broad dimensional nano-to-meso scale range to scatter heat-carrying phonons in a wide spectrum of wavelengths. Although, the microstructural defects, such as dislocations (few nm) and amorphous regions (few nm to tens of nm) are effective in scattering the short wavelength phonons, the matrix nanocrystallite (~5-30 nm) boundaries and residual nanopores (~ 20-200 nm) play an effective role in scattering the mid-to-high wavelength phonons [24, 26, 27], thus leading to a very low value of κ. The nano-to-meso scale pores can only scatter those heat-carrying phonons which are smaller than the size of the pores. As the wavelength of the charge carriers is very small (~ 5nm) compared to the size of the pores (20-200 nm), it is expected that although these fine pores would scatter phonons but not the charge carriers thereby decreasing κ without significantly affecting ρ.

To get a quantitative idea of the effect of nanostructuring on κ, the lattice thermal conductivity (κ_L) was obtained by subtracting the electronic contribution (κ_e), calculated from electrical conductivity

Accepted manuscript

ACCEPTED MANUSCRIPT

using the Wiedmann-Franz law ($\kappa_e = L_o\sigma T$), from the total thermal conductivity. The Lorentz number (L_o), calculated from the electrical conductivity data for nanostructured and bulk Cu_2Se samples was found to be, 2 x 10^{-8} V^2K^{-2} and 1.6 x 10^{-8} V^2K^{-2}, respectively and the resulting temperature dependence of κ_L is shown in Figure 5(d). A comparison of Figure 5(c) and 5(d) clearly suggests that in the bulk Cu_2Se sample the total κ has a substantial contribution from κ_L, which is reduced substantially on nanostructuring, as discussed earlier. It is evident that the reduction in κ for these samples is primarily due to nanostructuring, which introduces a high density of grain boundaries leading to abundant nanograin boundaries participating in phonon scattering process and the presence of microstructural defects, such as, dislocations and amorphous regions, introduced due to extended duration of ball-milling (as depicted by HRTEM, Figure 2c & d), which also contributes to phonon scattering process [20, 23, 24]. Another major factor contributing to the enhanced phonon scattering process is the residual nano to meso-scale porosity in these samples (see Figure 4), which also contribute significantly towards lowering κ as the nano-pores of varying nano to meso-scale dimensions (~ 20 - 200 nm) in the sintered samples can also act as centers for phonon scattering [30, 35-37, 41, 49, 50]. Although, a significant reduction in κ on nanostructuring has been earlier reported for a variety of thermoelectric materials [4, 20, 24-30], but this decrease of ~ 65% in thermal conductivity due to nanostructuring in Cu_2Se is among the highest reported thus far. It may be noted that the nanostructured Cu_2Se is only thermally stable up to a temperature of 800 K due to Se vaporization at higher temperatures [15, 16] *(Supplementary Content, inset in Figure S5)*.

Thermoelectric Performance

After combining the results of σ, S and κ, the calculated ZT as a function of temperature has been displayed in Figure 6(a). For better evaluation of our results, in this figure we have compared the ZT data with the recent reports from literature [8-10]. Figure 5(a) clearly shows that while the ZT ~ 1.5 in our melt-processed bulk Cu_2Se samples is comparable to those reported earlier in the literature [9, 10], this key parameter is ~2.1 at 973 K for our nanostructured sample, which translates into a gain of ~30-40 % over the reported values [9, 10] at the same temperature. In order to confirm the reproducibility of our

Accepted manuscript

ACCEPTED MANUSCRIPT

measurements, the temperature dependence of electrical and thermal transport properties was experimentally determined *(Supplementary Content, Figure S6)* by repeated thermal cycling between room temperature and 973 K and the resulting ZT for three consecutive cycles is plotted in Figure 6(b). This figure clearly suggests that the reproducibility in the ZT values is quite good, at all the temperatures and is within the experimental error of ZT.

We would like to emphasize that, despite moderate values of power factor, the drastic decrease in κ of the nanostructured Cu_2Se samples is due to a very low crystallite size (5 – 30 nm) and residual porosity (20 – 200nm) which owes its origin directly or indirectly to the consolidation and sintering of nanopowders employing SPS at optimized process parameters [42, 58-60]. Further, the presence of microstructural point defects, such as, dislocations and amorphous regions, due to extended periods of HEBM, also contributes in lowering κ. The combined effect of all these parameters leads to a very high value of ZT. It may, however, be noted that in order to achieve an optimum enhanced ZT, the size of residual porosity in thermoelectric material has be optimized depending on the material. Increasing the porosity in the thermoelectric material although may be favorable for decreasing κ [34, 35, 37], but in turn it would also lower the σ. Thus, the dimensional distribution of nano to meso-scale porosity in the thermoelectric material has to be optimized in order achieve a maximum enhancement in ZT, which can experimentally be realized by optimizing the SPS process parameters [39, 40, 42]. This strategy of reduction in thermal conductivity by incorporation of different defect features, especially residual nanoporosity, in a spectrum of nano to meso-scale dimensions, can also be applied to other thermoelectric materials for enhancing their ZT.

Conclusion

Accepted manuscript

ACCEPTED MANUSCRIPT

We report a simple experimental strategy for enhancing the ZT of nanostructured Cu_2Se by introducing different kinds of defect features, in a spectrum of nano to meso-scale dimensions, which were characterized employing FESEM and HRTEM. Employing this approach, nanostructured Cu_2Se is shown to yield a high ZT of 2.1 at 973 K, which is among the highest reported thus far and shows a ~ 40% increase over its bulk melt-processed counterpart. The nanostructured Cu_2Se was synthesized by controlled high energy ball milling followed by consolidation sintering of resulting nanopowders employing SPS at optimized process parameters at rapid heating rates. The main contribution to the enhanced ZT primarily originates from a very small value of thermal conductivity of 0.34 $Wm^{-1}K^{-1}$ (at 973 K), which owes its origin to the enhanced low-to-high wavelength phonon scattering by different kinds of defect features, in a wide spectrum of nano to meso-scale dimensions, involving microstructural defects (dislocations and amorphous regions) generated during high energy ball milling, abundant nanocrystalline grain boundaries due to very low crystallite size and nano to meso-sized residual porosity created due to spark plasma sintering at optimized process parameters. This strategy of significantly enhancing the ZT can be employed to all other existing thermoelectric materials.

Accepted manuscript

Acknowledgements

This work was supported by CSIR-TAPSUN (CSIR-NWP 54) programme entitled *"Novel approaches for solar energy conversion under technologies and products for solar energy utilization through networking."* The authors are grateful to Mr. Radhey Shyam and Mr. Naval Kishor Upadhyay for their technical support.

ACCEPTED MANUSCRIPT

FIGURE CAPTIONS

Figure 1: X-ray diffraction patterns of nanostructured Cu_2Se **(a)** at different temperatures **(b)** and **(c)** Reitveld refinement plot at room temperature (α-phase) and high temperature of 410 K (β-phase), respectively **(d)** crystal structure of β-Cu_2Se where blue spheres indicate Cu and green spheres indicate Se atoms.

Figure 2: HRTEM images of nanostructured Cu_2Se samples at room temperature showing **(a)** distribution of fine nanocrystallites abutting each other. Set of agglomerated nanocrystallites are marked as region A and a set of moiré patterns as region B. Inset A shows the magnified view of nanocrystallite aggregates in region A and inset B shows atomic scale image of region B exhibiting moiré patterns due to overlapped planes of monoclinic crystal **(b)** atomic scale image of nanocrystallites distributed randomly with different inter-planar spacing's of monoclinic crystal structure. Inset shows corresponding FFT revealing the crystallographic planes in reciprocal space **(c)** atomic scale image of a set of nanocrystallites showing a amorphous region at the boundary. Inset shows corresponding FFT revealing the crystallographic planes in reciprocal space and a diffused hallow ring elucidating the microstructural defects at the interface (marked with solid lines) **(d)** atomic-scale images of several randomly oriented nanocrystallites with presence of microstructural defects, marked with solid lines.

Figure 3: *In-situ* heating experiments showing atomic scale HRTEM images of nanostructured Cu_2Se **(a)** at 413 K after heating from RT at the heating rate of 10°C/minute exhibiting phase transformation of Cu_2Se (monoclinic) into cubic structure at 413 K. Image shows the presence of (111) planes with an interplanar spacing of about 0.34 nm, **(b)** at room temperature, after cooling from 413 K showing the presence of prominent planes with interplanar spacing of 0.33 nm (hkl:221) corresponding to monoclinic phase.

Figure 4: FESEM micrograph of nanostructured Cu_2Se showing nanocrystalline aggregates of Cu_2Se. (a & b) few nano-sized pores are marked with dotted lines. Inset depicts the EDS pattern showing the presence of Cu and Se. X-axis: 0.5 to 2 keV, Y-axis: Intensity (arb. unit).

Figure 5: Temperature dependence of electrical and thermal properties of nanostructured and bulk Cu_2Se **(a)** electrical resistivity (**b)** Seebeck coefficient (**c)** total thermal conductivity and **(d)** lattice thermal conductivity for bulk and nanostructured Cu_2Se samples.

Figure 6: Temperature dependence of ZT for nanostructured Cu_2Se **(a)** comparison with recently reported ZT values from the literature **(b)** reproducibility data of different thermal cycles on the same sample.

Accepted manuscript

ACCEPTED MANUSCRIPT

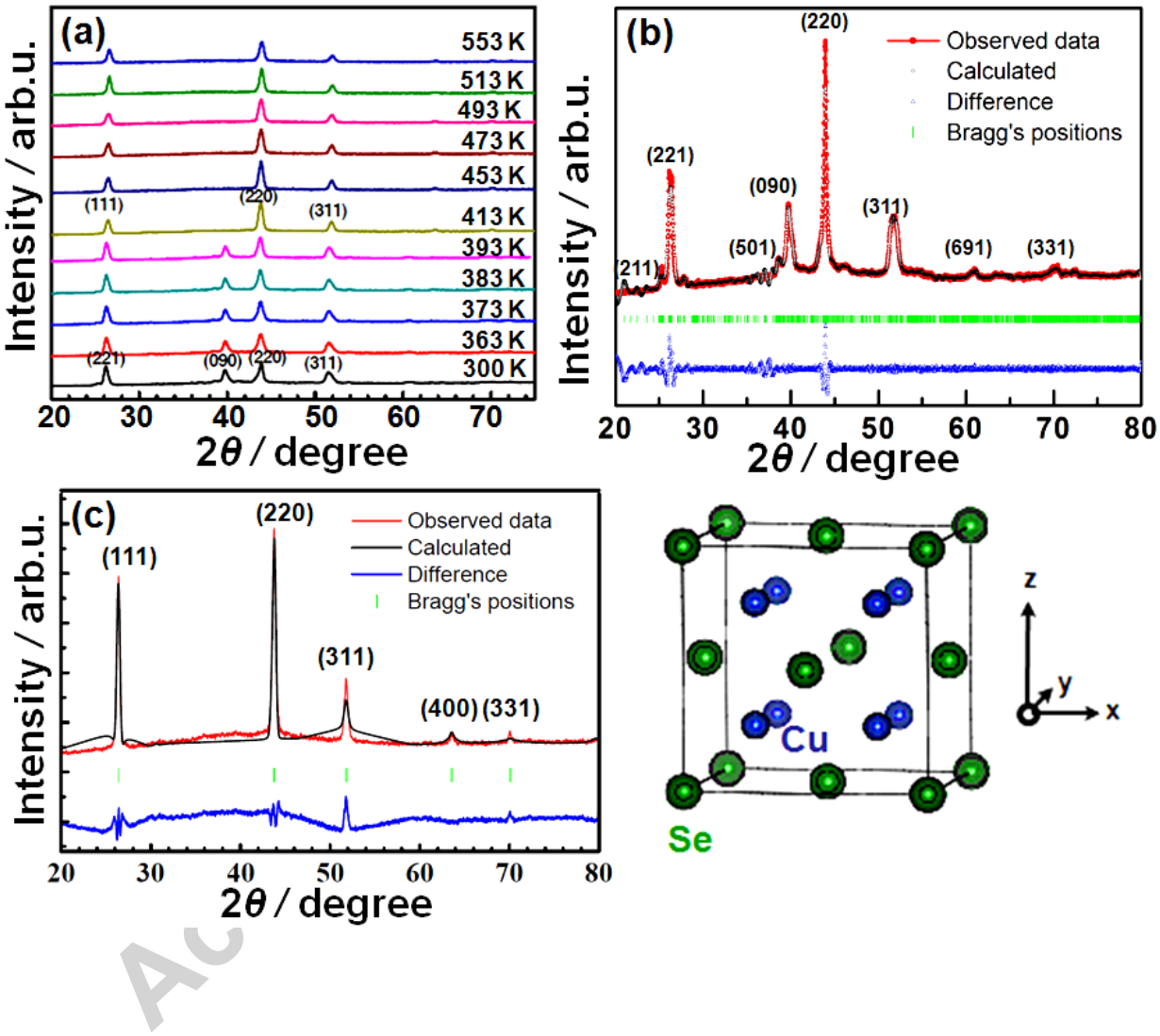

Figure 1

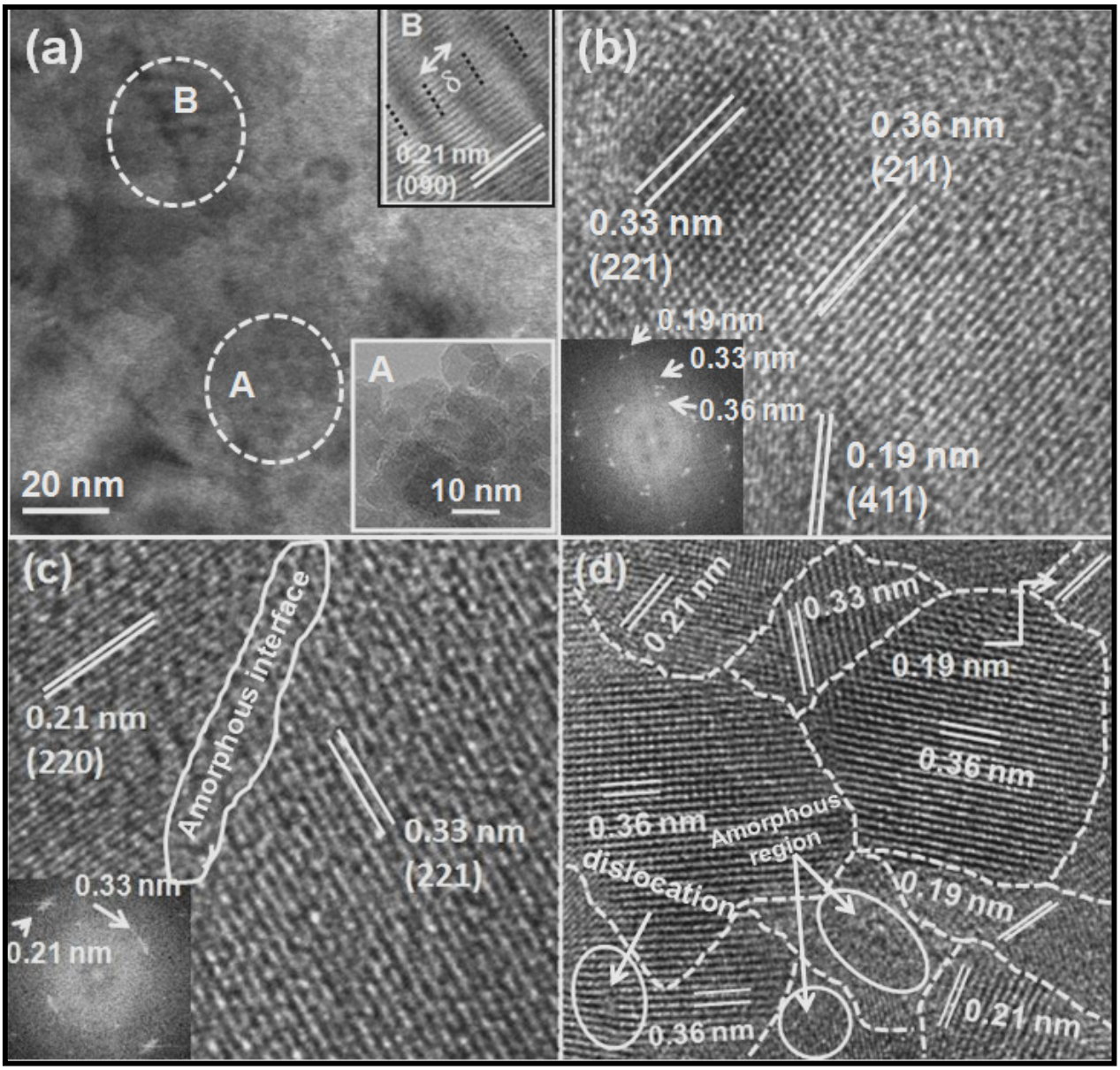
(a)
B
A
20 nm
B
0.21 nm
(090)
A
10 nm
(b)
0.36 nm
(211)
0.33 nm
(221)
0.19 nm
0.33 nm
0.36 nm
0.19 nm
(411)
(c)
0.21 nm
(220)
Amorphous interface
0.33 nm
(221)
0.33 nm
0.21 nm
(d)
0.21 nm
0.33 nm
0.19 nm
0.36 nm
0.36 nm
dislocation
Amorphous
region
0.19 nm
0.36 nm
0.21 nm

Figure: 2

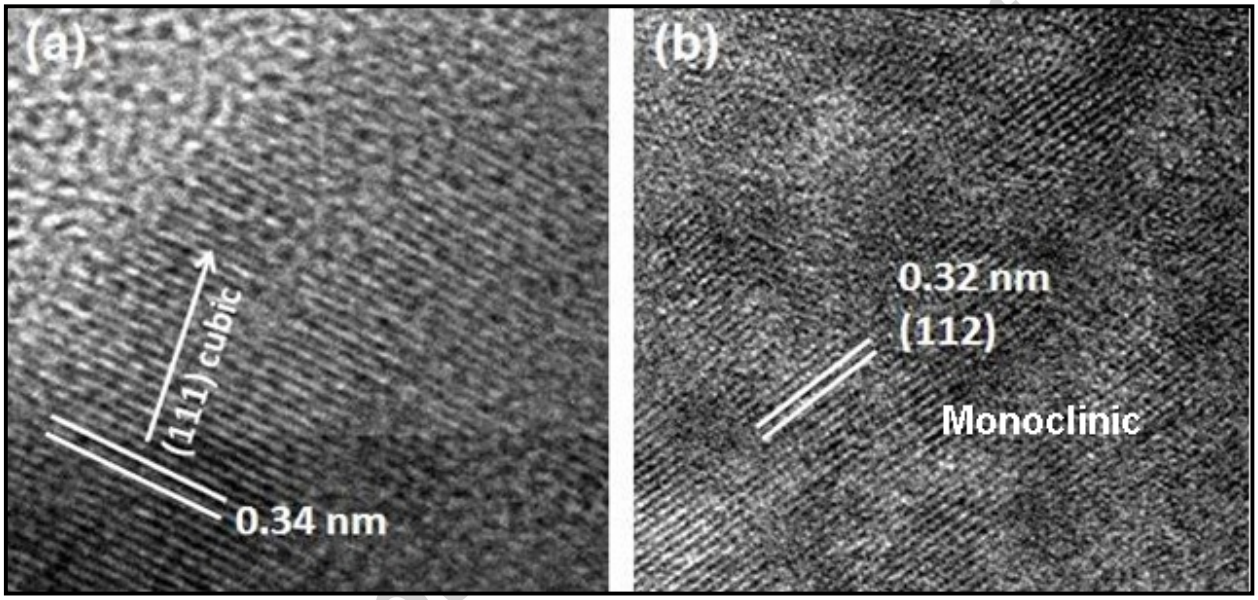

Figure: 3

Accepted

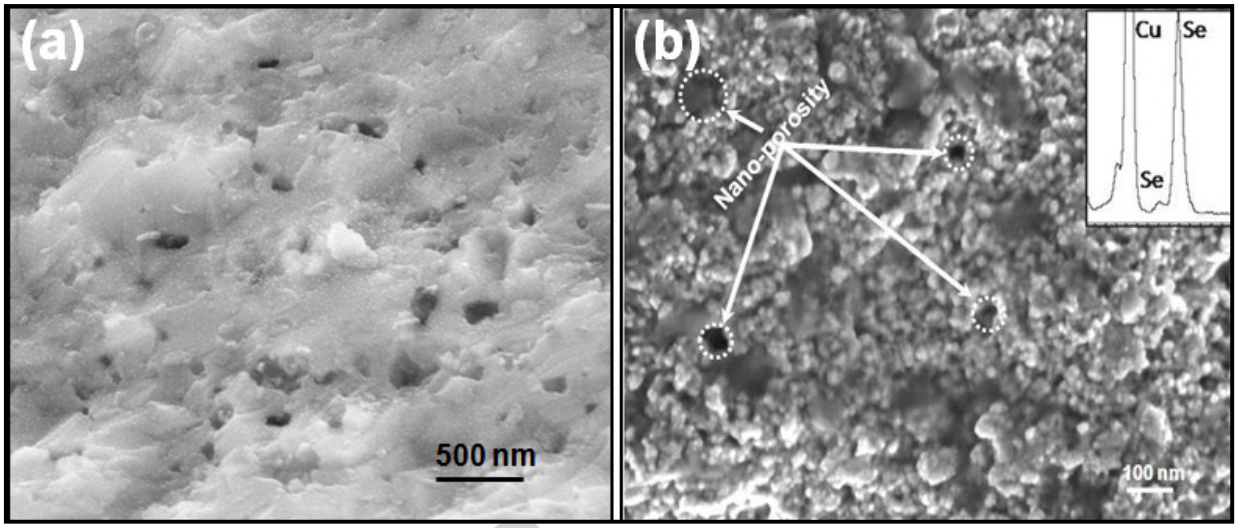

Figure: 4

Accepted

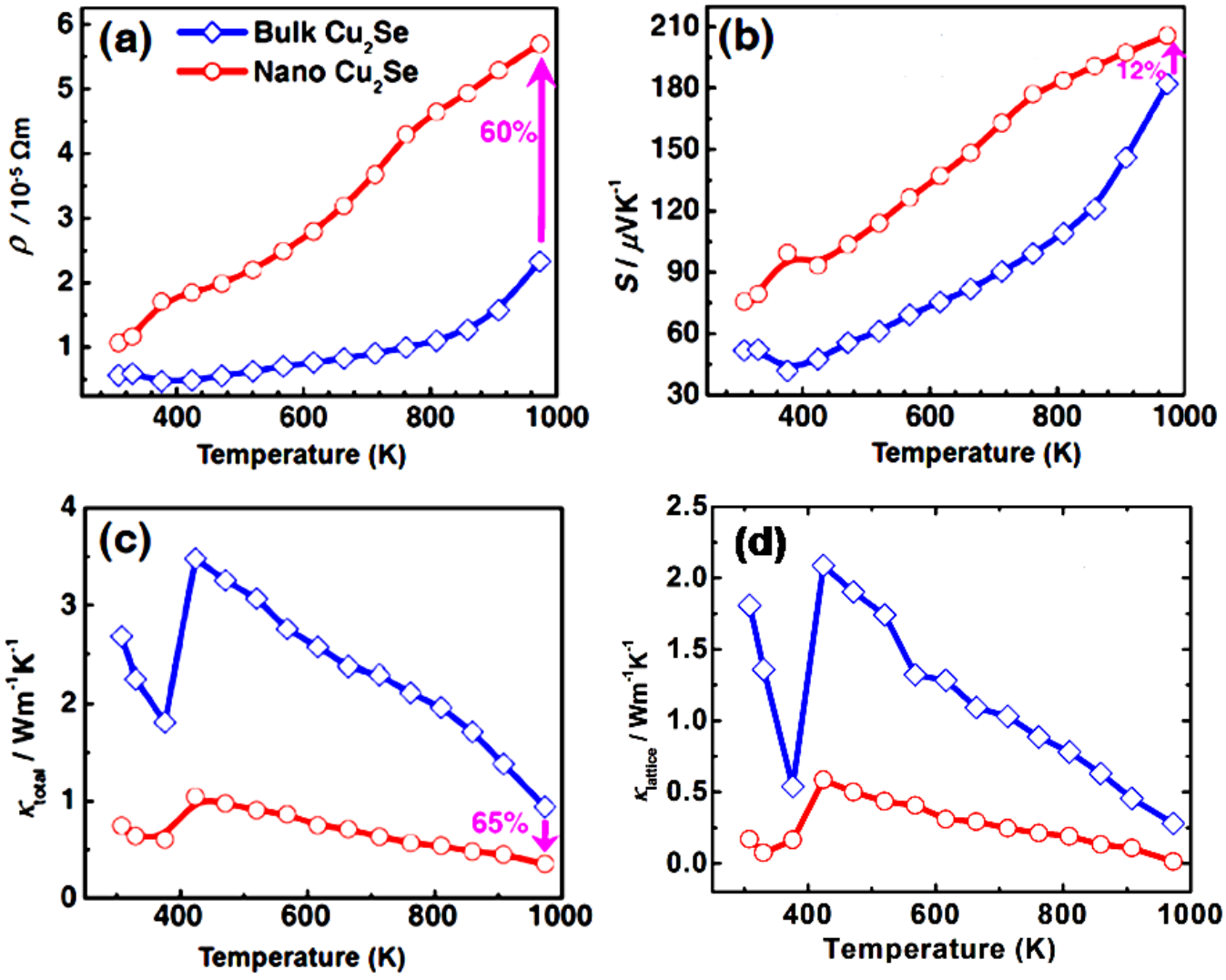
(a)
Bulk Cu2Se
Nano Cu2Se
60%
ρ /10-5 Ωm
Temperature (K)
(b)
12%
S / μVK-1
Temperature (K)
(c)
65%
κtotal / Wm-1K-1
Temperature (K)
(d)
κlattice / Wm-1K-1
Temperature (K)

Figure 5

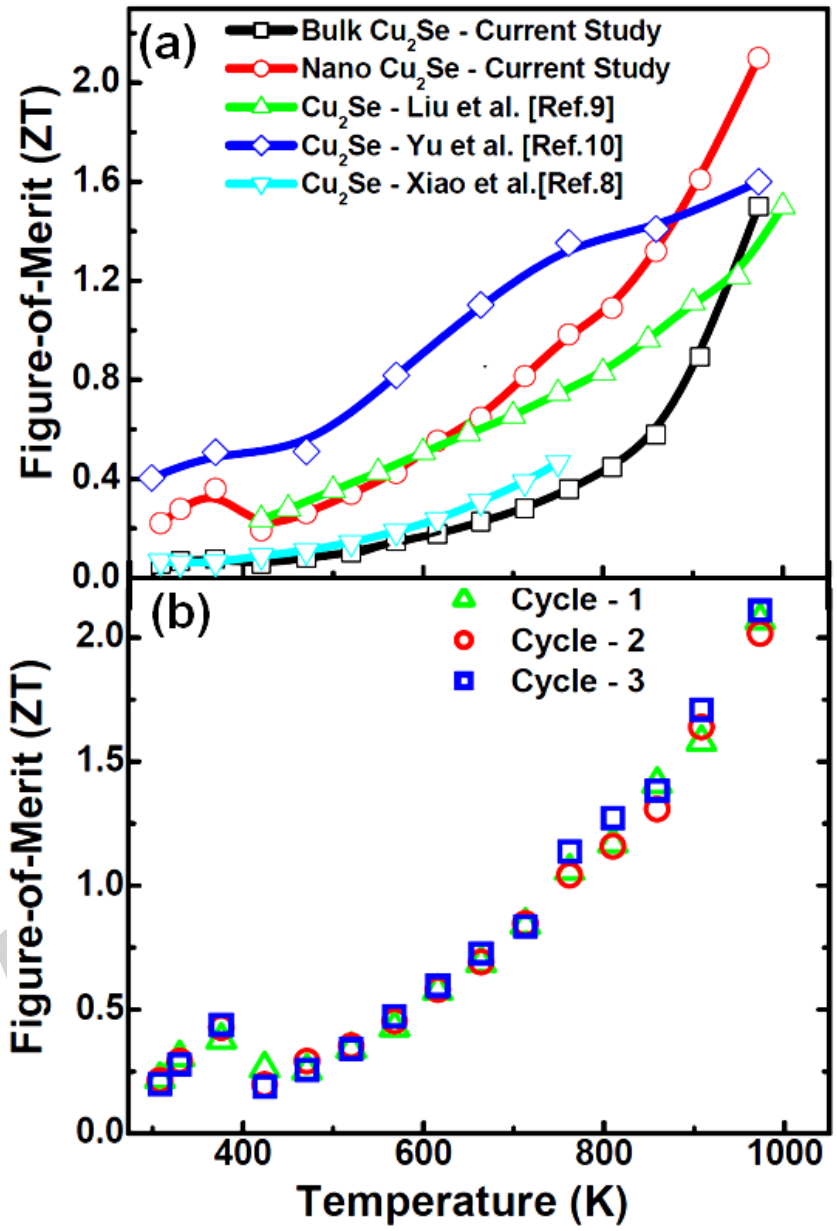
(a)
Bulk Cu2Se - Current Study
Nano Cu2Se - Current Study
Cu2Se - Liu et al. [Ref.9]
Cu2Se - Yu et al. [Ref.10]
Cu2Se - Xiao et al.[Ref.8]
Figure-of-Merit (ZT)
0.0
0.4
0.8
1.2
1.6
2.0
(b)
Cycle - 1
Cycle - 2
Cycle - 3
Figure-of-Merit (ZT)
0.0
0.5
1.0
1.5
2.0
400
600
800
1000
Temperature (K)

Figure 6

ACCEPTED MANUSCRIPT

References

[1] W. Liu, X. Yan, G. Chen, Z. Ren, Nano Energy 1 (2012) 42-56.
[2] H. Alam, S. Ramakrishna, Nano Energy 2 (2013) 190-212.
[3] G.J. Snyder, E.S. Toberer, Nature materials 7 (2008) 105-114.
[4] Y. Lan, A.J. Minnich, G. Chen, Z. Ren, Advanced Functional Materials 20 (2010) 357-376.
[5] M. Zebarjadi, K. Esfarjani, M. Dresselhaus, Z. Ren, G. Chen, Energy & Environmental Science 5 (2012) 5147-5162.
[6] J.R. Sootsman, D.Y. Chung, M.G. Kanatzidis, Angewandte Chemie International Edition 48 (2009) 8616-8639.
[7] T. Plirdpring, K. Kurosaki, A. Kosuga, T. Day, S. Firdosy, V. Ravi, G.J. Snyder, A. Harnwunggmoung, T. Sugahara, Y. Ohishi, Advanced Materials 24 (2012) 3622-3626.
[8] X. Xing-Xing, X. Wen-Jie, T. Xin-Feng, Z. Qing-Jie, Chinese Physics B 20 (2011) 087201.
[9] H. Liu, X. Shi, F. Xu, L. Zhang, W. Zhang, L. Chen, Q. Li, C. Uher, T. Day, G.J. Snyder, Nature materials, 11 (2012) 422-425.
[10] B. Yu, W. Liu, S. Chen, H. Wang, H. Wang, G. Chen, Z. Ren, Nano Energy 1 (2012) 472-478.
[11] S. Bhattacharya, R. Basu, R. Bhatt, S. Pitale, A. Singh, D. Aswal, S. Gupta, M. Navaneethan, Y. Hayakawa, Journal of Materials Chemistry A 1 (2013) 11289-11294.
[12] S. Ballikaya, H. Chi, J.R. Salvador, C. Uher, Journal of Materials Chemistry A 1 (2013) 12478-12484.
[13] H. Liu, X. Yuan, P. Lu, X. Shi, F. Xu, Y. He, Y. Tang, S. Bai, W. Zhang, L. Chen, Advanced Materials 25 (2013) 6607-6612.
[14] K. Tyagi, B. Gahtori, S. Bathula, A. Srivastava, A. Shukla, S. Auluck, A. Dhar, Journal of Materials Chemistry A 2 (2014) 15829.
[15] D.R. Brown, T. Day, T. Caillat, G.J. Snyder, Journal of electronic materials 42 (2013) 2014-2019.
[16] G. Dennler, R. Chmielowski, S. Jacob, F. Capet, P. Roussel, S. Zastrow, K. Nielsch, I. Opahle, G.K. Madsen, Advanced Energy Materials 4 (2014) 301581.
[17] D.M. Rowe, CRC handbook of thermoelectrics, CRC press, 1995.
[18] Y. Wu, S.W. Finefrock, H. Yang, Nano Energy 1 (2012) 651-653.
[19] M.S. Dresselhaus, G. Chen, M.Y. Tang, R. Yang, H. Lee, D. Wang, Z. Ren, J.P. Fleurial, P. Gogna, Advanced Materials 19 (2007) 1043-1053.
[20] K. Nielsch, J. Bachmann, J. Kimling, H. Böttner, Advanced Energy Materials 1 (2011) 713-731.
[21] G. Joshi, X. Yan, H. Wang, W. Liu, G. Chen, Z. Ren, Advanced Energy Materials 1 (2011) 643-647.
[22] S. Chen, K.C. Lukas, W. Liu, C.P. Opeil, G. Chen, Z. Ren, Advanced Energy Materials 3 (2013) 1210-1214.
[23] J. Yang, H.L. Yip, A.K.Y. Jen, Advanced Energy Materials 3 (2013) 549-565.
[24] S.K. Bux, R.G. Blair, P.K. Gogna, H. Lee, G. Chen, M.S. Dresselhaus, R.B. Kaner, J.P. Fleurial, Advanced Functional Materials 19 (2009) 2445-2452.
[25] W. Xie, J. He, H.J. Kang, X. Tang, S. Zhu, M. Laver, S. Wang, J.R. Copley, C.M. Brown, Q. Zhang, Nano Letters 10 (2010) 3283-3289.
[26] G. Zhu, H. Lee, Y. Lan, X. Wang, G. Joshi, D. Wang, J. Yang, D. Vashaee, H. Guilbert, A. Pillitteri, Physical Review Letters 102 (2009) 196803.

Accepted manuscript

ACCEPTED MANUSCRIPT

[27] S. Bathula, M. Jayasimhadri, N. Singh, A. Srivastava, J. Pulikkotil, A. Dhar, R. Budhani, Applied Physics Letters 101 (2012) 213902.
[28] C.J. Vineis, A. Shakouri, A. Majumdar, M.G. Kanatzidis, Advanced Materials 22 (2010) 3970-3980.
[29] B. Poudel, Q. Hao, Y. Ma, Y. Lan, A. Minnich, B. Yu, X. Yan, D. Wang, A. Muto, D. Vashaee, Science 320 (2008) 634-638.
[30] P. Puneet, R. Podila, S. Zhu, M.J. Skove, T.M. Tritt, J. He, A.M. Rao, Advanced Materials 25 (2013) 1033-1037.
[31] K. Biswas, J. He, I.D. Blum, C.-I. Wu, T.P. Hogan, D.N. Seidman, V.P. Dravid, M.G. Kanatzidis, Nature 489 (2012) 414-418.
[32] J. He, M.G. Kanatzidis, V.P. Dravid, Materials Today 16 (2013) 166-176.
[33] G. Chen, International Journal of Thermal Sciences 39 (2000) 471-480.
[34] W. Kim, J. Zide, A. Gossard, D. Klenov, S. Stemmer, A. Shakouri, A. Majumdar, Physical Review Letters 96 (2006) 045901.
[35] Y. He, D. Donadio, G. Galli, Nano Letters 11 (2011) 3608-3611.
[36] J.-H. Lee, G.A. Galli, J.C. Grossman, Nano Letters 8 (2008) 3750-3754.
[37] C. Bera, N. Mingo, S. Volz, Physical Review Letters 104 (2010) 115502.
[38] J.-H. Lee, J.C. Grossman, Applied Physics Letters 95 (2009) 013106.
[39] W.-Y. Zhao, Z. Liang, P. Wei, J. Yu, Q.-J. Zhang, G.-S. Shao, Acta Materialia 60 (2012) 1741-1746.
[40] Z. Zhang, P.A. Sharma, E.J. Lavernia, N. Yang, Journal of Materials Research 26 (2011) 475-484.
[41] Y. Zhang, G. Xu, F. Han, Z. Wang, C. Ge, Journal of electronic materials 39 (2010) 1741-1745.
[42] Z. Zhang, J.K. Yee, P.A. Sharma, N. Yang, E.J. Lavernia, Journal of Materials Research 28 (2013) 1853-1861.
[43] S. Bathula, R. Anandani, A. Dhar, A. Srivastava, Materials Science and Engineering: A 545 (2012) 97-102.
[44] G. Yamamoto, M. Omori, T. Hashida, H. Kimura, Nanotechnology 19 (2008) 315708.
[45] A. Minnich, M. Dresselhaus, Z. Ren, G. Chen, Energy & Environmental Science 2 (2009) 466-479.
[46] S. Kushwaha, K. Maurya, D. Haranath, G. Bhagavannarayana, Journal of Applied Crystallography 44 (2011) 1054-1061.
[47] B. Riscob, N. Vijayan, M. Shakir, M. Wahab, G. Bhagavannarayana, Journal of Applied Crystallography 46 (2013) 276-278.
[48] B.D. Cullity, SR Stock Elements of X-ray diffraction, Prentice Hall (New Jersey, USA), (2001).
[49] R. Orru, R. Licheri, A.M. Locci, A. Cincotti, G. Cao, Materials Science and Engineering: R: Reports 63 (2009) 127-287.
[50] J.H. Chae, K.H. Kim, Y.H. Choa, J.-i. Matsushita, J.-W. Yoon, K.B. Shim, Journal of alloys and compounds 413 (2006) 259-264.
[51] H. Zhang, M.-B. Tang, W. Schnelle, M. Baitinger, Z.-Y. Man, H.-H. Chen, X.-X. Yang, J.-T. Zhao, Y. Grin, Journal of Electronic Materials 39 (2010) 1772-1776.
[52] O. Guillon, J. Gonzalez-Julian, B. Dargatz, T. Kessel, G. Schierning, J. Räthel, M. Herrmann, Advanced Engineering Materials 16 (2014) 830-849.
[53] R. Chaim, R. Marder, C. Estournés, Z. Shen, Advances in Applied Ceramics 111 (2012) 280-285.
[54] Q. Zhang, Q. Zhang, S. Chen, W. Liu, K. Lukas, X. Yan, H. Wang, D. Wang, C. Opeil, G. Chen, Nano Energy 1 (2012) 183-189.

Accepted manuscript

ACCEPTED MANUSCRIPT

[55] M. Jak, E. Kelder, J. Schoonman, N. Van Der Pers, A. Weisenburger, Journal of Electroceramics 2 (1998) 127-134.
[56] J.R. Szczech, J.M. Higgins, S. Jin, Journal of Materials Chemistry 21 (2011) 4037-4055.
[57] G. Chen, Journal of Heat Transfer 121 (1999) 945-953.
[58] L.-D. Zhao, B.-P. Zhang, J.-F. Li, M. Zhou, W.-S. Liu, J. Liu, Journal of Alloys and Compounds 455 (2008) 259-264.
[59] Z. Munir, U. Anselmi-Tamburini, M. Ohyanagi, Journal of Materials Science 41 (2006) 763-777.
[60] M. Omori, Materials Science and Engineering: A 287 (2000) 183-188.

Dr. Bhasker Gahtori received his Ph.D. degree from Jamia Millia Islamia University, New Delhi in 2010 and is presently working as Scientist in Materials Physics and Engineering Division at CSIR-National Physical Laboratory, New Delhi, India. His current research is focused on Thermoelectric and Magnetic materials. He has published more than 30 research papers in scientific journals and presented his research work in more than 10 national and international conferences.

Mr. Sivaiah Bathula received his B.Tech. degree from NIT Waranagal in 2003 and M.Tech. degree from IIT Kanpur in Materials and Metallurgical Engineering in 2007. He is also a Faculty at the Academy of Scientific and Innovative Research (AcSIR). His current research is on the development of thermoelectric and structural materials. He has published more than 15 research papers in reputed scientific journals. Presently he is working as a Scientist in Materials Physics and Engineering Division at CSIR-National Physical Laboratory, New Delhi, India.

cepted manuscript

ACCEPTED MANUSCRIPT

Ms. Kriti Tyagi is a graduate student at CSIR-National Physical Laboratory, New Delhi, India registered at the Academy of Scientific and Innovative Research (AcSIR). She received her M.Tech. degree in Nanotechnology from Guru Gobind Singh Indraprastha University, New Delhi in 2011. Her current area of research is on Thermoelectric Materials and has published several research papers in prestigious journals.

Dr. M. Jayasimhadri received his Ph.D. degree in Physics from Sri Venkateswara University, India in 2006. Presently he is a Assistant Professor in Department of Applied Physics at Delhi Technological University, India. He has earlier worked as a post-doctoral fellow at POSTECH and CNU, South Korea. His current research interest are in the areas of optical/fluorescence spectroscopy of rare earth doped materials, nanotechnology and thermoelectric materials. He has published more than 50 research papers in scientific journals and presented his research work in more than 60 national and international conferences.

Dr. Avanish Kumar Srivastava received his Master's degree in from IIT Roorkee, M.Tech. from IIT Kanpur and doctorate from IISc, Bangalore, India He is presently working as a Principal Scientist at CSIR-NPL, India where he also a Faculty at the Academy of Scientific and Innovative Research (AcSIR). Dr. Srivastava has published more than 175 research papers in reputed journals and has received several awards including, Metallurgist of the Year Award and Materials Research Society of India Medal, both in 2011.

Dr. Sukhvir Singh is a Ph.D from Jamia Millia Islamia, New Delhi, India. Presently he is working as a Sr. Principal Scientist at CSIR-NPL, where he is the head of the electron and ion microscopy group and is also a Faculty at the Academy of Scientific and Innovative Research (AcSIR). His research interest

ACCEPTED MANUSCRIPT

include, nanostructured thin films and nanocomposites of compound semiconductors for various sensor and device applications. Currently, he is also working on the development of materials for efficient thermoelectric devices.

Prof. Budhani is currently a Professor of Physics at the Indian Institute of Technology Kanpur, India. He served the National Physical Laboratory as its Director during 2009- 2014. His research interests include correlated electron physics, magnetic and superconducting nanostructures, thin films and superlattices and thermoelectrics. Prof. Budhani has worked at several overseas laboratories including the University of California Los Angeles, Brookhaven National Laboratory, University of Maryland – College Park and ESPCI Paris as Joliot Fellow. He is a Fellow of the American Physical Society, the Indian Academy of Sciences, the National Academy of Sciences and the Indian National Science Academy New Delhi.

Accepted manuscript

Dr. Ajay Dhar holds Masters degrees in Science and Philosophy and a doctorate from University of Delhi, India. He is currently working as a Chief Scientist at the CSIR-National Physical Laboratory, New Delhi, India, where he heads the Metals & Alloys Group. Dr. Dhar was earlier a post-doctoral fellow and later a visiting faculty at Queen's University, Canada. He is a Professor and also the coordinator of Academy of Scientific and Innovative Research (AcSIR) at CSIR-NPL, Delhi. His current research interests among other include the development of cost-effective and non-toxic materials for efficient thermoelectric devices and rare-earth free permanent magnets.

ACCEPTED MANUSCRIPT

Graphic

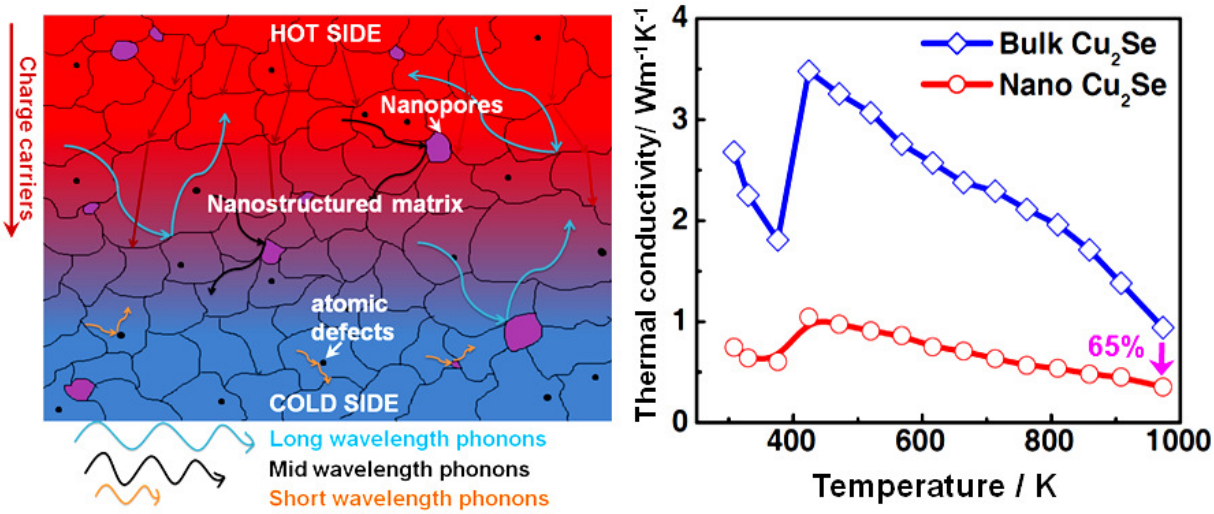

Accepted manuscript

Highlights

High ZT ~ 2.1 at 973 K realized in nanostructured Cu_2Se.

ZT of nanostructured Cu_2Se is ~ 40% higher than its bulk counterpart.

The enhanced ZT is due to a drastic reduction in lattice thermal conductivity.

Low-to-high wavelength phonons scattered by different nano-to-meso scale defects.

Nanoporosity in nanostructured Cu_2Se significantly reduced the thermal conductivity.

Appl Biochem Biotechnol (2014) 174:960–970
DOI 10.1007/s12010-014-0965-4

Graphene Oxide-Based Biosensor for Food Toxin Detection

Saurabh Srivastava · Md Azahar Ali · Sima Umrao · Upendra Kumar Parashar · Anchal Srivastava · Gajjala Sumana · B. D. Malhotra · Shyam Sudhir Pandey · Shuji Hayase

Received: 5 February 2014 / Accepted: 15 May 2014 /
Published online: 11 June 2014
© Springer Science+Business Media New York 2014

Abstract We report results of the studies relating to the fabrication of a highly sensitive label free biosensor based on graphene oxide (GO) platform for the detection of aflatoxin B1 (AFB_1) which is most toxic and predominant food toxin, using electrochemical impedance spectroscopy. The structural and optical characterization of GO/Au and anti-AFB_1/GO/Au has been done by electron microscopy, Raman, X-ray diffraction (XRD), UV–vis and electrochemical impedance spectroscopy (EIS). The impedimetric sensing response of immunoelectrode as a function of AFB_1 concentration reveals wider linear detection range (0.5–5 ng/ml), high sensitivity (639Ω ng^{-1} ml), improved detection limit (0.23 ng ml^{-1}) and good stability (5 weeks) for the label-free detection. Association constant (k_a) for antigen–antibody interaction obtained as 0.46 ng ml^{-1} indicates high affinity.

Keywords Graphene oxide · Aflatoxin B_1 · Immunosensor · Electrochemical impedance spectroscopy

Electronic supplementary material The online version of this article (doi:10.1007/s12010-014-0965-4) contains supplementary material, which is available to authorized users.

S. Srivastava · M. A. Ali · G. Sumana · B. D. Malhotra
Department of Science and Technology, Center on Biomolecular Electronics, Biomedical Instrumentation Section, CSIR-National Physical Laboratory, New Delhi 110012, India

S. Srivastava · S. Umrao · A. Srivastava
Department of Physics, Banaras Hindu University, Varanasi, Uttar Pradesh 221005, India

U. K. Parashar
Department of Physics, Indian Institute of Technology Kanpur, Kanpur, Uttar Pradesh 208016, India

B. D. Malhotra (✉)
Department of Biotechnology, Delhi Technological University, Delhi 110042, India
e-mail: bansi.malhotra@gmail.com

S. S. Pandey · S. Hayase
Department of Biological Functions and Systems, Graduate School of Life Science and Systems Engineering, Kyushu Institute of Technology, 2-4, Hibikino, Wakamatsu, Kitakyushu, Japan

Introduction

Graphene, the one-atomic 2D sheet of sp^2-bonded carbon atoms arranged into honeycomb lattice, is emerged as a rapidly rising star in the field of material science. Since its discovery in 2004, graphene-based material has been making a profound impact in many areas of science and technology due to its remarkable physicochemical properties such as high specific surface area (theoretically, 2,630 m^2/g for single-layer graphene), extraordinary electronic properties, strong mechanical strength and excellent thermal and electrical conductivities [13, 2, 30, 1]. One specific branch of graphene research deals with graphene oxide (GO). This can be considered as a precursor for graphene synthesis by either chemical or thermal reduction processes [25, 5]. GO consists of a single layer of graphite oxide and is usually produced by the chemical treatment of graphite through oxidation, with subsequent dispersion and exfoliation in water or suitable organic solvents. Chemically synthesized GO due to its easy and large-scale production, abundant electroactive defects and functional groups, facile surface modification, high surface area, fast electron transfer rate and biocompatibility, has a great potential in the area of electrochemical sensing and biosensing application [36, 11, 7]. The presence of oxygenated functional groups in GO render it strongly hydrophilic and make it highly dispersible in many solvents, including water that allow ease of processing and its modification [32]. The resulting GO-stable dispersion can be subsequently deposited on various conductive substrates in order to make excellent electrodes by means of common methods such as drop-casting, spraying, or spin-coating. In addition, using well-known chemical strategies, these functional groups serve as sites for chemical modification or functionalization of GO, which in turn can be employed to immobilize various electroactive species through covalent or noncovalent bonds for the design of sensitive electrochemical systems. The study of GO-based materials in recent years has been gaining increasing interest due to its facile synthesis, high dispersibility in a range of solvents, capability of coupling electroactive species onto the surface, and unique optical properties for cellular imaging and drug delivery [6, 27].

Electrochemical impedance spectroscopy (EIS) is the study of the resistive and capacitive behavior of the electrode–electrolyte interface in response to a small AC signal whose frequency may be varied over a wide range [14]. EIS is a sensitive, non-destructive and a useful analytical technique extremely sensitive to the biorecognition events happening at the electrode/electrolyte interface [18]. Importantly, EIS has an advantage of label free detection. Usually, labeling of antibody with dye molecules or enzyme (HRP) is used for fluorescence and amperometric sensing, respectively, to achieve high sensitivity. Such labeling processes would not only make experiments relatively complex and expensive, but also affect the binding affinity between the targets and biomolecules to a certain degree. In this regards, EIS provides label free detection with high sensitivity [18, 3, 34, 29].

Aflatoxins (AF) are a group of secondary fungal metabolites that are produced by *Aspergillus flavus* and *Aspergillus parasiticus* under certain conditions and are the most widely spread group of toxins resulting in contamination of food products [4]. There are four main aflatoxins: B_1, B_2, G_1, and G_2. Among these, AFB_1 is known to be most toxic and is responsible for human hepatocellular carcinoma (International Agency for Research on Cancer regards it as a human carcinogen) [9, 4]. Hence, there is an urgent need for availability of a rapid and sensitive detection of AFB_1. Tang et al. utilized multifunctional magnetic bead-based electrochemical immunoassay ($CoFe_2O_4$ nanoparticle as the core and Prussian blue nanoparticle (PBNP)-doped silica as the shell) for the detection of AFB_1 in food. A linear range of 0.05–12 ng/ml was achieved with a detection limit of 6.0 pg/ml [28]. Wang et al. reported a quartz crystal microbalance (QCM)-based biosensor to detect AFB_1 with the detection range of

0.3–7.0 ng/ml, using anti-AFB_1-functionalized magnetic core–shell Fe_3O_4/SiO_2 composite nanoparticles, where the bio-functionalized nanoparticles were attached to the surface of the QCM probe with an external magnet [31]. Singh et al. have recently reported a carboxylic multiwalled carbon nanotubes-based electrochemical biosensor for the sensitive detection of AFB_1. The biosensor shows high sensitivity of 95 μA/(ng/ml)/cm^2, a detection limit of 0.08 ng/ml in the linear detection range of 0.25–1.375 ng/ml. Additionally, the biosensor shows a good storage stability (42 days) [20]. This report aims towards the efficient and label free detection of AFB_1 using the GO-based biosensing platform (Table 1).

Materials and Methods

Materials

Graphite powder flakes (45 μm, >99.99 wt.%), monoclonal anti-AFB_1 antibody, AFB_1, *N*-ethyl-*N*-(3-dimethylaminopropyl)carbodiimide (EDC), *N*-hydroxysuccinimide (NHS) and bovine serum albumin (BSA) have been procured from Sigma-Aldrich.

Synthesis of Graphene Oxide

GO has been synthesized using modified Hummers method [12] with slight modification. In brief, 1.5 g of graphite powder is pre-oxidized by reacting it with the mixture of 40 ml of 98 % H_2SO_4, 5 g $K_2S_2O_8$ and 5 g of P_2O_5 for 4 h at 80 °C. The resulting suspension is washed with deionized water (DW) four to five times and is vacuum-dried at 50 °C. For the further oxidation pre-oxidized graphite is added to mixture of concentrated H_2SO_4/H_3PO_4 (180:13) with constant stirring. After 5 min, 9 g of $KMnO_4$ is added to the mixture and the stirring is continued for 15 h at 50 °C. The reaction is stopped after about 15 h and the reactants are

Table 1 Sensing characteristics of the proposed BSA-anti-AFB_1/GO/Au based biosensor compared to some of those reported in literature

Matrix	Sensitivity	Detection limit (ng/ml)	Detection range (ng/ml)	Stability (days)	Ref.
Ni-ITO	59 μA/(ng/ml)	0.327	0.05–1	60	[9]
SPCE	–	0.15	0.05–2	30	[17]
Au NPs	1.4 μS/(ng/ml)	0.1	0.5–10	12	[10]
Au Nps/PTH-GCE	1.23 μA/(ng/ml)	0.07	0.6–2.4		[15]
MMB	46 nA/(ng/ml)	0.006	0.05–12	17	[28]
Au/TiO_2/RTIL/Nafion/GCE	0.12 μA/(ng/ml)	0.05	0.1–12	19	[26]
RGO/ITO	68 μA/(ng/ml)	0.15	0.125–1.5	45	[23]
MWCNTs/ITO	95 μA/(ng/ml)	0.08	0.25–1.37	42	[20]
Pt/PANi–PSSA	869.6Ω ng^{-1} ml	100	1–6	–	[16]
Nanogold colloid (fluorescence based)	–	2.5	–	–	[33]
CdTe QDs (fluorescence based)	–	6.25×10^{-3}	$31.2–187.4\times10^{3}$	–	[35]
GO/Au	639Ω ng^{-1} ml	0.23	0.5–5	35	Present work

allowed to cool at room temperature after which 200 ml of ice has been poured into mixture followed by 1.5 ml of H_2O_2 (30 %). The fine material from the mixture is separated through U.S. standard testing sieve of pore size 30 μm and finally the filtration is done. The supernatant is discarded and the filtrate is subjected to centrifugation at 5,000 rpm for about 30 min. After that multiple washing of the sediment material has been carried out using distilled water, dilute HCl and ethanol (100 ml of each) followed by centrifugation separation. The final sediment is suspended in 100 ml of ether and is filtered through PTFE membrane with a pore size of 0.45 μm. The semisolid material obtained as GO is vacuum-dried overnight. The solid brown powder as GO is thus obtained.

Preparation of GO/Au Film

Gold electrodes (1.5×0.5 cm^2) are cleaned with piranha solution ($7H_2SO_4/3H_2O_2$). Ten microlitres of the aqueous GO solution (1 mg/ml) is uniformly spread onto Au electrodes followed by drying at 50 °C in vacuum oven overnight. The resulting GO/Au electrodes have been utilized for the immobilization of antibodies molecules.

Biofunctionalization of GO/Au Electrode Surface with Anti-AFB_1

Prior to the covalent immobilization process, COOH group of GO/Au electrode has been activated using EDC as the coupling agent and NHS as an activator [24]. The anti-AFB_1 antibody solution (10 μg/ml) is freshly prepared in phosphate buffer saline (PBS; pH 7.4). Then, 10 μl of this solution is uniformly spread on the activated GO/Au electrode surface and is incubated in humid chamber for about 4 h. The covalent interaction occurs via the formation of strong amide (CO–NH) bond between carboxyl group of GO and amino terminal of the anti-AFB_1. The anti-AFB_1/GO/ITO immunoelectrode is washed with PBS to remove the unbound antibodies molecules. Further the immunoelectrode is treated with BSA solution (1 mg/ml) which acts as a blocking agent for the non-specific active sites present on the electrode surface. The BSA-anti-AFB_1/GO/ITO immunoelectrode is then washed with PBS and stored at 4 °C, when not in use.

Results and Discussion

Structural Studies

Figure 1a shows powder X-ray diffraction (XRD) pattern (copper Kα radiation) of GO and in the range of 5–80°. The intense peak seen at 11.3° (7.96 Å) corresponds to the plane (002) and another peak found at 42.1° (2.12 Å) for the reflection plane (001) of GO (curve a). The number of layers (seven) of the GO has been obtained using the Debye–Scherrer equation [19, 22]

$$t = 0.89\lambda/\beta_{002}\cdot\cos\theta_{002} \tag{1}$$

$$n = t/d_{002}, \tag{2}$$

where t is thickness, β_{002} is the full width at half-maximum (FWHM), n is the number of graphene layers and d_{002} is interlayer spacing.

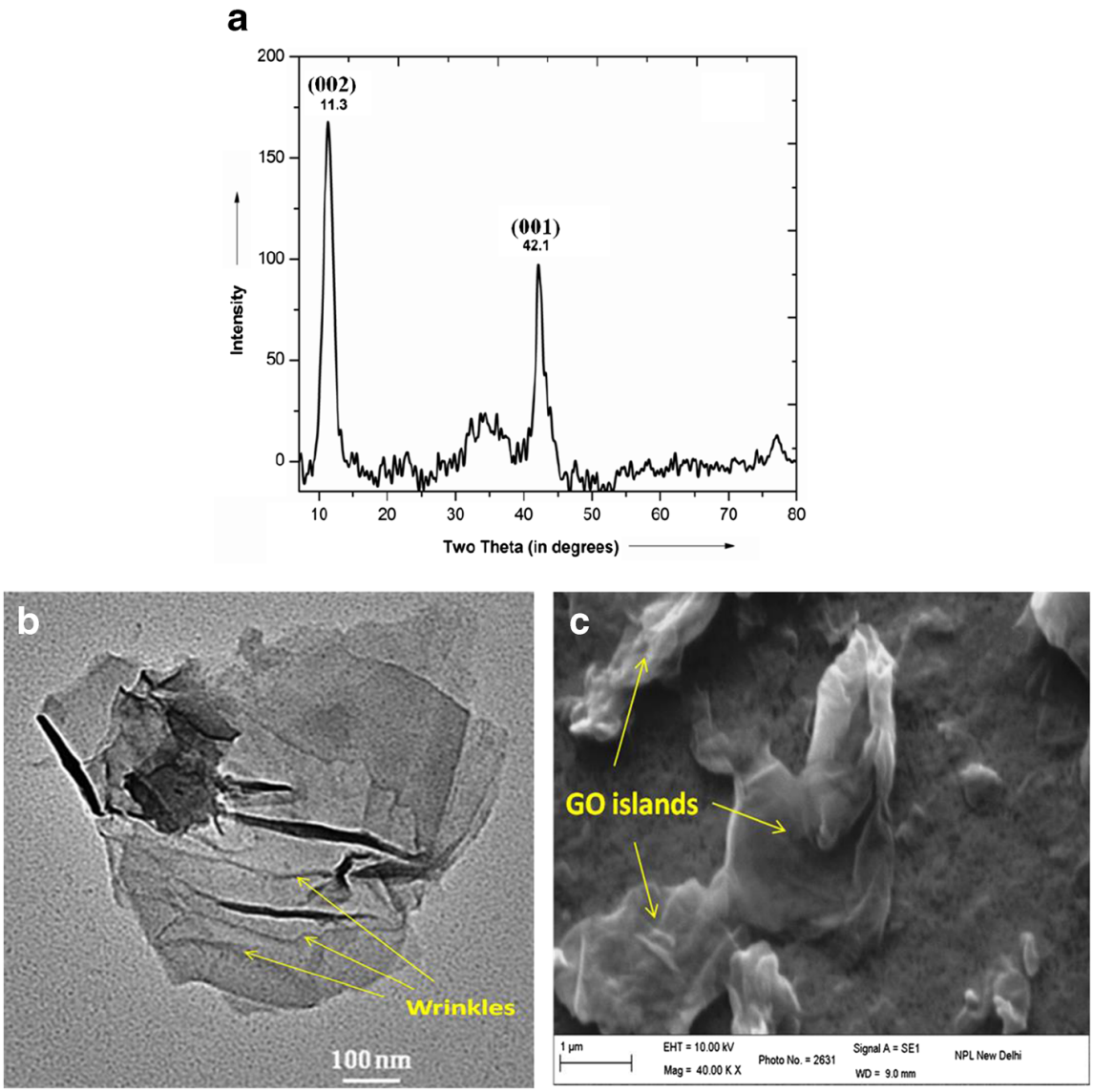

Fig. 1 **a** XRD pattern of graphene oxide shows the characteristic peaks at 11.3° corresponding to (002) plane. **b** Transmission electron micrograph of the graphene oxide indicating wrinkles and folding on the graphene sheets. **c** Scanning electron micrograph of graphene oxide film deposited onto Au electrode by drop cast method

Figure 1b shows the transmission electron micrograph (TEM) of GO. For TEM studies, well suspended GO has been prepared in water and drop casted onto carbon-coated copper grid. The image clearly demonstrates overlapped graphene layers and the folds and wrinkles are clearly visible. Some of the portion appears darker indicating more graphene sheets than the brighter region.

Figure 1c shows the scanning electron micrograph (SEM) of the GO/Au electrode surface, wherein micron sized island of GO sheet instead of a homogeneous layer clearly appears. It implies that the individual graphene sheets stack together to form larger sheets in the form of flake-like structures.

Optical Studies

Figure 2a indicates UV–vis spectroscopic studies of GO that has been carried out in wavelength range of 200–900 nm. The absorption of radiation starts increasing at 350 nm, wherein the maximum absorption has been seen at 226 nm. This may be assigned due to π–π^*

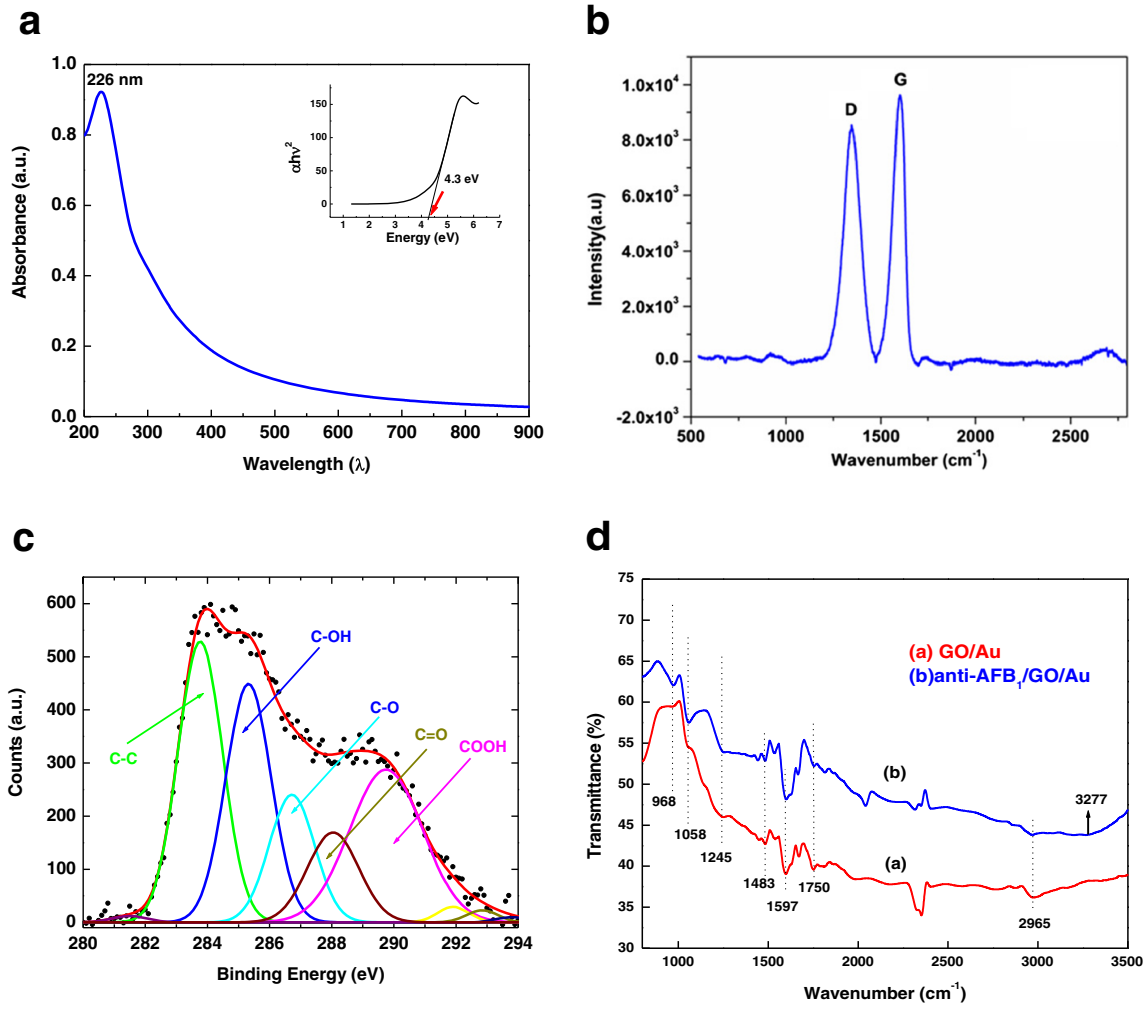

Fig. 2 **a** UV–visible spectra of graphene oxide indicating the maximum absorption seen at 226 nm corresponding to π–π* transition of aromatic C–C bonds. *Inset*: plot of $(\alpha h\nu)^2$ versus $h\nu$ for the estimation of optical band gap (4.11 eV). **b** Raman spectrum of graphene oxide. **c** X-ray photoelectron spectrum (*XPS*) of the C1s region of graphene oxide. **d** FTIR of GO/Au and anti-AFB_1/GO/Au film. The additional amide band seen at 3,277 cm^{-1} and reduction in the intensity of band seen at 2,977 cm^{-1} confirms the covalent immobilization of the antibody molecules

transition of aromatic C–C bonds in GO. The band gap of GO is found to be 4.3 eV estimated using the Tauc equation [21].

Figure 2b demonstrates Raman spectra of GO wherein well-defined D, G and 2D bands are observed. The prominent *D* peak may be seen at 1,348 cm^{-1}, which indicates the presence of disorder in the GO structure. This can be assigned to both the structural disorder (induced by the tears and folding over of the graphene sheets) and the presence of residual oxygen as well as point defects [8]. The G band seen at 1,598 cm^{-1} represents the planar sp^2 bonded carbon of GO. 2D band (overtone of the D band) found at 2,678 cm^{-1} is due to the second harmonic of D band indicating dispersive character as a function of excitation energy.

Figure 2c shows XPS spectrum of C 1 s region of the synthesized GO. The spectrum has been deconvoluted into the characteristic binding energy peaks using peak fit 1 software. Background subtraction and peak fitting of the spectra have been done using the Shirley function and Gaussian function, respectively. XPS measurements have been carried out in a Perkin Elmer XPS chamber (PHI 1257) with a base pressure of 5×10^{-9} Torr. The chamber is equipped with a dual anode Mg-K_α(energy 1,253.6 eV) and Al-K_α(energy 1,486.6 eV) X-ray source and a high-resolution hemispherical energy analyzer for energy resolved electron detection. An Mg-K_α X-ray source has been used for this study. The samples are sputtered

with 4 keV argon ions to remove surface contamination prior to XPS studies. The binding energy peak found at 283.7 eV is assigned to graphitic C–C bond. The binding energy peaks seen at 285.3 and 286.7 eV is due to the hydroxyl (C–OH) and epoxy (C–O) groups, respectively. Furthermore, the binding energy peak seen at 288 and 289.7 eV can be attributed to the carbonyl (C=O) and carboxylic acid (O–C=O) groups present in the samples [23]. Table 2 indicates the binding energy position of the various functional groups, FWHM and the corresponding relative percentage of these groups in the GO. These results indicate that the GO has abundant carboxylic acid functional groups as evident by their high relative atomic percentage (24.1 %). These carboxylic acid groups have been used to bind with amino terminal of the antibodies through the covalent immobilization process.

Figure 2d shows Fourier transform infrared spectra (FTIR) of the (a) GO/Au and (b) anti-AFB_1/GO/Au. The bands observed at 968 cm^{-1} represents the C–H stretching vibrations. The bands seen at 1,058 cm^{-1} represent the C–O–C stretching vibration of the epoxy group present in the GO. The band seen at 1,245 cm^{-1} represents the C–OH stretching vibrations of the hydroxyl group. The characteristic band observed at 1,750 cm^{-1} may be assigned to C=O stretching vibrations of the carboxylic/carbonyl groups present in the GO. The characteristic band seen at 1,597 cm^{-1} is due to the aromatic C=C stretching vibration, while a band seen at 1,483 cm^{-1} represents the H–C–H bending vibrations. Further, band at 2,965 cm^{-1} is due to the O–H stretch of the carboxylic acid group, the intensity of which get reduced after antibody immobilization (curve b). It indicates that the COOH group gets utilized in the formation of amide bond with antibodies molecules. Moreover, the additional band seen at around 3,277 cm^{-1} represents N–H stretching of the amide A (curve b).

Electrochemical Impedance Spectroscopic Studies

Figure 3a shows the Nyquist plot obtained for bare Au, GO/Au, anti-AFB_1/GO/Au and BSA/anti-AFB_1/GO/Au electrodes in the PBS containing 5 mM $[Fe(CN)_6]^{4-/3}$ in the frequency range 10^6–10^{-1} Hz at biasing potential of 10 mV. The charge transfer process in these electrodes has been investigated by measuring charge transfer resistance (R_{ct}) at the electrode/electrolyte interface. The value of the charge transfer resistance (R_{ct}) depends on the dielectric and insulating features at the electrode/electrolyte interface. It has been observed that magnitude of R_{ct} for Au electrode (312 Ω, curve a) increases to 363 Ω after its modification with GO. It may be attributed to the insulating characteristic of GO that reduces the conductivity of the gold surface (curve b). The R_{ct} value obtained for anti-AFB_1/GO/Au been found to enhance significantly up to 968 Ω. It is because the antibody molecules form an insulating layer on the electrode surface and creates hindrance in the electron transfer to the electrode surface. Further, the R_{ct} value, in the case of BSA-treated immunoelectrode (BSA/anti-AFB_1/GO/Au), increases to 1,122 Ω. It is because of the fact that BSA acts as blocking agent which blocks most of the non-specific active sites of the immunoelectrode surface.

Table 2 The C 1 s peak position, FWHM and the relative atomic percentage of various functional groups of the synthesized graphene oxide

Functional groups	Binding energy (eV)	FWHM (eV)	Relative percentage (%)
C–C	283.7	1.69	27.16
C–OH	285.3	1.72	23.45
C–O	286.7	1.72	12.54
C=O	288	1.58	9.99
O–C=O	289.7	2.6	24.13

Response Studies

EIS response studies of the BSA-anti-AFB_1/GO/Au immunoelectrode have been investigated as a function of AFB_1 concentration (0.5–5 ng/ml) using the EIS technique. Figure 3b indicates the Nyquist plot obtained for the immunoelectrode as a function of AFB_1 concentration. It has been observed that the charge transfer resistance (R_{ct}) increases with respect to the AFB_1 concentration. This is because the formation of antigen–antibody complexes reduces the conductivity of electrode surface and acts as a barrier in the electron transfer process. Figure 3b shows the calibration plot of R_{ct} values obtained for BSA-anti-AFB_1/GO/Au immunoelectrode as a function of the AFB_1 concentration. The linear variation of the R_{ct} value with AFB_1 concentrations (0.5–5 ng ml^{-1}) obeys Eq. 3.

$$R_{ct}(\Omega) = 783\,(\Omega) + 319.5\,\left(\Omega \mathrm{ng}^{-1}\mathrm{ml}\right) * \left[\text{concentration}\left(\mathrm{ng\,ml}^{-1}\right)\right] \tag{3}$$

Regression coefficient (R^2)=0.99.

This GO/Au-based immunosensor shows high sensitivity of 639 Ω ng^{-1} ml cm^{-2} and linear detection range as 0.5–5 ng ml^{-1}. The limit of detection has been evaluated using $3\sigma/m$ criteria,

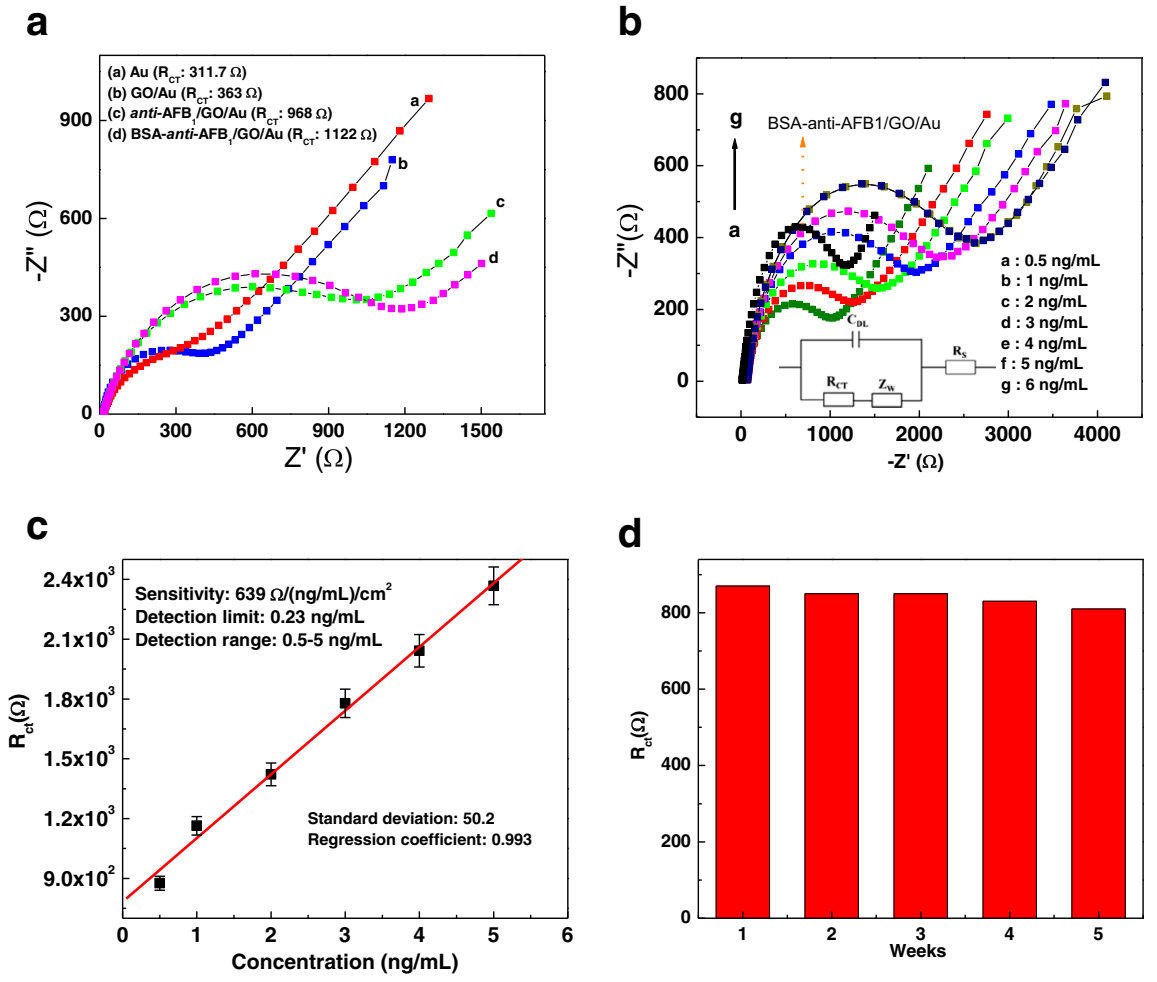

Fig. 3 **a** EIS (Nyquist plot) of various modified electrodes, obtained in PBS (pH 7.4) containing 5 mM $[Fe(CN)_6]^{3-/4-}$. **b** EIS response of the BSA-anti-AFB_1/GO/Au immunoelectrode obtained as a function of AFB_1 concentration. **c** Calibration plot between the magnitude of the charge transfer resistance (R_{ct}) and AFB_1 concentrations (0.5–5 ng ml^{-1}). **d** Plot of R_{ct} as a function of time indicating good storage stability of the biosensor (5 weeks)

where σ is the standard deviation and m is the sensitivity of calibration plot, and is found to be 0.23 ng ml^{-1}. The value of the association constant (K_a) obtained as 0.46 ng ml^{-1} using a Hanes–Woolf plot that indicates high affinity of AFB_1 towards anti-AFB_1. Furthermore, the large available surface area and abundant functional groups (carboxylic) of the graphene sheets provides high loading of anti-AFB_1 molecules resulting in wider linear detection range as well as high sensitivity. The storage stability of this BSA-anti-AFB_1/GO/Au-based impedimetric biosensor has been investigated by observing the charge transfer resistance (R_{ct}) at a regular interval of 1 week for 5 weeks with 1 ng/ml concentration of AFB_1 (Fig. 3d). Results of these studies indicate no significant decrease in the R_{ct} value (within 5 %) even after 5 weeks, revealing its good storage stability. The sensing performance of the proposed BSA-anti-AFB_1/GO/Au-based biosensor is summarized in Table 1 along with some of those reported in the literature.

We compared the EIS response of GO-based (BSA-anti-AFB_1/GO/Au) immunoelectrodes to that of Au (BSA-anti-AFB_1/Au) and graphite (BSA-anti-AFB_1/graphite/Au) in order to show the advantage of GO to the other two counterparts, for the detection of AFB_1 food toxin. Since both Au and graphite electrode surface have no functional groups, covalent immobilization of AFB_1 cannot be achieved. The anti-AFB_1 antibody molecules are physically adsorbed on Au as well as graphite electrode surface and then treated with BSA solution (1 mg/ml). Figure S1a shows the EIS response of the BSA-anti-AFB_1/Au immunoelectrode obtained as a function of AFB_1 concentration. Here, we do not observe any significant change in the Rct value for AFB_1 concentrations (0.5, 1 and 2 ng/ml). It has also been observed that above 2 ng/ml AFB_1 concentration, the EIS response saturates (Nyquist plots coincide). This may be due to the poor binding affinity of AFB_1 and Au. Figure S1b shows EIS response of the BSA-anti-AFB_1/graphite/Au immunoelectrode obtained as a function of AFB_1 concentration. Figure S1c shows calibration plot between the magnitude of the charge transfer resistance (R_{ct}) and AFB_1 concentrations (0.5–4 ng ml^{-1}). However, the response is found to be linear in the range of (1–4 ng/ml) (inset, Fig. S1c)]. The detection sensitivity estimated from the slope of linear calibration plot, in case of BSA-anti-AFB_1/graphite/Au immunoelectrode has been estimated as 74Ω ng^{-1} ml cm^{-2}, which is lower than that of BSA-anti-AFB_1/GO/Au (639Ω ng^{-1} ml cm^{-2}). This BSA-anti-AFB_1/graphite/Au shows detection limit of 0.7 ng/ml, which is higher than that of BSA-anti-AFB_1/GO/Au (0.23 ng/ml). It is also clear that GO-based immuosensor shows a wider linear detection range of 0.5–5 ng/ml as compared to graphite (1–4 ng/ml) and gold (0.5–2 ng/ml) electrodes. So, these studies clearly reveals the advantage of GO to the other two counterparts namely Au and graphite, in terms of sensing characteristics of the biosensor for the detection of food toxin (AFB_1).

Conclusions

GO has been synthesized using modified Hummers method and used to form thin film GO/Au electrode. The GO/Au electrode has been utilized for the covalent immobilization of the monoclonal antibody molecules (anti-AFB_1) using EDC-NHS protocol. The anti-AFB_1/GO/Au immunoelectrode has been successfully used as a label free biosensing platform to detect a range of AFB_1 concentration employing EIS. The fabricated impedimetric immunosensor shows wider linear detection range (0.5–5 ng/ml) along with high sensitivity (639Ω/(ng/ml)/cm^2) and good storage stability (5 weeks). In addition, this GO-based biosensing platform may efficiently be utilized for the label free detection of other important food toxins such as aflatoxin M_1 and ochratoxin-A.

Acknowledgments We thank the Director, CSIR-National Physical Laboratory, New Delhi, India, for providing the facilities. S.S. acknowledges the financial support from CSIR (SRF: 31/001(0302)/2008-EMRI), New Delhi, India. We thank Dr. V. Reddy and Prof. CheolGi Kim for the XPS measurements. The financial support received from Department of Science and Technology, India (Grant No. DST/TSG/ME/2008/18) and Indian Council of Medical Research, India (Grant No. ICMR/5/3/8/91/GM/2010-RHN) is gratefully acknowledged.

References

1. Alwarappan, S., Erdem, A., Liu, C., & Li, C.-Z. (2009). Probing the electrochemical properties of graphene nanosheets for biosensing applications. *Journal of Physical Chemistry C, 113*, 8853–8857.
2. Balandin, A. A. (2011). Thermal properties of graphene and nanostructured carbon materials. *Nature Materials, 10*, 569–581.
3. Bart, M., Stigter, E., Stapert, H., De Jong, G., & Van Bennekom, W. (2005). On the response of a label-free interferon-γ immunosensor utilizing electrochemical impedance spectroscopy. *Biosensors and Bioelectronics, 21*, 49–59.
4. Daly, S. J., Keating, G. J., Dillon, P. P., Manning, B. M., O'Kennedy, R., Lee, H. A., & Morgan, M. R. A. (2000). Development of surface plasmon resonance-based immunoassay for aflatoxin B1. *Journal of Agricultural and Food Chemistry, 48*, 5097–5104.
5. Dikin, D. A., Stankovich, S., Zimney, E. J., Piner, R. D., Dommett, G. H., Evmenenko, G., Nguyen, S. T., & Ruoff, R. S. (2007). Preparation and characterization of graphene oxide paper. *Nature, 448*, 457–460.
6. Dong, H., Gao, W., Yan, F., Ji, H., & Ju, H. (2010). Fluorescence resonance energy transfer between quantum dots and graphene oxide for sensing biomolecules. *Analytical Chemistry, 82*, 5511–5517.
7. Dreyer, D. R., Park, S., Bielawski, C. W., & Ruoff, R. S. (2010). The chemistry of graphene oxide. *Chemical Society Reviews, 39*, 228–240.
8. Eda, G., Fanchini, G., & Chhowalla, M. (2008). Large-area ultrathin films of reduced graphene oxide as a transparent and flexible electronic material. *Nature Nanotechnology, 3*, 270–274.
9. Kalita, P., Singh, J., Singh, M. K., Solanki, P. R., Sumana, G., & Malhotra, B. D. (2012). Ring like self assembled Ni nanoparticles based biosensor for food toxin detection. *Applied Physics Letters, 100*, 093702–093704.
10. Liu, Y., Qin, Z., Wu, X., & Jiang, H. (2006). Immune-biosensor for aflatoxin B1 based bio-electrocatalytic reaction on micro-comb electrode. *Biochemical Engineering Journal, 32*, 211–217.
11. Liu, Y., Yu, D., Zeng, C., Miao, Z., & Dai, L. (2010). Biocompatible graphene oxide-based glucose biosensors. *Langmuir, 26*, 6158–6160.
12. Chen, C., Li, J., Li, R., Xiao, G., & Yan, D. (2013). Synthesis of superior dispersions of reduced graphene oxide. *New Journal of Chemistry, 37*, 2778–2783.
13. Neto, A. C., Guinea, F., Peres, N., Novoselov, K. S., & Geim, A. K. (2009). The electronic properties of graphene. *Reviews of Modern Physics, 81*, 109.
14. Orazem, M. E. and Tribollet, B. (2011) *Electrochemical impedance spectroscopy*. Wiley.
15. Owino, J., Arotiba, O., Hendricks, N., Songa, E., Jahed, N., Waryo, T., Ngece, R., Baker, P., & Iwuoha, E. (2008). Electrochemical immunosensor based on polythionine/gold nanoparticles for the determination of aflatoxin B1. *Sensors, 8*, 8262–8274.
16. Owino, J. H., Ignaszak, A., Al-Ahmed, A., Baker, P. G., Alemu, H., Ngila, J. C., & Iwuoha, E. I. (2007). Modelling of the impedimetric responses of an aflatoxin B1 immunosensor prepared on an electrosynthetic polyaniline platform. *Analytical and Bioanalytical Chemistry, 388*, 1069–1074.
17. Piermarini, S., Micheli, L., Ammida, N. H. S., Palleschi, G., & Moscone, D. (2007). Electrochemical immunosensor array using a 96-well screen-printed microplate for aflatoxin B1 detection. *Biosensors and Bioelectronics, 22*, 1434–1440.
18. Ruan, C., Yang, L., & Li, Y. (2002). Immunobiosensor chips for detection of *Escherichia coli* O157: H7 using electrochemical impedance spectroscopy. *Analytical Chemistry, 74*, 4814–4820.
19. Sakintuna, B., Yürüm, Y., & Çetinkaya, S. (2004). Evolution of carbon microstructures during the pyrolysis of Turkish Elbistan lignite in the temperature range 700−1000 °C. *Energy & Fuels, 18*, 883–888.
20. Singh, C., Srivastava, S., Ali, M. A., Gupta, T. K., Sumana, G., Srivastava, A., Mathur, R., & Malhotra, B. D. (2013). Carboxylated multiwalled carbon nanotubes based biosensor for aflatoxin detection. *Sensors and Actuators B: Chemical, 185*, 258–264.
21. Singh, M. K., Mathpal, M. C., & Agarwal, A. (2012). Optical properties of SnO_2 quantum dots synthesized by laser ablation in liquid. *Chemical Physics Letters, 536*, 87–91.
22. Srivastava, R. K., Srivastava, S., Narayanan, T. N., Mahlotra, B. D., Vajtai, R., Ajayan, P. M., & Srivastava, A. (2011). Functionalized multilayered graphene platform for urea sensor. *ACS Nano, 6*, 168–175.

23. Srivastava, S., Kumar, V., Ali, M. A., Solanki, P. R., Srivastava, A., Sumana, G., Saxena, P. S., Joshi, A. G., & Malhotra, B. (2013). Electrophoretically deposited reduced graphene oxide platform for food toxin detection. *Nanoscale, 5*, 3043–3051.
24. Srivastava, S., Solanki, P. R., Kaushik, A., Ali, M. A., Srivastava, A., & Malhotra, B. D. (2011). A self assembled monolayer based microfluidic sensor for urea detection. *Nanoscale, 3*, 2971–2977.
25. Stankovich, S., Dikin, D. A., Piner, R. D., Kohlhaas, K. A., Kleinhammes, A., Jia, Y., Wu, Y., Nguyen, S. T., & Ruoff, R. S. (2007). Synthesis of graphene-based nanosheets via chemical reduction of exfoliated graphite oxide. *Carbon, 45*, 1558–1565.
26. Sun, A.-L., Qi, Q.-A., Dong, Z.-L., & Liang, K. (2008). An electrochemical enzyme immunoassay for aflatoxin B_1 based on bio-electrocatalytic reaction with room-temperature ionic liquid and nanoparticle-modified electrodes. *Sensing and Instrumentation for Food Quality and Safety, 2*, 43–50.
27. Sun, X., Liu, Z., Welsher, K., Robinson, J. T., Goodwin, A., Zaric, S., & Dai, H. (2008). Nano-graphene oxide for cellular imaging and drug delivery. *Nano Research, 1*, 203–212.
28. Tang, D., Zhong, Z., Niessner, R., & Knopp, D. (2009). Multifunctional magnetic bead-based electrochemical immunoassay for the detection of aflatoxin B1 in food. *Analyst, 134*, 1554–1560.
29. Tang, H., Chen, J., Nie, L., Kuang, Y., & Yao, S. (2007). A label-free electrochemical immunoassay for carcinoembryonic antigen (CEA) based on gold nanoparticles (AuNPs) and nonconductive polymer film. *Biosensors and Bioelectronics, 22*, 1061–1067.
30. Wang, C., Li, D., Too, C. O., & Wallace, G. G. (2009). Electrochemical properties of graphene paper electrodes used in lithium batteries. *Chemistry of Materials, 21*, 2604–2606.
31. Wang, L., & Gan, X.-X. (2009). Biomolecule-functionalized magnetic nanoparticles for flow-through quartz crystal microbalance immunoassay of aflatoxin B1. *Bioprocess and Biosystems Engineering, 32*, 109–116.
32. Wang, Y., Li, Z., Wang, J., Li, J., & Lin, Y. (2011). Graphene and graphene oxide: biofunctionalization and applications in biotechnology. *Trends in Biotechnology, 29*, 205–212.
33. Xiulan, S., Xiaolian, Z., Jian, T., Zhou, J., & Chu, F. (2005). Preparation of gold-labeled antibody probe and its use in immunochromatography assay for detection of aflatoxin B1. *International Journal of Food Microbiology, 99*, 185–194.
34. Yang, L., Li, Y., & Erf, G. F. (2004). Interdigitated array microelectrode-based electrochemical impedance immunosensor for detection of *Escherichia coli* O157: H7. *Analytical Chemistry, 76*, 1107–1113.
35. Zekavati, R., Safi, S., Hashemi, S. J., Rahmani-Cherati, T., Tabatabaei, M., Mohsenifar, A., & Bayat, M. (2013). Highly sensitive FRET-based fluorescence immunoassay for aflatoxin B1 using cadmium telluride quantum dots. *Microchimica Acta, 180*, 1217–1223.
36. Zhou, M., Zhai, Y., & Dong, S. (2009). Electrochemical sensing and biosensing platform based on chemically reduced graphene oxide. *Analytical Chemistry, 81*, 5603–5613.

Hardware Design of Dynamic Time Warping Algorithm based on FPGA in Verilog

Kriti Suneja, Dr. Malti Bansal
Department of Electronics and Communication Engineering,
Delhi Technological University
Delhi-110042, India

***Abstract* — The Dynamic Time Warping (DTW) algorithm is a software technique to quantify the diversity between two time varying sequences. In spite of its computational complexity, it is often used in speech recognition systems. In this work, hardware implementation of DTW modeled in VERILOG Hardware Description Language (HDL) has been done, with an aim to use it as an independent unit or as a co-processor in large embedded systems. The target device used for synthesis is xc3s400-4-pq208 in Xilinx. Simulations were performed in ModelSim. Hardware utilization analysis is provided to show its efficacy in warping a sequence in non linear fashion.**

Index Terms —dynamic time warping, verilog, time sequence data, Field Programmable Gate Array (FPGA), Look Up Tables (LUTs), Application Specific Integrated Circuits (ASICs)

I. INTRODUCTION

Dynamic Time Warping (DTW) algorithm finds the edit distance, which is the minimum number of editing operations required to convert one sequence into another, between two sequences by analysing three operations: substitution, insertion, and deletion [1]. Besides, it is a search algorithm which finds an optimal warping path dynamically for the minimal cost alignment of input on template.

Measuring the edit distance is best reflected as a 2-dimensional grid with the two sequences on the top and left side respectively. The central idea is to formulate optimal path to any intermediate point X in the grid in terms of optimal paths of all its immediate antecedents.
Let $\gamma(n,m)$ = Minimum path cost from origin to any point (n,m) in the grid.

$$\gamma(n,m) = d(n,m) + \min \{\gamma(n-1,m), \gamma(n,m-1), \gamma(n-1,m-1)\} \quad (1)$$

where d(n,m) is the square of the Euclidean distance between the two elements of the target sequences at X.
Hence, starting from the origin and computing minimum path cost for every grid point entry, proceeding from top left to bottom right corner provides the minimum edit distance as the last entry.

To determine the alignment, a back-pointer is maintained from X to its antecedent, which provides the minimum cost to it. At the end, back tracing gives the best alignment.

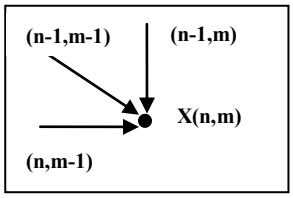

Fig.1 Point X and its antecedents to find minimum cost

DTW is very efficient in software computing. It has been used in isolated word speech recognition system for human computer interaction [2], hand gesture recognition [3], isolated musical pattern recognition [4], human action recognition [5]. Also, it provides excellent results in terms of accuracy. B.C. Bhokse and B.S. Thakare used DTW for *Devnagari* handwriting recognition system [6]. However, its application in real time processing is limited to literature because of space and time restrictions in its hardware implementation. In order to use specialized hardware for similarity search using DTW, we need to investigate the limitations of the target device and DTW computation. Ding et al. [7] stated the outperformance of DTW among all elastic distance measures. Sart et al. [8] investigated acceleration of DTW with GPUs and FPGAs using an open source C to VHDL compiler system, ROCCC. Tai, Li and Elmiligi [9] used VHDL for hardware space utilization and speed analysis of DTW which has its limitations as the data size grows.

In this paper, we propose an elementary DTW processing unit designed in VERILOG [10], in order to explicate its use in speech processing, such as, plagiarism detection in music by finding the distance between the song pairs after features extraction. Features' extraction can be done in MATLAB and then the scalar or vector data can be given as input to DTW hardware for comparison.

Though, implemented on SPARTAN FPGA, the goal of using VERILOG is to make DTW ASIC compatible and to exploit the use of VERILOG Programming Language Interface (PLI) and VERILOG Analog and

ISSN: 2278 – 909X All Rights Reserved © 2015 IJARECE

Mixed-Signal Extension (AMS) for large samples of speech.

The organization of this paper is as follows. In Section II, we describe the pseudo code and MATLAB implementation of DTW. We then describe how this can be incorporated in VERILOG. Next, we present results of experiments. Finally, we present our conclusions and suggestions for future work.

II. AN n-ELEMENT DTW PROCESSOR

Let us consider two sequences A and B of length n and m respectively. Pseudo code of DTW to find the edit distance between them is as follows:

```
for i := 1 to n
        for j := 1 to m
                cost :=  d(A[i] , B[j])
DTW[i,j] :=cost + minimum (DTW[i-1 , j],
                           DTW[i , j-1],
                           DTW[i-1,j-1])
        return DTW(n,m)
w=[]    //Optimal Path
k= n;
l=m;
                while (k+l ~=2)

[value , number]=
min([DTW(k-1,l),DTW(k,l-1),DTW(k-1,l-1)])
switch  number
case 1      k=k-1
case 2      l=l-1
case3       k=k-1;l=l-1
w = cat (1, w , [k,l])
```

where d(A[i],B[j]) is the square of Euclidean Distance and DTW(i,j) is the minimum edit distance between ith and jth elements of sequences A and B respectively.

For example, let A and B be :

A= [1 2 3 4 7 8] ; B= [1 1 2 2 3 3 3 4]

MATLAB simulations will give the results shown in Fig. 2 .

1	0	0	1	2	6	10	14	23
2	1	1	0	0	1	2	3	7
3	5	5	1	1	0	0	0	1
4	14	14	5	5	1	1	1	0
7	50	50	30	30	17	17	17	09
8	99	99	66	66	42	42	42	25

Fig.2 Matlab simulation results for the considered example

A. DTW in VERILOG with Xilinx ISE

In this paper, we propose the hardware design of DTW using VERILOG Hardware Description Language (HDL).

The system is implemented using Xilinx Integrated Software Environment (ISE) which is used to synthesize and process HDL algorithms on FPGA. Target device Spartan 3 with package pq208 has the following properties: 3584 Slices, 7168 Look Up Tables (LUTs) , 141 Input/ Output Blocks (IOBs). The input is taken as an array of binary numbers. Here, we have done it for example referred in Section II. If used for speech recognition, features of the samples, for example, Mel Frequency Cepstral Coefficients (MFCCs), tonalcentroids, zerocrossovers, etc., can be used as input.

First, the square of Euclidean distance is calculated for the first element of the matrix. Then, first row and first column elements, are calculated which require the previous element value and no comparisons. Finally, the rest of the entries in matrix are calculated with recursion. The minimum edit distance is found using ModelSim.

B. Experimental Results

The minimum edit distance in ModelSim for the example stated in section II is 25, as shown in Fig.3.

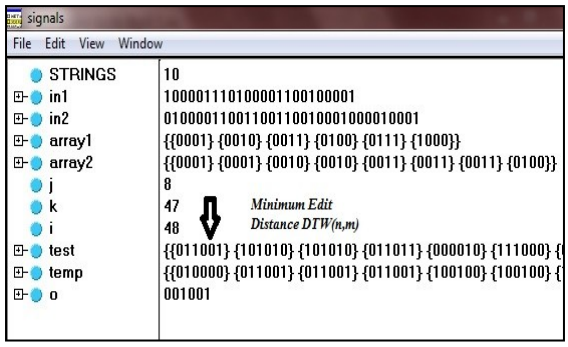

Fig.3 ModelSim simulation Results

MATLAB simulations give the same result along with the optimization path as shown in Fig.4.

The delay analysis shows that the delay increases linearly with the increase in number of elements in the sequences to be compared as shown in Fig.5.

When simulated in MATLAB, the execution time for 6 × 8 unit is 0.000138s and the delay obtained for the same unit in Xilinx is 95.49ns.

In the synthesis of DTW with input sequences of length 6 and 8 , 1024 out of 3584 Slices , 1982 out of 7168 4 input LUTs and 57 out of 141 IOBs are used which are only 28% , 27% and 40% respectively of the available resources.

However, number of slices and LUTs increase exponentially with the increase in input size; and IOBs increase linearly, as shown in Fig.6, Fig.7 and Fig.8 respectively.

ISSN: 2278 – 909X All Rights Reserved © 2015 IJARECE

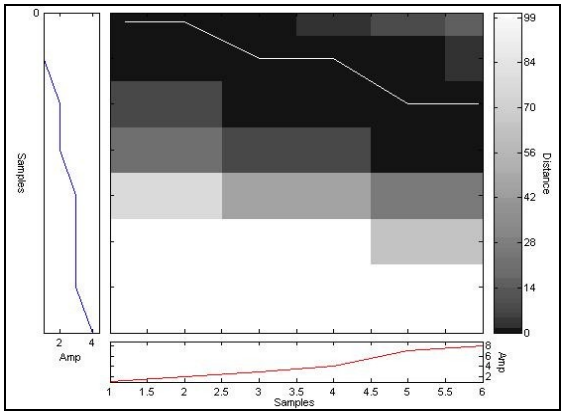

Fig.4 Accumulated Distance Matrix and Optimal path

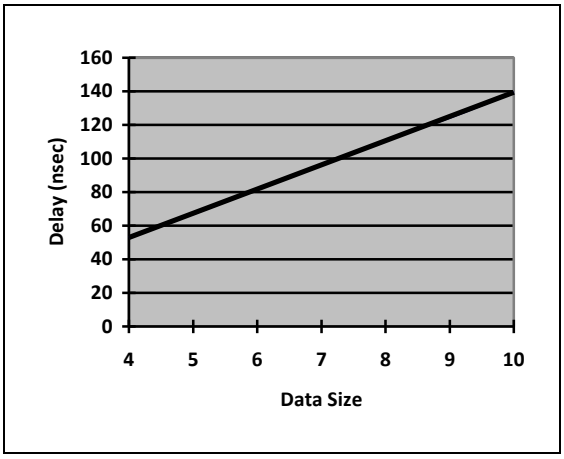

Fig.5 Delay Variation with number of elements

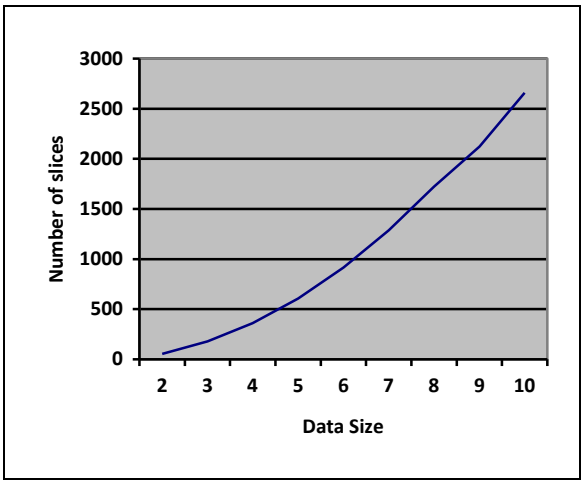

Fig.6 Number of Slices variation with data size

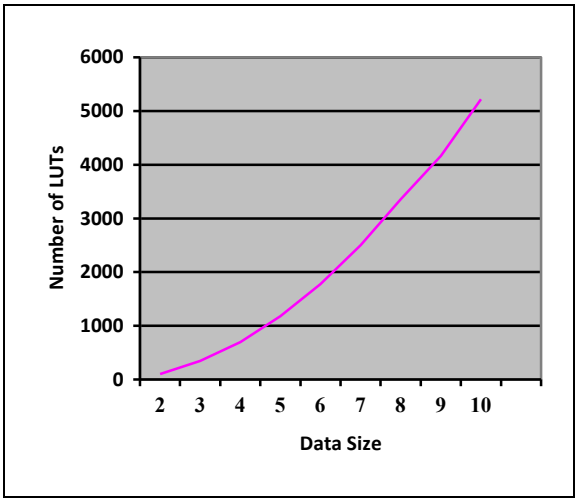

Fig. 7 Number of LUTs variation with Data size

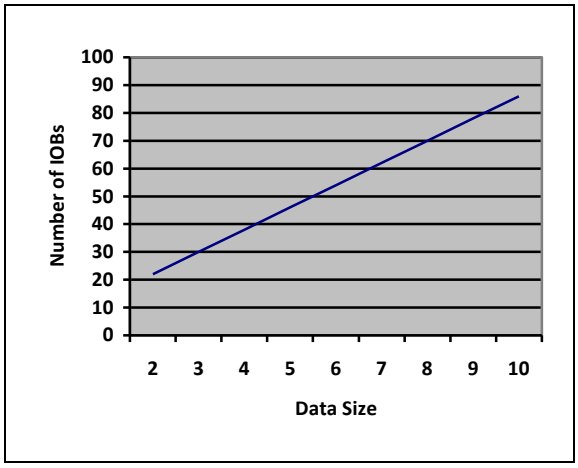

Fig.8 Number of IOBs variation with Data Size

III. CONCLUSION AND FUTURE WORK

DTW is an efficient software algorithm for comparing time sequences and is extensively used in speech and pattern recognition. However, in real time systems, speed and hardware utilization are critical parameters. Implementation of a basic DTW unit in this paper demonstrates that it can be used as an integral part of large processing units in FPGAs and ASICs. The device used in this paper has limited number of slices and LUTs available. However, if Virtex 7 is used, large data size can be used because it provides 408,000 programmable slices registers and 203,000 LUTs [9].

With the successful hardware implementation of DTW, it can be used as a built in coprocessor for speech processing embedded systems. Since, the algorithm requires a large number of multipliers proportional to the square of data size, there is a need of an efficient multiplication algorithm which can reduce the hardware utilization because the number of built in multipliers are limited.

ISSN: 2278 – 909X All Rights Reserved © 2015 IJARECE

REFERENCES

[1] M. Ravishankar, "Isolated word recognition using dynamic time warping," Design and implementation of ASR systems. http://asr.cs.cmu.edu/spring2010/class3/class3.25jan.dtw.pdf

[2] R. Makhijani and R. Gupta, "Isolated word speech recognition system using dynamic time warping," International Journal of Engineering Sciences & Emerging Technologies (IJESET), vol. 6, no. 3, pp.352-367, December 2013.

[3] K. Barczewska and A. Drozd, "Comparison of methods for hand gesture recognition based on dynamic time warping algorithm," IEEE Federation Conference on Computer Science and Information Systems (FedCSIS), pp. 207-210, September 2013.

[4] A. Pikrakis, S. Theodoridis and D. Kamarotos, "Recognition of isolated musical patterns using context dependent dynamic time warping," IEEE Transactions on Speech and Audio Processing, pp. 175-183, May 2003.

[5] S. Sempena, N.U. Maulidevi and P.R. Aryan, "Human action recognition using dynamic time warping," IEEE International Conference on Electrical Engineering and Informatics (ICEEI), pp. 1-5, July 2011.

[6] B.C. Bhokse and B.S. Thakare, "Devnagari handwriting recognition system using dynamic time warping algorithm," International Journal of Computer Applications(IJCA), vol. 52, no. 9, pp.7-13, August 2012.

[7] H. Ding, G. Trajcevski, P. Scheuermann, X. Wang, and E. Keogh, "Querying and mining of time series data: Experimental comparison of representations and distance measures," PVLDB, vol. 1, no. 2, pp.1542-1552, August 2008.

[8] D. Sart, A. Mueen, W. Najjar, E. Keogh and V. Niennattrakul, "Accelerating dynamic time warping subsequence search with GPUs and FPGAs," IEEE 10th International Conference on Data Mining, pp. 1001-1006, 2010.

[9] J.S. Tai, K.F. Li and H. Elmiligi, "Dynamic time warping algorithm: A hardware realization in VHDL," IEEE International Conference on IT Convergence and Security(ICITCS), pp. 1-4, December 2013.

[10] S. Palnitkar, "Verilog HDL- A guide to digital design and synthesis," SunSoft Press, 1996.

[11] B.K. Yi, H.V. Jagadish, C. Faloutsos, "Efficient retrieval of similar time sequences under time warping," IEEE 14th International Conference on Data Engineering, pp. 201-208, February 1998.

[12] Z. Qian, K. Takaya, "Dense stereo disparity maps by dynamic time warp with sparse features and FPGA acceleration" 24th Canadian Conference on Electrical and Computer Engineering, pp. 874-877, May 2011.

ISSN: 2278 – 909X All Rights Reserved © 2015 IJARECE

INVESTIGATION ON PROCESS PARAMETER OPTIMIZATION FOR SURFACE ROUGHNESS AND MICRO HARDNESS OF COLD SPRAYED COATINGS

Tarun Goyal[a*], R.S. Walia[b], T.S. Sidhu[c]

a Professor, Shaheed Udham Singh Engg. College, Tangori, Mohali, Punjab, India
b Associate Professor, Delhi Technological University, Delhi, India-110042
c Director, Shaheed Bhagat Singh State Technical Campus, Ferozepur, Punjab, India-152004
* *corresponding author e-mail*: goyaltarun1@gmail.com

ABSTRACT

Most of the existing multi-response optimization approaches focus on subjective and practical know how of the process. As a result some confusions and uncertainties are introduced in overall decision making process. In this investigation, an approach based on a Utility theory and Taguchi quality loss function (TQLF) has been applied to low-pressure cold spray (LPCS) process to deposit copper coatings, for simultaneous optimization of more than one response characteristics. In the present paper, two potential response parameters i.e. surface roughness (SR) and Micro hardness (MH) have been selected. Utility values based upon these response parameters have been analyzed for optimization by using Taguchi approach. The selected input parameters of powder feeding arrangement, substrate material, air stagnation pressure, air stagnation temperature and stand-off distance significantly improves the Utility function (raw data) comprising of quality characteristics (surface roughness and micro hardness). The percentage contribution of the parameters to achieve a higher value of utility function is: substrate material (32.27%), air stagnation pressure (29.72%), stand-off distance (14.41%), air stagnation temperature (3.19%) and powder feeding arrangement (3.04%) respectively.

Keywords: *Cold Spray (CS), optimization, Taguchi Method, Utility concept.*

1. Introduction

The cold gas-dynamic spray method (CGSM), hereafter referred to simply as cold spray (CS), is a relatively new process by which coatings of ductile materials (or composite materials with significant ductile phase content) can be produced without significant heating of the sprayed powder. The kinetic energy of the particles is sufficient to produce large deformations and high interfacial pressures and temperatures, which appear to produce a solid-state bond [1]. Cold-spray processing was developed in the former Soviet Union more than a decade ago as an offshoot of supersonic wind tunnel testing [2, 3].

CS is a process of applying coatings by exposing a metallic or dielectric substrate to a high velocity (300-1200 m/s) jet of small (1-50 μ m) particles accelerated by a supersonic jet of compressed gas. The two main clear cut distinctions of the Low Pressure Cold Gas Dynamic Spray (LPCGDS) system from the High Pressure Cold Gas Dynamic Spray (HPCGDS) system are: the utilization of low pressure gas (5-10 bars instead of 25-30 bars) and the radial injection of powder instead of axial injection. The accelerating gas (usually air or N_2) is injected at low pressure (5-10 bars) and preheated within the gas heater to temperatures up to about 400 ^{0}C to optimize its aerodynamic properties. Solid powder particles are radially introduced downstream of the throat section of the supersonic nozzle thus eliminating the need for a high pressure delivery system, which increases system portability, operational safety and significantly reduces spraying costs. Within the nozzle, static pressure is maintained below the atmospheric pressure ensuring that feedstock particles are effectively drawn in from the powder feeder by Venturi effect [4]. Fig. 1 shows a schematic of the LPCGDS system.

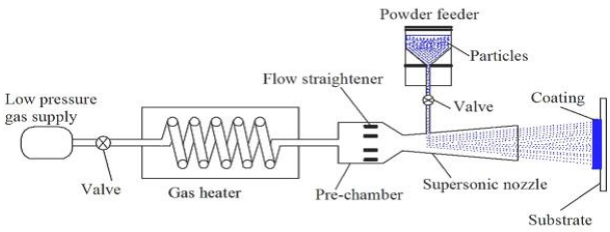

Fig. 1: A typical LPCGDS device [5]

To obtain good quality coatings, these spray parameters should be selected carefully and then optimized. In the process of optimization of process parameters, it is seen that one particular setting of input parameters for a response characteristics may not be suitable for other characteristics of the process/product. In most of the manufacturing processes, more than one quality characteristics has to be considered for optimization of process parameters making it necessary that several response characteristics have to be simultaneously optimized. Based on the foregoing discussions, in this paper, Taguchi method is briefly reviewed for the multi-response optimization. The multi-response optimization of the response parameters of Low

Pressure Cold Spray (LPCS) process is presented by using the experimental data. Optimization models have been developed by combination of the Taguchi Method and the Utility concept. The multi-response optimization of quality characteristics i.e. surface roughness and micro hardness of LPCS has been carried.

2. Experimental Procedure

Table 1 show the process parameters that were identified as potential important in affecting the quality characteristics of the LPCS process under consideration [6]. The process parameters, their designated symbols and ranges are also given in Table 1.

Table 1: Process parameters and their range

Symbol	Process Parameters	Range	Level 1	Level 2	Level 3
A	Feed Type	Gravity, Argon	Gravity	Argon	--------
B	Substrate Material	Al alloy, Brass, Ni alloy	Al alloy	Brass	Ni alloy
C	Stagnation pressure	104-120 psi	104	112	120
D	Stagnation temperature	350-400^0 C	350	375	400
E	Stand-off distance	2.5-7.5 mm	2.5	5.0	7.5
Nozzle type: Converging-diverging, Carrier gas: Air, Powder size: < 45 µm					

The Taguchi's mixed level design was selected as it was decided to keep two levels of powder feeding arrangement. The rest four parameters were studied at three levels. The effect of selected process parameters was studied on the following response characteristics of LPCS process:

a. Surface roughness (SR)
b. Micro hardness (MH)

Surface roughness is lower the better type of quality characteristic whereas micro hardness is "higher the better" type of quality characteristic. A simplified multi-criterion methodology based on Taguchi's approach and utility concept (given below) is used to achieve the objective of this study. The observed values of response parameters are given in Table 2.

Table 2: Experimental results of various response characteristics

Exp No.	Surface roughness () SR			S/N Ratio (dB)	Micro hardness ($H_{v0.3}$) MH			S/N Ratio (dB)
	R1	R2	R3		R1	R2	R3	
1	13.56	13.71	13.83	-22.73	122	126	124	41.86
2	10.87	10.91	10.36	-20.60	134	129	132	42.38
3	8.05	7.81	7.73	-17.91	131	132	122	42.15
4	9.20	10.04	10.68	-19.99	126	128	124	42.00
5	8.17	8.02	10.23	-18.95	124	125	128	41.98
6	8.70	7.50	8.60	-18.31	126	127	128	42.07
7	11.17	11.22	11.56	-21.07	129	131	132	42.32
8	6.69	6.68	7.35	-16.79	137	133	134	42.58
9	6.89	6.97	7.02	-16.85	134	135	139	42.66
10	8.31	8.26	9.59	-18.83	123	118	111	41.36
11	9.24	9.60	9.52	-19.51	119	115	117	41.36
12	8.42	8.29	8.92	-18.63	126	131	129	42.18
13	9.04	9.78	9.62	-19.54	125	121	122	41.77
14	7.19	7.79	7.82	-17.62	110	119	113	41.12
15	6.18	6.97	6.39	-16.28	122	120	124	41.72
16	7.94	8.13	8.15	-18.14	129	125	127	42.07
17	7.19	8.62	7.34	-17.77	125	127	128	42.05
18	7.94	7.11	7.84	-17.66	123	128	132	42.11
Total	154.75	157.41	162.55	-337.29	2265	2270	2266	755.80
	$\overline{T}_{SR}$ = overall mean of SR= 8.79				$\overline{T}_{MH}$ = overall mean of MH = 125.94			
R1, R2, and R3 represent repetitions								

A. Utility Concept

Utility can be defined as the usefulness of a product or a process in reference to the expectations of the users. The overall usefulness of a process/product can be represented by a unified index termed as *Utility* which is the sum of the individual utilities of various quality characteristics of the process/product. The methodological basis for Utility approach is to transform the estimated response of each quality characteristic into a common index.

If X_i is the measure of effectiveness of an attribute (or quality characteristic) i and there are n attributes evaluating the outcome space, then the joint Utility function can be expressed [7] as:

$$U(X_1, X_2, \ldots X_n) = f(U_1(X_1), U_2(X_2) \ldots U_n(X_n)) \quad (1)$$

where $U_i(X_i)$ is the utility of the i^{th} attribute.

The overall Utility function is the sum of individual utilities if the attributes are independent, and is given as follows:

$$U(X_1, X_2, \ldots X_n) = \sum_{i=1}^{n} U_i(X_i) \quad (2)$$

The attributes may be assigned weights depending upon the relative importance or priorities of the characteristics. The overall utility function after assigning weights to the attributes can be expressed as:

$$U(X_1, X_2, \ldots X_n) = \sum_{i=1}^{n} W_i U_i(X_i) \quad (3)$$

where W_i is the weight assigned to the attribute i, the sum of the weights for all the attributes must be equal to 1.

B. Determination of utility value

A preference scale for each quality characteristic is constructed for determining its utility value. Two arbitrary numerical values (preference number) 0 and 9 are assigned to the just acceptable and the best value of the quality characteristic respectively. The preference

number (P_i) can be expressed on a logarithmic scale as follows [8, 9]:

$$P_i = A \times \log\left(\frac{X_i}{X_i^{'}}\right) \quad (4)$$

where X_i = value of any quality characteristic or attribute *i*

$X_i^{'}$ = just acceptable value of quality characteristic or attribute *i*

A = constant

The value of *A* can be found by the condition that if X_i = X* (where X* is the optimal or best value), then P_i = 9

Therefore, $A = \frac{9}{\log \frac{X^*}{X_i^{'}}}$

The overall utility can be calculated as follows:

$$U = \sum_{i=1}^{n} W_i P_i \quad (5)$$

subject to the condition: $\sum_{i=1}^{n} W_i = 1$

Among various quality characteristics type viz. smaller the better, higher the better, and nominal the better, suggested by Taguchi, the Utility function would be higher the better type. Therefore, if the Utility function is maximized, the quality characteristics considered for its evaluation will automatically be optimized (maximized or minimized as the case may be).

3. Analysis and Discussions

Based upon the methodology developed in the previous section, following case have been considered to obtain the optimal settings of the process parameters of LPCS for predicting the optimal values of combined responses. Two quality characteristics i.e. Surface roughness and Micro hardness have been included in utility response.

Taguchi L_{18} orthogonal array (OA) [10] has been adopted for conducting the experiments. Powder feeding arrangement (A), Substrate material (B), air stagnation pressure (C), air stagnation temperature (D), and stand-off distance (E) were selected as input parameters. Response parameters (quality characteristics) were surface roughness and micro hardness, when they are optimized individually; the summary of results is produced in Table 3.

Table 3: Optimal setting and values of process parameters

Response characteristics	Optimal level of process parameters	Significant process parameters	Predicted optimal value of quality characteristics
SR	A2, B3, C3, D3, E3	A, B, C, D, E	4.92µm
MH	A1, B3, C3, D2, E2	A, B, C, D, E	138.36 $H_{v0.3}$

Following is the stepwise procedure for transforming experimental data into utility data.

A. Construction of preference scales

(a) Preference scale for SR (P_{SR}):

X* = Optimal value of SR = 4.92 (refer Table 3)

$X_i^{'}$ = Just acceptable value of SR = 14 (All the observed values of SR are lesser than 14)

Following equation is obtained from equation 4:

$$P_{SR} = -19.81 \times \log\left(\frac{X_{SR}}{14}\right) \quad (6)$$

(b) Preference scale for MH (P_{MH}):

X* = Optimal value of MH = 138.36 (refer Table 3)

$X_i^{'}$ = Just acceptable value of MH = 110 (All the observed values of MH are greater than 110)

Following equation is obtained from equation 4:

$$P_{MH} = 90.34 \times \log\left(\frac{X_{MH}}{110}\right) \quad (7)$$

B. *Calculation of utility value*

Equal weights (1/2 each) have been assigned to the selected quality characteristics assuming both the quality characteristics, are equally important. However, these weights can be varied depending upon the case or user requirements, if any.

The following relation was used to calculate the utility function based upon the experimental trials:

$$U(n,r) = P_{SR}(n,r) \times W_{SR} + P_{MH}(n,r) \times W_{MH} \quad (8)$$

where $W_{SR} = \frac{1}{2}$; $W_{MH} = \frac{1}{2}$

n is the trial number (n = 1,2,3,….,18) and *r* is the repetition number (r = 1,2,3). The calculated Utility values are shown in Table 4.

Table 4: Calculated utility data based on responses SR and MH

Trial Number	Utility Values			S/N Ratio (dB)
	R1	R2	R3	
1	2.17	2.75	2.40	7.63
2	4.96	4.20	4.87	13.32
3	5.81	6.09	4.59	14.59
4	4.47	4.40	3.52	12.15
5	4.67	4.91	4.32	13.28
6	4.71	5.50	5.07	14.09
7	4.10	4.38	4.40	12.64
8	7.48	6.91	6.64	16.88
9	6.92	7.02	7.56	17.08
10	4.44	3.65	3.81	11.87
11	3.33	2.50	2.87	9.06
12	4.85	5.68	5.07	14.26
13	4.39	3.41	3.65	11.48
14	3.87	4.07	3.03	11.04
15	5.55	4.71	5.73	14.43
16	5.57	4.85	5.15	14.25
17	5.38	4.91	5.75	14.50
18	4.63	5.89	6.07	14.66

R1, R2, R3 = repetitions of experiments against each of the trial conditions

C. Analysis of utility data for optimal settings of process parameters

The average and main response in terms of Utility values and S/N ratio (Tables 5 and 6) are plotted in Figure 2. It can be observed from Figure 2 (i) to (v) that the 1st level of powder feed arrangement (A 1), 3rd level of substrate material (B 3), 3rd level of air stagnation pressure (C 3), 3rd level of air stagnation temperature (D 3) and 2nd level stand-off distance (E 2) are expected to yield a maximum values of the utility and S/N ratio within the experimental space.

The pooled version of ANOVA for utility data and S/N ratio are given in Tables 7 and 8 respectively. It can be noticed from Table 7 that all the input parameters have significant effect (at 95% confidence level) on the utility function. Similarly, it had been found from Table 8 that all the chosen parameters in study have significant effect on the S/N ratio of utility function.

Table 5: Average and main Effects (Raw data: SR and MH)

Process parameter designation	Average Utility values			Main effects		Difference
	L1	L2	L3	L2-L1	L3-L2	(L3-L2)-(L2-L1)
A	4.99	4.55	-	-0.45	-	-0.45
B	4.11	4.44	5.76	0.33	1.31	0.98
C	3.97	4.70	5.64	0.73	0.93	0.20
D	4.55	4.69	5.07	0.14	0.38	0.24
E	3.99	5.26	5.07	1.27	-0.19	-1.46

L1, L2 and L3 represents average values of raw data of corresponding parameters at levels 1, 2 and 3 respectively. L2-L1 is the average main effect when the corresponding parameter changes from level 1 to level 2. L3-L2 is average main effect when the corresponding parameter changes from level 2 to level 3.
A-Powder feed arrangement, B- Substrate material, C-air stagnation pressure, D-air stagnation temperature, E-stand-off distance.

Table 6: Average S/N Values and main Effects (Raw Data: SR and MH)

Process parameter designation	S/N Average values			Main effects (dB)		Difference
	L1	L2	L3	L2-L1	L3-L2	(L3-L2)-(L2-L1)
A	13.5	12.8	-	-	-	-0.68
B	2	4	15.0	0.6	2.2	1.29
C	11.7	12.7	0	8	5	0.50
D	9	5	14.8	0.9	1.8	-0.29
E	11.6	13.0	5	6	4	-3.12

L1, L2 and L3 represents average values of S/N data of corresponding parameters at levels 1, 2 and 3 respectively. L2-L1 is the average main effect when the corresponding parameter changes from level 1 to level 2. L3-L2 is average main effect when the corresponding parameter changes from level 2 to level 3.
A-Powder feed arrangement, B- Substrate material, C-air stagnation pressure, D-air stagnation temperature, E-stand-off distance.

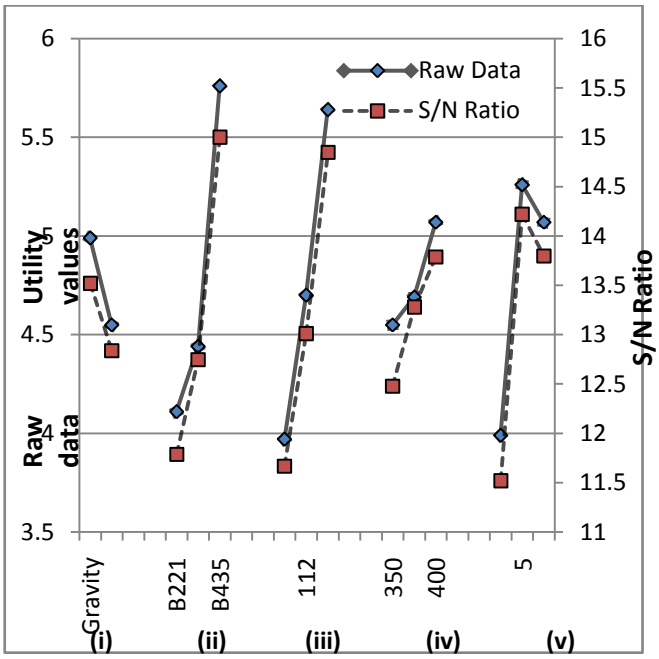

Fig. 2: Average and main response in terms of Utility values and S/N ratio

Table 7: Pooled ANOVA (Raw Data: SR and MH)

SOURCE	SS	DOF	V	F-Ratio	SS'	P %
A	2.69	1	2.69	8.11*	2.36	3.19
B	27.19	2	13.59	40.93*	26.53	32.27
C	25.04	2	12.52	8.11*	24.38	29.72
D	2.56	2	1.28	3.86*	1.90	3.04
E	12.14	2	6.07	18.28*	11.48	14.41
E (Pooled)	14.61	44	0.33	-	17.60	17.34
Total (T)	84.26	53	-	-	84.26	100

* Significant at 95% confidence level. SS= Sum of Squares, DOF= Degree of Freedom, V= Variance, SS'= Pure Sum of Squares

Table 8: S/N Pooled ANOVA (Raw Data: SR and MH)

SOURCE	SS	DOF	V	F-Ratio	SS'	P %
A	2.07	1	2.07	8.30*	1.82	2.12
B	32.67	2	16.33	65.33*	32.17	33.37
C	30.60	2	15.30	61.18*	30.10	31.25
D	5.23	2	2.61	10.46*	4.73	5.34
E	25.33	2	12.66	50.64*	24.83	25.86
E (Pooled)	2.00	8	0.25	-	4.25	2.04
Total (T)	97.92	17	-	-	97.92	100

* Significant at 95% confidence level. SS= Sum of Squares, DOF= Degree of Freedom, V= Variance, SS'= Pure Sum of Squares

D. Optimal values of quality characteristics (predicted means)

The optimal values of utility and thus the optimal values of response characteristics in consideration are predicted at the above levels of significant parameters.

The average values of all the response characteristics at the optimum levels of significant parameters with respect to Utility function are recorded in Table 9.

Table 9: Average values of various responses at optimal levels

Levels	Surface roughness, SR (µm)	Micro Hardness MH ($H_{v0.3}$)
A1	9.390	129.33.
B3	8.101	130.44
C3	7.629	128.28
D3	7.905	124.72
E2	8.454	128.33
Note: The above average values are taken from experimental data		

The optimal values of the predicted means (µ) of different response characteristics can be obtained from the following equation:

$$\mu = A1 + B3 + C3 + D3 + E2 - 4T \quad (9)$$

where, A1- First level of powder feed arrangement, B3- Third level of substrate material, C3- Third level of air stagnation pressure, D3- Third level of air stagnation temperature and E2- Second level of stand-off distance.

The 95% confidence interval of confirmation experiments (CI_{CE}) can be computed [10] by using the following equation:

$$CI_{CE} = \sqrt{F_{\alpha}(1, f_e) V_e \left[\frac{1}{n_{eff}} + \frac{1}{R}\right]} \quad (10)$$

where, $F_{\alpha}(1, f_e)$ = The F-ratio at the confidence level of (1-α) against DOF 1 and error degree of freedom f_e , R = Sample size for conformation experiments, V_e = Error variance, $n_{eff} = \frac{N}{1 + DOF}$ N= total number of trials, and DOF= Total degrees of freedom associated in the estimate of mean response.

(a) For Surface roughness (SR)

$$\mu_{SR} = A1 + B3 + C3 + D3 + E2 - 4T_{SR} = 6.319$$

where A1 = 90390, B3 = 8.101, C3 = 7.629, D3= 7.905, E2 = 8.454 (Table 9):

T_{SR} = 8.79 (Table 2)

The following values have been obtained by the ANOVA:

N = 54, f_e = 44, v_e = 0.00038, n_{eff} = 5.4, R= 3, $F_{0.05}$ (1, 44) = 4.064

From equation 10, CI_{CE} = ± 0.028

The predicted optimal range (for conformation runs of three experiments) for SR is given by

CI_{CE} : 6.291< μ_{SR} <6.347

(b) For Micro hardness (MH)

$$\mu_{MH} = A1 + B3 + C3 + D2 + E1 - 4T_{MH} = 135.51$$

where A1 = 129.33, B3 = 130.44, C3 = 128.28, D1= 127.83, E2 = 123.39, (Table 9):

T_{MH} = 125.94 (Table 2)

The following values have been obtained by the ANOVA:

N = 54, f_e = 44; v_e = 19.77, n_{eff} = 5.4, R= 3, $F_{0.05}$ (1, 44) = 4.064

From equation 10, CI_{CE} = ± 6.45

The predicted optimal range (for conformation runs of three experiments) for MH is given by

CI_{CE} : 129.06 < μ_{MH} < 141.96

D. Confirmation Experiment

For confirmation of experimental results, three experiments were performed at optimal settings as suggested by Taguchi analysis of Utility data. The observed values of various response characteristics have been given in Table 10. It can be noticed that overall average of the observed values of the response characteristics fall well within the 95% CI_{CE} of the optimal range of the respective response characteristics.

Table 10: Observed values of quality characteristics (Confirmation experiment)

Exp. No.	SR (µm)			MH ($H_{v0.3}$)		
	r_1	r_2	r_3	r_1	r_2	r_3
1	6.30	6.32	6.33	134	136	139
2	6.31	6.33	6.30	140	138	137
3	6.33	6.31	6.32	137	140	133
Overall average	6.32			137.1		

4. Conclusions

The important conclusions of this research work are enlisted below:

1. The optimal setting of the process parameters were predicted for optimization of surface roughness and micro hardness using the model. The optimal settings were A1- First level of powder feed arrangement, B3-Third level of substrate material, C3- Third level of air stagnation pressure, D3- Third level of air stagnation temperature and E2- Second level of stand-off distance.
2. The decreasing order of percentage contribution of the parameters to achieve a higher value of utility function is: substrate material (32.27%), air stagnation pressure (29.72%), stand-off distance (14.41%), air stagnation temperature (3.19%) and powder feeding arrangement (3.04%) respectively.
3. The overall average of quality characteristics was found to be 6.32µm for surface roughness and 137.1 $H_{v\ 0.3}$ for micro hardness which falls well within the 95% CI_{CE} of the optimal range of the respective response characteristics.

REFERENCES

1. *A.N. Papyrin "Cold Spray: State of the art and applications" in Cold Spray Technology, Albuquerque, NM, USA, 2006, pp 1 – 2.*

2. *J. R. Davis, (Ed.) et al., Handbook of Thermal Spray Technology, 1st Ed. OH, USA: ASM International® Materials Park, 2004.*

3. *A. Papyrin, V. Kosarev, S. Klinkov, A. Alkhimov and V. Fomin, Cold Spray Technology. London: Elsevier, 2007.*

4. *R.Gr. Maev and V. Leshchynsky, Introduction to Low Pressure Gas Dynamic Spray Physics and Technology. Weinheim: Wiley2VCH, 2008.*

5. *M. Grujicic, C. L. Zhao, C. Tong, W. S. DeRosset and D. Helfritch, "Analysis of the impact velocity of powder particles in the cold-gas dynamic-spray process", Materials Science and Engineering A368, Elsevier, 2004, pp 222 – 230.*

6. *Tarun Goyal, R.S. Walia, T.S. Sidhu, "Surface roughness optimization of cold sprayed coatings using Taguchi method", International Journal of Advanced Manufacturing Technology, Vol. 60, No.5-8, May 2012; pp. 611-623.*

7. *W. Bunn Derek, Analysis for optimal decisions. New York: John Wiley and Sons, 1982, pp. 275.*

8. *V. Gupta, P.N. Murthy, An introduction to Engineering Design Methods. New Delhi: Tata McGraw Hill, 1980, pp. 78-98.*

9. *P. Kumar, P.B. Barua, J.L. Gaindhar, "Quality optimization (Multi-Characteristics) through Taguchi Technique and Utility Concept", J. Quality and Reliability Engineering International, Vol. 16, 2000, pp. 475-485.*

10. *R.K. Roy, A primer on Taguchi method. New York: Van Nostrand Reinhold, 1990.*

Published by: South Asian Academic Research Journals
SAJMMR:
South Asian Journal of Marketing & Management Research
(A Double Blind Referred & Reviewed International Journal)

MACRO ECONOMIC DETERMINANTS OF FOREIGN DIRECT INVESTMENT IN BRIC NATIONS

Ms. Priya Gupta*; Dr. Archana Singh**

*Research Scholar,
Delhi School of Management,
Delhi Technological University,
New Delhi, India.
Assistant Professor,
Apeejay School of Management,
New Delhi, India.
**Assistant Professor,
Delhi School of Management,
Delhi Technological University,
Delhi, India.

www.IndianJournals.com
Members Copy, Not for Commercial Sale
Downloaded From IP - 14.139.251.107 on dated 24-Feb-2015

ABSTRACT

Foreign Direct Investment (FDI) has played a momentous role in the vigorous growth of countries across the world which in turn has triggered an interest in the minds of the researchers to focus on the determinants of such phenomenon.

Some of the identified factors for this observable fact are namely comparative labor costs, country size, economic openness, nature of exchange rate regime, return on investment, and political factors amongst many others. While several studies of the determinants of FDI have been published in the last years, most of them focus on a single country and are based on conceptual frameworks which have been developed to analyze FDI in developed countries. However, nothing much has been discussed about whether the logic of these frameworks can be directly applied to FDI in BRIC nations.

BRIC nations have been chosen because of their notable growth rates and rising shares in the worldwide trade and investment flows. The purpose of this study is, therefore, to explore the determinants of FDI in the BRIC nations from 1991 to 2010. We model foreign direct investment as a function of economic variables and it was

found that they play an important role in influencing the level of foreign direct investment in BRIC Nations.

KEYWORDS: *BRIC Nations, Economic Variables, Foreign Direct Investment, Growth Rate.*

INTRODUCTION

Foreign Direct Investment (FDI) is a driving force of globalization and an important engine of economic growth. Developing as well as developed countries seek to attract FDI due to its many advantages for economic development. FDI can not only bring capital to an economy, but also transfer knowledge, technology and skills, as well as generate employment and trade. (Jimmy J. Zhan (2006)).

G20 countries received, all in all, 64% of global FDI inflows in the first quarter of 2012 of which 49% was hosted by non-OECD partners of G20. Other significant FDI destinations were China (USD 64 billion representing 12% decrease from last quarter of 2011), Brazil (USD 15 billion, 8% decreases) and Russia (USD 13 billion). India, Indonesia, Argentina and South Africa attracted USD 13 billion (18% decrease). FDI inflows to Saudi Arabia were USD 4 billion in the last quarter of 2011. (OECD Report, 2012)

Since emerging markets have relied on foreign direct investment (FDI) as a source of investment and capital formation that is so urgently needed to grow, we document the economic determinants of foreign direct investment in BRIC nations.

This study is important because of the world-wide economic power shift that is evolving today. During the past 20 years, there has been a dramatic change in global business. Foreign Direct Investment has become a very important source of investment, capital formation, and growth for emerging markets. Emerging market economies compete for FDI.

This study highlights the determinants of foreign direct investment in BRIC Nations. FDI is considered to be an important driver of growth for capital starved economies. Policy makers of other countries that are classified as less developed countries and aspire to become emerging markets can learn from the experience of these countries such as China and India to attract FDI and move up from the category of less developed countries (LDC) to emerging market economies (EME).

LITERATURE REVIEW

Several studies have analyzed the determinants of FDI for individual countries or groups of countries that are part of developing markets. For an appropriate analysis, the literature is reviewed under the following segments:

1. Developing nations

2. Brazil, Russia, India and China as a part of BRIC Nations

www.IndianJournals.com
Members Copy, Not for Commercial Sale
Downloaded From IP - 14.139.251.107 on dated 24-Feb-2015

1. DEVELOPING NATIONS

Muhammad Azam and Ling Lukman (2010) revealed that market size, external debt, domestic investment, trade openness, and physical infrastructure are the important economic determinants of FDI in Pakistan, India and Indonesia. Magda Kandil, (2011) disclosed exchange rate movements as the prominent factor behind FDI inflows in both developing and advanced countries. Marcelo Braga Nonnemberg and Mario Jorge Cardoso de Mendonca (2004) concluded that FDI is correlated to level of schooling, economy's degree of openness, inflation, risk and average rate of economic growth in developing countries. Khondoker Abdul Mottaleb and Kaliappa Kalirajan (2010) also demonstrated that developing countries with larger GDPs, higher GDP growth rates, higher proportion of international trade and a more business-friendly environment are more successful in attracting FDI. Harinder Singh and Kwang W. Jun (1995) found export orientation as the strongest variable for explaining why a developing country attracts FDI. According to Recep Kok and Bernur Acikgoz Ersoy, (2009), interaction of FDI with the total debt service/ GDP and inflation have a negative impact and the most important determinant of FDI is the communication variable.

www.IndianJournals.com
Members Copy, Not for Commercial Sale
Downloaded From IP - 14.139.251.107 on dated 24-Feb-2015

Boopen Seetanah, Sawkut Rojid, (2011) in their study conducted for Mauritius emphasized on trade openness, wages and the quality of labor in the country as the most instrumental factors for attracting FDI. Andreia Alexandra Faria Severiano (2011) showed the importance of GDP per capita, degree of openness to trade, exchange rate, minimum wage, corporate tax rate and labor market flexibility while analyzing the determining factors for FDI in primary, secondary and tertiary sectors of Portugal. Another study which confirmed the results of the previous studies was by Gilmore et.al. (2003) who concluded that FDI is a preference to other forms of foreign market entry, size and growth of the host market, government emphasis on FDI and financial incentives, economic policy, cultural closeness, costs of transport, materials and labor, resources, technology, political stability and infrastructure are important determinants of FDI for Northern Ireland and Bahrain. Another study by Nguyen Ngoc Anh and Nguyen Thang (2007) in the Vietnam context gave importance to market, labor and infrastructure in attracting FDI.

Khondoker Abdul Mottaleb and Kaliappa Kalirajan (2010) demonstrated that developing countries with larger GDPs, higher GDP growth rates, higher proportion of international trade and a more business-friendly environment are more successful in attracting FDI. Elizabeth Asiedu (2001) suggested that good infrastructure, liberalized trade regimes and better government policies can help Africa to get more FDI flows. The main result is that natural resources and large markets promote FDI (Elizabeth Asiedu (2006)). Openness to trade, the size of the domestic market, stock of human capital played a positive role while political instability and labor cost a negative role in attracting FDI in the African markets as explored by Sawkut et. al.(2009). Yuko Kinoshita and Nauro F. Campos (2003) explored institutions, agglomeration and trade openness as main determinants for FDI inflows in transition economies.

2. BRIC NATIONS

Vijayakumar et. al. (2010) concluded that Market size, Labor cost, Infrastructure, Currency value and Gross Capital formation are the potential determinants of FDI inflows of BRICS countries. A study in China by Owen C. H. Ho (2004) indicated that market size, wage rate, degree of

economic reform and innovation activities are important determinants of sectoral FDI in China. Jones et. al. (2000) revealed that national infrastructural factors and Government policies were the major obstacles that Russia faced during the 1990s in attracting FDI. Political Risk also influences FDI in Russia as proved by Andrey Popovich (2007).

Alvin G. Wint, Densil A. Williams (2002), David Floyd and Sandhla Summan (2008) also focused on the role of Government policies as a major determinant of FDI. Balasundram Maniam, Amitava Chatterjee (1998) also conferred the importance of exchange rate for attracting US FDI in a developing country like India. Monica Singhania and Akshay Gupta (2011 revealed that GDP, inflation rate, scientific research, and FDI Policy changes have had a significant impact on FDI inflows into India. The financial strength of the state, development level of the state, size of the market and level of infra structure were some other determining factors for FDI in India as studied by Neerja Dhingra and H.S. Sidhu (2011).

Chien-Hsun Chen (1996), Lv Na and W.S. Lightfoot (2006) determined that market expansion potential, labor cost, allocative efficiency, transportation linkages, and technological filtering are able to attract more FDI in the mainland China. Junjie Hong (2008) also emphasized the labor cost as an essential determinant for attracting FDI flows in China. Angelo et. al. (2010) concluded the importance of the consumer market and strength of consumer sales as the most important factor in explaining capital movements into Brazil. Bergsman et. al. (1999) suggested that Russia should switch to a more modern policy approach to FDI by eliminating the relatively extensive non-tariff protection given to the domestic market, phasing out existing tax preferences for foreign investors, and reducing significantly restrictions on FDI to a limited number of activities.

Thus, the reviews would help in choosing the factors or alternatives that may gauge the FDI inflows of BRIC countries.

www.IndianJournals.com
Members Copy, Not for Commercial Sale
Downloaded From IP - 14.139.251.107 on dated 24-Feb-2015

OBJECTIVES OF THE STUDY

- To find out the most critical determinants influencing the FDI of BRIC Nations
- To study the relation between FDI and a set of explanatory variables by using a regression analysis

RESEARCH METHODOLOGY

RESEARCH DESIGN

For the purpose of the study, a set of explanatory economic variables were considered to define the impact on FDI flows in BRIC Nations. The data was drawn from World Investment Report by UNCTAD, International Direct Investment Statistics Yearbook by OECD, World Economic Outlook Database, IMF and The PRS Group, Inc., 1991-2010, East Syracuse, NY 13057 USA. The period of study has been since 1991 till 2010. Pearson Correlation has been applied to test the relationship between the dependent and independent variables. After this, the insignificant variables were dropped to run the Step- wise regression Test on SPSS so as to develop a model of significant determinants of FDI for all the four countries individually. Other relevant

econometric tests such as Coefficient of Determination (R^2), Standard error of coefficients, T-Statistics and F- ratio were carried out in order to assess the relative significance, desirability and reliability of model estimation parameters.

CONCEPTUAL FRAMEWORK

While several studies of the determinants of FDI have been published in the last years, most of them focus on a single country and are based on conceptual frameworks which have been developed to analyze FDI in developing or developed countries. However, nothing much has been discussed about whether the logic of these frameworks can be directly applied to FDI in BRIC nations. Thus, we model FDI as a function of economic variables. The following equation summarizes the model for determinants of FDI in BRIC Nations:

$$FDI = a + b_1(BB) + b_2(CAGDP) + b_3(CAXGS) + b_4(DS) + b_5(FD) + b_6(GDPG) + b_7(IL) + b_8(INF) + b_9(UNEM) + e_t$$

Where,

www.IndianJournals.com
Members Copy, Not for Commercial Sale
Downloaded From IP - 14.139.251.107 on dated 24-Feb-2015

DEPENDENT VARIABLE

FDI= U.S. Dollar amount of Foreign Direct Investment in the country/ economy

INDEPENDENT VARIABLES

BB= Budget Balance as a percentage of Gross Domestic Product (GDP)

CAGDP= Current Account as a percentage of GDP

CAXGS= Current Account as a percentage of Export of Goods and Services

DS= Debt Service as a percentage of Export of Goods and Services

FD= Foreign Debt as a percentage of GDP

GDPG= Real GDP Growth Rate

IL= International Liquidity of the country/ economy

INF= Percentage Inflation Rate in the country/ economy

UNEM= Percentage Unemployment in the country/ economy

e_t= The error term over the time t

a= Constant term of the model, and

b= Coefficients of the model

DATA ANALYSIS

The study has analyzed the four emerging countries Brazil, Russia, India and China individually to test the significance of the explanatory determinants on each of them and then formulate a model specifying the most significant variables for them.

FOR BRAZIL

After the Pearson Coefficient of Correlation, only two variables were found to be significant and thus were entered in SPSS for the Step-wise regression Statistics, i.e. Percentage Inflation Rate in the country and Percentage Unemployment in the country.

TABLE 1: STEP-WISE REGRESSION ANALYSIS OF FDI AND EXPLANATORY VARIABLES: MODEL SUMMARY[b]

Model	R	R Square	Adjusted R Square	Std. Error of the Estimate	Sig. F Change
1	.557[a]	.311	.272	12.10697	.011

a. Predictors: (Constant), percentage inflation rate in the economy

b. Dependent Variable: U.S. dollar amount of foreign direct investment in the country ($bn.)

In the model,

1. The regression coefficient is -.012 for percentage inflation rate in the economy. The fitted regression equation is FDI= 23.066 - .012INF.

2. The regression equation explains only 31.10% of the variation in FDI.

3. The standard error of the estimate is 12.10697%. This value is the measure of the amount of actual values from the fitted values.

4. The t- statistic of -2.848 for the inflation rate and its small p- value .011 indicate that the coefficient of inflation is significantly different from zero.

5. The computed F value (8.109) is used to test the significance of the regression. The large F-ratio and its small p-value (.011) show the regression is significant, i.e. the regression function explains a significant amount of variability in FDI.

FOR RUSSIA

After the Pearson Coefficient of Correlation, only two variables were found to be significant and thus were entered in SPSS for the Step-wise regression Statistics, i.e. International liquidity in the country and Real GDP growth rate.

www.IndianJournals.com
Members Copy, Not for Commercial Sale
Downloaded From IP - 14.139.251.107 on dated 24-Feb-2015

TABLE 2: STEP-WISE REGRESSION ANALYSIS OF FDI AND EXPLANATORY VARIABLES: MODEL SUMMARY[b]

Model	R	R Square	Adjusted R Square	Std. Error of the Estimate	Sig. F Change
1	.674[a]	.454	.424	16.08898	.001

a. Predictors: (Constant), international liquidity of the economy

b. Dependent Variable: U.S. dollar amount of foreign direct investment in the country ($bn.)

In the model,

1. The regression coefficient is 2.281 for international liquidity of the country. The fitted regression equation is FDI= 3.499 + 2.281IL.

2. The regression equation explains 45.40% of the variation in FDI.

3. The standard error of the estimate is 16.08898%. This value is the measure of the amount of actual values from the fitted values.

4. The t- statistic of 3.869 for international liquidity and its small p- value .001 indicate that the coefficient of international liquidity is significantly different from zero.

5. The computed F value (14.970) is used to test the significance of the regression. The large F-ratio and its small p-value (.001) show the regression is significant, i.e. the regression function explains a significant amount of variability in FDI.

www.IndianJournals.com
Members Copy, Not for Commercial Sale
Downloaded From IP - 14.139.251.107 on dated 24-Feb-2015

FOR INDIA

After the Pearson Coefficient of Correlation, three variables were found to be significant and thus were entered in SPSS for the Step-wise regression Statistics, i.e. Debt Service as a percentage of Export of Goods and Services, Foreign Debt as a percentage of GDP and Percentage Unemployment in the country.

TABLE 3: STEP-WISE REGRESSION ANALYSIS OF FDI AND EXPLANATORY VARIABLES: MODEL SUMMARY[b]

Model	R	R Square	Adjusted R Square	Std. Error of the Estimate	Sig. F Change
1	.870[a]	.757	.743	6.66566	.000

a. Predictors: (Constant), debt service as % of XGS

b. Dependent Variable: U.S. dollar amount of foreign direct investment in the country ($bn.)

In the model,

1. The regression coefficient is -1.071 for debt service as a percentage of export of goods and services of the country. The fitted regression equation is FDI= 30.923-1.071DS.

2. The regression equation explains 75.70% of the variation in FDI.

3. The standard error of the estimate is 6.66566%. This value is the measure of the amount of actual values from the fitted values.

4. The t- statistic of -7.483 for debt service as a percentage of export of goods and services and its small p- value .000 indicate that the coefficient of debt service as a percentage of export of goods and services of the country is significantly different from zero.

5. The computed F value (56.001) is used to test the significance of the regression. The large F-ratio and its small p-value (.000) show the regression is significant, i.e. the regression function explains a significant amount of variability in FDI.

www.IndianJournals.com
Members Copy, Not for Commercial Sale
Downloaded From IP - 14.139.251.107 on dated 24-Feb-2015

FOR CHINA

After the Pearson Coefficient of Correlation, six variables were found to be significant and thus were entered in SPSS for the Step-wise regression Statistics, i.e. Budget Balance as a percentage of Gross Domestic Product (GDP), Current Account as a percentage of GDP, Current Account as a percentage of Export of Goods and Services, Debt Service as a percentage of Export of Goods and Services, International Liquidity of the country and Percentage Unemployment in the country.

TABLE 4: STEP-WISE REGRESSION ANALYSIS OF FDI AND EXPLANATORY VARIABLES: MODEL SUMMARY[b]

Model	R	R Square	Adjusted R Square	Std. Error of the Estimate	Sig. F Change
5	.959[e]	.919	.891	15.30302	.017

e. Predictors: (Constant), international liquidity of the economy, current account as percentage of GDP, current account as percentage of XGS, budget balance as a percentage of GDP, percentage unemployment in the country

b. Dependent Variable: U.S. dollar amount of foreign direct investment in the country ($bn.)

In the model,

1. The regression coefficient is 3.206 for international liquidity of the economy, 6.786 for current account as percentage of GDP, -2.267 for current account as percentage of XGS, 11.760 for budget balance as a percentage of GDP and 24.722 for percentage unemployment in the country. The fitted regression equation is FDI= -45.672 + 3.206IL + 6.786CAGDP – 2.267CAXGS + 11.760BB + 24.722UNEM.

2. The fifth model explains 91.10% of the variation in FDI.

3. The standard error of the estimate is 15.3032%. This value is the measure of the amount of actual values from the fitted values.

4. The t- statistic of 3.470 for international liquidity of the economy, 3.441 for current account as percentage of GDP, -3.396 for current account as percentage of XGS , 4.016 for budget balance as a percentage of GDP and 2.701 for percentage unemployment in the country and their small p- value .004, .004, .004, .001 and .017 respectively indicate that the coefficient of is significantly different from zero.

5. The computed F value (31.953) is used to test the significance of the regression. The large F-ratio and its small p-value (.000) show the regression is significant, i.e. the regression function explains a significant amount of variability in FDI.

www.IndianJournals.com
Members Copy, Not for Commercial Sale
Downloaded From IP - 14.139.251.107 on dated 24-Feb-2015

CONCLUSION

It can be concluded that there are different determinants affecting the FDI flows in all the four nations. Inflation rate, international liquidity, debt service as a percentage of export of goods and services of the country, current account as percentage of GDP, current account as percentage of XGS, budget balance as a percentage of GDP, percentage unemployment in the country are amongst them. Thus, the BRIC countries appear to have prosperity of economic and social development in the forth coming decades, if these countries form a formal union like European Union, ASEAN, G6 and G8 etc, and pool their resources. The economic growth will be tremendous and can throw competition and challenges towards the developed countries.

REFERENCES

1. Alexandra, A. F. S (2011), “The determinants of FDI in Portugal – A Sectoral Approach” Dissertation submitted in partial fulfillment of requirements for the degree of Master of Science in Economics, at the Universidade Católica Portuguesa from www.clsbe.lisboa.ucp.pt/resources/.../Andreia%20Severiano.pdf.

2. Angelo et.al. (2010), "Determinants of FDI in emerging markets: evidence from Brazil", International Journal of Commerce and Management, Volume 20, Issue: 3 pp. 203 – 216.

3. Asiedu, E (2001), “On the Determinants of Foreign Direct Investment to Developing Countries: Is Africa Different?”, Available at SSRN: http://ssrn.com/abstract=280062 or http://dx.doi.org/10.2139/ssrn.280062.

4. Asiedu, E (2006), "Foreign Direct Investment in Africa: The Role of Natural Resources, Market Size, Government Policy, Institutions and Political Instability", The World Economy, Volume. 29, No. 1, pp. 63-77, Available at SSRN: http://ssrn.com/abstract=875105 or http://dx.doi.org/10.1111/j.1467-9701.2006.00758.x.

5. Muhammad, A and Ling, L (2010), "Determinants of Foreign Direct Investment in India, Indonesia and Pakistan: A Quantitative Approach", Journal of Managerial Sciences, Volume IV, Number 1, pp. 31-44.

6. Bergsman et. al. (1999), "Improving Russia's Foreign Direct Investment Policy Regime", Available at SSRN: http://ssrn.com/abstract=288774 or http://dx.doi.org/10.2139/ssrn.288774.

7. Chen, C-H (1996), "Regional determinants of foreign direct investment in mainland China", Journal of Economic Studies, Volume: 23, Issue: 2, pp. 18 – 30.

8. Dhingra, N and Sidhu, H.S. (2011), "Determinants of Foreign Direct Investment Inflows to India", European Journal of Social Sciences, Volume 25, Number 1, pp. 21-31.

9. Floyd, D (2003), "How can a flexible labor market influence the amount of foreign direct investment attracted by a host nation? The case of the UK", European Business Review, Volume 15, Issue: 5, pp. 334 – 339.

10. Gilmore et.al. (2003), "Factors influencing foreign direct investment and international joint ventures: A comparative study of Northern Ireland and Bahrain", International Marketing Review, Volume. 20, Issue: 2, pp. 195 – 215.

11. Ho. H. C. O (2004), "Determinants of foreign direct investment in China: a sectoral analysis", Volume 4; Volume 18 of Discussion paper, the University of Western Australia, Business School, Economics, pp-1-29.

12. Hong, J (2008), "WTO accession and foreign direct investment in China", Journal of Chinese Economic and Foreign Trade Studies, Volume 1, Issue: 2, pp. 136 – 147.

13. http://www.oecd.org/fr/daf/investissementinternational/statistiquesetanalysesdelinvestissement/oecdbenchmarkdefinitionofforeigndirectinvestment-4thedition.htm.

14. Jones et. al. (2000), "Obstacles to foreign direct investment in Russia", European Business Review, Vol. 12 Issue: 4, pp. 187 – 197.

15. Kandil, M (2011), "Financial flows to developing and advanced countries: determinants and implications", International Journal of Development Issues, Volume 10, Issue: 1, pp. 60 – 91.

16. Kinoshita, Y and Campos, N. F. (2003), "Why Does FDI Go Where it Goes? New Evidence from the Transition Economies", William Davidson Institute Working Paper No. 573, Available at SSRN: http://ssrn.com/abstract=414540 or http://dx.doi.org/10.2139/ssrn.414540.

www.IndianJournals.com
Members Copy, Not for Commercial Sale
Downloaded From IP - 14.139.251.107 on dated 24-Feb-2015

17. Kok, R and Ersoy, B. A. (2009), “Analyses of FDI determinants in developing countries", International Journal of Social Economics, Volume 36, Issue: 1, pp. 105 – 123.

18. Maniam, B and Chatterjee, A (1998), "The determinants of US foreign investment in India: implications and policy issues", Managerial Finance, Vol. 24 Issue: 7, pp. 53 – 62.

19. Mottaleb, K. A. and Kalirajan, K (2010), “Determinants of Foreign Direct Investment in Developing Countries: A Comparative Analysis”, Margin— The Journal of Applied Economic Research, Volume 4, Issue: 4, pp. 369–404.

20. Na, L and Lightfoot, W.S. (2006), "Determinants of foreign direct investment at the regional level in China", Journal of Technology Management in China, Volume 1, Issue: 3, pp. 262 – 278.

21. Nguyen, A. N. and Nguyen, T (2007), “Foreign Direct Investment in Vietnam: An Overview and Analysis the Determinants of Spatial Distribution across Provinces”, Available at SSRN: http://ssrn.com/abstract=999550 or http://dx.doi.org/10.2139/ssrn.999550.

22. Nonnenberg, M. B. and Mendonca, M. J. C. (2004), www.anpec.org.br/encontro2004/artigos/A04A061.pdf.

23. Popovich, Andrey (2007), “Investing in Emerging Markets: Finding Out how Political Risk Influences FDI in Russia”, Available at SSRN: http://ssrn.com/abstract=996414 or http://dx.doi.org/10.2139/ssrn.996414.

24. The PRS Group, Inc., 1991-2010, East Syracuse, NY 13057 USA.

25. Sawkut et. al. (2009), “Determinants of FDI: Lessons from the African Economies”, Journal of Applied Business and Economics, Vol. 9, No. 1, pp. 1-16.

26. Seetanah, B and Rojid, S (2011), "The determinants of FDI in Mauritius: a dynamic time series investigation", African Journal of Economic and Management Studies, Volume. 2, Issue: 1, pp. 24 – 41.

27. Singh, H and Jun, K. W. (1995), “Some New Evidence on Determinants of Foreign Direct Investment in Developing Countries”. World Bank Policy Research Working Paper No. 1531. Available at SSRN: http://ssrn.com/abstract=623885.

28. Singhania, M and Gupta, A (2011),"Determinants of foreign direct investment in India", Journal of International Trade Law and Policy, Volume 10, Issue: , pp. 64 – 82.

29. Vijayakumar et.al. (2010), “Determinants of FDI in BRICS Countries: A panel analysis”, International Journal of Business Science and Applied Management, Volume 5, Issue 3, pp. 1-13.

www.IndianJournals.com
Members Copy, Not for Commercial Sale
Downloaded From IP - 14.139.251.107 on dated 24-Feb-2015

30. Wint, A. G. and Williams D. A. (2002), "Attracting FDI to developing countries: A changing role for government?", International Journal of Public Sector Management, Volume. 15, Issue: 5, pp. 361 – 374.

31. Zhan, J. J. (2006), "FDI Statistics: A Critical Review and Policy Implications", World Association of Investment Promotion Agencies (WAIPA).

www.IndianJournals.com
Members Copy, Not for Commercial Sale
Downloaded From IP - 14.139.251.107 on dated 24-Feb-2015

International Journal of Current Engineering and Technology
E-ISSN 2277 – 4106, P-ISSN 2347 – 5161
©2015INPRESSCO®, All Rights Reserved
Available at http://inpressco.com/category/ijcet

Research Article

Magnetorheological Smart Automotive Engine Mount

Chiranjit Sarkar†*,Harish Hirani‡ and Abhijit Sasaneᴪ

†Mechanical Engineering Department, Delhi Technological University, Shahbad Daluatpur, Bawana Road, Delhi – 110042, India
‡Mechanical Engineering Department, Indian Institute of Technology Delhi, Hauz Khas, New Delhi – 110016, India
ᴪSenior Manager, Tata Motors, Mumbai, India

Accepted 18 Feb 2015, Available online 20 Feb 2015, **Vol.5, No.1 (Feb 2015)**

Abstract

An ideal engine mount system isolates vibrations caused by engine dynamic disturbances in various speed ranges, and prevents engine bounce originated by shock excitations. The stiffness and damping of the ideal engine mount are functions of the frequency and amplitude of vibration. To avoid transmission of medium to high frequency and low amplitude vibrations, an idle *engine mount should be 'Soft' (low dynamic stiffness). On the other hand, road excitations passing through the tires and vehicle suspension system cause the structural- vibrations of low frequency and high amplitude. To deal with this case, an idle engine mount should be 'Stiff' (high dynamic stiffness). Such contradictory requirements from an engine mount demands engine mount to be smart. The aim of the present paper is to target a smart mount which will perform similar to Ideal mount. The present paper proposes MRF mount to provide variable dynamic stiffness characteristics. A theoretical design of MRF mount system has been sketched and performance evaluation of MR mount approaching to the ideal engine mount has been presented.*

Keywords: *Comparative study among engine mounts, Active engine mount, Ideal engine mount, Magnetorheological engine mount.*

1. Introduction

Internal combustion engines are commonly used in automobile industries to produce the required driving power. The firing pulse in the engine-cylinders; and the inertia force and torque caused by the rotating and reciprocating parts (i.e. piston, connecting rod, and crank) generate engine dynamic disturbances. Frequency and amplitude of such disturbances for 4 cylinder-four stroke engine range between 30Hz to 250 Hz, and 0.1mm to 0.5mm respectively (Bernuchon, 1984). These disturbances increase the level of noise and vibrations of automobile structure. Further, objectives of engine-weight-minimization (Yu, *et al*, 2001) and engine-power-maximization lead an engine design of higher levels of vibration and noise (Singh, 2000). On the other hand, modern automobile industries(Yu, *et al*, 2001) are targeting the passengers' comfort, which is inversely proportional to noise and vibrations of automobile structure. To resolve these conflicting requirements, an engine mounting system is designed to bear the engine-weight and to isolate the unbalanced engine disturbance from transmission to the vehicle structure. To avoid transmission of medium to high frequency and low amplitude vibrations, an idle engine mount should be 'Soft' (low dynamic stiffness). On the other hand, road excitations passing through the tires and vehicle suspension system, cause the structural- vibrations of low frequency (0-30 Hz) and high amplitude (0.5mm to 1.5mm) at engine mount locations (Patrick and Ticks, 1984). To deal with such low-frequency and high-amplitude-vibrations, an idle engine mount should be 'Stiff' (high dynamic stiffness) to carry the engine along with chassis without any relative movement between them. In additions to these requirements from an idle engine mount, a special need arises during idling of engine, which imparts low-frequency and low-amplitude vibrations. To isolate chassis from such low frequency and low-amplitude vibrations, engine mount should show its 'soft' behaviour. Thus the dynamic characteristics of the mount, which is expressed as complex number, should vary along with the frequency and amplitude of vibrations. The magnitude of this complex number is named 'Dynamic Stiffness'. For an ideal mount the dynamic stiffness is characterized by the curve as shown in Fig.1. In this figure, red dotted lines demonstrate the behaviour of an ideal mount considering the low frequency high amplitude (road excitations), low frequency low amplitude (engine idling) and high frequency low amplitude (engine) vibrations. Unfortunately available engine mounts such as elastomeric/rubber mount (Regis, 1976), hydraulic mount with orifice (Concoran and Ticks, 1984), hydraulic mount with inertia track (Flower, 1985), and hydraulic mount with inertia track and decoupler

*Corresponding author: **Chiranjit Sarkar**

(Ushijima, 1988) do not meet the "ideal required dynamic stiffness". Therefore the present proposes a novel engine mount system, performance of which approaches to the "ideal engine mount". A systematic methodology of comparative study among available engine mounts has been presented and a need to design proposed novel Magnetorheological engine mount have been illustrated. The details of magnetorheological fluids (MRF) are available in the literature (Sarkar and Hirani, 2015), (Sarkar and Hirani, 2013), (Sukhwani, et al, 2009), (Sukhwani and Hirani, 2007), (Sukhwani and Hirani, 2008), (Sukhwani and Hirani, 2008), (Hirani and Manjunatha, 2007), (Sukhwani, et al, 2007), (Sukhwani, et al, 2006), (Gupta and Hirani, 2011), . In the present paper, design and analysis of Magnetorheological engine mount has been presented.

2. Literature Analysis

A comparative study of available engine mounts with their advantages and limitations has been described in following sub-sections.

2.1 Passive Elastomeric/Rubber Mount

Elastomeric mounts have been used to isolate vehicle structure from engine vibration since the 1930's (Regis, 1976). Gomes and Pouzada (2002) explained the effect of rubber compound formulation on the dynamic properties of elastomeric mount. To understand the behaviour of the elastomeric mount, it is often (Bernuchon, 1984), (Regis, 1976), (Choudhury, 2004), modelled as a nonlinear spring as function of the excitation frequency. One of such models provided by Rao, *et al.*(2001) is,

$$k_d = \sqrt{k^2 + (c\omega_{dr})^2} \qquad (1)$$

This equation clearly indicates that dynamic stiffness (k_d)is a function of static stiffness (k), damping property (C), and operating frequency. Using the Eq. 1, the variation in the value of dynamic stiffness of elastomeric mount (for k =6.98e7N/m, and c= 6.4e4 Ns/m) with operating frequency is plotted in Fig. 1.

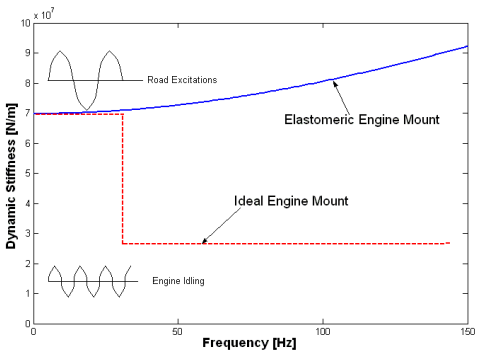

Fig.1 Dynamic Stiffness of Elastomeric Mount

On comparing (Fig. 1) this behaviour of dynamic stiffness with ideal dynamic stiffness, it can be concluded that elastomeric mount is suitable to deal with low frequency and high amplitude vibrations, but it is unable to isolate low-frequency-low amplitude and high-frequency-low-amplitude vibrations.

2.2 Hydraulic Engine Mount (HEM)

Corcoran and Ticks (1984) experimentally compared the performance of hydraulic engine mount with elastomeric mount on the basis of vibratory and acoustic comforts at operator's seat. They measured seat belt acceleration and sound power level for the comparison. They described advantages of hydraulic engine mount over elastomeric mount particularly during low frequency vibration such as engine bounce (motion of the engine with respect to chassis when vehicle is passing over bump) and idle shake (vibrations of engine when engine is in idling condition).

Three-dimensional exploded view of a typical HEM is shown in Fig.2. HEM consists of two fluid-filled chambers connected through a restricted (i.e. Orifice or narrow tubular path also termed as "inertia track") passage. The fluid used in HEM is generally having less viscosity for ease of flow across the chambers. Based on restricted passage, hydraulic mounts can be classified as: HEM with orifice (HEM-O), HEM with Inertia track (HEM-IT) and HEM with Inertia track and Decoupler (HEM-ITD) (Flower, 1985).

Flower, (1985) explained these three hydraulic mounts (HEM-O, HEM-IT and HEM-ITD) using mechanical system models and a set of the equations. However, equations for hydraulic engine mount with inertia track and decoupler were not covered by (Flower, 1985). These equations were detailed by Ushijima, *et al*,(1988). To simplify the understanding of the HEM, low- and high- frequency approaches were described by Adiguna,*et al*, (2003) and Kim and Singh, (1995). Adiguna,*et al*, (2003) provided the equations of HEM-ITD in frequency domain. The details of all three HEMs are described in following subsections.

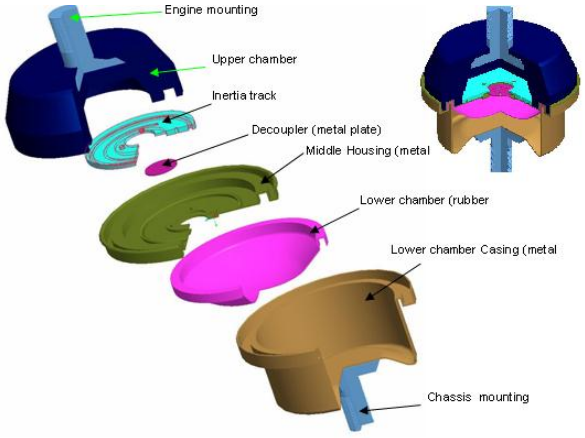

Fig.2 HEM with Inertia Track and Decoupler

2.2.1 HEM with Orifice

The orifice plate which divides the mount in two halves is made up of resilient material as shown in Fig.3a (Singh, 2007). During the operation when mounted engine cause the displacement of the upper chamber, the liquid is forced to pass through the small orifice opening from upper chamber to lower chamber or reverse. During this fluid motion, the resistance offered by the orifice is related to the amplitude of the excitation frequency. During large amplitudes (low frequencies 0 to 30 Hz) more resistance is offered and higher stiffness is exerted. Whereas during the low amplitudes (high frequencies 30 to 250 Hz) the resistance offered is less, so the stiffness is lesser. As per Flower, (1985) the characteristic equation of the HEM with orifice mount can be expressed as:

$$K(\omega_{dr}, j) = k_r + j\omega_{dr} b_r + \frac{A_p^2}{C_1} * \frac{j\omega + \frac{1}{R_o C_2}}{j\omega + \frac{1}{R_o}\left(\frac{1}{C_1} + \frac{1}{C_2}\right)} \quad (2)$$

The dynamic stiffness curve (k_r=2.25e^{5}N/m, b_r=100Ns/m, A_p=0.0025m^2, C_1=3e-^{11}m^5/N, R_o=, C_2=2.6e^{-9}, Amplitude =0.1mm etc.) of HEM-O is shown in fig.4.

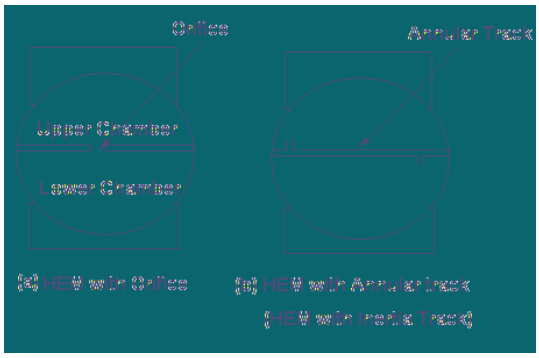

Fig.3 Schematic representation of Hydraulic mounts

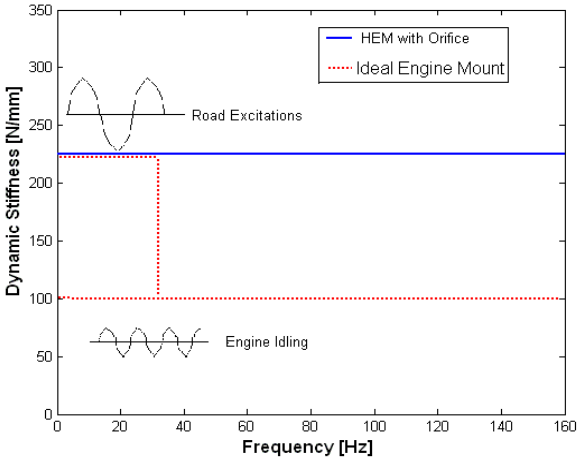

Fig.4 Dynamic Stiffness of HEM-O

Figure 4 illustrates almost constant value of the dynamic stiffness of the HEM-O mount, unlike elastomeric mount which shows increase in dynamic stiffness with increase in operating frequency. The requirement of ideal mount plotted in Fig. 4 indicates that in higher frequency zone HEM-O deviates from ideal mount. Improvement in dynamic performance of hydraulic mount can be achieved by replacing orifice geometry with an annular track as shown in Fig. 3b. HEM with such annular track connection between two chambers is termed as "HEM with Inertia track".

2.2.2 HEM with Inertia Track (HEM-IT)

The inertia track is a long annular pipe joining the two chambers. It is a part of a thin membrane which separates upper and lower chambers (Singh, 2000) or may be an external thin tube joining the chambers (Venezia, 1997).During the low amplitude high frequency vibrations, the displaced fluid is accommodated by thin membrane; hence HEM acts as "Soft HEM". In case of low frequency high amplitude vibrations, the membrane cannot accommodate all the displaced volume of the fluid and fluid enters in inertia track to get transferred from one chamber to other chamber. Long length and small cross sectional area of inertia track offers reasonable resistance to fluid-flow and adds to the stiffness of the mount. As the inertia of the fluid oscillating in the track adds to the total stiffness of the mount, the track is called as inertia track (Singh, 2000). The dynamic stiffness of HEM-IT can be (Ahmadian and Kong, 1999) expressed as,

$$\text{Dynamic stiffness } K^* = |K' + K''| \quad (3)$$

where

$$K' = k_r + A_p^2 \frac{\omega_{dr}^2[I_i\omega_{dr}^2(k_v I_i - b_v^2) - k_v(k_v I_i - R_i^2)]}{(k_v - I_i\omega_{dr}^2)^2 + [\omega_{dr}(R_i + b_v)]^2} \quad (4)$$

$$K'' = (b_r + A_p^2 b_v)\omega_{dr} + A_p^2 \frac{\{k_v^2(R_i - b_v)\omega_{dr} + \omega_{dr}^3[2k_v b_v I_i - b_v^2(R_i + b_v)]\}}{(k_v - I_i\omega_{dr}^2)^2 + [\omega_{dr}(R_i + b_v)]^2} \quad (5)$$

The term Resistance and Inertance expressed in equation 4 and 5 are given as

$$\text{Resistance} = R_i = \frac{32\mu L_i}{A_i} \quad (6)$$

$$\text{Inertance} = I_i = \frac{\rho L_i}{A_i} \quad (7)$$

By putting these expressions of resistance and inertance from equation 6 and 7 into equation 4 and 5, the characteristic equation of dynamic stiffness in terms of Area of Inertia Track (A_i) can be expressed as,

$$K' = k_r + A_p^2 \frac{\omega_{dr}^2[\omega_{dr}^2\rho L_i A_i(k_v\rho L_i - A_i b_v^2) - k_v(k_v\rho L_i A_i - 1024\mu^2 L_i^2)]}{(A_i^2 k_v - \omega_{dr}^2\rho L_i A_i)^2 + [\omega_{dr}(32\mu L_i + A_i b_v)]^2} \quad (8)$$

$$K'' = (b_r + A_p^2 b_v)\omega_{dr} + A_p^2 A_i \frac{\{k_v^2(32\mu L_i - b_v A_i)\omega_{dr} + \omega_{dr}^3[2k_v b_v\rho L_i - b_v^2(32\mu L_i + b_v A_i)]\}}{(A_i^2 k_v - \omega_{dr}^2\rho L_i A_i)^2 + [\omega_{dr}(32\mu L_i + A_i b_v)]^2} \quad (9)$$

Using Eqs. (3-9) the dynamic stiffness curve of HEM-IT versus frequency has been plotted in Fig.5.

The Fig. 5 illustrates that during "low frequency high amplitude" and "high frequency low amplitude" vibrations, the dynamic stiffness of HEM-IT approaches to dynamic stiffness required from an ideal mount. However, such performance is restricted by "notch frequency" (Ahmadian and Kong, 1999)as indicated in Fig. 5 and this observation provide a guideline that operating frequency of vibrations need to be lesser than notch frequency so that "resonance peak (Ahmadian and Kong, 1999)", which occurs just after notch frequency, can be avoided. This kind of HEM is better than elastomeric mount and HEM-O. However, this mount is unable to fulfil the required performance during "idle engine" conditions, as "HEM with Inertia track" shows relatively higher stiffness in lower frequency zone. In such case, engine vibrations pass to the chassis. To solve this problem, HEM with Inertia track and decoupler (Flower, 1985) was introduced.

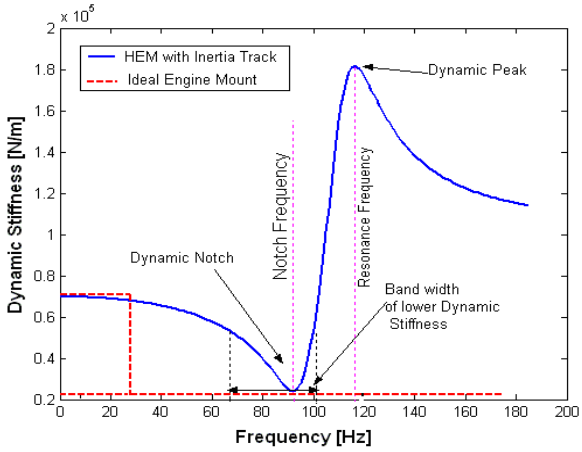

Fig.5 Dynamic Stiffness of HEM-IT

2.2.3 HEM with Inertia Track and Decoupler

HEM with Inertia track and decoupler (HEM-ITD), consists of two fluid-filled chambers connected through a decoupler and inertia track as shown in Fig.6. The decoupler plate has flexibility to travel within its cage. During floating condition of decoupler-plate, fluid flows freely. However once the plate rests in the cage, the fluid passes through the inertia track. In other words, during small amplitude excitations, the fluid passes freely through the decoupler from one chamber to other chamber, giving the low damping and stiffness characteristics. Fluid is forced through the inertia track during large amplitude vibrations, as the decoupler rest at bottom in its cage. To understand the complete dynamic behaviour of "HEM-ITD", it is necessary to model this HEM. The lumped parameter model of HEM-ITD is shown in Fig.7a. F_{in} is the input excitation force from the engine side and F_T is the transmitted force to the chassis. A_p (~2500mm^2) is the effective piston area which pumps the fluid from upper chamber to lower chamber. The k_r (225N/mm) and b_r (0.1e3Ns/m) are elastic stiffness and damping coefficient of upper chamber. C_1 (2.5e-4 mm^5/N) and C_2 (2.5e-6 mm^5/N) are the compliance of the upper and lower chambers respectively.

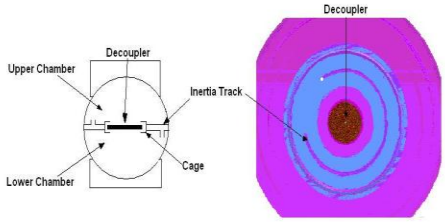

Fig.6 Schematic diagram of HEM-ITD

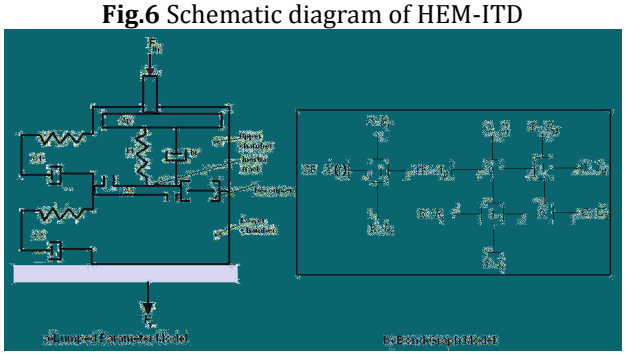

Fig.7 Lumped Parameter Model and Bond graph model of HEM-ITD

The bond graph diagram, which helps to derive mathematical differential equation, for the HEM-ITD is as shown in Fig.7b. In this bond graph, generalized variable 'source of flow (SF)', which is also known as power variable, has been used. In engine mount, this SF is the input to the system from engine which causes the flow inside the upper chamber. Along with the power variables, there are two more generalized variables called momentum p(t) and displacement Q(t). These are time integral of an effort and flow respectively. Terms 0 and 1 shows the 0-junction and 1 junction. In 0-junction the efforts are equal and algebraic sum of the flow is always zero (Thoma). In a 1-junction, the flows are equal and algebraic sum of effort is always zero (Thoma). The symbol ⇀ is used to indicate the flow of energy. The upper chamber acts as piston A_p which is equivalent to a transformer function (TF). After the transformer function the flow differs which is indicated by 0-junction. The flow Q_i and Q_d is the inertia track flow and decoupler flow which shows inertia element (I) and the resistance element (R). C elements are the capacity or capacitance element.

The vibration at the top of the engine mount displaces the fluid of the top chamber. The displaced fluid by the piston area A_p causes the bulging of upper chamber as well as flow through the inertia track and decoupler. The bulging is taken care by the parameter compliance C_1.The continuity equation for upper chamber becomes

$$C_1\dot{P}_1 = A_p\dot{X} - Q_i - Q_d \qquad (10)$$

Flow through the inertia track and decoupler enters the lower chamber which results in bulging of the lower chamber. The continuity equation of the lower chamber becomes

$$C_2\dot{P}_2 = Q_i + Q_d \quad (11)$$

Flow through inertia track and decoupler occur because of the pressure difference between the upper and lower chambers. Therefore momentum equations for inertia track and decoupler are given by 12 and 13 respectively.

$$P_1 - P_2 = I_i\dot{Q}_i + R_iQ_i \quad (12)$$

$$P_1 - P_2 = I_d\dot{Q}_d + R_dQ_d \quad (13)$$

To simplify the problem, it is analyzed in two different domains (Singh, *et. al*, 1992).The 'free floating decoupler' is characterized by low amplitude vibrations and 'fixed decoupler' is defined by high amplitude vibrations.

2.2.3 A. Free Floating Decoupler

Free floating condition of decoupler occurs when it does not contact the cage and almost complete flow passes freely through the decoupler, leaving negligible flow to pass through the inertia track (Q_i=0)(Singh, *et. al*, 1992). The continuity equations 10 and 11, for small amplitude high frequency become,

$$C_1\dot{P}_1 = A_p\dot{X} - Q_d \quad (14)$$

$$C_2\dot{P}_2 = Q_d \quad (15)$$

and the momentum equation 12 and 13 gives,

$$P_1 - P_2 = I_d\dot{Q}_d + R_dQ_d \quad (16)$$

By reframing the equations derived from the Bond graph (Fig 7b) excitation force equation becomes,

$$F = k_rX + b_r\dot{X} + A_pP_1 \quad (17)$$

Let us assume that each system variable can be expressed by sinusoidal form as shown in Eq. (18). Such representation helps to express the equations of HEM-ITD in terms of input vibration amplitudes X and the disturbing frequency ω_{dr}.

$$\begin{aligned} P_1 &= \tilde{P}_1e^{j\omega_{dr}t} \\ P_2 &= \tilde{P}_2e^{j\omega_{dr}t} \\ Q_d &= \tilde{Q}_de^{j\omega_{dr}t} \\ X &= \tilde{X}e^{j\omega_{dr}t} \end{aligned} \quad (18)$$

On differentiating with respect to time,

$$\begin{aligned} \dot{P}_1 &= j\omega_{dr}\tilde{P}_1e^{j\omega_{dr}t} \\ \dot{P}_2 &= j\omega_{dr}\tilde{P}_2e^{j\omega_{dr}t} \\ \dot{X} &= j\omega_{dr}\tilde{X}e^{j\omega_{dr}t} \end{aligned} \quad (19)$$

Now the continuity equation 14 becomes,

$$\begin{aligned} &C_1\dot{P}_1 = A_p\dot{X} - Q_d \\ &C_1j\omega_{dr}\tilde{P}_1e^{j\omega_{dr}t} = A_pj\omega_{dr}\tilde{X}e^{j\omega_{dr}t} - \tilde{Q}_de^{j\omega_{dr}t} \\ &\tilde{P}_1 = \frac{A_p}{C_1}\tilde{X} + j\frac{1}{\omega_{dr}C_1}\tilde{Q}_d \end{aligned} \quad (20)$$

Second continuity equation (Eq. 15),

$$\begin{aligned} &C_2\dot{P}_2 = Q_d \\ &C_2j\omega_{dr}\tilde{P}_1e^{j\omega_{dr}t} = \tilde{Q}_de^{j\omega_{dr}t} \\ &\tilde{P}_2 = -j\frac{1}{\omega_{dr}C_2}\tilde{Q}_d \end{aligned} \quad (21)$$

On substituting Eq. (20) and Eq. (21) into Eq. (16),

$$\frac{A_p}{C_1}\tilde{X} + j\frac{1}{\omega_{dr}C_1}\tilde{Q}_d + j\frac{1}{\omega_{dr}C_2}\tilde{Q}_d = j\omega_{dr}I_d\tilde{Q}_d + R_d\tilde{Q}_d$$

$$\text{or } \frac{A_p}{C_1}\tilde{X} = \left(R_d + j\left(I_d\omega_{dr} - \frac{1}{\omega_{dr}C_1} - \frac{1}{\omega_{dr}C_2}\right)\right)\tilde{Q}_d$$

$$\text{or } \tilde{Q}_d = \frac{\frac{A_p}{C_1}\tilde{X}}{R_d + j\left(I_d\omega_{dr} - \frac{1}{\omega_{dr}C_1} - \frac{1}{\omega_{dr}C_2}\right)}$$

$$\text{or, } \tilde{Q}_d = \frac{A_pC_2\omega_{dr}}{R_dC_1C_2\omega_{dr} + j(I_dC_1C_2\omega_{dr}^2 - C_2 - C_1)}\tilde{X} \quad (22)$$

Putting value of $\tilde{Q}_d$ from equation 22 into the equations (20) and (21),

$$\tilde{P}_1 = \left(\frac{A_p}{C_1} + \frac{A_pC_2j}{R_dC_1^2C_2\omega_{dr} + j(I_dC_1^2C_2\omega_{dr}^2 - C_1C_2 - C_1^2)}\right)\tilde{X} \quad (23)$$

$$\tilde{P}_2 = \left(\frac{-A_pj}{R_dC_1C_2\omega_{dr} + j(I_dC_1C_2\omega_{dr}^2 - C_2 - C_1)}\right)\tilde{X} \quad (24)$$

Equations 23 and 24 give the pressures inside the upper and lower chamber respectively in terms of input displacement amplitude. Similarly, writing the equation of the applied force (Eq. 17) in terms of frequency, and putting the value of P_1 from equation (23),

$$\tilde{F}e^{j\omega_{dr}t} = k_r\tilde{X}e^{j\omega_{dr}t} + j\omega_{dr}b_r\tilde{X}e^{j\omega_{dr}t} + A_p\left(\left(\frac{A_p}{C_1} + \frac{A_pC_2j}{R_dC_1^2C_2\omega_{dr} + j(I_dC_1^2C_2\omega_{dr}^2 - C_1C_2 - C_1^2)}\right)\tilde{X}\right)e^{j\omega_{dr}t}$$

On diving the applied force $\tilde{F}$ by $\tilde{X}$, the characteristic equation of dynamic stiffness, $K(\omega_{dr}, j)$

$$K(\omega_{dr}, j) = k_r + j\omega_{dr}b_r + \frac{A_p^2}{C_1} + \frac{A_p^2C_2j}{R_dC_1^2C_2\omega_{dr} + j(I_dC_1^2C_2\omega_{dr}^2 - C_1C_2 - C_1^2)} \quad (25)$$

The real part of the characteristic equation (25) is called as Dynamic stiffness.

Table1: Comparison of Engine Mount

Sr. No	Performance Zone → / Mount Type ↓	Low frequency large amplitude Vibrations (road excitations)	Low frequency low amplitude Vibrations (Engine idling)	High Frequency low amplitude Vibration (Engine running)	Remark
1 to 5 scale with 5 as the Best and 1 as worst.					
A	Elastomeric mount	3	2	2	Dynamic stiffness increases along with frequency
B	HEM with Orifice	4	3	3	Dynamic stiffness is almost constant
C	HEM with Inertia track	5	3	3	After Notch Frequency dynamic stiffness shows dynamic peak
D	HEM with inertia track and decoupler	5	5	3	High frequency Resonance of Dynamic Stiffness
E	Smart Mount	5	5	5	

2.2.3 B. Fixed Decoupler

It is expected that during large amplitude excitations the decoupler will spend the majority of time against the cage, and almost complete flow will pass through the inertia track. In such a situation terms Q_d and R_d will be equal to zero and equations 10 and 11 can be expressed in the following manner,

$$C_1\dot{P}_1 = A_p\dot{X} - Q_i \quad (26)$$

$$C_2\dot{P}_2 = Q_i \quad (27)$$

By converting these equations in frequency domain, it is possible to derive

$$K(\omega_{dr} j) = k_r + b_r\omega_{dr} j + \frac{A_p^2}{C_1} + \frac{C_2 A_p^2 j}{R_i C_1^2 C_2 \omega_{dr} + j(I_i C_1^2 C_2 \omega_{dr}^2 - C_2 C_1 - C_1^2)} \quad (28)$$

By using the dynamic stiffness Eq. (25) and Eq. (28), the graph plotted against the frequency is shown in Fig.8. In lower frequency zone, either decoupler or inertia track defines the property of the engine mount depending on the amplitude of excitation. During road excitations, fluid will flow through the inertia track giving higher values of the stiffness represented by the solid line (green colour). When the engine is idling without any disturbance from the road, the fluid will flow through the decoupler giving lower value of stiffness represented by dotted line (blue colour). It solves the problem of the engine idle shake which was present in the HEM with inertia track. However, this figure indicates that the dynamic stiffness provided by the free decoupler exceeds the value given by inertia track. In the high frequency zone, the amplitudes of vibration are low therefore decoupler represents the property of the engine mount. In this condition, inertia track will not be active as the magnitude of excitations amplitude is low.

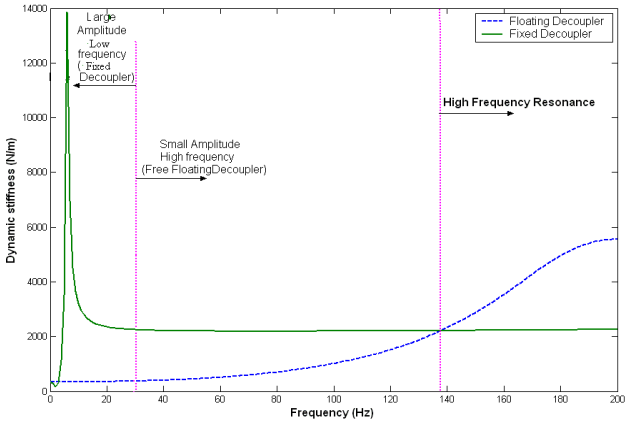

Fig. 8 Dynamic Stiffness of HEM –ITD

Thus it is observed that the HEM-ITD exhibit the high frequency resonance which is difficult to control as decoupler is sensitive only to amplitude, which is lower

in high frequency zone (Adiguna, *et al*, 2003), (Kim and Singh, 1995), (Colgate, et al, 1995). The HEM-ITD solves the problem of engine idling (2.2.3) if the assumptions of zero flow from inertia track during free decoupler and zero flow through decoupler during fixed decoupler are valid assumptions. However literature (Adiguna, *et al*, 2003), (Singh, 2007), (Ohadi and Maghsoodi, 2007) does not support practicality of these assumptions. In short, all three types of hydraulic mounts have limited operating range, as indicated in Table 1.The aim of the present paper is to target a smart mount which will perform similar to Ideal mount. Next subheading describes smart mounts to provide ideal behaviour from engine mount.

3. Smart Mount System

A typical architecture of a smart mount system is shown in Fig.9. Figure 9a shows a series combination of HEM and actuator, while Fig. 9b illustrates actuator as a part of HEM. This figure-9 indicates that signals from vibration sensors (mounted on chassis and engine) are passed to controller, which in turn instructs the actuator to counteract the vibrating energy. The vibration sensor may be a force sensor or an accelerometer. The controller adjusts the amplitude and phase of the force to be imposed by the actuator considering the behaviour of HEM to minimize the vibrations. Actuator adds or reduces the force applied against the input force offered by HEM. In the present design of smart mount, "HEM with inertia track" as basic structure has selected as it involves less number of non-linear parameters compared to the "HEM with inertia track and decoupler", therefore its control will be much easier.

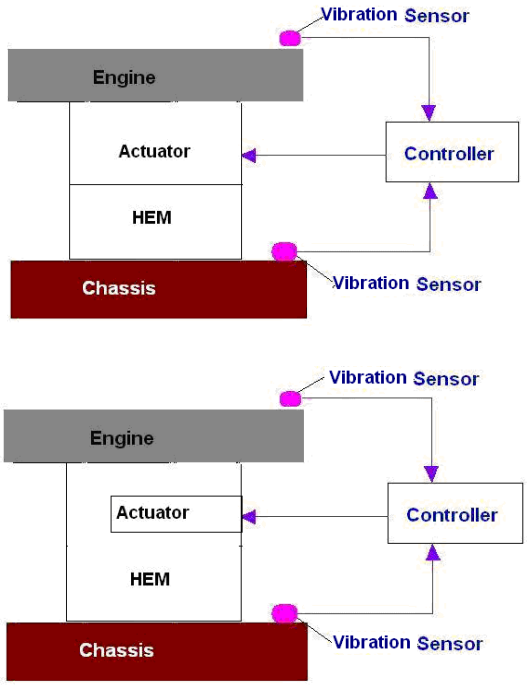

Fig. 9 Schematic representation of Smart Mount

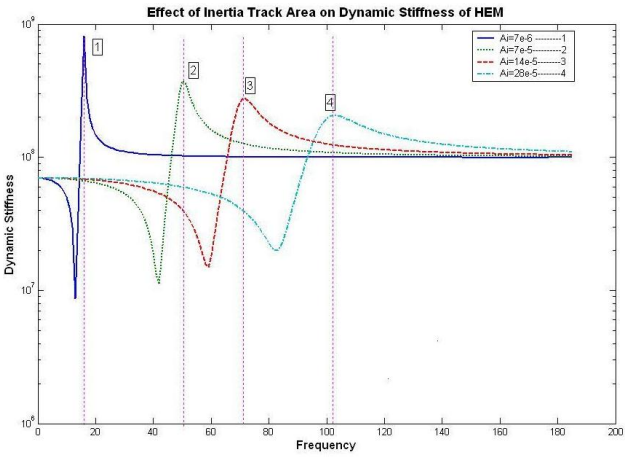

Fig. 10 Effect of Inertia track area on the Dynamic stiffness of HEM

The performance of the dynamic stiffness depends on the cross-sectional area of inertia track, which is given by equations 8 and 9. As it is very difficult to predict the behaviour of Inertia track area variation on the dynamic stiffness just by looking at the equations, MATLAB is used to plot the behaviour of the dynamic stiffness with area variation. The plot is as shown in the Fig. 10. This figure clearly shows that on increasing cross-sectional area of the inertia track, the peak values of dynamic stiffness decreases. Moreover increase in the area of inertia track shifts the 'peak' of dynamic stiffness toward the higher frequency zone. Thus by controlling the area, it is possible to control the dynamic 'notch frequency'.

Ahmadian and Kong, (1995) adopted a mechanism to control the area of inertia track. He explained the effect of complete closing of the inertia track on the dynamic stiffness. By putting the value of Inertia track equal to zero in equations 8 and 9, the characteristics equation of dynamic stiffness of closed HEM-IT becomes,

$$K^{*}_{closed} = (k_r + A_p^2 k_v) + j\omega_{dr}(b_r + A_p^2 b_v) \qquad (29)$$

Closing of inertia track after the notch avoids the resonance peak as shown in fig 11. The dynamic stiffness of closed inertia track is almost constant throughout the frequency. Also at every frequency, the value of dynamic stiffness of closed inertia track HEM is greater than the HEM with open inertia track (Ahmadian and Kong, 1995), (Kong, et al, 2005).As per Ahmadian and Kong, (1995) during the lower frequencies where amplitudes are larger, the closed valve condition provides higher dynamic stiffness and in higher frequency range (till the notch frequency), open valve offers lesser dynamic stiffness. At frequency greater than notch frequency again closed valve position is preferred to avoid the resonance peak (Ahmadian and Kong, 1995). To turn on and off the valve (Ahmadian and Kong, 1995) used a controllable Magneto Rheological Fluid (MRF). The fluid needs minimum energy i.e. magnetic induction of 1.3-2.0

Tesla which can be produced by 12V battery and minimum time (30msec) to respond to signal. Effort made by Ahmadian and Kong (1995) is appreciable, but still the performance of the mount does not match the performance of ideal mount. Engine idling and the performance after the notch frequency deviates from that of ideal mount.

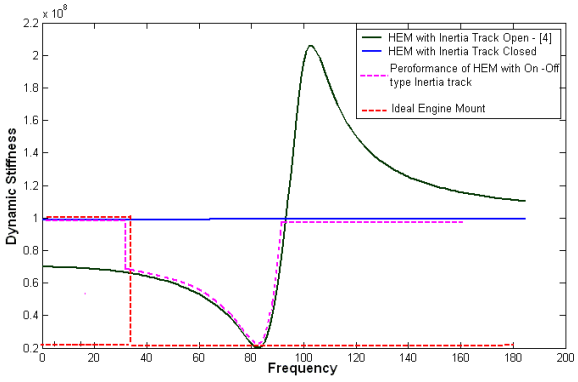

Fig. 11 Effect of Closed Inertia track on the Dynamic stiffness of HEM

3.1 Design Concept of Smart Mount

Study in previous paragraphs indicates that the dynamic notch and the resonance peak can be controlled by varying the area of inertia track area. In the present study controlling the area of inertia track has been targeted and mount which has such features is named as "Smart mount". Figure 12 shows that a close control on the area provides dynamic stiffness (shown by blue dotted line) approaching to the dynamic stiffness of idle mount. The transmissibility curves for Smart Mount, shown by blue dotted line, are plotted in fig.13. The red dotted line shows the performance of the ideal mount. These two figures (Figs. 12-13) encourage designing an engine mount having continuous control on the area of inertia track area. Such a design is explained in sub-section.

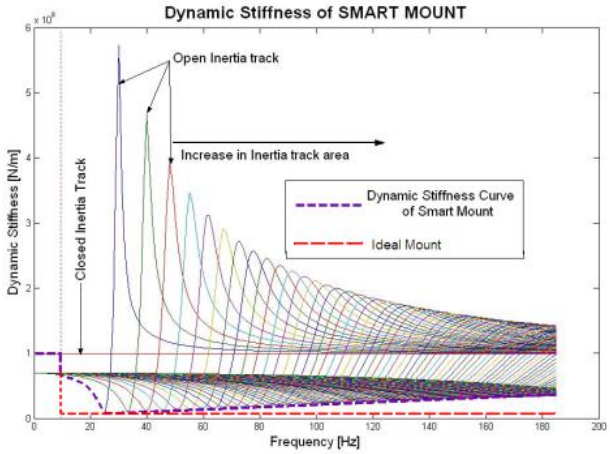

Fig. 12 Dynamic stiffness with Variable Inertia Track Area

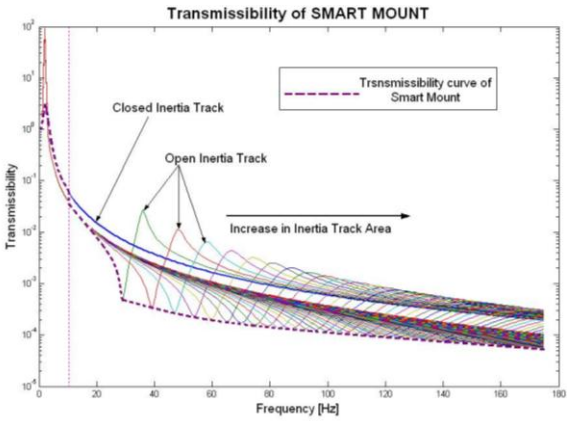

Fig. 13 Transmissibility with Variable Inertia Track Area

3.1.1 Variable Area of Inertia Track

In the present study, two concepts to dynamically controlled area of inertia track have been evolved. The first concept is to provide a valve on the inertia track which will be controlled by the sensors and the controller. To provide a valve on the inertia track is again a difficult task as inertia track is a part of mid housing and located inside the HEM. To solve this problem, HEM with external inertia track is useful solution. The schematic representation of the first concept is as shown in fig.14. This involves a valve which is fitted on the inertia track, a controller mechanism which will operate the valve. This concept requires extra space compared to elastomeric and hydraulic mounts. The fitment of the valve on the inertia track is again a difficult task as inertia track is very small in diameter (1.5 to 3mm ID). External inertia track if fitted with a small valve again has a drawback or reliability as it is prone to the leakages through the joineries. This concept in thus put a question marks on its application. The target is to now change the small area of the track without putting any additional part on it.

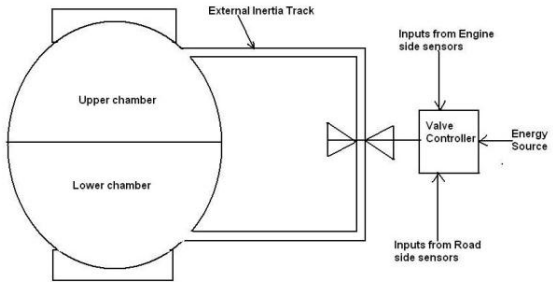

Fig. 14 Schematic valve mechanism for controlling area of inertia track Concept 1

To overcome the problem, the second concept is hypothesized, which is shown in fig.15. In this concept, the controllable MR fluid (MRF132) is filled inside the mount. External inertia track is passed through the core of the electromagnet. The change in value of

electric current supplied to electromagnet varies the magnet field (Li, et al, 1999) and affects the MRF particle chains. These chains restrict the movement of the fluid and thereby vary the shear strength of the suspension. MR fluids routinely exhibit shear strengths ranging between 50 to 100 kPa (Carlson) for applied magnetic field of 150 - 250 kA / m (for magnetic induction of 1.3-2.0 Tesla). The behaviour of such a controllable fluid is often represented as a Bingham plastic having variable shear strength.

$$\tau = \tau_{ys} + \eta\dot{\gamma} \tag{30}$$

Where yield stress, τ_{ys}, is expressed by

$$\tau_{ys} = 6^{1/2} * \phi * \mu_o * M_s^{1/2} * H^{3/2} \tag{31}$$

The relationship between the magnetic field intensity (*H)*, and voltage (*V*) is given by

$$H = nI \text{ (32) } H = n * \frac{V * \pi * D^2}{4 * \rho_{Cu} * l} \tag{33}$$

By putting the value of magnetic field intensity from equation 33 into equation 31, the relationship between the yield stress and voltage is given as,

$$\tau_{ys} = 6^{1/2} * \phi * \mu_o * M_s^{1/2} * \left(n * \frac{V * \pi * D^2}{4 * \rho_{Cu} * l} \right)^{3/2} \tag{34}$$

This equation indicates that increasing value of V increases τ_{ys}, which in turn increases the resistance against fluid flow. Such physical effect can be analyzed using 'valve mode' mechanism (Carlson).

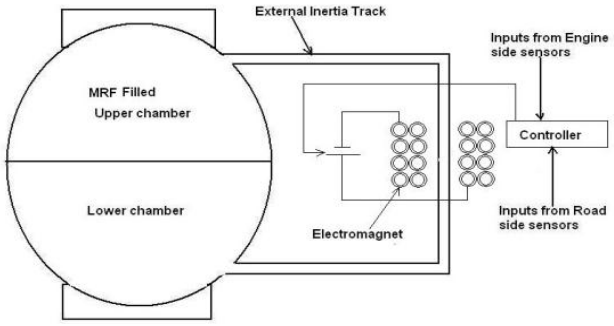

Fig. 15 Schematic valve mechanism for controlling area of inertia track Concept 2

To apply the concept of hardening of MR fluid on engine mount let us consider the displacement applied either at the base or at the top of the engine mount, which in turn vary the pressure inside the chambers. The pressure difference can be expressed in terms field independent viscous component (White, 1994) and field induced yield stress component (Carlson), such as, Field Independent Component,

$$\Delta P_\eta = \frac{32\mu L_i Q_i}{\rho g A_i} \tag{35}$$

Field Dependent Component,

$$\Delta P_\tau = \frac{c\tau_{ys} L_i}{g} \tag{36}$$

Where,

$$c = 2 \qquad for\left(\Delta P_\tau / \Delta P_\eta \right) < 1$$
$$c_{\max} = 3 \qquad for\left(\Delta P_\tau / \Delta P_\eta \right) > 3 \tag{37}$$

In case of normal fluids used for HEM, the pressure difference which causes the flow is given by the Eq. (35).In case of different types of HEM, the less stiffness is produced by less restricted flow across the chambers. This effect can be produced by larger area of the inertia track and less viscosity of the fluid. For getting the higher stiffness of the mount the restriction to the flow across the chambers should be more. This effect is produced by the lesser area for flow and higher viscosity of the fluid.

The behaviour of the pressure difference across two chambers with variation of the magnetic field intensity, expressed in Eq. 36, is shown in Fig 16. It shows that the pressure difference between upper chamber and lower chamber increases along with the increase in the yield stress of the MRF passing through the inertia track. At the saturation limit of MRF, the fluid becomes solid and the MRF based smart mount will act as elastomeric mount which will support the road shocks. By reducing the intensity of magnetic field (i.e. by reducing the applied voltage to the electromagnet), the mount stiffness can be reduced to achieve the dynamic notch.

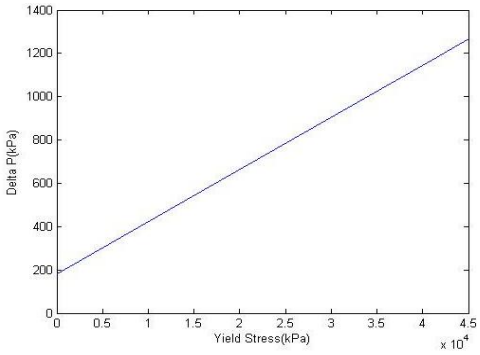

Fig. 16 Delta P as a function of yield stress

By summing Eqs. (35-36), total pressure drop is expressed as,

$$\Delta P = \frac{32\mu L_i Q_i}{\rho g A_i} + \frac{c\tau_{ys} L_i}{g} \tag{38}$$

This equation shows that increasing τ_{ys} and decreasing A_i the pressure difference increases. The behaviour of

pressure difference across chambers is plotted against the change in area of inertia track as shown in Fig. 17. These results indicate that MRF-based engine mounts perform as good as an ideal engine mount.

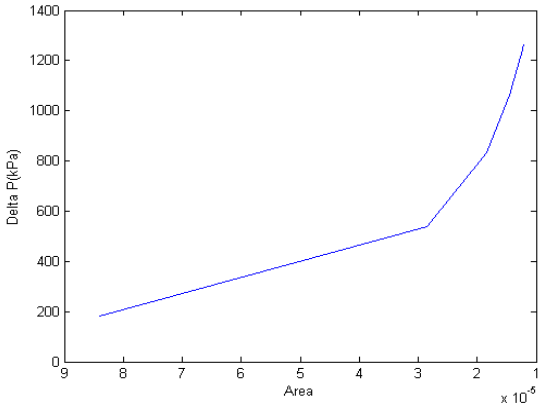

Fig. 17 Delta P as a function of area of inertia track

Conclusions

In the present study, the performance requirements from an ideal engine mount have been detailed. Commonly used elastomeric and hydraulic mounts have analyzed, and compared with smart engine mount. The design and analysis of Magnetorheological fluid (MRF) based engine mount have been described. The results of dynamic stiffness and transmissibility of MRF-smart mount have been compared with ideal engine mount. Finally it can be concluded that:

- Hydraulic mount with inertia track can be used as MRF-smart mount by replacing hydraulic fluid with Magnetorheological fluids, and
- Dynamic stiffness and transmissibility of MRF-smart mount is equivalent to the performance required from an ideal mount. Therefore MRF-mount can be treated as an "ideal engine mount".

References

A. R. Ohadi, G. Maghsoodi,(2007), Simulation of engine vibration on nonlinear hydraulic engine mounts,*Journal of Vibration and Acoustics,* 129, pp. 417-424.

C.Sarkar, H.Hirani, (2013), Theoretical and experimental studies on a magnetorheological brake operating under compression plus shear mode, *Smart Materials and Structures*, 22, art. no. 115032.

C.Sarkar, H.Hirani, (2013), Synthesis and characterization of antifriction magnetorheological fluids for brake, *Defence Science Journal*, 63, pp. 408-412.

C.Sarkar, H. Hirani, (2013), Design of a squeeze film magnetorheological brake considering compression enhanced shear yield stress of magnetorheological fluid, *Journal of Physics: Conference Series*, 412, 012045.

C.Sarkar, H.Hirani, (2015), Synthesis and characterization of nano-copper-powder based magnetorheological fluids for brake, International Journal of Scientific Engineering and Technology, 4, pp. 76-82.

C. Sarkar, H. Hirani, (2015), Effect of particle size on shear stress of magnetorheological fluids, *Smart Science,* (in press).

C. Sarkar, H. Hirani, (2015), Development of magnetorheological brake with slotted disc, *Proc. IMechE, Part D: Journal of Automobile Engineering*, (in press).

D. Carlson, D. Catanzarite, K. Clair, Commercial magneto-rheological fluid devices, *Lord Corporation. www.lord.com*.

F. M. White, (1994),Fluid Mechanics,*McGraw-Hill, Inc., Toronto*.

G. Kim, R. Singh, (1995), A study of passive and adaptive hydraulic engine mount systems with emphasis on non-linear characteristics. *Journal of Sound and Vibration*, 179, pp 427–453.

H. Hirani, C. S. Manjunatha, (2007), Performance evaluation of magnetorheological fluid variable valve, *Proc. of the Institution of Mechanical Engineers, Part D, Journal of Automobile Engineering*, 221, pp. 83-93.

H. Adiguna, M. Tiwari, R. Singh, H.Tseng, D. Hrovat, (2003), Transient response of a hydraulic engine mount, *Journal of Sound and Vibration*,268, pp 217–248.

J. Thoma, Simulation by bond-graphs, Springer-Verlag publications, ISBN0-387-51640-9.

J. Colgate, C. Chiou, W. Liu, L. Keer, (1995), Modelling of hydraulic engine mount focusing on response to sinusoidal and composite excitations,*Journal of Sound and Vibration*, 184, pp.503-528.

J. Venezia,(1997), Vibration modelling and experimental analysis of a locomotive cab,*Master Thesis, Virginia Polytechnic Institute and State University.*

M. Ahmadian, Y. Kong, (1999), Performance analysis of magneto rheological mounts,*Journal of Intelligent Material Systems and Structures*. 10, pp.248-256.

M. Bernuchon, (1984),Anew generation of engine mount. *SAE Technical Paper,* 840259.

M. D. Rao, S. Gruenberg, D. Griffiths, (2001), Measurement of dynamic parameters of automotive exhaust hanger, *Society of Automotive Engineers*, 01NVC-121 (8pp).

M. J. M. Gomes,A. S. Pouzada, (2002), Dynamic behaviour of rubber compounds for engine mounts,*Key Engineering Materials,*230-232, pp. 303-306.

P. E. Corcoran, G. H. Ticks, (1984), Hydraulic engine mount characteristics,*SAE Technical Paper,* 840407.

P.R. Choudhury, (2004), Workshop on Dynamic Testing of Rubber Sample and Rubber Products for Automobile Industry, May.

R. Singh, (2000), Dynamic design of automotive systems: Engine mounts and structural joints, *Sadhana*, 25, pp. 319-330.

R. Singh, (2007), Anatomy of a Real-Life Non-Linear Device: Hydraulic Engine Mount, *International Modal Analysis Conference, Orlando, FL*.

R. Singh, G. Kim, P. Ravindra, (1992), Linear analysis of automotive hydra-mechanical mount with emphasis on decoupler characteristics. *Journal of Sound and Vibration*, 158, pp.219-243.

Regis, (1976), Charles design of elastomeric vibration isolation mounting system for internal combustion engines, *SAE Technical Paper,* 760431.

S. Gupta, H. Hirani, (2011), Optimization of magnetorheological brake, *ASME/STLE 2011 International Joint Tribology Conference*, pp 405-406.

T. Q. Thanh, K.Kwan,Y. Kong, (2006), Optimal parameter control for multi-signal of semi-active engine mount,*The 1st International Forum on Strategic Technology (IFOST)*, pp. 20-23.

T. Ushijima, K. Takano, H. Kojima,(1998), High performance hydraulic mount for improving vehicle noise and vibration,*SAE Technical Paper Series*, 880073.

V. K. Sukhwani, V. Lakshmi, H. Hirani, (2006), Performance evaluation of MR brake: an experimental study, *Indian Journal of Tribology*, pp. 67-52.

V. K. Sukhwani, H. Hirani, T. Singh, (2007), Synthesis of magnetorheological grease, *Greasetech India*.

V. K. Sukhwani, H. Hirani, (2007), Synthesis and characterization of low cost magnetorheological (MR) fluids, *The 14th International Symposium on: Smart Structures and Materials & Nondestructive Evaluation and*

V.K.Sukhwani, H.Hirani, (2008), A comparative study of magnetorheological-fluid-brake and magnetorheological-grease-brake, *Tribology Online*, 3, pp. 31-35.

V.K.Sukhwani, H.Hirani, T.Singh, (2008), Synthesis and performance evaluation of MR grease, *NLGI Spokesman*,71.

V.K.Sukhwani, H. Hirani, (2008), Design, development and performance evaluation of high speed MR brake, *Proc. Institute Mech. Engineers., Part L, Journal of Materials: Design and Applications*, 222,pp.73-82.

V. K. Sukhwani, H. Hirani, T. Singh, (2009), Performance evaluation of a magnetorheological grease brake, *Greasetech India*, 9,pp. 5-11.

Y. Yu, S. Peelamedu, N. Naganathan, R. Dukkipati, (2001), Automotive vehicle engine mounting systems: A survey,*Journal of Dynamic Systems, Measurement, and Control*,123, pp.186-194.

Y. Kong, Y. Kim, B. Yang, M. Ahmadian, (2005), Optimal design of engine mount using an enhanced genetic algorithm with simplex method,*Vehicle System Dynamics*, 43, pp. 57-81.

W. C. Flower, (1985), Understanding hydraulic mounts for improved vehicle noise, vibration and ride qualities,*SAE Technical Paper,* 850975.

W. H. Li, G. Chen, S. Yeo, (1999), Viscoelastic properties of MR Fluids, Smart Materials and Structures, 8, pp. 460-468.

Volume 2, Issue 4 (2014) 784-789 ISSN 2347 - 3258
International Journal of Advance Research and Innovation

Methods for Improving Thermodynamic Performance of Vapour Compression Refrigeration Systems Using R134a Ecofriendly Refrigerant in Primary Circuit and Three Nano Particles Mixed with R718 used in Secondary Evaporator Circuit for Reducing Global Warming and Ozone Depletion

R. S. Mishra
Department of Mechanical Engineering, Delhi Technological University, New Delhi, India

Article Info

Article history:
Received 30 September 2014
Received in revised form
20 October 2014
Accepted 20 November 2014
Available online 15 December 2014

Keywords

Vapour Compression Refrigeration Systems,
Energy and Exergy Analysis,
First and Second Law Analysis,,
Irreversibility Analysis,
Efficiency Improvement using Nano Particles

Abstract

The methods for improving first law and second law efficiency have been considered in this paper by using three nano particles mixed with R718 refrigerants mixed in the secondary circuit and R134a in primary circuit is investigated in this paper. Detailed energy and exergy analysis for calculating performance parameters in the vapour compression refrigeration systems have been carried out. The numerical computations using three nano particles (i.e. CuO, Al_2O_3 and TiO_2) have been carried and it was observed that first law and second law efficiency improved from 15% to 18% and improvements in overall heat transfer coefficient in evaporator is ranging 79.58% to 91.41% using nano materials as compared to without nano particles.

Nomenclature

COP	Coefficient of Performance (Non-Dimensional)
VCR	Vapour Compression Refrigeration
CFC	Chlorofluorocarbon
HCFC	Hydrochlorofluorocarbon
Q	Rate of Heat Transfer (kW)
W	Work Rate (kW)
T	Temperature (K)
Δ	Efficiency Defect (Non-Dimensional)
ΔT_{sc}	Degree of Sub cooling
EP	Exergy Rate of Product (kW)
EV	Expansion Valve
EP	Evaporator

Subscript

e	Evaporator
comp	Compressor
H	Specific Enthalpy (kJ/kg)
P	Pressure (kPa)
IR	Irreversibility (kW)
E_x	Exergy Rate of Fluid (kW)
M	Mass Flow Rate (kg/s)
S	Specific Entropy (kJ/kgK)
EF	Exergy Rate of Fuel (kW)
EL	Exergy Loss Rate (kW)
H	Efficiency (Non-Dimensional)
R	Refrigerant, Space to be Cooled
ex	Exergetic
ev	Expansion Valve
C	Condenser
sc	Subcooler
K	kth Component

Corresponding Author,
E-mail address: professor_rsmishra@yahoo.co.in
All rights reserved: http://www.ijari.org

1. Introduction

Refrigeration is a technology which absorbs heat at low temperature and provides temperature below the surrounding by rejecting heat to the surrounding at higher temperature. Simple vapour compression system which consists of four major components compressor, expansion valve, condenser and evaporator in which total cooling load is carried at one temperature by single evaporator but in many applications like large hotels, food storage and food processing plants, food items are stored in different compartment and at different temperatures. Therefore there is need of multi evaporator vapour compression refrigeration system. The systems under vapour compression technology consume huge amount of electricity, this problem can be solved by improving performance of system.

Performance of systems based on vapour compression refrigeration technology can be improved by following:

- Refrigeration effect can also be increased using nano particles mixed with R718 in the secondary evaporator circuit and R134a in the primary evaporator circuit
- Evaporator overall heat transfer coefficient is also increases which enhanced refrigeration effect due to nano particles mixed with R718 in the secondary evaporator circuit and R134a in the primary evaporator circuit

Vapour compression refrigeration system based applications make use of refrigerants which are responsible for greenhouse gases, global warming and ozone layer depletion. Montreal protocol was signed on the issue of

substances that are responsible for depleting Ozone layer and discovered how much consumption and production of ozone depletion substances took place during certain time period for both developed and developing countries. Another protocol named as Kyoto aimed to control emission of green house gases in 1997[1]. The relationship between ozone depletion potential and global warming potential is the major concern in the field of GRT (green refrigeration technology) so Kyoto proposed new refrigerants having lower value of ODP and GWP. Internationally a program being pursued to phase out refrigerants having high chlorine content for the sake of global environmental problems [2].Due to presence of high chlorine content ,high global warming potential and ozone depletion potential after 90's CFC and HCFC refrigerants have been restricted. Thus, HFC refrigerants are used nowadays, showing much lower global warming potential value, but still high with respect to non-fluorine refrigerants. Lots of research work has been done for replacing "old" refrigerants with "new" refrigerants [3-8]and it was observed that researchers have gone through detailed first law analysis in terms of coefficient of performance and second law analysis in term of exergetic efficiency of simple vapour compression refrigeration system with single evaporator. Researchers did not go through the irreversibility analysis (second law analysis) of followings: Simple VCR with liquid vapour heat exchanger , flash intercooler, flash chamber, water intercooler, liquid subcooler and stages in compression(double stage and triple stage)multiple evaporators systems with multi-stage expansion and compound compression in vapour compression refrigeration systems detailed analysis of vapour compression refrigeration systems using several new ecofriendly refrigerants is required. For improving thermal performance of vapour compression refrigeration systems both multiple evaporator system by using liquid vapour heat exchanger for improving: First law efficiency (COP) , second law efficiency (Exergetic efficiency) and Reduction of system defect in components of system in terms of exergy destruction ratio which results into reduction of work inputis also required (30).

2. Literature Review

Reddy et al. [9] conducted numerical experiments on vapour compression refrigeration system using R134a, R143a, R152a, R404A, R410A, R502 and R507A , and find out the effect of evaporator temperature, degree of subcooling at condenser outlet, superheating of evaporator outlet, vapour liquid heat exchanger effectiveness and degree of condenser temperature on COP and exergetic efficiency. They observed that that evaporator and condenser temperature have significant effect on both COP and exergetic efficiency and also found that R134a has the better performance while R407C has poor performance in all respect. **Selladurai and Saravana kumar [10]** had compared the first law performance between R134a and R290/R600a mixture on a domestic refrigerator which is originally and observed that that R290/R600a hydrocarbon mixture gives higher first law efficiency (COP) and second law efficiency (exergetic efficiency) as compared with R134a. They observed in the vapour compression refrigeration system, that highest irreversibility obtained in the compressor as compared to condenser, expansion valve and evaporator. **Nikolaidis and Probert [11]** also observed analytically that change in evaporator and condenser temperatures in the two stage vapour compression refrigeration system using R22 adding considerable effect on system irreversibility. They reported that there is need for optimizing the conditions imposed upon the condenser and evaporator. **Kumar et al. [12]** conducted energy and exergy analysis of vapour compression refrigeration system by the use of exergy-enthalpy diagram. They analysized first law analysis (energy analysis)for calculating the coefficient of performance and exergy analysis (second law analysis) for evaluation of various losses occurred in different components of vapour compression cycle using R11 and R12 as refrigerants. **Mastani Joybari et al.[13]** conducted experimental studies on a domestic refrigerator originally manufactured to use of 145g of R134a.They concluded that exergetic defect occurred in compressor was highest as compare to other components and through their analysis it has been found that instead of 145g of R134a if 60g of R600a is used in the considered system gave same performance which ultimately result into economical advantages and reduce the risk of flammability of hydrocarbon refrigerants. **Anand and Tyagi [14]** conducted detailed exergy analysis of two ton of refrigeration capacity window air conditioning test rig using R22 as working refrigerantand found, that irreversibility in system components will be highest when the system is 100% charged and lowest when 25% charged and irreversibility in compressor is highest among system components. **Arora and Kaushik [7]** developed numerical model of actual vapour compression refrigeration system with liquid vapour heat exchanger and did energy and exergy analysis on the same in the specific temperature range of evaporator and condenser and concluded that R502 is the best refrigerant compared to R404A and R507A and compressor is the worst component and liquid vapour heat exchanger is best component of the system in case of exergy transfer. **Ahamed et al. [17]** had performed experiments on domestic refrigerator with hydrocarbons (isobutene and butane) and analysed thermal performance using energy and exergy analysis and observed that that energy efficiency ratio of hydrocarbons comparable with R134a, but exergy efficiency and sustainability index of hydrocarbons much higher than that of R134a at considered evaporator temperature. They found that compressor is showing highest system defect (69%) among components of in the considered vapour compression refrigeration system. **Ahamed et al. [15]** also used of hydrocarbons and mixture in the vapour compression system and found that compressor shows much higher exergy destruction as compared to rest of components in the vapour compression refrigeration system and this exergy destruction can be minimized by using of nanofluid and nanolubricants in compressor. **Bolaji et al. [18]** had conducted experimentally comparative analysis of R32, R152a and R134a refrigerants in vapour compression refrigerator and found that R32 showing lowest thermal performance whereas R134a and R152a showing nearly same thermal performance and excellent performance was obtained using R152a. **Yumrutas et al. [19]**carried out exergy analysis based on effect of condensing and evaporating

temperatures in the vapour compression refrigeration cycle in terms of pressure losses, COP, second law efficiency and exergy losses. Variation in temperature of condenser as well as have negligible effect on exergy losses of compressor and expansion valve, also first law efficiency and exergy efficiency increase but total exergy losses of system decrease with increase in evaporator and condenser temperature. **Padilla et al. [20] carried out** exergy analysis of domestic vapour compression refrigeration system with R12 and R413A was done. They concluded that performance in terms of power consumption, irreversibility and exergy efficiency of R413A is better than R12, so R12 can be replaced with R413A in domestic vapour compression refrigeration system due to global warming. **Getu and Bansal [21]** had optimized the design and operating parameters of like condensing temperature, subcooling temperature, evaporating temperature, superheating temperature and temperature difference in cascade heat exchanger R744-R717 cascade refrigeration system. They carried out regression analysis to obtain optimum thermodynamic parameters of same system. **Spatz and Motta [22]** had mainly focused on replacement of R12 using R410a through experimental investigation of medium temperature vapour compression refrigeration cycles. In terms of thermodynamic analysis, comparison of heat transfer and pressure drop characteristics, R410a gives best performance among R12, R404a and R290a. **Mohanraj et al. [23]** observed through experimental investigation in the domestic refrigerator and concluded COP variation with different environmental temperatures of system using mixture of R290 and R600a in the ratio of 45.2: 54.8 by weight showing up to 3.6% greater than same system using R134a, also discharge temperature of compressor with mixture of R290 and R600a is lower in the range of 8.5-13.4K than same compressor with R134a. **Han et al. [24]** considered different working conditions and experimental results revealed that there could be replacement of R12 by eco-friendly R407C in vapour compression refrigeration system having rotor compressor with mixture of R32/R125/R161 showing higher COP, less pressure ratio and slightly high discharge compressor temperature without any modification in the same system. **Halimic et al. [25]** had studied thermal first law performance of vapour compression refrigeration system using eco-friendly R401A, R290 and R134A refrigerants with R12 for replacing R12 because R12 gives more ozone depletion and global warming similar performance of R134a in comparison with R12, R134A can be replaced in the same system without any medication in the system components. But in reference to green house impact R290 presented best results. **Xuan and Chen [26]** studied vapour compression refrigeration by mixture of HFC-161 for replacing of R502 and conducted experiments. They found that mixture of HFC-161 gives same and higher performance than R404A at lower and higher evaporative temperature respectively on the vapour compression refrigeration system designed for R404A. **Cabello et al. [27]** had evaluated the effect of operating parameters on first law efficiency (COP), work input and cooling capacity of single-stage vapour compression refrigeration system. There is great influence on energetic parameters due change in suction pressure, condensing and evaporating temperatures .**Cabello et al. [28]** observed that the effect of condensing pressure, evaporating pressure and degree of superheating was experimentally investigated on single stage vapour compression refrigeration system using R22, R134a and R407C.It was observed that mass flow rate is greatly affected by change in suction conditions of compressor in results on refrigeration capacity because refrigeration capacity depended on mass flow rate through evaporator. It was also found that for higher compression ratio R22 gives lower COP than R407C. **Stanciu et al. [29]** also conducted numerical and graphical investigation on single stage vapour compression refrigeration system using R22, R134a, R717, R507a, R404a refrigerants in terms of first law efficiency (COP), compressor work, second law efficiency (exergetic efficiency) and refrigeration effect, effect of subcooling, superheating and compression ratio and did system optimization working with specific refrigerant in the vapour compression refrigeration system.

3. Summary of Literature Review and Research Gaps Identified

The study of above literatures and many other authors have not mentioned in the description presents in terms of following points-

Thermodynamic analysis of different vapour refrigeration systems have been carried out using various combinations. and thermal performance analysis have been done by employing different ecofriendly and new alternative refrigerants.

It has been concluded that different kinds of nano-particles such as Al_2O_3, TiO_2, CuO and Cu can be mixed with the new ecofriendly refrigerants for enhance performance enhancement.

But still a very vast area is available for exploration for using various combination/ modification/ hybrid systems and these systems could be tested with alternative and newer ecofriendly refrigerants which have low GWP values. Such as R1234yf and R1234ze

The following research objectives to be considered in the vapour compression refrigeration systems.

4. Research Objectives

- Thermodynamic first law analysis in terms of coefficiency of vapour compression system using alternative ecofriendly refrigerants in the primary evaporator circuit and nano particles mixed with R718 in the secondary evaporator circuit
- Thermodynamic second law analysis in terms of exergetic efficiency of vapour compression system using alternative ecofriendly refrigerants in the primary evaporator circuit and nano particles mixed with R718 in the secondary evaporator circuit

5. Research Methodology

The thermodynamic performance for the vapour compression refrigeration refrigeration is evaluated using Energy –exergy balance equations is based on the first law of thermodynamics. A numerical computer programme was developed for three nano particles mixed in R718 in the secondary evaporator circuit and R134a in the primary evapor circuit systems using EES software for finding the first law in terms of coefficient of performance (COP) and

second law efficiency in terms of exergetic efficiency and irreversibility in the system in terms of exergy Destruction ratio (EDR) which is a total irreversibility in the system in terms of total losses in the system to the exergety output evaluation and results are obtained on vapour compression refrigeration system by varying condenser and evaporator temperatures.

6. Numerical Computations

The study will provide the input on the usage of nano particles mixed with R718 in the secondary evaporator circuit which enhances evaporator heat transfer coefficient and increases refrigeration effect for a particular type of vapour compression refrigeration system, which could be suitable from the view point of its economic performance, and need as per the given objectives and conditions. It will also give an idea about the suitable nano materials mixed in R718 refrigerant effecting first law performance Similarly exergy equation based on second law of thermodynamics is to be formulated for these systems and second law effectiveness (exergetic efficiency) along with system exergy destruction ratio (EDR) for finding irreversibility occurred in the system components and as a whole system and suitable measures for removing irreversibilities in the components for enhances system performances in the refrigeration systems. as used in future for residential, industrial and medical applications.

7. Results and Discussions

Table: 1. Percentage First Law Performance Improvement (in terms of coefficient of performance) of vapour compression refrigeration system using three nano particles mixed with R718 in the Secondary Evaporator Circuit

Nano-particles	First law efficiency (COP)	% Improvement
Copper oxide	3.589	18.35
Copper	3.58	18.347
Al2O3	3.561	17.72
TiO2	3.516	11.23
Without Nano particles	3.025	_____

Table-1 shows the first law performance in terms of COP of vapour compression refrigeration system using three nano particles mixed with R718 refrigerant and it bwas observed that the first law performance improved using nano refrigerants from 11.23% to 18.35% as compared with without nano refrigerants in secondary circuit.

Table: 2. Percentage Second Law Performance Improvement (in terms of exergetic efficiency) of Vapour Compression refrigeration system using three nano Particles mixed with R718 in the Secondary Evaporator Circuit

Nano particles	Second law Efficiency	% improvement
Copper oxide	0.40071	18.31
Copper	0.4007	18.30
Al2O3	0.3986	17.6853
TiO2	0.3936	16.209
Without Nano Particles	0.3387	_____

Table-2 shows the second law performance in terms of exergetic efficiency of vapour compression refrigeration system using three nano particles mixed with R718 refrigerant and it bwas observed that the first law performance improved using nano refrigerants from 16.206% to 18.31% as compared with without nano refrigerants in secondary circuit.. Similarly the performance of vapour compression refrigeration is also compared using different eco-friendly refrigerants in the primary evaporator circuit without nano particles mixed in R718 in secondary evaporator circuit and it was observed that R 134a gives better first law and second law performance than R404a and R407c. The performance using R1234ze and R1234yf gives lesser thermodynamic first and second law performance as compared with R134a , but these refrigerants have low global warming potential (GWP) and zero ozone depletion potential (ODP) as compared to R134a.

Table: 3. Performance Parameters of Vapour Compression Refrigeration System using Ecofriendly Refrigerants and without Nano Materials

Refrigerants	COP	ED_Ratio	ETA_Second
R134a	2.973	2.447	0.2901
R404a	2.705	3.158	0.2717
R407c	2,754	2.333	0.30

Table: 4.a and Table-4.b gives the improvements in overall heat transfer coefficient using nano particles mixed with R718 in secondary evaporator circuit as compared without nano particles and significant improvement was observed. The variation of difference in temperatures in the evaporator and condenser is also increasing as compared to without nano prefrigerants in the secondary circuit.

Table: 4a. Effect of Overall Evaporator Heat Transfer Coefficient Using Different Nano Particles Mixed With R718 in the Secondary Evaporator Circuit and R134a in Primary Circuit

Nano particles	Overall heat transfer Coefficient (U_e)	Difference in water temperature (^oC)	Difference in Brine temperature (^oC)
Copper oxide	1372.14	15.71	11.58
Copper	1367.18	14.55	11.44
Al_2O_3	1318.0	14.62	11.5
TiO2	1242.43	14.43	11.32
Without Nano particles	691.04	12.24	9.29

Table: 4b. Effect of Overall Evaporator Heat Transfer Coefficient using Different Nano Particles Mixed with R718 in the Secondary Evaporator Circuit and R134a in Primary Circuit

Nano Particles	Overall heat transfer Coefficient (U_e)	% improvement
Copper oxide	1325.7	91.41
Copper	1324.25	91.4099
Al2O3	1318.70	90.6077
TiO2	1242.43	79.6
Without Nano particles	691.65	_____

8. Conclusions

In this paper, energy and exergy analysis of vapour compression refrigeration systems using R134a ecofriendly refrigerant in primary circuit and three nano particles mixed with R718 in the secondary evaporator is presented and following conclusions from the present analysis are summarized below:

1. The First law efficiency (COP) and Second law efficiency (Exergetic efficiency) of vapour compression refrigeration systems using three nano materials have been compared and copper oxide gives performance improvements in the range 11.23% to 18% without nano particles and better performance was found using copper oxide nano material
2. The First law efficiency (COP) and Second law efficiency (Exergetic efficiency) of using R134a eco-friendly refrigerant in primary evaporator circuit and Copper oxide mixed with R718 in the secondary evaporator circuit gives better first law efficiency (COP) and second law efficiency (Exergetic efficiency) as compared to TiO_2 nano particles mixed with R718
3. The COP improvement 18.35% and second law efficiency improvement is 18.31% observed using Al2O3 nano materials mixed with R718 in secondary circuit as compared to without nano refrigerants. Similarly 17.72% and 17.685% second law efficiency.

References

[1] Johnson. E. Global warming from HFC. Environ. Impact Asses. 18, 1998, 485-492
[2] QiyuChen, R. C Prasad. Simulation of a vapour compression refrigeration cycles HFC134A and CFC12.Int Comm.Heat Mass Transfer. 26, 1999; 513-521
[3] M. Padilla, R. Revellin, J. Bonjour. Exergy analysis of R413A as replacement of R12 in a domestic refrigeration system. Int J Energy Conversion and Management, 51, 2010, 2195-2201
[4] H.O. Spauschus, HFC 134a as a substitute refrigerant for CFC 12. Int J of Refrigeration, 11, 1988, 389-392
[5] J. U. Ahamed, R.Saidur, H. H.Masjuki, A review on exergy analysis of vapor compression refrigeration system. Int J Renewable and sustainable energy reviews, 15, 2011, 1593-1600
[6] R. L lopis, E. Torrella, R. Cabello, D. Sánchez. Performance evaluation of R404A and R507A refrigerant mixtures in an experimental double-stage of vapour compression plant. Int J Applied Energy, 87, 2010, 1546-1553
[7] Akhilesh Arora, S. C. Kaushik, Theoretical analysis of a vapour compression refrigeration system with R502, R404A and R507A. Int J Refrigeration, 31, 2008, 998-1005
[8] V. Havelsky. Investigation of refrigerating system with R12 refrigerant replacements .Int J Applied Thermal Engineering, 2000; 20:133-140
[9] V. Siva Reddy, N. L Panwar, S. C Kaushik, Exergy analysis of a vapour compression refrigeration system with R134a,R143a,R152a,R404A,R407C,R410A,R502 and R507A.Clean Techn Environ Policy, 14, 2012, 47-53
[10] R. Saravanakumar, V. Selladurai, Exergy analysis of a domestic refrigerator using eco-friendly R290/R600a refrigerant mixture as an alternative to R134a.Int J Therm Anal Calorim.2013
[11] C. Nikolaidis, D. Probert-Exergy method analysis of a two-stage vapour-compression refrigeration-plants performance. Int J Applied Thermal Engineering, 60, 1998, 241-256
[12] S. Kumar, M. Prevost, R. Bugarel, Exergy analysis of a vapour compression refrigeration system. Heat Recovery Systems & CHP, 9, 1989, 151-157
[13] Mahmood Mastani Joybari, Mohammad Sadegh Hatamipour, Amir Rahimi, Fatemeh Ghadiri Modarres- Exergy analysis and optimization of R600a as a replacement of R134a in a domestic refrigerator system. International Journal of refrigeration, 36, 2013, 1233-1242
[14] S. Anand, S. K Tyagi, Exergy analysis and experimental study of a vapour compression refrigeration cycle.Int J Therm Anal Calorim, 110, 2012, 961-971
[15] J. U Ahamed, R.saidur, H.H Masjuki, M. A Sattar, An analysis of energy, exergy and sustainable development of a vapour compression refrigeration system using hydrocarbon.International journal of Green energy, 9, 2012, 707-717
[16] Camelia Stanciu, Adina Gheorghian, Dorin Stanciu, Alexandru Dobrovicescu- Exergy analysis and refrigerant effect on the operation and performance lomits of a one stage vapour compression refrigeration system.Termotehnica, 1, 2011, 36-42
[17] J. U. Ahamed, R. Saidur, H. H. Masjuki, A review on exergy analysis of vapor compression refrigeration system. Int J Renewable and sustainable energy reviews, 15, 2011, 1593-1600
[18] B. O. Bolaji, M. A. Akintunde, T. O. Falade, Comparative analysis of performance of three ozone-friends HFC refrigerants in a vapor compression refrigerator. Int J Sustainable Energy & Environment, 2, 2011, 61-64
[19] RecepYumrutas, Mehmet Kunduz, Mehmet Kanoglu-Exergy analysis of vapor compression refrigeration systems. Exergy, An International Journal, 2, 2002, 266-272
[20] M. Padilla, R. Revellin, J. Bonjour, Exergy analysis of R413A as replacement of R12 in a domestic refrigeration system. Int J Energy Conversion and Management, 51, 2010; 2195-2201
[21] H. M Getu, P. K Bansal, Thermodynamic analysis of an R744-R717 cascade refrigeration system. Int J Refrigeration, 31, 2008, 45-54
[22] Mark W. Spatz, Samuel F. Yana Motta. An evaluation of options for replacing HCFC-22 in medium temperature refrigeration systems. Int J Refrigeration, 27, 2004, 475-483
[23] M. Mohanraj, S. Jayaraj, C. Muraleedharan, P. Chandrasekar, Experimental investigation of R290/R600a mixture as an alternative to R134a in a

domestic refrigerator. Int J Thermal Sciences, 48, 2009, 1036-1042
[24] X. H. Han, Q. Wang, Z. W. Zhu, G. M. Chen, Cycle performance study on R32/R125/R161 as an alternative refrigerant to R407C. Int J Applied Thermal Engineering, 27, 2007, 2559-2565
[25] E. Halimic, D. Ross, B. Agnew, A. Anderson, I. Potts, A comparison of the operating performance of alternative refrigerants. Int J Applied Thermal Engineering, 23, 2003, 1441-1451
[26] Yongmei Xuan, Guangming Chen. Experimental study on HFC-161 mixture as an alternative refrigerant to R502. Int J Refrigeration. Article in Press.
[27] R. Cabello, J. Navarro-Esbrı, R. Llopis, E. Torrella, Analysis of the variation mechanism in the main energetic parameters in a single-stage vapour compression plant. Int J Applied Thermal Engineering, 27, 2007, 167-176
[28] R. Cabello, E. Torrella, J. Navarro-Esbr. Experimental evaluation of a vapour compression plant performance using R134a, R407C and R22 as working fluids. Int J Applied Thermal Engineering, 24, 2004, 1905-1917
[29] S. A. Klein, F. Alvarado Engineering Equation Solver, Version 7.441. F Chart Software, Middleton, WI.2005
[30] I. Dincer. Refrigeration Systems and Applications. Wiley, UK, 26, 2003

Accepted Article

Humu-2014-0136

Informatics

mit-o-matic: a comprehensive computational pipeline for clinical evaluation of mitochondrial variations from next-generation sequencing datasets

Shamsudheen Karuthedath Vellarikkal [$,*,1], Heena Dhiman[$,2], Kandarp Joshi[3,*], Yasha Hasija[4], Sridhar Sivasubbu[1,*,#] and Vinod Scaria[2,*,#]

[$]Both authors contributed equally and would like to be known as joint first authors

[1] Genomics and Molecular Medicine, CSIR Institute of Genomics and Integrative Biology, Mathura Road, Delhi 110025, India

[2] GN Ramachandran Knowledge Center for Genome Informatics, CSIR Institute of Genomics and Integrative Biology, Mathura Road, Delhi 110025, India

[3] CSIR Open Source Drug Discovery Unit, Anusandhan Bhawan, Delhi 110001, India

[4] Department of Biotechnology, Delhi Technological University, Shahbad Daulatpur, Delhi, India

* Academy of Scientific and Innovative Research (AcSIR), Anusandhan Bhawan, Delhi 110001, India

[#] **Address for correspondence:**

Sridhar Sivasubbu: s.sivasubbu@igib.res.in

Vinod Scaria: vinods@igib.res.in

Grant Sponsor: Council of Scientific and Industrial Research (CSIR) – India (Grant No. BSC0122 – CARDIOMED)

This article has been accepted for publication and undergone full peer review but has not been through the copyediting, typesetting, pagination and proofreading process, which may lead to differences between this version and the Version of Record. Please cite this article as doi: 10.1002/humu.22767.

This article is protected by copyright. All rights reserved.

Accepted Article

ABSTRACT

The human mitochondrial genome has been reported to have a very high mutation rate as compared with the nuclear genome. A large number of mitochondrial mutations show significant phenotypic association and are involved in a broad spectrum of diseases. In recent years, there has been a remarkable progress in the understanding of mitochondrial genetics. The availability of Next Generation Sequencing technologies have not only reduced sequencing cost by orders of magnitude but has also provided us good quality mitochondrial genome sequences with high coverage, thereby enabling decoding of a number of human mitochondrial diseases. In this study, we report a computational and experimental pipeline to decipher the human mitochondrial DNA (mtDNA) variations and examine them for their clinical correlation. As a proof of principle, we also present a clinical study of a patient with Leigh disease and confirmed maternal inheritance of the causative allele. The pipeline is made available as a user-friendly online tool to annotate variants and find haplogroup, disease association and heteroplasmic sites. To the best of our knowledge, this is the first and the most comprehensive tool for clinical evaluation of mitochondrial genomic variations from Next Generation Sequencing datasets. The tool is freely available at http://genome.igib.res.in/mitomatic/.

Keywords: Mitochondria, Haplogroup, Heteroplasmy, Variation, Next Generation Sequencing

This article is protected by copyright. All rights reserved.

Accepted Article

Introduction

Mitochondrial diseases are one of the most common human genetic disorders (Taylor and Turnbull, 2005). Pediatric onset of mitochondrial diseases occurs with an estimated incidence of one in 5,000 individuals (Craigen, et al., 2013) and estimated prevalence of 1 in 7,634 (Skladal, et al., 2003). Recent years have seen a tremendous improvement in the understanding of the organization and function of the mitochondria in a variety of biological processes including bioenergetics of the cell, programmed cell death and also in the predisposition to a wide variety of disease conditions. The human mitochondria encode 37 genes including 13 protein coding genes, 22 transfer RNAs and 2 ribosomal RNAs (Shadel, 2008). The evolution of the organelle has seen a large scale reduction in the mitochondrial genome with subsequent contributions of components encoded by the nuclear genome (Adams and Palmer, 2003). The function and integrity of the mitochondria is largely dependent on import of a set of transcripts and proteins encoded by the nuclear genome (Lee, et al., 2008). Recent proteomics experiments have created a compendium of about 1000 proteins which are encoded by the nuclear genome and largely found in the mitochondria (Jensen and Johnson, 2001; Kunkele, et al., 1998; Mesecke, et al., 2005; Wiedemann, et al., 2003).

Apart from its functional importance, the peculiar maternal inheritance of the mitochondria has been widely applied as a tool towards understanding migration and population genetics (Pliss, et al., 2006; Underhill and Kivisild, 2007). Recent studies have increasingly shown mitochondrial variations and mitochondrial dysfunction to be associated with a number of pathophysiological conditions including neurological disorders such as Alzheimer's disease (Yan, et al., 2013) and metabolic disorders such as Type 2 Diabetes Mellitus (Tang, et al.,

This article is protected by copyright. All rights reserved.

Accepted Article

2005). The small genome size and availability of tools including tiling microarrays and sequencing has enabled us to understand the diversity of mitochondrial variations (Maitra, et al., 2004). This has been complemented by a number of informatics resources such as MITOMAP (Kogelnik, et al., 1996) and MitoLSDB (K, et al., 2013), which have systematically curated information from various resources on mitochondrial variations.

The advent of Next Generation Sequencing (NGS) technology has offered a fresh opportunity to understand mitochondrial variations. Many recent studies have extensively used NGS approaches to identify mitochondrial variants associated with diseases (Abaci, et al., 2014; Craigen, et al., 2013). It also provides additional advantages including large depth coverage, which could be effectively used to map heteroplasmic variations (Sosa, et al., 2012). In addition, recent exome capture methodologies also incorporate probes from the mitochondrial genome and offers additional opportunities towards understanding mitochondrial variations in clinical settings. With the drastic drop in cost of DNA sequencing, it is expected that affordable mitochondrial sequencing could be effectively employed for patients suffering from mitochondrial disorders (Sosa, et al., 2012). The widespread application of NGS by clinicians is in part limited by the paucity of appropriate systematic computational pipelines for data analysis, which are easy to operate and provide reports in easily interpretable formats. MitoSeek (Guo, et al., 2013) is one such tool for NGS data analysis from mtDNA, captured as a by-product of whole-exome or whole-genome sequencing. Although, a very expedient resource, it offers just a command-line version that works specifically on large abundance of paired-end sequencing data and does not support single-end data. It reports heteroplasmy, somatic mutations, structural variance, relative mtDNA copy number and annotations for amino acid changes, without any clinical correlation of the findings. To this end, mit-o-matic has been created to provide most comprehensive annotation with relevant clinical association that includes haplogroup classification.

This article is protected by copyright. All rights reserved.

Accepted Article

In the present work, we describe how a cloud-based data integration platform can leverage the high-quality and clinically relevant information distributed in disparate resources for clinical application towards understanding and annotating mitochondrial variations. As a proof of principle, we use datasets of mitochondrial sequencing from a patient with Leigh disease. To the best of our knowledge, mit-o-matic is to date one of the most comprehensive analysis pipelines for clinical annotation of mitochondrial sequencing data from Next Generation Sequencing platforms. The resource is freely available at http://genome.igib.res.in/mitomatic/.

Overview of mit-o-matic

mit-o-matic is a comprehensive computational pipeline for annotation of mitochondrial variations from next-generation datasets. It provides automation for alignment of NGS reads to the reference mitochondrial genome, fetching the variants above a set cut-off and creating a descriptive annotation of reported variants. The web based interface can accept data in form of FASTQ files directly and perform the analysis entirely online (Option 1), but with a size limitation, which allows an ample coverage of approximately 500x of the mitochondrial genome which is more than sufficient for most clinical applications. For large datasets above 500x coverage as in very specialized applications, the command-line option can be used for either running the complete pipeline or just parsing an already available pileup file. The parsed pileup files can be stored and used for analysis in future with the 'Option 2' on the home page. For each variant, the reference allele, alternate allele, percentage of allele frequency, corresponding gene, amino acid position, and amino acid change with its subsequent effect (Synonymous or Non-synonymous) are listed as per the revised Cambridge Reference Sequence (rCRS) (Andrews, et al., 1999). Apart from this the disease associated

This article is protected by copyright. All rights reserved.

Accepted Article

variants are reported with associated phenotype, population frequencies are reported for variants that are not novel and potential functional consequence is informed for non-synonymous novel variants. It provides an online user-friendly graphical user interface where the researcher or clinician can avail a comprehensive genetic report on the mitochondrial variations in a dataset. The delivery of computing as a service by integrating various tools and databases for the analysis of mitochondrial variations in the form of a free online user friendly interface makes mit-o-matic a useful cloud based data integration platform. An overview of the pipeline is summarized in Figure 1.

Sequence Mapping and Variant calling

The computational pipeline takes in standard high-quality trimmed FASTQ format files for mitochondrial sequences from any of the popular sequencing platforms. The resource supports both single-end and paired-end data from a variety of experimental protocols including amplicon sequencing using two or three sets of primers by different NGS approaches such as duplex sequencing (Schmitt, et al., 2012) or direct amplicon sequencing (Huang, 2011; Sosa, et al., 2012). The mtDNA below 500x coverage can be analyzed using the web-based option while the command-line version can be used for the analysis of whole-exome or targeted-exome containing mtDNA reads. The pipeline provides three options for alignment against the reference rCRS mitochondrial genome sequence modified according to the read length, and supports three popular quality-aware reference mapping algorithms – BWA (Li and Durbin, 2009), BOWTIE (Langmead, et al., 2009) and MAQ (Li, et al., 2008). Since the mitochondrial genome is circular, the reference genome has been modified to allow hundred percent mapping of reads on either end. For data with read length of x bp, x-1 bases would be added from the opposite end to start and stop of rCRS. The alignments thus generated are reformatted to pileups, and a custom formatted file is generated that includes

This article is protected by copyright. All rights reserved.

Accepted Article

frequencies and positions of the mismatches retrieved from the alignments. This file is further provided to the online reporting module of mit-o-matic, which provides a comprehensive annotation of the variations in the sample. An empirical minimum cutoff of 10% variants per site has been used by default to avoid spurious and low frequency variations (Li, et al., 2010). The frequency of each of the alleles was computed and tabulated with respect to the percentage of reads out of the total against the particular allele. Positions having more than one allele with frequency greater than the cutoff value are referred to as Heteroplasmic sites.

Resources and analysis tools integrated in mit-o-matic

mit-o-matic integrates a number of well-curated datasets and resources for providing the user with a rich annotation of the variants.

Mitochondrial Variations and Annotations

Mitochondrial variants and annotations were primarily derived from MITOMAP (Kogelnik, et al., 1996), mtDB (Ingman and Gyllensten, 2006) and MitoLSDB (K, et al., 2013). The variant data was compiled into compatible data files and uploaded into MySQL. This includes variations mapped onto 73 mtDNA function locations and 580 disease associations. The variant database stores 10,416 unique mitochondrial variations from the available resources (MITOMAP [11 July, 2014], MitoLSDB [v.2.0] and mtDB [1 March, 2007]). All the exonic non-synonymous variations were detected for their potential functional consequences using SIFT (Kumar, et al., 2009). This tool is widely used for predicting the effect of an amino acid substitution on protein function on the basis of sequence homology and the physical properties of amino acids.

This article is protected by copyright. All rights reserved.

Accepted Article

Frequency of variations

The frequencies of variations were retrieved from the MITOMAP database, which computes the population frequencies based on 18,363 sequences in GenBank.

Haplogroup annotations

Haplogroup annotations were performed using a popular approach as described by Fan L. and co-workers (Fan and Yao, 2013). To categorize the mitochondrial variome under most suitable haplogroup, a total of 3,737 haplogroups were derived from a comprehensive phylogenetic tree of global human mtDNA variation. As described in the approach, the variants in a sample were mapped to the variations forming each of the haplogroup and scored, and the best scoring haplogroup was reported by mit-o-matic.

Accuracy Estimation

We randomly introduced 100 mutations in the reference sequence (rCRS) and generated single end synthetic NGS reads of Illumina platform at discrete coverage values (100x, 200x, 300x, 400x and 500x) for Q30 phred quality using ART (Huang, et al., 2012). For a given coverage, the reads simulated from the mutated reference genome were mixed with the reads generated from non-mutated reference genome to create FASTQ files with varied maximum allele frequencies (10% - 90%) resulting in a dataset consisting of 45 samples. mit-o-matic was run on all these synthetic FASTQ files varying the cut-off values for alternate allele frequency with BOWTIE to check the number of true positive (TP) and false positive (FP) mutations reported by the pipeline. For each coverage data, TP and FP values were plotted across the mit-o-matic frequency cut-off values for all the samples independently (Supp. Figure S1). We show that the default cut-off (10%) used by Li et. al. (2010) provides for extremely accurate analysis of variants. Nevertheless the tool allows for specialized users to define their default cut-offs based on specific requirements if need arises.

This article is protected by copyright. All rights reserved.

Accepted Article

Case Study: Application of mit-o-matic for characterization of mitochondrial disorders

To test the utility of mit-o-matic, we used mitochondrial sequence derived from a patient diagnosed with potential Leigh disease and from the patient's mother. Blood sample was taken from individuals abiding all institutional ethical committee rules and regulations. DNA was isolated from 3ml of blood drawn and amplification of complete mitochondrial DNA was done with the help of long range PCR (La Taq, Takara) with three overlapping primer sets designed on rCRS (Dames, et al., 2013) (Supp. Table S1). All the three PCR products were pooled together to get uniform coverage across the mitochondria by normalizing the number of fragments from each amplicon pool based on the size. Fragmentation for sequencing was done by Covaris SS220 system. Fragmented products were processed further for library preparation using Truseq-DNA sample preparation kit (Illumina, USA) as per manufacturer's instruction to obtain an insert size of approximately 300bp. Sequence data was generated using single end read with a read length of 51bp on the Genome Analyzer IIx platform (Ilumina, USA).

The sequences from the two samples were mapped onto the modified rCRS reference mitochondrial genome to identify the variants (Supp. Tables S2 and S3). Allelic information was extracted and submitted to the mit-o-matic pipeline for further annotations using the standard pipeline (Table 1). The mit-o-matic pipeline identified a missense mutation from T to G at position 8,993 of the rCRS reference mitochondrial genome, which confirmed phenotypic association with Leigh disease for the patient (Tatuch, et al., 1992).

This article is protected by copyright. All rights reserved.

Accepted Article

The complete set of variations from the patient's mtDNA matches best to the haplogroup - U2a1. A very low frequency of the variant (T to G at position 8,993) was observed in the mother (0.12%), who shares the same haplogroup with the patient. Position 3107, represented by 'N' is the error nucleotide in the original CRS that is maintained in the revised sequence as a gap (Sondheimer, et al., 2011). The reports of the two cases are summarized as shown in Figure 2.

Conclusions and future perspective

Mitochondrial variations have been increasingly associated and implicated in a wide variety of human pathophysiological conditions. Conventional methods of mitochondrial variation analysis that include amplicon sequencing using a capillary sequencing approach (Cui, et al., 2013) or mitochondrial array based genotyping (Kassauei, et al., 2006) have been developed and employed in clinical practice.

Recent years have seen application of Next Generation Sequencing in clinical settings for many diseases. As the use of NGS technology becomes more popular, cost effective and well entrenched in clinical settings, one would potentially foresee its applications for diagnosis of mitochondrial disorders as well. Furthermore, the availability of NGS technologies offers a new opportunity to understand mitochondrial variations at a greater depth (Sosa, et al., 2012) with the additional advantage of the possibility to detect low frequency heteroplasmy sites (Goto, et al., 2011). A number of well-curated resources provide the wealth of mtDNA variations and their phenotypic correlates. However in general clinical practice the widespread application of NGS technology for mitochondrial disorders has been hampered by the non-availability of an integrated computational pipeline. The need of the hour is a

This article is protected by copyright. All rights reserved.

Accepted Article

pipeline, which could start from mitochondrial sequences, and perform assembly, annotation and evaluation of clinically relevant variations. mit-o-matic fills in this gap by providing a user-friendly computational pipeline that does not require specialized skills to operate, while giving a comprehensive overview of the variants and annotations of the disease associated variations in a user friendly and easily interpretable web interface. It can support any kind of high quality single-end or paired-end data that has been mapped to the mitochondrial genome, including amplicon sequencing, whole genome sequencing and custom enrichment.

The system has been built with future developments in mind, both in terms of usability and applicability. The major future developments would include possibility of integrating the reporting engine with the popular cloud analysis engines such as BaseSpace (http://www.illumina.com/software/basespace.ilmn) and Ion Reporter environments (https://ionreporter.lifetechnologies.com/ir/), which could provide a click-of-a-button ease of mitochondrial variation analysis. We also foresee integration of novel analytical resources and tools for functional annotation of novel mitochondrial variations.

Acknowledgments

The authors acknowledge funding support from the Council of Scientific and Industrial Research (CSIR) – India, through Grant No. BSC0122 (CARDIOMED). The authors thank Dr. Mohd Faruq and Dr. Binuja Varma for their insightful comments, technical help and reagents.

Disclosure statement: The authors declare no conflict of interest.

This article is protected by copyright. All rights reserved.

Accepted Article

References

Abaci N, Arikan M, Tansel T, Sahin N, Cakiris A, Pacal F, Sirma Ekmekci S, Gok E, Ustek D. 2014. Mitochondrial mutations in patients with congenital heart defects by next generation sequencing technology. Cardiol Young:1-7.

Adams KL, Palmer JD. 2003. Evolution of mitochondrial gene content: gene loss and transfer to the nucleus. Mol Phylogenet Evol 29(3):380-95.

Andrews RM, Kubacka I, Chinnery PF, Lightowlers RN, Turnbull DM, Howell N. 1999. Reanalysis and revision of the Cambridge reference sequence for human mitochondrial DNA. Nat Genet 23(2):147.

Craigen WJ, Graham BH, Wong LJ, Scaglia F, Lewis RA, Bonnen PE. 2013. Exome sequencing of a patient with suspected mitochondrial disease reveals a likely multigenic etiology. BMC Med Genet 14:83.

Cui H, Li F, Chen D, Wang G, Truong CK, Enns GM, Graham B, Milone M, Landsverk ML, Wang J and others. 2013. Comprehensive next-generation sequence analyses of the entire mitochondrial genome reveal new insights into the molecular diagnosis of mitochondrial DNA disorders. Genet Med 15(5):388-94.

Dames S, Chou LS, Xiao Y, Wayman T, Stocks J, Singleton M, Eilbeck K, Mao R. 2013. The development of next-generation sequencing assays for the mitochondrial genome and 108 nuclear genes associated with mitochondrial disorders. J Mol Diagn 15(4):526-34.

Fan L, Yao YG. 2013. An update to MitoTool: using a new scoring system for faster mtDNA haplogroup determination. Mitochondrion 13(4):360-3.

Goto H, Dickins B, Afgan E, Paul IM, Taylor J, Makova KD, Nekrutenko A. 2011. Dynamics of mitochondrial heteroplasmy in three families investigated via a repeatable re-sequencing study. Genome Biol 12(6):R59.

This article is protected by copyright. All rights reserved.

Accepted Article

Guo Y, Li J, Li CI, Shyr Y, Samuels DC. 2013. MitoSeek: extracting mitochondria information and performing high-throughput mitochondria sequencing analysis. Bioinformatics 29(9):1210-1.

He Y, Wu J, Dressman DC, Iacobuzio-Donahue C, Markowitz SD, Velculescu VE, Diaz LA, Jr., Kinzler KW, Vogelstein B, Papadopoulos N. 2010. Heteroplasmic mitochondrial DNA mutations in normal and tumour cells. Nature 464(7288):610-4.

Huang T. 2011. Next generation sequencing to characterize mitochondrial genomic DNA heteroplasmy. Curr Protoc Hum Genet Chapter 19:Unit19 8.

Huang W, Li L, Myers JR, Marth GT. 2012. ART: a next-generation sequencing read simulator. Bioinformatics 28(4):593-4.

Ingman M, Gyllensten U. 2006. mtDB: Human Mitochondrial Genome Database, a resource for population genetics and medical sciences. Nucleic Acids Res 34(Database issue):D749-51.

Jensen RE, Johnson AE. 2001. Opening the door to mitochondrial protein import. Nat Struct Biol 8(12):1008-10.

K S, Jalali S, Scaria V, Bhardwaj A. 2013. MitoLSDB: a comprehensive resource to study genotype to phenotype correlations in human mitochondrial DNA variations. PLoS One 8(4):e60066.

Kassauei K, Habbe N, Mullendore ME, Karikari CA, Maitra A, Feldmann G. 2006. Mitochondrial DNA mutations in pancreatic cancer. Int J Gastrointest Cancer 37(2-3):57-64.

Kogelnik AM, Lott MT, Brown MD, Navathe SB, Wallace DC. 1996. MITOMAP: a human mitochondrial genome database. Nucleic Acids Res 24(1):177-9.

Kumar P, Henikoff S, Ng PC. 2009. Predicting the effects of coding non-synonymous variants on protein function using the SIFT algorithm. Nat Protoc 4(7):1073-81.

This article is protected by copyright. All rights reserved.

Accepted Article

Kunkele KP, Heins S, Dembowski M, Nargang FE, Benz R, Thieffry M, Walz J, Lill R, Nussberger S, Neupert W. 1998. The preprotein translocation channel of the outer membrane of mitochondria. Cell 93(6):1009-19.

Langmead B, Trapnell C, Pop M, Salzberg SL. 2009. Ultrafast and memory-efficient alignment of short DNA sequences to the human genome. Genome Biol 10(3):R25.

Lee J, Sharma S, Kim J, Ferrante RJ, Ryu H. 2008. Mitochondrial nuclear receptors and transcription factors: who's minding the cell? J Neurosci Res 86(5):961-71.

Li H, Durbin R. 2009. Fast and accurate short read alignment with Burrows-Wheeler transform. Bioinformatics 25(14):1754-60.

Li H, Ruan J, Durbin R. 2008. Mapping short DNA sequencing reads and calling variants using mapping quality scores. Genome Research 18(11):1851-1858.

Li M, Schonberg A, Schaefer M, Schroeder R, Nasidze I, Stoneking M. 2010. Detecting heteroplasmy from high-throughput sequencing of complete human mitochondrial DNA genomes. Am J Hum Genet 87(2):237-49.

Maitra A, Cohen Y, Gillespie SE, Mambo E, Fukushima N, Hoque MO, Shah N, Goggins M, Califano J, Sidransky D and others. 2004. The Human MitoChip: a high-throughput sequencing microarray for mitochondrial mutation detection. Genome Res 14(5):812-9.

Mesecke N, Terziyska N, Kozany C, Baumann F, Neupert W, Hell K, Herrmann JM. 2005. A disulfide relay system in the intermembrane space of mitochondria that mediates protein import. Cell 121(7):1059-69.

Pliss L, Tambets K, Loogvali EL, Pronina N, Lazdins M, Krumina A, Baumanis V, Villems R. 2006. Mitochondrial DNA portrait of Latvians: towards the understanding of the genetic structure of Baltic-speaking populations. Ann Hum Genet 70(Pt 4):439-58.

This article is protected by copyright. All rights reserved.

Accepted Article

Schmidt O, Pfanner N, Meisinger C. 2010. Mitochondrial protein import: from proteomics to functional mechanisms. Nat Rev Mol Cell Biol 11(9):655-67.

Schmitt MW, Kennedy SR, Salk JJ, Fox EJ, Hiatt JB, Loeb LA. 2012. Detection of ultra-rare mutations by next-generation sequencing. Proc Natl Acad Sci U S A 109(36):14508-13.

Shadel GS. 2008. Expression and maintenance of mitochondrial DNA: new insights into human disease pathology. Am J Pathol 172(6):1445-56.

Skladal D, Halliday J, Thorburn DR. 2003. Minimum birth prevalence of mitochondrial respiratory chain disorders in children. Brain 126(Pt 8):1905-12.

Sondheimer N, Glatz CE, Tirone JE, Deardorff MA, Krieger AM, Hakonarson H. 2011. Neutral mitochondrial heteroplasmy and the influence of aging. Hum Mol Genet 20(8):1653-9.

Sosa MX, Sivakumar IK, Maragh S, Veeramachaneni V, Hariharan R, Parulekar M, Fredrikson KM, Harkins TT, Lin J, Feldman AB and others. 2012. Next-generation sequencing of human mitochondrial reference genomes uncovers high heteroplasmy frequency. PLoS Comput Biol 8(10):e1002737.

Tang DL, Zhou X, Zhou KY, Li X, Zhao L, Liu F, Zheng F, Liu SM. 2005. [Association of mitochondrial DNA variation with type 2 diabetes mellitus]. Zhonghua Yi Xue Yi Chuan Xue Za Zhi 22(6):636-40.

Tatuch Y, Christodoulou J, Feigenbaum A, Clarke JT, Wherret J, Smith C, Rudd N, Petrova-Benedict R, Robinson BH. 1992. Heteroplasmic mtDNA mutation (T----G) at 8993 can cause Leigh disease when the percentage of abnormal mtDNA is high. Am J Hum Genet 50(4):852-8.

Taylor RW, Turnbull DM. 2005. Mitochondrial DNA mutations in human disease. Nat Rev Genet 6(5):389-402.

Underhill PA, Kivisild T. 2007. Use of y chromosome and mitochondrial DNA population structure in tracing human migrations. Annu Rev Genet 41:539-64.

Wiedemann N, Kozjak V, Chacinska A, Schonfisch B, Rospert S, Ryan MT, Pfanner N, Meisinger C. 2003. Machinery for protein sorting and assembly in the mitochondrial outer membrane. Nature 424(6948):565-71.

Yan MH, Wang X, Zhu X. 2013. Mitochondrial defects and oxidative stress in Alzheimer disease and Parkinson disease. Free Radic Biol Med 62:90-101.

This article is protected by copyright. All rights reserved.

Accepted Article

Figure 1. Overview of the computational pipeline

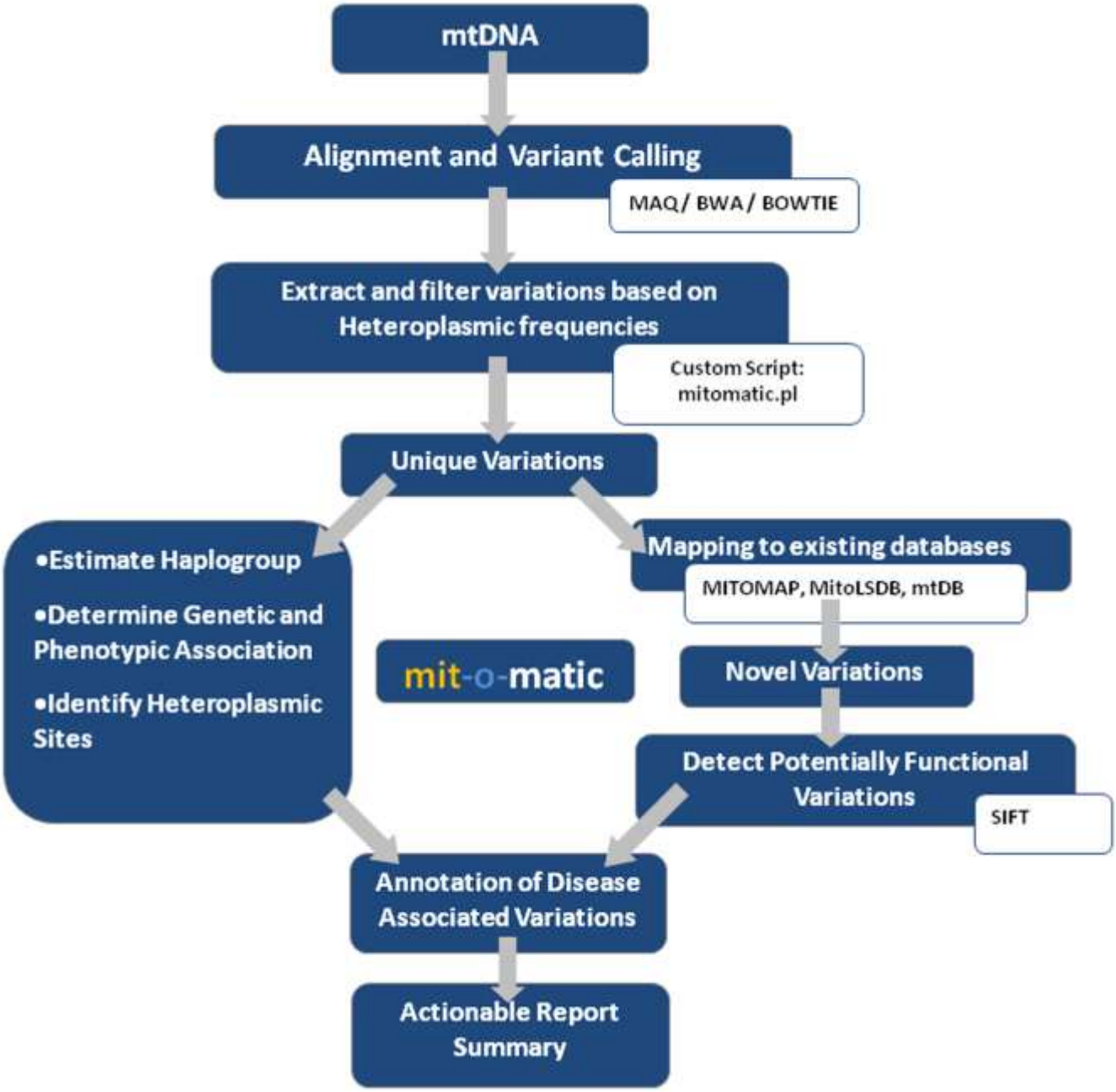

This article is protected by copyright. All rights reserved.

Figure 2. Snapshot of the report page of mit-o-matic. The report summarizes the analysis on top of the page followed by annotations for the variations detected in three different panels. (a) Summary includes haplogroup, number of heteroplasmic sites and counts of novel and disease associated variants. (b) Phenotype Association section enlists variants with confirmed or reported phenotypic association. (c) Novel variant section reports all the variations that have not been reported in MITOMAP, mtDB or MitoLSDB and their corresponding information details are detailed. (d) Variant map section details variants that have already been reported in the available resources.

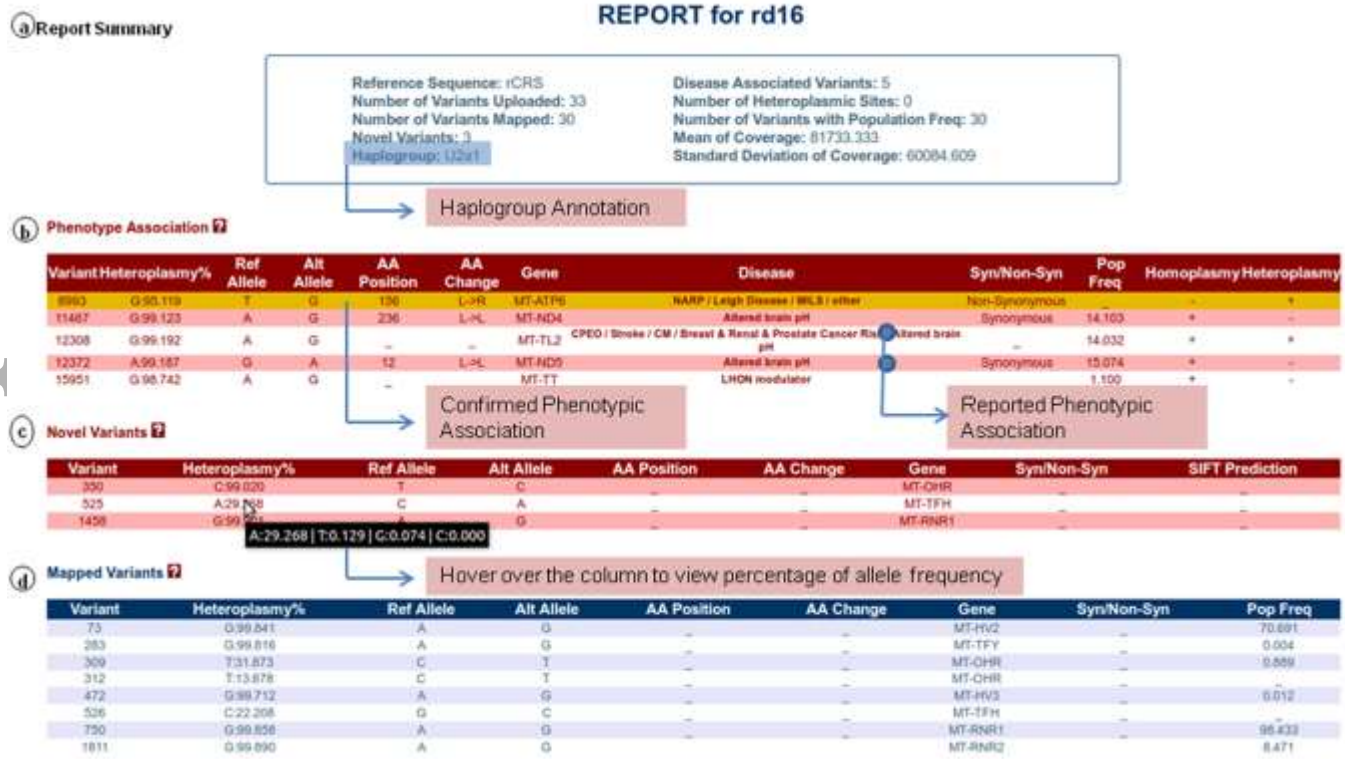

This article is protected by copyright. All rights reserved.

Accepted Article

Table 1. Data production and alignment results for the patient and the mother's sample

	Reads	**Mapped Reads**	**Mapping Percentage**	**Coverage**
Patient (rd16)	37,776,823	34,699,240	91.85%	106,805.56
Mother (rd22)	5,309,306	4,183,337	78.79%	8,584.31

Accepted Article

This article is protected by copyright. All rights reserved.

Appl Biochem Biotechnol (2014) 174:880–896
DOI 10.1007/s12010-014-0993-0

Nanomaterial-Based Biosensors for Food Toxin Detection

Bansi D. Malhotra · Saurabh Srivastava · Md. Azahar Ali · Chandan Singh

Received: 14 February 2014 / Accepted: 19 May 2014 /
Published online: 6 June 2014
© Springer Science+Business Media New York 2014

Abstract There is an increased interest toward the development of bioelectronic devices for food toxin (mycotoxins) detection. Mycotoxins are highly toxic secondary metabolites produced by fungi like *Fusarium*, *Aspergillus*, *and Penicillium* that are frequently found in crops or during storage of food including cereals, nuts, fruits, etc. The contamination of food by mycotoxins has become a matter of increasing concern. High levels of mycotoxins in the diet can cause adverse, acute, and chronic effects on human health and a variety of animal species. Side effects may particularly affect the liver, kidney, nervous system, endocrine system, and immune system. Among 300 mycotoxins known till date, there are a few that are considered to play an important part in food safety, and for these, a range of analytical methods have been developed. Some of the important mycotoxins include aflatoxins, ochratoxins, fumonisins, citreoviridin, patulin, citrinin, and zearalenon. The conventional methods of analysis of mycotoxins normally require sophisticated instrumentation, e.g., liquid chromatography with fluorescence or mass detectors, combined with extraction procedures for sample preparation. Hence, new analysis tools are necessary to attain more sensitive, specific, rapid, and reliable information about the desired toxin. For the last about two decades, the research and development of simpler and faster analytical procedures based on affinity biosensors has aroused much interest due to their simplicity and sensitivity. The nanomaterials have recently had a great impact on the development of biosensors. The functionalized nanomaterials are used as catalytic tools, immobilization platforms, or as optical or electroactive labels to improve the biosensing performance to obtain higher sensitivity, stability, and selectivity. Nanomaterials, such as carbon nanomaterials (carbon nanotubes and graphene), metal nanoparticles, nanowires, nanocomposites, and nanostructured metal oxide nanoparticles are playing an increasing role in the design of sensing and biosensing systems for mycotoxin determination. Furthermore, these nanobiosystems are also bringing advantages in terms of the design of novel food toxin detection strategies. We will focus on some of the recent results related to fabrication of nanomaterial-based biosensors for food toxin detection obtained in our laboratories.

B. D. Malhotra (✉)
Department of Biotechnology, Delhi Technological University, Delhi 110042, India
e-mail: bansi.malhotra@gmail.com

B. D. Malhotra · S. Srivastava · M. A. Ali · C. Singh
Department of Science and Technology Center on Biomolecular Electronics, Biomedical Instrumentation Section, CSIR-National Physical Laboratory, New Delhi 110012, India

Keywords Food toxins · Mycotoxins · Nanomaterials · Carbon nano materials · Graphene oxide

Introduction

The presence of various toxins in food and water is a major concern since it compromises food safety for public health. Food toxin is known as a substance which is synthesized by plant species, animal, and microorganisms. It can be categorized into four major groups such as plant toxins, bacterial pathogens and toxins, phycotoxins, and mycotoxins. Mycotoxins are toxic metabolises created by fungi or saprophytic molds that grow in a variety of foodstuffs including animal feeds and plant pathogens. They may be present in cereals, coffee, wine, fruits, feed, etc. and are potentially hazardous to animals [1]. Some plants are poisonous and they contain mainly phenolics, terpenoids, and nitrogen such as alkaloids, amines, amino acids, cyanogenic glycosides, glucosinolates, etc. Bacterial pathogens are known to be harmful and can cause several diseases. Tuberculosis is a bacterial disease caused by the bacterium *Mycobacterium tuberculosis*, which is mostly found in sub-Saharan Africa. Pathogenic bacteria can cause infections such as tetanus, typhoid fever, diphtheria, syphilis, and leprosy. Phycotoxins (marine toxins/shellfish toxins) are the secondary metabolites produced by toxicogenic microalgae. Mycotoxins including ochratoxins and aflatoxins are diminutive, toxic chemical products produced by fungal species that may contaminate them with toxins in the field or after harvest.

To protect consumers and maintain sustainability of agriculture, maximum permitted levels of toxins have been established in several matrices and analytical methods for their identification. It is essential to evolve new analytical tools for toxin quantification to obtain more specific and sensitive, rapid, robust, and reliable devices. Several European organizations including European Food Safety Authority, Food and Veterinary Office, and Community Bureau of Plant Varieties have recommended adequate sampling and analytical methods such as biosensors and biochemical assay analysis for toxin detection [2–4]. Vidal et al. have reviewed developments on electrochemical affinity biosensors for food mycotoxin detection [5]. It has been observed that electrochemical biosensors based on biochemical interactions provide high specificity and sensitivity. Besides this, electrochemical biosensors offer simplicity and cost-effective and disposable mass-produced electrodes. They may lead to the development of miniaturized, multiplexing, and portable devices for analysis of several compounds simultaneously. Kaushik et al. have recently reported advances in the electrochemical detection of ochratoxin A [6]. The nanostructured material including carbon materials plays an important role to improve the biosensor efficacy for food toxin detection. Integration of carbon materials with biosensor's transducer surface has led to interesting developments in biosensors due to their potential advantages such as higher specificity, higher sensitivity, higher operational stability, simpler and integrated sample treatment, and shorter analysis times [7, 8]. Carbon nanomaterials such as multiwalled carbon nanotubes (MWCNTs) and graphene and its derivatives (graphene oxide, reduced graphene oxide, etc.) are widely used in biosensors for food toxin detection [9, 10].

The field of carbon nanomaterials (CNMs) began with the discovery of the first synthetic allotrope of carbon, i.e., fullerene, in 1985 by Kroto et al. (Nobel Prize in Chemistry, 1996) which was further accompanied by the discovery of the carbon nanotubes in 1991 by S. Ijima and the recent discovery of graphene in 2004 by Geim and Novoselov (Nobel Prize in Physics, 2010). These synthetic allotropes of carbon have shown unique physical and chemical properties such as an ordered structure (with a high aspect ratio), ultra lightweight, high mechanical strength, high electrical and thermal conductivity, metallic or semi-metallic behavior, and high surface area, leading to considerable interest as a special class of materials. Figure 1 shows these synthetic carbon allotropes [11].

Wu et al. have used graphene oxide (GO) as an acceptor and multicolor upconversion fluorescent nanoparticle as a donor for multiplexed fluorescence resonance energy transfer-based aptasensor for mycotoxin determination [12]. This aptasensor provides a linear range from 0.05 to 100 ng/mL for ochratoxin A (OTA) and a detection limit of 0.02 ng/mL. An immunosensor has been demonstrated for ultrasensitive detection of aflatoxin B1 with an improved electrochemical performance using graphene/conducting polymer/gold nanoparticles/the ionic liquid nanocomposite film on modified gold electrode [13]. It has been observed that this nanocomposite shows an excellent sensitivity, long-term stability, and can be used to detect 1-fm concentration of aflatoxin B_1. Srivastava et al. have utilized antibody-functionalized reduced graphene oxide for aflatoxin B1 and obtained a detection limit of 0.12 ng/mL and a high sensitivity of 68 μA/(ng/mL)/cm^2 [10]. The functional and excellent electrochemical properties of CNMs may perhaps allow the selective immobilization of specific biomolecules for desired food toxin detection. Thus, it can be seen that the CNMs play an important role for the electrochemical detection of food toxins.

In this review, we focus the utilization of various carbon materials for food toxin, particularly for aflatoxin B1, detection. We present an overview of electrochemical properties of the carbon materials relating to recent development of biosensors for identification and quantification of various food contaminants. Besides this, we discuss the challenges and possible solutions of the various detection strategies for the development of compact analytical devices using carbon materials for food toxin determination.

Classification of Carbon Nanomaterials

Fullerenes

Fullerene is the zero-dimensional form of graphitic carbon. It can be visualized as an irregular sheet of graphene being curled up into a sphere by incorporating pentagons in its structure. Fullerenes come in various forms and sizes ranging from 30 to 3,000 carbon atoms. The smallest stable and most prominent is C_{60}. Each of C_{60} molecules is composed of 12 pentagons

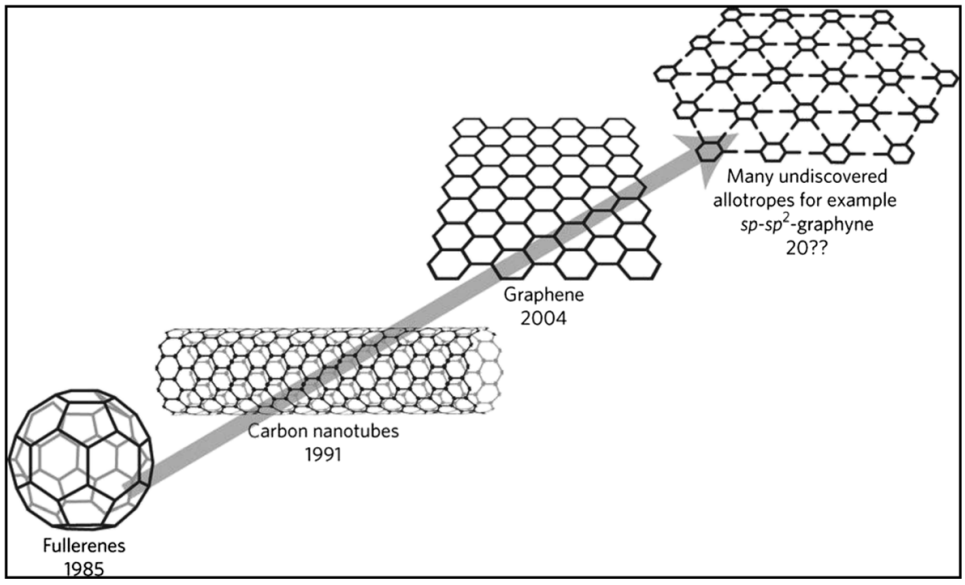

Fig. 1 Synthetic allotropes of carbon [11]

and 20 hexagons of sp^2-bonded carbon atoms. Many larger fullerenes such as C_{70}, C_{76}, C_{80}, C_{84}, etc. have also been found.

Carbon Nanotubes

Carbon nanotubes (CNTs) are one of the most promising materials offering unique physical and chemical properties for a wide range of applications in the field of physics, chemistry, and materials science. It consists of a sheet of graphite rolled into a tube with bonds at the end of the sheet. A single-walled carbon nanotube (SWCNT) has a diameter of 2 nm and a length of 100 μm, making it effectively a one-dimensional structure called a nanowire. Three types of nanotubes are possible, called armchair, zigzag, and chiral nanotubes, depending on how the two-dimensional graphene sheet is rolled up. MWCNTs are nanotubes with more than one wall, and their diameters are a few tens of nanometers. The interlayer distance in MWCNTs is close to the distance between the graphene layers in graphite, approximately 3.4 Å. CNTs exhibit extraordinary strength and unique electrical properties and are efficient thermal conductors. The chemical bonding of nanotubes is composed of entirely sp^2 bonds, which are stronger than the sp^3 bonds found in diamonds, and provide nanotubes with their unique strength. CNTs have attracted considerable interest since their discovery. They have been well investigated in order to exploit their superior properties and multifarious applications. CNTs have been extensively used for Li-ion secondary batteries [14, 15], nanofiltration [16, 17], hydrogen storage in fuel cells [18, 19], and supercapacitors [20, 21]. End/sidewall-localized COOH and NH_2 groups generated by oxidation of CNTs have been exploited for covalent attachment of biomolecular probes [22, 23], polymers [24], and metallic particles [25, 26]. They have been widely explored in highly sensitive electrochemical biosensing devices for food toxin detection owing to its unique electrochemistry [7, 23, 27].

Graphene

Graphene is a flat monolayer of carbon atoms, tightly packed into a two-dimensional (2D) honeycomb lattice. The single graphene layers were recently prepared successfully by means of a simple mechanical exfoliation of graphite using Scotch tape [28]. Andre Geim and Konstantin Novoselov, who headed the team behind the discovery of the exfoliation method and an associated investigation of the electronic properties of graphene, were awarded the 2010 Nobel Prize in Physics. The carbon bonds are sp^2-hybridized wherein the in-plane $\sigma_{c\text{-}c}$ bond is one of the strongest bonds in materials and out-of-plane π bond, which contributes to a delocalized network of electrons, is responsible for the electron conduction of graphene and provides the weak interaction among the graphene layers or between the graphene and substrate. With these unique structural characteristics, graphene has been shown to exhibit exceptional physical properties, which have attracted enormous research interest in both scientific and engineering communities.

Derivatives of Graphene

Being a standard 2D material for plethora of optoelectronics applications, graphene chemistry has not attracted significant interest. The main obstacle is the lack of functional groups for chemical and bimolecular functionalization. Progress in making graphene suspension rich in functional groups has opened up a new way to liquid-phase chemistry of graphene through chemical reduction method [29, 30]. Thus, the derivatives of graphene like graphene oxide (GO), reduced graphene oxide (rGO), and graphene quantum dots (GQDs) have entered into

the field of graphene research. These suspended forms of graphene have further broadened the area of applications such as in composite materials, biomedical, and biosensors.

Graphene Oxide

Graphene oxide (GO) is the oxidized form of graphite and is a layered material obtained by the exfoliation of graphite oxide. Although GO has been well known since its first synthesis by Brodie (1859), the material gained widespread popularity only after the discovery of graphene. Hence, it has been used as a source material for graphene synthesis by suitable reduction techniques [31]. In contrast to pristine graphite, the GO sheets are highly decorated by several oxygenated functional groups on its basal planes (hydroxyl and epoxies) and at its edges (carboxyl), resulting in a hybrid structure comprising of a mixture of sp^2- and sp^3-hybridized carbon atoms [29]. Both GO and graphite oxide are composed of stacked layer that are chemically functionalized on their basal planes and at their edges. However, GO possesses a monolayer or just a few stacked layers, while graphite oxide contains large number of stacked layers [32]. Oxygenated functional groups in graphite oxide make it easy to get exfoliated into monolayers of GO by stirring or mild sonication. GO has several captivating properties that offer several advantages over pure graphene for sensing and biosensing application [32]. Firstly, GO is dispersible in aqueous media, which is essential for biological applications. Secondly, it contains large amounts of oxygen-containing groups, which can be beneficial for the covalent immobilization of the biomolecules. GO has a highly disrupted sp^2 carbon lattice and exhibits a large number of defects, and functional groups make it insulator. Thus, to improve the conductivity, it is necessary to convert it into reduced graphene oxide (rGO). The rGO shows superior electrochemical behavior such as large voltammetric current and lower oxidation potential that makes it a promising candidate in the area of electrochemical biosensing. The molecular structure and high-resolution transmission electron microscopy (HRTEM) image of the graphene oxide is shown in Fig. 2.

Reduced Graphene Oxide

Reduced graphene oxide (rGO) is partly a reduced form of GO containing π-conjugated system. rGO resembles graphene with some residual oxygen and structural defects, whose conductivity is comparable to that of doped conductive polymers. GO can be converted to rGO

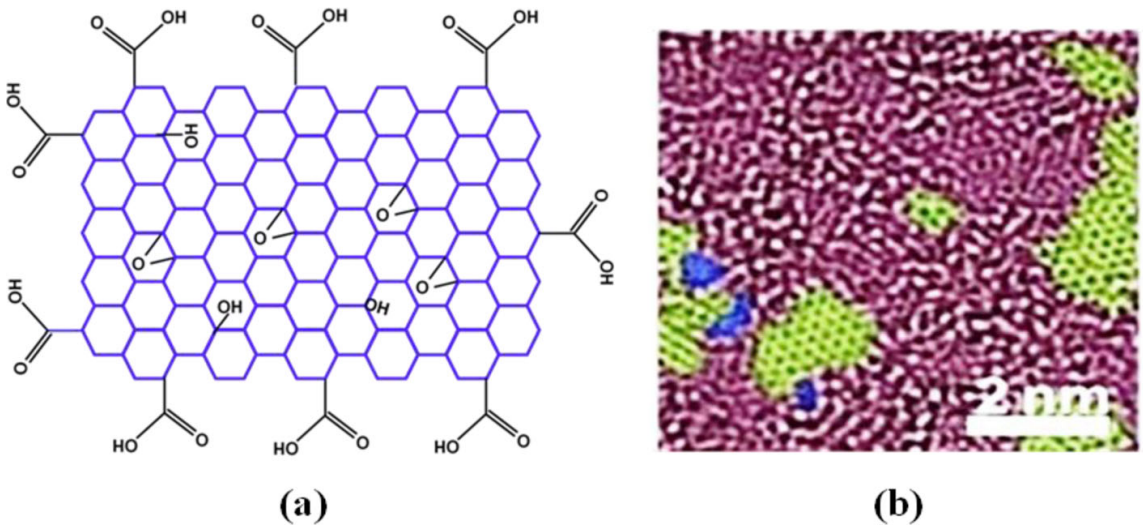

Fig. 2 Graphene oxide: **a** molecular and **b** HR-TEM image [33]

by thermal annealing, chemical reduction, or electrochemical reduction process [34]. rGO has been widely explored in the development of electrochemical sensors and biosensors because (1) its defects and chemical groups facilitate charge transfer and thus ensure high electrochemical activity; (2) the abundant functional groups on the rGO surface offer the convenience and flexibility for various functionalizations to enhance the sensor performance; (3) the chemical and electrical properties of rGO are highly tunable; and (4) as compared to non-conductive GO, rGO can efficiently transport charges. In addition, rGO can also be functionalized through covalent or non-covalent methods in order to further enhance its sensitivity, specificity, loading capacity, biocompatibility, etc. [35–39]. The molecular structure and HRTEM image of the reduced graphene oxide is shown in Fig. 3.

Carbon Nanomaterials for Biosensor Applications

The growing area of biomedical engineering has also embraced the increasing popularity of CNMs in recent years. The CNMs, especially CNTs and graphene, have been widely regarded as highly attractive biomaterials due to their multifunctional nature [40]. The physical properties of CNTs, such as mechanical strength, electrical conductivity, and optical properties, could be of great value for creating advanced biomaterials. The ability of functionalized CNT to penetrate into the cells offers the potential of using CNT as vehicles for the delivery of small drug molecules [41]. It has been observed that the functionalized carbon nanotubes enter non-adherent human cancer cells and by themselves are not toxic. While the fluoresceinated protein streptavidin by itself does not enter cells; it readily enters cells when it complexes to a nanotube–biotin transporter and exhibits dose-dependent cytotoxicity [42]. The biomedical application of graphene is a relative new area with significant potential. The intensive research on the biological applications of graphene and its derivatives is due to many fascinating properties, such as high specific surface area, exceptional electronic and thermal conductivity, high mechanical strength, and biocompatibility. GO produced via oxidation of graphite under acidic conditions is more commonly used, as it offers several advantages over using pure graphene. This is due to high dispersibility of GO in aqueous media, which is essential for biological applications. Moreover, low cost, scalable production, and facile biological/chemical functionalization are some of the other benefits of GO over pure graphene. The use of GO as an efficient nanocarrier for drug delivery was first reported by Dai et al., and

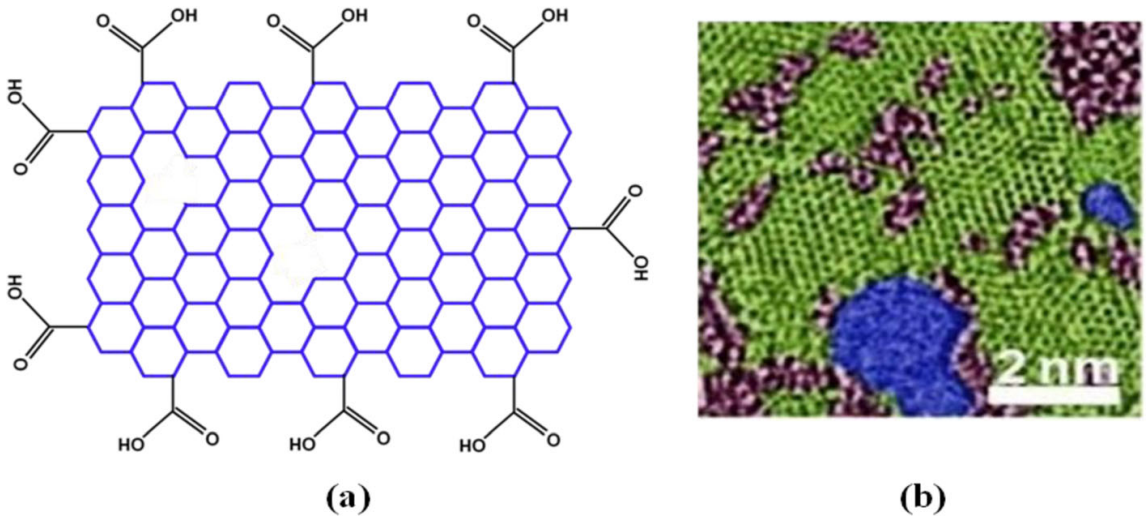

Fig. 3 Reduced graphene oxide: **a** Molecular and **b** HR-TEM image [33]

since then, a lot of interesting work has been carried out to explore the use of graphene for widespread biomedical applications, ranging from drug/gene delivery, biological sensing and imaging, and antibacterial materials to biocompatible scaffold for cell culture [43]. Zhang et al. explored the feasibility of GO as a nanocarrier for controlled loading and targeted delivery of mixed chemical drugs [44].

Food Toxins

Air, water, soil, and food are the unavoidable components of the human environment. Each of those elements influences the quality of human life, and each of them may be contaminated. Food is not only the elementary source of nutrients but may also contain natural chemical substances with toxic properties, e.g., cyanogenic glycosides (many plants), solanine (green parts of potatoes, sprouted potatoes, and potatoes stored in light), industrial pollutants (heavy metals), biogenic amines (fish), or mycotoxins (moldy foodstuffs). Food toxins include plant and microbial toxins that may contribute to common cases of food allergies, intolerance, and poisoning.

Plant Toxins

Natural substances in plants used for food impact the health of the human species. A few plants are poisonous and should not be ingested, but all plants used for food are nutritious and lack toxic effects. Grass pea (*Lathyrus sativus*) is an environmentally tolerant and protein-rich legume that is eaten on the Indian subcontinent, in the northeastern China, and the Horn of Africa that causes lathyrism, characterized by weakness, increased muscle tone, and hyperreflexia in the lower extremities. Continued ingestion results in progressive walking difficulties that eventuate in permanent inability to move the legs [45]. The ackee tree (*Blighia sapida*) synthesizes water-soluble toxic amino acids—known as hypoglycin A and B—and causes violent vomiting [46]. Ingestion of tree nuts, the edible kernels of the seed of several trees, may also cause immunological illness [47]. Sweet almonds (*Amygdalus communis*) and bitter almonds (*Prunus amygdalus*) comprise 22 % protein and contain multiple IgE-binding proteins that may trigger severe allergic reactions. Brazil nuts (*Bertholletia excelsa*, *Bertholletia myrtaceae*), ingestion of which has triggered allergic reactions in children and adults, contain 14 % protein, including a methionine-rich protein (Ber e 1) that constitutes the major allergen [48]. Several nuts and seeds other than tree nuts and legumes (groundnuts) may trigger allergic reactions [49]. Several plants (*Brassica* spp., cassava, and sorghum) eaten by humans possess glycosides that may attack the thyroid, brain, and, possibly, pancreas.

Bacterial Pathogens

Food-borne disease has been defined by the World Health Organization (WHO) as a disease of infectious or toxic nature caused by, or thought to be caused by, the consumption of food or water [50]. Food-borne disease takes a huge toll on human health and mortality. Food-borne pathogens vary considerably in their association with certain foods. In recent years, some bacterial pathogens have been linked to foods, including *Campylobacter* (milk and poultry), *Escherichia coli* O157:H7 (ground meats, unpasteurized apple cider, and cheese curds), *Salmonella* (eggs, fruits, and vegetables), and *Listeria monocytogenes* (raw milk, minimally processed and ready-to-eat meats). These food pathogens may cause major health problem such as abdominal pain, headache, bloody diarrhea, nausea, diarrhea, vomiting, and fever.

Phycotoxins

Phycotoxins are known to be as marine toxins or shellfish toxins and are found in the sea produced by toxicogenic microalgae. It is not exactly known as to why these microorganisms produce toxins and what their role is. Their production is a complex phenomenon that may be related to stringent climatic and ecological conditions. Although marine toxins do not entail a risk for shellfish, they are of major concern for human health. Usually, only acute intoxications are reported, but it is suspected that chronic exposure to marine toxins may induce immunotoxic, mutagenic, and carcinogenic effects [51–53].

Mycotoxins

Mycotoxins have low molecular weights and are natural products produced as secondary metabolites by filamentous fungi. More than 500 different mycotoxins are currently known, forming a structurally diverse group with different physicochemical properties. Aflatoxins; ochratoxins; fumonisins; patulin; trichothecenes such as T-2 toxin, HT-2 toxin, or deoxynivalenol (DON); zearalenone (ZEA); Alternaria toxins; and ergot alkaloids are types of major mycotoxins [54]. Mycotoxins are ubiquitous toxic compounds produced under certain weather conditions in the field and during improper storage, being mainly found in agricultural commodities and animal feedstuff [55]. Contamination by mycotoxins is a real problem, not only because of economical loss but especially also because of the serious human and animal health problems that their ingestion may cause. Such problems include liver and kidney diseases, nervous system damage, immunosuppression, and carcinogenicity [56]. As a result of the increasing concern related to mycotoxin contamination, legal regulations are continuously being updated [57].

The European Commission, scientifically assisted by the European Food Safety Authority (EFSA), has set MPLs for certain mycotoxins in individual foodstuffs trying to harmonize specific legislations to ensure protection of public health [58]. Table 1 summarizes classes of major mycotoxins and their physiological effects. The chemical structure of some of these important mycotoxins is shown in Fig. 4. Among these aforementioned mycotoxins, the detection of aflatoxin B1 (AFB1) is considered very important. AFB1 is considered as a first hazard class human carcinogen (according to the IARC classification), and it is the most prevalent and toxic among all the mycotoxins. In the following section, a brief discussion of AFB1 and its detection using analytical techniques has been described.

Aflatoxin B1 and Conventional Detection Methods

Aflatoxins (AF) are a group of secondary fungal metabolites that are produced by *Aspergillus Flavus* and *Aspergillus Parasiticus* under certain conditions and are the most widely spread group of toxins resulting in contamination of food products. *Aspergillus* molds grow mostly on crops, such as grains and nuts, and are found in milk, cheese, corn, peanuts, cottonseed, almonds, figs, spices, and a variety of other foods and feeds. Milk, eggs, and meat products are sometimes contaminated because of the animal consumption of aflatoxin-contaminated feed. *Aspergillus* also grows on substances like soil, hay, and decaying vegetation. The best conditions for *Aspergillus* to grow on organic materials are when the temperature is warm and when the material has a high level of moisture (7 % or more). Among the 18 different types of aflatoxins identified, major members are aflatoxin B1, B2, G1, and G2. The aflatoxins produce strong fluorescence in ultraviolet light (365 nm); B1 and B2 produce a blue fluorescence, whereas G1 and G2 produce green fluorescence. The aflatoxins are known to be potent

Table 1 Classes of major mycotoxins and their physiological effects

Toxin	Major effects on mammalian systems	References
Aflatoxins	Carcinogenic, acute hepatitis, impaired immune system	[59–61]
Ochratoxins	Carcinogenic, nephrotoxic, hepatotoxic, teratogenic	[62, 63]
Citrinin	Nephrotoxic	[64]
Citreoviridin	Neurotoxicity	[65, 66]
Fumonisins	Carcinogenic, hepatotoxic, causative agent of leukoencephalomalacia in horses	[67–69]
Patulin	Lung and brain hemorrhaging	[70, 71]
Trichothecenes	Immunodepressant, gastrointestinal hemorrhaging	[72]
Zearalenone	Estrogenic activity	[73]

toxic, carcinogenic, mutagenic, and immunosuppressive in the order of AFB1>AFG1>AFB2>AFG2. Among these, aflatoxin B1 (AFB1) is predominant and is a potent human carcinogen and is primarily responsible for liver cancer in animals. When AFB1 is ingested with feed by cows, it is transformed into its hydroxylated metabolite product, aflatoxin M1 (AFM1), which is then secreted in the milk. AFB1 is regulated by legislation in the EU at 2.0 μg/kg in foods for direct human consumption.

AFB1 occurs in the low sub-nanogram per gram range in a variety of food products. As low parts per billion (ppb) concentrations are usually involved, very sensitive analytical methods for AFB1 detection are needed [74]. Keeping this in view, the chromatographic analytical tools such as thin layer chromatography (TLC) and high-performance liquid chromatography (HPLC) with fluorescence or mass detector have been developed and are considered as the official methods for AFB1 monitoring. Routine screening of AFB1 is commonly performed by enzyme-linked immunosorbent assays (ELISAs), that can be used to process a large number of

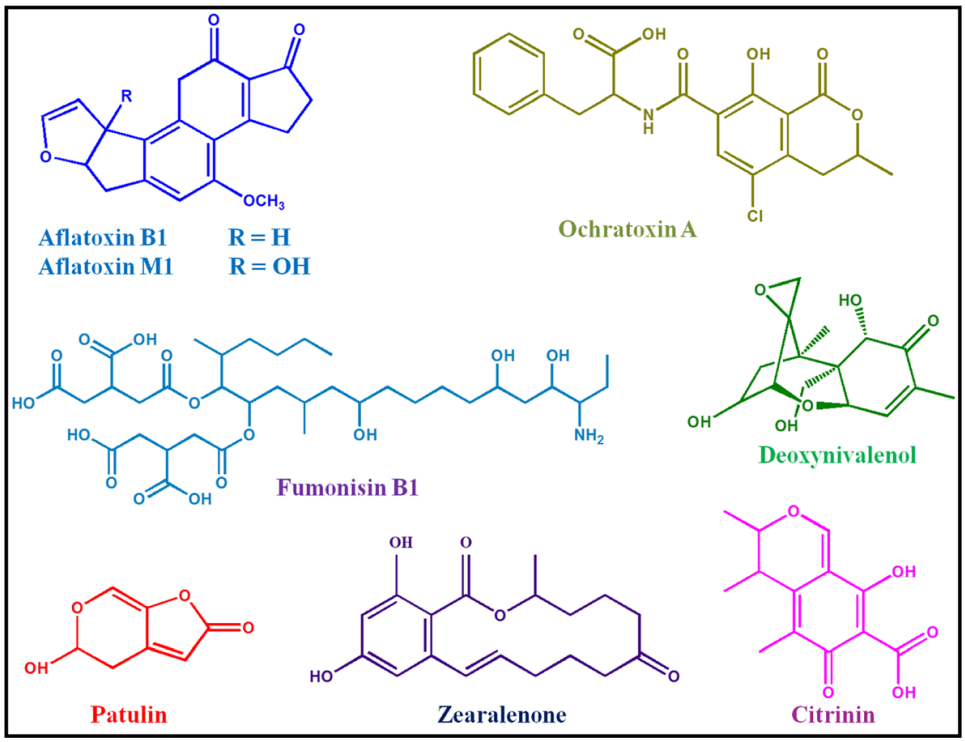

Fig. 4 Chemical structure of some of the important mycotoxins

samples in a single assay. Nevertheless, they involve long, laborious, and tedious procedures and cross-reactivity phenomena that, even though sometimes could be useful for the evaluation of the total toxicity, may yield false positive results for a single mycotoxin determination. These techniques usually yield very low detection limits, but sometimes their cost, need of skilled personnel, and limitations to perform in situ analysis can be overcome by alternative techniques. Patterson et al. detected several mycotoxins including AFB1 using 2D thin layer chromatography and appropriate solvent systems. AFB1 has been detected in mixed feedstuffs and various ingredients at levels ranging from 0.1 to 0.3 μg/kg [75].

Nakajima et al demonstrated a high-performance liquid chromatography technique linked with immunoaffinity chromatography to survey AFB1 and OTA in commercial green coffee beans. AFB1 and OTA were quantified with detection limits of 2 ng/kg and 0.1 μg/kg, respectively [76]. Candlish et al. developed a direct competitive enzyme-linked immunosorbent assay (ELISA) for AFB1. The sensitivity of the ELISA was 0–2 ng/mL with a working range up to 10 ng/mL for AFB1 [77]. These assays indicated broader detection ranges (4.2–99.9 μg/kg in sample) and showed no methanol effects up to 80 % with significantly reduced matrix interferences as a result of the shorter incubation times [78]. Xiulan et al. reported an immunochromatography assay for AFB1. The antibody-colloidal gold probe (conjugate) specific to AFB1 was prepared and used in developing a rapid AFB1 diagnostic method. Detection time (10 min) was found to lower by 6–10 times as compared to that of ELISA, whereas lower test limit was found to be around 2.5 ng/mL [79].

Biosensors for Aflatoxin B1 Detection

The biosensors have emerged as a reliable and promising alternative analysis tools as compared to those of classical methods because of their high sensitivity and selectivity, simplicity, ease of use, low cost, and in some cases, miniaturization and portability. According to IUPAC, biosensor is a self-contained integral device that is capable of providing specific quantitative or semi-quantitative analytical information using a biological element. In a biosensor, physiochemical change produced by specific interactions between the target analyte and biological element can be detected using a desired transducer. Biological element can be antibody, enzyme, receptor protein, nucleic acid, cell, or tissue. In the past decade, biosensing devices have aroused increasing interest for the point-of-care diagnostics and environmental monitoring such as for food toxins.

A typical biosensor has three major components such as a biorecognition element (DNA, enzyme, antibody, etc.) for recognition of an analyte also called bioreceptor; an immobilization matrix such as conducting polymers [80], nanomaterials [81, 82], sol–gel films [83], and self-assembled monolayers [84] have been used for the immobilization of a biomolecule; and a transducer unit for conversion of biochemical reaction product into a recognizable signal (Fig. 5). Bioreceptor and transducer together may also be referred to be as a biosensor membrane. Biomolecular recognition element, i.e., bioreceptor, is a biomolecule or molecular assembly that has the capability of recognizing a target/substrate, i.e., an analyte. The most commonly used bioreceptors in biosensors are enzymes, antibodies, DNA, or whole cells. The specificity of a biosensor comes from the specificity of the bioreceptor molecule used. In this context, CNMs have recently gained much interest in biosensor due to excellent electrocatalytic activity, large voltammetric current, and capability to demonstrate DET property for some proteins; the CNMs have been widely explored as a sensitive platform in electrochemical biosensor.

CNTs are commonly incorporated onto electrodes by directly growing CNTs on the electrode surface, adsorbing them on existing electrodes, imbedding them in polymer coatings, or combining CNTs and a binder to make a paste electrode [85]. The oxygen-containing species present on the graphene sheets generated during acid treatment are responsible for faster electron transfer kinetics. Since most atoms of the graphene sheets are exposed to the surface, slight changes in the charge environment due to the adsorption of biomolecules provide significant changes in their electrical properties which may help in the fabrication of more sensitive biosensors [36, 86]. The electrochemical sensors have been developed due to its simplicity and fast response, low-cost equipment, and real-time output over traditional techniques for AFB1 detection. In some cases, adsorptive accumulation by stripping voltammetry procedures has been required to electrochemically quantify aflatoxin B1 (AFB1) and aflatoxin B2 (AFB2) at trace levels [87, 88]. The ability of enzymes to catalyze specific reactions has been exploited to develop enzyme sensors for AFB1 analysis. Li et al. developed amperometric aflatoxin biosensor using aflatoxin-oxidase (AFO), embedded in sol-gel, linked to MWCNT-modified platinum electrode. This sensor exhibited a linear range from 3.2 to 721 nM (1 to 225 ng/mL) with limits of detection of 1.6 nM (signal-to-noise ratio=3) [89]. Most biosensors for mycotoxin detections are based on immunoreactions between antigen and antibody. It is known that the main advantage of these biosensors is that they do not require any tagging or labeled reagents. Nevertheless, labels can be used for signal amplification [90, 91]. Development of conductometric [92], potentiometric [93], and amperometric immunosensors has been often restricted by the requirement of electroactive labels [94, 95]. Recently, the label-free immunosensors based on electrochemical impedance spectroscopy (EIS) have emerged as simple, cost-effective, and highly sensitive devices for aflatoxin determination [96, 97]. They may lead to the development of miniaturized, multiplexing, and portable devices for in situ analysis of several compounds simultaneously. The formation of the antibody–antigen complex by a simple one-step immunoreaction between the immobilized anti-AFB1 and AFB1 in a sample solution introduced a barrier for direct electrical communication which resulted in the change in local conductivity variations could be detected. The proposed immune-biosensor exhibited a good conductometric response relative to AFB1 concentration in a linear range from 0.5 to 10 ng/mL with a relatively low

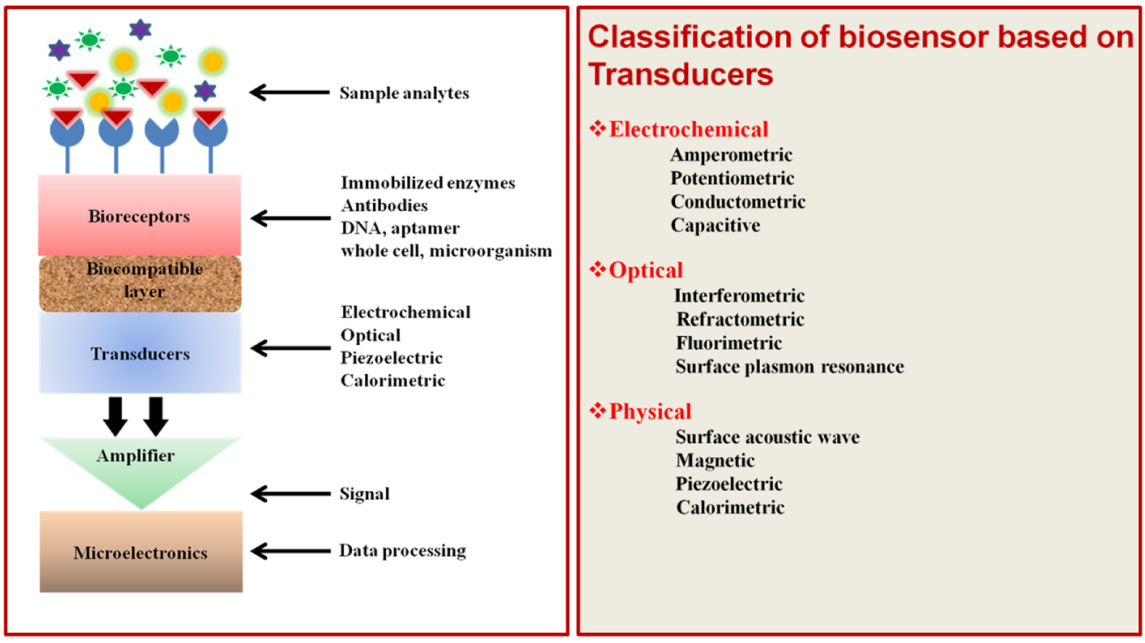

Fig. 5 Schematic of biosensors

detection limit of 0.1 ng/mL [98]. Piermarini et al. have demonstrated electrochemical immunosensor array using a 96-well screen-printed microplate for aflatoxin B1 detection. AFB1 can be measured at a level of 30 pg/mL and with a working range between 0.05 and 2 ng/mL [99, 100]. Pemberton et al. reported the development of a screen-printed carbon electrochemical immunosensor array for AFB1 detection. The screen-printed carbon electrodes bearing a surface-adsorbed antibody against AFB1 were used in a competitive immunoassay, based on competition of free analyte with a biotinylated aflatoxin B1 conjugate. The detection range of 0.15 to 2.5 ng/mL and a detection limit of around 0.15 ng/mL were achieved [101]. It is clear from the above reports that there is a considerable scope to improve the sensing characteristic of AFB1 using electrochemical immunosensor. Singh et al. fabricated carboxylated multiwalled carbon nanotubes based biosensor for aflatoxin detection. The carboxylated MWCNTs that have been electrophoretically deposited onto indium tin oxide (ITO) substrate and the electrode surface were functionalized with monoclonal anti-aflatoxin B1 (anti-AFB1). The antibody molecules were covalently immobilized via EDC-NHS coupling chemistry to ensure the high stability (Fig. 6). The c-MWCNT-based electrochemical immune-biosensor showed high sensitivity (95 μA/(ng/mL)/cm^2) and improved detection limit (0.25 ng/mL) in the linear detection range of 0.25–1.25 ng/mL [102].

The rGO, due to its excellent electrochemical properties and large surface area, has recently aroused much interest for electrochemical biosensing application. Srivastava et al. synthesized chemically active RGO, deposited onto indium tin oxide (ITO)-coated glass substrate. This novel platform has been utilized for covalent attachment of the monoclonal antibodies of aflatoxin B1 (anti-AFB1) for food toxin (AFB1) detection [10]. The electrochemical sensing results of the anti-AFB$_1$/RGO/ITO-based immunoelectrode obtained as a function of aflatoxin concentration showed high sensitivity (68 μA/(ng/mL)/cm^2) and improved detection limit

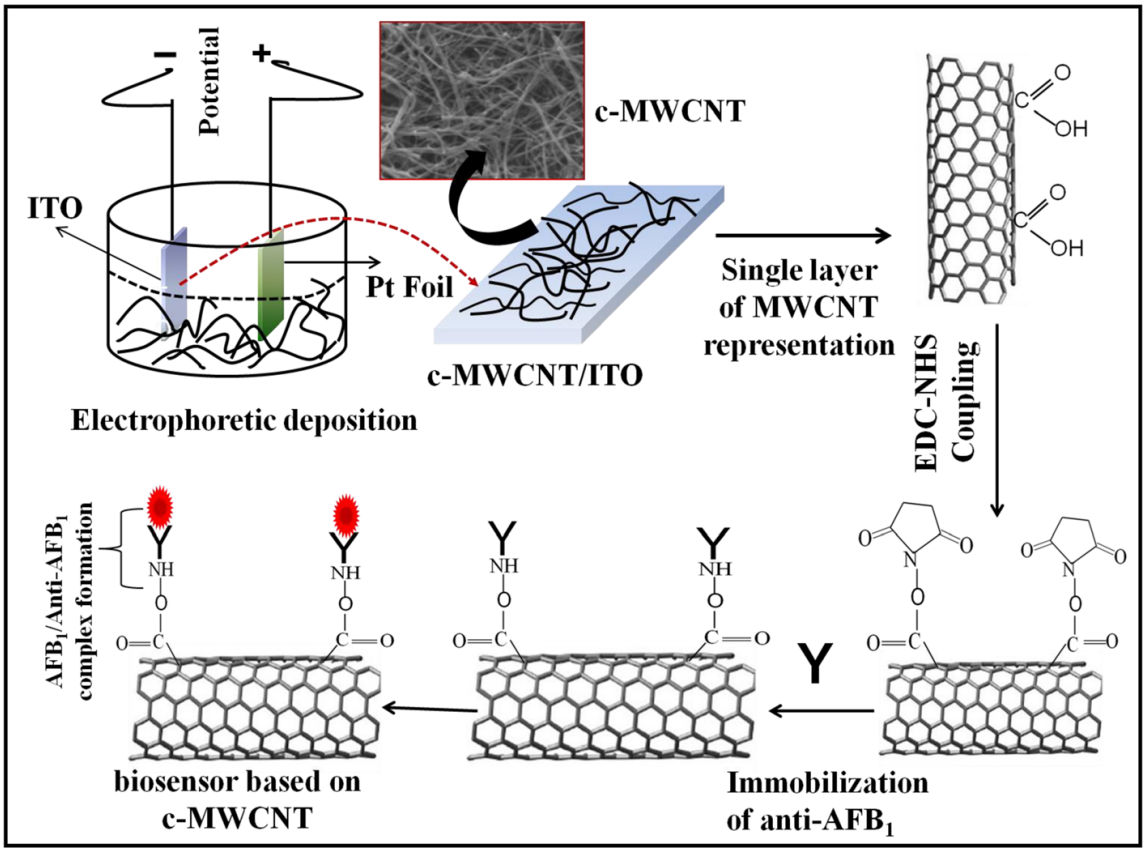

Fig. 6 Schematic representation of c-MWCNT based biosensor for Aflatoxin B$_1$ detection [102]

(0.12 ng/mL). The association constant (k_a) for antigen–antibody interaction obtained as 5×10^{-4} ng/mL indicated high affinity of antibodies toward the antigen (AFB1) (Fig. 7).

The insulating GO was found to be the excellent candidate for AFB1 determination via the impedimetric immuno-biosensor. We have recently fabricated a highly sensitive label free impedimetric immune-biosensor based on GO platform for the detection of AFB1 using EIS technique. The impedimetric sensing response of immunoelectrode as a function of AFB1 concentration has revealed wider linear detection range as 0.5–5 ng/mL, sensitivity as 639Ω/ng/mL, and detection limit as 0.23 ng/mL for the label-free detection. The wider linear detection range of this biosensor could be attributed to the presence of larger number of functional groups (carboxyl) as compared to that based on MWCNTs and rGO [103].

Conclusions

This review demonstrated the work relating to the development of carbon nanomaterial-based biosensing devices for the food toxin detection. The potential merit and various prospects of biosensors for food toxin detection have been explained. Especially, we have covered the utilization of carbon nanomaterials in the development of compact devices for food toxin monitoring. Compared to the conventional detection methods that require sophisticated instrumentation and excessive procedures for sample preparation, the electrochemical biosensors have been found to exhibit sensitive, specific, rapid, robust, and reliable toxin quantifications. The study suggests that the carbon nanomaterials including MWCNTs, graphene, and their derivatives, owing to their exceptional properties, have a great potential to meet the challenges in the development of rapid, ultrasensitive, and efficient biosensor for food toxin detection in the real samples. These CNM-based biosensors could be a better alternative over the conventional detection techniques.

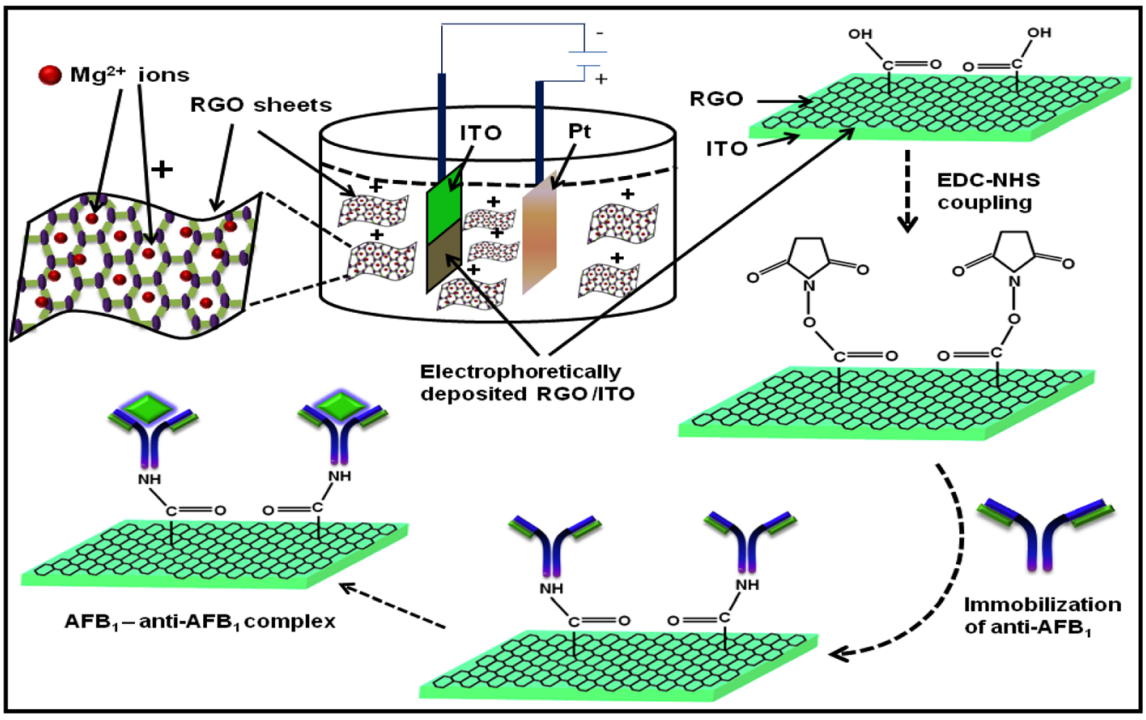

Fig. 7 Schematic representation of the proposed RGO based immunosensor [10]

Acknowledgments We thank Dr Anchal Srivastava (Banaras Hindu University, India) and Dr G. Sumana (CSIR-National Physical Laboratory, India) for interesting discussions. S.S. acknowledges the financial support from CSIR (SRF: 31/001(0302)/2008-EMRI), New Delhi, India. The financial support received from Department of Science and Technology, India (Grant No. DST/TSG/ME/2008/18) and Indian Council of Medical Research, India (Grant No. ICMR/5/3/8/91/GM/2010-RHN) is gratefully acknowledged.

References

1. Kralj Cigić, I., & Prosen, H. (2009). An overview of conventional and emerging analytical methods for the determination of mycotoxins. *International Journal of Molecular Sciences, 10*(1), 62–115.
2. Palchetti, I., & Mascini, M. (2008). Electroanalytical biosensors and their potential for food pathogen and toxin detection. *Analytical and Bioanalytical Chemistry, 391*(2), 455–471.
3. Ligler, F. S., Taitt, C. R., Shriver-Lake, L. C., Sapsford, K. E., Shubin, Y., & Golden, J. P. (2003). Array biosensor for detection of toxins. *Analytical and Bioanalytical Chemistry, 377*(3), 469–477.
4. Rasooly, A., & Herold, K. E. (2006). Biosensors for the analysis of food- and waterborne pathogens and their toxins. *Journal of AOAC International, 89*(3), 873–883.
5. Vidal, J. C., Bonel, L., Ezquerra, A., Hernández, S., Bertolín, J. R., Cubel, C., et al. (2013). Electrochemical affinity biosensors for detection of mycotoxins: a review. *Biosensors and Bioelectronics, 49*, 146–158.
6. Kaushik, A., Arya, S. K., Vasudev, A., & Bhansali, S. (2013). Recent advances in detection of ochratoxin-A. *Open Journal of Applied Biosensor, 2*, 1.
7. Wang, J. (2005). Carbon nanotube based electrochemical biosensors: a review. *Electroanalysis, 17*(1), 7–14.
8. Kuila, T., Bose, S., Khanra, P., Mishra, A. K., Kim, N. H., & Lee, J. H. (2011). Recent advances in graphene-based biosensors. *Biosensors and Bioelectronics, 26*(12), 4637–4648.
9. Singh, C., Srivastava, S., Ali, M. A., Gupta, T. K., Sumana, G., Srivastava, A., et al. (2013). Carboxylated multiwalled carbon nanotubes based biosensor for aflatoxin detection. *Sensors and Actuators B: Chemical, 185*, 258–264.
10. Srivastava, S., Kumar, V., Ali, M. A., Solanki, P. R., Srivastava, A., Sumana, G., et al. (2013). Electrophoretically deposited reduced graphene oxide platform for food toxin detection. *Nanoscale, 5*(7), 3043–3051.
11. Hirsch, A. (2010). The era of carbon allotropes. *Nature Materials, 9*(11), 868–871.
12. Wu, S., Duan, N., Shi, Z., Fang, C., & Wang, Z. (2014). Simultaneous aptasensor for multiplex pathogenic bacteria detection based on multicolor upconversion nanoparticles labels. *Analytical Chemistry, 86*(6), 3100–3107.
13. Linting, Z., Ruiyi, L., Zaijun, L., Qianfang, X., Yinjun, F., & Junkang, L. (2012). An immunosensor for ultrasensitive detection of aflatoxin B1 with an enhanced electrochemical performance based on graphene/conducting polymer/gold nanoparticles/the ionic liquid composite film on modified gold electrode with electrodeposition. *Sensors and Actuators B: Chemical, 174*, 359–365.
14. Hu, L., Wu, H., La Mantia, F., Yang, Y., & Cui, Y. (2010). Thin, flexible secondary Li-ion paper batteries. *ACS Nano, 4*(10), 5843–5848.
15. de las Casas, C., & Li, W. (2012). A review of application of carbon nanotubes for lithium ion battery anode material. *Journal of Power Sources, 208*, 74–85.
16. Mostafavi, S., Mehrnia, M., & Rashidi, A. (2009). Preparation of nanofilter from carbon nanotubes for application in virus removal from water. *Desalination, 238*(1), 271–280.
17. Srivastava, A., Srivastava, S. Kalaga K. (2013). *Carbon nanotube membrane filters. Springer handbook of nanomaterials*: Springer, p. 1099–1116.
18. Cheng, H.-M., Yang, Q.-H., & Liu, C. (2001). Hydrogen storage in carbon nanotubes. *Carbon, 39*(10), 1447–1454.
19. Dillon, A. C., Jones, K., Bekkedahl, T., Kiang, C., Bethune, D., & Heben, M. (1997). Storage of hydrogen in single-walled carbon nanotubes. *Nature, 386*(6623), 377–379.
20. Kaempgen, M., Chan, C. K., Ma, J., Cui, Y., & Gruner, G. (2009). Printable thin film supercapacitors using single-walled carbon nanotubes. *Nano Letters, 9*(5), 1872–1876.
21. Zhang, L. L., & Zhao, X. (2009). Carbon-based materials as supercapacitor electrodes. *Chemical Society Reviews, 38*(9), 2520–2531.
22. Cha, C., Shin, S. R., Annabi, N., Dokmeci, M. R., & Khademhosseini, A. (2013). Carbon-based nanomaterials: multifunctional materials for biomedical engineering. *ACS Nano, 7*(4), 2891–2897.
23. Wohlstadter, J. N., Wilbur, J. L., Sigal, G. B., Biebuyck, H. A., Billadeau, M. A., Dong, L., et al. (2003). Carbon nanotube-based biosensor. *Advanced Materials, 15*(14), 1184–1187.

24. Coleman, J. N., Khan, U., Blau, W. J., & Gun'ko, Y. K. (2006). Small but strong: a review of the mechanical properties of carbon nanotube–polymer composites. *Carbon, 44*(9), 1624–1652.
25. Kim, B., & Sigmund, W. M. (2004). Functionalized multiwall carbon nanotube/gold nanoparticle composites. *Langmuir, 20*(19), 8239–8242.
26. Li, W., Liang, C., Zhou, W., Qiu, J., Zhou, Z., Sun, G., et al. (2003). Preparation and characterization of multiwalled carbon nanotube-supported platinum for cathode catalysts of direct methanol fuel cells. *The Journal of Physical Chemistry B, 107*(26), 6292–6299.
27. Rivas, G. A., Rubianes, M. D., Rodríguez, M. C., Ferreyra, N. F., Luque, G. L., Pedano, M. L., et al. (2007). Carbon nanotubes for electrochemical biosensing. *Talanta, 74*(3), 291–307.
28. Novoselov, K. S., Geim, A. K., Morozov, S. V., Jiang, D., Zhang, Y., Dubonos, S. V., et al. (2004). Electric field effect in atomically thin carbon films. *Science, 306*(5696), 666–669.
29. Dikin, D. A., Stankovich, S., Zimney, E. J., Piner, R. D., Dommett, G. H., Evmenenko, G., et al. (2007). Preparation and characterization of graphene oxide paper. *Nature, 448*(7152), 457–460.
30. Hernandez, Y., Nicolosi, V., Lotya, M., Blighe, F. M., Sun, Z., De, S., et al. (2008). High-yield production of graphene by liquid-phase exfoliation of graphite. *Nature Nanotechnology, 3*(9), 563–568.
31. Park, S., & Ruoff, R. S. (2009). Chemical methods for the production of graphenes. *Nature Nanotechnology, 4*(4), 217–224.
32. Dreyer, D. R., Park, S., Bielawski, C. W., & Ruoff, R. S. (2010). The chemistry of graphene oxide. *Chemical Society Reviews, 39*(1), 228–240.
33. Erickson, K., Erni, R., Lee, Z., Alem, N., Gannett, W., & Zettl, A. (2010). Determination of the local chemical structure of graphene oxide and reduced graphene oxide. *Advanced Materials, 22*(40), 4467–4472.
34. Pei, S., & Cheng, H.-M. (2012). The reduction of graphene oxide. *Carbon, 50*(9), 3210–3228.
35. Pumera, M. (2010). Graphene-based nanomaterials and their electrochemistry. *Chemical Society Reviews, 39*(11), 4146–4157.
36. Pumera, M. (2011). Graphene in biosensing. *Materials Today, 14*(7), 308–315.
37. Shao, Y., Wang, J., Wu, H., Liu, J., Aksay, I. A., & Lin, Y. (2010). Graphene based electrochemical sensors and biosensors: a review. *Electroanalysis, 22*(10), 1027–1036.
38. Zhou, M., Zhai, Y., & Dong, S. (2009). Electrochemical sensing and biosensing platform based on chemically reduced graphene oxide. *Analytical Chemistry, 81*(14), 5603–5613.
39. Pumera, M., Ambrosi, A., Bonanni, A., Chng, E. L. K., & Poh, H. L. (2010). Graphene for electrochemical sensing and biosensing. *TrAC Trends in Analytical Chemistry, 29*(9), 954–965.
40. Harrison, B. S., & Atala, A. (2007). Carbon nanotube applications for tissue engineering. *Biomaterials, 28*(2), 344–353.
41. Pantarotto, D., Briand, J.-P., Prato, M., & Bianco, A. (2004). Translocation of bioactive peptides across cell membranes by carbon nanotubes. *Chemical Communications, 1*, 16–17.
42. Shi Kam, N. W., Jessop, T. C., Wender, P. A., & Dai, H. (2004). Nanotube molecular transporters: internalization of carbon nanotube-protein conjugates into mammalian cells. *Journal of the American Chemical Society, 126*(22), 6850–6851.
43. Liu, Z., Robinson, J. T., Sun, X., & Dai, H. (2008). PEGylated nanographene oxide for delivery of water-insoluble cancer drugs. *Journal of the American Chemical Society, 130*(33), 10876–10877.
44. Zhang, L., Xia, J., Zhao, Q., Liu, L., & Zhang, Z. (2010). Functional graphene oxide as a nanocarrier for controlled loading and targeted delivery of mixed anticancer drugs. *Small, 6*(4), 537–544.
45. Spencer, P.S., ed. (1995). *Lathyrism, handbook of clinical neurology*. Amsterdam: Elsevier.
46. Meda, H. A., Diallo, B., Buchet, J. P., Lison, D., Barennes, H., Ouangre, A., et al. (1999). Epidemic of fatal encephalopathy in preschool children in Burkina Faso and consumption of unripe ackee (Blighia sapida) fruit. *Lancet, 353*, 536–540.
47. Taylor, S.L., Hefle, S.L. & Gauger, B.J., ed. (2001). *Food toxicology*. Florida: CRC Press.
48. Bush, R. K., & Hefle, S. L. (1996). Food allergens. *Critical Reviews in Food Science & Nutrition, 36*(S1), 119–163.
49. Malish, D., Glovsky, M., Hoffman, D., Ghekiere, L., & Hawkins, J. (1981). Anaphylaxis after sesame seed ingestion. *Journal of Allergy and Clinical Immunology, 67*(1), 35–38.
50. World Health Organization (WHO). (1997). Food safety and foodborne diseases. World Health Statistics Quarterly.
51. Dominguez, H. J., Paz, B., Daranas, A. H., Norte, M., Franco, J. M., & Fernández, J. J. (2010). Dinoflagellate polyether within the yessotoxin, pectenotoxin and okadaic acid toxin groups: characterization, analysis and human health implications. *Toxicon, 56*(2), 191–217.
52. Etheridge, S. M. (2010). Paralytic shellfish poisoning: seafood safety and human health perspectives. *Toxicon, 56*(2), 108–122.
53. Lefebvre, K. A., & Robertson, A. (2010). Domoic acid and human exposure risks: a review. *Toxicon, 56*(2), 218–230.

54. Köppen, R., Koch, M., Siegel, D., Merkel, S., Maul, R., & Nehls, I. (2010). Determination of mycotoxins in foods: current state of analytical methods and limitations. *Applied Microbiology and Biotechnology, 86*(6), 1595–1612.
55. Richard, J. L. (2007). Some major mycotoxins and their mycotoxicoses—an overview. *International Journal of Food Microbiology, 119*(1), 3–10.
56. Turner, N. W., Subrahmanyam, S., & Piletsky, S. A. (2009). Analytical methods for determination of mycotoxins: a review. *Analytica Chimica Acta, 632*(2), 168–180.
57. Van Egmond, H. P., Schothorst, R. C., & Jonker, M. A. (2007). Regulations relating to mycotoxins in food. *Analytical and Bioanalytical Chemistry, 389*(1), 147–157.
58. Commission regulation (EC) no. 1881/2006. (2006). *Official Journal of the European Communities: Legis, 364*, 5.
59. Ellis, W., Smith, J., Simpson, B., Oldham, J., & Scott, P. M. (1991). Aflatoxins in food: occurrence, biosynthesis, effects on organisms, detection, and methods of control. *Critical Reviews in Food Science & Nutrition, 30*(4), 403–439.
60. Ngindu, A., Kenya, P., Ocheng, D., Omondi, T., Ngare, W., Gatei, D., et al. (1982). Outbreak of acute hepatitis caused by aflatoxin poisoning in Kenya. *The Lancet, 319*(8285), 1346–1348.
61. Probst, C., Njapau, H., & Cotty, P. J. (2007). Outbreak of an acute aflatoxicosis in Kenya in 2004: identification of the causal agent. *Applied and Environmental Microbiology, 73*(8), 2762–2764.
62. Peckham, J. C., Doupnik, B., & Jones, O. H. (1971). Acute toxicity of ochratoxins A and B in chicks. *Applied Microbiology, 21*(3), 492–494.
63. Pfohl-Leszkowicz, A., & Manderville, R. A. (2007). Ochratoxin A: an overview on toxicity and carcinogenicity in animals and humans. *Molecular Nutrition & Food Research, 51*(1), 61–99.
64. Friis, P., Hasselager, E., & Krogh, P. (1969). Isolation of citrinin and oxalic acid from Penicillium viridicatum Westling and their nephrotoxicity in rats and pigs. *Acta Pathologica Microbiologica Scandinavica, 77*(3), 559–560.
65. Datta, S. C., & Ghosh, J. J. (1983). Action of citreoviridin, a mycotoxin from Penicilliumcitreoviride on the gamma-aminobutyric acid metabolism of the central nervous system. *Toxicon, 21*, 89–92.
66. Ueno, Y. (1970). Production of citreoviridin, a neurotic mycotoxin of Pénicillium citreo-viride Biourge. Production of citreoviridin, a neurotic mycotoxin of Penicillium citreo-viride Biourge, 115–32.
67. Dutton, M. F. (1996). Fumonisins, mycotoxins of increasing importance: their nature and their effects. *Pharmacology & Therapeutics, 70*(2), 137–161.
68. Gelderblom, W., Jaskiewicz, K., Marasas, W., Thiel, P., Horak, R., Vleggaar, R., et al. (1988). Fumonisins—novel mycotoxins with cancer-promoting activity produced by Fusarium moniliforme. *Applied and Environmental Microbiology, 54*(7), 1806–1811.
69. Norred, W. P., & Voss, K. A. (1994). Toxicity and role of fumonisins in animal diseases and human esophageal cancer. *Journal of Food Protection, 57*(6), 522–527.
70. Johanning, E. & Ammann, H. M. (2003). *Encyclopedia of Environmental Microbiology*, John Wiley & Sons, Inc.
71. Osswald, H., Frank, H., Komitowski, D., & Winter, H. (1976). Long-term testing of patulin administered orally to Sprague-Dawley rats and Swiss mice. *Food and Cosmetics Toxicology, 16*(3), 243–247.
72. Ueno, Y. (1984). Toxicological features of T-2 toxin and related trichothecenes. *Fundamental and Applied Toxicology, 4*(2), S124–S132.
73. Shier, W., Shier, A., Xie, W., & Mirocha, C. (2001). Structure-activity relationships for human estrogenic activity in zearalenone mycotoxins. *Toxicon, 39*(9), 1435–1438.
74. Krska, R., & Molinelli, A. (2007). Mycotoxin analysis: state-of-the-art and future trends. *Analytical and Bioanalytical Chemistry, 387*(1), 145–148.
75. Patterson, D., & Roberts, B. (1979). Mycotoxins in animal feedstuffs: sensitive thin layer chromatographic detection of aflatoxin, ochratoxin A, sterigmatocystin, zearalenone, and T-2 toxin. *Journal-Association of Official Analytical Chemists, 62*(6), 1265.
76. Nakajima, M., Tsubouchi, H., Miyabe, M., & Ueno, Y. (1997). Survey of aflatoxin B1 and ochratoxin A in commercial green coffee beans by high-performance liquid chromatography linked with immunoaffinity chromatography. *Food and Agricultural Immunology, 9*(2), 77–83.
77. Candlish, A., Stimson, W., & Smith, J. (1985). A monoclonal antibody to aflatoxin B1: detection of the mycotoxin by enzyme immunoassay. *Letters in Applied Microbiology, 1*(3), 57–61.
78. Lee, N. A., Wang, S., Allan, R. D., & Kennedy, I. R. (2004). A rapid aflatoxin B1 ELISA: development and validation with reduced matrix effects for peanuts, corn, pistachio, and soybeans. *Journal of Agricultural and Food Chemistry, 52*(10), 2746–2755.
79. Xiulan, S., Xiaolian, Z., Jian, T., Zhou, J., & Chu, F. (2005). Preparation of gold-labeled antibody probe and its use in immunochromatography assay for detection of aflatoxin B1. *International Journal of Food Microbiology, 99*(2), 185–194.

80. Gerard, M., Chaubey, A., & Malhotra, B. (2002). Application of conducting polymers to biosensors. *Biosensors and Bioelectronics, 17*(5), 345–359.
81. Pandey, P., Datta, M., & Malhotra, B. (2008). Prospects of nanomaterials in biosensors. *Analytical Letters, 41*(2), 159–209.
82. Solanki, P. R., Kaushik, A., Agrawal, V. V., & Malhotra, B. D. (2011). Nanostructured metal oxide-based biosensors. *NPG Asia Materials, 3*(1), 17–24.
83. Ansari, A. A., Kaushik, A., Solanki, P., & Malhotra, B. (2008). Sol–gel derived nanoporous cerium oxide film for application to cholesterol biosensor. *Electrochemistry Communications, 10*(9), 1246–1249.
84. Arya, S. K., Solanki, P. R., Datta, M., & Malhotra, B. D. (2009). Recent advances in self-assembled monolayers based biomolecular electronic devices. *Biosensors and Bioelectronics, 24*(9), 2810–2817.
85. Jacobs, C. B., Peairs, M. J., & Venton, B. J. (2010). Review: carbon nanotube based electrochemical sensors for biomolecules. *Analytica Chimica Acta, 662*(2), 105–127.
86. Pumera, M. (2009). Electrochemistry of graphene: new horizons for sensing and energy storage. *The Chemical Record, 9*(4), 211–223.
87. Molina, P. G., Zón, M. A., & Fernández, H. (2008). Novel studies about the electrooxidation of a deoxynivalenol (DON) mycotoxin reduction product adsorbed on glassy carbon and carbon paste electrodes. *Electroanalysis, 20*(15), 1633–1638.
88. Hajian, R., & Ensafi, A. (2009). Determination of aflatoxins B1 and B2 by adsorptive cathodic stripping voltammetry in groundnut. *Food Chemistry, 115*(3), 1034–1037.
89. Sc, L., Chen, J., Cao, H., Yao, D. S., & Liu, D. L. (2011). Amperometric biosensor for aflatoxin B1 based on aflatoxin-oxidase immobilized on multiwalled carbon nanotubes. *Food Control, 22*(1), 43–49.
90. Jin, X., Jin, X., Chen, L., Jiang, J., Shen, G., & Yu, R. (2009). Piezoelectric immunosensor with gold nanoparticles enhanced competitive immunoreaction technique for quantification of aflatoxin B_1. *Biosensors and Bioelectronics, 24*(8), 2580–2585.
91. Jin, X., Jin, X., Liu, X., Chen, L., Jiang, J., Shen, G., et al. (2009). Biocatalyzed deposition amplification for detection of aflatoxin B_1 based on quartz crystal microbalance. *Analytica Chimica Acta, 645*(1), 92–97.
92. Liu, Y., Qin, Z., Wu, X., & Jiang, H. (2006). Immune-biosensor for aflatoxin B_1 based bio-electrocatalytic reaction on micro-comb electrode. *Biochemical Engineering Journal, 32*(3), 211–217.
93. Rameil, S., Schubert, P., Grundmann, P., Dietrich, R., & Märtlbauer, E. (2010). Use of 3-(4-hydroxyphenyl)propionic acid as electron donating compound in a potentiometric aflatoxin M1-immunosensor. *Analytica Chimica Acta, 661*(1), 122–127.
94. Pohanka, M., Malir, F., Roubal, T., & Kuca, K. (2008). Detection of aflatoxins in capsicum spice using an electrochemical immunosensor. *Analytical Letters, 41*(13), 2344–2353.
95. Parker, C. O., Lanyon, Y. H., Manning, M., Arrigan, D. W., & Tothill, I. E. (2009). Electrochemical immunochip sensor for aflatoxin M1 detection. *Analytical Chemistry, 81*(13), 5291–5298.
96. Vig, A., Radoi, A., Muñoz-Berbel, X., Gyemant, G., & Marty, J.-L. (2009). Impedimetric aflatoxin M1 immunosensor based on colloidal gold and silver electrodeposition. *Sensors and Actuators B: Chemical, 138*(1), 214–220.
97. Zaijun, L., Zhongyun, W., Xiulan, S., Yinjun, F., & Peipei, C. (2010). A sensitive and highly stable electrochemical impedance immunosensor based on the formation of silica gel–ionic liquid biocompatible film on the glassy carbon electrode for the determination of aflatoxin B1 in bee pollen. *Talanta, 80*(5), 1632–1637.
98. Liu, Y., Qin, Z., Wu, X., & Jiang, H. (2006). Immune-biosensor for aflatoxin B1 based bio-electrocatalytic reaction on micro-comb electrode. *Biochemical Engineering Journal, 32*(3), 211–217.
99. Piermarini, S., Micheli, L., Ammida, N., Palleschi, G., & Moscone, D. (2007). Electrochemical immunosensor array using a 96-well screen-printed microplate for aflatoxin B1 detection. *Biosensors and Bioelectronics, 22*(7), 1434–1440.
100. Owino, J. H., Arotiba, O. A., Hendricks, N., Songa, E. A., Jahed, N., Waryo, T. T., et al. (2008). Electrochemical immunosensor based on polythionine/gold nanoparticles for the determination of aflatoxin B1. *Sensors, 8*(12), 8262–8274.
101. Pemberton, R., Pittson, R., Biddle, N., Drago, G., & Hart, J. (2006). Studies towards the development of a screen printed carbon electrochemical immunosensor array for mycotoxins: a sensor for aflatoxin B1. *Analytical Letters, 39*(8), 1573–1586.
102. Singh, C., Srivastava, S., Ali, M. A., Gupta, T. K., Sumana, G., Srivastava, A., Mathur, R. & Malhotra, B. D. (2013). Carboxylated multiwalled carbon nanotubes based biosensor for aflatoxin detection. *Sensors and Actuators B: Chemical, 185*, 258–264.
103. Accepted in the special issue on *Applied Biochemistry and Biotechnology* 2014. doi:10.1007/s12010-014-0965-4.

Neural Network Based Black Box Testing

Harsh Bhasin
Department of Computer Science
Delhi Technological University
Delhi, India
+91-9818730508
i_harsh_bhasin@yahoo.com

Esha Khanna
M. Tech Scholar, CE Department
A. I. T. M.
Palwal, India
+91-9711332464
eshakhanna30@gmail.com

ABSTRACT
Black Box Testing is immensely important because the source code of a module is not always available. Enterprise Resource Planning systems are also tested using Black Box Testing wherein all the test cases are not equally important. The prioritization of these test cases would be helpful in case of premature termination of testing, due to lack of resources. This paper proposes a Neural Network based method to prioritize test cases. The paper also presents guidelines for prioritizing test cases. The technique has been tested using a financial management system and the results are encouraging. This paper paves way for applying Neural Network in Black Box Testing and presents a framework, which would help both researchers and practitioners.

Categories and Subject Descriptors
D.2.5 [**Software Engineering**]: Testing and Debugging – *Testing Tools (e.g., data generators, coverage testing)*

General Terms
Algorithms, Reliability, Verification.

Keywords
Neural Network, Black Box Testing, Test case design, Prioritizing Test Cases

1. INTRODUCTION
Software should be of high quality and bug free. In order to accomplish the task of developing such software, we need to have sound and robust testing techniques. We must also take into consideration the point that the source code of the module under test might not be available in the testing phase. In such cases Black Box Testing (BBT) can be used. The methodology adopted should be good enough to reveal the maximum number of faults. During an extensive literature review, it was observed that most of the conventional BBT techniques did not use Computational Intelligence (CI) methods.

The paper proposes a Neural Network (NN) based model to prioritize test cases for BBT. A CI technique that has pattern recognizing capabilities could be used in BBT in order to improve efficiency and effective error finding capabilities. NN is a technique that has the capability of recognizing patterns and therefore it can help in carrying out tasks like data mining and network security. The paper proposes a new framework, which applies Neural Networks in BBT. A set of programs has been tested using the technique. The technique has also been applied to an Enterprise Resource Planning (ERP) system. The proposed system will henceforth be referred to as Neural Network Based Black Box Testing (NNBBBT).

The organization of the paper is as follows. Section two discusses the literature review, section three discusses testing in general and BBT in particular, section four discusses test cases, section five presents the proposed framework, section six discusses the experiments and the results and section seven of the paper concludes.

The goals of this paper are as follows.

1. To propose a NN based model, which prioritizes test cases in BBT.
2. To enlist a set of policies for prioritizing test cases developed for GUIs.

2. BACKGROUND
An extensive literature review has been carried out to find gaps in the existing literature. The review was carried out according to the guidelines proposed by Kitchenham [1]. The following databases have been searched.

1. IEEE Explore
2. ACM Digital
3. Springer
4. Wiley Online

Several techniques of testing using NN have been studied. Some of these techniques have been selected by a group of lecturers and assistant professors. Table 1 shows the techniques and verification methods used in the papers selected for review.

In the work by Lilan Wu, a Back Propagation Neural Network methodology has been used to derive test cases [2]. In order to accomplish the task, all basic input variables and their ranges are extracted using the requirement and test management tools. However, the system works only for data-driven modules. The system also makes use of a random test generator whose output is used to test the database module.

The core component of the system, which implements Back Propagation Neural Network, makes use of a random number generator for initialization of weights. The database is tested and the outputs are fed to the Back Propagation Neural Network model. The threshold function used in the system is a sigmoid function. If the input is greater than a particular threshold then it is fed to the next neuron. The author has developed a recurrence relation for sensitivity and has compared the actual output to the expected output. The weights are adjusted as per the steepest descent rule.

The above paper does not mention the number of layers in the neural network, the procedure of assigning weights or even the results in order to make the work convincing. As such there is nothing novel in the work. The premise of the above paper is not clear. No theoretical approach has been followed and the work is not based on the problem reduction approach. It may be stated here that NNs are not used just for the sake of using them. It would be better to stop considering them as a magical box that corrects any inputs and gives the desired output. Rather a sound problem reduction technique must be developed explaining the reason to use NN.

DOI: 10.1145/2579281.2579292 http://doi.acm.org/10.1145/2579281.2579292

Table 1.

Literature Review

Author Name	Premises	Verification
Lilan, wu et. al. [2]	Back Propagation Neural Network has been used to reveal faults in functional testing. Test cases have been generated , covering the functionality of the software, using the above method	The methodology was used to test software for an Automatic teller machine (ATM). The Neural Network was built using all the inputs to the application, except the preconditions. Trial and error was used to determine the number of hidden layers of the neural network.
Saraph, P. et. al.[3]	The work uses Neural Networks as classifiers in order to reduce the number of test cases. This has been done using the identification of input output relations, feature ranking and formation of equivalence classes of input domain. The proposed method is based on three phase algorithm for network pruning.	The number of test cases was reduced using Neural Network pruning and rule extraction.
Paul, A.L, Byrne, P.C [4]	Two conditions have been proposed for reducing the number of learning iterations. The first is to scale the output with respect to the input and the second is to learn the input selectively, not sequentially.	The work was applied on XOR learning algorithm and considerable reduction in the number of rules was observed.
Last, M. et. al. [5]	"The work demonstrates the use of data mining algorithm to automatically induce functional requirements from the execution data. The induced requirements have been used to recover missing or incomplete specifications and minimize the set of test cases."	The technique was validated by solving partial differential equations, In order to accomplish the task data mining algorithm called Info-Fuzzy network (INF) was applied to the execution code data.
Dick, S. et. al. [6]	Machine learning techniques have been used for re-sampling a dataset. This has been done to overcome the skewness problem in software metrics databases. The effects of re-sampling on the results of the data mining algorithm have also been studied in the paper.	Re-sampling in three dataset of software metrics was used to show how re-sampling alters the results of data mining.
Vanmali, M. et.al. [7]	"The work presents artificial neural network as an automated oracle to determine whether a test case passes or fails. The neural network has been trained by back propagation algorithm. The network has been trained using Black Box testing."	Two layer Neural Network was used to detect the faults in mutated code.
Last, M. et. al. [8, 9]	"The work uses data mining algorithm for automated modeling of tested system. The data mining algorithms have been used for recovering system requirements, designing minimal set of regression test cases and evaluating correctness of the software's output."	The work was applied to a data mining algorithm called Info Fuzzy Network (IFN). It used execution data of complex mathematical package.
Last, M., Friedman, M. [10]	"The work uses Info Fuzzy Networks for automatic induction of functional requirements from the execution data. These requirements have then been used for recovering missing or incomplete specifications and designing minimal set of test case."	The proposed methodology was validated by solving differential equations. This task was accomplished by using the execution data of an expert system..
Aggarwal D. et. al. [11]	"The work compares Artificial neural network and Info Fuzzy Networks as automated oracles. The task has been accomplished on the basis of ROC curves, training time and dispersion analysis."	The paper reported results of experiments on a set experiments designed to compare two methods based on ROC curves.
Anderson, C. et. al. [12]	"The work presents a mechanism for automatically generating test cases that yields more faults/failures. The mechanism learns on the basis of past history."	Experimental results using Neural Network for pruning a test case set was presented.
Larry V. Kirkland, R. Glenn Wright [13]	The work uses Neural Network for diagnostic circuit faults.	When different functions are invoked by a test case, the output signal from unit under test varies. Neural Network was trained to classify the variation of the signals obtained.

DOI: 10.1145/2579281.2579292 http://doi.acm.org/10.1145/2579281.2579292

3. SOFTWARE TESTING

Software testing has become one of the most essential ingredients of the recipe that makes delicious software. Software testing starts from the beginning of a project and continues till the end. It not only helps to find bugs, faults and errors but also reduces the overall cost of a project. The overall cost of a project is reduced because had software testing been incomplete, errors would have cropped in the later phases and required more manpower and time, thus escalating the cost of the project. The importance of software testing can also be gauged from the fact that the lack of testing of Electronic Voting Machines in one of the elections has been considered as one of the major factors of win of George Bush, which cost the States a war and thousands of lives [14].

Software testing can be classified as static or dynamic. Static testing techniques require fewer resources because they do not rely on the actual run of a program. Dynamic testing, on the other hand requires more resources as it depends on the actual execution of the code. In dynamic testing, the module output is compared with the expected output and the module under test is labeled as "correctly run" or "having a bug." Various techniques for static testing are reviews, inspections and walkthroughs.

Another way of classifying testing techniques is Black Box, White Box and Grey Box. Black box testing is based on the functional requirements of the module under test. It does not take into account the internal structure of the code. At times, this becomes an advantage as the technique can be employed for the software under test whose executable is available but not the source code. One of the major techniques of black box testing is analyzing the requirements and predicting the output. There are many methodologies for Black box testing like Boundary Value Analysis, Robustness, Equivalence Partitioning, Decision Table, Static Table and Error Guessing. In "Boundary Value Analysis, test cases are chosen on or near the boundaries of the input domain of variables, with the underlying rationale that many defects tend to concentrate near the extreme values of inputs" [15, 16]. Robustness Testing is an extension of the Boundary Value Analysis technique. "In Boundary Value Analysis test cases are also selected from outside the input domain. This is essential, in order to test program robustness to unexpected and erroneous inputs" [15, 16]. In the Equivalence Partitioning Technique, the input domain is subdivided into a collection of subsets which are equivalent according to a given relation. In this technique, the test case suite is crafted by taking one or more test cases from each class [15, 16]. Decision Tables represent logical relationships between inputs and outputs. The concept of combinational testing is applied to derive the test cases in this method [15, 17]. In State Based Testing, "test cases are designed by modeling a program as a finite state machine; tests can be selected in order to cover states and transitions on it" [15, 17]. In Error Guessing, test cases are designed in order to figure out the most obvious faults in a given program. This task can be accomplished by the history of faults discovered in earlier projects as well as the tester's expertise [16].

White box testing, on the other hand, analyzes the code and employs techniques like path testing in order to incorporate the concept of flow of data in testing. The various methods employed by white box testing are as follows. "In Flow-Graph based testing techniques, the control structure of a program is graphically represented using a flow graph, i.e., a directed graph whose nodes and arcs correspond to the program elements" [15, 17]. The Data Flow-based testing is done by annotating the control flow graph with details about the definition and usage of program variables. "A reference notion is a definition-use pair, which is a triplet (d, u, V) such that: V is a variable, d is a node in which V is defined. 'u' is a node in which V is used, such that there exists a path between d and u in which the definition of V in disused in u" [15, 17, 18]. Mutant Testing is carried out by creating mutants of the program. "A mutant is a modified version of the program under test. The modified version differs from the original program by a small, syntactic change. Every test case is run in the original and all generated mutants. If a test case is successful in identifying the difference between the program and a mutant, the latter is said to be killed" [18, 19].

4. TEST CASES

"A test case is defined as a set of test inputs, execution conditions, and expected results developed for a particular objective, such as to exercise a particular program path or to verify compliance with a specific requirement" [20]. "A test case can also be considered as documentation used to compute the task of testing." According to IEEE std. 829-1983, a test case is a documentation specifying inputs, predicted results, and a set of execution conditions for a test item [21]. The writing of good test cases, prior to actual testing of software, is the most important task of a testing team. Test cases are then prioritized on the basis of time, resources and cost of the software. Test cases can be manual or automated. Advantages of a Good Test Case (GTC) are as follows.

1. A GTC has a high probability of finding the maximum number of undiscovered errors.
2. A GTC has a high potential to improve the quality of the software. This quality can be measured in the terms of reliability, usability, robustness etc.
3. A GTC removes the majority of potential threats to the proper execution of the software and therefore reduces the overall cost of the product.
4. It also helps in reducing post development risks.

A GTC has the following characteristics.

1. A test case should be comprehensive in nature. It should include all the necessary details i.e. what to test and how to test. A test case should state preconditions and post conditions along with a description of each test case.
2. Test cases must be designed to test both individual units and interactions among these units. Each and every factor should be tested thoroughly.
3. Test cases should be thoughtful and creative in nature. This characteristic depends on the experience of each test case developer.
4. Test cases should be developed in accordance to the Requirement Analysis and Design Specification.
5. Test cases can be positive or negative [22].
    - Positive Test Case: "Testing conducted to determine the system does what it is supposed to do is called positive testing and the test cases written for this purpose are positive test cases." E.g. Check a client side C# Window Form with correct inputs.
    - Negative Test Case: "Testing software with a test case which does not satisfy the constraints specified in the Requirement Analysis and Design Specifications is called a negative test case" e.g. Checking a client side, C# Windows Form with incorrect input can be considered as a negative test case.

The automation of test cases has been dealt with in our previous works [23, 24].

DOI: 10.1145/2579281.2579292 http://doi.acm.org/10.1145/2579281.2579292

5. PROPOSED WORK

This section explains the architecture of Neural Network Based Black Box Testing (NNBBBT). The various components and their functions are explained in this section.

The various components of the proposed system are as follows.

5.1 Module State Diagram Generator

Software is made up of many modules. The basic component of a procedural program is a method and even in the case of Object Oriented software, the classes in the software interact through methods (or functions). The flow of software is determined by the order in which modules call each other. This essence is captured in the Module State Diagram (MSD), which was proposed in one of our previous works [25]. The Module State Diagram can be defined as follows.

Definition:

The Module State Diagram (MSD) is a graph in which each node depicts a function and the edges between the nodes indicate the calling sequence. The MSD captures the function flow of a program.

The MSD can be created by one of the following methods.

- Stack Trace (ST) of a program
- Software Specifications (SS)

If a program is developed in the .NET framework, then it is quite easy to obtain its ST. However, it would be difficult to capture the ST of the programs developed in C or C++. In that case the specifications can be used to obtain the module signatures and the calling sequences. The first component of the proposed system generates the MSD.

5.2 Test Case Generator (TCG)

The most important part of testing is creation of appropriate test cases. The test cases are generated with the help of test case generators. A test case generator based on Cellular Automata (CA) has already been implemented and verified in earlier works [26]. The test cases created by the CA based system would be used in the following steps.

The test cases developed are classified into three categories: Unit Test Case (UTC), Interaction Test Case (ITC) and System Test Case (STC). This paper proposes a BBT technique for the testing phase. Some of the modules have already been tested while being developed. The interaction between the modules might not have been dealt with completely. The test STC's have not been touched as yet. Figure 1 shows the various test cases.

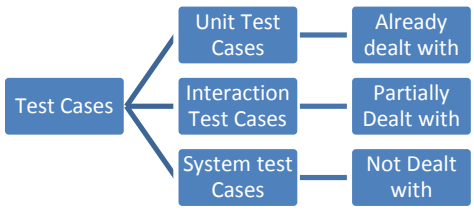

Figure 1. Categorization of Test Cases

Thousands of test cases may be required in order to find out errors in software. Therefore, it is important to assign priorities to them. The work assigns priorities to these test cases. This priority would help in black box testing.

The second component of the proposed system generates the test cases and prioritizes them.

5.3 Module Interaction Assigner (MIA)

Interactions between the modules are found using MSD. The calling module passes arguments to the called module and the called module returns some data to the calling module. These module interactions can be prioritized by assigning them a value from 1 to 10. The value 1 depicts the most important interactions and the value 10 depicts the least important interactions. This assignment would also help at the time of regression testing. The third component of the proposed system assigns a priority to each interaction. These priorities are used to train the neural network.

5.4 Training of Neural Networks

Neural Networks are trained for prioritizing module interactions. The inputs to the Neural Network are the module interactions and the output is a number having range 1-10, where 1 depicts an interaction having highest importance and 10 denotes the lowest importance interaction. The trained neural network is then used for prioritization of module interactions.

The fourth phase of the proposed system trains the neural network. For example if a thousand test cases have been developed, then seven hundred test cases can be used to train the network and 300 test cases can be used for the verification purposes.

5.5 Installation

Finally, the neural network developed would assess the priority of interaction based on the training provided to it in step 4. The process of assigning importance to Black Box Test cases is depicted in Figure 2.

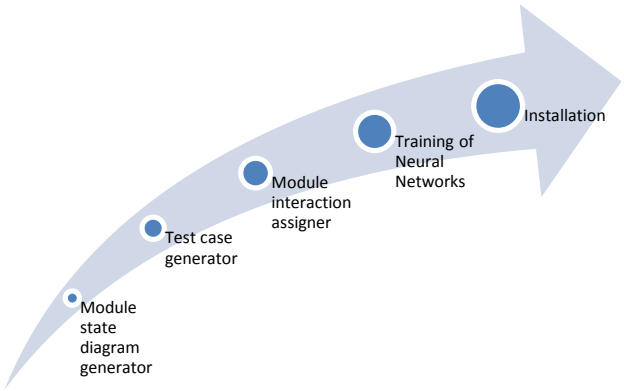

Figure 2. Neural Network Based Black Box Testing (NNBBBT)

6. VERIFICATION

The methodology proposed in the previous section has been verified as follows. An ERP system, which keeps track of the Systematic Investment Plans of the customers of a financial management company, DFPL, has been chosen for verification of the technique. The ERP system is about 12 K lines of code and is developed in C#. Test Cases have been developed for each form of the system. Tables 2 and 3 show the controls of one of the forms and the corresponding database fields respectively. The Test Cases have been assigned a value indicating the importance as per the following policies.

Table 2. Frontend of customer details form

Field ID	Field Name	Field Type
1	First Name	Textbox
2	Middle Name	Textbox
3	Last Name	Textbox
4	Date Of Birth	DateTimePicker

DOI: 10.1145/2579281.2579292 http://doi.acm.org/10.1145/2579281.2579292

5	PAN Number	Textbox
6	Nationality	Textbox
7	House Number	Textbox
8	City	Textbox
9	State	Combo box
10	Phone Number	Textbox
11	Phone Number 2	Textbox
12	Landline	Textbox
13	E - mail	Textbox
14	Pin Code	Textbox
15	Occupation	Textbox
16	KYC	Combo box

Table 3. Database of customer details form

Field ID	Database name
1	Firstname
2	middleName
3	lastName
4	dateOfBirth
5	CustPanNumber
6	custNationality
7	addressHouseNumber
8	addressCity
9	AddressState
10	Phone1
11	Phone2
12	Landline
13	eMail
14	Pincode
15	Occupation
16	custKYC

6.1 Policies For Assigning Importance To Test Cases

1. The controls, which associate the frontend with the Database, are more important as compared to labels and images in a form.
2. From amongst these controls those that appear in multiple tables are more important as compared to others.
3. From amongst the above controls those that help in calculating the results and are used in crystal reports, are more important as compared to others.
4. Labels that display results are more important than the labels which do not display results.
5. Combo boxes that are populated from the database are more important as compared to other combo boxes.
6. BLOB and CLOB handling events are more important than rest of the events.
7. Rests of the test cases are prioritized using Design Specifications and Software Requirement Specification (SRS).

As per the above rules the Test Cases have been prioritized.

1. Test cases that satisfy the constraints are assigned a low priority.
2. Test cases that do not satisfy the constraints, imposed at the beginning, are assigned a higher priority. Test cases that violate constraints are assigned a still higher priority.
3. Test cases that displays data that has been extracted from the database are assigned a priority more than that assigned for the test cases satisfying point 4.
4. Test cases that are a result of some operation that depends on the database value are assigned priority more than that assigned for the test cases satisfying point 5.
5. Test cases that are results of calculations and part of crystal reports are assigned priority near to point 5.
6. For assigning priorities to rest of the test cases manual description along with policies stated previously has been used.

As an example, the input and display data forms of the system were chosen. Table 4 shows priorities assigned to some of the test cases. The priorities have been assigned on the scale 1-10.

Table 4. Priorities assigned to test cases

Test Case ID	Priority Assigned	18	2
1	2	19	4
2	3	20	4
3	3	21	3
4	2	22	2
5	3	23	3
6	4	24	4
7	3	25	4
8	2	26	2
9	4	27	2
10	3	28	4
11	3	29	4
12	3	30	2
13	4	31	4
14	2	32	4
15	4	33	4
16	4	34	2
17	4	35	4

The whole data set is fed into the model depicted in Figure 3. The model takes test case priority assignment policies and database test cases as inputs. A Multilayer Feedback Neural Network has been used for training and information processing. The output of the model is the prioritized test cases, which have been prioritized using the above policies.

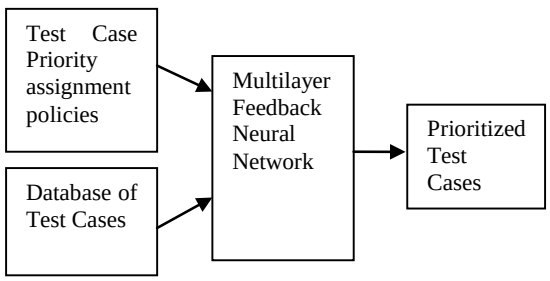

Figure 3: Model of NNBBBT

DOI: 10.1145/2579281.2579292 http://doi.acm.org/10.1145/2579281.2579292

70 % of these test cases are then given to the NN in the training phase and the rest are used in order to validate the system.

7. RESULTS AND CONCLUSION

The quality and robustness of software depends on the quality of its test cases. This paper proposes a set of policies to prioritize test cases. The technique has been tested on a medium sized ERP system. This paper also proposes a NN based system that prioritizes the test cases based on the above policies. The system helps in assigning importance to test cases thus making BBT more efficient. The results obtained are similar to the priorities assigned manually as per the policies. The technique is an important step towards developing a complete testing solution that would generate test cases and prioritize them.

8. REFERENCES

[1] Kitchenham, B.A et. al. 2010. Systematic literature reviews in software engineering .A tertiary study, Information & Software Technology .*INFSOF* , vol. 52, no. 8, pp. 792-805, 2010

[2] Wu, L., Liu, B., Jin, Y. and Xie, X. 2008 .Using Back-propagation Neural Networks for Functional Software Testing. *Anti-counterfeiting, Security and Identification*, . ASID 2008. 2nd International Conference on 20-23 Aug. 2008. DOI= 10.1109/IWASID.2008.4688385

[3] Saraph, P., Last, M., and Kandel, A.2004 .Test Set Generation and Reduction with Artificial Neural Networks. in M. Last, A. Kandel, and H. Bunke (Editors),.*Artificial Intelligence Methods in Software Testing*. World Scientific, 2004, pp. 101-132.

[4] Paul, A.L, Byrne, P.C .1990.An efficient learning algorithm for the Back Propagation Artificial Neural Network. *IEEE DOI*= 10.1109/SECON.1990.117770

[5] Last, M., Friedman M. and Kandel, A. 2003. The Data Mining Approach to Automated Software Testing. *Conference on Knowledge Discovery* in Data, 2003.

[6] Dick, S. and Kandel, A.2004 .Data Mining with Resampling in Software Metrics Databases. In M. Last, A. Kandel, and H. Bunke (Editors), *Artificial Intelligence Methods in Software Testing*, World Scientific, pp. 175-208.

[7] Vanmali M., Last M., Kandel A.2002. Using a Neural Network in the Software Testing Process. *International Journal of Intelligent Systems* 2002, 17, 1: 45-62.

[8] Last M., Friedman M., and Kandel A.2003 .The Data Mining Approach to Automated Software Testing. Proceedings of the Ninth *ACM SIGKDD* International Conference on Knowledge Discovery and Data Mining (KDD-2003), pp. 388 - 396, Washington, DC, USA August 24 -27,2003.

[9] Last M., Friedman M., and Kandel A..2004..Using Data Mining for Automated Software Testing. *International Journal of Software Engineering and Knowledge Engineering*, Special Issue on Data Mining for Software Engineering and Knowledge Engineering, Vol. 15, No. 5, October 2004.

[10] Last, M. and Friedman, M.2004.Black-Box Testing with Info-Fuzzy Networks. in M. Last, A. Kandel, and H. Bunke (Editors), *Artificial Intelligence Methods in Software Testing* World Scientific, pp. 21-50,2004.

[11] Aggarwal, D., Tamir, D.E., Last, M., Kandel, A. .2012. A comparative study of Artificial Neural Network and Info Fuzzy Network as automated oracles in software testing. Systems, Man and Cybernetics, Part A, Sytems and Humans, *IEEE Transactions* on volume:42 issue 5

[12] Anderson, C. ,Mayrhauser, A, Marz, R . 1995. On the use of neural networks to guide software testing activities. *International test conference IEEE* .ISBN 0-7803-2992-9. DOI= 10.1109/TEST.1995.529902

[13] Larry V. Kirkland, R. Glenn Wright.1995 .Using Neural Network for functional testing. *IEEE INSPEC 5154796 DOI*= 10.1109/AUTEST.1995.522718

[14] Gore, Al (September 23, 2002). "Iraq and the War on Terrorism" *(Text of speech given by Al Gore). CommonwealthClub.org.* Archived from the original on May 31, 2010. Retrieved June 30, 2010.

[15] Jorgensen, P.C.1995. *Software Testing A Craftsman's Approach*, CRC Press.

[16] Kaner, C., Falk, J., and Nguyen, H. Q.1999.*Testing Computer Software*. 2nd Edition, Wiley.

[17] Beizer, B.1990. *Software Testing Techniques* 2nd Edition. Van Nostrand Reinhold.

[18] Zhu, H., Hall, P.A.V., and May, J.H.R.1997. Software Unit Test Coverage and Adequacy *ACM Computing Surveys*, 29, 4 (Dec. 1997) 366-427.

[19] Perry, W.1995. *Effective Methods for Software Testing*, Wiley.

[20] IEEE Standard 610 (1990) definition of test cases [online].

[21] IEEE std 829-1983 definition of test cases.

[22] ERP Testing "Test Case Structure" [online] available at http://erp-testing.blogspot.in/2012/04/test-case-structure.html.

[23] Bhasin, H., Singla, N., Sharma, S. (2013, July) "Cellular Automata Based Test data Generation" ACM SIGSOFT Software Engineering Notes.

[24] Bhasin, H., Singla, N. (2013, September) .Cellular-Genetic Test data Generation. *ACM SIGSOFT Software Engineering Notes*, Volume 38 Number 5

[25] Bhasin, H., Shewani, and Goyal, D. (2013). Test Data Generation using Artificial Life, *International Journal of Computer Application*. 67, 12, 34-39.

[26] Bhasin, H., Shewani, and Goyal, D. (2013). *On Application Of Artificial Life Based Tes*t Data Generation, *International Journal on Computer Science and Engineering* ISSN : 0975-3397 Vol. 5 No. 06 Jun 2013

Appl. Math. Inf. Sci. **9**, No. 3, 1541-1548 (2015)

Applied Mathematics & Information Sciences
An International Journal

http://dx.doi.org/10.12785/amis/090350

Non-Additive Entropy Measure and Record Values

Vikas Kumar[1,*] *and H. C. Taneja*[2]

[1] Department of Applied Science, UIET, M. D. University, Rohtak-124001, India
[2] Department of Applied Mathematics, Delhi Technological University, Delhi - 110042, India

Received: 20 Aug. 2014, Revised: 20 Nov. 2014, Accepted: 21 Nov. 2014
Published online: 1 May 2015

Abstract: Non-additive entropy measures are important for many applications. We study Havrda and Charvat entropy for record values and have shown that this characterizes the underlying distribution function uniquely. Also the non-additive entropy of record values has been derived in case of some specific distributions. Further we propose a generalized residual entropy measure for record value.

Keywords: Generalized entropy, Record value, Probability integral transformation, Residual entropy.

1 Introduction

Suppose $X_1, X_2, \cdots, X_n$ be a sequence of independent and identically distributed (i.i.d.) random variables with a common absolutely continuous distribution function (cdf) F, probability density function (pdf) f, and survival function $\overline{F} = 1 - F$. An observation X_j will be called an *upper record value* if its value exceeds that of all previous observations. Thus X_j is an upper record if $X_j > X_i$ for every $i < j$. An analogous definition can be given for a lower record value. Let $R(j)$ denote the time (index) at which the jth record value is observed. Since the first observation is always a record value, we have

$$R(1) = 1, \cdots, R(J+1) = min\left\{i : X_i > X_{R(j)}\right\},$$

where $R(0)$ is defined to be 0. The sequence of upper record values can thus be defined by $U_j = X_{R(j)}, j = 1,2,3,\cdots$ Let $D(j) = R(j+1) - R(j)$ denote the inter-record time between the jth record value and $(j+1)$th record value, and let the jth record value $X_{R(j)}$ be denoted by X_j for simplicity. Then the probability density function of the jth record value X_j is given by

$$g_{X_j}(x) = \frac{\{-\ln(1-F(x))\}^{j-1} f(x)}{\Gamma(j)}, \; x > 0 \qquad (1)$$

The survival function is

$$\bar{G}_{X_j}(x) = \sum_{j=0}^{n-1} \frac{\{-\ln(1-F(x))\}^{j} \bar{F}(x)}{\Gamma(j)} = \frac{\Gamma(n\,; -\log \bar{F}(x))}{\Gamma(n)}, \qquad (2)$$

where $\Gamma(a;x)$, the incomplete gamma function, is defined as

$$\Gamma(a;x) = \int_x^\infty x^{a-1} e^{-x} dx, \; x, \; a > 0,$$

refer to, David and Nagaraja (2003, p.32).

Records can be viewed as order statistics from a sample whose size is determined by the values and the order of occurrence of the observations. In reliability theory, order statistics and record values are used for statistical modeling. The $(n-m+1)$th order statistics in a sample of size n represents the life length of an $'m$ *out of* n' system. Record values are used in shock models and minimal repair systems, refer to Kamps (1994). Record values arise naturally in problems such as industrial stress testing, meteorological analysis, hydrology, sporting and athletic events, and economics, refer to Arnold et al. (1998), Nevzorov (2001) and Ahsanullah (2004). Several authors have studied the characterization of distribution function F based on the properties of order statistics and record values, refer to Nagaraja and Nevzorov (1997), Raqab and Awad (2000), and Balakrishnan and Stepanov (2004).

The idea of information-theoretic entropy was first introduced by Shannon (1948) and later by Weiner (1949) in Cybernetics. Let X be an absolutely continuous random variable which denotes the lifetime of a device or, a system with probability density function $f(x)$. Then the average amount of uncertainty associated with the random

* Corresponding author e-mail: vikas_iitr82@yahoo.co.in

© 2015 NSP
Natural Sciences Publishing Cor.

variable X, as given by Shannon entropy (1948) is

$$H(X) = -\int_0^\infty f(x)\log f(x)dx\,. \tag{3}$$

The measure (3) is additive in nature in the sense that for two independent random variables X and Y

$$H(X*Y) = H(X)+H(Y)\,,$$

where $X*Y$ denotes the joint random variable. In literature many authors have generalized Shannon entropy (3) in different ways. A well-known parametric extension of the Shannon entropy measure was defined by Havrda and Charvat (1967) as

$$H_\alpha(X) = \frac{1}{1-\alpha}\left\{\int_0^\infty f^\alpha(x)dx - 1\right\},\ \alpha\neq 1,\ \alpha>0\,. \tag{4}$$

Although entropy measure (4) was first introduced by Havrda and Charvat (1967) in the context of cybernetics theory, it was Tsallis (1988) who exploited its non-extensive features and placed it in a physical setting. Hence entropy measure (4) is also known as Tsallis entropy (1988). Clearly as $\alpha\to 1$, (4) reduces to (3). This entropy is similar to Shannon entropy except for its non-additive nature, that is

$$H(X*Y) = H(X)+H(Y)+(1-\alpha)H(X)H(Y).$$

In general, the non-additive measures of entropy find justifications in many biological and chemical phenomena. Some properties and applications of non-additive entropy measure (4) have been studied by Tsallis (1998, 2002) and, Tsallis and Brigatti (2004). Baratpour et al. (2007, 2008) obtained results for the Shannon entropy and Renyi entropy of the order statistics and record values.

In this communication we study results for the record values based on the non-additive entropy measure (4). The paper is organized as follows. A general expression for the entropy measure (4) of a record value distribution is derived in Section 2. The entropies of record values associated with the uniform, exponential, weibull, pareto, finite range and gamma are presented in Section 3. In an attempt to establish a coherence between the entropies of the parent and the corresponding record value distributions, Section 4 is devoted to a characterization result. Generalized residual entropy of record values has been studied in Section 5.

2 Generalized Entropy for Different Univariate distribution

In this section, we derive generalized entropy measure (4) for some specific univariate continuous distributions.

2.1 Exponentiated Exponential Distribution

A random variable X is said to have the exponentiated exponential distribution denoted by $X\sim EE(\gamma,\ \theta)$, if its probability density function (pdf) and cumulative distribution function (cdf) are given by

$$f(x) = \gamma\theta\exp(-\theta x)\{1-\exp(-\theta x)\}^{\gamma-1},\ \ x>0 \tag{5}$$

and

$$F(x) = \{1-\exp(-\theta x)\}^{\gamma},\ \ \gamma>0,\ \theta>0, \tag{6}$$

respectively. In particular for $\gamma=1$, (5) is the exponential distribution.

The exponentiated exponential distribution introduced by Gupta and Kundu (1999) has some interesting physical interpretations. Consider a parallel system consisting of γ components, the system works, only when at least one of the γ-components works. If the lifetime distributions of the components are independent identically distributed (i.i.d.) exponential random variables, then the lifetime distribution of the system is defined as (6).

Entropy of a random variable X is a measure of its uncertainty. Let $X\sim EE(\gamma,\ \theta)$; we derive explicit form for the generalized entropy measure (4) for X. For the pdf given by (5),

$$\int_0^\infty f^\alpha(x)dx = (\gamma\theta)^\alpha\int_0^\infty \exp(-\theta\alpha x)\{1-\exp(-\theta x)\}^{\alpha\gamma-\alpha}dx. \tag{7}$$

On substituting $y=\exp(-\theta x)$, (7) reduces to

$$\gamma^\alpha\theta^{\alpha-1}\int_0^1 y^{\alpha-1}\{1-y\}^{\alpha\gamma-\alpha}dy = \gamma^\alpha\theta^{\alpha-1}B(\alpha;\alpha\gamma-\alpha+1).$$

So (4) takes the form

$$H_\alpha(X) = \frac{1}{1-\alpha}\left\{\gamma^\alpha\theta^{\alpha-1}B(\alpha;\alpha\gamma-\alpha+1)-1\right\}. \tag{8}$$

If $\gamma=1$, then (8) reduces to $H_\alpha(X) = \frac{1}{1-\alpha}\left\{\frac{\theta^{\alpha-1}}{\alpha}-1\right\}$, the entropy measure (4) for exponential distribution.

Table 1 gives the non-additive Havrda and Charvat entropy measure (1967) for some specific probability distributions.

3 Generalized Entropy of Record Value Obtained for Specific Distributions

We will use the probability integral transformation of the random variable $U=F(x)$, where the distribution of U is the standard uniform distribution. The probability integral transformation provides the following useful

© 2015 NSP
Natural Sciences Publishing Cor.

Table 1: yyyyyy

Distribution	Density function $f(x)$	Entropy $H_\alpha(X)$
Uniform	$\frac{1}{(b-a)}$; $x \in [a,b]$	$\frac{1}{(1-\alpha)}\{(b-a)^{1-\alpha}-1\}$
Exponential	$\theta e^{-\theta x}$; $x>0,\ \theta>0$	$\frac{1}{(1-\alpha)}\left\{\frac{\theta^{\alpha-1}}{\alpha}-1\right\}$
Pareto	$\frac{\theta\beta^\theta}{x^{(\theta+1)}}$; $x \geq \beta>0,\ \theta>0$	$\frac{1}{(1-\alpha)}\left[\frac{\theta^\alpha}{[\alpha\theta+\alpha-1]\beta^{\alpha-1}}-1\right]$
Finite Range	$\frac{a}{b}(1-\frac{x}{b})^{a-1}$; $0 \leq x \leq b,\ a>1$	$\frac{1}{(1-\alpha)}\left\{\frac{a^\alpha b^{1-\alpha}}{(1+(a-1)\alpha)}-1\right\}$
Beta	$\frac{x^{a-1}(1-x)^{b-1}}{\beta(a,b)}$; $0 \leq x \leq 1,\ a,\ b>0$	$\frac{1}{(1-\alpha)}\left[\frac{\beta(\alpha(a-1)+1,\alpha(b-1)+1)}{\beta^\alpha(a,b)}-1\right]$
Levy	$(\frac{\sigma}{2\pi})^{1/2}\frac{1}{(x-\mu)^{3/2}}e^{-\frac{\sigma}{2(x-\mu)}}$; $x>\mu,\ \mu>0$	$\frac{1}{(1-\alpha)}\left\{(\frac{\sigma}{2})^{\frac{3(1-\alpha)}{2}}(\frac{\alpha^{1-\frac{3\alpha}{2}}}{\pi^{1/2}})\Gamma(\frac{3\alpha}{2}-1)-1\right\}$
Folded Cramer	$\frac{\theta}{(1+\theta x)^2}$; $x \geq 0,\ \theta>0$	$\frac{1}{(1-\alpha)}\left\{\frac{\theta^{\alpha-1}}{(2\alpha-1)}-1\right\}$

representation of the entropy measure (4) for the random variable X

$$H_\alpha(X)=\frac{1}{1-\alpha}\left\{\int_0^1 f^{(\alpha-1)}(F^{-1}(u)du-1\right\}. \qquad (9)$$

Next we prove the following result.

Lemma 31*The entropy measure (4) of the j^{th} record value X_j can be expressed as*

$$H_\alpha(X_j)=\frac{\Gamma[(j-1)\alpha+1]}{\{\Gamma(j)\}^\alpha(1-\alpha)}E[f^{\alpha-1}\{F^{-1}(1-e^{-v})\}]-\frac{1}{(1-\alpha)}, \qquad (10)$$

where $v \sim \Gamma\{(j-1)\alpha+1\}$ and E is the expectation.

Proof Generalized entropy (4) of the j^{th} record value is defined as

$$H_\alpha(X_j)=\frac{1}{1-\alpha}\left\{\int_0^\infty\{g_{X_j}(x)\}^\alpha dx-1\right\},\ \alpha\neq 1,\ \alpha>0\,.$$

Using (1), this can be rewritten as

$$H_\alpha(X_j)=\frac{1}{(1-\alpha)\{\Gamma(j)\}^\alpha}\{\int_0^\infty\{-\ln\bar{F}(x)\}^{(j-1)\alpha} f^\alpha(x)dx-\{\Gamma(j)\}^\alpha\}$$

Substituting $-\ln\bar{F}(x)=u$, and hence, $x=F^{-1}(1-e^{-u})$, we have

$$H_\alpha(X_j)=\frac{1}{(1-\alpha)\{\Gamma(j)\}^\alpha}\{\int_0^\infty u^{(j-1)\alpha}e^{-u}\left[f^{\alpha-1}\{F^{-1}(1-e^{-u})\}\right]du-\{\Gamma(j)\}^\alpha\} \qquad (11)$$

It can be rewritten as

$$H_\alpha(X_j)=\frac{1}{(1-\alpha)}\{\frac{\Gamma[(j-1)\alpha+1]}{\{\Gamma(j)\}^\alpha}E[f^{\alpha-1}\{F^{-1}(1-e^{-v})\}]-1\}.$$

So, the result follows.

3.1 Uniform Distribution

If a random variable X is uniformly distributed over $(a,\ b),\ a<b$, then its density and distribution functions are given respectively by

$$f(x)=\frac{1}{b-a}\ \text{and}\ F(x)=\frac{x-a}{b-a}\,,\ a<x<b.$$

We have

$$H_\alpha(X_j)=\frac{1}{(1-\alpha)\{\Gamma(j)\}^\alpha}\{\int_0^\infty u^{(j-1)\alpha}e^{-u}\ f^{\alpha-1}(x)du-\{\Gamma(j)\}^\alpha\}.$$

Thus generalized entropy (4) of the j^{th} record value for uniform distribution is given as

$$H_\alpha(X_j)=\frac{1}{(1-\alpha)\{\Gamma(j)\}^\alpha}\left\{\frac{\int_0^\infty u^{(j-1)\alpha}e^{-u}du}{(b-a)^{\alpha-1}}-\{\Gamma(j)\}^\alpha\right\},$$

which gives

$$H_\alpha(X_j)=\frac{1}{(1-\alpha)\{\Gamma(j)\}^\alpha}\left\{\frac{\Gamma\{(j-1)\alpha+1\}}{(b-a)^{\alpha-1}}-\{\Gamma(j)\}^\alpha\right\}.$$

The generalized entropy of the first record, that is, X_1, is

$$H_\alpha(X_1)=\frac{(b-a)^{1-\alpha}}{1-\alpha}-\frac{1}{1-\alpha}. \qquad (12)$$

This is the entropy of the parent distribution for uniform variate as indicated in Table 2.1. The entropy of the non-trivial record, that is, X_2, is given as

$$H_\alpha(X_2)=\frac{1}{(1-\alpha)}\left\{\frac{\Gamma(\alpha+1)}{(b-a)^{\alpha-1}}-1\right\}.$$

3.2 Exponential Distribution

Let X be a random variable having the exponential distribution with pdf $f(x)=\theta\{\exp-(\theta x)\}$. Substituting

© 2015 NSP
Natural Sciences Publishing Cor.

$-\ln\bar{F}(x)=u$, hence, $\frac{u}{\theta}=F^{-1}(1-e^{-u})$ we have

$$f^{\alpha-1}\{F^{-1}(1-e^{-u})\}=\left[f\left(\frac{u}{\theta}\right)\right]^{\alpha-1}=\theta^{\alpha-1}e^{-u(\alpha-1)}. \tag{13}$$

Thus generalized entropy (4) of the j^{th} record value for exponential distribution is given as

$$H_\alpha(X_j)=\frac{1}{(1-\alpha)\{\Gamma(j)\}^\alpha}\{\frac{\int_0^\infty u^{(j-1)\alpha}e^{-\alpha u}du}{\theta^{1-\alpha}} -\{\Gamma(j)\}^\alpha\},$$

which gives

$$H_\alpha(X_j)=\frac{1}{(1-\alpha)\{\Gamma(j)\}^\alpha}\{\frac{\Gamma\{(j-1)\alpha+1\}\theta^{\alpha-1}}{\alpha^{(j-1)\alpha+1}} -\{\Gamma(j)\}^\alpha\}. \tag{14}$$

For $j=1$, that is, the entropy of the first record, we have

$$H_\alpha(X_1)=\frac{\theta^{\alpha-1}}{\alpha(1-\alpha)}-\frac{1}{1-\alpha}.$$

This is the entropy of the parent distribution. The entropy of the non-trivial record, that is, X_2, is given as

$$H_\alpha(X_2)=\frac{1}{(1-\alpha)}\left\{\frac{\Gamma(\alpha+1)\theta^{\alpha-1}}{\alpha^{\alpha+1}}-1\right\}.$$

3.3 Pareto Distribution

Let X be a random variable having Pareto distribution with pdf

$$f(x)=\frac{\theta\beta^\theta}{x^{\theta+1}},\ x\geq\beta>0,\ \theta>0. \tag{15}$$

Substituting $-\ln\bar{F}(x)=u$, we observe that $x=F^{-1}(1-e^{-u})=\beta e^{\frac{u}{\theta}}$ and for computing $H_\alpha(X_j)$, we have

$$f^{\alpha-1}\{F^{-1}(1-e^{-u})\}=\left(\frac{\theta}{\beta}\right)^{\alpha-1}e^{-u(\alpha-1)(1+\frac{1}{\theta})}.$$

Thus generalized entropy (4) of the j^{th} record value for Pareto distribution is given as

$$H_\alpha(X_j)=\frac{1}{(1-\alpha)\{\Gamma(j)\}^\alpha}\{\left(\frac{\theta}{\beta}\right)^{\alpha-1}\int_0^\infty u^{(j-1)\alpha} e^{-(\alpha+\frac{\alpha-1}{\theta})u}du-\{\Gamma(j)\}^\alpha\},$$

which gives,

$$H_\alpha(X_j)=\frac{1}{(1-\alpha)\{\Gamma(j)\}^\alpha}\{\frac{\Gamma\{(j-1)\alpha+1\}\theta^{j\alpha}}{\beta^{\alpha-1}[\alpha\theta+\alpha-1]^{(j-1)\alpha+1}} -\{\Gamma(j)\}^\alpha\}. \tag{16}$$

Therefore,

$$H_\alpha(X_1)=\frac{1}{1-\alpha}\left\{\frac{\theta^\alpha}{[\alpha\theta+\alpha-1]\beta^{\alpha-1}}-1\right\},$$

the entropy for the parent distribution. The entropy for non trivial record X_2 is given as

$$H_\alpha(X_2)=\frac{1}{1-\alpha}\left\{\frac{\Gamma(\alpha+1)\theta^{2\alpha}}{\beta^{\alpha-1}[\alpha\theta+\alpha-1]^{\alpha+1}}-1\right\}. \tag{17}$$

3.4 Finite Range Distribution

The pdf of the finite range distribution is given by

$$f(x)=\frac{a}{b}\left(1-\frac{x}{b}\right)^{a-1},\quad a>1,\ 0\leq x\leq b. \tag{18}$$

The survival function is

$$\bar{F}(x)=1-F(x)=\left(1-\frac{x}{b}\right)^a.$$

Substituting $-\ln\bar{F}(x)=u$, we observe that $x=F^{-1}(1-e^{-u})=b(1-e^{-\frac{u}{a}})$ and for computing $H_\alpha(X_j)$, we have

$$f^{\alpha-1}\{F^{-1}(1-e^{-u})\}=\left(\frac{a}{b}\right)^{\alpha-1}e^{-u(\alpha-1)(1-\frac{1}{a})} \tag{19}$$

Lemma 3.1 gives

$$H_\alpha(X_j)=\frac{1}{(1-\alpha)\{\Gamma(j)\}^\alpha}\{\frac{\Gamma\{(j-1)\alpha+1\}a^{j\alpha}}{b^{\alpha-1}[a\alpha-\alpha+1]^{(j-1)\alpha+1}} -\{\Gamma(j)\}^\alpha\}. \tag{20}$$

For $j=1$, the entropy for parent distribution is

$$H_\alpha(X_1)=\frac{1}{1-\alpha}\left\{\frac{\theta^\alpha}{[\alpha\theta+\alpha-1]\beta^{\alpha-1}}-1\right\}$$

The entropy for non trivial record X_2 is given as

$$H_\alpha(X_2)=\frac{1}{1-\alpha}\left\{\frac{\Gamma(\alpha+1)a^{2\alpha}}{b^{\alpha-1}[a\alpha-\alpha+1]^{\alpha+1}}-1\right\}. \tag{21}$$

3.5 Weibull Distribution

A non-negative random variable X is Weibull distributed, if its pdf is

$$f(x)=\lambda\beta x^{\beta-1}\exp\left\{-\lambda x^\beta\right\},\ \lambda,\ \beta>0,\ x>0$$

where λ and β are scale and shape parameters respectively. The survival function is

$$\bar{F}(x)=1-F(x)=e^{-\lambda x^\beta}.$$

© 2015 NSP
Natural Sciences Publishing Cor.

Substituting $-\ln\bar{F}(x)=u$, we observe that $x=F^{-1}(1-e^{-u})=\{\frac{u}{\lambda}\}^{\frac{1}{\beta}}$ and for computing $H_\alpha(X_j)$, we have

$$f^{\alpha-1}\{F^{-1}(1-e^{-u})\}=\left(\beta\lambda^{\frac{1}{\beta}}\right)^{\alpha-1}\{u\}^{\frac{(\alpha-1)(\beta-1)}{\beta}}e^{-u(\alpha-1)}$$

Lemma 3.1 gives

$$H_\alpha(X_j)=\frac{1}{(1-\alpha)\{\Gamma(j)\}^\alpha}\{\frac{\left(\beta\lambda^{\frac{1}{\beta}}\right)^{\alpha-1}\Gamma\{j\alpha-\frac{\alpha-1}{\beta}\}}{\{\alpha\}^{j\alpha-\frac{\alpha-1}{\beta}}}-\{\Gamma(j)\}^\alpha\}. \tag{22}$$

For $j=1$ the entropy for parent distribution is

$$H_\alpha(X_1)=\frac{1}{(1-\alpha)}\left\{\frac{\left(\beta\lambda^{\frac{1}{\beta}}\right)^{\alpha-1}\Gamma\{\alpha-\frac{\alpha-1}{\beta}\}}{\{\alpha\}^{\alpha-\frac{\alpha-1}{\beta}}}-1\right\}.$$

For $\beta=1$, (22) reduces to (14), the entropy for j^{th} record of exponential distribution.

4 Characterization Problem

In this section, we show that the distribution function F can be uniquely specified up to a location change by the equality of Tsallis entropy of record values. First we state the following lemma, due to Goffman and Pedrick (1965).

Lemma 41*A complete orthogonal system for the space $L_2(0,\infty)$ is given by sequence of Laguerre function*

$$\phi_n(x)=\frac{1}{n!}e^{-\frac{x}{2}}L_n(x),\ n\geq 0.$$

where $L_n(x)$ is the Laguerre polynomial, defined as the sum of coefficients of e^{-x} in the nth derivative of x^ne^{-x}, that is

$$L_n(x)=e^x\frac{d^n}{dx^n}(x^ne^{-x})=\sum_{k=0}^{n}(-1)^k n(n-1)\cdots(k+1)x^k. \tag{23}$$

The completeness of Laguerre functions in $L_2(0,\infty)$ means that if $f\in L_2(0,\infty)$ and $\int_0^\infty f(x)e^{-\frac{x}{2}}L_n(x)dx=0,\ \forall n\geq 0$, then f is zero almost everywhere.

Theorem 41*Let X and Y be two random variables with pdfs $f(x)$ and $g(x)$ and absolutely continuous cdfs $F(x)$ and $G(x)$ respectively, with $E[\log f(x)]^2<\infty$ and $E[\log g(x)]^2<\infty$. Then F and G belong to the same location family of distribution, if, and only if*

$$H_\alpha(X_j)=H_\alpha(Y_j)\ ,\ \forall j\geq 1, \tag{24}$$

where X_j and Y_j are the j^{th} upper records of X and Y respectively.

Proof The necessary part is obvious. We only need to prove the sufficiency part. Let

$$H_\alpha(X_j)=H_\alpha(Y_j)\ ,\ \forall j\geq 1.$$

We Know that

$$H_\alpha(X_j)=\frac{1}{(1-\alpha)\{\Gamma(j)\}^\alpha}\{\int_0^\infty\{-\ln\bar{F}(x)\}^{(j-1)\alpha}f^\alpha(x)dx-\{\Gamma(j)\}^\alpha\}. \tag{25}$$

Substituting $\{-\ln\bar{F}(x)\}^\alpha=u$, and hence, $x=F^{-1}\left\{1-\exp\left(-u^{\frac{1}{\alpha}}\right)\right\}$, in (25) we get

$$H_\alpha(X_j)=\frac{1}{(1-\alpha)\{\Gamma(j)\}^\alpha}\{\int_0^\infty u^{j-1}u^{\frac{1}{\alpha}-1}e^{-(u)^{\frac{1}{\alpha}}}f^{\alpha-1}\{F^{-1}(1-e^{-(u)^{\frac{1}{\alpha}}})\}du-\{\Gamma(j)\}^\alpha\}.$$

Similarly, we get

$$H_\alpha(Y_j)=\frac{1}{(1-\alpha)\{\Gamma(j)\}^\alpha}\{\int_0^\infty u^{j-1}u^{\frac{1}{\alpha}-1}e^{-(u)^{\frac{1}{\alpha}}}g^{\alpha-1}\{G^{-1}(1-e^{-(u)^{\frac{1}{\alpha}}})\}du-\{\Gamma(j)\}^\alpha\}.$$

If for two cdfs F and G, these differences coincide, we can conclude that

$$\int_0^\infty u^{\frac{1}{\alpha}-1}e^{-(u)^{\frac{1}{\alpha}}}[f^{\alpha-1}\{F^{-1}(1-e^{-(u)^{\frac{1}{\alpha}}})\}-g^{\alpha-1}\{G^{-1}(1-e^{-(u)^{\frac{1}{\alpha}}})\}]u^{n-1}L_n(u)du=0, \tag{26}$$

for all $n\geq 1$, By (26), we can conclude that

$$\int_0^\infty u^{\frac{1}{\alpha}-1}e^{\frac{u}{2}-(u)^{\frac{1}{\alpha}}}[f^{\alpha-1}\{F^{-1}(1-e^{-(u)^{\frac{1}{\alpha}}})\}-g^{\alpha-1}\{G^{-1}(1-e^{-(u)^{\frac{1}{\alpha}}})\}]e^{-\frac{u}{2}}u^{n-1}L_n(u)du=0, \tag{27}$$

for all $n\geq 1$, where $L_n(u)$ is Laguerre polynomial given in Lemma 4.1. Using the assumption $E[\log f(x)]^2<\infty$ and $E[\log g(x)]^2<\infty$, and Minkowski inequality, we can conclude that

$$u^{\frac{1}{\alpha}-1}e^{\frac{u}{2}-(u)^{\frac{1}{\alpha}}}\{f^{\alpha-1}\{F^{-1}(1-e^{-(u)^{\frac{1}{\alpha}}})\}-g^{\alpha-1}\{G^{-1}(1-e^{-(u)^{\frac{1}{\alpha}}})\}\}\in L^2(0,\ 1).$$

Hence, by the completeness property of Lemma 4.1, we conclude that

$$f(F^{-1}(v))=g(G^{-1}(v)),\ \forall\ v\in(0,1).$$

As, $\frac{d(F^{-1}(v))}{dv}=\frac{1}{f(F^{-1}(v))}$. Therefore, we have

$$F^{-1'}(v)=G^{-1'}(v),\ \forall\ v\in(0,1)$$

or, $F^{-1}(v)=G^{-1}(v)+c$,

where c is a constant. This concludes the proof.

© 2015 NSP
Natural Sciences Publishing Cor.

5 Generalized Residual Entropy of Record Values

In reliability theory and survival analysis, X usually denotes a duration such as the lifetime of a component. The residual lifetime of the system when it is still operating at time t is $(X_t = X - t|X > t)$ which has the probability density $f(x;t) = \frac{f(x)}{\bar{F}(t)}$, $x \geq t > 0$, where $\bar{F}(t) = 1 - F(t) > 0$. Ebrahimi (1996) proposed the entropy of the residual lifetime X_t as

$$H(X;t) = -\int_t^\infty \frac{f(x)}{\bar{F}(t)} \log \frac{f(x)}{\bar{F}(t)} dt \ , t > 0. \qquad (28)$$

This measures the uncertainty of the residual lifetime of the system when it is still operating at time t. The role of residual entropy as a measure of uncertainty in order statistics and record values has been studied by many researchers, refer to, Zarezadeh and Asadi (2010), Bartapour et al. (2007, 2008). The generalized residual entropy of order α is defined as

$$H_\alpha(X;t) = \frac{1}{(1-\alpha)} \left[\frac{\int_t^\infty f^\alpha(x)dx}{\bar{F}^\alpha(t)} - 1 \right]; \ \alpha > 0, \ \alpha \neq 1 \ . \qquad (29)$$

For more details and application of this dynamic information measure refer to Nanda and Paul (2005), and Kumar and Taneja (2011). Obviously, when $t = 0$, (28) and (29) reduce to information measures (3) and (4) respectively.

Let $X_1, X_2, \cdots X_n$ are i.i.d. random variables with an absolutely continuous distribution F and density function f, denoting the lifetime of n components. Then $Z = min(X_1, X_2, ..., X_n)$ represents the lifetime of the system, whose components are connected in series. The residual entropy measure (29) of the series system is independent of t, when X_i's are exponentially variate. In this context, we prove the following theorem.

Theorem 51*If $X_1, X_2, ..., X_n$ are independent random variables having an exponential distribution with parameters $\theta_i, i = 1, 2, ..., n$, then the residual entropy (29), of the random variable $Z = min(X_1, X_2, ..., X_n)$ is independent of the parameters t.*

Proof Since $Z = min(X_1, X_2, ..., X_n)$, therefore the cumulative distribution function (c.d.f.) Z is

$$F_Z(z) = P(Z \leq z) = 1 - \prod_{i=1}^n (\exp(-\theta_i z)) = 1 - \exp(-z \Sigma_{i=1}^n \theta_i).$$

Survival function of Z is

$$\bar{F}_Z(z) = 1 - F_Z(z) = \exp\left(-z \sum_{i=1}^n \theta_i \right).$$

Then its p.d.f. is given by

$$f_Z(z) = \frac{d}{dz} F_Z(z) = \sum_{i=1}^n \theta_i \left[\exp\left(-z \sum_{i=1}^n \theta_i \right) \right].$$

Substituting these values in (29) and simplify, we obtain

$$H_\alpha(Z;t) = \frac{1}{1-\alpha} \left(\frac{\sum_{i=1}^n \{\theta_i\}^{\alpha-1}}{\alpha} - 1 \right),$$

which is independent of t.

Corollary 51*If $X_1, X_2, ..., X_n$ are independent and identically distributed (i.i.d.) random variables, then :*

$$H_\alpha(Z;t) = \frac{1}{1-\alpha} \left(\frac{\sum_{i=1}^n \{n\theta\}^{\alpha-1}}{\alpha} - 1 \right).$$

The role of residual entropy as a measure of uncertainty in order statistics and record value has been studied by Zarezadeh and Asadi (2010). Next, we derive generalized residual entropy of order α for the jth upper record value. Before the main result we state the following two lemmas which are easy to prove.

Lemma 51*Let U_j^* be the j^{th} upper record value for a sequence of observations from uniform distribution on $(0,1)$. Then*

$$H_\alpha(U_j^*;t) = \frac{1}{1-\alpha} \left\{ \frac{\Gamma[(j-1)\alpha + 1; -\log(1-t)]}{\Gamma^\alpha(n; -\log(1-t))} - 1 \right\}. \qquad (30)$$

Proof For uniform distribution, using (29) we have

$$H_\alpha(U_j^*;t) = \frac{1}{(1-\alpha)} \left[\frac{\int_t^\infty g_{X_j}^\alpha(x)dx}{G_{X_j}^\alpha(t)} - 1 \right]; \ \alpha > 0, \ \alpha \neq 1 \ . \qquad (31)$$

Putting values from (1) and (2) in (31), we get the desired result (30).

Lemma 52*Let $\bar{U}_j$ be the j^{th} upper record values for a sequence of observations from standard exponential distribution. Then*

$$H_\alpha(\bar{U}_j;t) = \frac{1}{1-\alpha} \left\{ \frac{\Gamma[(j-1)\alpha + 1; t]}{\Gamma^\alpha(n;t)} E\{e^{-(\alpha-1)U_t}\} - 1 \right\}, \qquad (32)$$

where $U_t \sim \Gamma\{(j-1)\alpha + 1; t\}$

The proof follows on the same lines as in Lemma 5.1.
Now we state the main result.

Theorem 52*Let X_n, $n > 1$ be a sequence of i.i.d. continuous random variable from the distribution $F(x)$ with density function $f(x)$ and the quantile function $F^{-1}(.)$. Let U_j denote the j^{th} upper record . Then the dynamic generalized entropy (29) of j^{th} upper record value can be expressed as*

$$H_\alpha(\bar{U}_j;t) = \frac{1}{1-\alpha} \{ \frac{\Gamma[(j-1)\alpha + 1; -\log\bar{F}(t)]}{\Gamma^\alpha(n; -\log F(t))} E\{ f^{\alpha-1}\{F^{-1}(1-e^{-V_z})\}\} - 1\}, \qquad (33)$$

where $z = -\log\bar{F}(t)$ and $V_z \sim \Gamma\{(j-1)\alpha + 1; -\log\bar{F}(t)\}$ and E is the expectation.

© 2015 NSP
Natural Sciences Publishing Cor.

Proof Dynamic generalized entropy (29) of the j^{th} upper record value is defined as

$$H_\alpha(U_j;t) = \frac{1}{(1-\alpha)}\left[\frac{\int_t^\infty g_{X_j}^\alpha(x)dx}{G_{X_j}^\alpha(t)} - 1\right];\ \alpha>0,\ \alpha\neq 1$$

$$= \frac{1}{(1-\alpha)}\left\{\frac{\int_t^\infty \{-\ln\bar{F}(x)\}^{(j-1)\alpha} f^\alpha(x)dx}{\Gamma^\alpha\{n;-\log F(t)\}} - 1\right\}. \qquad (34)$$

Substituting $-\log\bar{F}(x) = u$ and $x = F^{-1}(1-e^{-u})$, we have

$$H_\alpha(U_j;t) = \frac{\left\{\int_{-\log\bar{F}(t)}^\infty u^{(j-1)\alpha}e^{-u} \times\left[f^{\alpha-1}\{F^{-1}(1-e^{-u})\}\right]du\right\}}{(1-\alpha)(\Gamma^\alpha\{n;-\log F(t)\}-1)}$$

It can be rewritten as

$$H_\alpha(\bar{U}_j;t) = \frac{1}{1-\alpha}\{\frac{\Gamma[(j-1)\alpha+1;-\log\bar{F}(t)]}{\Gamma^\alpha(n;-\log F(t))} E\{f^{\alpha-1}\{F^{-1}(1-e^{-V_z})\}\}-1\}.$$

So, the result follows.

Example Let X have Weibull distribution with density

$$f(x) = \lambda\beta x^{\beta-1}\exp\left\{-\lambda x^\beta\right\},\ \lambda,\ \beta>0,\ x>\ 0$$

Here, $x = F^{-1}(1-e^{-u}) = \{\frac{u}{\lambda}\}^{\frac{1}{\beta}}$. Then we have

$$f^{\alpha-1}\{F^{-1}(1-e^{-u})\} = \left(\beta\lambda^{\frac{1}{\beta}}\right)^{\alpha-1}\{u\}^{\frac{(\alpha-1)(\beta-1)}{\beta}}e^{-u(\alpha-1)}$$

Therefore

$$H_\alpha(\bar{U}_j;t) = \frac{1}{1-\alpha}\left\{\frac{\beta^{(\alpha-1)}\lambda^{\frac{\alpha-1}{\beta}}\Gamma\left[j\alpha-\frac{\alpha-1}{\beta};\lambda t^\beta\right]}{\Gamma^\alpha\{n;\lambda t^\beta\}[\alpha]^{j\alpha-\frac{\alpha-1}{\beta}}} - 1\right\}. \qquad (35)$$

Remark 1 For $b=2$, (35) reduces to

$$H_\alpha(\bar{U}_j;t) = \frac{1}{(1-\alpha)}\left\{\frac{\{2\sqrt{\lambda}\}^{\alpha-1}\Gamma\{j\alpha-\frac{\alpha-1}{2};\lambda t^2\}}{\Gamma^\alpha\{n;\lambda t^2\}\{\alpha\}^{\{j\alpha-\frac{\alpha-1}{2}\}}} - 1\right\}; \qquad (36)$$

the residual entropy of the jth record value from a Rayleigh distribution, that is, $X\sim Rayleigh(\lambda>0)$.

Remark 2 For $b=1$, (35) reduces to

$$H_\alpha(\bar{U}_j;t) = \frac{1}{(1-\alpha)}\left\{\frac{\{\lambda\}^{\alpha-1}\Gamma\{j\alpha-\alpha+1;\lambda t\}}{\Gamma^\alpha\{n;\lambda t\}\{\alpha\}^{\{j\alpha-\alpha+1\}}} - 1\right\}; \qquad (37)$$

the residual entropy of the jth record value from a exponential distribution, that is, $X\sim\exp(\lambda)$.

6 Conclusion

Information theoretic measures of Shannon and Renyi which are additive in nature have been studied by many researchers for record values. It is of interest to study non-additive entropy measures, which find applications in many phenomena, for record values. We have seen that Havrda and Charvat entropy measure for record values characterize the underlying distribution function uniquely except for the location. Also the concept generalized residual entropy for record values has been studied which can be explored further both theoretical interest and application point of view.

References

[1] Ahsanullah, M. Record Values-Theory and Applications, University Press of America Inc., New York, 2004.

[2] Arnold, B. C. Balakrishnan, N. Nagaraja, H. N. Records, Wiley, New York, 1998.

[3] Baratpour, S. Ahmadi, J. Arghami, N. R. (2007). Entropy properties of record statistics, Statistical Papers, 48, 197-213.

[4] Baratpour, S. Ahmadi, J. Arghami, N. R. (2008). Characterizations based on Renyi entropy of order statistics and record values, Journal of Statistical Planning and Inference, 138, 2544-2551.

[5] David, H. A. Nagaraja, H. N. (2003) Order Statistics. Wiley, Hoboken, New Jersey.

[6] Ebrahimi, N. (1996). How to measure uncertainty in the residual lifetime distributions, Sankhya A, 58, 48-57.

[7] Goffman, C. Pedrick, G. First course in functional analysis. Prentice Hall Inc. (1965).

[8] Havrda, J. and Charvat, F. (1967). Quantification method of classification process:concept of structural α-entropy, Kybernetika, 3, 30-35.

[9] Kumar, V. Taneja, H. C. (2011). A generalized entropy-based residual lifetime distributions, International Journal of Biomathematics, 4(2), 171-184.

[10] Kamps, U. (1994). Reliability properties of record values from non-identically distributed random variables. Communications in Statistics Theory and Methods, 23, 2101-2112.

[11] Nanda, A. K. Paul, P. (2006). Some results on generalized residual entropy, Information Sciences, 176, 27-47.

[12] Nevzorov, V. Records: Mathematical Theory, Translation of Mathematical Monographs, vol. 194, American Mathematical Society Providence, RI, USA, 2001.

[13] Raqab, M. Z., Awad, A. M. (2000). Characterizations of the Pareto and related distributions. Metrika, 52,63-67.

[14] Shannon, C. E. (1948). A mathematical theory of communication, Bell System Technical Journal, 27, 379-432.

[15] Tsallis, C. (1988). Possible generalization of Boltzmann-Gibbs statistics, Journal Statistical Physics, 52, 479-487.

[16] Tsallis, C. and Brigatti, E. (2004). Non-extensive statistical mechanics: a brief introduction, Continuum Mechanics and Thermodynamics, 16, 223-235.

© 2015 NSP
Natural Sciences Publishing Cor.

[17] Zahedi, H. and Shakil, M. (2006). Properties of entropies of record values in reliability and life testing context, Communications in Statistics - Theory and Methods, 35, 997-1010.
[18] Zarezadeh, S. and Asadi, M. (2010). Results on residual Renyi entropy of order statistics and record values, Information Sciences, 180, 4195-4206.

Vikas Kumar has obtained his M.Sc and M.Phil degree in Applied Mathematics from IIT Roorkee and ISM University, Dhanbad in 2005 and 2007 respectively. He received the Ph.D. degree in Mathematics from University of Delhi, Delhi. Currently, he is a Assistant Professor in Mathematics, UIET, M. D. University, Rohtak, India. His research interests are information theory and its applications and mathematical modeling. He has published research articles in reputed international journals of Mathematics and Statistical sciences.

H. C. Taneja presently Professor in Applied Mathematics and Dean (Alumuni & International Affairs) at Delhi Technological University, Delhi got his Ph.D. in the field of Information Theory in the year 1985. He has vast experience of about 35 years of teaching in mathematics and statistics both at UG and PG levels at different universities and technical institutions. Dr. Taneja has published more than sixty research papers in the field of Information Theory & Coding in journals of international repute and is a member of various national and international societies. He has authored two books, one ?Advanced Engineering Mathematics? and the second ?Statistical Methods for Engineering and Sciences?.

© 2015 NSP
Natural Sciences Publishing Cor.

Performance characteristics of a single cylinder diesel engine fuelled with 1-octanol diesel blends

Rashi Koul
Department of Mechanical Engineering
Bio Diesel Laboratory
Delhi Technological University;Bawana;Delhi, India

Abstract- Various research related to the use of alcohols so far as alternative fuels for internal combustion engines has been focused on the employment of short chain alcohols, mainly methanol and ethanol, blended with fossil fuels. Despite of their adequate combustion properties, long chain alcohols have been barely investigated.
There is a growing interest on using alcohols to substitute diesel fuel, as the use of oxygenated fuels involves oxygen enrichment leading to enhancement of premixed combustion phase and improved emissions.
The main objective of this paper is to study higher chain alcohol like Octanol which may provide a real insight in to the potential usage of these largely unexplored alternative fuels in diesel engines. The present study deals with the utilisation of 1-Octanol and diesel blends on a single cylinder diesel engine to characterise performance.
The 1-octanol was volume wise substituted by 5%, 10%, 15% and 20% in the mineral diesel and named as OC5, OC10, OC15 and OC20 respectively. Neat diesel was named as D100. The experimental engine trial results showed an increase in brake thermal efficiency (BTE) and reduction in brake specific fuel consumption (BSFC) and increased exhaust temperature.

Keywords: Engine performance, 1-octanol diesel blends.

I. INTRODUCTION

Energy is one of the most important building blocks in human development, and, as such, acts as a key factor in determining the economic development of all countries. Reduction in engine emissions becomes a major task in engine development due to the increasing concern of environmental protection and more stringent emission norms. In addition to this, efforts are needed to reduce dependence on the petroleum fuels as it is obtained from limited reserves [1]. Diesel engine has a higher thermal efficiency and produces higher power that can save more fuel compared to gasoline engine [2]. Hence diesel engines are usually used for heavy duty vehicles. Several experimental studies have been carried out around the world to evaluate the engine performance of methanol diesel blends and ethanol diesel blends [4, 6-14].

This experiment was conducted by taking higher carbon chain alcohol like 1-octanol, as its various property values were almost same to that of the diesel. 1-octanol was easily miscible in diesel, hence overcoming the disadvantage of immiscibility of methanol and ethanol with diesel fuel [4,5]. However, in case of methanol, ethanol diesel blends problem to some extent can be solved by adding octyl nitrate [5] or methyl ester [7,8].

1-octanol has number of advantages. It is produced industrially by the oligomerisation of ethylene using triethylaluminium followed by oxidation of the alkylaluminium products.
An idealised synthesis is shown

$$Al(C_2H_5)_3 + 9C_2H_4 \rightarrow Al(C_8H_{17})_3$$

$$Al(C_8H_{17})_3 + 3O + 3H_2O \rightarrow 3C_8H_{17}OH + Al(OH)_3$$

The experiment was carried on a Kirloskar make, single cylinder, air cooled, direct injection, DAF8 model diesel engine. Break thermal efficiency, break specific fuel consumption and exhaust temperature were found out for different proportions like D100, OC5, OC10, OC15 and OC20.

II. EXPERIMENTAL SET UP & PROCEDURE

The present study is conducted on an engine installed in Bio-fuel laboratory of Mechanical Engineering Department at Delhi Technological University, Delhi.

Table 1. Specifications of the Diesel Engine

Make	**Kirloskar**
Model	DAF 8
Rated Brake Power (bhp/kW)	8 / 5.9
Rated Speed (rpm)	1500
Number of Cylinder	One
Bore X Stroke (mm)	95 x 110
Compression Ratio	17.5:1
Cooling System	Air Cooled (Radial Cooled)
Lubrication System	Forced Feed
Cubic Capacity	0.78 Lit
Inlet Valve Open (Degree)	4.5 BTDC
Inlet Valve Closed (Degree)	35.5 ABDC
Exhaust Valve Open (Degree)	35.5 BBDC
Exhaust Valve Closed (Degree)	4.5 ATDC
Fuel Injection Timing (Degree)	26 BTDC

The main features of an engine are presented in the Table 1.

Table 2. Fuel properties

Property	**Mineral Diesel**	**1-Octanol Diesel blend**
Density(kg/m^3)	810	823.56
Kinematic Viscosity at 40°C (cSt)	2.5	3.387
Cold Filter Plugging Point (CFPP) (°C)	-13	-10
Calorific value (kJ/kg)	42,200	37634.68

The Table 2 compares the properties of mineral diesel and 1-octanol diesel blend.

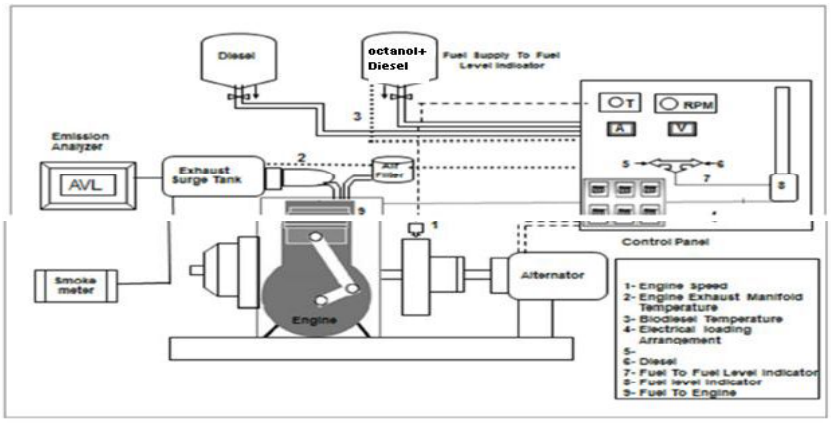

Figure 1. Schematic Diagram of the Experimental Set Up

The Figure 1. gives the complete layout of the experimental setup.

It is a single cylinder, naturally aspirated, four stroke, vertical, air-cooled engine. It has a provision of loading electrically since it is coupled with single phase alternator through flexible coupling. The engine can be

hand started using decompression lever and is provided with centrifugal speed governor. The cylinder is made of cast iron and fitted with a hardened high-phosphorus cast iron liner. The lubrication system used in this engine is of wet sump type, and oil is delivered to the crankshaft and the big end by means of a pump mounted on the front cover of the engine and driven from the crankshaft. The inlet and exhaust valves are operated by an overhead camshaft driven from the crankshaft through two pairs of bevel gears. The fuel pump is driven from the end of camshaft.

Once the parameters like power, engine speed, fuel consumption, temperature were selected, the essential instruments required for sensing these parameters were installed at the appropriate points in the experimental set-up.

In the present set up volumetric fuel consumption was measured using a glass burette. The time taken by the engine to consume a fixed volume of 10cc was measured using a stopwatch. The volume divided by the time taken for fuel consumption gave the volumetric flow rate. After stable operating conditions were experimentally achieved, the engine was subjected to similar loading conditions. Starting from no load, observations were recorded at 20%, 40%, 60%, 80% and 100% of the rated load. Chromel-Alumel K-type thermocouples were connected to a 6 channel digital panel meter to measure temperatures of exhaust gas.

The engine was started at no load. After feed control was adjusted so that engine attains rated speed and was allowed to run (about 30 minutes) till the steady state condition was reached. With the fuel measuring unit and stop watch, the time elapsed for the consumption of 10cc of fuel was measured for OC5, OC10, OC15 and OC20 at varying load. Fuel Consumption, RPM, exhaust temperature were measured. The engine was loaded gradually keeping the speed with in the permissible range and the observations of different parameters were evaluated. Short term performance tests were carried out on the engine with diesel to generate the base line data and subsequently blend was used to evaluate its suitability as a fuel. The performance characteristics of the blend fuel were evaluated and compared with diesel fuel.

III. RESULTS AND DISCUSSIONS

3.1. Performance Characteristics

The performance characteristic of test engine on octanol diesel blends is summarized below.

3.1.1. Brake Thermal Efficiency

Figure 2. shows the variation of different octanol diesel blends in comparison to neat diesel. It is clear that the Brake Thermal Efficiency (BTE) first increase with increase in load and thereafter it decreases. It is also found that BTE is increasing with increasing volume of octanol in octanol diesel blends. The maximum BTE observed for the blends OC 5, OC 10, OC 15 and OC 20 are 24.46%, 25.59%, 26.19% and 27.02% respectively. The maximum BTE in case of neat diesel is 23.71%. The increase in BTE with addition of octanol in diesel may be due to the fact that octanol is oxygenated which results in improved combustion. Moreover, addition of octanol in diesel also reduces kinematic viscosity which makes atomization better [9]. The results are similar to the results obtained by Rakapoulus [16] and O.Dogan [17].

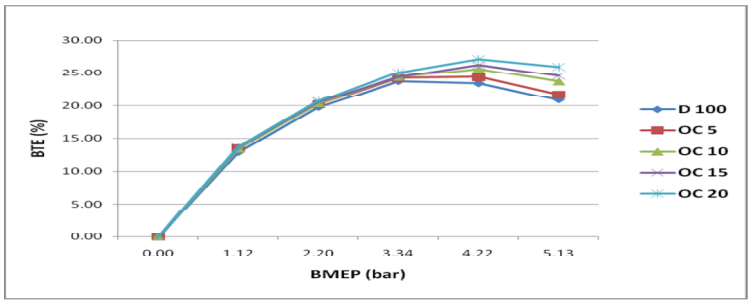

Figure 2. BTE v/s BMEP

3.1.2. Brake Specific Energy Consumption

Since Brake Specific Fuel Consumption (BSFC) is not a very reliable parameters to compare the performance of two different fuels since density and calorific value of both the fuel are significantly different. Therefore, brake specific energy consumption (BSEC) was taken as a parameter to compare the energy requirement for producing unit power in case of different test fuels.

As seen from the Fig. 3, the BSEC reduces with the increase in Brake Mean Effective Pressure (BMEP). BSEC of the octanol-diesel blend is lower than the baseline data for the neat diesel. This is mainly because of presence of oxygen in octanol which helps in better combustion. Due to better combustion of fuel blends, requirement for energy is reduced and hence BSEC of blends decreases in comparison to baseline data. Decrease in kinematic viscosity of blends due to presence of octanol also helps in better atomization on fuel and subsequent better consumption [9,12].

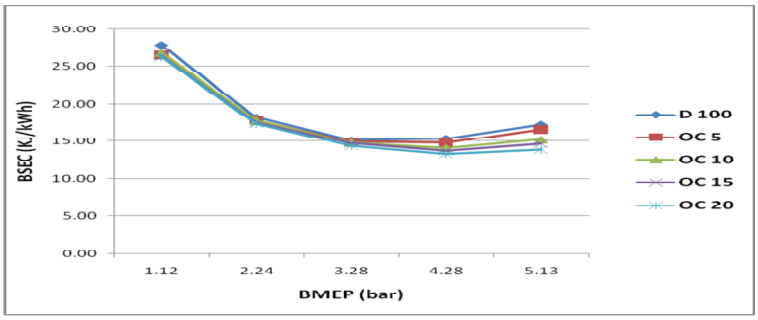

Figure 3. BSEC v/s BMEP

3.1.3.Exhaust Temperature

Figure. 4. shows the variation of exhaust temperature with brake mean effective pressure for different blends of octanol and neat diesel. The result shows that the exhaust temperature increases with the increase in brake power in all the cases. The increase in exhaust temperature with octanol addition may be due to better combustion, which leads to increased cylinder temperature and hence increased exhaust temperature [12, 20].

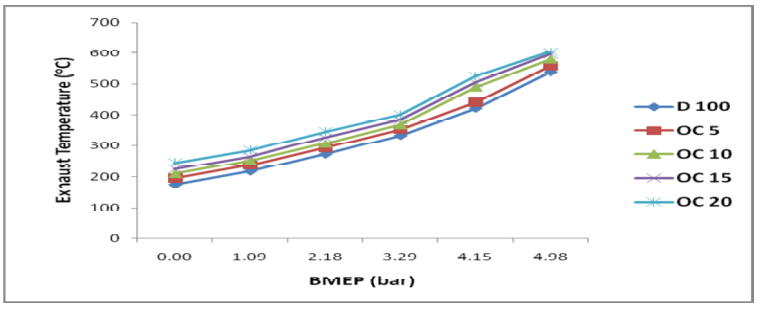

Figure.4. Exhaust temperature v/s BMEP

IV. CONCLUSIONS AND SCOPE FOR FUTURE WORK

4.1 Conclusion

The purpose of the present study was to evaluate the performance characteristics of a higher carbon chain alcohol diesel blend, i.e; octanol diesel blend on an unmodified diesel engine. On the strength of exhaustive engine trial, the following major conclusions have been drawn:

1. The brake thermal efficiency of the octanol diesel blends (OC 5, OC 10, 0C 15 and OC 20) were found higher than neat diesel (D100).
2. The brake specific energy consumption was found to be lower for the blends in comparison to neat diesel.
3. 1-octanol was easily miscible in diesel, hence overcoming the disadvantage of immiscibility of methanol and ethanol with diesel fuel

V. FUTURE WORK

On the basis of present work done, the following directions are indicated for further investigations and developments.

In the present study, octanol concentration was limited up to 20%. It is suggested that higher concentration of octanol may be explored in the near future work.

In the present study, an unmodified diesel engine was used, however, it is expected that certain modifications may be required for better performance. Therefore, the engine design may be modified, specially the injection system for using blends of 1-octanol and diesel.

The short term trial of engine was carried out in the present work. There is an urgent need to carry out long term endurance test to assess the suitability of 1-octanol-diesel blends on an engine.

REFERENCES

[1] Hulwanm DB, Joshi SV. Performance, emission and combustion characteristic of a multicylinder DI diesel engine running on diesel–ethanol–biodiesel blends of high ethanol content. *Applied Energy* 2011;**8 (12)**:5042–55.

[2] Huang J, Lin J, Wang Y, Qin J, Roskilly AP, Li L, Ouyang T, Yu Y. Experimental study of the performance of and emission characteristics of diesel engine using direct and indirect injection systems and different fuels. Fuel Process Tech 2011; 92: 1380-1386.

[3] Can O, Celikten I, Usta N. Effects of ethanol addition on performance and emissions of a turbocharged indirect injection diesel engine running at different injection pressures. Energy Convers Manage 2004;45:2429-2440.

[4] Shi X, Pang X, Mu Y, He H, Shuai S, Wang J, Chen H, Li R. Emission Reduction Potential of Using Ethanol-Biodiesel-Diesel Fuel Blend on a Heavy-duty Diesel Engine. Atmospheric Environment 2006;40:2567-2574.

[5] Rakopoulos DC, Rakopoulos CD, Karakas EC, Giokoumis EG. Effects of ethanol–diesel fuel blends on the performance and exhaust emissions of heavy duty DI diesel engine. Energy Convers Manage 2008;49:3155-3162.

[6] Sayin C, Cacakci M. Effects of injection timing on the engine performance and exhaust emissions of a dual-fuel diesel engine. Energy Convers Manage 2009;50:203–213.

[7] Cetin M, Yuksel F, Kus H. Emission characteristics of a converted diesel engine using ethanol as fuel. Energy for Sustainable Development 2009;13:250–254.

[8] Surawski NC, Ristovski ZD, Brown RJ, Situ R. Gaseous and particle emissions from an ethanol fumigated compression ignition engine. Energy Conversion and Management 2012;54:145–151.

[9] Kumar MS, Kerihuel A, Bellettre A, Tazerout M. Ethanol animal fat emulsions as a diesel engine fuel – part 2: engine Test analysis. Fuel 2006;85:2646–2652.

[10] Pidol L, Lecointe B, Starck L, Jeuland N. Ethanol–biodiesel–diesel fuel blends: performances and emissions in conventional diesel and advanced low temperature combustions. Fuel 2012;93:329–338.

[11] Huang J, Wang Y, Li S, Roskilly AP, Yu H, Li H. Experimental investigation on the performance and emissions of a Diesel engine fuelled with ethanol–diesel blends. Appl Therm Eng 2009;29:2484–2490.

[12] Park HS, Youn IM, Lee CS. Influence of ethanol blends on the combustion performance and exhaust emission characteristics of a four-cylinder diesel engine at various engine loads and injection timings. Fuel 2011;90:748–755.

[13] Hulwan DB, Joshi SV. Performance, emission and combustion characteristic of a multicylinder DI diesel engine running On diesel–ethanol–biodiesel blends of high ethanol. Appl Energy 2011;88:5042–5055.

[14] D.C.Rakopoulos, C.D.Rakopoulos, E.G.Giakoumis, A.M.Dimaratos and D.C.Kyritis. Effects of butano-diesel fuel blends on the performance of a high speed DI diesel engine, Energy Conversion and Management, Vol.51, NO.10, 2010, 1989-1997.

[15] O.Dogan; the influence of n-butanol/diesel fuel blends utilisation on a small diesel engine performance and emissions fuel; Vol-90, pp 2467-2472, 2011.

[16] AC Hansen, MR Gratton, Yuan W. Diesel engine performance and NOx emissions from oxygenated biofuels and blends with diesel fuel. Trans ASABE 2006;49(3):589–95.

[17] Deepak Agarwal, Lokesh Kumar, Avinash Kumar Agarwal ,Performance evaluation of vegetable oil fuelled compression ignition engine, Renewable Energy 33 (2008) 1147–1156.

[18] Labeckas G, Slavinskas S. Comparative performance of direct injection diesel engine operating on ethanol, petrol and rapeseed oil blends. Energy Convers Manage 2008;50(3):792–801.

Indian J Phys (May 2014) 88(5):489–496
DOI 10.1007/s12648-014-0445-2

ORIGINAL PAPER

Piezoelectric and pyroelectric properties of zirconium substituted barium titanate ferroelectric ceramics

P A Jha[1] and A K Jha[1,2]*

[1]Thin Film and Material Science Laboratory, Department of Applied Physics, Delhi Technological University (Formerly Delhi College of Engineering), Bawana Road, Delhi 110042, India

[2]Department of Applied Sciences, Ambedkar Institute of Advanced Communication Technologies and Research, Geeta Colony, Delhi 110031, India

Received: 23 October 2013 / Accepted: 08 January 2014 / Published online: 23 January 2014

Abstract: In present study, Piezoelectric and pyroelectric properties of zirconium substituted barium titanate compositions ($BaZr_xTi_{1-x}O_3$) ($x = 0$–0.1) have been investigated, as Zr^{+4} possesses more chemical stability than Ti^{+4} ions. The grain size increases from 0.55 μm for $x = 0.0$–3.2 μm for $x = 0.025$ and 6.15 μm for $x = 0.05$. With further Zr substitution, grain size decreases to 0.5 μm for $x = 0.075$ and 0.33 μm for $x = 0.1$. With increase in sintering temperature from 1,200 to 1,300 °C, the piezoelectric coefficient of $BaZr_{0.025}Ti_{0.975}O_3$ increases from 40.1 to 189.2 pC/N and this is correlated to the type of domain structures. Zr content influences grain size and domain structures leading to an appreciable change in dielectric constant as well as piezoelectric and pyroelectric properties. The value of pyroelectric coefficients increases from 72.23 μC/m^2 °C for $x = 0.0$–5,984.095 μC/m^2 °C for $x = 0.025$ and decreases to 2,719.68 μC/m^2 °C for x = 0.05 and 5.96 μC/m^2 °C for $x = 0.1$. The value of figure of merit of $x = 0.025$ i.e. 1.22 proves its better suitability for infrared detectors.

Keywords: Barium titanate; Sintering temperature; Dielectrics; Ferroelectrics

PACS Nos.: 77.84.Cg; 81.20.Ev; 77.84.-s

1. Introduction

In piezoelectric and pyroelectric materials the spontaneous polarization depends upon mechanical stress and temperature respectively [1]. When constant stress and temperature are applied, free charges inside the sample compensate the material's internal electric field originating from intrinsic dipoles by creating a layer of bound charge [2]. Spontaneous polarization occurs more easily in perovskite crystal structure (e.g. Barium titanate) due to higher value of Lorentz factor ($\gamma = 10^2$) than the other crystal structures [3].

There have been considerable interests on structural and electrical properties of various ferroelectric materials [4–8]. Among those ferroelectric materials, barium titanate is the most widely studied lead-free piezoelectric materials due to its application in uncooled infra red detectors among large number of other applications. These detectors depend on pyroelectric and ferroelectric materials as ferroelectric detectors operate close to the Curie temperature [3]. The phase transition temperature can be altered with A- or B-site substitutions. In particular, Zr^{+4} has higher ionic radius and more chemical stability than Ti^{+4}, hence compositionally modified barium zirconate titanate has received large attention due to its tunable structure and electrical properties for specific applications.

Moreover, the zirconium substituted polycrystalline $BaTiO_3$ are suitable materials for transverse mode and pyroelectric charge coupled device (CCD) arrays and 3–4 % substitution of Zr^{4+} ions to barium titanate alters phase transformation temperature and electric properties [9]. The substitution changes the Curie temperature where pyroelectric coefficient is extremely high relative to dielectric permittivity. These materials show a very high figure of merit for dielectric bolometer applications than the existing materials. Moreover, these materials can be synthesized easily [10–12]. An extensive literature survey reveals that there is hardly any report on the correlation

*Corresponding author, E-mail: prof.akjha@gmail.com

© 2014 IACS

between the domain structures, density and piezoelectric and pyroelectric properties of barium zirconate titanate. Also there is hardly any report regarding the detailed discussions on the influence of small Zr^{+4} substitutions i.e. $x \leq 0.1$ on the domain structures and electrical properties of barium titanate. This has prompted the authors to present a detailed discussion on the electrical properties of barium zirconate titanate.

2. Experimental details

Compounds $BaZr_xTi_{1-x}O_3$ ($x = 0$, 0.025, 0.05, 0.075, 0.1) were prepared by the solid state reaction method [13], using high purity $BaCO_3$, TiO_2 and ZrO_2 (all from M/s Aldrich, USA). The powder mixtures were thoroughly ground in an agate mortar and passed through a sieve of appropriate size. The powder mixtures were then calcined at 1,150 °C for 2 h in an alumina crucible. The calcined mixtures were ground and admixed with polyvinyl alcohol (PVA) as a binder and then pressed at 150 MPa into disk shaped pellets. The pellets were then sintered at 1,300 °C for 2 h in air. X-ray diffractograms of all the sintered samples were recorded using a Bruker X-ray diffractometer with CuKα ($\lambda = 1.5406$ Å) radiations in the range $10° \leq 2\theta° \leq 70°$ at a scanning rate of 2°/minute. The X-ray diffractograms were fitted with tetragonal structure (P4 mm) in Reitveld refinement using FULL PROF Suite package. The microstructural studies of the samples were carried out using a scanning electron microscope (Hitachi S-3700N). The sintered pellets were polished to a thickness of 1 mm and coated with silver paste on both sides to act as electrodes and then finally cured at 300 °C for 30 min. The dielectric measurements were carried out in the temperature range of room temperature to 300 °C at 1 kHz using a high precision LCR meter (HP 4284A) at rms voltage of 1 V. P-E hysteresis loops were recorded at room temperature using a P-E loop tracer based on Sawyer–Tower circuit. The pyroelectric coefficient was measured using the Byer–Roundy technique [14]. Before measurement, the compositions were poled at a field of 2 kV at temperature less than Curie temperature i.e. ferroelectric region ($\sim$100 °C), for 2–3 h in silicon oil. Then the poled specimen was heated at 1 °C/min to measure pyroelectric current generated in the sample using a high precision electrometer (Keithley 6517 A). Piezoelectric coefficient (d_{33}) was measured using a piezometer system (PiezoTest, PM300).

3. Results and discussion

Figure 1 shows the X-ray diffractograms for $BaZr_xTi_{1-x}O_3$ ($x = 0$, 0.025, 0.05, 0.075, 0.1), while Fig. 2 shows the

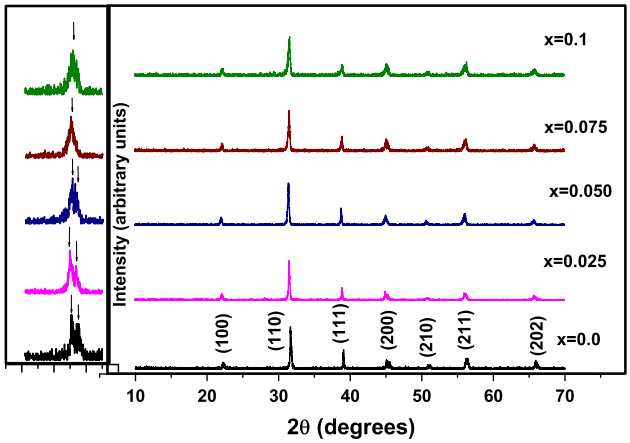

Fig. 1 X-ray diffractograms for different compositions of $BaZr_xTi_{1-x}O_3$

Reitveld refinement of the above mentioned specimens. X-ray diffractograms have been fitted with tetragonal structure (P4 mm) in Reitveld refinement using FULL PROF Suite package. The splitting of tetragonal peaks (200) and (002) is observed at $2\theta = 45.262°$ in the specimen with $x = 0$, i.e. pure barium titanate [15]. However, with the increasing content of Zr^{+4}, splitting disappears. For the clarity, the slow scan of the (200) peak is shown in the left side of Fig. 1, clearly indicating the splitting of this peak in the specimens with lower Zr content [16]. This is because of the higher ionic radius of the Zr^{+4} ion (0.87 Å) than that of Ti^{+4} ion (0.68 Å) and with the substitution of Zr^{+4} ions reaction kinetics change leading to the formation of dense ceramics at different sintering temperature [17]. It is well known that the diffusion coefficient is directly proportional to the sintering temperature and inversely proportional to the radius of the diffusing particles [18]. Hence, higher sintering temperature will be required for the diffusion of large sized Zr^{+4} ions. In the sample with higher Zr content i.e. $x = 0.1$ no splitting of peak is observed showing the transformation towards cubic structure i.e. lattice parameters are nearly same for $x = 0.1$ as Zr substitution has decreased c- parameter (shown in Fig. 3) as is also seen by the reduced value of tetragonal strain (c/a) in Fig. 3 inset. This can be due to the substitution of higher ionic radii and chemically more stable Zr^{4+} ions.

Figure 4(a) shows SEM micrographs for x = 0.0, Fig. 4(b) shows SEM micrographs for x = 0.025, Fig. 4(c) shows SEM micrographs for x = 0.05, Fig. 4(d) shows SEM micrographs for x = 0.075 and Fig. 4(e) shows SEM micrographs for x = 0.1. Pure barium titanate specimen has smaller grains and porous microstructures whereas in Zr substituted barium titanate specimens well developed larger grains are seen. The average grain size increases initially but decreases subsequently with the increase in the Zr content (0.55, 3.2, 6.15, 0.5 and 0.33 μm respectively for $x = 0.0$,

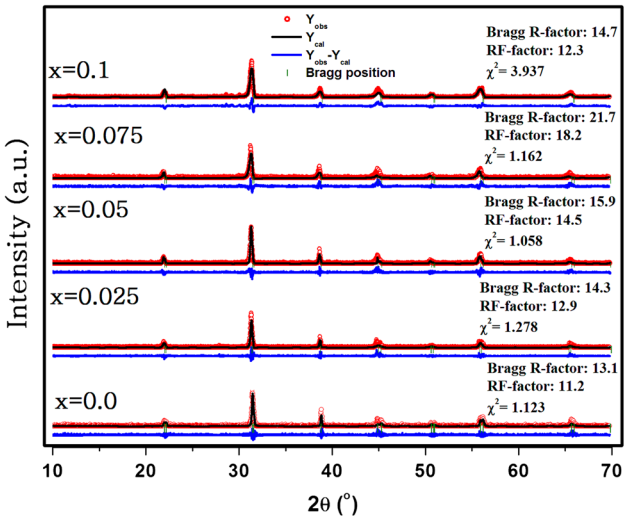

Fig. 2 Reitveld refinement for the same compositions in Fig. 1. Further, the Bragg R-factor, RF-factor and χ^2 has been mentioned

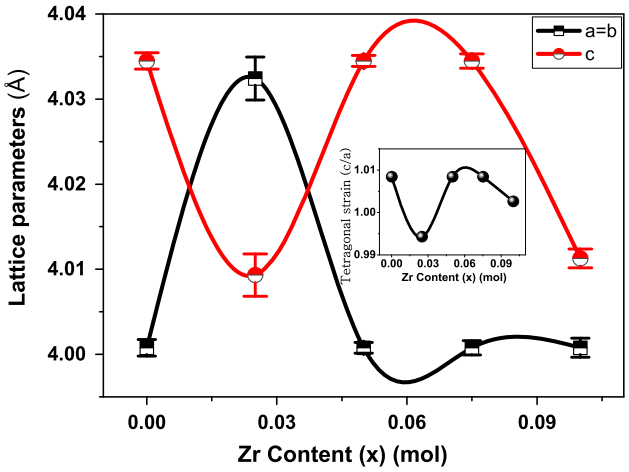

Fig. 3 Lattice parameters for different compositions of ($BaZr_xTi_{1-x}O_3$)

0.025, 0.05, 0.075 and 0.1). This is because of dominant mechanism for grain growth during sintering is diffusion and higher grain size is attributed to the diffusion of larger Zr^{+4} ions onto the B-sites [19]. Further, the domain structures are observed in the SEM micrographs of the Zr^{+4} substituted samples. The domain structures in SEM images in these compounds have also been earlier reported by Wei Cai et al. [17]. The domains with "lamellar" and "watermark" characters are shown in Fig. 4 by circles A, B, C and D. It is also observed that the domain structures are larger in number in specimen with lower Zr content.

Figure 5 shows the measured density of the studied samples by measuring dimensions. Theoretical density of BZT ceramics was calculated to be 6.02 g/cm^3 as per JCPDS file card # 31-0174. It is observed that relative density first increases from 90 % for $x = 0.0$–98 % for $x = 0.05$ and decreases to 71 % for $x > 0.05$ (Fig. 5). As seen in SEM micrographs, sample with $x = 0.025$ and $x = 0.05$ possess larger grains and less number of pores. This results in the increase in density of the specimen. As mentioned earlier, higher sintering temperature is required for the diffusion of large sized Zr^{+4} ions for higher Zr content specimens to form higher dense specimens.

Figure 6(a) Shows permittivity with temperature, Fig. 6(b) shows dielectric loss with temperature for different compositions of ($BaZr_xTi_{1-x}O_3$) and Fig. 6(c) shows the permittivity around Curie temperature for $x = 0.075$ and $x = 0.1$ The broad permittivity peak is indicating the diffuse phase transition [20]. There is a noticeable increase in the dielectric constant i.e. from 2,920 for $x = 0.0$, 4,840.437 for $x = 0.025$, 10,680 for $x = 0.05$ has been observed. With the increase in Zr content i.e. for $x > 0.05$, the dielectric constant reduces considerably i.e. 417 for $x = 0.075$ and 190 for $x = 0.1$. Increase in dielectric constant can be attributed to the increase in grain size. This can be explained as follows. At higher sintering temperature, average grain size increases leading to the easier domain wall motion resulting in an increased polarization and hence dielectric constant [21]. The lattice undergoes reoxidation on sintering in air and it forms a strong insulating layer of oxygen vacancies around a grain with a higher bulk resistance. It results in high interfacial polarization leading to the increase in dielectric constant [22]; as the grain boundaries have large resistance and capacitance as compared to the bulk [23]. Moreover, the difference in the conductivity of the bulk and grain boundary results in an increase in surface charge accumulation which results in the increase of interfacial polarization. While the dielectric loss is independent of temperature up to about 150 °C and then increases with increase in temperature. Whereas for 5 mol% Zr substituted sample, firstly the dielectric loss decreases up to about 75 °C and then is independent of temperature of about 150 °C and increases rapidly at higher temperatures. It is also observed that the loss is higher for $x = 0.05$. The onset temperature of dielectric loss decreases with the increase in Zr-content. This variation in onset temperature clearly suggests the presence of impurities arising from defects or vacancies in the sample [24].

Figure 7(a) shows the P–E loop for x = 0.0, Fig. 7(b) shows the P–E loop for x = 0.025, Fig. 7(c) shows the P–E loop for x = 0.05, Fig. 7(d) shows the P–E loop for x = 0.075 and Fig. 7(e) shows the P–E loop for x = 0.1. Well saturated hysteresis loops with regular shape having high remanent polarization, i.e. $P_r = 34$ μC/cm^2 and coercive field, $2E_c$ of 14 kV/cm at 1,300 °C for $x = 0.0$. With the substitution of zirconium for $x \leq 0.05$, well saturated loops and for $x > 0.05$, lossy elliptic loops are obtained. As zirconium is chemically more stable than

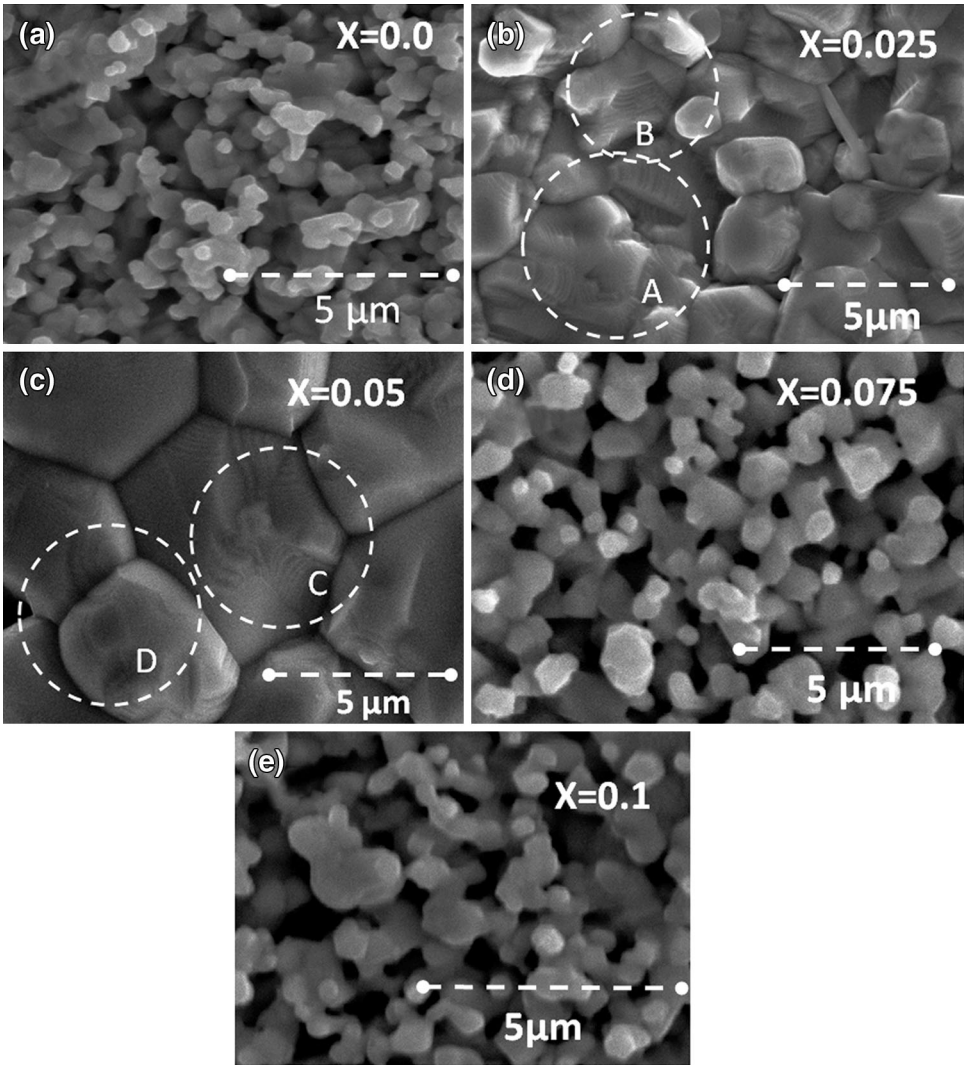

Fig. 4 (**a**) Shows SEM micrographs for x = 0.0, (**b**) shows SEM micrographs for x = 0.025, (**c**) shows SEM micrographs for x = 0.05, (**d**) shows SEM micrographs for x = 0.075, (**e**) shows SEM micrographs for x = 0.1

titanium and this can reduce ferroelectricity. The remanent polarization increases decreases from 24 μC/cm^2 for $x = 0.025$, 22 μC/cm^2 for $x = 0.05$, 3.56 for $x = 0.075$ and 3.52 for $x = 0.1$. On further addition of zirconium i. e. for $x > 0.05$, the P–E hysteresis loop has an elliptic shape which is attributed to paraelectric state [25]. The reduction in remanent polarization, P_r can be related to the changes in crystal structure [26] as the structure is cubic for $x = 0.1$. With the Zr substitution, coercive field ($2E_c$) decreases for all $x \neq 0$ samples indicating that reversal polarization process of a ferroelectric domain becomes easier with Zr-substitution in BT-lattice [27]. This is explained on the basis of effect of grain boundary on polarization. The decrease in grain size leads to the increase in the number of grain boundaries [17] and grain boundaries are low capacitive regions, hence poor ferroelectricity. On the other hand there is a difference between the polarization of bulk and grain boundary leading to the polarization discontinuity and hence remanent polarization ($2P_r$) decreases. Unsaturated loops in the higher Zr content region can be due to absence of "imprint" phenomena indicating that our ceramics possess defects as oxygen vacancies which pin the domain walls [28]. As it is well known that the ferroelectric properties depend on the microstructure and nature of substituent etc. [29–31], hence, the above observed behavior can be due to the Zr substitution.

Piezoelectric constants (d_{33}) and quadratic electrostriction coefficient (K_{33}) are plotted as a function of Zr content in Fig. 8(a). The relation between piezoelectric coefficient, spontaneous polarization and the electrostriction coupling coefficient is [32]:

$$d_{33} = 2\varepsilon_{33}\varepsilon_o k_{33} P_s \tag{1}$$

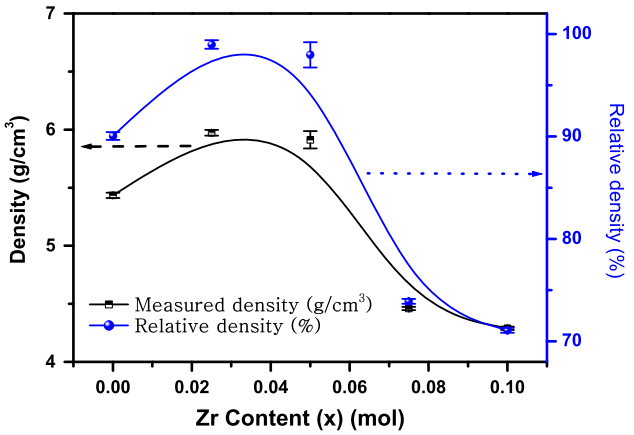

Fig. 5 Relative density for different compositions of ($BaZr_xTi_{1-x}O_3$)

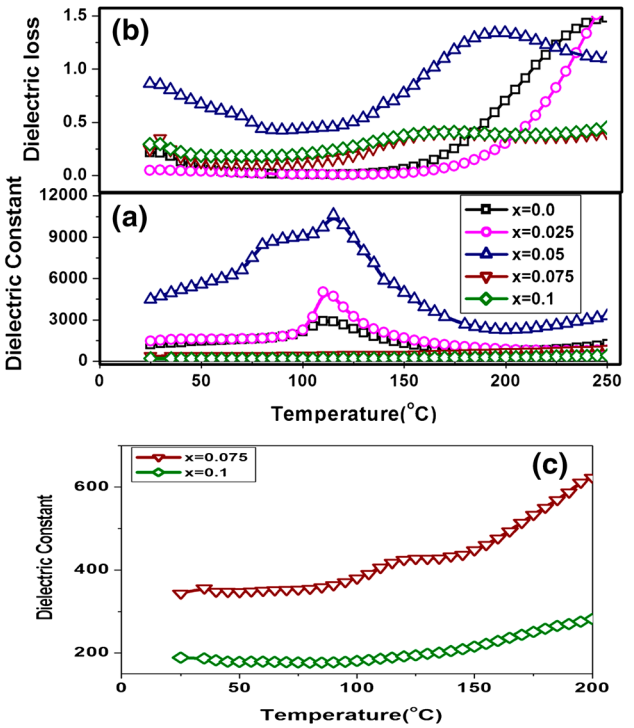

Fig. 6 (**a**) Shows permittivity with temperature, (**b**) shows dielectric loss with temperature for different compositions of ($BaZr_xTi_{1-x}O_3$) and (**c**) shows the permittivity around Curie temperature for $x = 0.075$ and $x = 0.1$

where ε_{33} is the dielectric constant, ε_o is dielectric constant of free space. The electrostrictive coupling originates from the anharmonic motion of dipoles in the materials and this causes a change in the lattice parameter and produces a strain. The electrostriction coefficient does not depend upon temperature and its value varies in between 0.05 and 0.1 m^4/C^2 for different materials. It is observed that up to x = 0.025, piezoelectric coefficients increases from 40.1 to 189.2 pC/N and for $x \geq 0.05$, the value of the coefficients decreases from 54.8 pC/N for $x = 0.05$, 27 pC/N for $x = 0.075$ and 26 pC/N for $x = 0.1$. This can be understood as follows. There are two major contributions to the piezoelectric coefficients: extrinsic and intrinsic. Influence of grain size, preferred orientation and the morphotrophic phase boundary conditions determine the intrinsic component of the piezoelectric constant in a specimen [33, 34]. The extrinsic contribution is related to 180° and 90° domain wall motion in the specimen [35]. The increase in piezoelectric coefficient is due to the increase in grain size as grain size affects the intrinsic responses and domain wall motion. As seen in SEM micrographs, grain size increases for $x \leq 0.05$ and then grain size decreases for $x > 0.05$. The grain size affects the coercive field (E_c) and low E_c values facilitate the orientation of ferroelectric domains during electrical poling and hence the intrinsic responses of the piezoelectric constant. On the other hand, near the Curie temperature, lattice distortion introduces large strains in the individual grains leading to domain structures that influence permittivity and hence piezoelectric constant. Moreover, in SEM micrographs, it is observed that domains are continuous as well as discontinuous across grain boundaries. Continuous ferroelectric domains across the grain boundary decreases the electrostrictive stress under an external applied electric field and hinders the formation of other oriented domains near the grain boundary leading to the enhancement in the piezoelectric properties [36]. Therefore, at $x = 0.025$, minimum value of tetragonal strain (as shown in Fig. 3 inset) and larger number of continuous domains led to the increase in piezoelectric coefficient.

Piezoelectric coefficient (d_{33}) of the composition $BaZr_{0.025}Ti_{0.975}O_3$ increases from 40.1 to 189.2 pC/N with the increase in sintering temperature from 1,200 to 1,300 °C, as seen in Fig. 8(b). It is observed in the studied sample that the grain size is directly proportional to sintering temperature, reported elsewhere [13]. Hence the increase in piezoelectric coefficient can be due to increase in intrinsic responses and domain wall motion. This also depends upon the type of domains present i.e. the extrinsic component of the piezoelectric coefficient i.e. 180° domain wall motion present in the sample sintered at 1,300 °C [13].

Pyroelectric coefficient as a function of temperature in the studied specimens is shown in Fig. 8(c). The pyroelectric coefficient relates a change in temperature to a change in electrical displacement D ($\mu C/m^2$) as change in temperature causes variation in spontaneous polarization. The pyroelectric coefficient is expressed as [2]

$$p = \frac{P_I}{A(dT/dt)} \tag{2}$$

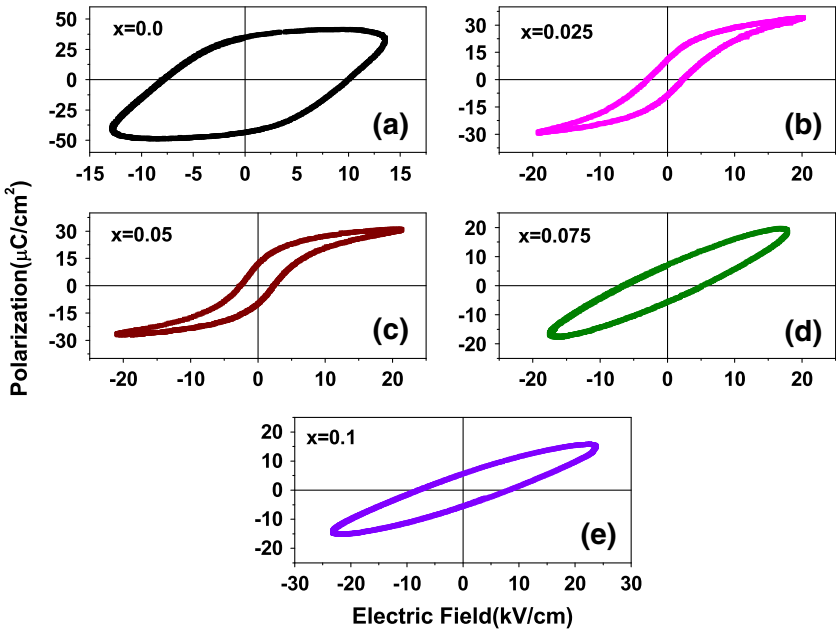

Fig. 7 (**a**) Shows the P–E loop for x = 0.0, (**b**) shows the P–E loop for x = 0.025, (**c**) shows the P–E loop for x = 0.05, (**d**) shows the P–E loop for x = 0.075, (**e**) shows the P–E loop for x = 0.1

where p is pyroelectric coefficient, P_I is pyroelectric current, A is the area of electrodes and dT/dt is the rate of change of temperature.

It is observed that pyroelectric coefficient possesses a peak at a temperature lower than the Curie temperature (T_c). The maximum pyroelectric coefficient increases from 72.23 μC/m^2 °C for $x = 0.0$–5,984.054 μC/m^2 °C for $x = 0.025$ and for $x > 0.05$, the pyroelectric coefficient decreases considerably i.e. 2,719.68 μC/m^2 °C for $x = 0.05$, 59.64 μC/m^2 °C for $x = 0.075$ and 5.96 μC/m^2 °C for $x = 0.1$. It can be explained as follows:

The pyroelectric coefficient is represented as the sum of primary and secondary pyroelectric effect as mentioned by Zhang et al. [34]:

$$p_i^{\sigma} = (\partial P_s/\partial T)_{E,S} + d_{31}(C_{11}\alpha_1 + C_{12}\alpha_1 + C_{13}\alpha_3) + d_{33}(2C_{13}\alpha_1 + C_{33}\alpha_3) \quad (3)$$

where p_i^{σ} is the total pyroelectric coefficient measured at constant stress and $(\partial P/\partial T)_{E,\ S}$ is the primary pyroelectric coefficient and the other terms in the expression represent the secondary pyroelectric effect which is contributed by the piezoelectric effect and the symbols have their usual meanings. Since d_{33} at $x = 0.025$ is higher than the other studied compositions as seen in Fig. 8(a), hence the pyroelectric coefficient of $x = 0.025$ is higher than the other studied specimens. This is attributed to higher secondary pyroelectric effect than the primary pyroelectric coefficient [37].

The pyroelectric figure of merit (R_v) for infrared detector materials with the Zr substitution for the studied samples is shown in Fig. 8(d). The expression used for the calculation of R_v is defined as [3]

$$R_v = p/\varepsilon_r$$

where p is the peak pyroelectric coefficient and ε_r is the permittivity at T_c. It is maximum for $x = 0.025$, i.e. 1.22, which is in accordance with the observed pyroelectric coefficient. The figure of merit increases from 0.0251 to 1.22 for $x = 0.0$ to $x = 0.025$ and thereafter decreases from 0.258 for $x = 0.05$–0.0213 for $x = 0.1$. The variation of figure of merit to Zr content is similar to the variation observed in the relative density curve. The value of piezoelectric coefficient and figure of merit can be attributed to the relative density of the specimens.

The variation in pyroelectric coefficient of $BaZr_{0.025}Ti_{0.975}O_3$ with sintering temperature is shown in Fig. 8(e). The presence of peak in diffuse phase transition at a temperature below T_c has been confirmed in the present work [38]. With the increase in sintering temperature, the value of coefficient increases. This can be due to increase in grain size and density with the substitution of large sized Zr^{+4} ions on the Ti^{+4} sites, i.e., secondary pyroelectric effect. The variation of pyroelectric figure of merit (R_v) of $BaZr_{0.025}Ti_{0.975}O_3$ with the sintering temperature is shown in Fig. 8(f). The figure of merit increases from 0.025 to 1.22 with the increase in sintering temperature from 1,200 to 1,300 °C. The pyroelectric figure of merit has increased considerably in sample sintered at 1,300 °C due to increase in pyroelectric coefficient of this specimen.

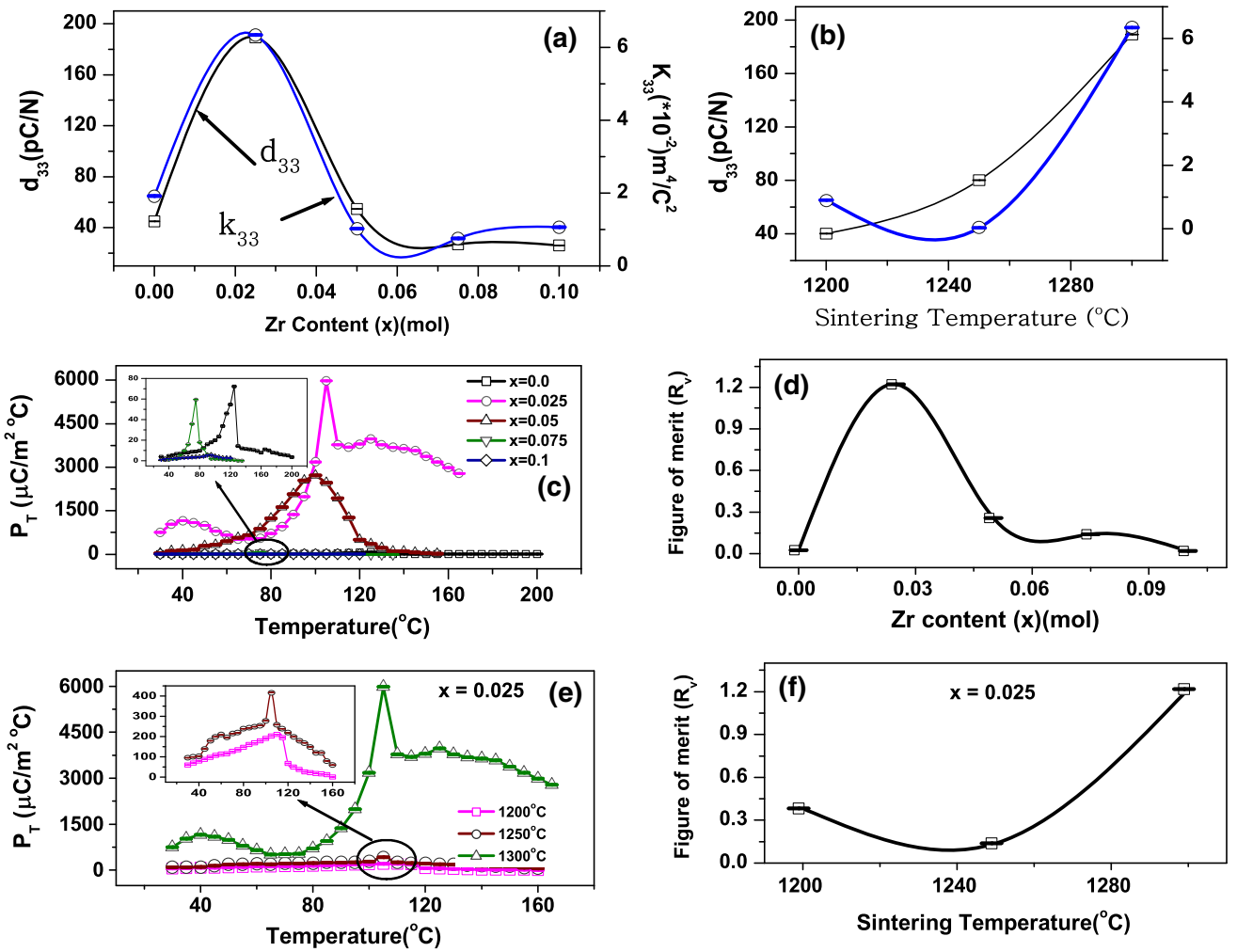

Fig. 8 (**a**) Piezoelectric constants (d_{33}) and quadratic electrostriction coefficient (K_{33}) as a function of Zr content, (**b**) piezoelectric constants (d_{33}) and quadratic electrostriction coefficient (K_{33}) for $x = 0.025$ as a function of sintering temperature, (**c**) pyroelectric coefficient as a function of Zr content, (**d**) figure of merit as a function of Zr content, (**e**) pyroelectric coefficient at $x = 0.025$ as a function of sintering temperature and (**f**) figure of merit at $x = 0.025$ as a function of sintering temperature

4. Conclusions

In present work, the correlation between domain structures and ferroelectric, piezoelectric and pyroelectric properties has been studied. Ferroelectric, piezoelectric and pyroelectric properties seem to be dependent on Zr content, sintering temperature and grain size. It is observed that specimen $BaZr_{0.025}Ti_{0.975}O_3$ sintered at 1,300 °C possesses 180° type domains as seen in micrographs and higher piezoelectric and pyroelectric coefficient i.e. 189.2 pC/N and 5,984.095 μC/m^2 °C respectively, than the other studied specimens. Hence these properties seem to be some intrinsic and complex function of density and the grain size, along with spontaneous polarization and breakdown strength.

References

[1] S B Lang *Sourcebook of Pyroelectricity* (New York: Gordon and Breach) (1974)
[2] A Batagiannis, M Wiibbenhorst, J Hulliger *Curr. Opin. Solid State Mater. Sci.* **14** 107 (2010)
[3] K Uchino *Ferroelectric Devices* (New York: Marcel Dekker Inc.) (1960)
[4] A Govindan, A Sharma, A K Pandey and S K Gaur *Indian J. Phys.* **85** 1829 (2011)
[5] T Chen, H L Wang, T Zhang, J F Zhou, J W Zhang, Y H Liu and G C Wang *Indian J. Phys.* **87** 629 (2013)
[6] B N Dash, P Dash, H Rath, P Mallick, R Biswal, P K Kulriya and N C Mishra *Indian J. Phys.* **84** 1315 (2010)
[7] N C Pop and O F Căl̨un *Indian J. Phys.* **86** 283 (2012)
[8] T Chen, T Zhang, J F Zhou, J W Zhang, Y H Liu and G C Wang *Indian J. Phys.* **86** 443 (2012)
[9] Z Yu, C Ang, R Guo, and A S Bhalla *Mater. Lett.* **61** 326 (2007)

[10] K K Deb, M D Hill and J F Kelly *J. Mater. Res.* **7** 3296 (1992)
[11] P Zheng, J L Zhang, S F Shao, Y Q Tan, and C L Wang *Appl. Phys. Lett.* **94** 3 (2009)
[12] E M Sabolsky, L Maldonado, M M Seabaugh, and S L Swartz *J. Electroceram.* **25** 77 (2010)
[13] P A Jha and A K Jha *J. Alloys Comp.* **513** 580 (2012)
[14] C B Roundy and R L Byer *J. Appl. Phys.* **44** 929 (1973)
[15] S Devi and A K Jha *Physica B* **404** 4290 (2009)
[16] P A Jha and A K Jha *J. Mater. Sci. Mater. Electron* **24** 1511 (2013)
[17] W Cai, C Fu, J Gao and H Chen *J Alloys Comp.* **480** 870 (2009)
[18] K Huang *Statistical Mechanics* (New York: Wiley) (1987)
[19] S W Zhang, H Zhang, B P Zhang and G Zhao *J Euro. Ceram. Soc.* **29** 3235 (2009)
[20] D Hennings, A Schnell and G Simon *J. Am. Ceramic Soc.* **65** 539 (1982)
[21] S B Reddy, K P Rao and M S R Rao *Appl. Phys. Lett*. **91** 022917 (2007)
[22] D C Sinclair and A R West *J. Appl. Phys.* **66** 3850 (1989)
[23] D C Sinclair, T B Adams, F D Morrison and A R West, *Appl. Phys. Lett.* **80** 2153 (2002)
[24] P Ganguly and A K Jha *J. Alloys Comp.* **495** 7 (2010)
[25] F Moura, A Z Simoes, B D Stojanovic, M A Zaghete, E Longo and J A Varela *J. Alloys Comp.* **462** 129 (2008)
[26] N Nanakorn, P Jalupoom, N Vaneesorn and A Thanaboonsombut *Ceram. Int.* **34** 779 (2008)
[27] E Antonelli, R S Silva and A C Hernandes *Ferroelectrics* **334** 75 (2006)
[28] C Hongwei, Y Chuanren, Z Jihua, W Bo and J Hong *App. Sur. Sci.* **255** 4585 (2009)
[29] S Devi and A K Jha *Indian J. Phys*. **86** 279 (2012)
[30] A K Jha and R G Mendiratta *Indian J. Phys*. **68** 491 (1994)
[31] Sugandha and A K Jha *Indian J. Phys.* **87** 325 (2013)
[32] A V Bune, C Zhu, S Ducharme, L M Blinov and V M Fridkin *J. Appl. Phys*. **85** 7869 (1999)
[33] Y Chang, Z Yang and L Wei *J. Am. Ceram. Soc.* **90** 1656 (2007)
[34] K Ramam and M Lopez *J. Mater. Sci. Mater. Electron.* **19** 1140 (2008)
[35] F Xu, S T McKinstry, W Ren, B Xu, Z L Xie and K J Hemker *J. Appl. Phys.* **89** 1336 (2001)
[36] S Tsurekawa, K Ibaraki, K Kawahara and T Watanabe *Scrip. Mater.* **56** 577 (2007)
[37] J Zhang, B I Lee, R W Schwartz and Z Ding *J. Appl. Phys*. **85** 8343 (1999)
[38] E S Gomez, R G Ballesteros and V C Rivas *Mater. Char.* **50** 349 (2003)

J Inf Process Syst
http://dx.doi.org/10.3745/JIPS.04.0013

ISSN 1976-913X (Print)
ISSN 2092-805X (Electronic)

Prediction & Assessment of Change Prone Classes Using Statistical & Machine Learning Techniques

Ruchika Malhotra* and Ravi Jangra*

Abstract—Software today has become an inseparable part of our life. In order to achieve the ever demanding needs of customers, it has to rapidly evolve and include a number of changes. In this paper, our aim is to study the relationship of object oriented metrics with change proneness attribute of a class. Prediction models based on this study can help us in identifying change prone classes of a software. We can then focus our efforts on these change prone classes during testing to yield a better quality software. Previously, researchers have used statistical methods for predicting change prone classes. But machine learning methods are rarely used for identification of change prone classes. In our study, we evaluate and compare the performances of ten machine learning methods with the statistical method. This evaluation is based on two open source software systems developed in Java language. We also validated the developed prediction models using other software data set in the same domain (3D modelling). The performance of the predicted models was evaluated using receiver operating characteristic analysis. The results indicate that the machine learning methods are at par with the statistical method for prediction of change prone classes. Another analysis showed that the models constructed for a software can also be used to predict change prone nature of classes of another software in the same domain. This study would help developers in performing effective regression testing at low cost and effort. It will also help the developers to design an effective model that results in less change prone classes, hence better maintenance.

Keywords—Change Proneness, Empirical Validation, Machine Learning Techniques, Software Quality

1. INTRODUCTION

The software industry has grown considerably faster than any other industry. Software is evolving with time to incorporate newer demands or to amend any present defects. The cycle of change is becoming shorter as technology progresses. The effort required from development to testing has increased manifold with this time crunch. Resources, such as time, cost, and effort, are limited in the software industry while working to develop and maintain a software. A lot of research has been done to study the relationship between object-oriented (OO) metrics and various quality attributes of a software like fault proneness and maintainability [1-7]. The prediction of these software attributes helps in identifying the weak classes of software. Thus, we can effectively plan a project's constraint resources by assigning appropriate resources to the

Manuscript received November 21, 2013; first revision May 29, 2014; second revision September 11, 2014; accepted October 28, 2014.
Corresponding Author: Ruchika Malhotra (ruchikamalhotra2004 @yahoo.com)
* Department of Software Engineering, Delhi Technological University, New Delhi, India (ruchikamalhotra2004 @yahoo.com, ravi_jangra25@yahoo.co.in)

Copyright ⓒ 2015 KIPS

weak classes of software, so that these classes are better maintained and tested.

Maintenance accounts for about 40%–70% of the total cost of the software. Thus, it is critical to evaluate the probability of change in a particular part of the software (change proneness). The prediction of change prone classes can help in optimizing the maintenance and testing phases of a software project. Change prone classes must be thoroughly tested and tracked as the software evolves. This would lead to better quality software with less defects and changes. It would also lead to the effective and economic utilization of resources by focusing resources on these classes. The identification of change prone classes in the early phases of the software development life cycle also aids in the drastic reduction of maintenance costs. This is because the sooner an error is detected in a product, the fewer amount of resources there are that are consumed to correct that error. Otherwise, the cost to correct an error increases exponentially in each undetected phase of the software's life cycle. Thus, the development of models that predict change prone classes aids software developers in delivering a better quality product at optimum costs, as minimum changes and errors are propagated to the later stages of software development.

In order to develop change prediction models, researchers need to assess the effectiveness of a number of methods. These methods could be traditional statistical methods or machine learning methods. It is important to explore a number of methods as different methods may give varied results on different data sets. Thus, the search for a method that develops an effective model on a number of data sets continues. Apart from using different methods, it is crucial to evaluate whether a model that has been developed using the training data from a specific data set can provide good prediction results for another data set. This type of procedure is known as inter project validation. In order to develop inter-project models, we need to train the model on a specific data set and provide a different data set for validating the model. The development of an inter project model is useful, due to the fact that it saves a lot of effort. The training data for each specific data set may not be available and may be scarce in nature. As such, reusing the training data for another software data set saves a lot of time, as well as effort.

The aim of this study is to develop effective change prediction models that would help in ascertaining the change prone classes in a software. The various objectives of the study are as follows:

1) To perform a comprehensive study to investigate the relationship between OO metrics and the change proneness of classes.
2) To analyze and assess the capability of various machine learning and statistical methods for developing change prediction models.
3) To evaluate the effectiveness of inter-project models and to determine if they are practical and useful. The study determines whether a model trained on a specific software data set can be used for predicting the change prone classes of another data set.

In order to explore the relationship between various OO metrics and change prone classes, we developed change prediction models using the two open source software data sets of Art-of-Illusion (AOI) and Sweet-Home-3D, which were developed in the Java language. Two versions of each software system was taken and analyzed for changes. The changes were analyzed in binary form. If any line was added, deleted, or modified from among the two versions it was then marked as a change. The OO metrics were calculated for classes that are common to both versions of the software and were combined with change statistics that were calculated beforehand, to serve as data points for further analysis. Various machine learning methods and the logistic regression method (a statistical method) were analyzed for their performance in

predicting the change prone classes of a software. The results show that the machine learning methods perform well in predicting change prone classes and that they are on par with the statistical methods. We also performed a statistical test (t-test) to test the hypothesis of whether various methods are statistically different from each other for developing change prediction models.

It is very intuitive for researchers to validate the results from the same data set from which it was derived from. Hence, for validation purposes we took two versions of open source software (AOI and Sweet-Home-3D), which were written in the Java language. However, we also used the Sweet-Home-3D software system data set as a test set for the inter-project validation of the change proneness prediction model, which was developed using training data from AOI software. The performance of various models was assessed using receiver operating characteristic (ROC) analysis. The results of this study are phenomenal and helpful for allowing testers and developers to effectively utilize their resources during the maintenance and testing phases.

This paper is organized as follows: Section 2 summarizes the related work in this field. Section 3 summarizes the research methodology used in the study, along with the different variables of the study, research hypothesis, and data collection procedure. Section 4 describes the experimental framework with a description of all the methods used in the study, along with the performance measures and model building techniques. Section 5 gives the results of the study and Section 6 presents the threats to validity in this work. Section 7 provides how the work presented in this study can be applied and the conclusion is given in Section 8.

2. RELATED WORK

Software keeps on evolving with time, which leads to changes in the functionality of the system or to the removal of defects that were previously present in it. Prediction models for identifying change prone classes in the software can help to resolve these issues with ease. Various models have been proposed in this field using machine learning techniques and statistical techniques. Han et al. [8] used the behavioral dependency measurement (BDM), which is a method used for rating classes according to the probability of change, in order to predict change proneness in UML 2.0 models. BDM was found to be an effective indicator of change proneness.

Ajrnal Chaumum et al. [9] carried out a study on the telecommunication system to analyze the impact of a change. They defined a change impact model and mapped it to C++ language to study the consequences of changes made to the classes of a system. Their result showed that the design of a system defines the system's reaction to incoming changes, and that well-chosen OO metrics can function as indicators of changeability.

When we add or modify a class it changes the OO design of the system. Tsantalis et al. [10] analyzed this effect on change proneness in their work. Their work categorizes three axes, namely change inheritance, reference, and dependency. Probabilities were extracted from two open source multi-version software projects (JFlex and JMol) for studying the stability of design over successive versions of the software project and to identify a level beyond which the remodeling of a design cannot be pursued. They performed statistical analysis on the projects. The results of their analysis revealed an improved correlation between extracted probabilities and actual changes in each class, in comparison to the prediction model that relies upon past data.

Sharafat and Tavildari [11] used a reverse engineering technique to collect code metrics for various versions of a software project (JFlex). They proposed a probabilistic model that predicts the probability of a change in each class. This approach is based upon the change history and source code of the class.

Zhou et al. [12] found the effect of size on the associations between OO metrics and change proneness of a class. They considered the following three size metrics: SLOC, which is available only after the implementation stage has been completed; NMIMP (the number of methods implemented in a class); and NumPara (the sum of the parameters of these methods), which is available earlier during the high level design stage. They concluded that the confounding effect of size on the relationship between the metrics and change proneness exists and thus, should be removed to avoid misleading results. Another study by Lu et al. [1] has investigated the relationship between OO metrics and change proneness. The study considered a large number of OO metrics (62 metrics) and the empirical validation was conducted using a large number of systems (102 systems) so that they could generalize their results. However, both the studies by Zhou et al. [12] and Lu et al. [1] used statistical methods for developing change prediction models.

Our previous work [13] also established a relationship between OO metrics and change proneness. The study developed change prediction models using various machine learning (AdaBoost, LogitBoost, Naïve Bayes, Bayes Net, and J48) and statistical (logistic regression) methods. However, the dataset used is in the previous study is different than in this study. Frinika, which is a complete music workstation, was the type of dataset used in the previous study. Moreover, we only used a single dataset in our previous work. Whereas, in our present work, we have collected the changes of two completely different, open source software data sets (AOI and Sweet-Home-3D). In this work, we also performed inter-project validation. In other words, we have used one project for training the model and the other project for testing the model. This type of cross validation was also not done in our previous work.

The study is different from existent previous work as it analyzes and evaluates ten different machine learning and statistical methods for developing change prediction models. Even though certain researchers have developed change prediction models, these models only assess the capability of the widely used statistical method (logistic regression) and very few machine learning methods. Moreover, we performed a statistical test (t-test) in our study to evaluate whether or not the pairwise comparison between the capabilities of different methods is statistically significant. This is important for providing definite conclusions about the capabilities of different methods. This study also explores the applicability of inter-project validation using machine learning methods. Inter-project validation saves a lot of effort and time as the training data of a project can be reused to predict the change prone classes of a different software project. Such models could be effectively used when the project has constraint resources and when the training data of a project is too expensive to collect and may not be easily available for developing effective models. Thus, this study has a significant impact on both academia and the software industry as it explores a variety of methods for change prediction and guides academia and the software industry in choosing an effective method. Moreover, the study also advocates the use of inter-project validation for change prediction, which is a novel technique for developing models in the field of change prediction.

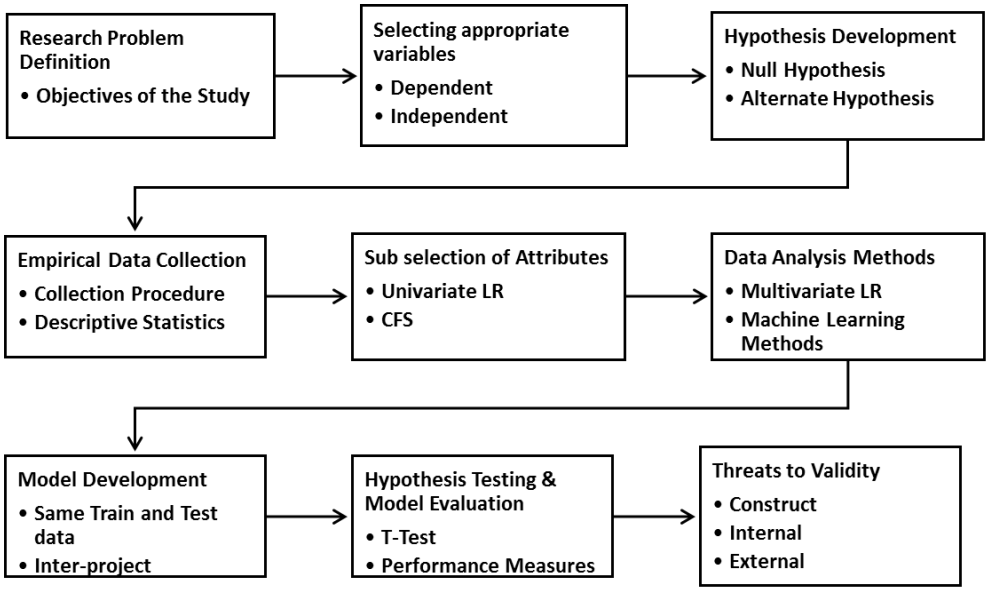

Fig. 1. Basic steps followed.

3. RESEARCH METHODOLOGY

We will briefly explain the basic methodology and describe each step in detail in the subsequent sections. The methodology is explained via a diagram in Fig. 1. The various research steps involved in the study are as listed below.

- We first selected the dependent and the independent variables for this study. Section 3.1 states the variables of this study in detail. These variables were selected in order to explore the relationship between various OO metrics and change prone classes. In the next step, we state the hypothesis that we evaluated (Section 3.2). The hypothesis was developed in order to explore the second objective statistically.
- The data from both of the software data sets was collected from an open source repository named sourceforge.net. A detailed description of the data collection procedure and the details of the data sources are explained in Section 3.3. The descriptive statistics of both of the data sets used in this study are also provided in this section.
- All of the change prediction models were developed using the 13 metrics explained in Table 1. However, in order to develop an effective prediction model, we needed to reduce the dimensions of our input set. We did so by finding a subset of independent variables that were significant in predicting the dependent variable and change prone classes. We used univariate logistic regression (Section 4.1) for reducing the number of input variables, while developing a model using the statistical method and the correlation-based feature selection (CFS) technique for input variables reduction when using the machine learning methods. The CFS technique is explained in Section 4.2.1. The metrics that were selected after these methods were applied are presented in Section 5.1.
- We analyzed the change prediction models that were developed by using both the statistical and the machine learning methods. Brief descriptions of all of the methods that we used in this study are presented in Sections 4.1 and 4.2.

- Next, we constructed of various machine learning and statistical models to predict change proneness for both of the projects. The various models were developed with the aid of a WEKA tool. These models have been developed using ten-fold cross validation technique where the same software is used for training and validation. We also evaluated inter-project models. A brief description of the model development techniques that we used is given in Section 4.3.
- All of the prediction models developed in this study were evaluated on three performance measures: sensitivity, specificity, and area under the ROC curve (AUC). All of which are briefly explained in Section 4.4. In order to validate the hypothesis, we used the t-test; the results of which are presented in Section 5.4.
- We performed inter-project validation using Sweet-Home-3D software as the test set and AOI software as the training set. These results are stated in Section 5.5.
- The various threats to the validity of this study were also evaluated. The three threats to validity of this study are as follows: construct validity, internal validity, and external validity. The threats are presented in Section 6.

3.1 Independent and Dependent Variables

The independent and dependent variables that were used in this study are described below.

3.1.1 Independent Variables

Object-oriented metrics are used to quantify the various aspects of a software process. A single metric is not sufficient for studying all of the aspects related to a software. As such, a combination of a number of metrics needs to be used. The independent variables (i.e., various OO metrics) in this study are summarized in Table 1. The metrics that we included in our study account for various characteristics of a software like its coupling, size, cohesion, inheritance, etc. These metrics were evaluated for all of the classes of a software using the scientific tool of Understand [14,15].

3.1.2 Dependent Variables

Rapid changes in the utility of a software require modifications and upgrades in the code of the software. Change proneness prediction would be a great help for low cost enhancements. This study aims at studying the relationship between OO metrics and the change prone attributes of classes in software. In this context, change is anything that is added, deleted, or modified in terms of SLOC. Thus, the dependent variable in our study is change proneness.

3.2 Research Hypothesis

We aimed to perform a statistical test to evaluate whether or not the differences amongst various methods is statistically significant with the help of t-test. In our hypothesis, we used the LogitBoost method as the baseline method. The hypothesis that we tested is as explained below.

- Null Hypothesis: The change prediction model developed using the LogitBoost technique is similar to the change prediction models that were developed using the other nine methods (Bagging, AdaBoost, LR, MLP, Bayes Net, Naïve Bayes, Random Forest, J48, and NNge).

Table 1. Independent variables

S. No.	Metric	Definition	Source	Dimension
1	Number of base classes (NIB)	Number of immediate base classes	[16]	Inheritance
2	Coupling between objects (CBO)	Number of classes to which a class is coupled and vice versa	[17,18]	Coupling
3	Number of children (NOC)	Number of immediate subclasses of a class	[17,18]	Inheritance
4	Number of attribute (NOA)	Total number of attributes/variables defined in a class	[18,19]	Size
5	Response for a class (RFC)	Number of methods in the class including the methods accessible to an object class due to inheritance	[17,18]	Coupling
6	Number of private methods (NPRM)	Number of local (not inherited) private methods	[16]	Size
7	Number of protected methods (NPROM)	Number of local protected methods	[16]	Size
8	Number of public methods (NPM)	Number of local public methods	[20]	Size
9	Source lines of code (SLOC)	The number of lines that contain source code	[21]	Size
10	Depth of inheritance tree (DIT)	Maximum number of steps from the class node to the root node of the inheritance tree	[22,23]	Inheritance
11	Maximum nesting level (MNL)	Maximum nesting of control constructs	[16]	Inheritance
12	Lack of cohesion amongst methods (LCOM)	For each data field in a class, the percentage of the methods in the class using that data field; the percentages are averaged and then subtracted from 100%	[17,18,23]	Cohesion
13	Weighted methods per class (WMC)	Sum of complexities of all the methods in a class	[17,18]	Size

- Alternate Hypothesis: The change prediction model developed using the LogitBoost technique is better than the change prediction models that were developed using other nine methods (Bagging, AdaBoost, LR, MLP, Bayes Net, Naïve Bayes, Random Forest, J48, and NNge).

3.3 Empirical Data Collection

This section presents a detailed description of our data sources and the data collection method that we used. We examined two open source software, which were written in Java, from the open source repository of sourceforge.net (http://sourceforge.net). The changes in each software were characterized by the changes in the classes of different versions of the corresponding software. Two stable versions of each software were analyzed by extracting the common classes that were present in both versions of the software. We then analyzed the changes in these common classes.

We investigated the AOI software, which is a full-featured 3D modeling, rendering, and animation studio that is available for all operating systems. The two stable versions evaluated for AOI in this study were v2.9.2 and v2.7. Version 2.7 was released on January 27, 2009 and consists of 439 classes and v2.9.2 was released on October 21, 2012 and consists of 458 classes. The test data set for inter-project validation was collected from another open source software named Sweet-Home-3D, which is an interior design application that helps you quickly draw the floor plan of your house, arrange furniture in it, and view the results in 3D. We analyzed two

versions of Sweet-Home-3D, which were v3.6 (349 classes) and v3.7 (350 classes). The details of the software used in the study are shown in Table 2. The analyzed versions of each software, its programming language (P/L used), the total LOC of each software, the total number of common classes extracted in the software (total classes), the number of common classes exhibiting changes (classes exhibiting change), and the number of classes that did not undergo changes (classes without change) of each software are all given in Table 2.

Table 2. Summary of data set used

Name	Version 1	Version 2	P/L used	Total LOC	Total classes	Classes exhibiting change	Classes without change
Art-of-Illusion	2.7	2.9.2	Java	88,444	434	131	303
Sweet-Home-3D	3.6	3.7	Java	74,762	348	15	333

3.3.1 Data Collection Procedure

In this work, we followed the steps given below to collect OO metrics and the changes between multiple versions of a software.

Step I (Metrics collection): The source code of both versions of the software was taken from http://sourceforge.net. The metrics listed in Table 1 were collected with the help of Understand software for the previous version of the software (i.e., AOI v2.7 and Sweet-Home-3D v3.6). The Understand software can provide the metric results for files, methods, etc. However, because we were assessing and predicting changes in only the OO classes, only the metrics for these classes were collected.

Step II (Preprocess versions): In this step, we extracted the common classes in both versions of the software. Changes in the common classes of both of the versions (current and previous) were taken into account. Zhou et al. [12] followed a similar approach in their work.

Step III (Compare classes): The common classes that were received after the preprocessing step were then compared line by line with the help of WinMerge software. Each common class of software was designated a binary status of 'change' or 'no change.' All of the classes were initially given a 'no change' status.

The standards that we followed for determining the status of the class are as follows:

- If there was any added, deleted, or modified line of source code in the current (newer) version of the class with respect to the previous version, it was marked as 'change.'
- The presence of any added, deleted, or modified comment in the class did not affect the status of the class. The status remained as 'no change.'
- The presence of any added or deleted blank line of source code in a class did not affect the status of the class. The status remained as 'no change.'
- If there was any change in the scope of class or class definition, it was marked as 'change.'
- If two lines were present in both versions of the class but were reordered then this did not affect the status of the class. The status remained as 'no change.'
- If there was any deletion or addition of unnecessary blank spaces or lines in a class, it did not affect the status of the class. The status remained as 'no change.'

Thus, all classes with a change in the lines of source code, class scope, or class definition were given a 'change' status and all other classes were given a 'no change' status. The status given to each class was the dependent variable of our study.

Step IV (Collection of data points): The change status from Step III and the metrics from Step I were combined to generate data points. Metric values and the change proneness (status) that corresponded to a class defined a data point. The number of data points in each software was the number of common classes found in both versions of the software. According to Table 2, the number of data points in AOI software is 434. In AOI software, 434 classes are present in both versions and 5 classes are absent in v2.9.2. A total of 131 classes exhibited a change in AOI (i.e., almost 30% of the total classes present in both versions). The data points collected from Sweet-Home-3D had 348 classes common in both the versions and only 1 class was absent in v3.7. Out of these 348 classes, only 15 classes were found changed. These details are summarized in Table 2.

3.3.2 Descriptive Statistics

We analyzed the characteristics of the data sets that were used in this study on the basis of the descriptive statistics of various OO metrics given in Tables 3 and 4 for AOI and Sweet-Home-3D software, respectively. The table shows the minimum, maximum, mean, median, and standard deviation for each of the metrics analyzed in the study. The following observations were derived from these statistics:

1. The size of the class is measured in terms of lines of source code. It ranges from 4 to 3,053 LOC and 4 to 7,959 LOC for the AOI software and Sweet-Home-3D, respectively.
2. The mean value of the NOC metric (AOI, 0.463; Sweet-Home-3D, 0.433) and the DIT metric (AOI, 1.772; Sweet-Home-3D, 1.693) are low in the software systems that shows that number of children are very few and inheritance is least used in the systems under study. Similar results have been shown by others [4,5,24].
3. The LCOM measure (AOI, 100; Sweet-Home-3D, 100) is high for the software systems, which counts the number of classes with no common attribute usage.

Table 3. Descriptive statistics for AOI software

Metric	Min	Max	Mean	Median	SD
NIB	1	3	1.196	1	0.42
CBO	0	98	8.763	5.5	10.114
NOC	0	55	0.463	0	3.082
NOA	0	33	1.523	0	3.931
RFC	0	149	26.394	17.5	27.819
NPRM	0	23	1.581	0	3.05
NPROM	0	10	0.355	0	1.175
NPM	0	90	10.475	7	11.306
SLOC	4	3053	203.788	107	295.249
DIT	1	6	1.772	2	0.79
MNL	0	8	2.06	2	1.581
LCOM	0	100	50.696	59	31.243
WMC	0	554	35.267	19	54.295

All abbreviations are listed in Table 1.

Table 4. Descriptive statistics for Sweet-Home-3D software

Metric	Min	Max	Mean	Median	SD
NIB	1	5	1.473	1	0.667
CBO	0	70	5.994	4	8.319
NOC	0	37	0.433	0	2.547
NOA	0	45	0.908	0	3.542
RFC	1	279	17.662	10	25.119
NPRM	0	111	3.009	0	9.106
NPROM	0	52	0.616	0	3.126
NPM	0	84	7.891	4	11.524
SLOC	4	7959	214.573	65	557.09
DIT	1	4	1.693	2	0.678
MNL	0	9	1.854	1	1.765
LCOM	0	100	49.576	60	34.897
WMC	1	636	27.235	10	56.042

All abbreviations are listed in Table 1.

4. EXPERIMENTAL FRAMEWORK

This section briefly describes all of the methods that we used in the study. It also gives a brief description of the model development techniques and the performance measures used to evaluate various change prediction models.

4.1 Statistical Model

Logistic regression is a method that is commonly used to predict a dependent variable from a set of independent variables (a detailed description is given in [2,25,26]). It is used when the dependent variable is dichotomous or binary. Univariate and multivariate regression, which are two types of logistic regression analysis, were used in this study. Univariate regression finds a connection between the dependent variable and each independent variable and it finds the significance of their association. On the other hand, multivariate regression builds a prediction model for the change proneness of classes. It analyzes the usefulness of metrics when the metrics are used in combination. Logistic regression results in a subset of significant metrics. To find this type of independent metrics subset, two stepwise selection methods are used, which are known as forward selection and backward elimination [26]. Forward selection analyzes one metric at the entry of each step. In backward elimination, all of the metrics in the model are selected at the initial step and are then removed one by one from the model until the stopping criteria is fulfilled. In this study, we used forward selection for statistical modeling.

Multivariate LR can be mathematically formulated as:

$$\text{probab}(X_1, X_2, \ldots\ldots X_n) = \exp^{f(x)} / 1 + \exp^{f(x)} \quad (1)$$

$$f(x) = C_0 + C_1X_1 + C_2X_2 + \ldots\ldots\ldots + C_nX_n \quad (2)$$

where X_i, i = 1,2,….,n are the independent variables. ‘Probab’ is the probability of a class being change prone.

These are the following statistics for each significant metric in this particular model:

1. Odds ratio (OR): OR is calculated for each independent metric using C_is. The formula for the odds ratio is OR = exp(C_i). This is the ratio of probability that the event will occur to the probability of the non-occurrence of an event. The event is our case study of finding a change in the recent version of the class and non-occurrence is the failure to detect any change in the class [2,26].
2. Maximum-likelihood estimation (MLE) and coefficients (C_is): The coefficients of a model are estimated by this statistical method. It is a likelihood function that records the probability of observing the set of dependent variables [25]. MLE finds the coefficients that make the log for the likelihood functions as large as possible. The larger the value, the better the impact of the independent variable on the predicted outcome variable [2,26].
3. The statistical significance (sig): Every coefficient has a significance level described by sig. The greater the value of the statistical significance, the lesser the impact of the independent OO metrics in prediction is. In our study we considered 0.05 to be the threshold for the significance level [2].

4.2 Machine Learning Methods

This section explains the machine learning methods that were used for conducting the analysis in our study. We used the default setting of the WEKA tool [27].

4.2.1 Correlation-Based Feature Selection

Recognizing a representative set of features (i.e., OO metrics [independent variables]) is very important for building a classification model using machine learning methods [28]. A good feature set contains features that are highly correlated with the change in the class but that are not dependent on each other [29]. CFS helps to find the unwanted and noisy features that are correlated with other features. Hall [28] proved in his study that the "classification accuracy using a reduced feature set is equal to or better than the accuracy that is obtained when using a complete feature set." We utilized this method in our study for feature selection. The advantages of feature selection are reduction in dimensionality, improved predictive accuracy, and reduced execution time [28,29].

4.2.2 Random Forest (RF)

This is constructed from a collection of decision trees. Each of the trees is constructed by the random selection of a subset from a training dataset by using replacement. A decision tree is created from the random subset of the available variables. This helps us to create the best partitions for the dataset at each node. The final outcome is the one that is selected by the majority. Each decision tree gives its own vote for the result and the majority vote wins. RF is built using the unknown number of decision trees in which each decision tree has reached its full size. The advantages of RF are as follows: very little preprocessing of data and no need to select a variable to start building a model. RF itself selects the most useful variables [30,31].

4.2.3 AdaBoost

This stands for adaptive boosting. It can be used with other machine learning algorithms to

improve the efficiency and performance of the model. It adapts to the error rates of the individual weak hypothesis. As the name suggests, it boosts the efficiency of a weak learning algorithm and converts it into a strong learning algorithm. The important concept of AdaBoost is that it maintains a distribution of weights over the training set. At the initial step, all of the weights are equal but with each successive iteration the weights of incorrect classified examples are increased so that the weak learning algorithm focuses more on the hard examples in the training set. This concept converts a weak algorithm into a strong one. The advantage of AdaBoost is that it is less susceptible to the over fitting problem than most other learning algorithms are [32].

4.2.4 Bagging

Bootstrap aggregating is a technique that repeatedly samples (with replacement) from a data set according to a uniform probability distribution [33]. It is also called bagging. The size of the bootstrap sample is same as the original data. As sampling is carried out with replacement, some instances may appear more than once in the same training set, while others may not be present at all. Every bootstrap sample contains 63% of the original training data on average. This is because each sample has the probability of $1 – (1 – 1/n)^n$ of being selected in each training set D_i. If n is sufficiently large enough the probability converges to $1 – 1/e = 0.632$. A test instance is assigned a class based on voting after training the k classifiers [7].

4.2.5 Multilayer Perceptron

Multilayer perceptron (MLP) are models that are used for computations that simulate biological neurons. MLP models complex relationships between inputs and outputs and is used to find patterns in data [34]. Multilayer feed-forward networks are those that have one input layer, one output layer, and one or more hidden layers that are used for complex mapping and to extract higher order statistics [34]. Back-propagation is the most commonly used learning paradigm to train multilayer feed-forward networks. It consists of two passes through that run the different layers of network. In the forward pass, a training input data set is applied and a set of outputs is produced as the actual response. In the backward pass, an error signal is generated, which is propagated backward through the network so that the synaptic weights can be readjusted to make the actual response closer to the desired response. The advantages of a neural network are its adaptive nature, non-linearity, parallel architecture, and fault tolerance.

4.2.6 Bayes Net

The Bayesian networks [35] are quite a powerful probabilistic representation and that is why they are often used for classification purposes. Unfortunately, perform poorly when learned in a standard way. Bayes Net is a graphical representation for probabilistic relationships among a set of random variables. Given a finite set X (X_1,X_2,X_3,…,X_n) of discrete random variables where each variable X_i may take values from a finite set, denoted by Val(X_i). A Bayes Net is an annotated directed acyclic graph ‘G’ that encodes a joint probability distribution over X. In Bayes networks, the nodes of the graph correspond to the random variables X_1, X_2,…X_n. The links of the graph correspond to the direct influence from one variable to the other. If there is a directed link from variable X_i to variable X_j, variable X_i will be a parent of variable X_j. Each node is annotated with a conditional probability distribution (CPD) that represents $p(X_i/P_a(X_i))$, where $P_a(X_i)$ denotes the parents of X_i in G. The pair (G, CPD) encodes the joint distribution $p(X_i,…X_n)$ [36].

4.2.7 Naïve Bayes

This is a well-established Bayesian method that was primarily formulated for performing classification tasks. Given its simplicity (i.e., the assumption that the independent variables are statistically independent), Naïve Bayes models are effective classification tools that are easy to use and interpret. Naïve Bayes is particularly appropriate when the dimensionality of the independent space (i.e., number of input variables) is high (a problem known as the curse of dimensionality). For the reasons given above, Naïve Bayes can often outperform other more sophisticated classification methods [37].

4.2.8 J48

J48 is an open implementation of the C4.8 algorithm by the WEKA tool in Java. This decision tree-based algorithm builds the tree in the same way as ID3 along with some improvements. Ros Quinlan developed this algorithm and it is now widely used for classification purposes. In this algorithm, first the base cases are checked and then for each attribute, the normalized information gain is found. The attribute that has the highest information gain is made the root node and this process is done recursively [38]. J48 is an evolved and refined offshoot of ID3 that accounts for unavailable values, continuous attribute value ranges, the pruning of decision trees, rule derivations, and so on. These properties make it more fruitful.

4.2.9 LogitBoost

LogitBoost is one of the boosting techniques that were proposed by Friedman et al. [39]. Boosting helps to change a weak learning algorithm into a strong learning algorithm. This is done by assigning equal weights to all the training examples and then increasing the weights of incorrectly classified examples. In this way, a weak learner is forced to focus on the hard examples. In other words, boosting is the process of applying a classification algorithm to the training instances, reweighting them again and again, and then taking a majority vote on the number of classifiers thus produced. The LogitBoost algorithm takes the AdaBoost algorithm as an additive model and applies the cost function of logistic regression [39]. LogitBoost is suitable for problems involving two class situations.

4.2.10 NNge

NNge is the nearest-neighbor-like algorithm that uses non-nested generalized exemplars (which are hyper-rectangles that can be viewed as ‘if-then’ rules). It is an algorithm that was developed to determine the solution to the famous travelling salesman problem. It classifies a new example ‘a’ by finding the training example (a,b) that is nearest to ‘a’ according to the Euclidean distance. The nearest neighbor algorithm follows the greedy approach to find the shortest distance. It is easy to implement and executes quickly. The disadvantage of the NNge algorithm is that it may not find a feasible route at all, even when one exists.

4.3 Model Development Techniques

This study evaluates the following two types of change prediction models: 1) models developed using ten-fold cross validation where the training, as well as the validation set belongs to the same software and 2) models developed using inter-project validation. We briefly explain the two procedures as laid out below.

1. *Ten-Fold Cross Validation:* This procedure involves the random division of data into ten parts. Each time, nine parts are used as a training set and the left out part is used as a test set [40]. Therefore, we obtain the change proneness of all ten parts. Applying a prediction model to different data sets gives a better view of its accuracy. Hence, we developed models using the ten-fold cross validation procedure. However, while using this procedure we used the data points of the same software while performing model training or during model validation. This study analyzes the ten-fold cross validation results of both the AOI data set and the Sweet-Home-3D data set.
2. *Inter-Project Validation:* A model would be more effective and useful if it can give good results on a validation set that is different (belongs to a different data set) from the training set. This procedure involves using data points of a specific type of software for model training and validating the model on the data points of a different type of software. Thus, inter project validation can assess the possibility of using developed models on different software data sets, which can lead to a lot of saving of resources. In order to perform inter-project validation, this study uses the AOI software as the training data set and the Sweet-Home-3D data set as the test set. A good inter-project model supports the reusability of the already established models on different data sets effectively.

4.4 Performance Measures

We used the measures described below to evaluate the performance of the change proneness prediction models that we developed in our study.

1. *Sensitivity and Specificity:* Sensitivity and specificity represents the correctness of these models. The percentage of classes that have been correctly predicted to be prone to change from among all the actual change prone classes is known as the sensitivity of the model. The opposite of sensitivity (i.e., the percentage of classes correctly predicted to be not change prone) is called the specificity of the model. The values of both the sensitivity and specificity should be high, in order to predict change-prone and non-change prone classes correctly.
2. *ROC Analysis:* Outputs of prediction models are evaluated using ROC analysis. The ROC curve is plotted between 1-specificity on the x-axis and sensitivity on the y-axis, which effectively predicts the quality of predicted models [3,41]. We selected many cutoff points between 0 and 1 while constructing ROC curves and calculated the sensitivity and specificity on those points. The optimal choice of the cutoff point (that maximizes both sensitivity and specificity) can be selected from the curve [3,41]. AUC is a combined measure of sensitivity and specificity [3]. The AUC, which is computed by using ROC analysis, computes the accuracy of a model.

5. ANALYSIS AND RESULTS

This section describes the type of analysis that is performed to find the relationship between OO metrics and the change proneness of classes. We employed a statistical method, which is the multivariate logistic regression, to find the combined effect of OO metrics on the change proneness attribute of a class. Apart from this method, we also employed nine machine learning

methods to analyze the relationship between OO metrics and the change proneness of classes. The methods we used are Bayes Net, Naive Bayes, MLP, Bagging, AdaBoost, LogitBoost, J48, NNge, and RF.

5.1 Attribute Selection Results

In order to construct an effective prediction model, a subset of metrics from Table 1 was selected by applying the CFS technique. The selected subset of metrics for the AOI data set was comprised of CBO, NPRM, SLOC, LCOM, and WMC metrics. CFS is only applied for model development using the machine learning methods. For the statistical method (LR), stepwise forward selection was used, which selected the CBO, RFC, NPRM, and DIT metrics for AOI software. Table 5 shows the results of the metrics that were selected using the CFS or the forward stepwise selection on the AOI data set. The set of metrics selected after the CFS technique was applied to the Sweet-Home-3D data set were the NPRM, SLOC, and WMC metric. The metrics that were selected by using forward stepwise selection on the Sweet-Home-3D data sets was NPRM and NPROM (Table 5).

Table 5. Metrics selected by CFS and stepwise forward selection LR method

Software name	Metric selection method	Metrics selected
Art-of-Illusion	CFS	CBO, NPRM, SLOC, LCOM, WMC
	Forward LR	CBO, RFC, NPRM, DIT
Sweet-Home-3D	CFS	NPRM, SLOC, WMC
	Forward LR	NPRM, NPROM

All abbreviations are listed in Table 1.

5.2 Result Analysis for Art-of-Illusion

This section describes the validation results of the various models that were developed using the AOI software. Table 6 shows the coefficient (B), standard error (SE), statistical significance (sig), and odds ratio (OR) for the metrics included in the multivariate LR prediction model for the AOI data set. Table 7 shows the ten-fold cross validation results on the system that were studied (i.e., AOI). The sensitivity and specificity values for the model developed using the LR method were 63.4% each with a cutoff point of 0.235. The AUC for LR was 0.719, which is much less than the AUC achieved by the model developed using the Bagging method, which is 0.803. The sensitivity and specificity values for the Bagging model are also much higher at 71% and 71.3%, respectively. The cutoff point for Bagging was 0.291. The RF method gives some competitive results with an AUC value of 0.784 and the sensitivity and specificity values of 75.6% and 67%, respectively. The cutoff point for the RF method was 0.25. The Bayes Net and LogitBoost methods also gave good results. Detailed results of the validation for all the change proneness prediction models using AOI software are stated in Table 7.

Table 6. Result of multivariate LR analysis of Art-of-Illusion Software

Metric	B	SE	Sig.	OR
CBO	0.078	0.021	0.000	1.081
RFC	0.024	0.008	0.001	1.025
NPRM	0.242	0.052	0.000	1.273
DIT	-0.878	0.234	0.000	0.416
Constant	-1.044	0.312	0.001	0.352

Table 7. Art-of-Illusion validation results

Method	Specificity	Sensitivity	Cutoff Point	AUC
LR	63.4	63.4	0.235	0.719
Bayes Net	68.0	67.9	0.252	0.765
Naïve Bayes	67.3	66.4	0.012	0.712
MLP	67.0	67.2	0.251	0.730
Bagging	71.3	71.0	0.291	0.803
AdaBoost	67.0	66.4	0.386	0.752
LogitBoost	69.3	68.7	0.298	0.782
NNge	81.8	55.0	0.500	0.684
J48	57.4	66.4	0.245	0.684
RF	67.0	75.6	0.250	0.784

5.3 Result Analysis for Sweet-Home-3D

The results of multivariate LR analysis for the Sweet-Home-3D data set are shown in Table 8. Ten-fold cross validation results for the prediction models of the Sweet-Home-3D, along with the forward LR model, are provided in detail, as shown in Table 9. According to Table 9, Naïve Bayes provides the best prediction results with an AUC value of 0.879 and high specificity (79.6%) and sensitivity (80%) values. Other machine learning models also performed well in comparison to the statistical model. The performances by J48 and NNge were the lowest among

Table 8. Result of multivariate LR analysis of Sweet-Home-3D software

Metric	B	SE	Sig.	OR
NPRM	0.289	0.051	0.000	1.336
NPROM	-27.262	1695.25	0.987	0.000
Constant	-4.394	0.506	0.000	0.012

Table 9. Sweet-Home-3D validation results

Method	Specificity	Sensitivity	Cutoff point	AUC
LR	72.7	73.3	0.018	0.780
Bayes Net	81.7	80.0	0.005	0.819
Naïve Bayes	79.6	80.0	0.011	0.879
MLP	79.6	80.0	0.030	0.846
Bagging	75.7	80.0	0.037	0.796
AdaBoost	77.2	80.0	0.013	0.821
LogitBoost	68.2	73.3	0.013	0.802
NNge	98.2	20.0	0.500	0.591
J48	49.5	33.3	0.044	0.414
RF	89.2	53.3	0.050	0.730

Table 10. t-test to check statistical significance

Method	Art-of-Illusion	Sweet-Home-3D
Bagging	0	0
AdaBoost	+	0
LR	+	0
MLP	+	0
Bayes Net	0	0
Naïve Bayes	+	0
Random Forest	0	0
J48	+	+
NNge	+	+

other models with AUC values at 0.414 and 0.591, respectively. Sensitivity and specificity for J48 and NNge were also low in the case of the Sweet-Home-3D software system. The performance of the Naïve Bayes method was slightly better than the MLP method with a high AUC value (0.846) and a very good sensitivity value (80%).

5.4 Hypothesis Validation

We compared the percentage of correct statistics of one of the machine learning methods (LogitBoost) with the other nine methods. This was done in order to check whether the different methods used in the study were statistically significantly different from each other for developing change prediction models. For this, we used the t-test with a significance level of 0.05. We used the open source tool, WEKA, to perform this test.

The number '0' indicates that this particular method is not statistically different from the baseline method (LogitBoost) at the specified significance level of 0.05. Whereas, the symbol '+' indicates that the method is statistically superior to the baseline method (LogitBoost) at the specified significance level of 0.05. We performed this test for both the AOI and Sweet-Home-3D software. We can observe from Table 10 that for AOI, that Adaboost, LR, MLP, Naïve Bayes, J48, and NNge are statistically better or superior than LogitBoost (rejection of the null hypothesis). Whereas, for Sweet-Home-3D, we can observe that the majority of the methods are statistically the same as the baseline method of LogitBoost (acceptance of the null hypothesis). Thus, overall we can say that the results are either statistically superior or the same as the baseline method and that no method has shown statistically worse performance than the baseline method.

5.5 Inter-Project Validation of the Prediction Model Using Sweet-Home-3D

In order to perform inter project validation, we developed a model using AOI software as the training set and Sweet-Home-3D software as the validation set. Inter-project models were developed using only machine learning methods. The results of the developed models are shown in Table 11. According to the table, the results of all the prediction models are very good. The Bayes Net model outperformed other machine learning models with a maximum AUC value of 0.913. The sensitivity and specificity values for the model developed by using the Bayes Net method were 79.6% and 80%, respectively, with a cutoff 0.664. LogitBoost and Naïve Bayes models also gave competitive results with AUC values of 0.882 and 0.901, respectively. The sensitivity and specificity values were also high for these models. Other prediction models that were developed using machine learning methods for change prone classes also demonstrated high efficiency, as indicated in Table 11.

Table 11. Inter-project validation results with Sweet-Home-3D test set

Method	Specificity	Sensitivity	Cutoff point	AUC
Bayes Net	79.6	80.0	0.664	0.913
Naïve Bayes	83.8	80.0	0.250	0.901
MLP	79.6	80.0	0.355	0.873
Bagging	79.9	80.0	0.419	0.847
AdaBoost	68.8	73.3	0.411	0.844
LogitBoost	80.2	80.0	0.417	0.882
NNge	83.8	80.0	0.500	0.819
J48	93.7	66.7	0.545	0.799
RF	73.6	73.3	0.350	0.814

5.6 Discussion of Results

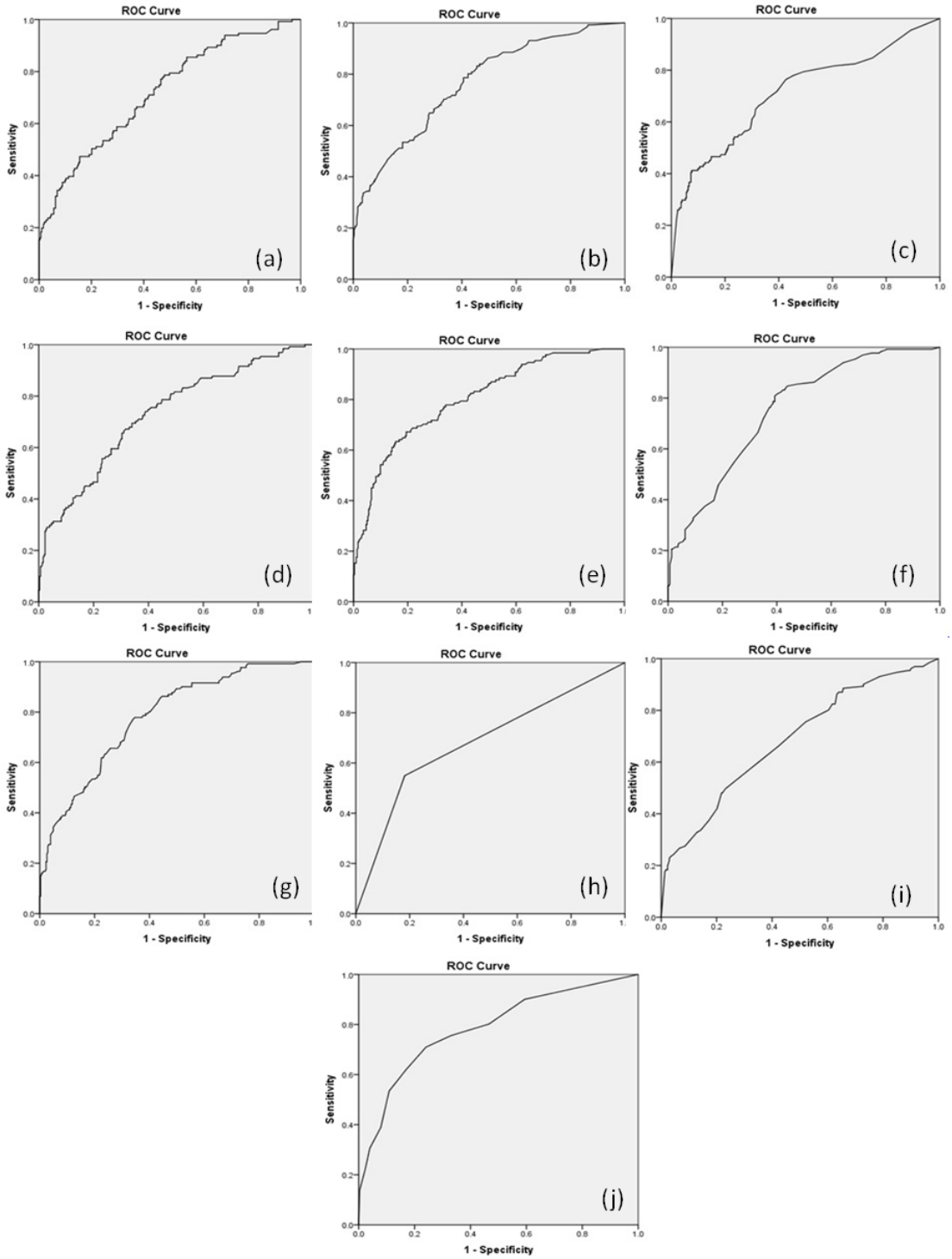

Fig. 2. Validation curves of AOI: (a) Forward LR, (b) Bayes Net, (c) Naïve Bayes, (d) MLP, (e) Bagging, (f) AdaBoost, (g) LogitBoost, (h) NNge, (i) J48, and (j) RF.

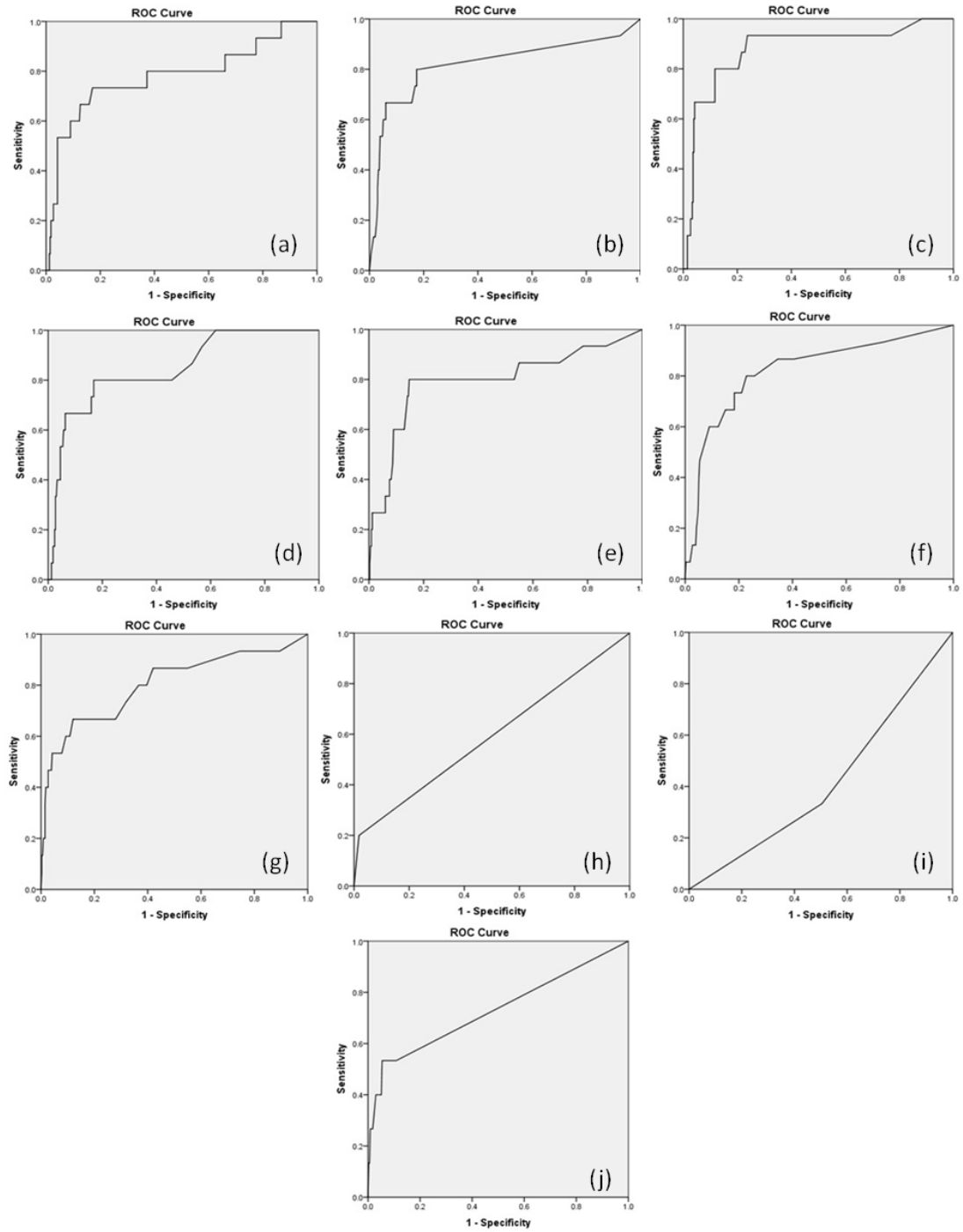

Fig. 3. Validation curves of Sweet-Home-3D: (a) Forward LR, (b) Bayes Net, (c) Naïve Bayes, (d) MLP, (e) Bagging, (f) AdaBoost, (g) LogitBoost, (h) NNge, (i) J48, and (j) RF.

In this section, we compare the performance of the models predicted for both of the projects (AOI and Sweet-Home-3D). Various machine learning and statistical models were predicted and their performance was measured using various performance measures, such as sensitivity, specificity, and area under the ROC curve. As per the definitions of these measures (provided in Section 5), high values of these measures are desired. The higher the values, the better the model

is in terms of accuracy.

The ten-fold cross validation results for the AOI data set suggests Bagging as being the best method from among all of the machine learning and statistical methods with an AUC value of 0.803. However, the validation results for Sweet-Home-3D have shown that the model that was developed using Naïve Bayes as being the best prediction model with high values of AUC (0.879) and sensitivity (80%). Thus, we can say that the validation results vary as the dataset changes and are not alike for different datasets. However, if we have a dataset with similar characteristics, then the results may be similar (i.e., we may get the same machine learning method as being the best one). The other machine learning methods viz. Bayes Net, RF, and LogitBoost also gave comparable performances.

These models can be used for predicting the change proneness of classes. The prediction of change prone classes in the early phases of software development will help us in effectively planning testing resources. Change prone classes should be rigorously tested by allocating more resources to them, as a change prone class requires a greater effort to be made during the maintenance phase. A major source of change in change prone classes could be defects and testing these classes meticulously would decrease the probability of a defect. Thus, the early prediction of such classes reduces our efforts during testing and maintenance phases.

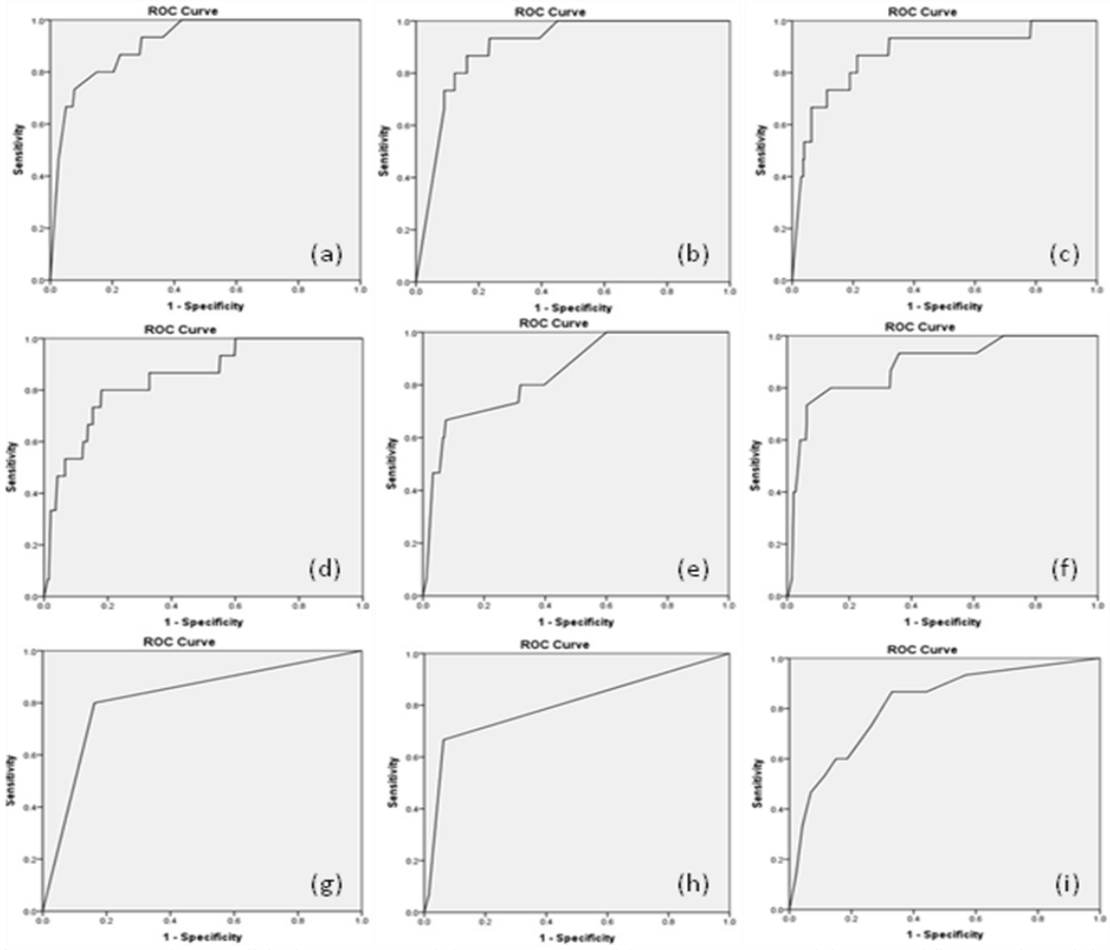

Fig. 4. Inter-project validation curves: (a) Bayes Net, (b) Naïve Bayes, (c) MLP, (d) Bagging, (e) AdaBoost, (d) LogitBoost, (e) NNge, (f) J48, and (g) RF.

Fig. 2 shows the ROC curves of prediction models for AOI, Fig. 3 shows the ROC curves for Sweet-Home-3D, and Fig. 4 shows the ROC curves for inter-project validation. Thus, we can conclude that the results of machine learning methods are competitive and comparable to the statistical method (i.e., LR). Another conclusion from our study is that NPRM, SLOC, and WMC are good indicators of change proneness as they are selected in the reduced feature sets of both data sets after the CFS technique is applied. Another important result concluded from our analysis of inter-project validation models is that we can use already constructed models for predicting the change prone classes of other software from the same domain.

6. THREATS TO VALIDITY

This section discusses the three areas of concern related to this study, which are as follows: construct validity, external validity and internal validity, which are common to all empirical studies.

6.1 Construct Validity

Construct validity refers to the extent to which the dependent and independent variables accurately measure the concept that they are supposed to measure [1]. Corrective, adaptive, and perfective or preventive are different classes of change in software [1,41]. The types of change that a class goes through are not segregated in our study. A similar approach was followed in [1,43]. The metrics included in our study cover concepts like cohesion, coupling, inheritance, etc. These metrics were already validated in previous studies [4,44,45] (i.e., they are accurate measure of the concepts that they represent). The change proneness or dependent variable is calculated manually with the help of WinMerge software. Thus, the threat of collecting an incorrect dependent variable is removed.

6.2 Internal Validity

Zhou et al. [12] stated that "Internal validity is the degree to which a conclusion can be drawn about the causal effect of independent variables on the dependent variables." We empirically determined the relation between independent variables and the change proneness attribute of a class. However, we did not demonstrate the causal relationship of various attributes on the dependent variable. This can only be evaluated by varying a particular measure (like coupling) and keeping the functionality constant [46]. This type of controlled experiment is difficult to carry out in practice and this threat exists in various studies [46]. Our main focus was not to analyze the causal relationship between OO metrics and change proneness.

6.3 External Validity

This refers to the degree of generalization of the results. This can be achieved by analyzing and comparing the results that were achieved on a vast number of data sets [1]. We only used two open source software in our study. Thus, the results cannot be generalized to all software systems. However, previous studies in this area with different projects in different languages have proved the relationship between OO metrics and the change proneness attribute of a class. Furthermore, we have successfully performed the inter-project validation of prediction models

using other software from the same domain (i.e., 3D modeling). The results conclude that these models can be used for predicting the change prone classes of the software systems from the same domain, but we cannot generalize these models for software systems from other domains. We can eliminate this threat by carrying out replicated studies in this area with different data sets belonging to different domains.

7. APPLICATION OF THE WORK

This study has developed various models for predicting the change prone classes during the early phases of the software development life cycle. The prediction of change prone classes would help developers in judiciously allocating the resources and pay focused attention in terms of cost, time and effort on these classes. This would help in delivering better quality software products as effective testing would decrease the number of defects in a software and would lead to more satisfied customers.

Change prediction models were developed using various OO metrics that are available at the design phase. From a suite of 13 OO metrics, the univariate analysis gave CBO and NPRM metrics as significant predictors of change proneness for both of the projects (AOI and Sweet-Home-3D). Using the CFS technique, NPRM, SLOC, and WMC were found to be significant indicators of change proneness. Researchers and practitioners can use these significant predictors in the earlier phases of software development to measure the quality of the systems. Thus, closely monitoring these metrics would give developers an idea of the ideal values of these metrics. Thus, we can alter the design measurements if we find the design to be inappropriate. These design measurements can be used throughout different organizations as quality benchmarks to assess and compare different industrial projects. Furthermore, within this same project, we are able to check the design of the upcoming release and suggest any alternations, if required. This helps in checking the quality of the new versions, which are released on a regular basis. In order to draw stronger conclusions, more replicated studies are required.

8. CONCLUSIONS

The aim of the study was to analyze the relationship between OO metrics (independent variables) and change proneness of a class. In order to explore this relationship, we empirically validated the results of change prediction models on two open source software, AOI and Sweet-Home-3D. The second objective of the study was to analyze, compare and evaluate the performance of logistic regression and machine learning methods in predicting change prone classes of a software. The study evaluates the performances of a number of machine learning and statistical change prediction models developed on the two software data sets of the study using ROC analysis. This study also performed a statistical test (t-test) to statistically compare the models developed using different methods on both the data sets. Another objective of the study was to ascertain whether inter-project change prediction models can be successfully used for predicting the change prone classes of a different software. To achieve this objective, we performed inter-project validation by using the prediction model developed with AOI software as the training set and Sweet-Home-3D software as the test set. Since both the software were

from the same domain, our results would help the industry and academia to analyze whether these prediction models can be used to predict change prone classes for the software data sets belonging to a similar domain. Thus, the contribution of this work can be summarized as follows: First, we performed analysis on both open source software data sets taking change in classes in account for predicting change proneness. Second, apart from statistical method, we applied nine different machine learning methods to construct prediction models for change prone classes and evaluated their performances. Third, we analyze and assess the applicability of inter-project models for change prediction. The key findings and recommendations of the study are summarized as follows:

1. NPRM, SLOC and WMC metrics are significant indicators of change proneness in both the data sets as they were selected after applying the feature subset selection technique, CFS. CBO and NPRM metrics were found significant using univariate LR analysis. Thus, the values of these metrics (NPRM, SLOC, WMC, CBO, and NPRM) should be closely monitored during development and maintenance of a product as they are closely associated with change in a class. Developers can formulate quality benchmarks stating appropriate values for these metrics so that the quality of the software product can be monitored regularly. Corrective actions should be taken if at any point the product is not in accordance with the quality benchmarks.
2. For both the software data sets used in the study, the models developed using the Bagging, RF, Bayes Net, LogitBoost and MLP methods outperformed the model developed using the LR method. These models yielded good AUC values. This concludes that machine learning methods are competitive and comparable with statistical methods for predicting change prone classes in a software. Thus, software developers can use machine learning methods for developing effective change prediction models.
3. The results of validation for 'AIO' project showed the best performance by Naïve Bayes method, whereas the results of validation for 'Sweet-Home-3D' showed the best performance by Bagging method. Thus we conclude that it is not necessary that the results of validation for different projects will be similar. Researchers and developers should take into account the characteristics of the data sets as well as the properties of the methods before choosing them to develop change prediction model for a particular data set.
4. The AUC of machine learning based prediction models range from 0.799 to 0.913 when we performed inter-project validation on Sweet-Home-3D data set. Hence, inter-project validation using Sweet-Home-3D as test data set, concludes that prediction models can successfully predict the change prone classes for other software data set from the same domain. Inter-project models save a lot of effort and time as we do not need to collect training data specific to a project. Such models are useful when training data specific to a project may not be previously available or is very expensive to compute.
5. The results of this study (effective change prediction models) can be used by researchers and practitioners in the early phases of software development life cycle to reduce the maintenance effort and costs. It can also be used for effectively planning testing resources. This is possible as change prone classes need more attention and resources while maintenance and testing. These classes are changed due to existing errors or a new requirement. Constantly monitoring and focusing resources on these classes would

help in identifying probable errors and changes in the early phases of software development. Thus, developers can correct errors and may perform corrective design measures to reduce the changes and errors in the later stages of software development. Thus, there is a reduction in maintenance costs and effective allocation of test resources.

This work is limited to a medium-sized object oriented open source project. So, it may not work well in case of large software systems. We plan to replicate our study to predict models based on other highly popular machine learning methods like ant colony optimization and particle swarm optimization. We also plan to study the economical benefit of change proneness models.

REFERENCES

[1] H. Lu, Y. Zhou, B. Xu, H. Leung, and L. Chen, "The ability of object-oriented metrics to predict change-proneness: a meta-analysis," *Empirical Software Engineering*, vol. 17, no. 3, pp. 200-242, 2012.

[2] K. K. Aggarwal, Y. Singh, A. Kaur, and R. Malhotra, "Empirical analysis for investigating the effect of object-oriented metrics on fault proneness: a replicated case study," *Software Process: Improvement and Practice*, vol. 14, no. 1, pp. 39-62, 2009.

[3] Y. Singh, A. Kaur, and R. Malhotra, "Empirical validation of object-oriented metrics for predicting fault proneness," *Software Quality Journal*, vol. 18, no. 1, pp. 3-35, 2010.

[4] L. C. Briand, J. Wust, J. W. Daly, and D. Victor Porter, "Exploring the relationships between design measures and software quality in object-oriented systems," *Journal of Systems and Software*, vol. 51, no. 3, pp. 245-273, 2000.

[5] M. Cartwright and M. Shepperd, "An empirical investigation of an object-oriented software system," *IEEE Transactions on Software Engineering*, vol. 26, no. 8, pp. 786-796, 2000.

[6] M. English, C. Exton, I. Rigon, and B. Clearyp, "Fault detection and prediction in an open source software project," in *Proceedings of the 5th International Conference on Predictor Models in Software Engineering (PROMISE2009)*, Vancouver, Canada, 2009.

[7] R. Malhotra and A. Jain, "Software effort prediction using statistical and machine learning method," *International Journal of Advanced Computer Science and Applications*, vol. 2, no.1, pp. 145-152, 2011.

[8] A. Han, S. Jeon, D. Bae, and J. Hong, "Behavioral dependency measurement for change proneness prediction in UML 2.0 design models," in *Proceedings of the 32nd Annual IEEE International Conference on Computer Software and Applications (COMPSAC2008)*, Turku, Finland, 2008, pp. 76-83.

[9] M. Ajrnal Chaumum, H. Kabaili, R. K. Keller, and F. Lustman, "A change impact model for changeability assessment in object oriented software systems," in *Proceedings of the 3rd European Conference on Software Maintenance and Reengineering*, Amsterdam, 1999, pp. 130-138.

[10] N. Tsantalis, A. Chatzigeorgiou, and G. Stephanides, "Predicting the probability of change in object oriented systems," *IEEE Transactions on Software Engineering*, vol. 31, no. 7, pp. 601-614, 2005.

[11] A. R. Sharafat and L. Tavildari, "A probabilistic approach to predict change in object-oriented software systems," in *Proceedings of the 11th European Conference on Software Maintenance and Reengineering (CSMR2007)*, Amsterdam, 2007, pp. 27-38.

[12] Y. Zhou, H. Leung, and B. Xu, "Examining the potentially confounding effect of class size on the associations between object-oriented metrics and change-proneness," *IEEE Transactions on Software Engineering*, vol. 35, no. 5, pp. 607-623, 2009.

[13] L. Malhotra and A. J. Bansal, "Prediction of change prone classes using machine learning and statistical techniques," in *Advanced Research and Trends in New Technologies, Software, Human-Computer Interaction and Communicability*. Hershey, PA: IGI Global, 2014, pp. 193-202.

[14] Understand your code official website [Online]. Available: http://www.scitools.com.

[15] Understand your code – About SciTools [Online]. Available: http://www.scitools.com/about/index.php.
[16] Understand your code - Metrics [Online]. Available: https://scitools.com/feature/metrics/.
[17] S. R. Chidamber and C. F. Kemerer, "A metrics suite for object oriented design," *IEEE Transactions on Software Engineering*, vol. 20, no. 6, pp. 476-493, 1994.
[18] K. K. Aggarwal, Y. Singh, A. Kaur, and R. Malhotra, "Empirical study of object-oriented metrics," *Journal of Object Technology*, vol. 5, no. 8, pp. 149-173, 2006.
[19] B. Henderson-Sellers, *Object-Oriented Metrics: Measures of Complexity*. Englewood Cliffs, NJ: Prentice Hall, 1996.
[20] M. Lorenz and J. Kidd, *Object-oriented Software Metrics: A Practical Guide*. Englewood Cliffs, NJ: Prentice Hall, 1994.
[21] Understand your code - County metrics [Online]. Available: https://scitools.com/support/metrics_list.
[22] Understand your code - Complexity metrics [Online]. Available: https://scitools.com/support/metrics_ list.
[23] Understand your code - Object oriented metrics [Online]. Available: https://scitools.com/support/ metrics_list.
[24] S. R. Chidamber, D. P. Darcy, and C. F. Kemerer, "Managerial use of metrics for object-oriented software: an exploratory analysis," *IEEE Transactions on Software Engineering*, vol. 24, no. 8, pp. 629-639, 1998.
[25] V. R. Basili, L. C. Briand and W. L. Melo, "A validation of object-oriented design metrics as quality indicators," *IEEE Transactions on Software Engineering*, vol. 22, no. 10, pp. 751-761, 1996.
[26] D. W. Hosmer and S. Lemeshow, *Applied Logistic Regression*. New York, NY: Wiley, 1989.
[27] Weka 3: Data Mining Software in Java [Online]. Available: http://www.cs.waikato.ac.nz/ml/weka/.
[28] M. A. Hall, "Correlation based feature selection for discrete and numeric class machine learning," in *Proceedings of the 17th International Conference on Machine Learning (ICML2000)*, Stanford, CA, 2000, pp. 359-366.
[29] K. Michalak and H. Kwasnicka, "Correlation based feature selection strategy in neural classification," in *Proceedings of the 6th International Conference on Intelligent Systems Design and Applications (ISDA2006)*, Jinan, China, 2006, pp. 741-746.
[30] I. H. Witten, E. Frank, and M. A. Hall, *Data Mining: Practical Machine Learning Tools and Techniques*, 3rd ed. Burlington, MA: Morgan Kaufmann, 2011.
[31] Y. Freund, R. E. Schapire, and N. Abe, "A short introduction to boosting," *Journal of Japanese Society for Artificial Intelligence*, vol. 14, no. 5, pp. 771-780, 1999.
[32] AdaBoost [Online]: Available: http://en.wikipedia.org/wiki/AdaBoost.
[33] L. Breiman, "Bagging predictors," *Machine Learning*, vol. 24, no. 2, pp. 123-140, 1996.
[34] S. Haykin, *Neural Networks: A Comprehensive Foundation*, 2nd ed. Delhi: Pearson education, 1999.
[35] J. Pearl, Bayesian Networks, 1988 [Online]: Available: http://ftp.cs.ucla.edu/pub/stat_ser/R246.pdf.
[36] Bayes Nets [Online]. Available: http://www.bayesnets.com/.
[37] K. P. Murphy, "Naive Bayes classifiers," *Technical Report*, University of British Columbia, Canada, 2006.
[38] C4.5 algorithm [Online]. Available: http://en.wikipedia.org/wiki/C4.5_algorithm.
[39] J. Friedman, T. Hastie, and R. Tibshirani, "Additive logistic regression: a statistical view of boosting," *The Annals of Statistics*, vol. 28, no. 2, pp. 337-407, 2000.
[40] M. Stone, "Cross-validatory choice and assessment of statistical predictions," *Journal of the Royal Statistical Society Series B: Methodological*, vol. 36, no 2, pp. 111-147, 1974.
[41] K. El-Emam, S. Benlarbi, N. Goel, and SN. Rai, "A validation of object-oriented metrics," *Technical Report ERB-1063*, National Research Council of Canada, 1999.
[42] K. K. Aggarwal and Y. Singh, *Software Engineering*, 2nd ed. New Delhi: New Age International Publishers, 2007.
[43] A. G. Koru and J. Tian, "Comparing high-change modules and modules with the highest measurement values in two large-scale open-source products," *IEEE Transactions on Software Engineering*, vol. 31, no. 8, pp. 625-642, 2005.
[44] L. C. Briand, J. Daly, and J. Wust, "A unified framework for cohesion measurement in object-oriented

systems," *Empirical Software Engineering*, vol. 3, no. 1, pp. 65-117, 1998.
[45] L. C. Briand, J. Daly, and J. Wust, "A unified framework for coupling measurement in object-oriented systems," *IEEE Transactions on Software Engineering*, vol. 25, no. 1, pp. 91-121, 1999.
[46] L. C. Briand, J. Wust, and H. Lounis, "Replicated case studies for investigating quality factors in object-oriented designs," *Empirical Software Engineering*, vol. 6, no. 1, pp. 11-58, 2001.

Ruchika Malhotra

She is an Assistant Professor at the Department of Software Engineering, Delhi Technological University (formerly Delhi College of Engineering), Delhi, India. She has been awarded the prestigious UGC Raman postdoctoral fellowship by the Indian government and is currently pursuing postdoctoral research from Department of Computer and Information Science, Purdue University, Indianapolis, USA. She was an assistant professor at the University School of Information Technology, Guru Gobind Singh Indraprastha University, Delhi, India. She has received her master's and doctorate degree in software engineering from the University School of Information Technology, Guru Gobind Singh Indraprastha University, Delhi, India. She has received IBM Faculty Award 2013. She is executive editor of Software Engineering: An International Journal. She is co-author of a book on *Object Oriented Software Engineering* published by PHI learning. Her research interests are in software testing, improving software quality and the definition and validation of software metrics. She has published more than 80 publications in international journals and conferences.

Ravi Jangra

He is pursuing his masters in software engineering from Delhi Technological University (formerly called Delhi College of Engineering), Delhi, India. He completed his graduation from YMCA Institute of Engineering, Faridabad, India. His research interests are software quality, software metrics and statistical and machine learning models.

This article was downloaded by: [Delhi Technological University]
On: 03 February 2015, At: 20:00
Publisher: Taylor & Francis
Informa Ltd Registered in England and Wales Registered Number: 1072954 Registered office: Mortimer House, 37-41 Mortimer Street, London W1T 3JH, UK

Click for updates

Journal of Industrial and Production Engineering
Publication details, including instructions for authors and subscription information:
http://www.tandfonline.com/loi/tjci21

Selecting competitive supply chain using fuzzy AHP and extent analysis

Rajesh Kumar Singh[a] & Milind Kumar Sharma[b]

[a] Department of Mechanical and Production Engineering, Delhi Technological University, Shahbad Daulatpur, Main Bawana Road, New Delhi, Delhi 110042, India

[b] Department of Production & Industrial Engineering, M.B.M. Engineering College, Faculty of Engineering & Architecture, Engineering College, Jai Narain Vyas University, Jodhpur, Residency Road, Jodhpur 342011, India

Published online: 30 Jan 2015.

To cite this article: Rajesh Kumar Singh & Milind Kumar Sharma (2015): Selecting competitive supply chain using fuzzy AHP and extent analysis, Journal of Industrial and Production Engineering, DOI: 10.1080/21681015.2014.999723

To link to this article: http://dx.doi.org/10.1080/21681015.2014.999723

PLEASE SCROLL DOWN FOR ARTICLE

Taylor & Francis makes every effort to ensure the accuracy of all the information (the "Content") contained in the publications on our platform. However, Taylor & Francis, our agents, and our licensors make no representations or warranties whatsoever as to the accuracy, completeness, or suitability for any purpose of the Content. Any opinions and views expressed in this publication are the opinions and views of the authors, and are not the views of or endorsed by Taylor & Francis. The accuracy of the Content should not be relied upon and should be independently verified with primary sources of information. Taylor and Francis shall not be liable for any losses, actions, claims, proceedings, demands, costs, expenses, damages, and other liabilities whatsoever or howsoever caused arising directly or indirectly in connection with, in relation to or arising out of the use of the Content.

This article may be used for research, teaching, and private study purposes. Any substantial or systematic reproduction, redistribution, reselling, loan, sub-licensing, systematic supply, or distribution in any form to anyone is expressly forbidden. Terms & Conditions of access and use can be found at http://www.tandfonline.com/page/terms-and-conditions

Journal of Industrial and Production Engineering, 2015
http://dx.doi.org/10.1080/21681015.2014.999723

Taylor & Francis
Taylor & Francis Group

Selecting competitive supply chain using fuzzy AHP and extent analysis

Rajesh Kumar Singh[a] and Milind Kumar Sharma[b]*

[a]*Department of Mechanical and Production Engineering, Delhi Technological University, Shahbad Daulatpur, Main Bawana Road, New Delhi, Delhi 110042, India;* [b]*Department of Production & Industrial Engineering, M.B.M. Engineering College, Faculty of Engineering & Architecture, Engineering College, Jai Narain Vyas University, Jodhpur, Residency Road, Jodhpur 342011, India*

(*Received April 2014; accepted October 2014*)

An integrated supply chain has an advantage on the competitiveness of the individual companies. This article compares supply chains of three Indian passenger car manufacturing industries using Fuzzy AHP and extent analysis technique. Different factors pertaining to supply chain competitiveness have been identified. These factors are further grouped under three main factors, namely, assets, processes, and performance. Finally, the most competitive supply chain among the available alternatives is determined.

Keywords: supply chains; competitiveness; Fuzzy AHP; extent analysis

Downloaded by [Delhi Technological University] at 20:00 03 February 2015

1. Introduction

A supply chain or logistics network is a system of organizations, people, technology, activities, information, and resources involved in moving a product or service from supplier to customer. Supply chain management (SCM) includes a set of approaches and practices to effectively integrate suppliers, manufacturers, distributors, and customers for improving the long-term performance of the individual firms. Supply chain as a whole is a cohesive and high-performing business model [18]. As defined by the Council of Supply Chain Management Professionals (CSCMP), SCM, and related strategies are crucially important to the success of a manufacturing firm because the cost and quality of goods and services sold are directly related to the cost and quality of goods and services purchased.

An integrated supply chain has an advantage on the competitiveness of the individual companies. As a result, the chain–chain competition has started to take over the enterprise–enterprise competition [37]. The forward-looking enterprises today are dynamic in their operation. They collaborate with suppliers, customers, and even with competitors; share information and knowledge aiming to create a supply chain that is capable of competing. Hence, gaining competitive edge under such a cut-throat environment becomes increasingly difficult, if not impossible. Survival and success of the industries depend upon the competitiveness of the supply chain, i.e. the ability to compete in the marketplace. Supply Chain competitiveness has been described as a multi-dimensional and relative concept. According to [1], competitiveness is the firm's ability to provide goods and services more efficiently than others involved in the marketplace. For this purpose, organizations need to manage their resources and processes more efficiently than their competitors. Competitiveness of a supply chain depends on its ability to perform well in dimensions such as cost, quality, delivery, dependability and speed, innovation, and flexibility to adapt itself to variations in demand [13].

Today's competitive environment is characterized by thin profit margins, high consumer expectations for quality products, and short lead times, companies are required to take advantage of every opportunity to optimize their business processes [66]. In order to achieve these objectives, several important and critical decisions have to be taken at tactical as well as strategic levels. But for such decisions the information and data available are not always accurate, it is usually imprecise in nature. It cannot be described deterministically. So to deal with such kind of uncertainty, Zadeh [69] introduced fuzzy set theory which deals with imprecise situations. The technique was used to tackle the imprecise or vague data. The data can be collected in linguistic terms which are in the form of triangular fuzzy numbers [47]. Subsequently, a fuzzy AHP and extent analysis, a multi-criteria decision-making (MCDM) technique have been applied to integrate various linguistic assessments and weights in order to determine the best selection.

Key objectives of this paper are as follows:

(1) Factors responsible for supply chain competitiveness have been identified from the literature review and opinions of experts both from industries and academia.
(2) These factors are further grouped under three main factors, namely, Assets, Processes, and Performance.
(3) These factors are subsequently sub grouped into different factors.
(4) A hierarchy model has been developed comprising of these factors.

*Corresponding author. Email: milindksharma@rediffmail.com

© 2015 Chinese Institute of Industrial Engineers

(5) Further, by using Fuzzy AHP and extent analysis technique prioritization of the factors has been done and global weights were determined.
(6) Later supply chains of three Indian passenger car manufacturing industries are compared using Fuzzy AHP and extent analysis technique and finally, the most competitive supply chain among the available alternatives was determined.

The organization of this paper is as follows: first a brief introduction about supply chain has been discussed followed by a literature review for identification of the factors for supply chain competitiveness. Further Fuzzy AHP and extent analysis methodology is discussed. Proposed hierarchy model for prioritization of identified factors is presented with case illustrations. Lastly, the results are discussed followed by key conclusions.

Downloaded by [Delhi Technological University] at 20:00 03 February 2015

2. Literature review

In recent years, a number of firms have realized the potential of SCM in day-to-day operations management [5, 6]. In this section, factors of supply chain competitiveness are identified from the previous research work and from the opinions of experts from industries and academia. These factors are further grouped under three main factors, assets, processes, and performance. Assets and processes consist of four sub-factors each and Performance consists of three sub-factors. A brief literature review has been presented articulating these factors.

Assets: [1] defined assets as inherited (natural resources) or created infrastructures to achieve economic gains from sales to customers. Information and communication technology (ICT) is a very important strategic factor in determining whether the company is competitive or not. It acts as the disseminator and enabler for process and product communication along with reducing paperwork and lead times [30,60]. Email/faxes, worldwide web (www), Electronic data interchange (EDI), electronic funds transfer (EFT), Radio-frequency identification (RFID), etc., are the few that comes under the IT [60]. Use of IT technology such as internet, intranet, software applications packages, and decision support system can be applied to facilitate the information flow within the supply chain members [25]. The effective use of ICT is essential in developing an IT infrastructure that operates quickly and efficiently [34]. To meet rapidly changing product features and customer needs, company should build a dynamic capability to develop new to market products [56]. According to [42], a company can compete with their larger rivals by developing new-to-market products. Investment in product research and development will also help in improving quality and in reducing cost. For the development of new product, employees must be skilled and properly trained. According to [43], automation is the replacement of manual operations by computerized methods, or execution of decisions with the least human intervention. Some of the tools used in factory automation are CAD/CAM software's, computerized controlled machine tools, material handling system, and rapid prototyping [43].

2.1. *Processes*

To improve the efficiency of various processes, initiatives have to be taken by top management [54]. Leadership plays a significant role in framing organization strategy and in shaping the quality focus of companies [51]. To achieve this, top management must develop a system that motivates workers to think and act flexibly and productively to meet company goals. Alliances with suppliers, customers, and other external partners should be intensified to make the supply chain more effective. By aligning and coordinating the business processes and activities, overall performance and effectiveness of the supply chain can be improved [49]. According to [26], it is important to have top management support, for cross-functional training, integration of department within the organization, vendor development. Top management is also responsible for allocating resources in order to achieve an organization's purpose [64]. Trust is a favorable attitude that exists when one supply chain (SC) member has confidence in another SC member [2]. It is required for flow of reliable and accurate information in the supply chain. Lack of trust is one of the major factors that contribute to supply chain risks [57]. According to [23], risk and reward sharing is important for decision-making and developing the trust and partnership among the supply chain members.

Different organizations have formed different SCM strategies to compete in the market. They have learnt that to be successful, they must be focused, as they cannot be best and outperform their rivals in all areas [65]. Success of the supply chain depends on the effective strategies of the SCM [58]. Information sharing between the supply chain members is essential for a supply chain [25]. Information sharing may be of sharing of the inventory data, demand data, and product quality data.

2.2. *Performance*

Performance measurement for supply chains is becoming increasingly crucial in today's competitive business scenario [7, 8]. Performance of an enterprise is often measured as a ratio of output to input. The outputs constitute the products of the enterprise and the inputs are the resources used by the enterprise. Rise in global competition has compelled the firms to increase performance standards in many dimensions such as quality, cost, productivity, product introduction time, and smooth-flowing operations [31]. It is noteworthy that quality is important for both efficiency and responsiveness [61]. Quality is determined by the extent to which a product or service successfully serves the purpose of the user during usage

Downloaded by [Delhi Technological University] at 20:00 03 February 2015

[45]. Customers require products and services of a given quality to be delivered by, or be available by, a given time, and to be at a price that reflects value for money. These are the needs of customers. An organization will survive only if it creates and retains satisfied customers and this can only be achieved if the products or services meet customer needs and expectations. In context of product quality, reliability of the product and its service during the use is the most important factor for measuring product quality [48]. Responsiveness is defined as the ability of a supply chain to respond rapidly to the changes in demand, both in terms of volume and mix of products [19,32]. The responsiveness of a supply chain describes how quickly it responds to customer (i.e. the rate of communication). It includes the delivery of product in right quantity, of right quality, and at right time. The "'supply chain lead time"' is the time spent by the supply chain to process the raw materials to obtain the final products and to deliver them to the customer. It includes supplier lead time, manufacturing lead time, distribution lead time, and logistics lead time for transport of raw materials and semi-finished/finished goods [6]. More importantly, lead time can play a major role in achieving competitive advantages through quick response to customer requirement [68]. And as such it is an important performance measure and source of competitive advantage; it directly interacts with customer service in determining effectiveness of supply chain. According to [16], the profit of an enterprise is directly affected by the cost of its operations. Total cost is a sum of all its complex attributes such as distribution cost, manufacturing cost, inventory cost, raw material cost, etc. Distribution cost includes the transportation and handling cost, safety stock cost, and duty. Manufacturing cost includes labor, maintenance, and reworks cost. Inventory cost includes the work-in process and finished goods inventories.

On the basis of above literature, main and sub-factors for supply chain competitiveness are summarized in the Table 1.

3. Research methodology

Supply chain selection is a multi-criteria decision-making problem in which all the information available is not precise but vague in nature. To deal with impreciseness, fuzzy logic is used extensively. So the Fuzzy AHP and extent analysis is used for prioritize the factors and select the most competitive supply chain by comparing them.

3.1. *Fuzzy logic*

Fuzzy logic is a form of multi-valued logic derived from fuzzy set theory to deal with reasoning that is approximate rather than precise. Most real-world decision problems take place in a complex environment where conflicting systems of logic, uncertain and imprecise knowledge, and possibly vague preferences have to be considered. To face such complexity, the use of specific tools, techniques, and concepts which allow the available information to be represented with the appropriate granularity is believed as crucial. Particularly, fuzzy set theory can ideally cope with this kind of problems.

3.2. *Fuzzy set theory*

Let U be the universe of discourse, $U = \{\mu_1, \mu_2, \mu_3 \ldots \mu_n\}$. According to Zadeh [69], a fuzzy set Ã of U is a set of ordered pairs $\{(\mu_1, f_{\tilde{A}}(\mu_1)), (\mu_2, f_{\tilde{A}}(\mu_2)), \ldots (\mu_n, f_{\tilde{A}}(\mu_n))\}$, where $f_{\tilde{A}}, f_{\tilde{A}} : U \to [0, 1]$ is the membership function of Ã and $f_{\tilde{A}}(\mu_i)$ indicates the grade of membership of μ_i in Ã. Among various membership function, the triangular fuzzy number is the most prominently applied in engineering applications. According to [22], this fuzzy number is characterized by triangular distribution functions with the linear and symmetric sides, which is parameterized by a triple (m, n, p). In this methodology, $t\ (m, n, p)$ is denoted as triangular fuzzy number Ã, with $m \le n \le p$, where m and p stands for the lower and upper values for the support of Ã, respectively, and n stands for moderated value. Its membership function can be defined as:

$$f_{\tilde{A}}(\mu) = \begin{cases} 0, & \mu < m, \\ \frac{\mu - m}{m - n}, & m \le \mu \le n, \\ \frac{p - \mu}{p - n}, & n \le \mu \le p, \\ 0, & \mu > p. \end{cases} \tag{1}$$

The curve of membership function is shown in Figure 1.

The algebraic operations on triangular numbers [22] say $\tilde{A}$ and $\tilde{B}$ parameterized by triplet (m_1, n_1, p_1) and (m_2, n_2, p_2), respectively, are stated below:

$$\begin{gathered} \tilde{A} + \tilde{B} \approx (m_1 + m_2, n_1 + n_2, p_1 + p_2) \\ \tilde{A} - \tilde{B} \approx (m_1 - p_2, n_1 - n_2, p_1 - m_2) \\ \tilde{A}.\tilde{B} \approx (m_1.m_2, n_1.n_2, p_1.p_2) \\ \tilde{A}/\tilde{B} \approx (m_1/p_2, n_1/n_2, p_1/m_2) \\ 1/\tilde{A} \approx (1/p_1, 1/n_1, 1/m_1) \\ \ln(\tilde{A}) \approx (\ln(m_1), \ln(n_1), \ln(p_1)) \\ \exp(\tilde{A}) \approx (\exp(m_1), \exp(n_1), \exp(p_1)) \end{gathered} \tag{2}$$

The distance between $\tilde{A}$ and $\tilde{B}$ can be calculated using the vertex method as in the following equation:

$$d(\tilde{A}, \tilde{B}) = \sqrt{\frac{1}{3}\left[(m_1 - m_2)^2 + (n_1 - n_2)^2 + (p_1 - p_2)^2\right]} \tag{3}$$

3.3. *Fuzzy AHP*

Analytic hierarchy process (AHP) has been widely used as a useful MCDM tool or a weight estimation technique in many areas such as selection, evaluation, planning and development, decision-making, forecasting, and many more. The traditional AHP requires exact judgments. However, due to the complexity and uncertainty involved

Table 1. Factors for supply chain competitiveness.

Main factors	Sub-factors	References
Assets (AST)	(1) IT Infrastructure (IT) • Intranet/Extranet facility • Bar coding • Use of Electronic Data Interchange (EDI) • Radio-frequency identification (RFID)	[25,34,43,46,38,60]
	(2) Research and Development (R&D) • New product development capability • Skilled employees • Employee's training • Adoption of latest technologies	[1,17,50,54,56]
	(3) Automation (AUT) • Material handling • Equipment	[15,43,54]
	(4) Plant Infrastructure (PINF) • Plant location • Capability • Availability of Suitable utilities • Distributer network	[21,45,59]
Processes (PRO)	(1) Strategy development (SD) • Product analysis • Process analysis • Market analysis • Performance measurement system (PMS) • Selection of appropriate SCM practices • Vendor development • Customer relationship management (CRM)	[9,28,33,40,54,56,58,62,65]
	(2) SC integration (SCI) • Risk and reward sharing • Trust development in SC members • Collaborative decision-making and planning • Partnership with dealers, distributors, and retailers	[3,4,11,12,17,20,40,62,67],
	(3) Top management commitment (TMC) • Resource allocation (labor, machine, capacity, energy) • Long-term investment motives • Employee's training and participation	[15,24,26,36,40,50,54,56,58]
	(4) Information Sharing (IS) • Point of sales data • Inventory Data • Product quality data • Product design and development data	[3,10,27,41,44,52,67]
Performance (PERF)	(1) Product quality (QUA) • Reliability • Serviceability	[1,21,45,48,50,55,59,61]
	(2) Responsiveness (RES) • Reduced lead time • On-time delivery • Right quality • Right quantity • Transport optimization	[23,28,45,50,61,68]
	(3) Cost (COST) • Low cost • Distribution cost • Manufacturing cost • Inventory cost	[1,15,29,39,45,50,55,59,61]

Downloaded by [Delhi Technological University] at 20:00 03 February 2015

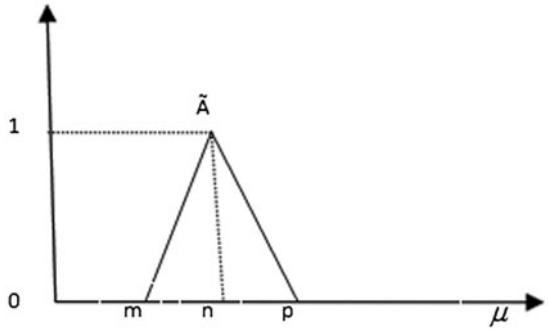

Figure 1. Triangular fuzzy number.

in real-world decision problems, a decision-maker (DM) may sometimes feels more confident to provide fuzzy judgments than exact comparisons.

A number of methods have been developed to handle fuzzy comparison matrices. Some of them are given below:

- Logarithmic least squares method (LLSM) [63], to obtain triangular fuzzy weights from a triangular fuzzy comparison matrix.
- Geometric mean method to calculate fuzzy weights [14].
- Extent analysis method by Chang [16], which derives crisp weights for fuzzy comparison matrices.
- Fuzzy preference programming method.
- Lambda-Max method, which is the direct fuzzification of the well-known kmax method.

Among the above approaches, the extent analysis method has been employed in quite a number of applications due to its computational simplicity.

3.4. *Fuzzy AHP and extent analysis*

Extent analysis is the technique used to prioritize the weights. In this paper, the extension of fuzzy AHP method, extent analysis is considered which was proposed by Kahraman et al. [35]. The algorithm of this method can be described as follows:

Let $X = \{x_1, x_2 \ldots x_n\}$ be an object set, and $U = \{u_1, u_2 \ldots u_m\}$ be a goal set. According to the method of Chang (1992) extent analysis, each object is taken and extent analysis for each goal, g_i, is performed, respectively. Therefore, m extent analysis values for each object can be obtained, with the following signs:

$$M_{g_i}^1, \quad M_{g_i}^2, \ldots, \quad M_{g_i}^m \quad i = 1, 2, \ldots, n. \tag{4}$$

where all the M_{gi}^j ($j = 1, 2 \ldots m$) are TFNs.

The steps of Chang's extent analysis can be given as in the following:

Step 1: The value of fuzzy synthetic extent with respect to the ith object is defined as:

$$S_i = \sum_{j=1}^{m} M_{g_i}^j \otimes \left[\sum_{i=1}^{n}\sum_{j=1}^{m} M_{g_i}^j\right]^{-1} \tag{5}$$

To obtain $\sum_{j=1}^{m} M_{g_i}^j$ perform the fuzzy addition operation of m extent analysis values for a particular matrix such that

$$\sum_{j=i}^{m} M_{g_i}^j = \left(\sum_{j=1}^{m} l_j \sum_{j=1}^{m} m_j \sum_{j=1}^{m} u_j\right) \tag{6}$$

and to obtain $\left[\sum_{i=1}^{n}\sum_{j=1}^{m} M_{g_i}^j\right]$, perform the fuzzy addition operation of $M_{g_i}^j$ ($j = 1, 2 \ldots m$) values such that

$$\sum_{i=1}^{n}\sum_{j=i}^{m} M_{g_i}^j = \left(\sum_{i=1}^{m} l_i \sum_{i=1}^{m} m_i \sum_{i=1}^{m} u_i\right) \tag{7}$$

The inverse of the vector in Equation (4) can be computed as:

$$\left[\sum_{i=1}^{n}\sum_{j=1}^{m} M_{g_i}^j\right]^{-1} = \left(\frac{1}{\sum_{i=1}^{n} u_i}, \frac{1}{\sum_{i=1}^{n} m_i}, \frac{1}{\sum_{i=1}^{n} l_i}\right) \tag{8}$$

Step 2: The degree of possibility of $M_2 = (1_2, m_2, u_2)$ $M_1 = (l_1, m_1, u_1)$ is defined as:

$$V(M_2 \geq M_1) = \sup_{y \geq x}\left[\min\left(\mu_{M_1}(x), \mu_{M_2}(y)\right)\right] \tag{9}$$

and can be equivalently expressed as follows:

$$V(M_2 \geq M_1) = hgt(M_1 \cap M_2) = \mu_{M_2}(d) = \begin{cases} 1, & \text{if } m_2 \geq m_1, \\ 0, & \text{if } l_1 \geq u_2, \\ \frac{l_1 - u_2}{(m_2 - u_2) - (m_1 - l_1)} & \text{otherwise,} \end{cases} \tag{10}$$

where d is the ordinate of the highest intersection point D between μ_{M_1} and μ_{M_2} (Figure 2).

To compare M_1 and M_2, we need both the values of $V(M_2 \geq M_1)$ and $V(M_1 \geq M_2)$.

Step 3: The degree possibility for a convex fuzzy number to be greater than k convex fuzzy numbers M_i ($i = 1, 2, \ldots, k$) can be defined by,

$$\begin{aligned} &V(M \geq M_1, M_2, \ldots, M_k) \\ &= V[(M \geq M_1) \text{ and } (M \geq M_2) \text{ and } \ldots \text{ and } (M \geq M_k)] \\ &= \min\ V(M \geq M_i), \quad i = 1, 2, 3, ..., k \end{aligned} \tag{11}$$

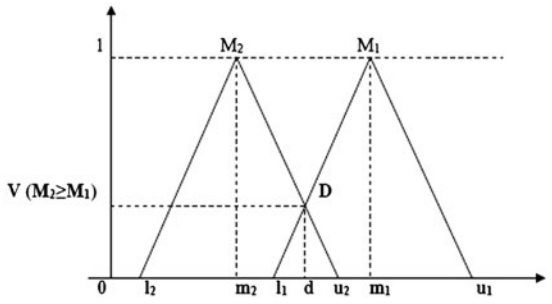

Figure 2. The interaction between M_1 and M_2.

Downloaded by [Delhi Technological University] at 20:00 03 February 2015

Assume that,

$$d'(A_i) = \min \ V(S \geq S_k) \tag{12}$$

for, $k = 1, 2, \ldots, n$ and $k \neq 1$. Now the weight vector can be given by the following formulae:

$$W' = (d'(A_1), d'(A_2), ..., d'(A_n))^T, \tag{13}$$

where A_i ($i = 1, 2, 3 \ldots, n$) are n elements.

Step 4: via normalization, the normalized weight vectors are given as:

$$W' = (d'(A_1), d'(A_2), ..., d'(A_n))^T,$$

where W is a non-fuzzy number.

4. Case illustration

In order to demonstrate the use of fuzzy AHP and extent analysis, an industrial case has been discussed in this paper. First the factors of supply chain competitiveness identified in the section of literature review are prioritized and then supply chains of three different Indian car manufacturing industries have been identified and compared on the basis of the identified factors using the same method. The company profile and the salient features of supply chains of the industries are discussed later on in this section.

4.1. *ABC Ltd*

ABC Ltd. is one of India's leading automobile manufacturers and the market leader in the car segment, both in terms of volume of vehicles sold and revenue earned. It was established in 1981 with a joint venture with a Japanese leading automobile company C's Ltd. Until recently, 18.28% of the company was owned by the Indian government, and 54.2% by C Ltd. of Japan. Its manufacturing facilities are located at two facilities Gurgaon and Manesar south of Delhi. ABC's Gurgaon facility has an installed capacity of producing 350,000 units per annum. The Manesar facilities launched in February 2007 comprise a vehicle assembly plant with a capacity of 300,000 units per year. Manesar and Gurgaon facilities have a combined capability to produce over 700,000 units annually. ABC Ltd. offers 15 models. Nearly 75,000 people are employed directly by ABC Ltd. and its partners. It has been rated first in customer satisfaction among all car makers in India from 1999 to 2009 by J D Power Asia Pacific. Currently, ABC has a market share of 47.4%. Table 2 indicates last two years sales performance of ABC Ltd.

Table 2. Performance statistics of ABC Ltd.

Indicators	2008–2009	2009–2010
Installed capacity (units/year)	600,000	600,000
Unit sold	812,063	924,193
Capacity utilization (%)	135.3	154
% Swing in sales		13.8
Market share (%)	52.3	47.4

4.2. *Salient features of supply chain of ABC Ltd*

- ABC Ltd. has two plants in Gurgaon and Manesar in Haryana. The Gurgaon plant is spread over 300 acre areas with installed capacity of 350,000 vehicles annually and Manesar plant is spread over 600 acre with capacity of 300,000 vehicles annually.
- It currently has 100 vendors and 800-plus dealerships across more than 500 cities in India.
- To ensure the vehicles sold by them are serviced properly, ABC has 1945 Authorized Service Stations and 30 Express Service Stations on 30 National Highways across 1314 cities in India.
- The R&D of the company is carried out by its Japanese collaborative C Ltd.
- ABC utilizes CAD-CAM tools and Robots for the manufacturing. It currently employs more than 150 robots in their manufacturing plant.
- ABC has 2.0 mbps high-speed LAN provided by BSNL, for their connectivity and information sharing within the plant.
- ABC's vendors lie within 100 km from their manufacturing plant, which helps in improving product quality, cost reduction, and also help in vendor development.
- ABC received ISO 9001:2000 certification for their quality products.

4.3. *XYZ Ltd*

XYZ was established in 1996 in India by a South Korean company X Ltd. XYZ is fully owned by the parent group and is the second largest car manufacturer and the largest passenger car exporter from India. XYZ presently markets six models of passenger cars in 37 variants across segments. It has two plants at Sriperambudur and Irungattukottai in Tamil Nadu. Plant in Sriperumbudur, Tamil Nadu, capable of producing 350,000 vehicles annually while Irungattukottai plant has a capacity to make 120,000 cars and 130,000 engine transmission units per annum and is the largest overseas investment made by the Korean Company. Irungattukottai plant is spread over 500 acre land area. XYZ's market share is 21.2%. Table 3 indicates last two years sales performance of XYZ Ltd.

4.4. *Salient features of supply chain of XYZ Ltd*

- It has two manufacturing plants at Sriperambudur and Irungattukottai in Tamil Nadu having producing

Downloaded by [Delhi Technological University] at 20:00 03 February 2015

Table 3. Performance statistics of XYZ Ltd.

Indicators	2008–2009	2009–2010
Installed capacity (units/year)	600,000	600,000
Unit sold	281,039	428,950
Capacity utilization (%)	46.8	71.5
% Swing in sales		52.6
Market share (%)	18.1	22

Table 4. Performance statistics of PQR Ltd.

Indicators	2008–2009	2009–2010
Installed capacity (Units/Year)	190,000	500,000
Unit sold	122,663	167,680
Capacity utilization (%)	64.6	33.5
% Swing in sales		36.7
Market share (%)	7.9	8.6

capacity of 350,000 and 120,000 vehicles per annum, respectively. Irungattukottai plant is spread over 500 acre land area.

- XYZ's total production capacity is 600,000 units per annum.
- XYZ has 355 dealerships and 610 Authorized Service Centers in 325 cities across India.
- XYZ has a R&D section at their Irungattukottai plant.
- They have also established a research center in Hyderabad, India, for R&D purposes, which has 450 engineers. The engineers are constantly looking for new innovations which would help in improving their technology and hence, providing good quality and innovative products.
- They employ tools like Uni-graphics, automation, robots, etc. for their manufacturing and R&D section.
- XYS has an extensive Wi-Fi system in their plants which enables effective and efficient information sharing and connectivity.
- XYZ has established a wide network of the vendors across their manufacturing plant. Continues vendor development programs have been incorporated by XYZ in order to improve the performance and efficiency of the vendors.
- XYZ is using a flexible manufacturing system in their plant in order to achieve high productivity, reduce lead time, good quality products, etc.
- XYZ has been awarded the benchmark ISO 14,001 certification for its sustainable environment management practices.

4.5. *PQR Ltd*

PQR Ltd. is one of the India's leading automobile manufacturing industries. It has a market share of 8.6%. It manufactures eight different models of four wheelers with 13 variants. It has two manufacturing plants in India, one in Nasik with a capacity of producing 190,000 units/annum. The other plant is at Chakan near Pune, India. It is 700 acres in area with a manufacturing capacity of 300,000 units/annum. At Chakan, it uses a cluster of 70 solar dishes to power the chillers in its paint shop, thereby reducing electricity consumption by 1.8 lakh units a year, LPG consumption by 1500 tones, and carbon dioxide emissions by 3500 tones. PQR Ltd. has featured in Forbes' Asian Fab 50 list, which is a compilation of the best listed companies in the Asia-Pacific region in 2009. Table 4 indicates last two years sales performance of PQR Ltd.

4.6. *Salient features of supply chain of PQR Ltd*

- PQR sells car through 295 dealership in 165 cities across India.
- PQR has two passenger car manufacturing plants at Nasik and Chakan (near Pune) in Maharashtra, India. Nasik plant is capable of producing 190,000 units/annum while on the other hand Chakan plant is capable of producing 300,000 units/annum which rising the PQR's total production capacity to nearly 500,000 units/year.
- Nasik plant is spread over 115 acre land area and Chakan plant is over 700 acres.
- PQR has a world class R&D section at their newly opened plant at Chakan. The R&D work is carried out by the team of 310 highly trained & educated engineers. Engineers are working at Pro-E design software.
- Plants are having Intranet and Internet facilities. Intranet is being done by high-speed local area network for sharing data/information within the plants and for internet 8.0 mbps line is used.
- PQR utilizes computer-aided manufacturing techniques and Robots for the manufacturing. It currently employs more than 60 robots in their manufacturing plant at Chakan.
- The R&D facility at Chakan is ISO/TS 16949 certified. The Nasik plant has also been recommended for the TPM excellence award.

4.7. *Development of the hierarchy model*

The Figure 3 below shows a hierarchy model for selecting a competitive supply chain. It shows the factors for supply chain competitiveness, which have been grouped under three main factors as written in Table 1. The AHP model developed is used for the prioritization of the factors and selection of the supply chain. Fuzzy AHP and extent analysis is used to prioritize the main and sub-factors.

Downloaded by [Delhi Technological University] at 20:00 03 February 2015

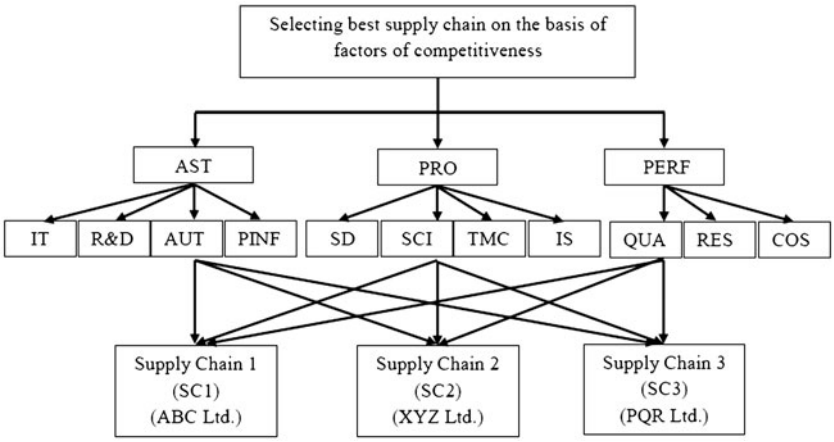

Figure 3. Schematic of the hierarchy model for selecting competitive supply chain.

Downloaded by [Delhi Technological University] at 20:00 03 February 2015

4.8. *Working steps of calculations and applications of Fuzzy AHP and extent analysis*

For the supply chain selection, the judgments based on observation are fed into the Fuzzy AHP model for each main factors and sub-factors of all the levels of hierarchy. Pairwise comparison of the factors at each level is done on a linguistic scale of relative importance as shown in Table 5.

The steps to follow in using the Fuzzy AHP and extent analysis:

(1) Define the problem and determine the objective.
(2) Structure the hierarchy from the top through the intermediate levels to the lowest level.
(3) Construct a set of pairwise comparison matrices for each of the lower levels. An element in the higher level is said to be a governing element for those in lower level, since it contributes to it or affects it. The elements in the lower level are then compared to each other based on their effect on the governing element above. This yields a square matrix of judgments. The pairwise comparisons are done in terms of which an element dominates another. These judgments are expressed in fuzzy environment.
(4) The fuzzy values of paired comparison were converted to crisp values via the Chang's *extent analysis* as mentioned in the Research Methodology section. First, the fuzzy synthetic extent values were calculated using Equation (2) with the help of Equations (1)–(5). Equations (6) and (7) were applied to express the degree of synthetic extent values. To have a weight vector given by as in Equation (10). After normalizing weight vector is defined, the obtained priority weight vector of criteria was figured out.

Table 5. Linguistic variable for importance weight of each factor.

Linguistic variable	Triangular fuzzy numbers
Absolutely important	(7/2, 4, 9/2)
Strongly important	(5/2, 3, 7/2)
Fairly important	(3/2, 2, 5/2)
Weakly important	(2/3, 1, 3/2)
Equally important	(1, 1, 1)

Source: Ref. [35].

From the Table 6 and Equation (5), fuzzy synthetic extent values can be obtained as follows:

$$s_{\mathrm{AST}} = (2.07, 2.50, 3.17)\left[\frac{1}{12}.35, \frac{1}{10}, \frac{1}{8}.14\right] = (0.17, 0.25, 0.39)$$

$$s_{\mathrm{PRO}} = (3.17, 4.00, 5.00)\left[\frac{1}{12}.35, \frac{1}{10}, \frac{1}{8}.14\right] = (0.27, 0.40, 0.62)$$

$$s_{AST} = (2.90, 3.50, 4.17)\left[\frac{1}{12}.35, \frac{1}{10}, \frac{1}{8}.14\right] = (0.24, 0.35, 0.51)$$

Using Equations (9) and (10), the vectors obtained are as follows:

$$V(S_{\mathrm{AST}} \geq S_{\mathrm{PERF}}) = \frac{(0.24 - 0.39)}{(0.25 - 0.39) - (0.35 - 0.24)} = 0.60$$

Table 6. The fuzzy evaluation matrix with respect to the goal.

	AST	PRO	PERF
AST	(1, 1, 1)	(2/3, 1, 3/2)	(2/5, 1/2, 2/3)
PRO	(2/3, 1, 3/2)	(1, 1, 1)	(3/2, 2, 5/2)
PERF	(3/2, 2, 5/2)	(2/5, 1/2, 2/3)	(1, 1, 1)

Table 7. The fuzzy evaluation matrix of the sub factors with respect to ASSETS.

	IT	R&D	AUT	PINF
IT	(1, 1, 1)	(5/2, 3, 7/2)	(3/2, 2, 5/2)	(2/3, 1, 3/2)
R&D	(2/7, 1/3, 2/5)	(1, 1, 1)	(1, 1, 1)	(2/3, 1, 3/2)
PERF	(2/5, 1/2, 2/3)	(1, 1, 1)	(1, 1, 1)	(2/5, 1/2, 2/3)
PINF	(2/3, 1, 3/2)	(2/3, 1, 3/2)	(3/2, 2, 5/2)	(1, 1, 1)

The weight vector from this table is calculated as $W_{\mathrm{AST}} = (0.44, 0.10, 0.16, 0.30)^T$.

Table 8. The fuzzy evaluation matrix of the sub factors with respect to PROCESSES.

	SD	SCI	TMC	IS
SD	(1, 1, 1)	(2/3, 1, 3/2)	(1, 1, 1)	(3/2, 2, 5/2)
SCI	(2/3, 1, 3/2)	(1, 1, 1)	(2/5, 1/2. 2/3)	(2/3, 1, 3/2)
TMC	(1, 1, 1)	(3/2, 2, 5/2)	(1, 1, 1)	(3/2, 2, 5/2)
IS	(2/5, 1/2, 2/5)	(2/3, 1, 3/2)	(2/5, 1/2, 2/3)	(1, 1, 1)

The weight vector from this table is calculated as $W_{\mathrm{PRO}} = (0.34, 0.18, 0.43, 0.05)^T$.

Table 9. The fuzzy evaluation matrix of the sub factors with respect to PERFORMANCE.

	QUA	RES	COST
QUA	(1, 1, 1)	(3/2, 2, 5/2)	(2/3, 1, 3/2)
RES	(2/5, 1/2, 2/3)	(1, 1, 1)	(2/3, 1, 3/2)
COST	(2/3, 1, 3/2)	(2/3, 1, 3/2)	(1, 1, 1)

The weight vector from this table is calculated as $W_{\mathrm{PERF}} = (0.45, 0.22, 0.33)^T$.

$$V(S_{\mathrm{PRO}} \geq S_{\mathrm{AST}}) = 1$$

$$V(S_{\mathrm{PRO}} \geq S_{\mathrm{PERF}}) = 1$$

$$V(S_{\mathrm{PERF}} \geq S_{\mathrm{AST}}) = 1$$

$$V(S_{\mathrm{PERF}} \geq S_{\mathrm{PRO}}) = \frac{(0.27 - 0.51)}{(0.35 - 0.51) - (0.40 - 0.27)} = 0.83$$

Now, using Equation (12),

$$d'(S_{\mathrm{AST}}) = V(S_{\mathrm{AST}} \geq S_{\mathrm{PRO}}, S_{\mathrm{PERF}}) = \min(0.44, 0.60) = 0.44$$

$$d'(S_{\mathrm{PRO}}) = V(S_{\mathrm{PRO}} \geq S_{\mathrm{AST}}, S_{\mathrm{PERF}}) = \min(1, 1) = 1$$

$$d'(S_{\mathrm{PERF}}) = V(S_{\mathrm{PERF}} \geq S_{\mathrm{AST}}, S_{\mathrm{PRO}}) = \min(1, 0.83) = 0.83$$

Hence, the Weight vector is written as (Equation 13):

$$W' = (0.44, 1, 0.83)^T$$

via normalization, we get

Table 10. Global wt. of the main and sub-factors of supply chain competitiveness.

S. no.	Factors	Individual wt.	Global wt.
1.	Assets (ast)	0.20	0.20
	• It infrastructure (it)	0.44	0.09
	• Research & development (r&d)	0.10	0.02
	• Automation (aut)	0.16	0.03
	• Plant infrastructure (pinf)	0.30	0.06
2.	Processes (pro)	0.44	0.44
	• Strategy development (sd)	0.34	0.15
	• Sc integration (sci)	0.18	0.08
	• Top management commitment (tmc)	0.43	0.19
	• Information sharing (is)	0.05	0.02
3.	Performance (perf)	0.36	0.36
	• Product quality (qua)	0.45	0.16
	• Responsiveness (res)	0.22	0.08
	• Cost (cost)	0.33	0.12

Downloaded by [Delhi Technological University] at 20:00 03 February 2015

Downloaded by [Delhi Technological University] at 20:00 03 February 2015

Table 11. Evaluation of the supply chains with respect to IT INFRASTRUCTURE.

	SC1	SC2	SC3
C1	(1, 1, 1)	(2/3, 1, 3/2)	(2/5, 1/2, 2/3)
C2	(2/3, 1, 3/2)	(1, 1, 1)	(2/3, 1, 3/2)
C3	(3/2, 2, 5/2)	(2/3, 1, 3/2)	(1, 1, 1)

The weight vector from this table is calculated as W_{IT} = (0.22, 0.33, 0.45)^T.

Table 12. Evaluation of the supply chains with respect to RESEARCH & DEVELOPMENT.

	SC1	SC2	SC3
C1	(1, 1, 1)	(2/9, 1/4, 2/7)	(2/9, 1/4, 2/7)
C2	(7/2, 4, 9/2)	(1, 1, 1)	(3/2, 2, 5/2)
C3	(7/2, 4, 9/2)	(2/5, 1/2, 2/3)	(1, 1, 1)

The weight vector from this table is calculated as $W_{R\&D}$ = (0.00, 0.65, 0.35)^T.

Table 13. Evaluation of the supply chains with respect to AUTOMATION.

	SC1	SC2	SC3
C1	(1, 1, 1)	(2/3, 1, 3/2)	(2/5, 1/2, 2/3)
C2	(2/3, 1, 3/2)	(1, 1, 1)	(2/3, 1, 3/2)
C3	(3/2, 2, 5/2)	(2/3, 1, 3/2)	(1, 1, 1)

The weight vector from this table is calculated as W_{AUT} = (0.54, 0.17, 0.29)^T.

Table 14. Evaluation of the supply chains with respect to PLANT INFRASTRUCTURE.

	SC1	SC2	SC3
C1	(1, 1, 1)	(3/2, 2, 5/2)	(5/2, 3, 7/2)
C2	(2/5, 1/2, 2/3)	(1, 1, 1)	(3/2, 2, 5/2)
SC3	(2/7, 1/3, 2/5)	(2/5, 1/2, 2/3)	(1, 1, 1)

The weight vector from this table is calculated as W_{PNIF} = (0.82, 0.18, 0.00)^T.

Table 15. Evaluation of the supply chains with respect to STRATEGY DEVELOPMENT.

	SC1	SC2	SC3
C1	(1, 1, 1)	(2/3, 1, 3/2)	(5/2, 3, 7/2)
C2	(2/3, 1, 3/2)	(1, 1, 1)	(3/2, 2, 5/2)
C3	(2/7, 1/3, 2/5)	(2/5, 1/2, 2/3)	(1, 1, 1)

The weight vector from this table is calculated as W_{SD} = (0.58, 0.41, 0.00)^T.

Table 16. Evaluation of the supply chains with respect to SC INTEGRATION.

	SC1	SC2	SC3
C1	(1, 1, 1)	(2/3, 1, 3/2)	(2/3, 1, 3/2)
C2	(2/3, 1, 3/2)	(1, 1, 1)	(3/2, 2, 5/2)
C3	(2/3, 1, 3/2)	(2/5, 1/2, 2/3)	(1, 1, 1)

The weight vector from this table is calculated as W_{SCI} = (0.33, 0.45, 0.22)^T.

Table 17. Evaluation of the supply chains with respect to TOP MANAGEMENT COMMITMENT.

	SC1	SC2	SC3
C1	(1, 1, 1)	(3/2, 2, 5/2)	(2/3, 1, 3/2)
C2	(2/5, 1/2, 2/3)	(1, 1, 1)	(3/2, 2, 5/2)
C3	(2/3, 1, 3/2)	(2/5, 1/2, 2/3)	(1, 1, 1)

The weight vector from this table is calculated as W_{TMC} = (0.44, 0.36, 0.20)^T.

Table 18. Evaluation of the supply chains with respect to INFORMATION SHARING.

	SC1	SC2	SC3
C1	(1, 1, 1)	(2/3, 1, 3/2)	(2/5, 1/2, 2/3)
C2	(2/3, 1, 3/2)	(1, 1, 1)	(2/3, 1, 3/2)
C3	(3/2, 2, 5/2)	(2/3, 1, 3/2)	(1, 1, 1)

The weight vector from this table is calculated as W_{IS} = (0.17, 0.29, 0.54)^T.

Table 19. Evaluation of the supply chains with respect to PRODUCT QUALITY.

	SC1	SC2	SC3
C1	(1, 1, 1)	(3/2, 2, 5/2)	(5/2, 3, 7/2)
C2	(2/5, 1/2, 2/3)	(1, 1, 1)	(2/3, 1, 3/2)
C3	(2/7, 1/3, 2/5)	(2/3, 1, 3/2)	(1, 1, 1)

The weight vector from this table is calculated as W_{QUA} = (1.00, 0.00, 0.00)^T.

Table 20. Evaluation of the supply chains with respect to RESPONSIVENESS.

	SC1	SC2	SC3
C1	(1, 1, 1)	(2/3, 1, 3/2)	(5/2, 3, 7/2)
C2	(2/3, 1, 3/2)	(1, 1, 1)	(3/2, 2, 5/2)
C3	(2/7, 1/3, 2/5)	(2/5, 1/2, 2/3)	(1, 1, 1)

The weight vector from this table is calculated as W_{RES} = (1.00, 0.72, 0.00)^T.

Table 21. Evaluation of the supply chains with respect to COST.

	SC1	SC2	SC3
C1	(1, 1, 1)	(2/3, 1, 3/2)	(5/2, 3, 7/2)
C2	(2/3, 1, 3/2)	(1, 1, 1)	(2/3, 1, 3/2)
C3	(2/7, 1/3, 2/5)	(2/3, 1, 3/2)	(1, 1, 1)

The weight vector from this table is calculated as W_{COST} = (0.64, 0.29, 0.07)^T.

Table 22. Summary combination of priority weights.

	IT	R&D	AUT	PINF	Alternative priority weight
Sub-factors of assets					
Weight	0.44	0.10	0.16	0.30	
Alternatives					
SC1	0.22	0	0.54	0.82	0.43
SC2	0.33	0.65	0.17	0.18	0.29
SC3	0.45	0.35	0.29	0	0.28
	SD	SCI	TM	IS	Alternative priority weight
Sub-factors of processes					
Weight	0.34	0.18	0.43	0.05	
Alternatives					
SC1	0.58	0.33	0.44	0.17	0.45
SC2	0.41	0.45	0.36	0.29	0.39
SC3	0	0.22	0.20	0.54	0.16
	QUA		RES	COST	Alternative priority weight
Sub-factors of performance					
Weight	0.45		0.22	0.33	
Alternatives					
SC1	1		0.58	0.64	0.79
SC2	0		0.41	0.29	0.19
SC3	0		0	0.07	0.02
	AST		PRO	PERF	Alternative priority weight
Main factors of the goal					
Weight	0.20		0.44	0.36	
Alternatives					
SC1	0.43		0.45	0.79	0.57
SC2	0.29		0.39	0.19	0.30
SC3	0.28		0.16	0.02	0.13

$$W_G = (0.20, 0.44, 0.36)^T$$

where W is a non-fuzzy number (Tables 7–10).

All the factors for supply chain competitiveness listed in Table 1 are important. But more importance should be given to main factor and sub-factor according to their priority weight given to the factors as shown in Table 11. Factor having more weight should be given more importance as compare to the factors having less weight So to make a supply chain well competitive, an organization should give importance in the following order: first is to Processes (0.44), then Performance (0.36), and in the end, Assets (0.20). And similarly, importance should be given to the sub-factors.

4.9. *Application of Fuzzy AHP and extent analysis for selection of competitive supply chain*

As discussed previously, the supply chain of three different Indian passenger car manufacturer have been selected (namely, SC1, SC2, and SC3) and are then evaluated on the basis of factors of supply chain competitiveness shown in Table 1.

5. Result and discussion

In this study, various factors of supply chain competitiveness have been identified by an extensive literature survey and opinions of experts both from industries and academia. The factors were grouped under three main factors, namely, Assets, Processes, and Performance (as shown in Table 1). A hierarchy model was developed of the identified factors (Figure 2) and prioritize weights were calculated using Fuzzy AHP and extent analysis (Tables 11–21).

All the factors for supply chain competitiveness listed in Table 1 are important. But from the analysis reported above suggests that more importance should be given to main factors and sub-factors according to their weights given to the factors as shown in Table 10. Factor having more weights are considered to be more critical than the factors having less weights. Results shown in Table 22 suggest that in order to make a supply chain more competitive, an organization should give more importance to the Processes (0.44) followed by Performance (0.36), and Assets (0.20). Similar analogy may be drawn for sub-factors also.

Downloaded by [Delhi Technological University] at 20:00 03 February 2015

Downloaded by [Delhi Technological University] at 20:00 03 February 2015

The results further show that SC1 (0.57) is far more competitive than SC2 (0.30) and SC3 (0.13). So there is a need for improvement in the supply chains of XYZ Ltd. and PQR Ltd. in order to improve their competitiveness, and hence, compete in the market. It may be emphasized here that first supply chain (SC1) has got more score as compared to other supply chains. Reason for it may be that SC1 gives more focus on research and development of products, use of advanced technology in processes, and extensive use of high speed internet. In present globalized markets, customers' requirements are very dynamic in terms of features, specifications, service level, maintainability, flexibility, etc. [53] have also observed that manufacturing flexibility is very important for competitiveness of supply chains. Organizations can meet these market requirements only by giving more focus on R&D. Organizations also need to maintain high process capability to reduce rejection and improve productivity to overcome continuous increase in raw material and resources cost. SC1 is meeting this objective using advanced manufacturing technologies in their processes. Organizations also need to eliminate all kind of waste by integrating different operations in whole value chain. For this purpose, SC1 is using high-speed internet. These findings may help manufacturing organizations to frame their strategies to improve their competitiveness. Similar models based on AHP, Balanced scorecard (BSC), Preemptive goal programming (PGP), and hybrid use of AHP-PGP, AHP-BSC have also been reported in the literature. Bhagwat and Sharma [5–7] and Bhagwat et al. [8] suggested performance measurement models for SCM. These papers proposed SCM evaluation models based on different multi-criteria decision-making approaches. Performance measurement of SCM is done based on SCM performance metrics whilst classify them according to different decision levels, namely, strategic, tactical, and operational levels. These models prioritize different decision levels depending upon their criticality and also suggest the degree of importance of the various performance metrics. Whereas this study articulates on supply chain competitiveness while focusing on three main factors, Assets, Processes, and Performance as described in preceding sections.

6. Conclusion

In order to increase the competitive advantage in the current era of globalization and intensive world-wide competition along with the technological advancements, many organizations are paying serious attention to set their competitive priorities. To achieve the same, in this research work, a framework has been developed to prioritize the factors of supply chain competitiveness and evaluate the supply chain on the basis of the factors. Comparison of supply chains and selection of the best of them is a fuzzy multi-criteria decision-making problem in which data available are vague and imprecise for decision-making. So to make decision in uncertain condition, we used Fuzzy AHP and extent analysis methodology to prioritize the factors and evaluate the supply chain on the basis of these factors.

From this work, we can conclude that fuzzy AHP and extent analysis is a useful technique for prioritization of the factors and also for selection of the supply chain among the given alternatives. However, the systematic framework for supply chain selection in a fuzzy environment presented in this work can be easily extended to the analysis of other management decision problems.

This article has contributed to important issues of supply chain competitiveness theory and practices:

(a) This study contributes to competitiveness of supply chains.
(b) It points out the key factors and sub-factors crucial for supply chain competitiveness.
(c) This research work suggests a framework to prioritize the factors of supply chain competitiveness and evaluate the supply chain on the basis of such factors.
(d) This article further proposes the method to rank different supply chains on the basis of their performance and suggests the lagging and leading supply chains on the basis of their competitiveness.

This paper should be viewed in the light of some limitations. As this analysis and findings are based on Indian companies, and this necessitates caution in interpreting the results. The limited number of interviewed managers in a company restricts the generalizability of the results. Though the company selected for this study is typical of developing country businesses, the findings of the paper may not be readily extensible to other companies. Future research could examine these results using a larger sample set or field surveys in developing country settings. Secondly, this study used retrospective settings, based on the interviewed feedback after the events had occurred. This method naturally poses limitations due to respondent recall and the accuracy of information provided. Thirdly, the problem chosen for this study is based in a single country context and further additional research will be required to examine if the findings could be extended to other companies in other developing nations.

Acknowledgment

Authors thank anonymous referees for their helpful and constructive comments.

Notes on contributors

Rajesh Kumar Singh is an associate professor at Delhi Technological University, Delhi, India. His research interest includes Competitiveness Strategies, small business management, quality management, and supply chain management. He has about 80 research papers published in reputed international/national journals and conferences. He has published research papers in journals such as Industrial Management

Data Systems, Singapore Management Review, International Journal of Productivity, and Performance Management, Benchmarking: An International Journal, Journal of Modeling in Management, Competitiveness Review: An International Business Journal, Global Journal of Flexible Systems and Management, International Journals of Productivity and Quality Management, International Journal of Services and Operations Management, International Journal of Automotive Industry and Management, International Journal of Logistic Systems Management, IIMB Management Review, and Productivity Promotion. He is also on editorial board of some reputed journals.

Milind Kumar Sharma has taught many subjects related to production and industrial engineering and operations management. Prior to joining the Department of Production & Industrial Engineering, M.B. M. Engineering College, J.N.V. University, Jodhpur in 1998, he has served in industry for four years. He has been awarded research projects under the SERC fast track scheme for young scientist by Department of Science & Technology (DST), Career Award for Young Teacher Scheme by the All India Council for Technical Education (AICTE) and University Grants Commission (UGC), New Delhi, India. His areas of research interests include management information system, performance measurement, supply chain management, and small business development. He has published research papers in Production Planning and Control, Computers & Industrial Engineering, International Journal of Productivity and Quality Management, Journal of Manufacturing Technology Management, International Journal of Globalization and Small Business, International Journal of Enterprise Network Management, Measuring Business Excellence.

Downloaded by [Delhi Technological University] at 20:00 03 February 2015

References

[1] Ambastha, A. and K. Momaya, "Competitiveness of firms: Review of theory, frameworks and models," *Singapore Management Review*, 26, 45–61 (2004).

[2] Anderson, J. C. and J. A. Narus, "A model of distributor firm and manufacturer firm working partnerships," *Journal of Marketing*, 54, 42–58 (1990).

[3] Stentoft Arlbjørn, J., H. de Haas, R. Caspersen, J. Johansen and J. Nørmølle, "Improved change readiness through supply chain competency development," *Industrial and Commercial Training*, 38, 128–136 (2006).

[4] Arshinder, A. K. and S. G. Desmukh, "Supply chain coordination issues: An SAP-LAP frame work," *Asia Pacific Journal of Marketing and Logistics*, 19, 240–264 (2006).

[5] Bhagwat, R. and M. K. Sharma, "An integrated BSC-AHP approach for supply chain management performance evaluation," *Measuring Business Excellence*, 11, 57–68 (2007a).

[6] Bhagwat, R. and M. K. Sharma, "Performance measurement of supply chain management using the analytical hierarchy process," *Production Planning and Control*, 18, 666–680 (2007b).

[7] Bhagwat, R. and M. K. Sharma, "An application of the integrated AHP-PGP model for performance measurement of supply chain management," *Production Planning and Control*, 20, 678–690 (2009).

[8] Bhagwat, R., M. K. Sharma and F. T. S. Chan, "Performance measurement model for supply chain management in SMEs," *International Journal of Globalisation and Small Business*, 2, 428–445 (2008).

[9] Bhaskar, V. and P. Lallement, "Modeling a supply chain using a network of queues," *Applied Mathematical Modelling*, 34, 2074–2088 (2010).

[10] Bhatnagar, R. and C. Teo, "Role of logistics in enhancing competitive advantage: A value chain framework for global supply chains," *International Journal of Physical Distribution & Logistics Management*, 39, 202–226 (2009).

[11] Blome, C., A. Paulraj and K. Schuetz, "Supply chain collaboration and sustainability: A profile deviation analysis," *International Journal of Operations & Production Management*, 34, 639–663 (2014).

[12] Cachon, G. P. and M. A. Lariviere, "Supply chain coordination with revenue-sharing contracts: Strengths and limitations," *Management Science*, 51, 30–44 (2005).

[13] Carpinetti, L. C. R., M. C. Gerólamo and M. Dorta, "A conceptual framework for deployment of strategy-related continuous improvements," *The TQM Magazine*, 12, 340–349 (2000).

[14] Cebeci, U. and C. Kahraman, "Measuring customer satisfaction of catering service companies using fuzzy AHP: The case of Turkey," *Proceedings of International Conference on Fuzzy Systems and Soft Computational Intelligence in Management and Industrial Engineering, Istanbul*, 29, 315–325 (2002).

[15] Chan, F. T. S., "Performance measurement in a supply chain," *The International Journal of Advanced Manufacturing Technology*, 21, 534–548 (2003).

[16] Chang, D.Y., "Applications of the extent analysis method on fuzzy AHP," *European Journal of Operational Research*, 95(3), 649–655 (1996).

[17] Charan, P., R. Shankar and R. K. Baisya, "Analysis of interactions among the variables of supply chain performance measurement system implementation," *Business Process Management Journal*, 14, 512–529 (2008).

[18] Chopra, S., P. Meindle and D. V. Kalra, Supply Chain Management: Strategic, Planning and Operation, Pearson Education, New Delhi (2009).

[19] Christopher, M., "The agile supply chain," *Industrial Marketing Management*, 29, 37–44 (2000).

[20] Disney, S. and D. Towill, "Vendor-managed inventory and bullwhip reduction in a two-level supply chain," *International Journal of Operations & Production Management*, 23, 625–651 (2003).

[21] Du, L., "Acquiring competitive advantage in industry through supply chain integration: A case study of Yue Yuen Industrial Holdings Ltd," *Journal of Enterprise Information Management*, 20, 527–543 (2007).

[22] Dubois, D. and H. Prade, Fuzzy Sets and Systems: Theory and Applications, Academic Press, New York, NY (1980).

[23] Nishat Faisal, M., D. K. Banwet and R. Shankar, "Supply chain risk mitigation: Modeling the enablers," *Business Process Management Journal*, 12, 535–552 (2006).

[24] Aissa Fantazy, K., V. Kumar and U. Kumar, "An empirical study of the relationships among strategy, flexibility, and performance in the supply chain context," *Supply Chain Management: An International Journal*, 14, 177–188 (2009).

[25] Fawcett, S. E., C. Wallin, C. Allred and G. Magnan, "Supply chain information-sharing: Benchmarking a proven path," *Benchmarking: An International Journal*, 16, 222–246 (2009).

Downloaded by [Delhi Technological University] at 20:00 03 February 2015

[26] Ganesan, K. and B. Saumen, "Corporate turnaround through effective supply chain management: The case of a leading jewellery manufacturer in India," *Supply Chain Management: An International Journal*, 10, 340–348 (2005).

[27] Groznik, A. and M. Maslaric, "Achieving competitive supply chain through business process re-engineering: A case from developing country," *African Journal of Business Management*, 4, 140–148 (2010).

[28] Gunasekaran, A., C. Patel and R. E. McGaughey, "A framework for supply chain performance measurement," *International Journal of Production Economics*, 87, 333–347 (2004).

[29] Halley, A. and M. Beaulieu, "Mastery of operational competencies in the context of supply chain management," *Supply Chain Management: An International Journal*, 14, 49–63 (2009).

[30] Handfield, R. B. and E. L. Nichols, Introduction to Supply Chain Management, Prentice-Hall, Upper Saddle River, NJ (1999).

[31] Hitt, M. A., R. D. Ireland and R. E. Hoskisson, Strategic Management. Competitiveness and Globalisation: Concepts and Cases, Thompson Learning, Mason, OH (2001).

[32] Holweg, M., "The three dimensions of responsiveness," *International Journal of Operations & Production Management*, 25, 603–622 (2005).

[33] Huo, B., Y. Qi, Z. Wang and X. Zhao, "The impact of supply chain integration on firm performance," *Supply Chain Management: An International Journal*, 19, 369–384 (2014).

[34] Jharkharia, S. and R. Shankar, "IT enablement of supply chains: Modeling the enablers," *International Journal of Productivity and Performance Management*, 53, 700–712 (2004).

[35] Kahraman, C., U. Cebeci and D. Ruan, "Multi-attribute comparison of catering service companies using fuzzy AHP: The case of Turkey," *International Journal of Production Economics*, 87, 171–184 (2003).

[36] Kayakutlu, G. and G. Büyüközkan, "Effective supply value chain based on competence success," *Supply Chain Management: An International Journal*, 15, 129–138 (2010).

[37] Koh, S. C. L., S. M. Saad and S. Arunachalam, "Competing in the 21st century supply chain through supply chain management and enterprise resource planning integration," *International Journal of Physical Distribution & Logistics Management*, 36, 455–465 (2006).

[38] Lin, H., W. Lo and C. Chiang, "Using RFID in supply chain management for customer service," IEEE International Conference on Systems, Man, and Cybernetics, Oct. 8–11, Taipei, Taiwan (2006).

[39] Lockmay, A. and W. Smith, "Target costing for supply chain management: Criteria and selection," *Industrial Management and Data Systems*, 100, 210–218 (2000).

[40] Mehrjerdi, Y. Z., "Excellent supply chain management," *Assembly Automation*, 29, 52–60 (2009).

[41] Michelino, F., F. Bianco and M. Caputo, "Internet and supply chain management: Adoption modalities for Italian firms," *Management Research News Journal*, 31, 359–374 (2008).

[42] Mosey, S., "Understanding new to market product development in SMEs," *International Journal of Operations & Production Management*, 25, 114–130 (2005).

[43] Pandey, V. C. and S. Garg, "Analysis of interaction among the enablers of agility in supply chain," *Journal of Advances in Management Research*, 6, 99–114 (2009).

[44] Pawlak, M. and E. Malyszek, "A local collaboration as the most successful co-ordination scenario in the supply chain," *Industrial Management & Data Systems Journal*, 108, 22–42 (2008).

[45] Phusavat, K. and K. Kanchana, "Future competitiveness: Viewpoints from manufacturers and service providers," *Industrial Management & Data Systems*, 108, 191–207 (2008).

[46] Poon, T. C., K. L. Choy, H. K. H. Chow, H. C. W. Lau, F. T. S. Chan and K. C. Ho, "A RFID case-based logistics resource management system for managing order-picking operations in warehouses," *Expert Systems with Applications*, 36, 8277–8301 (2009).

[47] Prabhu, T. R. and K. Vizaya, "'Fuzzy hierarchical decision making method (FHDM)', A methodology for technology choice," *International Journal of Computer Application in Technology*, 9, 322–329 (1996).

[48] Sahay, B. S., J. N. D. Gupta and R. Mohan, "Managing supply chains for competitiveness: The Indian scenario," *Supply Chain Management: An International Journal*, 11, 15–24 (2006).

[49] Sarmah, S. P., D. Acharya and S. Goyal, "Buyer vendor coordination models in supply chain management," *European Journal of Operational Research*, 175, 1–15 (2006).

[50] Si, S., J. Takala and Y. Liu, "Competitiveness of Chinese high-tech manufacturing companies in global context," *Industrial Management & Data Systems*, 109, 404–424 (2009).

[51] Sila, I. and M. Ebrahimpour, "Critical linkages among TQM factors and business results," *International Journal of Operations & Production Management*, 25, 1123–1155 (2005).

[52] Singh, R. K., "Prioritizing the factors for coordinated supply chain using analytic hierarchy process (AHP)," *Measuring Business Excellence*, 17, 80–97 (2013).

[53] Singh, R. K. and M. K. Sharma, "Prioritising the alternatives for flexibility in supply chains," *Production Planning and Control*, 25, 176–192 (2014).

[54] Singh, R. K., S. K. Garg and S. G. Deshmukh, "Interpretive structural modelling of factors for improving competitiveness of SMEs," *International Journal of Productivity and Quality Management*, 2, 423–440 (2007a).

[55] Singh, R. K., S. Garg, S. G. Deshmukh and M. Kumar, "Modelling of critical success factors for implementation of AMTs," *Journal of Modelling in Management*, 2, 232–250 (2007b).

[56] Singh, R. K., S. K. Garg and S. G. Deshmukh, "Strategy development by SMEs for competitiveness: A review," *Benchmarking: An International Journal*, 15, 525–547 (2008).

[57] Sinha, P. R., L. E. Whitman and D. Malzahn, "Methodology to mitigate supplier risk in an aerospace supply chain," *Supply Chain Management: An International Journal*, 9, 154–168 (2004).

[58] Sun, S.-Y., M.-H. Hsu and W.-J. Hwang, "The impact of alignment between supply chain strategy and environmental uncertainty on SCM performance," *Supply Chain Management: An International Journal*, 14, 201–212 (2009).

[59] Tracey, M. and C. L. Tan, "Empirical analysis of supplier selection and involvement, customer satisfaction, and firm performance," *Supply Chain Management: An International Journal*, 6, 174–188 (2001).

[60] Tummala Rao, V. M., L. M. Cheryl Phillips and M. Johnson, "Assessing supply chain management success factors: A case study," *Supply Chain Management: An International Journal*, 11, 179–192 (2006).

[61] Vachon, S., A. Halley and M. Beaulieu, "Aligning competitive priorities in the supply chain: The role of interactions with suppliers," *International Journal of Operations & Production Management*, 29, 322–340 (2009).

[62] Varma, S., S. Wadhwa and S. G. Deshmukh, "Evaluating petroleum supply chain performance," *Asia Pacific Journal of Marketing and Logistics*, 20, 343–356 (2008).

[63] Weck, M., F. Klocke, H. Schell and E. Ruenauver, "Evaluating alternative production cycles using the extended fuzzy AHP method," *European Journal of Operational Research*, 100, 351–366 (1997).

[64] Wu, B. Y., C. H. Chi, Z. Chen, M. Gu and J. Sun, "Workflow-based resource allocation to optimize overall performance of composite services," *Journal of Production Economics*, 125, 199–212 (2009).

[65] Xia, L. X. X., M. Bin and R. Lim, "AHP Based Supply Chain Performance Measurement System", IEEE, Washington, DC, 1308–1315 (2007).

[66] Yadav, V. and M. K. Sharma, "An application of hybrid data envelopment analytical hierarchy process approach for supplier selection," *Journal of Enterprise Information Management*, 28 (*2*) (in press).

[67] Yang, J., "Supply chain agility: Securing performance for Chinese manufacturers," *International Journal of Production Economics*, 150, 104–113 (2014).

[68] Ye, F. and X. Xu, "Cost allocation model for optimizing supply chain inventory with controllable lead time," *Computers & Industrial Engineering* (in press).

[69] Zadeh, L. A., "The concepts of linguistic variable and its application to approximate reasoning," *International journal of Science*, 8, 199–249 (1975).

Downloaded by [Delhi Technological University] at 20:00 03 February 2015

International Journal of Scientific Engineering and Technology (ISSN : 2277-1581)
Volume No.4 Issue No.2, pp : 76-82 01 Feb2015

Synthesis and Characterization of Nano-Copper-Powder Based Magnetorheological Fluids for Brake

Chiranjit Sarkar[1], Harish Hirani[2]
[1]Mechanical Engineering Department, Delhi Technological University, Delhi – 110042
[2] Mechanical Engineering Department, Indian Institute of Technology Delhi, New Delhi - 110016
Corresponding Email: chiranjit.ju@gmail.com

Abstract: ***Magnetorheological (MR) fluids can be used as brake friction materials [1-6]. During braking, kinetic energy of machines gets converted into heat and shear thinning of MR fluid due to increase in temperature occurs which in turn reduces the braking effect. To lessen the effect of heat generation on MR fluids due to heat, synthesis of magnetorheological fluid using nano-copper-powder has been proposed. To explore the feasibility of incorporating copper powder, four carbonyl iron (CI) powder based MR fluids (without any copper powder, with 0.25% weight, 0.5% weight and 0.75% weight copper powder) have been synthesized. Yield stress of all four MR fluids have been estimated using magnetorheometer.***

A flywheel based MR brake experimental setup has been developed to analyze the performance of synthesized MR fluids. To increase the braking torque of MR brake, compression mode along with the shear mode has been introduced. The comparison of the braking torque in shear and compression modes has been presented. "T" type thermocouples have been used to measure the temperature distribution of the fabricated MR brake. Results of braking torque and corresponding temperature distribution are presented.

Keywords — **Magentorheological fluids; Nano – copper powder; Shear mode; Compression mode; Temperature distribution**

I. Introduction

MR fluid is a dispersion of micron sized pure iron particles in a non-magnetic fluid carrier [7, 8]. Under the presence of the magnetic field, particles form chains in the direction of magnetic flux and increase its yield stress. In MR brake [1-8], increase in fluid's yield stress restricts the rotational movement of disk and reduces the kinetic energy of the disk. The change in kinetic energy gets converted into heat that increases the temperature of MR fluid and shear thinning of MR fluid results. Shear thinning due to increase in temperature limits the usage of MR fluids in disk brakes [8-9].

The effects of temperature on the performance of MR devices have been explored by a number of researchers [8-10].In experimental study on MR brake by Wang et al. [8], torque reduction from 300 Nm to 180 Nm on increasing operating temperature from 30°C to 180°C was observed. Weiss et al. [9] experimentally found that on increasing temperature from - 40 to 150°C, the plastic viscosity and dynamic yield stress of the MR fluid decreased by 95 and 10%, respectively. Liao [10] witnessed sharp decay in the damping force of the MR damper when the temperature of the MR fluid increased from 20 to 80°C.To deal with shear thinning problem of MR devices due to heat, Wang et al. [8] proposed water cooling method. Dogruoz et al. [11] employed radiating fins in the shell to accelerate the heat dissipation from the MR fluid damper and control the temperature rise. Tian and Hou [12] proposed forced cooling of MR clutch. Zheng et al. [13] utilized rotary heat pipes to achieve forced cooling of the MR transmission device. Mistik et al. [14] synthesized and characterized MR fluids filled with spacer fabric. Their investigation showed that the thermal conductivity of the MR fluids with spacer fabric structures increased upon the application of magnetic field. In the present study, MR fluids with nano copper-powder have been synthesized to increase the heat transmission rate from the MR brake.

Four MR fluid samples have been synthesized using mechanical stirrer and then characterized using MCR-102 magnetorheometer at different temperatures. To confirm the outcome of synthesized MR fluids, a MR brake test rig has been developed; experiments have been performed; and the results of braking torque and temperature distribution are presented. The surface temperature of MR brake housing have been measured using eight thermocouples. The MR brake has been operated in "shear" and "compression assisted shear" modes as detailed in the literatures [1, 15]. The results of temperature distribution and torque using various MR fluids have been compared and presented.

II. Synthesis and Characterization

In this research work, four MR fluid samples have been synthesized using microns sized (3 to 394 microns) carbonyl iron (purity 99%) particles purchased from SIGMA ALDRICH. The particle size distributions were measured using HORIBA Laser Scattering Particle Size Distribution Analyzer LA-950.The probability volume density graph of iron particles are shown in Figure 1.For MR brake or clutches applications where two rotating bodies are relatively moving (mechanical stirring action), sedimentation is not a problem. One percent impurities, in iron sample, contain As: $\leq$5mg/kg, Cu: $\leq$100 mg/kg, Mn: $\leq$1000 mg/kg, Ni: $\leq$500 mg/kg, Pb: $\leq$20 mg/kg and Zn: $\leq$50 mg/kg.

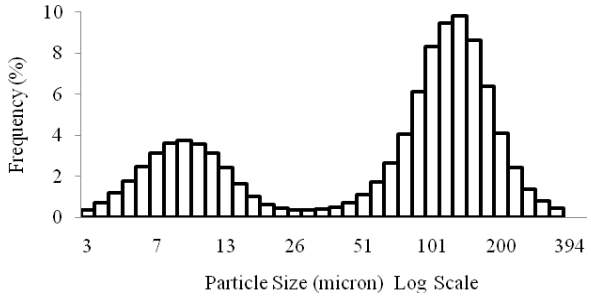

Fig 1.Probability volume density graph of particle sizes

First MR fluid sample MRF85 contains 14.5% by wt silicone oil, 0.5% by wt oleic acid, and 85% by wt carbonyl iron powder as indicated in Table 1. Similarly three other MR fluid samples contain 0.5% by wt oleic acid, 85% by wt carbonyl iron powder, specification of which is listed in Table 1.

Table 1.MR fluid compositions

MR fluids samples	Silicone Oil (% by wt.)	Iron particle (% by wt)	Oleic acid (% by wt)	Cu nano powder (% by wt)
MRF85	14.50	85	0.50	0
MRF85_0.25Ag	14.25	85	0.50	0.25
MRF85_0.50Ag	14	85	0.50	0.50
MRF85_0.75Ag	13.75	85	0.50	0.75

Copper nano-powder suspensions, purchased from Reinste Nano Ventures, contains copper particle size of 40±5 nm in ethanol (30 % by weight) and metal impurities lesser than 0.1% including Fe (<0.02%). The shear stress of MRF85, MRF85_0.25Cu, MRF85_0.50Cu and MRF85_0.75Cuat various magnetic fields measured using magnetorheometer ANTON PAAR MCR-102, are plotted in Figure 2. The shear stress of each sample was measured thrice. From figure 2, it can be inferred that the shear stress of all four MR fluids samples lie within the error bar. There is no significant variation in the stress values. To explore the spread of copper on iron particles, SEM and EDX of MR particles was performed.

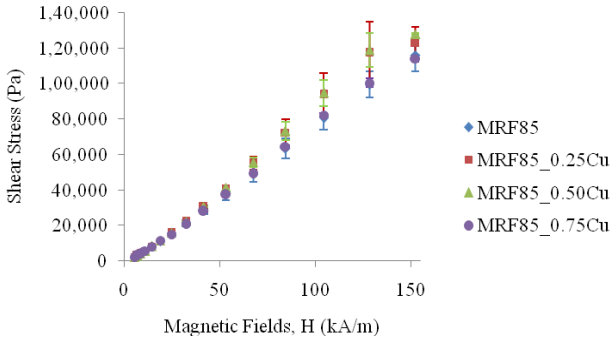

Fig 2.Shear stress of MR fluids at various magnetic fields

The scanning electron micro scope photographs of iron particles (Sigma Aldrich) are shown in Figure 3(a). These iron particles of different sizes are nearly spherical in shape. The iron particles extracted from MRF85_0.75Cu, and the scanning electron microscopic photograph of this iron particles have been captured and shown in Figure 3(b). It shows that Cu nano powder make a layer over the iron particles. Figure 4 shows EDX analysis of extracted iron particles from MRF85_0.75Cu. It confirms the presence of Cu nano powder with the iron particles.

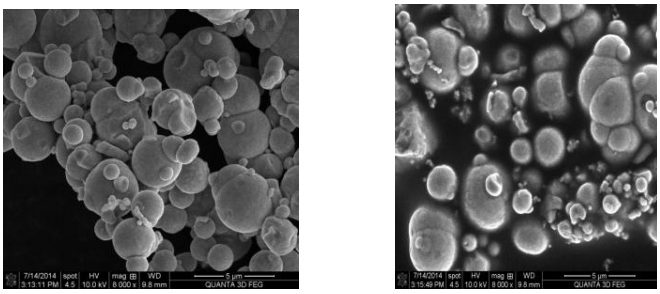

(a) Iron particles (Sigma Aldrich) (b) Iron particles coated with Cu nano-powder

Fig 3.Scanning electron microscopic photograph of iron particles coated and uncoated

To observe the effect of temperature rise on the shear stress of MR fluids, all four samples were subjected to temperature 30, 35, 40, 45, 50 and 55 degree centigrade. The results of shear measured at those samples are plotted in Figure 5.

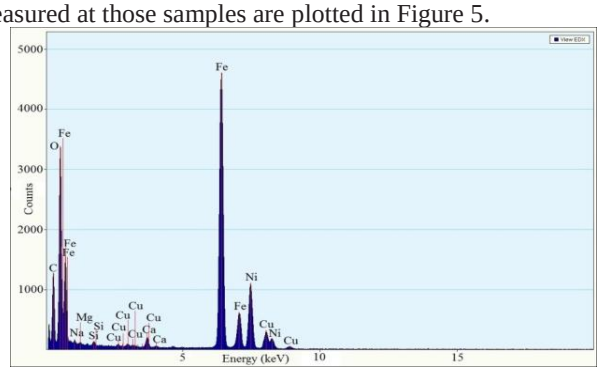

Fig 4.EDX analysis of extracted iron particles from MRF85_0.75Cu

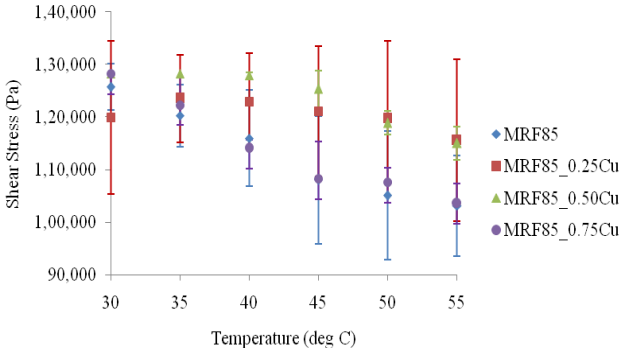

Fig 5.Thinning of MR fluids at different temperatures

Figure 5 shows the thinning behaviour of the four MR fluids with increase in temperature. It can be said that shear stress of all MR fluids decreases with increase in temperature. To validate the shear stress results of MR fluids, performance of MR brake has been carried in experimental test rig.

International Journal of Scientific Engineering and Technology (ISSN : 2277-1581)
Volume No.4 Issue No.2, pp : 76-82 01 Feb2015

III. Design and development of MR brake operating under shear and compression assisted shear modes

A schematic of proposed MR brake is shown in Figure 6. Rod seal has been used to stop the leakage of MR fluid. The stator is mounted on the bearing. A side electromagnet has been used to slide the housing plate towards the disk to compress the MR fluid. Both the stator and housing plates are made of low carbon steel. The shaft is made of stainless steel.

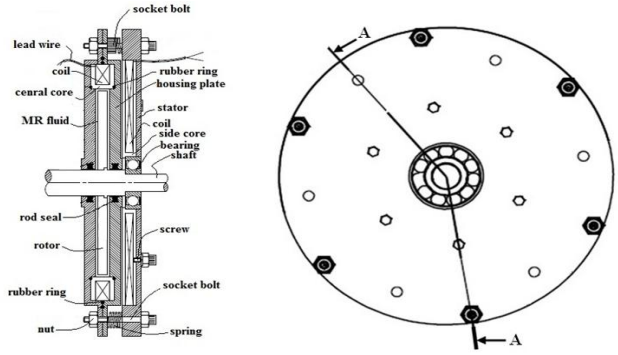

Fig 6.Schematic drawing of MR brake

A schematic of MR brake, developed in the present study has been shown in Figure 7. Initially, in the absence current supply in the coil of central core, MR particles remain uniformly distributed in the fluid as shown in Figure 7. Figure 8 depicts the alignment of MR particles in the direction of magnetic field when the current is supplied in the central electromagnet. These MR particles make chains/clusters to resist the motion of disk and such braking action from MR brake is named as "shear mode" of MR brake.

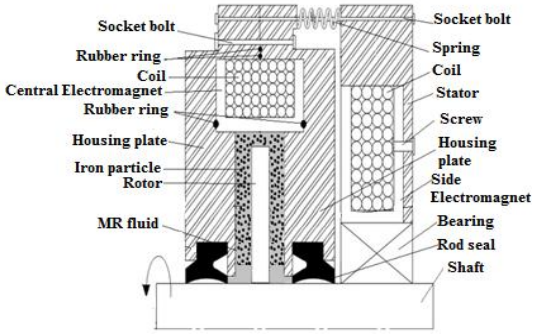

Fig 7.Random distribution of iron particles

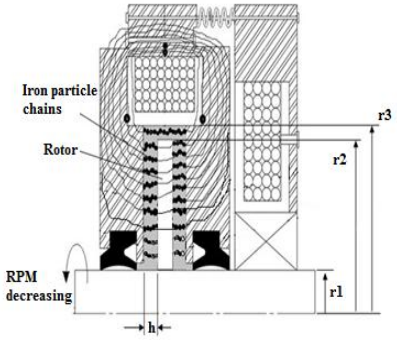

Fig 8.Chain of iron particle in MR brake

When current is gradually applied in the side electromagnet, the stator acts as a magnet and the housing plate assembly acts as an armature which slides in the direction Da by compressing the springs as shown in Figure 9. When current is applied in the central electromagnet, compressed iron particles make stronger chains in compression zone and weak chain in expansion zone. Such braking action is named as "compression assisted shear mode" of MR brake.

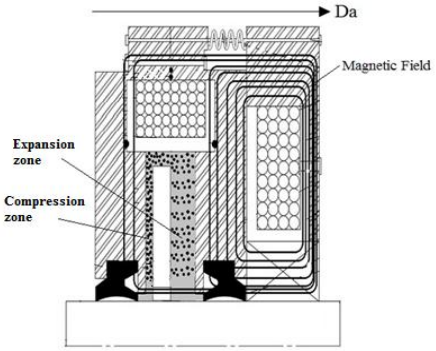

Fig 9.Iron particle after compression

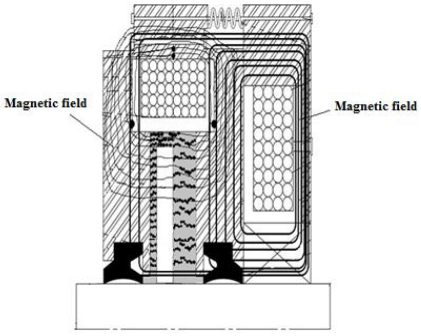

Fig 10.Iron particle chain after compression

IV. Experimental study on MR brake

The block diagram of the MR brake test rig is shown in Figure 11. It comprises of 3-phase 5-HP D.C. motor with speed controller, jaw coupling, a flywheel (20kg), and MR brake through bearing brackets. A D.C. (30 V and 5 A) power supply has been used to regulate the current in the electromagnet of MR brake. A tachometer has been used to measure the rotational speed. A number of experiments at various operating conditions (magnetic field 0 to 300 kA/m and speed 200 and 600 rpm) have been performed.

After completing each experiment, a table fan was used to reduce the time to cool brake back to the room temperature. Figure 12 displays the MR brake test rig. Figure 13 illustrates the position of the thermocouples on surface of the MR brake housing. Eight thermocouples have been used to measure the localized temperature on the surface of the housing of MR brake. The rotor has inner radius (r1) 10 mm and outer radius (r2) 44 mm. Three thermocouples has been installed at minimum P.C.D (24mm) and five thermocouples has been installed at the maximum P.C.D (80mm) on the housing surface at equal distance so that the temperature can be measured at the

International Journal of Scientific Engineering and Technology (ISSN : 2277-1581)
Volume No.4 Issue No.2, pp : 76-82 01 Feb2015

housing surface area where MR fluids make a chain between the housing and rotor.

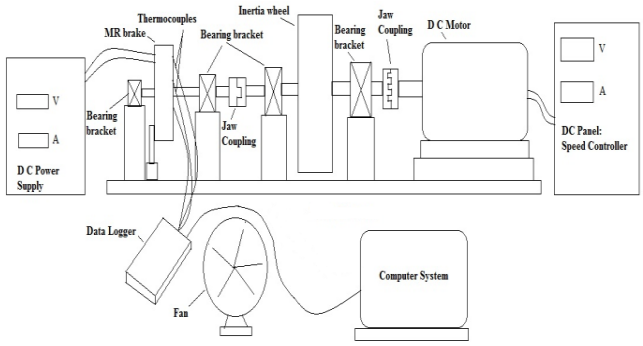

Fig 11.Schematic diagram of the MR brake test rig

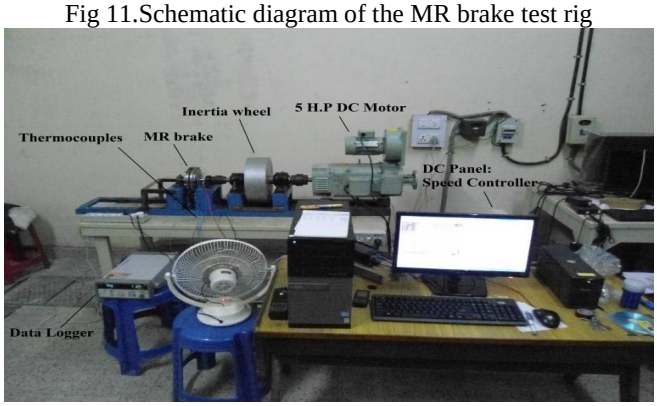

Fig 12.Photograph of MR brake test rig

The present setup can be used to find braking torque under "shear mode" as well as "compression assisted shear mode". To evaluate the brake torque and temperature rise at any particular speed (i.e. 200 rpm, 600 rpm) in shear mode, following procedure have been charted:

- Maintain the motor speed at the specified rpm using speed controller. Record the readings of voltmeter and ammeter to estimate the power supplied. Use the tachometer to measure the speed of the brake shaft.
- Supply current to the central electromagnet of MR brake. In the presence of magnetic field, MR brake reduces the speed of the motor.
- Increase the voltage of the speed controller to maintain the specified speed (RPM) of the MR brake shaft. Record the new readings the voltmeter and ammeter to estimate the final supplied power. Estimate braking torque using $BT = \left(PW_f - PW_i\right)/\omega$. Here, PW_i and PW_f are initial and final power loss; ω is the specified angular speed.
- After stabilization of temperature, record the readings of thermocouples in the desktop computer using data logger.
- Switch off the power supply to the electromagnet and reduce the RPM of the DC motor to zero.
- Switch on table fan to cool the MR brake to get back to initial temperature. Repeat the same procedure for another experiment (different current to electromagnet and different motor speed).
- Similar procedures have been used to find braking torque "compression assisted shear mode" except one additional step of supplying the desired current in the side electromagnet to compress the MR fluid and then supplying the desired current in central electromagnet.

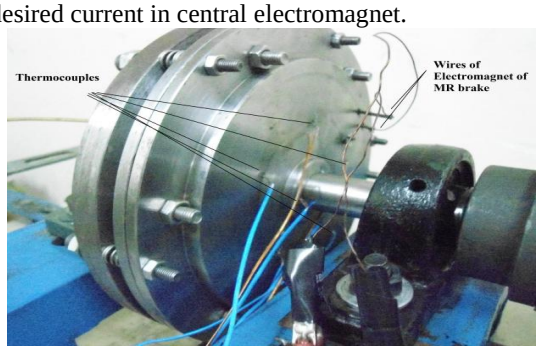

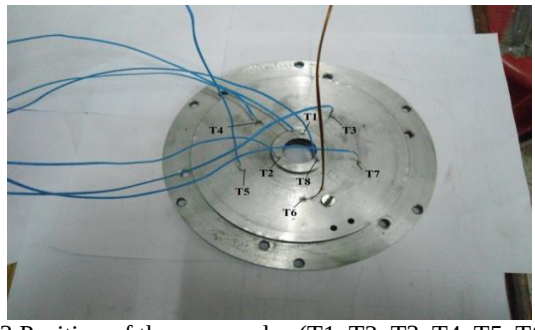

Fig 13.Position of thermocouples (T1, T2, T3, T4, T5, T6, T7, T8) on the surface of the brake housing

V. Results and Discussions

Figures 14 shows the braking torque and surface temperature of the MR brake housing using two MR fluids (MRF85 and MRF85_0.25Cu) in shear mode at 200 RPM. For both the fluids increase in braking torque as well as temperature with increase in current supplied to the central electromagnet can be noticed. It is important to notice that the braking torque for both MR fluids is same. Temperature of the MR brake containing MRF85 is higher than that of MRF85_0.25Cu. This proves that the heat transfer rate of the MRF85_0.25Cu is higher than that of MRF85.

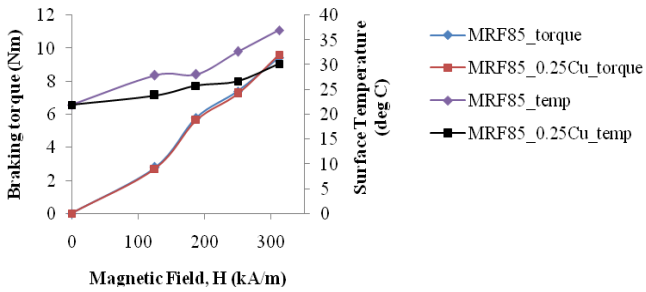

Fig 14.Braking torque and surface temperature in shear mode at 200 RPM

Figure 15 shows the braking torque and surface temperature of the MR brake in "compression assisted shear mode" at 200 RPM. As per the Figure 15, there is insignificant difference in torque exerted using MRF85 and MRF85_0.25Cu based MR brakes. It is worth noting that braking torques under "compression assisted shear mode" (Figure 15) are higher compared to that obtained under shear mode (Figure 14). Another important observation is reduction in surface temperature in "compression assisted shear mode" compared to "shear mode" of MR brake. This indicates that due to compression of MR fluids, heat dissipation rate increases. The heat transfer mechanism of compressed iron particles of MR fluids is shown in Figure 16.

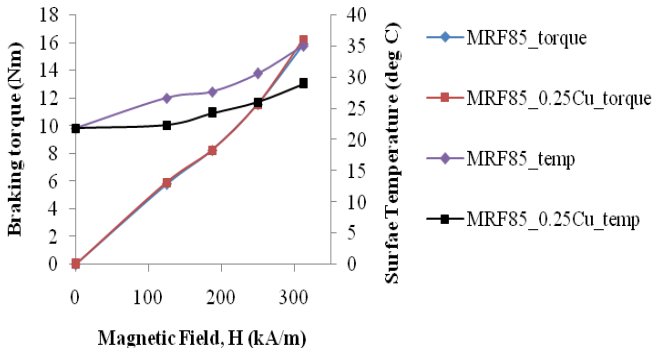

Fig 15.Braking torque and surface temperature in compression assisted shear mode at 200 RPM

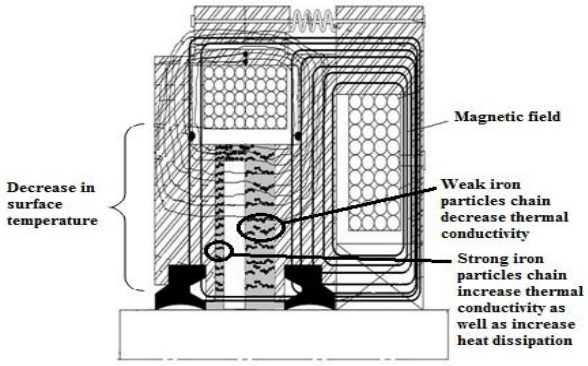

Fig 16.Heat Transfer mechanism of MR brake

At 200 RPM, the braking torque of MR brake in shear mode for MRF85 and MRF85_0.25Cu are 9.45 Nm and 9.62 Nm respectively. The surface temperature for MRF85 and MRF85_0.25Cu are 37.04°C and 30.18°C in shear mode. In compression assisted shear mode, the braking torque of MR brake for MRF85 and MRF85_0.25Cu are 15.89 Nm and 16.26 Nm respectively, whereas the surface temperature for MRF85 and MRF85_0.25Cu are 35.07 °C and 28.94°C respectively. There is 1.79% increase in braking torque with 22.73% decrease in surface temperature using copper nano powder in MR fluids in shear mode at 200 RPM and 2.23 % increase in braking torque with 17.49 % decrease in surface temperature in "compression assisted shear mode".

In order to capture the performance of MR brake at higher speed, experiments were performed at 600 rpm speed. The braking torque and surface temperature in "shear mode" and "compression assisted shear mode", have been measured and plotted in Figure 17 and Figure 18. At 600 RPM, the braking torque in shear mode for MRF85 and MRF85_0.25Cu are 7.67 Nm and 7.74 Nm respectively. The surface temperature for MRF85 and MRF85_0.25Cu are 54.05°C and 45.32°C in shear mode. In compression assisted shear mode, the braking torque of MR brake for MRF85 and MRF85_0.25Cu are 9.31 Nm and 9.67 Nm respectively, whereas the surface temperature for MRF85 and MRF85_0.25Cu are 41.89°C and 38.82°C respectively. It shows that the braking torque decreases with increase in the speed.

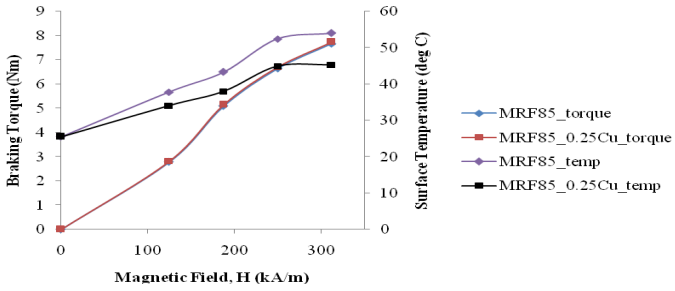

Fig 17.Braking torque and surface temperature in shear mode at 600 RPM

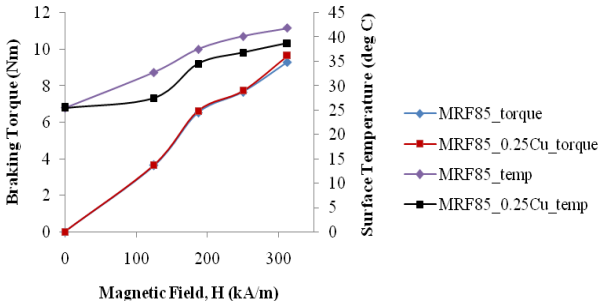

Fig 18.Braking torque and surface temperature in compression assisted shear mode at 600 RPM

To observe the effect of 0.50% Cu and 0.75% Cu, the experiments on MR brake using MRF85_0.50Cuand MRF85_0.75Cu have been performed. Figure19 and Figure 20 show the braking torque and maximum surface temperature of housing using four MR fluid samples at 600 RPM in "shear" and "compression assisted shear" modes, respectively. The braking torque and maximum localized surface temperature for MR brake containing MRF85, MRF85_0.25Cu, MRF85_0.50Cu and MRF85_0.75Cu are 7.67 Nm, 7.74 Nm, 7.74 Nm and 7.70 Nm respectively in shear mode and 54.05°C, 45.32°C, 41.45°C and 38°C respectively. The braking torque and maximum localized surface temperature using MRF85, MRF85_0.25Cu, MRF85_0.50Cu and MRF85_0.75Cu are 9.31 Nm, 9.67 Nm, 9.67 Nm and 9.54 Nm respectively in compression assisted shear mode and 41.89°C, 38.82°C, 37.77°C and 36.12°C respectively.

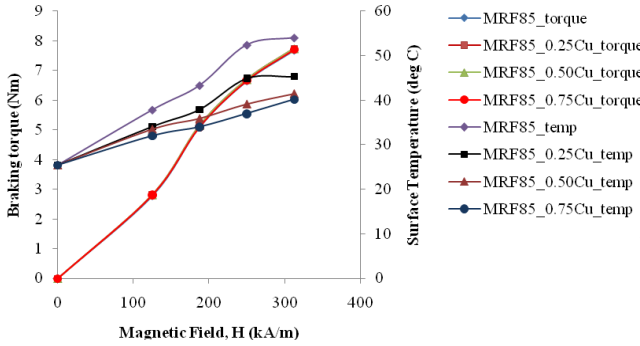

Fig 19.Braking torque and surface temperature using four different MR fluids in shear mode at 600 RPM

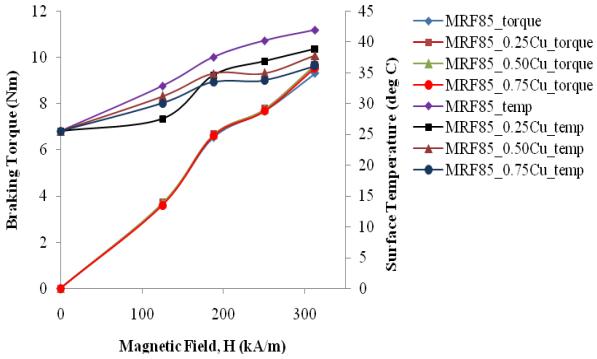

Fig 20.Braking toque and surface temperature using four different MR fluid samples in compression assisted shear mode at 600 RPM

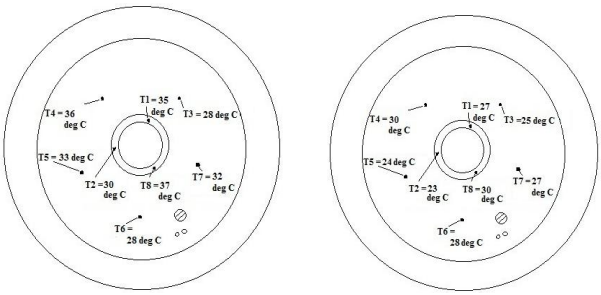

(a) MRF85 (b) MRF85_0.25Cu

Fig 21.Thermocouple readings using MRF85 and MRF85_0.25Cu at 200 RPM

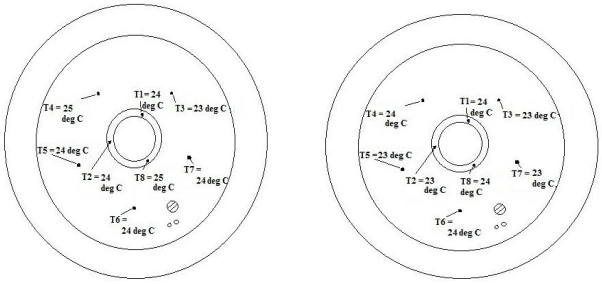

(a) MRF85_0.50Cu (b) MRF85_0.75Cu

Fig 22.Thermocouple readings using MRF85_0.50Cu and MRF85_0.75Cu at 200 RPM

Figure 21 and Figure 22 show the thermocouple readings (at maximum magnetic field in shear mode) using MRF85 and MRF85_0.25Cu samples at 200 RPM; using MRF85_0.50Cu and MRF85_0.75Cu samples at 200 RPM respectively. Figure 23 and Figure 24 show the thermocouple readings (at maximum magnetic field in shear mode) using MRF85 and MRF85_0.25Cu samples at 600 RPM; using MRF85_0.50Cu and MRF85_0.75Cu samples at 600 RPM respectively. On the basis of Figure 21, Figure 22, Figure 23 and Figure 24 it can be said that increase in percentage (0 to 0.75) of copper nano-powder reduces the temperature of brake surface. The maximum temperature of the surface MR brake in shear mode without Cu nano-powder is 54°C while the maximum temperature of MR brake with 0.75% Cu nano-powder is 40.15°C. It can be said that the nano-copper powder increases the heat transfer rate of MR fluid. This method of cooling MR fluid is economic and better (in terms of required geometrical space) than other cooling methods [5, 8-10]. The Cu based MR fluids shall be used if there is a need to impart the cooling capabilities in MR fluid devices. The variation of the temperature of thermocouples indicates that there is some misalignment between the disk and MR brake housing.

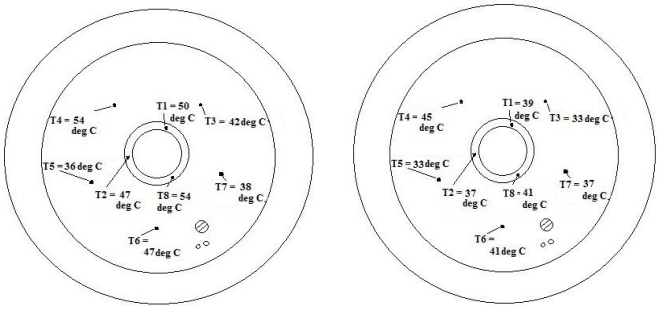

(a) MRF85 (b) MRF85_0.25Cu

Fig 23.Thermocouple readings using MRF85 and MRF85_0.25Cu at 600 RPM

VI. Conclusions

In the present manuscript effects of copper nano powder on the shear stress and heat transfer rate of MR fluid have been explored. Four MR fluid samples were synthesized. Shear stresses of all synthesized MR fluids at various temperatures were measured using MCR-102 magnetorheometer. Each experiment was repeated thrice and no significant change in shear stress due to mixing of MR fluid was observed. In other words, shear stress of MR fluids does not decrease with increase in weight percentage of copper nano-powders. To observe the increase in heat transfer rate due to mixing of copper nano powder, MR brake test rig was been developed. Experiments performed on MR brake rig indicate that on increasing copper nano-powder percentage, surface temperature of MR brake decreases. Based on these results it can be concluded that the use of Cu nano-powder is effective cooling method. It does not require any extra space to cool the MR brake. The Cu based MR fluids shall be used if there is a

need to impart the cooling capabilities in MR fluid devices.

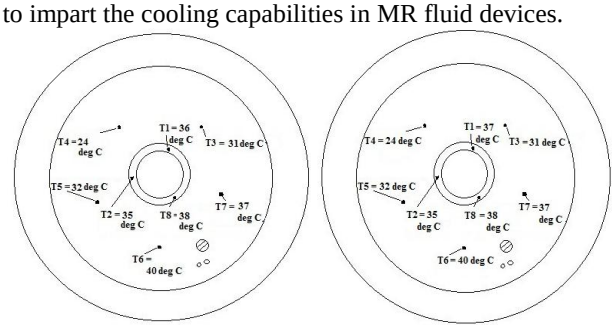

(a) MRF85_0.50Cu (b) MRF85_0.75Cu

Fig 24.Thermocouple readings using MRF85_0.50Cu and MRF85_0.75Cu at 600 RPM

REFERENCES

i. *Sarkar, C. and Hirani, H. Theoretical and experimental studies on a magnetorheological brake operating under compression plus shear mode, Smart Mater. Structure, 2013, 22, 115032 (12pp).*

ii. *Sarkar, C. and Hirani, H. Synthesis and characterization of antifriction magnetorheological fluids for brake, Defence Science Journal, 2013, 63, 408-12.*

iii. *Sukhwani, V. K. and Hirani, H. Design, development and performance evaluation of high speed MR brake, Proc. Institute Mech. Engineers., Part L, Journal of Materials: Design and Applications, 2008, 222, 73-82.*

iv. *Sukhwani, V. K.; Lakshmi, V. and Hirani, H. Performance evaluation of MR brake: an experimental study, Indian Journal of Tribology, 2006, 1, 47-52.*

v. *Karakoc, K.; Park, E. J. and Suleman, A. Design considerations for an automotive magnetorheological brake, Mechatronics, 2008, 18, 434–47.*

vi. *Li, W. H. and Du, H. Design and experimental evaluation of a magnetorheological brake, Int. J. Adv. Manuf. Technol., 2003, 21, 508–15.*

vii. *Nam, T. H. and Ahn, K. K. A new structure of a magnetorheological brake with the waveform boundary of a rotary disk, Smart Mater. Struct., 2009,18, 115029 (14pp)*

viii. *Wang, D. M.; Hou, Y. F.; and Tian, Z. Z. A novel high-torque magnetorheological brake with a water cooling method for heat dissipation, Smart Mater. Struct., 2013, 22, 025019 (11pp).*

ix. *Wiess, K. D. and Duclos, T. G. Controllable fluids: the temperature dependence of post-yield properties., Int. J. Mod. Phys. B.,1994, 8, 3015-32.*

x. *Liao, C. R. Study on Magnetorheological Fluid Damper for Automobile Suspension System, 2001 (Chongqing: Chong Qing University) (in Chinese)*

xi. *Dogruoz, M. B.; Gordaninejad, F.; Wang, E. L. and Stipanovich, A. J. Heat transfer from fail-safe magnetorheological fluid dampers, Proc. SPIE Conf. Smart Mater.Struct., 2001, 4331, 343–353.*

xii. *Tian, Z. Z. and Hou, Y. F. A double-disk magnetorheological clutch, CN Patent Application 201110041597, 2011.*

xiii. *Zheng, J.; Zhang. G. H. and Cao, X. J. Design and experiment for magnetorheological transmission device with heat pipes, Chin. J. Mech. Eng., 2009, 45, 305–311.*

xiv. *Mistik, S. I.; Shah, T.; Hadimani, R. L. and Siores, E. Compression and thermal conductivity characteristics of magnetorheological fluid–spacer fabric smart structures, J. Int. Mater. Syst. and Struct., 2012, 23, 1277-1283.*

xv. *Sarkar, C. and Hirani, H. Design of a squeeze film magnetorheological brake considering compression enhanced shear yield stress of magnetorheological fluid, Journal of Physics: Conference Series, 2013, 412, 012045 (12pp).*

Theoretical modeling of temperature dependent catalyst-assisted growth of conical carbon nanotube tip by plasma enhanced chemical vapor deposition process

Aarti Tewari and Suresh C. Sharma

Citation: Physics of Plasmas (1994-present) **22**, 023505 (2015); doi: 10.1063/1.4906876
View online: http://dx.doi.org/10.1063/1.4906876
View Table of Contents: http://scitation.aip.org/content/aip/journal/pop/22/2?ver=pdfcov
Published by the AIP Publishing

Articles you may be interested in

Role of plasma activation in kinetics of carbon nanotube growth in plasma-enhanced chemical vapor deposition
J. Appl. Phys. **111**, 074307 (2012); 10.1063/1.3699310

Transition from single to multi-walled carbon nanotubes grown by inductively coupled plasma enhanced chemical vapor deposition
J. Appl. Phys. **110**, 034301 (2011); 10.1063/1.3615945

Different growth mechanisms of vertical carbon nanotubes by rf- or dc-plasma enhanced chemical vapor deposition at low temperature
J. Vac. Sci. Technol. B **28**, 1081 (2010); 10.1116/1.3497030

Effect of hydrogen on catalyst nanoparticles in carbon nanotube growth
J. Appl. Phys. **108**, 053303 (2010); 10.1063/1.3467971

Formation of carbon nanotubes by plasma enhanced chemical vapor deposition: Role of nitrogen and catalyst layer thickness
J. Appl. Phys. **92**, 6188 (2002); 10.1063/1.1515126

This article is copyrighted as indicated in the article. Reuse of AIP content is subject to the terms at: http://scitation.aip.org/termsconditions. Downloaded to IP: 14.139.251.107 On: Mon, 16 Feb 2015 05:06:34

PHYSICS OF PLASMAS **22**, 023505 (2015)

Theoretical modeling of temperature dependent catalyst-assisted growth of conical carbon nanotube tip by plasma enhanced chemical vapor deposition process

Aarti Tewari and Suresh C. Sharma
Department of Applied Physics, Delhi Technological University (DTU), Shahbad Daulatpur, Bawana Road, Delhi 110 042, India

(Received 3 November 2014; accepted 7 January 2015; published online 10 February 2015)

A theoretical model has been developed to examine the effect of substrate temperature on the growth of the conical carbon nanotube (CNT) tip assisted by the catalyst in a reactive plasma. The growth rate of the CNT with conical tip because of diffusion and accretion of ions on catalyst nanoparticle including the charging rate of the CNT, kinetics of plasma species, and the evolution of the substrate temperature in reactive plasma has been taken into account. The effect of substrate temperature for different ion densities and temperatures on the growth of the conical CNT tip has been investigated for typical glow discharge plasma parameters. The results of the present model can serve as a major tool in better understanding of plasma heating effects on the growth of CNTs.
© *2015 AIP Publishing LLC*. [http://dx.doi.org/10.1063/1.4906876]

I. INTRODUCTION

Plasma enhanced chemical vapor deposition (PECVD) has been one of the best techniques to produce multi-walled carbon nanotubes (MWCNTs) on the patterned substrate. The nanofibres produced by PECVD are vertically aligned[1,2] which can be either free standing or forest like.

CNTs prepared by PECVD are expected to have lesser growth temperatures than those by CVD. As the plasma dissociates the feedstock gas, more and more number of carbon radicals and higher stable hydrocarbons become readily available for nanotube growth.[3] In recent years, during the growth of CNTs by PECVD, an external heating source beneath the substrate has been used for substrate heating.[1,2,4] There have been works, where the external source for the substrate heating was not used.[5,6]

Teo *et al.*[7] have synthesized straight and well-aligned carbon nanofibres (CNFs) by a substrate exposed to the plasma in a simple, parallel plate dc PECVD reactor for nanotube growth and it heats up to high temperatures (700 °C) without the aid of an external heater.

The present work aims to investigate the mechanism by which feedstock gas in PECVD chamber leads to an increase in substrate temperature and the effect of increase of substrate temperature on the growth rate of CNTs.

The temperature has been identified to play an important role in the growth of catalyst-assisted growth of CNTs. Numerous works have been done to highlights the role of temperature on the growth of CNTs.[8–15]

Han *et al.*[8] have demonstrated that as the growth temperature increases, the average diameter of CNTs increased from 40 to 110 nm and the growth rate was enhanced from 2 to 15 μm/h.

Baratunde *et al.*[9] have shown that as the growth temperature was decreased, the associated decrease in CNT density and average CNT diameter resulted in an increased thermal resistance at the interface.

Lee *et al.*[10] have demonstrated that the growth rate and the average diameter increase nonlinearly with temperature. The growth rate enhances from 1.6 μm/min by a factor of 18 and the average diameter increases from 20 to 150 nm for the temperature rise from 800 to 1100 °C.

Loffler *et al.*[11] have shown that at higher temperatures of the substrate and catalyst the hydrocarbon gas dissociates faster, aided by the catalyst. A higher diffusion rate of carbon atoms through the catalytic particle can be expected, which results in considerably longer CNTs at the same growth time.

The motivation for the present article stems from the recent works where the dependence of growth rate of nanostructures on various parameters including substrate temperatures, electron and ion densities, the flux ratio of etching and hydrocarbon ions, etc., has been widely studied.[12–15]

Denysenko *et al.*[12] have studied the growth of single walled CNTs (SWCNTs) in a PECVD using the surface deposition model. In this case, it was shown that at low substrate temperatures (1000 K), the atomic hydrogen and ion fluxes from the plasma could strongly affect the nanotube growth.

Mehdipour *et al.*[13] have studied the growth rate of carbon nanofibre as a function of substrate temperature for different electron and ion temperatures. They have observed that the growth rate as a function of substrate temperature increases as ion and electron temperatures are increased.

Denysenko and Ostrikov[14] have described the plasma-assisted growth of CNFs that accounts for the nanostructure heating by ion and etching gas fluxes from the plasma. They have shown that fluxes from the plasma environment can substantially increase the temperature of the catalyst nanoparticle located on the top of the CNF with respect to the substrate temperature.

More recently, Burmaka *et al.*[15] have shown that the growth rates of SWCNT array and the film between the nanotubes, as well as the length of SWCNTs can be

 © 2015 AIP Publishing LLC

This article is copyrighted as indicated in the article. Reuse of AIP content is subject to the terms at: http://scitation.aip.org/termsconditions. Downloaded to IP: 14.139.251.107 On: Mon, 16 Feb 2015 05:06:34

successfully controlled by adjusting neutral and ion fluxes to the nanotubes, SWCNT surface temperature and the penetration depths of the neutral and ionic species.

Tips of CNT grown by PECVD are seen to have various shapes. Conical tip CNTs have been obtained by many researchers.[16–18]

Srivastava *et al.*[16] have obtained films containing randomly oriented conical CNTs with varying length and density were grown on Si substrates by microwave PECVD (MPECVD) process at relatively low temperature by judicious control of the process parameters such as microwave power and growth time.

The detailed mechanism of the growth of carbon nanotube in plasma medium assisted by the catalyst–substrate surface has been demonstrated by Tewari and Sharma.[19] In this case, the substrate temperature was taken as a constant during the growth process. In the present paper, we are studying the effect of substrate temperatures on the growth of catalyst-assisted growth of the CNT (both the cylindrical CNT surface and conical CNT tip) in the reactive plasma medium.

In Sec. II, a theoretical model is developed involving energy balance of catalyst particle, growth rate equation of the CNTs, and kinetics of various plasma species. Results and discussions are given in Sec. III. Finally, conclusion is given in Sec. IV.

II. MODEL

Consider a catalyst particle of nickel (Ni) over the substrate of silicon (Si) in a plasma chamber. The plasma is composed of ions of acetylene (C_2H_2) and hydrogen (H_2), neutrals of acetylene and hydrogen, and electrons. The ions of acetylene and hydrogen are designated as A and B ions, respectively. In Argon (Ar) + H_2 + C_2H_2 plasma, C_2H_2 acts as a carbon source gas.

The main processes for the CNT growth over the catalyst-substrate surface in plasma considered in the present model are:

(1) It is assumed that the applied plasma power ionizes the gas within the chamber, thereby creating plasma species of relatively higher energy. These highly energetic ions initiate the fragmentation of catalyst particle to form catalyst nanoparticle, which then seed nanotube growth on them.
(2) The acetylene ions traverses through the plasma sheath to the catalyst-substrate surface and then thermal dissociation, ion induced dissociation, and decomposition of positively charged ions, interaction of adsorbed acetylene ions with atomic hydrogen from plasma, thermal dissociation of carbon source gas of acetylene ions, and other processes occurs to finally result in the adsorption, surface diffusion, and accretion of acetylene ions to determine the height of growing CNT.
(3) Then, there is decomposition of positively charged hydrogen ions, incorporation of hydrogen ions due to thermal dissociation of acetylene ions, and the diffusion of hydrogen ions into catalyst–substrate surface. The hydrogen ions effectively shape the nanoparticle tip due to etching effects.

In Table I, the assumed processes in the model that occur during CNT growth in a PECVD chamber with their corresponding terms are given.

The electric field is directed towards z-axis. Following Tewari and Sharma,[19] the continuity equation

$$\left(\hat{i}\frac{\partial}{\partial x}+\hat{j}\frac{\partial}{\partial y}+\hat{k}\frac{\partial}{\partial z}\right).(n_j u_j)=\nu_{iz}n_e, \tag{1}$$

where n_e = number density of electron; ν_{iz} = ionization frequency; u_j = fluid velocity of electrons, $C_2H_2^+$, Ar^+ and H^+; n_j = number density of electrons, $C_2H_2^+$, Ar^+, and H^+. The ion momentum balance equation

$$Mn_j u_j\frac{du_j}{dz}=en_jE-Mn_j\nu_{jn}u_j, \tag{2}$$

where M is the mass of ions in plasma, ν_{jn} is the collision frequency, and E is the electric field.

Using Poisson's equation, we determine potential within the sheath

$$\frac{d^2\phi}{dz^2}=-4\pi\Sigma q_j\delta_j n_j, \tag{3}$$

where $\delta_j\left(=\frac{n_{ij}}{n_e}\right)$ is the j_{th} ion to electron number density ratio and ϕ is the electrostatic potential, i.e., $\sum_j\delta_j=1$ and $0<\delta_j<1$ as electron density is greater in plasma bulk than in sheath.

A. Energy balance equation for catalyst particle

Initially, a catalyst particle Ni of radius 30 nm is considered to be placed over a silicon substrate surface.

As Srivastava *et al.*[20] highlight that an increase in microwave power causes more ionization of the gas, which increases the density of plasma species of relatively higher energy. Following experimental results of Srivastava *et al.*,[20] we assume that as the applied rf power increases, it ionizes the gas more which creates more energetic ions, which implies that plasma species of relatively higher energy are created. Since energy of ions corresponds to the number density and temperature of ions, we assume that with an increase in rf power the number density and temperature of plasma species increases.

These highly energetic ions then accretes at the surface of catalyst particle and any increase in their number density and temperature results in catalyst particles of smaller radii

$$\begin{aligned} rfpower &= \frac{d}{d\tau}(C_p m_p T_s)\\ &= \left[n_{iActP}\left(\varepsilon^s{}_{iAc}+I_{pA}\right)+n_{iBctP}\left(\varepsilon^S{}_{iBc}+I_{pB}\right)\right]\\ &\quad -\left(\frac{3}{2}k_B\right)[(1-\gamma_{Ai})n_{iActP}+n_{iBctP}]T_S\\ &\quad -4\pi r_P^2\varepsilon\sigma\left(T_S^4-T_a^4\right), \end{aligned} \tag{4}$$

where $m_p\left(=\frac{4}{3}\pi r_P^3\rho_P\right)$ is the mass of catalyst particle and r_p is the radius of catalyst particle. ρ_P is the mass density of catalyst particle, C_p is the specific heat of catalyst particle (Ni) and is 0.44 KJ/Kg K, and T_s is the substrate temperature. I_{pA}

This article is copyrighted as indicated in the article. Reuse of AIP content is subject to the terms at: http://scitation.aip.org/termsconditions. Downloaded to IP: 14.139.251.107 On: Mon, 16 Feb 2015 05:06:34

TABLE I. Outline of the main processes during the growth of catalyst-assisted CNT in the plasma medium, considered in the present model.

Assumed processes in the model that occur during CNT growth in a PECVD chamber	Corresponding terms
1.Thermal dissociation of C_2H_2 ions[13]	$2n_{CH}\nu\exp\left(\frac{-\delta E_t}{k_B T_s}\right)$
2. Ion Induced dissociation of C_2H_2[13]	$2\theta_{CH} j_{iA} y_d$
3. Decomposition of positively charged acetylene ions[13]	$2j_{iA}$
4. Interaction of acetylene ions atomic hydrogen[14]	$\frac{j_{iA}\sigma_{ads} j_{iB}}{\nu}$
5. Incoming flux of carbon atoms[13]	j_c
6. Adsorption of C_2H_2 ions to the catalyst-substrate surface[13]	$j_{iA}(1-\theta_t)$
7. Thermal dissociation of C_2H_2[13]	$j_{iA}\exp\left(\frac{-\delta E_t}{k_B T_s}\right)$
8. Accretion of neutral acetylene atoms to the cylindrical surface of CNT[19]	$\gamma_{C_2H_2}\pi r_P^2 n_{C_2H_2 ctcys}$
9. Diffusion of hydrogen atom into catalyst-substrate surface[13]	$j_{iB}\exp\left(\frac{-E_b}{k_B T_s}\right)$
10. Incoming flux of hydrogen due to the dehydrogenation of C_2H_2[13]	$j_{iB}\exp\left(\frac{-\delta E_{th}}{k_B T_s}\right)$
11. Adsorption of hydrogen ions to the catalyst-substrate surface[14]	$j_{iB}(1-\theta_t)$
12. Decomposition of hydrogen ions[14]	j_{iB}
13. Ion induced dissociation of hydrogen[13]	$\theta_{CH} j_{iB} y_d$
14. Incorporation of hydrogen ions due to thermal decomposition of acetylene ions[13]	$\theta_{CH}\nu_0\nu\exp\left(-\frac{\delta E_i}{k_B T_s}\right)$
15. Accretion of neutral acetylene atoms to the conical tip of CNT[19]	$\gamma_{C_2H_2}\pi r_{conct}^2 n_{C_2H_2 conct}$
16. Adsorption flux of acetylene ions and hydrogen ions to catalyst-substrate surface[19]	$J_{aij} = \frac{P_i}{(2\pi m_{ij} k_B T_{ij})^{\frac{1}{2}}} \times \frac{n_{ij}}{j_{ij}}$
17. Desorption flux of acetylene ions and hydrogen ions from catalyst-substrate surface[19]	$J_{desorptionj} = n_{ij}\nu\left(-\frac{\varepsilon_{ai}}{k_B T_{ij}}\right)$
18. Ion collection current to the CNT(both conical tip and cylindrical surface)[19]	$n_{iBconcts} + n_{iBcysct}$ or $n_{iAconcts} + n_{iAcysct}$
19. Neutral collection current to the CNT(both conical tip and cylindrical surface)[19]	$n_{Bconcts} + n_{Bcysct}$ or $n_{Aconcts} + n_{Acysct}$
20. Electron collection current to the CNT(both conical tip and cylindrical surface)[19]	$n_{econcts} + n_{ecysct}$

and I_{pB} are the ionization energies of atoms A (acetylene) and B (hydrogen), respectively (Ref. 19). T_a is the ambient temperature, ε is the emissivity of the material of the catalyst, and σ is the Stefan–Boltzmann constant. Here, we assume that the applied rf power not only ionizes the feedstock gas in the chamber but also heats up the substrate as well. In the present problem, we have assumed the substrate and catalyst temperature to be the same

$$\varepsilon_{ijc}^{s}(Z)\left\{=\left(\left(\frac{(2-Z\gamma_{ji})}{(1-Z\gamma_{ji})}\right)-Z\gamma_{ji}\right)k_B T_{ij}\right\}$$

are the mean energy collected by the ions j where j refers to ion A (acetylene) or B (hydrogen) at the surface of the catalyst particle and $\gamma_{ji} = \left(\frac{e^2}{r_P k_B T_{ij}}\right)$.

$$n_{ijctP} = \pi {r_P}^2 \left(\frac{8k_B T_i}{\pi m_{ij}}\right)^{\frac{1}{2}} n_{ij}(x)\left[1 - Z\gamma_{ji}\right] \times \exp\left[-\frac{E_b}{k_B T_s}\right]\exp\left[-\frac{eU_s}{k_B T_s}\right]$$

is the ion collection current at the surface of catalyst particle, where j refers to ion A or B.

In solving Eq. (4), we consider that at rf power of 100 W, and at $\tau = 0$ feeding $n_{iB0} = n_{iA0} = 10^9\,cm^{-3}$, $T_{i0} = 2100\,K$, $T_s = 550\,^{\circ}C$, $E_b = 1.6\,eV$, $U_s = -50\,V$, and $r_{P0} = 30\,nm$ in expression for n_{iActP} and n_{iBctP}, we can calculate n_{iActP0}, n_{iBctP0}.

Feeding n_{iActP0} and n_{iBctP0} and the other parameters, i.e., $\varepsilon_{iAc}^{s} = 8.2\,eV$, $\varepsilon_{iBc}^{s} = 13.2\,eV$, $I_{pA} = 11.87\,eV$, and $I_{pB} = 13.7\,eV$ in Eq. (4), we can get the value of catalyst particle radius r_P and its temperature T_s at any time τ.

The terms on the right side of Eq. (4) is the rate of energy transferred to the catalyst particle due to the ions collected at the surface of catalyst particle because of ionization of neutral atoms A and B and mean energy collected by the ions at the surface of catalyst particle, and due to the accretion of ions A and B at the catalyst particle site. The last term is the rate of energy dissipation of the catalyst particle through radiation and conduction to the host gas.

The resulting value of catalyst nanoparticle at time τ serves as the initial base radius of the cylindrical part of nanotube.

This article is copyrighted as indicated in the article. Reuse of AIP content is subject to the terms at: http://scitation.aip.org/termsconditions. Downloaded to IP: 14.139.251.107 On: Mon, 16 Feb 2015 05:06:34

B. Growth rate equation of the curved surface area of CNT

Following Tewari and Sharma[19]

$$r_P \frac{d(2\pi h)}{d\tau} = \left(\left\{ 2n_{CH}\nu \exp\left(\frac{-\delta E_t}{k_B T_s}\right) + 2\theta_{CH} j_{iA} y_d + 2j_{iA} + \frac{j_{iA}\sigma_{ads} j_{iB}}{\nu} + j_c \right\} m_c + \left\{ j_{iA}(1-\theta_t) + \frac{j_{iA}\sigma_{ads} j_H}{\nu} + j_{iA} \exp\left(\frac{-\delta E_t}{k_B T_s}\right) \right\} m_{iA} \right) \times \frac{D_s \times 2\pi r_p}{\pi r_p^2 \rho_p} \left(\frac{1}{n_{iActcys}}\right) + \gamma_{C_2H_2} \pi r_p^2 n_{C_2H_2 ctcys} \tag{5}$$

$$\frac{d(\pi r_{conct} l)}{d\tau} = \left\{ j_{iB} \exp\left(\frac{-E_b}{k_B T_s}\right) + j_{iB} \exp\left(\frac{-\delta E_{th}}{k_B T_s}\right) + j_{iB}(1-\theta_t) + j_{iB} + \theta_{CH}\left(j_{iB} y_d + \nu_0 \nu \exp\left(\frac{-\delta E_i}{k_B T_s}\right)\right)\right\} \frac{h(\tau)}{n_{iB}} + \gamma_{C_2H_2} \pi r_{conct}^2 n_{C_2H_2 conct}. \tag{6}$$

Since the opening angle[21] of conical CNT tip is 45°, the slanted length (l) of conical CNT tip becomes

$$l = \left(h'^2 + r_{conct}^2\right)^{\frac{1}{2}}.$$

h' is the height of conical CNT tip

$$\tan\theta = \frac{r_{conct}}{h'}.$$

Since θ is 45°,

$$l = \sqrt{2r^2_{conct}} = \sqrt{2} r_{conct},$$

where $n_{CH} = (\theta_{CH}\nu_0)$ is the number density of CH (see Ref. 13), (CH denotes C_2H_2); $\nu_0 (\approx 1.3 \times 10^{15} cm^{-2})$ is the number of adsorption sites per unit area; θ_{CH} is the total surface coverage of C_2H_2; j_c ($= n_c v_{thC}/4$) is the ion flux of carbon ions and v_{thC} is the thermal velocity of C ions; δE_t is thermal energy barrier; $j_{iA} = n_{iA}(k_B T_{ij}/m_{iA})^{1/2}$ and $j_{iB} = n_{iB}(k_B T_{ij}/m_{iB})^{1/2}$ are the ion flux of types A and B, respectively; n_{iA} and n_{iB} are the number densities of A and B type ions, respectively; $y_d \approx \varepsilon_{icH}/\varepsilon_{dis}$, where ε_{icH} is kinetic energy associated with the motion of hydrocarbon ions impinging on the substrate and ε_{dis} is the dissociation energy of C_2H_2; σ_{ads} is the cross section for the reactions of atomic hydrogen with adsorbed particles $\approx (6.8 \times 10^{-16}\ cm^2)$; E_b is the energy barrier for bulk diffusion ($\approx$1.6eV); D_s is the surface diffusion coefficient $[D_s = D_{s0}\exp(-E_s/k_B T_s)]$; E_s is the energy barrier for diffusion of Carbon (C) on the catalyst and is 0.3 eV; and $D_{s0} = \nu a_0^2$, where a_0 is inter atomic distance (see Ref. 13); ν is the thermal vibrational frequency; θ_t is the total surface coverage (see Ref. 13); ε_{th} is the energy due to thermal dehydrogenation; $\delta\varepsilon_t$ is the energy due to thermal dissociation (see Ref. 13); $\gamma_{C_2H_2}$ is the sticking coefficient of C_2H_2 molecules; m_C is the mass of a carbon atom (12 a.m.u.); m_{iA} is the mass of type A ions (26 a.m.u. for $C_2H_2^+$); and h is the height of cylindrical CNT surface.

In Eq. (5), the first term in the first bracket (see Ref. 13) describes the generation of carbon atoms on the catalyst surface due to thermal dissociation of acetylene ions (with energy barrier δE_t); second term (see Ref. 13) describes the ion induced dissociation of C_2H_2; third term (see Ref. 13) denotes the decomposition of positively charged ions of type A, i.e., $C_2H_2^+$ (see Ref. 14); fourth term (see Ref. 13) is the interaction of ions with atomic hydrogen from the plasma; fifth term (see Ref. 13) accounts for the incoming flux of carbon atoms per unit time onto the catalyst particle; sixth term denotes the adsorption of type A ions to the surface; seventh term is the interaction of adsorbed type A ions with atomic hydrogen from plasma; and the eighth term is due to thermal dissociation of carbon source gas C_2H_2 (see Ref. 13). The factor $n_{iActcys}$ accounts for the ion collection current on the growing cylindrical part of the CNT. The term $\frac{D_s \times 2\pi r_p}{\pi r_p^2 \rho_p}$ denotes the surface diffusion of species onto the catalyst surface across the catalyst nanoparticle per unit area mass density. Finally, the last term denotes the sticking of neutral atoms of acetylene to the cylindrical surface of the CNT.

In Eq. (6), the first term (see Ref. 13) denotes hydrogen atom diffusing into catalyst–substrate surface; second term (see Ref. 13) accounts for the incoming flux of hydrogen ion due to thermal dehydrogenation of type A ions; third term (see Ref. 13) is adsorption of type B ions to the surface; fourth term (see Ref. 14) is the decomposition of positively charged ions of type B; fifth term (see Ref. 14) is due to ion induced dissociation of C_2H_2; sixth term is due to the incorporation of hydrogen ions due to thermal dissociation of acetylene ions. The last term denotes the sticking of neutrals of acetylene on the conical tip of CNT.

C. Charge kinetics of the CNT surface

Equation (7) describes the charge developed on the entire CNT (i.e., the conical tip over the cylindrical surface)

$$Z'[\tau] = n_{iAconcts} + n_{iAcysct} + n_{iBconcts} + n_{iBcysct} - \gamma_e(n_{econcts} + n_{ecysct}), \tag{7}$$

where Z is the charge over the entire CNT (i.e., conical tip and cylindrical surface),

(a) For electron on the conical CNT tip $n_{econcts} = \pi r_{conct} l \left(\frac{8k_B T_e}{\pi m_e}\right)^{\frac{1}{2}} n_e(x) \exp\left[\frac{Z\alpha_e}{k_B T_e} + \frac{eU_s}{k_B T_s}\right]$ is the electron collection current at the surface of the conical CNT tip and r_{conct} is the conical nanoparticle tip radius $\alpha_e = eVcon(z)$, where

This article is copyrighted as indicated in the article. Reuse of AIP content is subject to the terms at: http://scitation.aip.org/termsconditions. Downloaded to IP: 14.139.251.107 On: Mon, 16 Feb 2015 05:06:34

$$V_{con}(z) = \sigma\left(\frac{3\sqrt{h^2 - 2hz + 2z^2} + (-2h + 4z)\log\left[\frac{-2h + 4z + 2\sqrt{2}\sqrt{h^2 - 2hz + 2z^2}}{\sqrt{2}}\right]}{4\sqrt{2}\varepsilon_0}\right).$$

$V_{con}(z)$ is explained in the Appendix.

$n_e(x) = n_{e0}\exp\left[\frac{|e|\phi(x)}{k_B T_e}\right]$ is the electron density in plasma sheath; $\phi(x)$ is the electrostatic potential; n_{e0} is plasma density in bulk and it decreases towards the substrate; T_e is the electron temperature; $\phi(x) = \phi_0\exp\left(-\frac{|x|}{\lambda_d}\right)$; ϕ_0 is the negative potential at the surface; λ_d is the plasma Debye length

(b) For electrons on cylindrical surface:

$n_{ecysct} = n_e(x) r_P h\left(\frac{2\pi k_B T_e}{m_e}\right)^{\frac{1}{2}}\exp\left[\frac{eV_s}{k_B T_e} + \frac{eU_s}{k_B T_s}\right]$ is the electron collection current on the cylindrical surface of the CNT and V_s is the surface potential on the cylindrical surface of the CNT and h is the height of cylindrical surface of the CNT, m_e is the mass of electron

(c) For ions on the cylindrical surface

$$n_{ijcysct} = n_{ij}(x) r_P h\left(\frac{2\pi k_B T_{ij}}{m_{ij}}\right)^{\frac{1}{2}}\left\{\frac{2}{\sqrt{\pi}}\left(\frac{eV_s}{k_B T_{ij}}\right)^{\frac{1}{2}} + \exp\left[\frac{eV_s}{k_B T_{ij}}\right] erfc\left[\left(\frac{eV_s}{k_B T_{ij}}\right)^{\frac{1}{2}}\right]\right\} \times \exp\left[-\frac{E_b}{k_B T_s}\right]\exp\left[-\frac{eU_s}{k_B T_s}\right]$$

is the ion collection current on the cylindrical surface[24] of CNT, T_{ij} is the ion temperature, m_{ij} is the ion mass (j refers to either A or B positively charged ion as explained earlier), E_b is the energy barrier for bulk diffusion (≈ 1.6 eV), T_s is the substrate or catalyst temperature.

(d) For ions on the conical tip surface

$$n_{ijconcts} = \pi r_{conct} l\left(\frac{8k_B T_{ij}}{\pi m_{ij}}\right)^{\frac{1}{2}} n_{ij}(x)\left[1 - \frac{Z\alpha_i}{k_B T_{ij}}\right] \times \exp\left[-\frac{E_b}{k_B T_s}\right]\exp\left[-\frac{eU_s}{k_B T_s}\right]$$

is the ion collection current on the conical CNT tip $n_{ij}(x) = n_{ijo}\left(1 - \frac{2e\phi(x)}{m_i v_{i0}^2}\right)$, where $n_{ij}(x)$ is the ion density in plasma sheath, v_{io} is the ion velocity at any point within the plasma and $\alpha_i = eV_{con}(z)$.

In Eq. (7), first and second term denote charge developed on the entire CNT (i.e., the conical tip over cylindrical surface) due to accretion of positively charged ions of acetylene, third and fourth term denote the charge developed on the entire CNT (i.e., the conical tip over cylindrical surface) due to accretion of positively charged ions of hydrogen. The last term describes the loss in charge due to electron collection current at the surface of the CNT (i.e., the conical tip over cylindrical surface).

D. Stability equation of electron number density

The equation describes the balance of electron number density in the plasma bulk because of ionization of neutrals, recombination of electron and neutrals and electron collection current at the surface of CNT

$$\frac{dn_e}{d\tau} = (\beta_A n_A + \beta_B n_B) - (\alpha_A n_e n_{iA} + \alpha_B n_e n_{iB}) - \gamma_e n_{ct}(n_{econcts} + n_{ecysct}), \quad (8)$$

where β_j is the coefficient of ionization of the constituent neutral atoms due to external field; $\alpha_j(T_e) = \alpha_{j0}\left(\frac{300}{T_e}\right)^k \text{cm}^3/\text{s}$ is the coefficient of recombination of electrons and positively charged ions;[23] n_e is the electron number density; and n_{iA} and n_{iB} are the ion number density of ions A and B, respectively; $\kappa = -1.2$ is a constant; and n_{ct} is the CNT number density.

The first term on the right side of Eq. (8) is the rate of gain in electron density per unit time because of ionization of neutral atoms of acetylene and hydrogen; the second term is the decaying rate of the electron density due to the electron–ion recombination. The third term is the electron collection current at the surface of the CNT (i.e., the conical tip over the cylindrical surface).

E. Stability equation of positively charged ion number density

$$\frac{dn_{iA}}{d\tau} = \beta_A n_A - \alpha_A n_e n_{iA} - n_{ct}(n_{iAconcts} + n_{iAcysct}) - J_{aiA} + J_{desorptionA}, \quad (9)$$

$$\frac{dn_{iB}}{d\tau} = \beta_B n_B - \alpha_B n_e n_{iB} - n_{ct}(n_{iBconcts} + n_{iBcysct}) - J_{aiB} + J_{desorptionB} + J_{th}. \quad (10)$$

$J_{aij} = \frac{P_i}{(2\pi m_{ij} k_B T_{ij})^{\frac{1}{2}}} \times \frac{n_{ij}}{j_{ij}}$ is the adsorption flux onto the catalyst –substrate surface, P_i is the partial pressure of adsorbing species, $J_{desorptionj} = n_{ij}\nu\exp\left(\frac{-\varepsilon_{ai}}{k_B T_{ij}}\right)$ is the desorption flux from the catalyst – substrate surface, j refers to either A or B ions, ν is the thermal vibrational frequency, ε_{ai} is the adsorption energy, j_{ij} is the ion flux on the catalyst substrate surface. $J_{th} = n_H\nu\exp\left(\frac{-\delta\varepsilon_{th}}{k_B T_s}\right)$ is the flux of type B ion (namely, hydrogen) on account of thermal dehydrogenation. $\delta\varepsilon_{th}$ is the activation energy of thermal dehydrogenation, n_H is the hydrogen ion flux at catalyst–substrate surface.

The first term in Eqs. (9) and (10) is the gain in ion density per unit time because of ionization of neutral atoms; the

This article is copyrighted as indicated in the article. Reuse of AIP content is subject to the terms at: http://scitation.aip.org/termsconditions. Downloaded to IP: 14.139.251.107 On: Mon, 16 Feb 2015 05:06:34

second term is the electron-ion recombination. The third term is the ion collection current to the surface of the CNT (i.e., conical tip over the cylindrical surface). The fourth term is the loss of ions because of their adsorption to the catalyst–substrate surface and fifth term, is the gain of ion density due to the desorption of ions from the catalyst–substrate surface into plasma. The last term in Eq. (10) describes the increase of hydrogen ion number density in plasma because of thermal dehydrogenation.

F. Stability equation of neutral atom number density

The equation describes the balance of neutral particles[23] in plasma due to recombination of electrons-ions, ionization of neutral molecules, ion and neutral collection current on the CNT surface

$$\frac{dn_A}{d\tau} = \alpha_A n_e n_{iA} - \beta_A n_A + n_{ct}(1-\gamma_{iA})(n_{iAconcts} + n_{iAcysct}) - n_{ct}\gamma_A(n_{Aconcts} + n_{Acysct}), \quad (11)$$

$$\frac{dn_B}{d\tau} = \alpha_B n_e n_{iB} - \beta_B n_B + n_{ct}(1-\gamma_{iB})(n_{iBconcts} + n_{iBcysct}) - n_{ct}\gamma_B(n_{Bconcts} + n_{Bcysct}), \quad (12)$$

where $n_{jconcts} = \pi r_{conct} l \left[\frac{8k_B T_n}{\pi m_j}\right]^{\frac{1}{2}} n_j$ is the neutral collection current at the surface of conical CNT tip, $n_{jcysct} = \pi r_P h \left[\frac{2k_B T_n}{m_j}\right]^{\frac{1}{2}} n_j$ is the neutral collection current on the cylindrical surface of CNT. γ_{iA} is the ion sticking coefficient and γ_A is the neutral atom sticking coefficient, T_n is the neutral atom temperature, n_j is the neutral atom density, and m_j is the neutral atom mass.

The first term in Eqs. (11) and (12) is the gain in neutral atom density per unit time due to electron–ion recombination; the second term is the decrease in neutral density due to ionization of neutrals of either A(acetylene) or B (hydrogen). The third term is the gain in neutral density due to neutralization of the particles collected at the surface of the CNT. The last term is the accumulation of neutral atoms of species A and B on the surface of the CNT (i.e., the conical tip and cylindrical surface).

III. NUMERICAL RESULT AND DISCUSSIONS

The present paper investigates the role of substrate temperature on the growth of carbon nanotubes by PECVD process. In the present model, we assume the inhomogeneous deposition of ions on CNT growing in a plasma medium assisted by catalyst. The calculations have been formed to investigate the dependence of the height of cylindrical CNT surface and radius of the conical CNT tip as a function of substrate temperature for different ion density and ion temperature by simultaneous solution of Eqs. (1)–(12) at appropriate boundary conditions.

The values of height and radius of the CNT as obtained by Eqs. (5) and (6) are obtained at different times as a function of temperature but since in the present paper, we are interested in studying the variation of height and radius of the CNT as a function of substrate temperature, the value of height and radius of CNT are plotted for a fixed time interval, i.e., $\tau = 0$ min to 30 min for varying substrate temperature.

For Ar plasma, using the values of ion number density and temperature from Chai *et al.*,[22] the initial boundary conditions for the present calculations are at $\tau = 0$, ion number density ($n_{iA0} = 0.6 n_{e0}$ and n_{iB0}=$0.4 n_{e0}$), neutral atom density ($n_{A0} = n_{B0} = 1 \times 10^{14}\,cm^{-3}$), electron number density ($n_{e0} = 1.12 \times 10^{9}\,cm^{-3}$), electron temperature (T_{e0}) = 1.5 eV, ion temperature (T_{iA0}) = 2200 K, neutral temperature (T_{n0}) = 2000 K, mass of ion A $m_{iA} = 26$ amu (acetylene ($C_2H_2^+$)), mass of ion B (m_{iB}) = 1 amu(H^+), coefficient of recombination of electrons and ions ($\alpha_{A0} \approx \alpha_{B0}$) = $1.12 \times 10^{-7} cm^3/s$, $\kappa = -1.2$, and density of Ni (ρ_P) = 8.908 g/cm^3. Other parameters used in the calculation are substrate temperature (T_s) = 550 °C, thermal energy barrier on the catalyst surface (δE_t), energy barrier for bulk diffusion E_b = 1.6 eV, energy due to thermal dissociation of methyl ions, dissociation energy of C_2H_2 (see Ref. 13) ε_{dis} = 4.35 eV, Ionization energies of neutral atom A (I_{pA}) = 8.76 eV, Ionization energies of neutral atom B (I_{pB}) = 6.56 eV, the mean energy collected by the ion A at the surface of catalyst particle (ε_{iA}) = 5.915 eV, the mean energy collected by the ion B at the surface of catalyst particle (ε_{iB}) = 9.80 eV. Substituting all the above values in Eqs. (1)–(12), we simultaneously solve the first order differential Eqs. (1)–(12) using MATHEMATICA software to investigate the dependence of height and radius of CNT for different substrate temperature (T_s) and ion density and temperature of either acetylene (n_{iA0}&T_{iA0}) or hydrogen ions (n_{iB0}&T_{iB0}).

Fig. 1 sketches the variation of potential at a conical surface (V_{con}) as a function of axial distance (z). It can be seen from Fig. 1 that the potential on the conical surface decreases with the axial distance (z). The decrease in the potential at a conical surface (V_{con}) with axial distance (z) follows the same trend as the electrostatic potential at the surface behaves as the distance from the surface is increased. The electrostatic potential at the surface decreases as the distance from the surface is increased.

Fig. 2 traces the evolution of the height of the cylindrical part of the CNT as a function of substrate temperature for different ion densities and temperature of type A (e.g., $n_{iA0} = 10^9\,cm^{-3}$, T_{iA0} = 2250 K; $n_{iA0} = 2 \times 10^{10}\,cm^{-3}$, T_{iA0} = 2300 K and $n_{iA0} = 3 \times 10^{11}\,cm^{-3}$, T_{iA0} = 2400 K). It can be seen from Fig. 2 that as substrate temperature is increased for a fixed ion density and temperature of type A ion (i.e., acetylene ion) the height of the CNT increases.

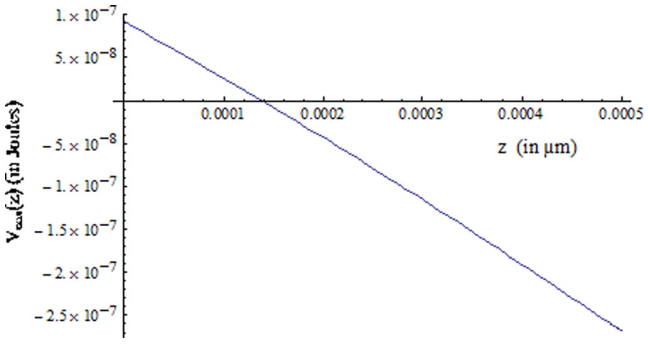

FIG. 1. Sketches the variation of potential of conical CNT tip with axial distance.

This article is copyrighted as indicated in the article. Reuse of AIP content is subject to the terms at: http://scitation.aip.org/termsconditions. Downloaded to IP: 14.139.251.107 On: Mon, 16 Feb 2015 05:06:34

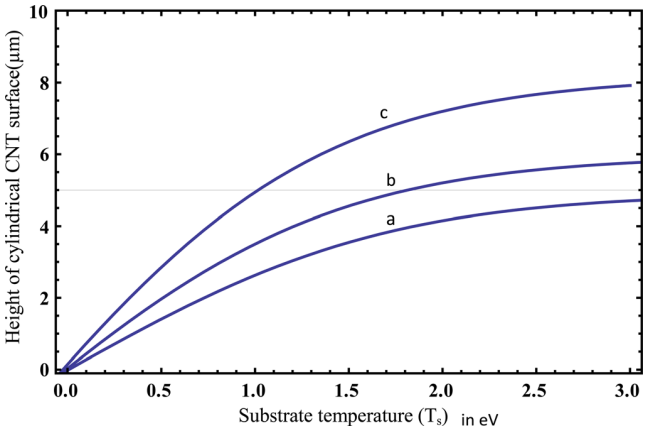

FIG. 2. Depicts the evolution of the height of cylindrical CNT surface as a function of substrate temperature for different ion density and temperature of type A ions (where a, b, and c correspond to $n_{iA0} = 10^9\,cm^{-3}$, $T_{iA0} = 2250\,K$; $n_{iA0} = 2 \times 10^{10}\,cm^{-3}$, $T_{iA0} = 2300\,K$; and $n_{iA0} = 3 \times 10^{11}\,cm^{-3}$, $T_{iA0} = 2400\,K$). The other parameters are given in the text.

This is because with increasing substrate temperature, the hydrocarbon gas dissociates faster, leading to higher diffusion of carbon through catalyst particle thereby giving enhanced growth rates. Moreover, with increasing ion density and temperature of type A ions, the effective carbon flux to the catalyst surface increases which results in better CNTs growth.

Fig. 3 traces the evolution of the radius of the conical CNT tip as a function of substrate temperature for different ion densities and temperature of type A (i.e., $n_{iA0} = 10^9\,cm^{-3}$, $T_{iA0} = 2250\,K$; $n_{iA0} = 2 \times 10^{10}\,cm^{-3}$, $T_{iA0} = 2300\,K$, and $n_{iA0} = 3 \times 10^{11}\,cm^{-3}$, $T_{iA0} = 2400\,K$). It can be seen from Fig. 3 that as substrate temperature is increased for a fixed ion density and temperature of type A ion (i.e., acetylene ion), the radius of the conical CNT tip increases. This is because with increasing substrate temperature, the hydrocarbon gas dissociates faster, leading to higher diffusion of carbon through catalyst particle thereby giving larger radius. Also, as the ion density and temperature of type A ions (i.e., acetylene ion) is

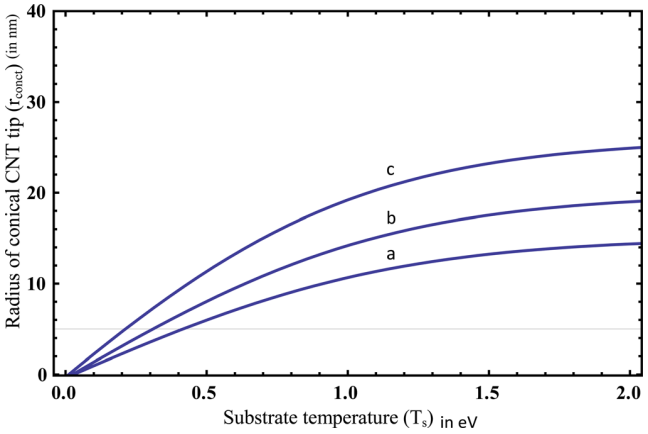

FIG. 3. Depicts the time evolution of the radius of the conical CNT tip for different density and temperature of type A ions (where a, b, and c correspond to $n_{iA0} = 10^9\,cm^{-3}$, $T_{iA0} = 2250\,K$; $n_{iA0} = 2 \times 10^{10}\,cm^{-3}$, $T_{iA0} = 2300\,K$; and $n_{iA0} = 3 \times 10^{11}\,cm^{-3}$, $T_{iA0} = 2400\,K$). The other parameters are given in the text.

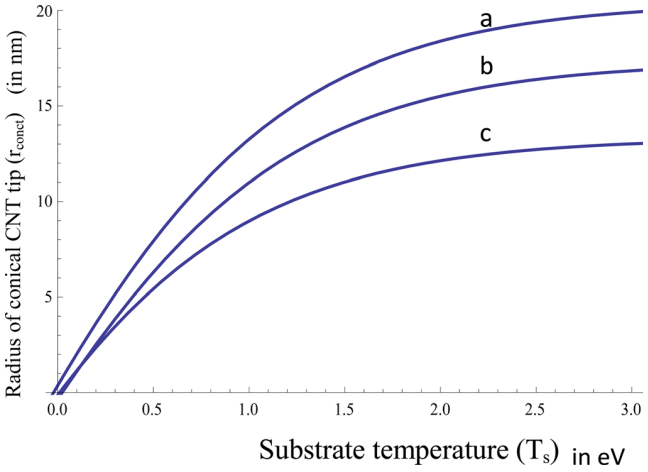

FIG. 4. Illustrates the evolution of the radius of the conical CNT tip as a function of substrate temperature for different ion density and temperature of type B ions (where a, b, and c correspond to $n_{iB0} = 10^9\,cm^{-3}$, $T_{iB0} = 2300\,K$; $n_{iB0} = 5 \times 10^{10}\,cm^{-3}$, $T_{iB0} = 2350\,K$; and $n_{iB0} = 4 \times 10^{11}\,cm^{-3}$, $T_{iB0} = 2400\,K$).

increased, the effective carbon flux to the catalyst surface increases which results in a larger radius of the CNT tip.

The observations of Figs. 2 and 3, i.e., the enhanced growth rate of the CNT with substrate temperatures are in principle with the experimental observations of Han *et al.*,[8] Baratunde *et al.*,[9] Lee *et al.*,[10] Loffler *et al.*,[11] and theoretical findings of Mehdipour *et al.*[13]

Fig. 4 traces the evolution of the radius of the conical CNT tip as a function of substrate temperature for the different ion density and temperature of type B ions (i.e., $n_{iB0} = 10^9\,cm^{-3}$, $T_{iB0} = 2300\,K$; $n_{iB0} = 5 \times 10^{10}\,cm^{-3}$, $T_{iB0} = 2350\,K$ and $n_{iB0} = 4 \times 10^{11}\,cm^{-3}$, $T_{iB0} = 2400\,K$). It can be seen from Fig. 4 that as substrate temperature is increased for a fixed ion density and temperature of the type B ion (i.e., hydrogen ion), the radius of CNT decreases. This is imputable to the fact that as the substrate temperature is increased for a fixed ion density and temperature of type B ions (i.e., hydrogen ion) the radius of the conical CNT tip increases because with increasing substrate temperature, the feedstock gas dissociates more and, consequently, a larger number of carbon radicals and higher stable hydrocarbons become easily available for CNT growth. But as the density of type B ion (i.e., hydrogen ion) increases, the radius of the conical CNT tip decreases because of etching effects of hydrogen. The results of Fig. 4 comply with Mehdipour *et al.*,[13] and Denysenko and Ostrikov.[14]

IV. CONCLUSION

A theoretical model to study the substrate temperature effects on the growth of CNTs in plasma assisted by catalyst is developed. The issue of substrate temperature with ion density and temperature on the radius of the conical CNT tip and the height of cylindrical CNT surface has been examined. It is found that the height of cylindrical CNT surface and the radius of the conical CNT tip increases with the substrate temperature for a fixed density and temperature of acetylene ion. The radius of the conical CNT tip increases with substrate temperature for a fixed

This article is copyrighted as indicated in the article. Reuse of AIP content is subject to the terms at: http://scitation.aip.org/termsconditions. Downloaded to IP: 14.139.251.107 On: Mon, 16 Feb 2015 05:06:34

density and temperature of hydrogen ion. The increase in the density and temperature of acetylene ion results in larger height of the cylindrical CNT surface and radius of the conical CNT tip increases owing to faster diffusion of carbon through a catalyst particle. But the increase in the hydrogen ion density and temperature results in smaller radius of the conical CNT tip because of etching effects of hydrogen. The above work can be extended to improve the understanding of plasma heating effects on nanotube growth.

APPENDIX: POTENTIAL AT A POINT ON THE SURFACE OF A CONE

Following Ref. 21 and considering a conical surface with uniform surface charge density, the height of the cone is h and radius is "r_{conct}." The geometry of the problem is same as in Ref. 21. The surface charge density is

$$\sigma = \frac{e}{2\pi r_{conct} l}.$$

The differential electric field, along z axis[21]

$$dE_{conz} = \frac{1}{4\pi\varepsilon_0}\frac{2\sqrt{2}\pi\sigma z(h-z)dz}{\left((h-z)^2+z^2\right)^{\frac{3}{2}}}. \tag{A1}$$

Integrating Eq. (A1) over the entire cone surface

$$E_{con}\hat{z} = \frac{\sigma}{\sqrt{2}\varepsilon_0}\int\frac{2\sqrt{2}\pi\sigma z(h-z)d_z}{\left((h-z)^2+z^2\right)^{\frac{3}{2}}}\hat{z}. \tag{A2}$$

Solving Eq. (A2), we get

$$E_{con}\hat{z} = \frac{\sigma\left(-2h+4z-\sqrt{2}\sqrt{h^2-2hz+2z^2}\log\left[-2h+4z-2\sqrt{2}\sqrt{h^2-2hz+2z^2}\right]\right)}{4\sqrt{2}\sqrt{h^2-2hz+2z^2}}. \tag{A3}$$

Now, solving for potential on the surface of a cone

$$V_{con}(z) = -\int_{\infty}^{z} E.dz$$

or

$$V_{con}(z) = \sigma\left(\frac{3\sqrt{h^2-2hz+2z^2}+(-2h+4z)\log\left[\frac{-2h+4z+2\sqrt{2}\sqrt{(h^2-2hz+2z^2)}}{\sqrt{2}}\right]}{4\sqrt{2}\varepsilon_0}\right). \tag{A4}$$

[1]L. Delzeit, I. McAninch, B. A. Cruden, D. Hash, B. Chen, J. Han, and M. Meyyappan, J. Appl. Phys. **91**, 6027 (2002).
[2]V. I. Merkulov, D. H. Lowndes, Y. Y. Wei, G. Eres, and E. Voelkl, Appl. Phys. Lett. **76**, 3555 (2000).
[3]M. Meyyappan, L. Delzeit, A. Cassell, and D. Hash, Plasma Sources Sci. Technol. **12**, 205 (2003).
[4]M. Chhowalla, K. B. Teo, C. Ducati, N. L. Rupesinghe, G. A. J. Amaratunga, A. C. Ferrari, D. Roy, J. Robertson, and W. I. Milne, J. Appl. Phys. **90**, 5308 (2001).
[5]Y. C. Choi, D. J Bae, Y. H. Lee, B. S. Lee, G. S. Park, W. B. Choi, N. S. Lee, and J. M. Kim, J. Vac. Sci. Technol. A **18**, 1864 (2000).
[6]J. I. B Wilson, N. Scheerbaum, S. Karim, N. Polwart, P. John, Y. Fan, and A. G. Fitzgerald, Diamond Relat. Mater. **11**, 918 (2002).
[7]K. B. K. Teo, D. B. Hash, R. G. Lacerda, N. L. Rupesinghe, M. S. Bell, S. H. Dalal, D. Bose, T. R. Govindan, B. A. Cruden, M. Chhowalla, G. A. J. Amaratunga, M. Meyyappan, and W. I. Milne, Nano Lett. **4**, 921 (2004).
[8]J.-H. Han, S. H. Choi, T. Y. Lee, J.-B. Yoo, C.-Y. Park, H. J. Kim, I.-T. Han, S. Yu, W. Yi, G. S. Park, M. Yang, N. S. Lee, and J. M. Kim, Thin Solid Films **409**, 126 (2002).
[9]A. Cola Baratunde, B. Amama Placidus, X. Xianfan, and S. Fisher Timothy, J. Heat Transfer **130**, 114503 (2008).
[10]Y. T. Lee, J. Park, Y. S. Choi, H. Ryu, and H. Joo Lee, J. Phys. Chem. B **106**, 7614 (2002).
[11]R. Loffler, M. Haffner, G. Visanescu, H. Weigand, X. Wang, D. Zhang, M. Fleischer, A. J. Meixner, J. Fortagh, and D. P. Kern, Carbon **49**, 4197 (2011).
[12]I. Denysenko, K. Ostrikov, M. Y. Yu, and N. A. Azarenkov, J. Appl. Phys. **102**, 074308 (2007).
[13]H. Mehdipour, K. Ostrikov, and A. E. Rider, Nanotechnology **21**, 455605 (2010).
[14]I. B. Denysenko and K. Ostrikov, J. Phys. D: Appl. Phys. **42**, 015208 (2009).
[15]G. Burmaka, I. B. Denysenko, K. Ostrikov, I. Levchenko, and N. A. Azarenkov, Plasma Processes Polym. **11**, 798 (2014).
[16]S. K. Srivastava, V. D. Vankar, and V. Kumar, Nanoscale Res. Lett. **3**, 25 (2008).
[17]S. Iijima, P. M. Ajayan, and T. Ichihashi, Phys. Rev. Lett. **69**, 3100 (1992).
[18]D. L. Carroll, P. Redlich, P. M. Ajayan, J. C. Charlier, X. Blase, A. De Vita, and R. Car, Phys. Rev. Lett. **78**, 2811 (1997).
[19]A. Tewari and S. C. Sharma, Phys. Plasmas **21**, 063512 (2014).
[20]S. K. Srivastava, A. K. Shukla, V. D. Vankar, and V. Kumar, Thin Solid Films **492**, 124 (2005).
[21]See http://www2.warwick.ac.uk/fac/sci/physics/current/teach/module_-home/px.263/assignments/assignment1_soln.pdf.
[22]K. B. Chai, C. R. Seon, C. W. Chung, N. S. Yoon, and W. Choe, J. Appl. Phys. **109**, 013312 (2011).
[23]M. S. Sodha, S. Misra, S. K. Mishra, and S. Srivastava, J. Appl. Phys. **107**, 103307 (2010).
[24]M. S. Sodha, S. K. Mishra, and S. Misra, Phys. Plasmas **16**, 123701 (2009).

This article is copyrighted as indicated in the article. Reuse of AIP content is subject to the terms at: http://scitation.aip.org/termsconditions. Downloaded to IP: 14.139.251.107 On: Mon, 16 Feb 2015 05:06:34

International Journal of Current Engineering and Technology
E-ISSN 2277 – 4106, P-ISSN 2347 – 5161
©2015INPRESSCO®, All Rights Reserved
Available at http://inpressco.com/category/ijcet

Research Article

Transient Thermo Elastic Analysis of Disk Brake

Chiranjit Sarkar†* and Harish Hirani‡

†Mechanical Engineering Department, Delhi Technological University, Shahbad Daluatpur, Bawana Road, Delhi – 110042, India
‡Mechanical Engineering Department, Indian Institute of Technology Delhi, Hauz Khas, New Delhi – 110016, India

Accepted 19 Feb 2015, Available online 20 Feb 2015, **Vol.5, No.1 (Feb 2015)**

Abstract

Thermo elastic instability is caused by frictional heating and thermal deformation of the surfaces when two bodies slide against each other, and alters the original contact configuration. Even if the surfaces are perfectly flat at the outset, instability will lead to a departure from flatness. Above a certain critical speed, a nominally uniform pressure distribution is unstable, giving way to localization of load, excessive heat generation and hence to hot spots at the sliding interface (Barber, 1969), (Kennedy and Ling, 1974), (Floquet and Dubourg, 1994), (Bryant, et al, 1995), (Kao et al., 2000). The problem is particularly prevalent in energy dissipation systems such as brakes and clutches. Hot spots can cause material damage (i.e. wear) and undesirable frictional vibrations, known as ``hot roughness'' or ``hot judder'' (Kreitlow, et al, 1985), (Inoue, 1986), (Zagrodzki, 1990), (Anderson, 1990), (Lee, 1998).The present paper describes the use of ANSYS simulation software to perform a transient analysis of the thermo elastic contact problem for disk brakes. The numerical simulation for the thermo elastic behavior of disk brake is obtained in the repeated brake testing carried out on a dynamometer. The computational results are presented for the distribution of heat flux and temperature on each friction surface between the contacting bodies.. In addition, comparisons of the thermal behavior of the different brake pad materials with respect to disk materials have been discussed.

Keywords:*Volvo Disk Brake, Finite Element Analysis, Thermo Elastic Instability.*

1. Introduction

Magnetorheological (MR) brake (Sarkar and Hirani, 2015), (Sarkar and Hirani, 2013), (Gupta and Hirani, 2011), (Sukhwani, *et al*, 2009), (Sukhwani and Hirani, 2008), (Sukhwani and Hirani, 2008), (Hirani and Manjunatha, 2007), (Sukhwani, *et al*, 2007), (Sukhwani, *et al*, 2006), (Huang, et al, 2002), (Li and Du, 2003) is a device, where MR fluids are used as brake friction materials. During braking, kinetic energy of machines gets converted into heat and shear thinning of MR fluid due to increase in temperature occurs which in turn reduces the braking effect. Similarly, in conventional disk brake during the braking action, the kinetic energy produced at the wheel is transformed into heat energy, which doesn't dissipate fast enough into the air stream from the brake and the brake disk, as a result, one of the disk brake material properties; the thermal conductivity plays a critical role in handling such friction heat generated. Thermal judder occurs as a result of non-uniform contact cycles between the pad and the disk brake rotor, which is primarily an effect of the localized Thermo-Elastic Instabilities (TEI) at the disk brake rotor surface. Localized TEI act at the friction ring surface generating intermittent hot bands around the rubbing path which may in turn leads to the development of so-called hot spots (Eggleston, 2000).

The mechanism of the TEI phenomena taking place during the braking process has been of interest to many researchers (Lee, 2000), (Jang and Khonsari, 2003), (Lee and Brooks, 2003), (Dufrenoy, 2004). However, in this paper an assumption has been made that the thermo mechanical phenomenon of each disk is symmetrical about the disk's mid-plane. Also, the wear action taking place during the braking process, resulting from the friction between the disk brake and the pad, is assumed to be so small and thus to be neglected in the analysis. A FEA model has been suggested to simulate the braking action by investigating both the thermal and elastic actions occurring during the friction between the two sliding surfaces (the disk brake and the pad).The results obtained from the suggested model are compared with actualmeasurements performed by Kumar,*et al, 2009*.

2. Methodology

The FEA simulation was performed into two stages: thermal and elastic. During the analysis, the braking parameters,such as rotational speed of the disk brake, the cycle of the pressure applied and the time period

*Corresponding author: **Chiranjit Sarkar**

(shown in Fig. 1) of the different phases: braking, dragging, and release, were set to the values, extracted from the literature.

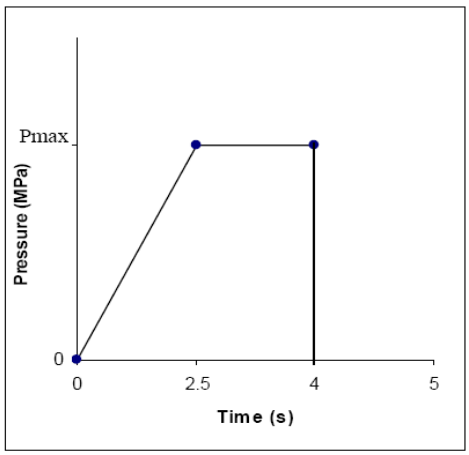

Fig.1 The change in applied pressure during breaking process

As shown in figure 1, during the braking process, it is assumed that the pressure will first increase linearly until it reaches the maximum value P_{max} within 2.5 s, then the pressure remains constant for another 1.5 s, then it dropsto zero.

The governing equation for the transient heat transfer problem is:

$$\rho C * \frac{\partial T}{\partial t} + \nabla(-k\nabla T) = Q - \rho.Cp.u.\nabla T \quad (1)$$

Where, ρ is density, C is heat capacity, T is temperature, k is thermal conductivity, Q is heat source or heat sink, *Cp*is the specific heat capacity and u is the velocity.

The governing equation for the elastic problem is:

$$\rho * \frac{\partial^2 u}{\partial t^2} - \nabla c \nabla u = K \quad (2)$$

where, K is the force vector.

Figure 2 shows the boundary conditions assumed during the simulation of the heat transfer problem.

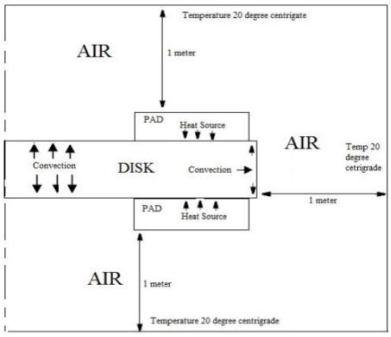

Fig.2 Heat Transfer Boundary Condition

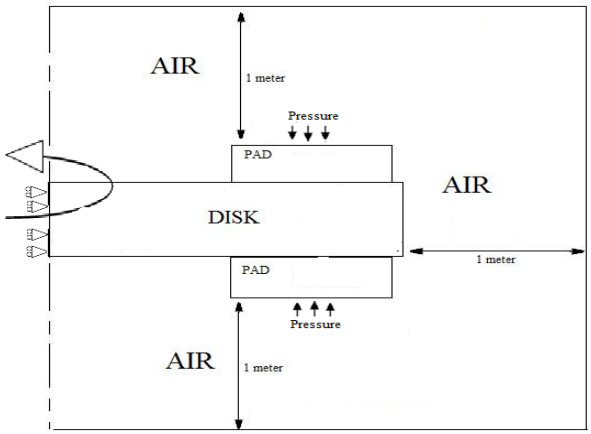

Fig.3 Elastic Problem Boundary condition

The boundary conditions stated for the elastic problem are represented in figure 3.

The objective of the study presented in this paper is to simulate the thermo elastic phenomenon taking place during the braking process. In addition, comparisons of the thermal behavior of the different brake pad materials with respect to disk materials have been discussed. Table1 shows the disk material's properties and Table2 shows the brake pad material's properties. The coefficient of friction values varies from 0.35 to 0.45 for these materials.

Table 1 Disk Material properties

Material	Grey Cast Iron
Density, ρ(Kg/m^3)	7031
Specific Heat, C (J/Kg K)	495
Thermal Conductivity, K (W/m/k)	56.72
Elastic Modulus, E (Pa)	1.50E+11
Poisson's Ratio	0.265
Thermal Expansion Coefficient, α (/k)	1.30E-07

Table 2 Physical, chemical and mechanical properties of VOLVO brake pads series

Parameters	P	A
Density (g/cc)	2.24	2.21
Acetone extraction (%)	1.25	1.35
Hardness ® (ASTM D 785)	95-102	89
Th. Conductivity (W/mK) (ASTM-E1461-01)	2.03	1.97

Table 3 shows the material properties of P series of composites.Table 4 shows the other mechanical properties of composites. Table 5 shows the operating conditions.

The elastic problem was simulated in order to investigate the mechanical action taking place at the disk's contact surface during the braking process. The deformation obtained from the elastic problem was approximately 200 μm.

Table 3 Physical and mechanical properties of the Series P composites (4th series)

Properties	BP Series	CP Series	IP Series
	BP_1	CP_1	IP_1
Density (g/cc)	2.30	2.31	2.29
Porosity (%)	4.33	4.30	4.10
Acetone extraction (%)	1.38	1.18	1.28
Tensile strength (MPa)	12.37	12.65	14.56
Young's modulus (GPa))	2.28	2.30	2.16
Flexural strength (MPa)	24.15	23.89	30.43
Flexural modulus (GPa)	4.33	4.80	5.70
Rockwell Hardness (S-scale)	78-88	88-93	85-95
Compressibility (%)	1.07	1.02	1.26
Thermal Conductivity (W $m^{-1}K^{-1}$)	2.22	2.41	2.11
Thermal diffusivity $x10^{-4}(cm^2s^{-1})$	80	97	71
Specific heat (J $kg^{-1}K^{-1}$)	1207	1076	1298
Effusivity (J $m^{-2}K^{-1}s^{-1/2}$)	2482	2447	2504

Table 4 Other Mechanical Properties of Composites

Material	Specific Heat, C (J/Kg K)	Elastic Modulus, E (Pa)	Poisson's Ratio, γ	Thermal Expansion Coefficient, α (/K)
Composites	800	4e11	0.25	6e-6

Table 5 Operating conditions.

Operating Conditions	Brake	Disk
Hydraulic pressure, P (MPa)	1	
Angular velocity, w (R.P.M)		150

3. Results and Discussions

The developed finite element analysis model contains a total of 32242 elements and 23 degrees of freedom, while the time step used during thenumerical computation was 0.01s. The initial temperature used during the simulation was set as 20 ºC.

As mentioned before, the suggested model was applied to the stated materials in order toinvestigate which of these materials possess better temperature distribution as well as themaximum temperature produced when subjected to the same braking conditions.

Figure 4 depicts one of the typical temperature distributions developed under the mentioned braking conditions using the suggested finite element analysis model. It's shown how the temperature increases further from the center of the brake disk to the point of the maximum temperature within the contact area between the disk and the pad, and then it decreases.

Figure 5 shows the Von misses stress distribution and average displacements of the disk brake.

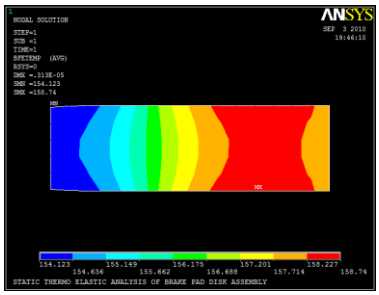

(a) Pad P: Maximum temperature: 158.74º C

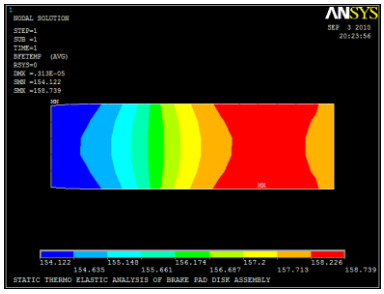

(b) Pad A: Maximum temperature 158.739º C

Fig .4 Temperature distributionat Pad A and Pad B

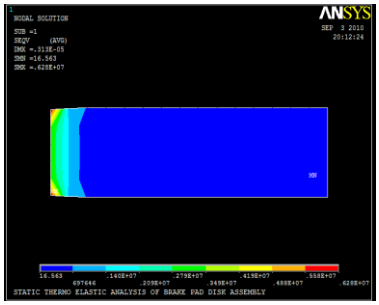

(a) Pad P: Von misses stress: 0.628 e7 Pa

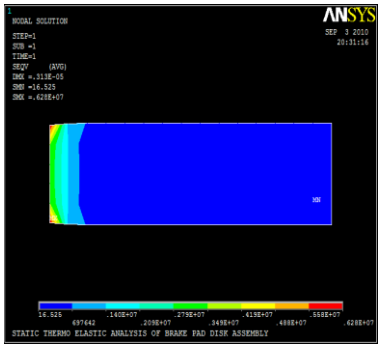

(b) Pad A: Von misses stress: 0.628e7

Fig .5 Von misses stress at Pad P and Pad A

From the above results, it can be observed that temperature distributions and generated Von-misses stresses for both pads are same.

The temperature distribution during the braking process at different application is shown in Figure 6, in which the temperature distribution of the brake disk is presented at 1, 2, 3, 4, 5, 6, 7 and 8 no of application.

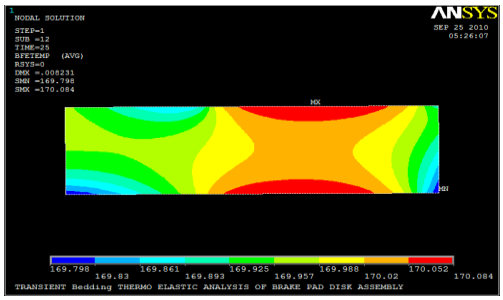

Brake Application No. 1

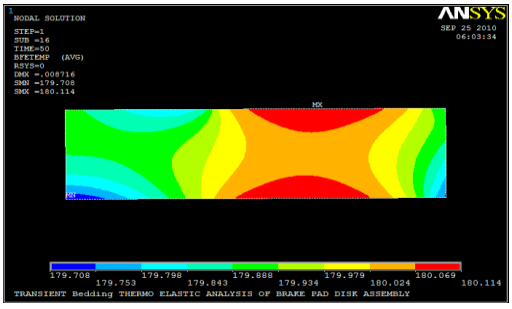

Brake Application No 2

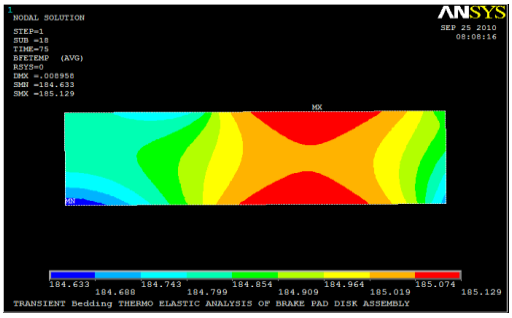

Brake Application No 3

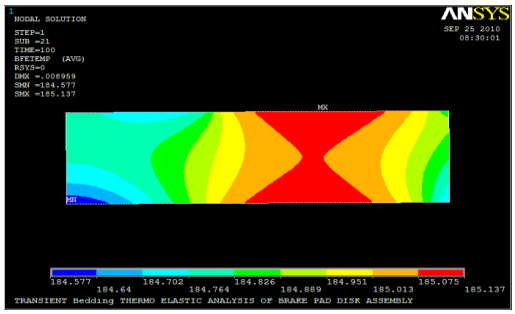

Brake Application No 4

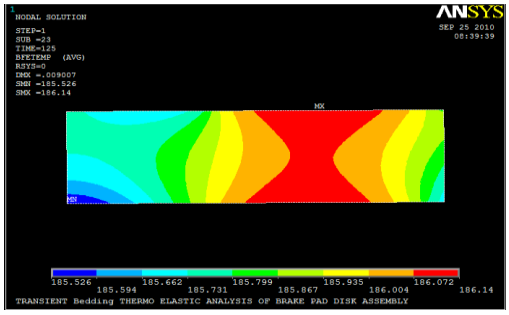

Brake Application No 5

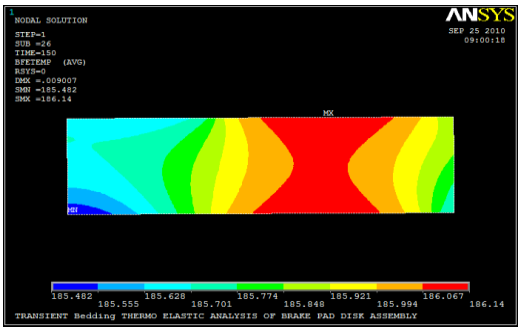

Brake Application No 6

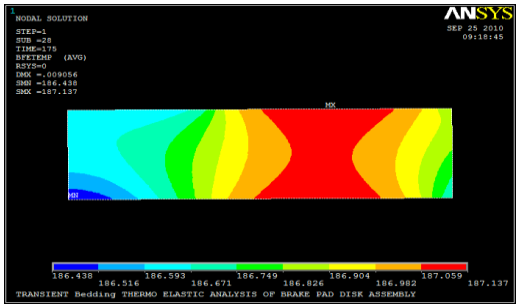

Brake Application No 7

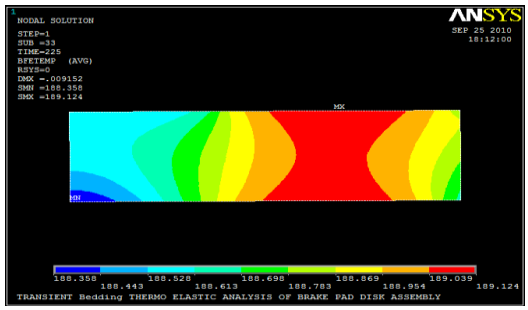

Brake Application No 8

Fig. 6 Temperature distribution of the brake disk

In order to validate the proposed model, the maximum temperatures obtained from the proposed model were compared to the actual measurement performed (Kumar, *et al*, 2009). The results are listed in Table 6.

Table 6 Comparison between the actual temperatures measured (Kumar, *et al*, 2009) and the simulated values obtained from the suggested finite element analysis model

No of Appl.	Actual temperature measured (° C) at **5.8 Bar**	Simulated temperature (°C)	Difference (%)
1	165	147	11
2	173	170	1.7
3	183	180	1.6
4	187	185	1.1
5	185	185	0
6	186	186	0
7	187	186	0.5
8	188	187	0.5
9	190	189	0.5

From the Table 6, it can be concluded that the suggested model produced a maximum difference of 11% at initial conditions, but subsequent to that difference between the calculated temperature and the measured temperature decreases. This comparison provides confidence in finite element model used to simulate the braking cycles.

The comparison of the maximum is also plotted in the Figure 7, which shows a very close fit between the proposed model and the experimental results Kumar, *et al* (2009).

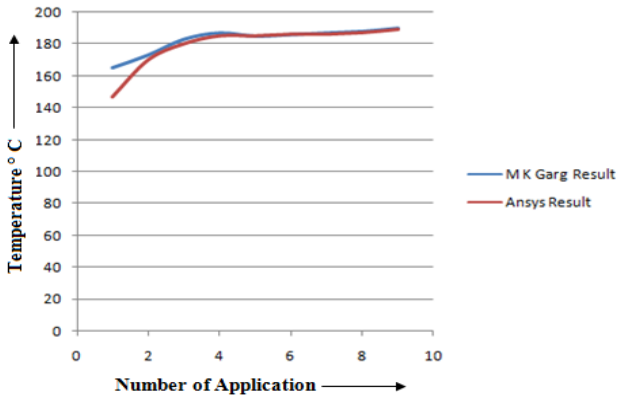

Fig.7 Comparison of Temperature Distribution

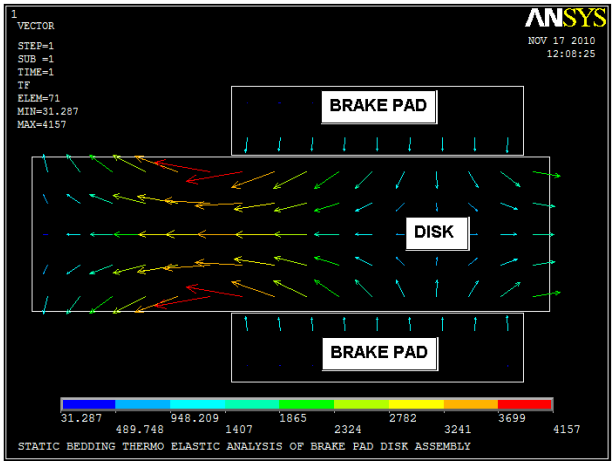

Fig. 8 ANSYS graphics shows the direction of heat flux

The vector plot showing the heat flow from the brake pad to the disk has been presented in Figure8. The red arrow is for high value of the heat flux.

Conclusions

A finite element analysis model was developed in order to investigate both the thermal and mechanical behaviors taking place between the disk brake and the pad, during the braking process. The developed model was compared with actual measurements performed (Kumar, et al, 2009) in order to validate the proposed model. The simulated results match very close to the experimental results.

References

A.E.Anderson, R.A.Knapp, (1990), Hot spotting in automotive friction systems,*Wear*, 135,pp. 319-337.

A.Floquet,M.C.Dubourg, (1994), Non-axisymmetric effects for 3D thermal analysis of abrake, *ASME J.Tribology*, 116,pp. 401-408.

C.Sarkar, H.Hirani, (2015), Effect of particle size on shear stress of magnetorheological fluids, *Smart Science,* (in press).

C.Sarkar, H.Hirani,(2015),Development of magnetorheological brake with slotted disc, *Proc. IMechE, Part D: Journal of Automobile Engineering*, (in press).

C.Sarkar, H.Hirani, (2015), Synthesis and characterization of nano-copper-powder based magnetorheological fluids for brake, *International Journal of Scientific Engineering and Technology*, 4, pp. 76-82.

C.Sarkar, H.Hirani, (2013), Theoretical and experimental studies on a magnetorheological brake operating under compression plus shear mode, *Smart Materials and Structures*, 22, art. no. 115032.

C.Sarkar, H.Hirani, (2013), Synthesis and characterization of antifriction magnetorheological fluids for brake, *Defence Science Journal*, 63, pp. 408-412.

C.Sarkar, H. Hirani, (2013), Design of a squeeze film magnetorheological brake considering compression enhanced shear yield stress of magnetorheologicalfluid, *Journal of Physics: Conference Series*, 412, 012045.

D. Eggleston, (2000), Thermal Judder, *EURACTechnical Bulletin*, 34056.

F.E. Kennedy, F.F.Ling, (1974), A thermal, thermoelastic and wear simulation of a highenergy sliding contact problem, *ASME J.Lub.Tech.*, 96,pp. 497--507.

H.Hirani, C. S. Manjunatha, (2007), Performance evaluation of magnetorheological fluid variable valve, *Proc. of the Institution of Mechanical Engineers, Part D, Journal of Automobile Engineering*, 221, pp. 83-93.

H. Li, H. Du,(2003), Design and experimental evaluation of magnetorheologicalbrake, *International Journal of Advanced Manufacturing Technology*, 21, pp. 508-515.

H. Inoue, (1986), Analysis of brake judder caused by thermal deformation of brake disk rotors,*SAE 865131*.

J. Huang, J.Q.Zhang,Y. Yang, Y.Q. Wei, (2002), Analysis and design of cylindrical magnetorheological fluid brake, *Journal of Materials Processing Technology*, 129, pp. 559-562.

J.R.Barber, (1969),Thermoelastic instabilities in the sliding of conforming solids, *Proc. R. Soc. Lond.*, A312,pp. 381-394.

J.Y.Jang, M.M. Khonsari, (2003), A generalized thermo elastic instability analysis,*Proceedings of the royal society*, A459, pp. 309-329.

K. Lee, R.B. Dinwiddie, (1998), Conditions of frictional contact in disk brakes and theireffects on brake judder, *SAE 980598*.

K. Lee, (2000), Frictionally excited thermo elastic instability in automotive drum brakes,*ASME Journal of Tribology*, 122,pp. 849-855.

K.Lee, F.W. Brooks, (2003), Hot spotting and judder phenomena in aluminum drum brakes,*Transactions of the ASME*, 125, pp. 44-51.

M.D.Bryant, J.P.Wang, J.W.Lin, (1995), Thermal mounding in high speed dry sliders - experiment, theory and comparison, *Wear*, 181, pp. 668-677.

M.Kumar, S.Mallik, J.Bijwe, (2009), Volvo bus disc brake testing on a brake inertia dynamometer, *Proceedings of TRIBO-INDIA conference*, Delhi, pp. 54-57.

P.Zagrodzki, (1990), Analysis of thermomechanical phenomena in multidisc clutches andbrakes, *Wear,* 140 pp. 291-308.

P.Dufrenoy, (2004), Two-/three dimensional hybrid model of the thermo mechanical behaviorof disc brakes, *Proceedings of the Institution of Mechanical Engineers, Journal of Railand Rapid Transit*, 218,pp. 17-30.

T.K.Kao, J.W.Richmond, A.Douarre, (2000),Brake disc hot spotting and thermal judder:an experimental and finite element study,*Int. J. Vehicle Design*, 23,pp. 276-296.

S.Asfour, M.Almakky, C.Hung, (2006), Thermoelasticinstability in disk brakes: simulation of the heat generation problem, *Proceedings of the COSMOS Users Conference*, Boston.

S. Gupta, H. Hirani, (2011), Optimization of magnetorheological brake, ASME/STLE 2011 International Joint Tribology Conference, pp 405-406.

V.K.Sukhwani, H.Hirani, T. Singh, (2009), Performance evaluation of a magnetorheological grease brake, *Greasetech India*, 9,pp. 5-11.

V.K.Sukhwani, H.Hirani, (2008), A comparative study of magnetorheological-fluid-brake and magnetorheological-grease-brake, *Tribology Online*, 3, pp. 31-35.

V.K.Sukhwani, H.Hirani, T.Singh, (2008), Synthesis and performance evaluation of MR grease, *NLGI Spokesman*,71.

V.K.Sukhwani, H. Hirani, (2008), Design, development and performance evaluation of high speed MR brake, *Proc. Institute Mech. Engineers., Part L, Journal of Materials: Design and Applications*, 222,pp.73-82.

V.K.Sukhwani,H.Hirani,T.Singh,(2007), Synthesis of magnetorheologicalgrease,*GreasetechIndia*.

V.K.Sukhwani, V.Lakshmi, H. Hirani, (2006), Performance evaluation of MR brake: an experimental study, *Indian Journal of Tribology*, pp. 67-52.

W.Kreitlow, F.Schrödter, H.Matthäi, (1985), Vibration and hum of disc brakes under load,*SAE 850079*.